Jai Balaji Maharaj

UNIVERSITÄT DUISBURG ESSEN

Open-Minded

The Multifunctional Potential of Bismuth Ferrite Nanoparticles

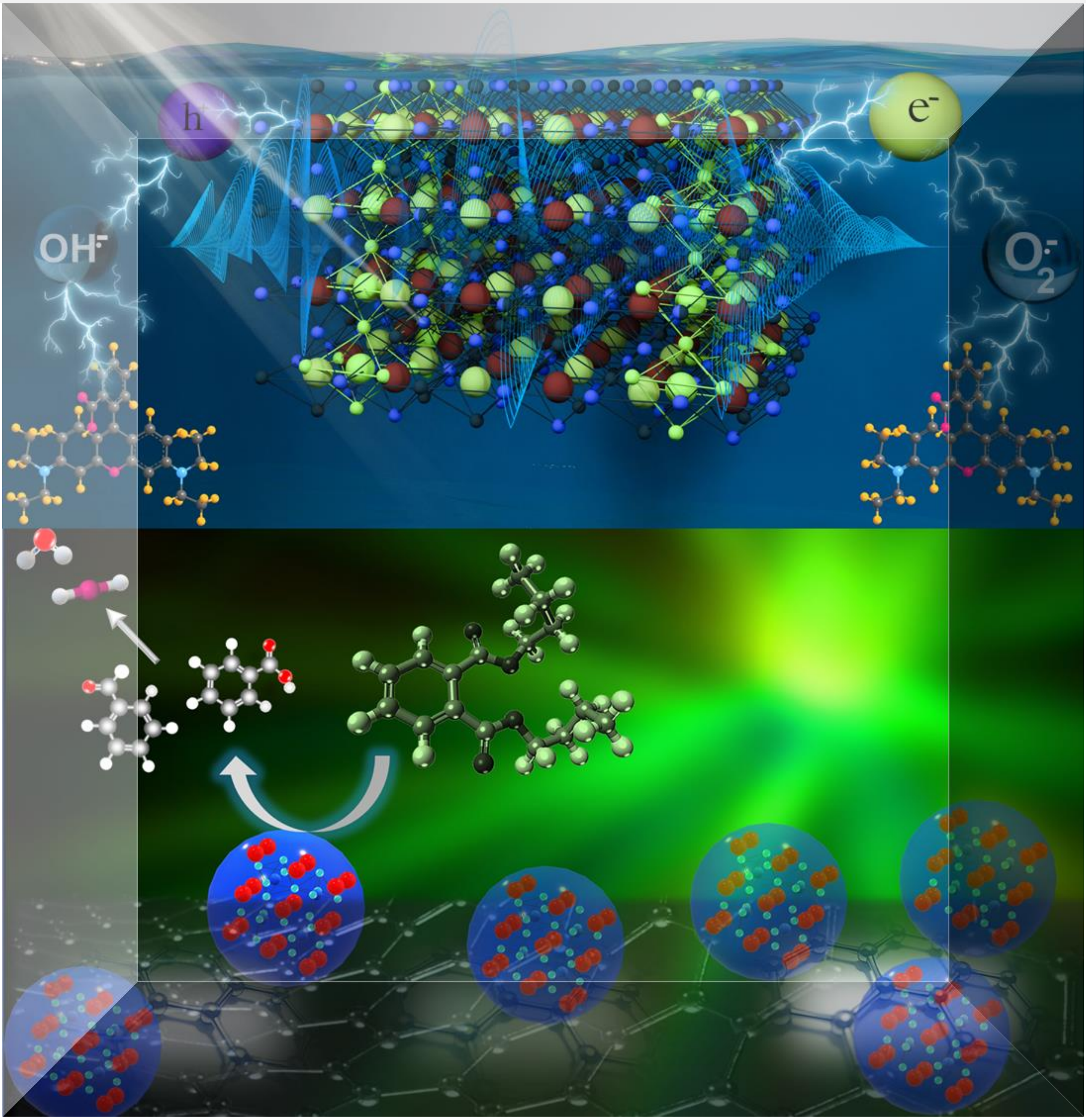

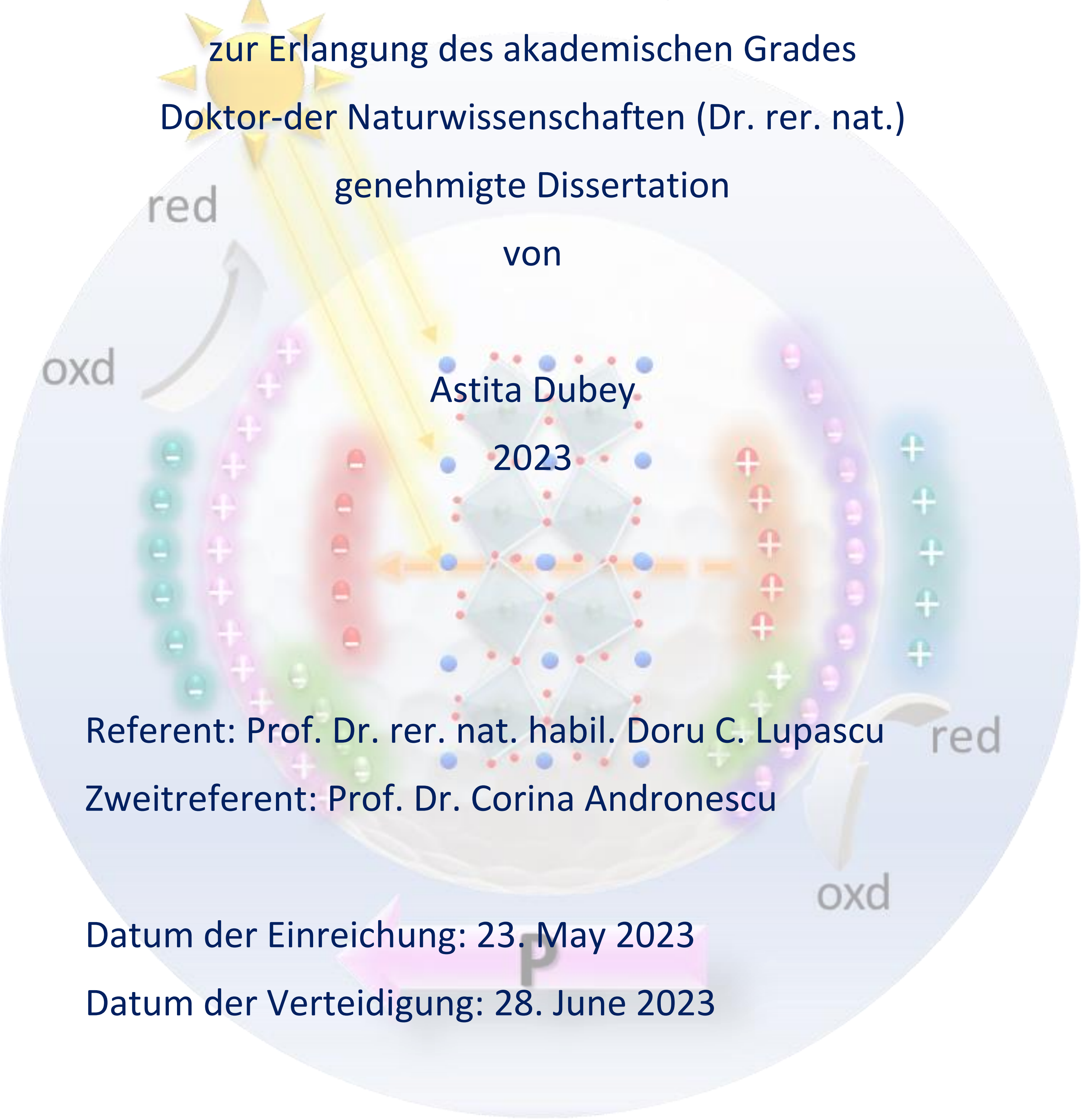

Von der Fakultät für Chemie
der Universität Duisburg-Essen
zur Erlangung des akademischen Grades
Doktor-der Naturwissenschaften (Dr. rer. nat.)
genehmigte Dissertation
von

Astita Dubey
2023

Referent: Prof. Dr. rer. nat. habil. Doru C. Lupascu
Zweitreferent: Prof. Dr. Corina Andronescu

Datum der Einreichung: 23. May 2023
Datum der Verteidigung: 28. June 2023

Jai Balaji Maharaj

Dedicated to my Grandparents

Late. Mrs. Tara Pandey (Naniji)
Late. Mrs. Saraswati Dubey (Dadiji)
Late Mr. Brahmadutt Dubey (Daddji)
Mr. Shambhunath Pandey (Nanaji)

DOI: 10.17185/duepublico/78735
URN: urn:nbn:de:hbz:465-20230712-101717-4

ॐ

Jai Balaji Maharaj

"In the quest for truth, science reigns,
Exploring the world with logic's chains,
Yet spirituality seeks a deeper way,
To find the essence, the truth to say.

So let us bridge these paths with care,
To bridge the divide, a wisdom to share"

Astita Dubey

Acknowledgments

It is with profound reverence and a sense of deep gratitude that I acknowledge the immeasurable impact that Lord Hanuman's perspective has had on my spiritual journey. His unwavering devotion, strength, patience, intelligence, greatness, simplicity, uniqueness, and omnipresence have not only inspired me, but have also bestowed upon me a newfound sense of creativity and expanded dimensions of thought. To be in the company of such great deity is a rare and precious privilege, and I count myself extremely fortunate to have been granted the status of his devotee. Through his mythological stories, I have gleaned invaluable lessons on the importance of critical thinking and problem-solving and have come to cherish and strive towards the ideal of working with noble intentions for the betterment of society. Lord Hanuman's exalted status as a superhero, endowed with the power to vanquish any obstacle, fills me with a sense of awe and wonder. His constant presence in every moment of my life is a source of comfort and reassurance, and I am deeply thankful for his guidance and protection. I offer my heartfelt gratitude to the universe, for granting me the inestimable privilege of walking alongside the great Lord Hanuman, and for bestowing upon me the opportunity to deepen my spiritual understanding and evolve towards a more enlightened state of being. My life has been enriched by his presence, and I am eternally grateful.

****

गुरूर्ब्रह्मा गुरूर्विष्णुः गुरूर्देवो महेश्वरः ।

गुरूर्साक्षात परब्रह्म तस्मै श्री गुरवे नमः ।।

"The Guru is Lord Brahma; the Guru is Lord Vishnu. The Guru is also Lord Shiva, and the Guru is the very embodiment of the primal source, the Adi Brahma. I offer my salutations to that Guru."

A guru is an important guide who can help a person gain knowledge and wisdom and can be revered as a source of divine inspiration.

I show my huge respect and highest gratitude to my gurus Professor Doru C. Lupascu, and Dr. Vladimir V. Shvartsman for their invaluable contribution to my Ph.D. journey.

My Ph.D. father (Prof. Lupascu) has guided and supported me throughout my research journey. He has helped me to develop several research skills, taught to set deadlines, and provided feedback to improve any piece of work. He has nurtured my personal and professional growth by instilling great scientific ethics in me. Furthermore, he has provided me with unwavering emotional support and acted as a sounding board whenever I have faced difficult situations. He is a great human being that’s what I admire the most, an extraordinary scientist who is great storyteller. I am very lucky and more than grateful to have him as my Ph.D. supervisor.

Throughout the course of my research, I was awed by the unyielding dedication and unwavering support shown by Dr. Vladimir V. Shvartsman. Right from the start, his insatiable hunger for knowledge and his genuine curiosity in my research work made a deep impact on me. His astute insights and prompt inspirations propelled me towards greater heights, igniting my own passion for science. His profound understanding of the subject matter was matched only by his boundless enthusiasm and zeal for scientific exploration. He was always eager to lend his expertise and guidance, providing me with timely suggestions that proved invaluable in solving many scientific problems. His unwavering support enabled me to push beyond my own perceived limits, helping me to realize my full potential as a scientist. In short, his profound impact on my scientific journey cannot be overstated. I am eternally grateful for his guidance.

I am immensely grateful to Dr. Marianela Escobar for introducing me to the great idea of exploring doped Bismuth Ferrite nanoparticles. It was clear to me that she is a veritable powerhouse of expertise and a true master of her craft. I am thankful to her for shaping my ideas with her feedback, insightful thoughts, and experience. I still remember sharing the first photocatalytic results with her in late evening, after a work of 7 hrs continuous measurements. She has always been my cheer leader, and very valuable critic has helped me grow as a scientist. I will always remember her quote “wrap up this work, then we will talk about another one”. I am very thankful to her for having patience with me and trusting my promises.

I am immensely thankful to all my collaborators who were with me during the most important moments of my thesis. For Raman measurements, I am thankful to the group of Prof. Brahim Dkhil from CNRS, France. I am grateful to Prof. Gerd Bacher's group for giving me the opportunity to do photoluminescence measurements, which were quite helpful. I show my gratitude to Prof. Julia Stähler from Helmholtz University, Berlin, for trusting my ideas and giving me a opportunity to learn ultrafast transient spectroscopy. I am highly thankful to Prof. Hana Ursic's group and Dr. Uros Prah for teaching me several sintering methods and ceramic processing methods. I thank to Prof. Jacob Jones and his team, who admired the idea to perform high temperature XRD-in situ for doped BFO NPs, which was a successful measurement in his lab. I am thankful to Prof. Barcikowski and Prof. Bilal Gökce, and Dr. Friedrich Waag to provide resources and help in laser ablation techniques for synthesis. I am very thankful to Prof. Hari Srikanth and his team from the University of South Florida, USA, who helped me with hyperthermia measurements and trusted my ideas, even giving me cool suggestions during our discussions on magnetic anisotropy.

I am grateful to have found Prof. Corina Andronescu on campus. I am thankful for her acceptance of our collaboration. When I was thrilled to study hydrogen evolution reaction, she welcomed it wholeheartedly, and allowed me to do the measurements and learn the technique. It was great working with Dr. Ignacio Sanjuán Moltó, and I am thankful to him for introducing me to electrochemical setups. I am thankful to Prof. R. K. Dutta and Prof. A Kazmi from the Indian Institute of Technology Roorkee, India, who gave me the opportunity to photodegrade plasticizers. I show my sincere gratitude to ICAN team especially, Dr. Ulrich Hagemann, and Dr. Markus Heidelmann for support in XPS and TEM measurements. I am also very thankful to Mrs. Claudia Schenck for support in BET-BJH measurements.

During Ph.D., I was fortunate to supervise, bachelor and intern students. The first one Mr. Chin Hon Keat, we both shared same excitement with photocatalytic results in lab and celebrated it in form of publication later. Then I had Ms. Maisarah Ismadi, who proved that

there is no short cut of success. She finished her thesis with great results, related publication is under the process. Later, Ms. Syaidah, Ms. Keshalini and Mr. Dhruvil all of them have showed their smart and efficient approaches while their work. Our scientific discussions made us to generate new ideas and helped to finish the projects successfully. *Kudos guys!* I am very proud of you, and it was great working with you all.
I express my huge gratitude to Dr. Andrei Salak who helped me with printing the first draft and motivated me for doing best. I am extremely thankful to him.

In expressing my gratitude, I would be remiss not to acknowledge the support and encouragement of my loved ones, whose unwavering belief in my PhD journey has been a source of great strength and solace. I am deeply grateful to acknowledge the role that my father, Mr. Arvind Kumar Dubey, and my mother, Mrs. Beena Dubey, have as advisors towards my attitude during the tough times in Ph.D. Their perpetual support and guidance have given me the confidence to trust my own vision and pursue my ambitions. They have motivated and encouraged me in every step of the way, allowing me to spread my wings and soar towards my goals. I feel truly fortunate to have parents who believe in my abilities and give me the courage to take on the world and pursue my dreams.

My younger siblings, Mr. Ashutosh Dubey and Ms. Ayushi Dubey, are my powerhouses. They can never see me down, and they immediately boost my confidence. They are an inspiration to me, as their smart and intellectual approach towards any challenge astonishes me very positively. They have always motivated me and boosted my confidence whenever I faced difficult times. I am grateful to be their 'bhai' and extremely thankful to both of them for always listening to me.

I would also like to express my gratitude to my friends and well-wishers who have supported me throughout my journey. Your encouragement and warmth have been invaluable. I am immensely grateful to Varun Karthik for his invaluable assistance, positivity, and for teaching me the virtues of composure and patience in facing life's challenges. Thank you to help me with your optimistic approach and teach me calmness and patience to deal any challenges in the life. I am particularly grateful for your sincere concern regarding work-life balance, as well as your insights on health and dietary habits, which have proven to be valuable and informative. I want to express my gratitude for your wisdom and companionship in life outside of lab. I am also thankful to Mohit for his genuine thoughtfulness for my well-being, and for his steadfast support and encouragement throughout my Ph.D. journey. Moreover, the recollections of our shared experiences at IIT Delhi, along with his delightful repertoire of Bollywood songs and timeless humour, have made the journey seem effortless and pleasant.

Pursuing Ph.D. 6168 km away from home is already a brave decision. However, it was a best decision ever cause of nice workplace and work environment. The best thing of UDEMAT group is the great people here. I am so grateful to Dr. Hans J. Keck, Mrs. Sabine Kriegel, Mr. Menze, Mr. Merlin Schmuk, Mr. Andreas Schmidt, Mr. Stefan Nawrath and Mr. Christoph to laugh at my poor jokes, to make me laugh every time whenever we meet, and to make me feel like family. I have my lovely people who are so close to my heart and have shower their love and care in many ways. I call it "*my guys*", whenever I needed small to big help, they were always there for me. I am so thankful to all of you guys' Dr. Nicole Bartek, Dr. Tommy, Dr. Martina Pantaler, Dr. Amazad Farooq, Dr. Yusra Hambal, Thanh Dang, Andrei Karabanov, Young Un Jin, Felix Paul, Sobhan Fathabad, Eva Kroell, Daniil Lewin, Gustave Semugaza, Neshable Noel, Dr. Miriana Vadala, Susi, Anne, Ian Yap, and Witchaya Aparavate.

Last but not least, I express my gratitude to the German Research Funding (DFG project number 396469149) for their direct support of my research project throughout my Ph.D. program. Additionally, I am thankful to DAAD for giving me the opportunity to cultivate my research skills through my Master's project and for planting the seed of becoming a researcher within me in 2018.

"Vasudhaiva Kutumbakam"

(The whole universe is a family)

Every facet of the universe has played a role in making this possible, and for that, I am deeply grateful to my entire family.

Astita Dubey

Essen, 23rd May 2023

Erklärung

Ich versichere an Eides statt durch meine Unterschrift, dass ich die vorstehende Arbeit selbständig und ohne fremde Hilfe angefertigt habe und dass ich alle Stellen, die ich wörtlich oder annähernd wörtlich aus Veröffentlichungen entnommen habe, als solche kenntlich gemacht habe. Ich habe mich auch keiner anderen als der angegebenen Literatur oder sonstiger Hilfsmittel bedient. Die Arbeit hat in dieser oder ähnlicher Form noch keiner anderen Prüfungsbehörde vorgelegen.

“I hereby declare under oath by my signature that I have independently completed the above-mentioned work without any external assistance and have clearly indicated all places where I have taken literal or nearly literal quotes from publications and have not used any sources other than those specified in the literature or other aids. The work has not been submitted to any other examination authority in this or a similar form.”

23.05.2023

Essen, den

Astita Dubey

Abstract

In 2023, the world is facing problems such as global warming, hazardous chemicals, non-destructible plasticizers, similar to viruses. All of these issues are major concerns for our environment. To address these issues, there is a strong need for a multifunctional material that serves as a catalyst, which is stable, efficient, selective, and reusable. The conventional catalyst based on photoinduced charge carriers is insufficient. The intrinsic properties of a material, such as ferroelectricity, piezoelectricity, and magnetism, can play a role in the catalysis process and enhance the catalyst's activity by driving forces such as spontaneous polarization, piezoelectric coefficient, and ferromagnetism at room temperature.

These qualities are found and cherished in the classic ceramic semiconductor Bismuth Ferrite ($BiFeO_3$; BFO), commonly known as the "The drosophila of multiferroics." BFO exhibits ferroic orderings at room temperature. For catalytic purposes, a large surface area is required to have a high number of active sites. Therefore, nanosized BFO particles are chosen. Although BFO nanoparticles (NPs) absorb visible light, they have smaller ferroelectric polarization than bulk BFO due to reduced crystal asymmetry, and they also possess weak ferromagnetic properties. To achieve a larger surface area while maintaining increased ferroelectric and magnetic properties, ionic engineering at Bi and Fe sites is utilized. The dopants not only further reduce the particle size of BFO NPs but also influence the shape of NPs, resulting in different morphologies. The macroscopic and local crystal structure of doped BFO NPs is examined using several techniques. The alteration in Bi-O and Fe-O bond parameters and the increase in microstrain of the BFO crystal structure due to doping are major factors responsible for altered ferroic properties.

Doping magnetic ions at the Fe site of BFO NPs leads to an increase in total magnetization mainly through superexchange interaction, disrupting the spin cycloid. Further co-doping at the Bi site results in even higher magnetization due to changes in the Fe-O-Fe bond angle and the presence of uncompensated spins on the surface of small-sized NPs. Doping also influences the coercive field and anisotropy of the NPs, making them suitable for magnetic hyperthermia. Doped BFO NPs exhibit efficiency in converting magnetic energy into heat when exposed to an alternating magnetic field, showing promise for applications in magnetic hyperthermia for cancer treatment. The local ferroelectricity and piezoelectric response in doped BFO NPs are found to be higher than in pristine BFO NPs due to crystal structure distortion caused by asymmetrical Bi-O bonds in the BiO_{12} cuboctahedron and resulting alterations in the FeO6 octahedron. Doping Mn at the Fe site does not significantly influence the ferroelectricity of BFO NPs. However, further doping of divalent cations (Ca^{2+} or Ba^{2+}) at the Bi site in $BiFe_{0.95}Mn_{0.05}O_3$ (BFM) NPs reduces the local ferroelectricity, while doping of trivalent (Dy^{3+}) and monovalent (Ag^{+}) cations into BFM NPs increases the ferroelectric properties of BFM NPs approximately three times.

This study finds that single doping at the Fe site has a substantial influence on the band gap compared to doping at the Bi site, primarily due to the indirect effect on the electronic structure of BFO NPs. The band gap of BFO, which is 2.2 eV, can be reduced to 1.6 eV with the appropriate ratio of Ba and Mn co-doping. This provides the maximum utilization of the solar

spectrum to generate photoinduced charge carriers for catalytic purposes. Dopants at the Bi site have a slight impact on the light absorption properties of the BFO NPs, creating oxygen vacancies or defect states in the band gap.

The catalytic activity of the doped BFO NPs for the degradation of organic pollutants under visible and UV light illumination is compared. Ba-doped BFM NPs exhibit enhanced photocatalytic efficiency compared to pristine BFM and BFO NPs. 1 mol% Ba-doped BFM NPs degrade rhodamine B and methyl orange dyes within 60 and 25 minutes under UV and visible illumination, respectively. The increased photocatalytic efficiency in Ba-doped BFM NPs is attributed to a cooperative effect of factors such as increased light absorption ability, large surface area, active surface, reduced recombination of charge carriers, and spontaneous polarization to mitigate photoinduced charge carrier recombination. In piezo-photocatalysis, Dy-BFM and Ag-BFM NPs show the best photocatalytic activity under ultrasonication conditions. The increase in spontaneous polarization by mono- and trivalent doping is one of the major factors in enhancing the photocatalytic performance, along with stronger light absorption in the visible range, low recombination rate of charge carriers, and larger surface area of NPs.

Dibutyl phthalate (DBP) is notorious as an endocrine disruptor, making it a significant threat to both human health and the environment. Successful photodegradation of DBP is achieved under UV light irradiation within 2.5 hours using Ag-doped BFM NPs supported on graphene oxide (GO) nanosheets. Gas chromatography and mass spectrometry (GCMS) show that Ag-BFM NPs supported on GO have a higher photodegradation efficiency than the pristine free-standing BFO NPs alone. The photodegradation process of DBP generates various intermediate products, such as phthalic acid, benzoic acid, benzaldehyde, and 3-methyl butyric acid, before achieving complete mineralization into carbon dioxide and water.

The investigation delves into the functionality exhibited by doped BFM NPs concerning the hydrogen evolution reaction (HER). The electrocatalytic activity of BFM NPs undergoes a transformative shift as a consequence of mono-, di-, and trivalent cation substitutions. Notably, strategic engineering of doping at the Bi site within BFM NPs yields a remarkable outcome, namely the reduction of the kinetic overpotential prerequisite for HER. This diminished overpotential in doped BFM NPs arises from the confluence of multifarious factors: diminished charge transfer resistance, augmented specific surface area, a discernible distribution of pore sizes ranging from narrow to broad, particles endowed with a shape boasting abundant active facets, and the integration of dopants as novel active sites upon the surface. Furthermore, the presence of surface defects, oxygen vacancies, and amplified microstrain within doped BFM NPs contributes to the reduced overpotential.

This study underscores the successful synthesis of phase-pure doped and undoped BFO NPs with diverse morphologies using different methods and the profound impact of doping on their magnetic, electrical, optical, and catalytic properties. The findings highlight the tremendous multifunctional potential of doped BFO NPs in a wide range of applications. These doped BFM NPs encapsulate immense potential to revolutionize the realm of HER in the photoelectrochemical domain, owing to their profound light absorption capabilities and aptitude for catalysis.

In German

Im Jahr 2023 steht die Welt vor Problemen wie der globalen Erwärmung, gefährlichen Chemikalien und unzerstörbaren Kunststoffen, ähnlich wie bei Viren. All diese Probleme sind eine große Sorge für unsere Umwelt. Um diese Probleme anzugehen, besteht ein dringender Bedarf an einem multifunktionalen Material, das als Katalysator dient, stabil, effizient, selektiv und wiederverwendbar ist. Der herkömmliche Katalysator, der auf photoinduzierten Ladungsträgern basiert, ist unzureichend. Die intrinsischen Eigenschaften eines Materials, wie Ferroelektrizität, Piezoelektrizität und Magnetismus, können im Katalyseprozess eine Rolle spielen und die Aktivität des Katalysators durch treibende Kräfte wie spontane Polarisation, piezoelektrischen Koeffizienten und Ferromagnetismus bei Raumtemperatur erhöhen.

Diese Eigenschaften sind in dem klassischen keramischen Halbleiter Bismutferrit (BFO) zu finden, der gemeinhin als "Drosophila der Multiferroika" bezeichnet wird. BFO weist bei Raumtemperatur ferroische Ordnungen auf. Für katalytische Zwecke ist eine große Oberfläche erforderlich, um eine hohe Anzahl aktiver Stellen zu haben. Daher werden BFO-Partikel in Nanogröße gewählt. Obwohl BFO-Nanopartikel (NPs) sichtbares Licht absorbieren, haben sie aufgrund einer geringeren Kristallasymmetrie eine geringere ferroelektrische Polarisation als BFO-Masse und besitzen auch schwache ferromagnetische Eigenschaften. Um eine größere Oberfläche bei gleichzeitiger Beibehaltung verbesserter ferroelektrischer und magnetischer Eigenschaften zu erreichen, wird ionisches Engineering an Bi- und Fe-Stellen eingesetzt. Die Dotierstoffe verringern nicht nur die Partikelgröße der BFO NPs, sondern beeinflussen auch die Form der NPs, was zu unterschiedlichen Morphologien führt. Die makroskopische und lokale Kristallstruktur der dotierten BFO NPs wird mit verschiedenen Techniken untersucht. Die Veränderung der Bi-O- und Fe-O-Bindungsparameter und die Zunahme der Mikrodehnung der BFO-Kristallstruktur infolge der Dotierung sind die Hauptfaktoren, die für die veränderten ferroischen Eigenschaften verantwortlich sind.

Die Dotierung magnetischer Ionen an der Fe-Stelle von BFO NPs führt zu einer Erhöhung der Gesamtmagnetisierung, hauptsächlich durch Superexchange-Wechselwirkung, wodurch die Spin-Zykloide unterbrochen wird. Eine weitere Co-Dotierung an der Bi-Stelle führt zu einer noch höheren Magnetisierung aufgrund von Änderungen des Fe-O-Fe-Bindungswinkels und des Vorhandenseins von unkompensierten Spins auf der Oberfläche der kleinen NPs. Die Dotierung beeinflusst auch das Koerzitivfeld und die Anisotropie der NPs, was sie für die magnetische Hyperthermie geeignet macht. Dotierte BFO NPs zeigen eine hohe Effizienz bei der Umwandlung von magnetischer Energie in Wärme, wenn sie einem magnetischen Wechselfeld ausgesetzt werden, was vielversprechend für Anwendungen in der magnetischen Hyperthermie zur Krebsbehandlung ist. Die lokale Ferroelektrizität und die piezoelektrische Reaktion in dotierten BFO-NP sind höher als in reinen BFO-NP, was auf eine Verzerrung der Kristallstruktur zurückzuführen ist, die durch asymmetrische Bi-O-Bindungen im BiO_{12}-Kuboktaeder und daraus resultierende Veränderungen im FeO_6-Oktaeder verursacht wird. Die Dotierung von Mn an der Fe-Stelle hat keinen signifikanten Einfluss auf die Ferroelektrizität von BFO NPs. Eine weitere Dotierung von zweiwertigen Kationen (Ca^{2+} oder Ba^{2+}) an der Bi-Stelle in $BiFe_{0,95}Mn_{0,05}O_3$ (BFM) NPs verringert jedoch die lokale

Ferroelektrizität, während die Dotierung von dreiwertigen (Dy^{3+}) und einwertigen (Ag^{+}) Kationen in BFM NPs die ferroelektrischen Eigenschaften von BFM NPs etwa dreimal erhöht.

Diese Studie zeigt, dass eine einfache Dotierung an der Fe-Stelle im Vergleich zur Dotierung an der Bi-Stelle einen wesentlichen Einfluss auf die Bandlücke hat, was in erster Linie auf den indirekten Effekt auf die elektronische Struktur von BFO-NP zurückzuführen ist. Die Bandlücke von BFO, die 2,2 eV beträgt, kann mit einem geeigneten Verhältnis von Ba- und Mn-Codotierung auf 1,6 eV reduziert werden. Dies ermöglicht die maximale Nutzung des Sonnenspektrums zur Erzeugung photoinduzierter Ladungsträger für katalytische Zwecke. Dotierstoffe an der Bi-Stelle haben einen geringen Einfluss auf die Lichtabsorptionseigenschaften der BFO-NP, indem sie Sauerstofflücken oder Defektzustände in der Bandlücke erzeugen.

Die katalytische Aktivität der dotierten BFO NPs für den Abbau organischer Schadstoffe unter sichtbarer und UV-Licht-Beleuchtung wird verglichen. Ba-dotierte BFM NPs zeigen eine verbesserte photokatalytische Effizienz im Vergleich zu unbehandelten BFM und BFO NPs. 1 mol% Ba-dotierte BFM NPs bauen die Farbstoffe Rhodamin B und Methylorange innerhalb von 60 bzw. 25 Minuten unter UV + sichtbarer Beleuchtung ab. Die erhöhte photokatalytische Effizienz in Ba-dotierten BFM NPs wird auf einen kooperativen Effekt von Faktoren wie erhöhter Lichtabsorptionsfähigkeit, großer Oberfläche, aktiver Oberfläche, reduzierter Rekombination von Ladungsträgern und spontaner Polarisation zur Abschwächung der photoinduzierten Ladungsträgerrekombination zurückgeführt. In der Piezo-Photokatalyse zeigen Dy-BFM und Ag-BFM NPs die beste photokatalytische Aktivität unter Ultraschallbedingungen. Die Erhöhung der spontanen Polarisation durch ein- und dreiwertige Dotierung ist einer der Hauptfaktoren für die Verbesserung der photokatalytischen Leistung, zusammen mit einer stärkeren Lichtabsorption im sichtbaren Bereich, einer niedrigen Rekombinationsrate der Ladungsträger und einer größeren Oberfläche der NPs.

Dibutylphthalat (DBP) ist als endokriner Disruptor berüchtigt, was es zu einer erheblichen Bedrohung für die menschliche Gesundheit und die Umwelt macht. Mit Ag-dotierten BFM-Nanopartikeln, die auf Graphenoxid (GO)-Nanoblätter aufgebracht sind, wird DBP unter UV-Lichtbestrahlung innerhalb von 2,5 Stunden erfolgreich photochemisch abgebaut. Gaschromatographie und Massenspektrometrie (GCMS) zeigen, dass Ag-BFM NPs auf GO eine höhere Photodegradationseffizienz haben als die ursprünglichen freistehenden BFO NPs allein. Beim Photodegradationsprozess von DBP entstehen verschiedene Zwischenprodukte wie Phthalsäure, Benzoesäure, Benzaldehyd und 3-Methylbuttersäure, bevor eine vollständige Mineralisierung zu Kohlendioxid und Wasser erreicht wird.

Die Untersuchung befasst sich mit der Funktionalität von dotierten BFM NPs in Bezug auf die Wasserstoffentwicklungsreaktion (HER). Die elektrokatalytische Aktivität von BFM NPs erfährt durch die Substitution mit ein-, zwei- und dreiwertigen Kationen eine transformative Veränderung. Insbesondere die strategische Dotierung der Bi-Stelle in den BFM NPs führt zu einem bemerkenswerten Ergebnis, nämlich der Verringerung des kinetischen Überpotentials, das für die HER erforderlich ist. Dieses verringerte Überpotenzial in dotierten BFM-NP ergibt sich aus dem Zusammenwirken zahlreicher Faktoren: verringerter Ladungstransferwiderstand, vergrößerte spezifische Oberfläche, eine erkennbare Verteilung der Porengrößen von eng bis weit, Partikel mit einer Form, die zahlreiche aktive Facetten aufweist, und die Integration von Dotierstoffen als neue aktive Stellen auf der Oberfläche. Darüber hinaus trägt das Vorhandensein von Oberflächendefekten, Sauerstoffleerstellen und verstärkter Mikroverformung in den dotierten BFM-NP zu einer geringeren Überspannung bei.

Diese Studie unterstreicht die erfolgreiche Synthese von phasenreinen dotierten und undotierten BFO NPs mit unterschiedlichen Morphologien unter Verwendung verschiedener Methoden und den tiefgreifenden Einfluss der Dotierung auf ihre magnetischen, elektrischen, optischen und katalytischen Eigenschaften. Die Ergebnisse unterstreichen das enorme multifunktionale Potenzial von dotierten BFO NPs in einem breiten Spektrum von Anwendungen. Diese dotierten BFM-NP besitzen ein immenses Potenzial, den Bereich der HER in der Photoelektrochemie zu revolutionieren, und zwar aufgrund ihrer tiefgreifenden Lichtabsorptionsfähigkeit und ihrer Eignung für die Katalyse.

Table of Contents

1 Foundations

1.1 Introduction

In this century, we face an array of challenges that threaten the sustainability of our planet. Our environment, once taken for granted, is now at the forefront of our attention. As we seek ways to keep our Earth as “Earth”, we must confront a host of daunting tasks that were unimaginable just a century ago. The need for renewable energy sources, for instance, is a pressing concern. Fossil fuels, still the backbone of our economy, have proven to be unsustainable and environmentally destructive. To combat this issue, we need to harness the power of materials science to develop new energy sources that are clean, efficient, and affordable like hydrogen.

The degradation of plastics is another serious issue that demands our attention. Microplastics, plasticizers, phthalates and toxic dyes are all contributing to the contamination of our oceans and the destruction of our aquatic ecosystems. Here, too, materials science can provide solutions. New materials are being developed that can break down plastics into their component parts, allowing us to recycle and reuse them. The field of materials science has given us many astonishing examples of how we can use new materials to combat the world's biggest problems.

Nanotechnology, in particular, has been a game-changer in this regard. By manipulating matter at the nanoscale, scientists have developed materials that can be used for drug delivery, nanocatalysts, and even to produce “Green fuel” hydrogen and life saviour oxygen.[1–3]

Semiconductor nanoparticles (NPs) have revolutionized the fields of energy storage, catalysis, and biomedicines.[4] However, despite their extensive applications, NPs face a number of challenges, such as toxicity (due to Pb content), stability, low quantum yield, reproducibility, and contest among themselves for the best for a particular application.[5–7]

This is where multifunctional Bismuth Ferrite (BFO) comes in as a new approach. BFO is an extremely versatile material with unique room temperature magnetoelectric properties and visible light absorbing capability. The multifunctional nature makes it a material that is being explored in many fields including spintronics,[8] and memory storage devices[9]. Furthermore, there are several other fields such as bio-medicine, piezophotocatalysis, phthalates degradation, and virus-killing applications that have not been explored yet. BFO is referred to as “the drosophila of multiferroics”,[10] as its study has been ongoing since the 1960s.[11–13]

In this work, BFO NPs have been exploited by taking a broad approach, and properties have been tuned through doping engineering. The role of dopants in its properties has been systematically studied and doped and co-doped elements have been chosen for specific properties like catalysis, and hyperthermia tests. The dopants have been selected based on their valence state from monovalent (Ag) to divalent (Ca, and Ba) to trivalent (La and lanthanides), their magnetic moments (Mn, and Co), and their outermost electronic configuration with *s*-orbital, *d*-orbital, and *f*-orbitals. The combination of these dopants into BFO NPs has provided the opportunity to explore the world of BFO NPs and unlock fascinating aspects that alter the overall properties of the material.

Three different synthesis methods to produce BFO NPs are compared: the sophisticated modified-sol-gel methodology, the hydrothermal method, and pulsed laser ablation (PLAL). After conducting an in-depth analysis of these synthesis methods, the modified-sol-gel methodology stands out as the most efficient and reliable way to synthesize BFO NPs. By modifying the reaction conditions, modified-sol-gel can produce highly reproducible single-phase NPs with a controlled size and narrow size distribution. Additionally, the ease of use of modified-sol-gel makes it the ideal choice for our current research.

The modified-sol-gel route is employed to produce moderately (5 mol%) doped BFO NPs, which exhibit distinct morphology, shape, and size. These single-phase NPs feature distorted crystal structure, resulting in increased microstrain and reduced crystallite size maintaining the pristine rhombohedral (*R*3*c*) crystal symmetry. The reduced particle size leads to a larger surface area and an abundance of surface-active sites, ideal for catalytic applications.

The doped BFO NPs display a range of shapes, from cuboidal to spherical, rhombohedron to distorted pentagonal, and elliptical. The diverse shapes provide additional functionality from active facets, enhancing the weak ferromagnetism and piezoelectric responses of these NPs via alteration in anisotropy (magnetic and crystalline). Intriguingly, not only magnetic dopants (Mn and Co at Fe-site), but also the non-magnetic ion (Ag/Ca/Ba/La at Bi-site) increases the magnetic properties of pristine BFO NPs. This may be due to a change in magnetic anisotropy, destruction of magnetic spin cycloid, canting of spin cycloid, and uncompensated magnetic spins at the surface of NPs as per their large surface due to small particle's size (less than 35 nm). The enhanced magnetism of the some doped BFO NPs was tested for hyperthermia application, and their ability to generate heat under an applied AC field shows large potential in cancer treatment.

The optical properties of doped BFO NPs (2.3 eV) are investigated, especially the role of dopants with different outermost electronic configuration and effect of Jahn-Teller cation and lanthanides on the band gap of BFO NPs. The single doping at Fe-site has larger influence on the band gap of BFO NPs as compared to doping at Bi-site. The radiative and nonradiative recombination and dynamics of photoinduced charge carriers are comparatively studied for doped BFO NPs.

Catalysis is one of the largest and most significant markets in the world. In 2019, the chemical industry generated approximately US$4 trillion in revenue,[14] with an estimated 85 % of this value being attributed to catalytic processes. Industrial chemical processes, including the production of commodity, petro-products, pharmaceutical and clean fuels, and pollution abatement technologies, heavily rely on catalysis. One major agenda is to degrade harmful chemicals such as plasticizers and toxic colourful dyes from the environment. Additionally, research on renewable sources of energy such as hydrogen generation based on efficient and selective catalysts is highly researched, aiming to establish the term "Green Energy and Green Work."

This study among others, examines the potential of doped BFO NPs as an electrocatalyst for the hydrogen evolution reaction (HER) in the absence of light. It is found that doped BFO NPs exhibit lower overpotential and higher conductivity of charge transportation to generate hydrogen than BFO NPs. In the future, this preliminary study could be extended to include photo-electrocatalysis by utilizing the light absorption capabilities of doped BFO NPs.

The narrow band gap, the piezoelectric, and the ferroelectric properties of doped BFO NPs were exploited to completely degrade harmful organic dyes and plasticizers under UV and visible light sources at different pH. The increased photocatalytic activity of doped BFO NPs is due to their high light absorption ability, reduced recombination of photoinduced charge carriers, large surface area, and appropriate defects.

Additionally, the piezoresponse of these ferrocatalysts was used to enhance photocatalytic reaction for degradation of organic pollutants under ultrasonic agitation. The catalytic activity increases based on the piezoresponse and linearly proportional spontaneous polarization of doped BFO NPs, by leveraging their ferroelectric and piezoelectric properties.

1.2 Multiferroics

The history of multiferroics materials, interesting filed of research with many coupled ordering parameters. Though the terms "magnetoelectric" and "multiferroic" are often used interchangeably, there is a subtle difference between the two. Magnetoelectric materials are those that exhibit a coupling between magnetic and electric properties [Figure 1.1 (a-b)], whereas multiferroic materials exhibit two or more ferroic properties that need not necessarily coupled. In 1993, Hans Schmid has introduced the term "multiferroic".[15] Schmid's definition of multiferroics encompasses materials that exhibit two or more fundamental ferroic states, such as ferroelasticity, ferroelectricity, ferromagnetism, and ferrotoroidicity, within the same phase as shown in Figure 1.1c.

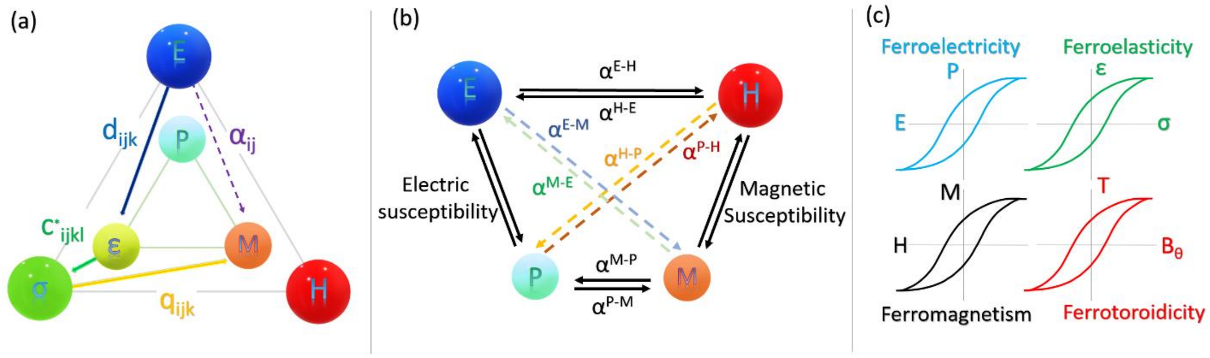

Figure 1.1: Heckmann diagrams[16] *show order parameters (a), and magnetoelectric coupling coefficients (b). Primary four ferroic orders (c). Ferroelectricity has a spontaneous electric polarization (**P**) which switches by application of an electric field (**E**). Ferroelasticity exhibit spontaneous strain (**ε**) switched by application of stress (σ). In ferromagnetism, the macroscopic magnetic moment (**M**) is switched by a applied magnetic field (H), and in Ferrotoroidicity a vortex-like alignment of spins with a toroidization (**T**) is switched by applied toroidal field ($\mathbf{B}_{\vartheta}$).*

From an experimental standpoint, the physical phenomena that involve the combination of magnetic and ferroelectric order were still in their nascent stages during the 1950s. It was during this time that the former Soviet Union initiated the first attempts to merge these two order parameters. Notably, Smolenskii and Ioffe proposed the introduction of magnetic ions into ferroelectric perovskites to create a magnetic long-range order, while still preserving the ferroelectric state.[17] Their research ultimately led to the successful synthesis of single-crystals such as Pb(Fe$_{0.5}$Nb$_{0.5}$)O$_3$ (PFN), and polycrystalline solid-solutions (1–x)Pb(Fe$_{0.66}$W$_{0.33}$)O$_3$–xPb(Mg$_{0.5}$W$_{0.5}$)O$_3$, which are called the first multiferroics that were designed.[12,18] Smolenskii and Ioffe referred to these systems as ferroelectromagnets, which were originally known as seignettomagnets at that time.[19]

Multiferroics can be categorized into two groups, namely type I, also known as "proper" multiferroics, and type II, also known as "improper" multiferroics. In the former group, magnetism and ferroelectricity coexist, but each arises from distinct sources. In the latter group, magnetic order gives rise to ferroelectricity. The classic example of type I multiferroics is Bismuth Ferrite (BFO; BFO). Type II multiferroics comprise the manganites like TbMnO$_3$, and MnWO$_4$ that have spiral magnetic structures capable of breaking inversion symmetry. Mixed valent materials, such as $LuFe_2O_4$ or Ca_3CoMnO_6, are also included in this group, where the ferroelectric polarization results from the magnetically induced polar charge ordering.

BFO and manganites ($RMnO_3$; R = Sc, Y, In, Dy-Lu) were first stated as multiferroic materials in the 1960s.[13,20,21] In a remarkable breakthrough, in 1966 a colossal linear magnetoelectric effect was found in $Ni_3B_7O_{13}I$, which facilitated the switching of a multiferroic state by means of electric or magnetic fields.[22] In 2000, Spaldin et. al. started research based on the original concept of Ioffe and Smolenskii's. They proposed that in classical perovskites, ferroelectric ordering induced by displacement and magnetic order are incompatible.[23] Numerous developments ensued after the initial discoveries, such as the detection of pronounced magnetoelectric interactions in $YMnO_3$,[24] $TbMnO_3$,[25] and $TbMn_2O_5$.[26]

BFO exhibits a large electric polarization and very small magnetoelectric coupling at room temperature.[27] It is intriguing to note that BFO remains the only established system of lone pair type including the another promising candidate $BiMnO_3$.[28]

Multiferroics have the potential to be used in sensors, actuators, and energy harvesting devices. One of the most promising applications of multiferroics is spintronics, where the electron spin is utilized to store and process information. These materials offer an additional degree of freedom for controlling the spin by manipulating both magnetic and electric fields simultaneously. A multiferroic tunnel junction can be used to control the magnetic state of a ferromagnetic layer, and thus modulate the spin-dependent tunnelling current, which is the basis of magnetic random-access memory (MRAM) devices.[29] The use of multiferroics in spintronic field-effect transistors (FETs) where the electric field is used to control the spin current and thus enable the efficient modulation of spin signals.[30] These applications have the potential to revolutionize the field of spintronics and pave the way for the development of next generation computing and memory devices.

Apart of this, multiferroics are not typically used for catalytic applications. This research is still in the early stages and more work is required to fully explore the potential of multiferroics in the field of catalysis. For heterogenous catalysis, one would like to start with famous multiferroic BFO, as so many structural, optical, magnetic, and electrical properties are already known and discussed.

1.3 Bulk bismuth ferrite: A promising material

"The symmetry of the causes is to be found in the effect" – Pierre Curie (1894)

BFO is widely recognized as the sole perovskite (ABO_3) compound that possesses multiferroic characteristics at room temperature.[27] Synthesized in the late 1950s, BFO was later characterized in the early 1960s.[27] Bulk BFO features a rhombohedral $R3c$ space group (R-phase), which comprises of ten atoms with lattice parameters of a_{rh} = 5.63 Å, α_{rh} = 59.35°. In pseudo-cubic form, the lattice parameters are a_C = 3.965 Å, α_C = 89.45°, whereas the most common hexagonal representation has lattice parameters of a_{hex} = 5.58 Å and c_{hex} = 13.87 Å as shown in Figure 1.2.[31,32]

BFO exhibits non-centrosymmetric crystal symmetry, with a ferroelectric transition at T_C ≈ 1103 K and an antiferromagnetic phase transition at T_N = 640 K.[31,33–35] These properties make it a potential material for a wide range of applications high temperature piezoelectricity in information storage, in spintronics (magnetoelectric random-access memory) and also for 'Quantum Electromagnets'.[36–39] The antisymmetric superexchange (Fe-O-Fe) of unpaired electrons of the d-shell of Fe^{+3} leads to a canted G-type antiferromagnetic ordering, which also allows for weak ferromagnetism due to the canting of the sub-lattice magnetization caused by the Dzyaloshinskii-Moriya [D-M] interaction.[40] However, the incommensurate cycloidal modulation of magnetic moments having a periodic length of approximately 62 nm cancels the net magnetization and obstructs the linear magnetoelectric [M-E] effect in BFO.[41,42] The ferroelectricity in BFO exists due to a stereochemically active $6s^2$ lone pair of Bi^{+3}, which generates a spontaneous polarization along the $[111]_C$ axis.[40]

In a hexagonal representation, where there is three-fold rotational symmetry parallel to the c-axis, the spontaneous electric polarization exists along the c-axis $[001]_{hex}$ as shown in Figure 1.2. The rhombohedral structure is derived from the ideal cubic (Pm-$3m$) perovskite structure, which is made up of corner-sharing BX_6 octahedra, by tilting the octahedron. The two most important axes can be converted into the pseudo-cubic or rhombohedral structures using the following relationships.

$$[0\ 0\ 1]_{hex} = 2[1\ 1\ 1]_{pc} = [1\ 1\ 1]_{rh}$$

and

$$[1\ 1\ 0]_{hex} = [1\ \text{-}1\ 0]_{pc} = [\text{-}1\ 1\ 0]_{rh}$$

BFO has Fe^{3+} ions at B-sites that are surrounded by six oxygen anions forming FeO_6 octahedra, and BiO_{12} cuboctahedra, which are linked to each other by sharing their corners. The FeO_6 octahedra tilt at an angle of approximately 11-14°,[31,32,43] a phenomenon that typically occurs when the A and B cations have different ionic radii. The tolerance factor "*t*" is related to the packing of ions in the perovskite cell. It was suggested by Megaw to determine the stability of the perovskite phase for a given set of ions.[44] It can be described by the Goldschmidt's tolerance factor (t).[45]

$$t = \frac{[(1-x)r_{Bi} + xr_A] + r_O}{\sqrt{2}[\{(1-y)r_{Fe} + yr_B\} + r_O]} \tag{1.1}$$

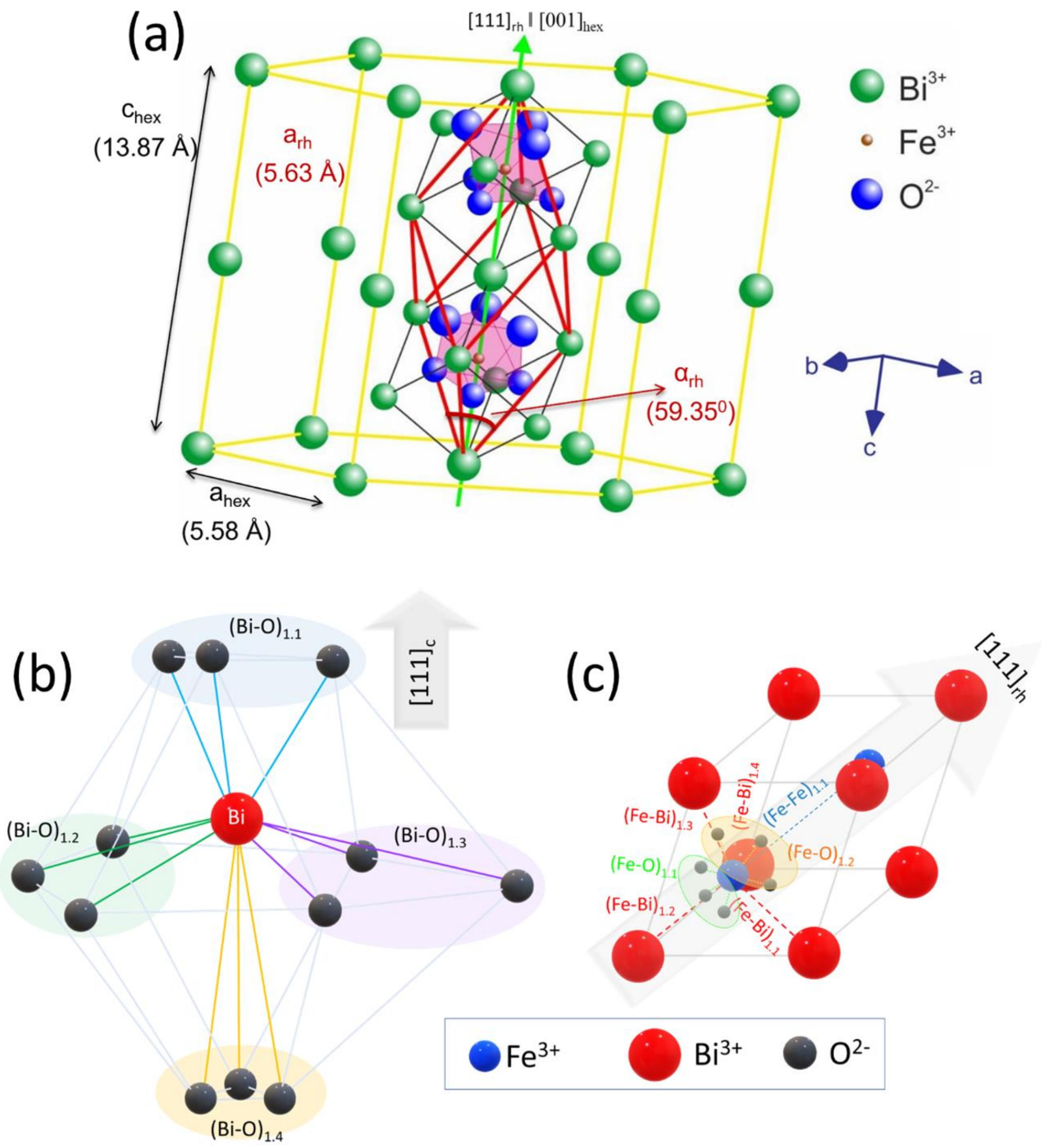

Figure 1.2: (a) Schematic of crystal symmetry of Bismuth Ferrite (BFO), where a primitive rhombohedral unit cell is represented by red lines, hexagonal unit cell by yellow lines and pseudo-cubic by black line. (b) $[111]_c$ $=[111]_{rh}$ is the polar axis of BFO. Bi-cuboctahedron (BiO_{12}) schematic in rhombohedral representation of BFO, where four groups of oxygens atoms are shown in different colors based on different Bi-O bond distances. (c) Schematic of Fe-O, Fe-Bi and Fe-Fe bond distances in the rhombohedral unit cell of BFO (c). [© 2022 Adv. Func. Mater., with permission][46]

In Equation 1.1, the r_{Bi}, r_{Fe}, and r_O represent ionic radii of Bi, Fe and O respectively. Whereas r_A, and r_B stand for the ionic radii of the A-site dopant, B-site dopant, respectively. The ionic radii can be obtained from Shannon's tables on effective ionic radii.[47] When *t* = 1, a perfect cubic cell is formed. When *t* deviates from 1, the perovskite cell gets deformed, and the symmetry is lowered. The smaller the tolerance factor (which is the case for BFO), the greater the buckling between the oxygen octahedra. This occurs because the smaller A-site ions cannot fully fill the empty space, resulting in the tilting of the octahedra thereby reducing the available space. As a result, the bond angle of Fe^{3+}–O^{2-}–Fe^{3+} deviates from 180°. For BFO, the octahedral tilt (~11-14°) is around the polar $[111]_c$ axis, with the related Fe–O–Fe angle being 154–156°.[48] The Fe–O–Fe angle is crucial because it controls both the magnetic exchange and orbital overlap between Fe and O, determining the magnetic and conduction properties.

The tilt of octahedra plays a crucial role in determining the material properties, particularly in the case of BFO. In the 1970s, Mike Glazer developed a system to categorize 23 possible tilts within the perovskite structure, based on the assumption that the BX_6 octahedron is rigid and only in-phase or out-of-phase tilting is allowed with respect to neighbouring octahedra.[49,50] However, an anomaly that was discovered with the $SrRuO_3$ system led to the reduction of the original 23 Glazer tilting systems to only 15.[51] As per the "Glazer notations," the *R*3*c* space group of BFO (space group 161) is denoted by $a_+^- a_+^- a_+^-$. The first, second, and third characters correspond to tilting angles along the principal x, y, and z-axes in the ideal cubic perovskite structure, while the subscripts and superscripts denote atomic displacements and octahedral tilting along each axis, respectively. Subscripts + indicate non-zero displacement, while superscripts shows out-of-phase tilting (meaning that adjacent octahedra tilt in opposite directions).

The *R*3*c* space group has out-of-phase tilts with atomic displacement along the $[111]_C$, resulting in broken inversion symmetry, as shown in Figure 1.3. At room temperature, BFO's FeO_6 octahedron is experimentally found to be tilted out-of-phase along $[111]_C$, and the Bi and Fe cations are shifted along the same $[111]_C$ direction, breaking the inversion symmetry. These cation shifts correspond to a ferroelectric (FE) distortion. The FE distortion arises from the stereochemical activity of the Bi^{3+} $6s^2$ lone pair, which hybridizes with 6p orbitals, resulting in an asymmetric wave function. This causes the bonding between Bi and O to be asymmetric and stabilizes an off-centering displacement of the Bi ions with respect to the oxygen sublattice. Electrostatic repulsion then causes a cooperative displacement of Fe^{3+} ions, resulting in a finite electric polarization.[52] In the distorted cuboctahedron of bulk BFO, six oxygen atoms are in the plane perpendicular to the polar axis $[111]_c$, forming a hexagon with Bi at the top of it and off displaced from the center. Three oxygens are in the plane below the hexagon and three oxygens are in the plane above it, forming the triangular base. Based on the Bi-O bond distances, four groups are divided from shortest: $(1.1)_3$, $(1.2)_3$, $(1.3)_3$, to longest: $(1.4)_3$ and are represented in different colors in Figure 1.2 (b-c).

The octahedral tilting is also called an antiferrodistortive (AFD) rotation. The octahedron rotation may arise from the shortening of certain Bi-O bonds with respect to others bonds which leads to the rigid FeO_6 octahedra to rotate to accommodate this position.[53] Both distortions (AFD and FE) compete with each other since each lowers the total energy of BFO with respect to the cubic structure by ≈ 0.7 eV, but their combination is only ≈1 eV lower in energy than the perovskite structure.[53,54] The AFD affects the Fe–O–Fe bond angle, so influencing the superexchange and Dzyaloshinskii–Moriya (DM) interaction, whilst the FE distortion enhances the single ion anisotropy.[53,54]

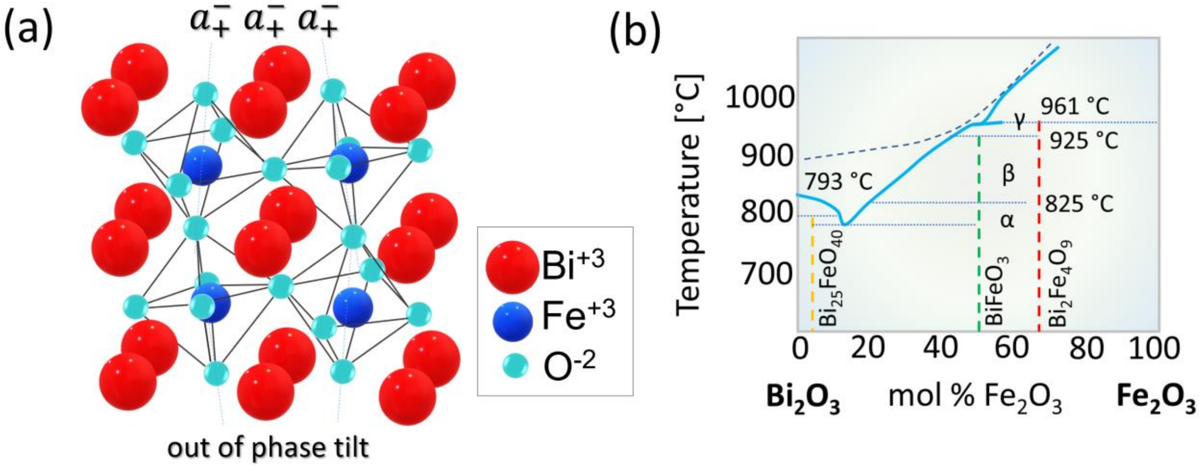

Figure 1.3: (a) Octahedral tilt in Bismuth Ferrite (BFO) of type a_+^- a_+^- a_+^- *as per Glazer's notation.*[55] *(b) Compositional phase diagram of synthesis of bulk BFO (b),*[27] *where two main impurities* $Bi_{25}FeO_{40}$ *and* $Bi_2Fe_4O_9$ *appear.*

Existing Challenges with bulk BFO

BFO is a promising material for various applications, but it is not without its limitations. One of the major drawbacks is the high leakage current that leads to low resistivity, presumably due to defect and nonstoichiometry. This limits its practical applications in high-performance electronic devices due to power dissipation and associated reliability issues. The leakage current for bulk BFO samples can be in the range of 10^{-7} to 10^{-9} A/cm^2.[56]

Furthermore, BFO ceramics are difficult to process due to the high melting point, which requires high temperature processing methods, thereby limiting its scalability and commercial production. Processing-induced defects also negatively affect its properties and reliability.[57] The pseudo-binary phase diagram of the Bi_2O_3–Fe_2O_3 system is shown in Figure 1.3b. It contains three phases at room temperature: sillenite ($Bi_{25}FeO_{39}$), the perovskite (BFO) and mullite ($Bi_2Fe_4O_9$). The formation of the sillenite and mullite phases is a challenge during a route to obtain pure BFO. These unsolicited parasitic phases ($Bi_{25}FeO_{40}$ and $Bi_2Fe_4O_9$) tend to nucleate at grain boundaries are an obstacle in studying the properties of single phase BFO. Hence, there has been a pressing need to generate high-quality micro sized grains and nanosized BFO ceramic.

BFO exhibits high ferroelectricity (90–100 μC/cm^2),[58] and also making it a reliable high temperature piezoelectric. However, the antiferromagnetic nature of BFO limits its use in applications that require strong magnetism, such as data storage devices and magnetic sensors. Although BFO exhibits multiferroic behaviour, which allows it to exhibit coupled ferroelectric and magnetic orderings, however, the magnetoelectric coupling is not strong enough for any practical use.[42] Therefore, developing approaches to enhance the magnetic properties of BFO is important for its realistic commercialization. Therefore, the factors such as synthesis method, and processing conditions are crucial for achieving low leakage current and improving the performance of bulk BFO-based devices.

Addressing Issues: Our Approach

To address these issues from a wider viewpoint, a systematic and strategic approach needs to be taken. The primary objective is to synthesize a single phase of BFO with improved magnetic properties and with retention of its ferroelectric properties. This can be achieved by carefully selecting the appropriate synthesis method and optimizing the processing conditions to ensure the desired phase is obtained. This can be achieved by utilizing nanostructuring techniques such as sol-gel synthesis or hydrothermal methods or modern methods like pulsed laser ablation in liquid (PLAL). Large surface area of the nanostructure material can also be utilizable for other applications like catalysis.

Furthermore, to enhance light absorption, the optical band gap of BFO needs to be reduced and modified. This can be accomplished through various methods such as doping with suitable elements, modifying the processing parameters, or altering the composition of the material. Additionally, engineering its local crystal structure is crucial to enhance its optical and electrical properties.

In summary, a multidisciplinary approach involving careful selection of synthesis methods for nanostructured BFO, optimization of processing conditions, and choice of dopants both at Bi and Fe sites can lead to the synthesis of BFO with improved magnetic and ferroelectric properties, narrower optical band gap, and with increased surface area.

1.4 Bismuth ferrite nanoparticles

Bulk Bismuth Ferrite (BFO) was first reportedly synthesized in 1957, and first studied in 1960 by Royen et. al and Filipev et. al, respectively.[11,59] Efforts for unveiling its exact atomic structure were going with high interest.[60,61] In 2002, the attempt to synthesise smaller sized (less than 100 nm) polycrystalline NPs are successful, which was further improved by Ghosh et. al in 2005.[62,63] Using a modified Pechini's method,[62] it was possible to synthesize single phase BFO nanoparticles (NPs). Similar to bulk BFO, nanosized BFO retains the primitive rhombohedral $R3c$ crystal structure.[10] From Figure 1.4, one can observe that the SEM image of bulk BFO (synthesized in our lab) shows a polycrystalline structure with multiple grains and grain boundaries, while TEM images of nano-sized BFO (synthesized in our lab) reveal a narrow size distribution of single-crystalline NPs.

The alteration of BFO nanoparticle size to probe the related properties (mainly magnetic and ferroelectric) was started by Park et al in 2007.[64] The strong size-dependent magnetic properties of BFO NPs were correlated with suppression of the spin cycloid (∼62 nm) with decreasing NPs size and uncompensated spins and strain anisotropies at the surface.[64] Motivated by this research, in 2010 Jaiswal et al, showed magnetoelectric coupling evidence in BFO NPs of size ~50-60 nm, using temperature dependent Raman and dielectric measurements.[65] The size effect studies of BFO NPs (23 to 80 nm) showed that as the particle size decreases, the lattice expands, the Néel temperature (T_N) decreases, and it diffuses more for smaller sized NPs.[63,66] An expansion of the unit cell volume was reported with the decrease in particle size from the bulk to nano samples. In addition, the reduction in coordination number also observed for 20 nm sized BFO NPs compared to bulk counterpart (For 20 nm coordination number of 7.6 Bi- atoms at approximately 3.5 Å as compared to the bulk of 8.0 Bi- atoms.).[67] In 2013, PFM studies showed that the spontaneous polarization decreases with reducing particle size, and 50 nm sized NPs still manifest ferroelectric behaviour.[68] The spin cycloidal structure in BFO NPs also has received much attention. Mössbauer spectra for 50 nm sized BFO NPs, show the anharmonicity of the long-range cycloidal structure to decrease upon rising temperature.[69] The cycloid parameters were found to be comparable to bulk, while for NPs of about 50 nm enhanced quadrupole splitting, means a change in the polarization, and a reduced Néel temperature of ~631 K were found. However, they could not observe any clear particle size dependence of the anharmonicity, the temperature dependence showed a region of constant anharmonicity up to ~170 K, followed by a decrease, reaching the harmonic state above 400 K.

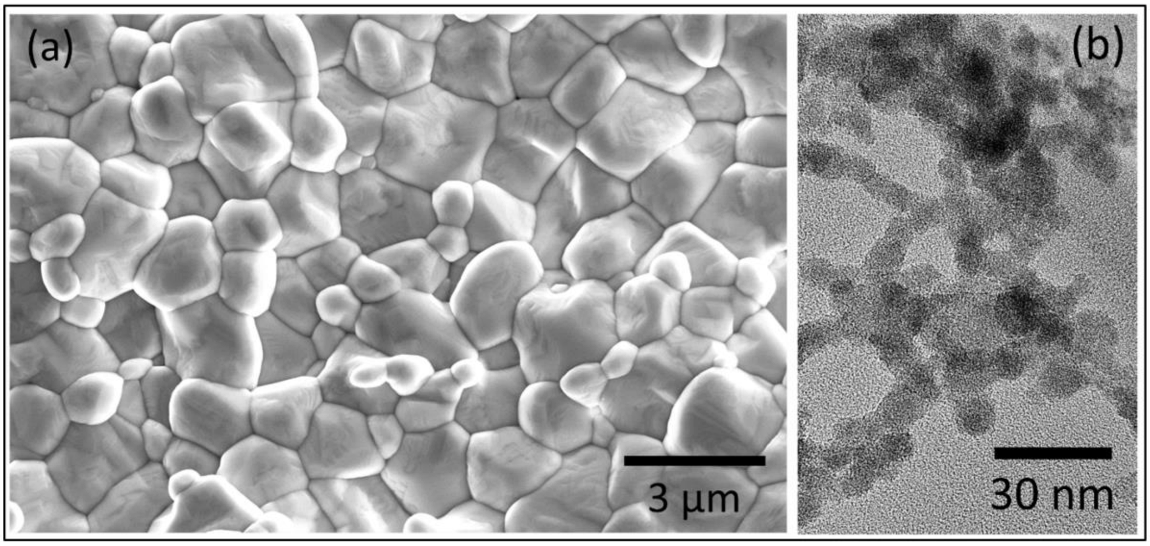

Figure 1.4: The SEM image of bulk Bismuth Ferrite (BFO) synthesized by solid-state method (a). The TEM image of nanosized particles of BFO, synthesized by pulsed laser ablation method (PLAL) (b).

Hence a huge interest in BFO NPs has arisen due to their enhanced magnetization,[70,71] sizable polarization,[68,72,73] and significant magnetoelectric coupling.[70,72] They also have a smaller band gap than their bulk counterpart, which is exploitable in the field of catalysis.[74] Nevertheless, the disadvantage is the weak magnetism in BFO NPs, which is not good enough for data storage devices and magnetic sensors. The magneto electric coupling is also too small and cannot be used for any realistic application.

One possible solution to these issues is to reduce the size of the BFO NPs further less than 50 nm (more uncompensated spins at the surface and for a larger surface area also useful for catalysis), but this may decrease the ferroelectricity due to the increased symmetry of the crystal structure. So, this is not a viable solution on its own, but one has to do the experimental measurements to check ferroelectricity in small sized BFO NPs. What is needed is a smart ionic engineering tool that can be used to address these issues in a more effective manner. To achieve this, the substitution by moderate amounts of dopants is required, which can distort the crystal structure a bit and reduce the symmetry, enhancing ferroelectricity. Additionally, magnetic or non-magnetic, aliovalent dopants can be used to enhance the magnetism in BFO NPs providing a more robust solution for data storage and magnetic sensor applications.

In summary, while there are challenges to be addressed in the realm of BFO NPs, an ionic engineering that employs the use of dopants of various sizes can help to overcome these obstacles and pave the way for more effective and efficient data storage and magnetic sensor technologies and catalysis.

1.5 Magnetism in bismuth ferrite

All materials in nature possess some form of diamagnetic response to an applied magnetic field. As a rule of thumb, all materials are magnetic, but not all types of magnetism are of interest for experimental purposes. To discuss this, materials are classified according to their response to an external magnetic field, described by the magnetic susceptibility. It comes from latin susceptibilis, "receptive", and in case of linear volume susceptibility, it is described by equation 1.2,

$$M = \chi H \tag{1.2}$$

M is the magnetization of the material, in Am^2/kg in case of mass normalization, while H is the magnetic field strength [A/m]. The susceptibility χ is a dimensionless quantity, with a positive suSsceptibility denoting para-, ferro- and ferri-magnetic materials (strengthening of the magnetic field in the material due to induced magnetization) and a negative susceptibility denoting diamagnetic materials (magnetic field weakened by the induced magnetization).

Paramagnetism is a state where the magnetization is randomly oriented and with a positive magnetic susceptibility, meaning that the material is in a state where it is attracted to the magnetic field. Under applied magnetic field, the material is magnetized, and thermal motion causes the spins to become randomly oriented, reducing the total magnetization to zero when the field is removed unlike ferromagnetism, where induced magnetic moment is retained in the absence of an external applied magnetic field. In antiferromagnetism, the overall magnetic moment is zero due to neighbouring spins pointing in opposite directions, whereas ferrimagnetism occurs when neighbouring spins are pointing in opposite directions but of unequal size, resulting in a net magnetic moment. [Figure 1.5 (a-d)]

The materials most relevant for our purpose are those that exhibit magnetism even after an external magnetic field is removed, known as remanent magnetization (M_r). Ferromagnets are a well-known class of magnetic materials whose properties cannot be fully explained by classical approaches, as they are based on quantum mechanical effects arising from the magnetic dipole moments of electrons. The presence of unpaired spins in atoms with partially filled electron shells can lead to spontaneous magnetization without an applied field, where the exchange interaction being the primary force responsible for the parallel orientation of spins. Temperature plays a role, as thermal energy can overcome spin coupling energy at the Curie temperature (T_C), leading to the formation of magnetic domains separated by domain walls. Hysteresis curves can be used to measure the strength of magnetization, coercive field, and remanence, which are the defining characteristics of ferromagnetism.

Antiferromagnetism is similar to ferromagnetism but with sublattices of spins that are aligned antiparallel to each other resulting in equal and opposite magnetization that cancels out the net magnetization of the material. This makes it challenging to characterize this state through magnetometry methods. Mössbauer spectroscopy can reveal the magnetic order of antiferromagnets through the local hyperfine fields, making detailed characterization possible. Thermal agitation can also disrupt the ordering if the material is heated above the Néel temperature (T_N).

Ferromagnetic materials undergo a transition from a ferromagnetic to a paramagnetic state above Curie temperature, T_C. Similarly, antiferromagnetic materials exhibit a phase transition from an antiferromagnetic to a paramagnetic state above the Néel temperature, T_N. This behaviour reflected in maximum magnetic susceptibility at the T_N. The sublattices with antiparallel alignment become unstable to reorientation under an applied magnetic field at T_N.

In 1963, the magnetic susceptibility of BFO was measured, revealing its antiferromagnetic properties below the Neel temperature of T_N 370 °C.[75] Neutron diffraction[34] showed that BFO exhibits a G-type anti-ferromagnetic spin configuration, where the Fe^{3+} ions possess six nearest neighbours with anti-parallel spins [Figure 1.5f]. Every iron center has a magnetic moment of about 4 µB. A high-resolution neutron diffraction study conducted by Sosnowska et al. in 1982 demonstrated that the spin structure of BFO is inadequately described by G-type ordering as shown in Figure 1.5e.[76] Rather, they suggested that BFO's magnetic ordering follows a cycloidal spiral in the $[110]_{hex}$ direction with a period of 620 Angstrom. Furthermore, according to Sosnowska et al., BFO exhibits weak ferromagnetism at room temperature due to residual magnetic moments caused by a canted spin magnetic structure.

The antiferromagnetic spin structure arises from the superexchange (SE) interaction between the spins of the next neighbour Fe ions mediated via oxygen atoms as shown in Figure 1.5g. The Hamiltonian corresponding to the SE interaction in BFO is described in the Equation 1.3.[55]

$$H_{SE} = J \sum_{\vec{r},\vec{\alpha}} (\overrightarrow{S_{\vec{r}}} \bullet \vec{S}_{\vec{r}+\vec{\alpha}}) + J' \sum_{\vec{r},\vec{\beta}} (\overrightarrow{S_{\vec{r}}} \bullet \vec{S}_{\vec{r}+\vec{\beta}}) \tag{1.3}$$

$$H_{DM} = - \sum_{\vec{r},\vec{\delta}} \vec{D}_{\vec{\delta}} \, (\overrightarrow{S_{\vec{r}}} \times \vec{S}_{\vec{r}+\vec{\delta}}) \tag{1.4}$$

Where, $\overrightarrow{S_{\vec{r}}}$ is the spin of Fe at site vector $\overrightarrow{r}$, $\vec{S}_{\vec{r}+\vec{\alpha}}$ and $\vec{S}_{\vec{r}+\vec{\beta}}$ are the spins of nearest-neighbour and next-nearest-neighbours of spin $\overrightarrow{S_{\vec{r}}}$ with displacement vectors $\vec{\alpha}$ and $\vec{\beta}$. *J* and *J′* are the interaction parameters as sketched in Figure 1.5g. The spin structure of BFO stabilizes in the G-type antiferromagnetic spin arrangement. The Dzyaloshinskii-Moriya (DM) interaction arises due to the antisymmetric exchange interaction between neighbouring spins of Fe. If the spin orbit coupling is considered as a perturbation to the SE interaction, the second order energy correction is of the form of an antisymmetric exchange interaction. Thus, the microscopic origin of the DM interaction is related to spin-orbit coupling.

In fact, the DM interaction can only exist in a material, if the midpoint of neighbouring spins is not a point of inversion. This criterion is indeed satisfied in BFO, where the ferroelectric distortion causes the oxygen atom in the Fe-O-Fe bond to be displaced. The Hamiltonian for DM interaction is shown in Equation 1.4.[55] $\vec{D}_{\vec{\delta}}$ corresponds to the DM vector at displacement vector $\vec{\delta}$. The DM interaction favours perpendicular spin alignment whereas SE interaction favours antiparallel spin alignment.

The competition between the DM and the superexchange interactions leads to a canted spin structure. In case of BFO, this canted spin structure forms spin cycloid in a regular fashion over a distance of 62 nm. [Figure 1.5h] The average magnetic moment over the spin cycloid is found to be zero as each spin has its mirror image in the cycloidal spin arrangement. Therefore, a macroscopic magnetization of BFO does not arise due to the cycloidal spin arrangement.

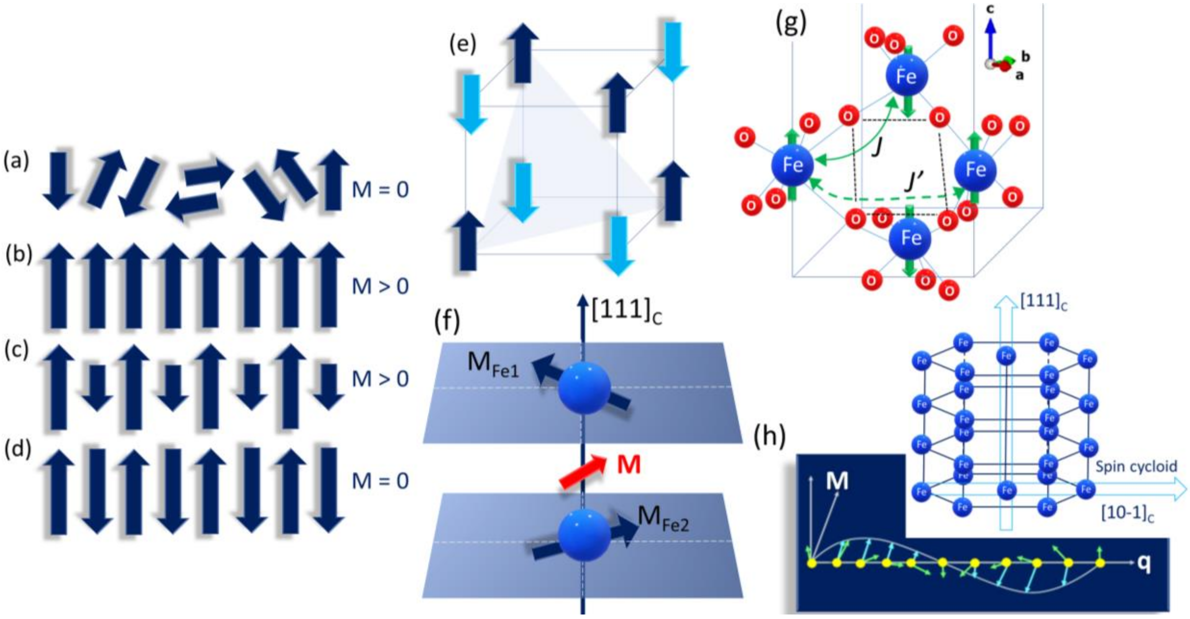

Figure 1.5: A schematic of the spin ordering in paramagnetic (a), ferromagnetic (b), ferrimagnetic (c), and antiferromagnetic (d) materials. Schematic of G-type antiferromagnetism (e) and canted antiparallel spins in neighbouring Fe atoms of BFO shown in (f). A representation of super exchange interaction between nearest-neighbour and next-nearest-neighbour Fe spins via oxygen atoms (g),[55] and incommensurate spin cycloid in BFO of periodicity 62 nm shown in (h) along [10-1]$_c$.

In the in the cycloidal spin arrangement of BFO, the single ion anisotropy (SIA) related to the interaction between orbital magnetic moment and crystal field, plays an important role. A large SIA suppresses the spin cycloid, but small SIA causes anharmonicity in the spin cycloid modulation. In BFO, origin of SIA is from the anisotropic deformation resulting from the ferroelectric distortion, where BFO has an easy axis type anisotropy.[54,69,77] In addition, the spin cycloid in BFO is not harmonic, as SIA is introduced by antiferrodistortive rotation and ferroelectric distortion. The anharmonicity in the modulation of the spin cycloid of BFO has been reported using NMR and Mössbauer spectroscopy.[27,78] These studies suggest that a large anharmonicity is present in the spin cycloid of BFO.[69]

The existence of both ferroelectric and anti-ferromagnetic ordering makes BFO a magnetoelectric material. However, the existence of a spin cycloid averages out any linear magnetoelectric (*M-E*) coupling between polarization (*P*) and magnetization (*M*). Any macroscopic magnetoelectric coupling must therefore be of higher order (quadratic) as observed by Tabaré's group.[79] Indeed, up to magnetic fields of several Tesla the magnetically induced polarization is found to be proportional to the square of the magnetic field. The full quadratic magnetoelectric tensor was first characterized by Tabares-Munoz et al.,[79] and is given by in hexagonal coordinate axis with P_3 parallel to the spontaneous polarization.

Despite very limited evidence of direct coupling, the dependence of spontaneous magnetization and spontaneous polarization on the electric and magnetic fields, respectively, has created much interest for its use in applications in the field of information storage, sensors and electric field controlled ferromagnetic resonance devices and transducers with magnetically modulated piezoelectricity.

With the increasing trends towards device miniaturization, it is both technologically and scientifically interesting to synthesize nanostructured BFO. Nano-sizing of BFO enhances the magnetization that is ascribed to the suppression of spin cycloid structure, surface induced magnetization and decrease in oxygen vacancies, which are discussed in the following.[68,71]

Size effect: When the particle size of BFO is reduced to the nanoscale, the ratio of surface area to volume increases enormously (~1/r). This increased surface area can lead to the presence of more uncompensated spins at the surface,[71] which can contribute to a higher overall magnetization.

Crystal structure and strain: BFO has a rhombohedral crystal structure at room temperature. However, as the particle size decreases, the crystal structure can become distorted and contain large microstrain.[73] This slight alteration in crystal structure can lead to the emergence of a ferromagnetic phase, which can contribute to higher magnetization.

Overall, a higher magnetization of BFO NPs compared to bulk BFO can be attributed to a combination of size effect, crystal structure, and microstrain in the material, which can be further utilised in several bio-medical applications.

1.6 Bismuth ferrite nanoparticles in hyperthermia therapy

Hyperthermia refers to the condition where the temperature or a specific part of a body surpasses the normal temperature of 37 °C.[80] When cancerous tissues are subjected to high temperatures, various physical and physiological mechanisms lead to their destruction. Hyperthermia is known to promote apoptosis within the tissue when the temperature is increased to above 42 °C for about 30 minutes.[81] The threshold temperature may differ based on the type of tissue, but the cytotoxicity level sharply rises once it's surpassed, with as little as a 0.2 °C difference between cytotoxic and noncytotoxic temperatures. Furthermore, hyperthermia can lead to necrosis, the death of most or all cells when the tissue is heated to 46 °C for about 30 minutes. As the temperature increases, the time required for heating decreases, and coagulative necrosis happens within 1-2 seconds at temperatures of approximately 60 °C.

Based on biological research, it can be stated that although hyperthermia is not potent on its own, it is one of the best radiation modifiers available today. The mechanism of magnetic hyperthermia relies firstly on the selective uptake of MNPs on cancer cells and secondly on the heating of tumours by increasing the local temperature (up to 41–45 °C) leading either to cell degradation or even to apoptotic death as shown in Figure 1.6a.

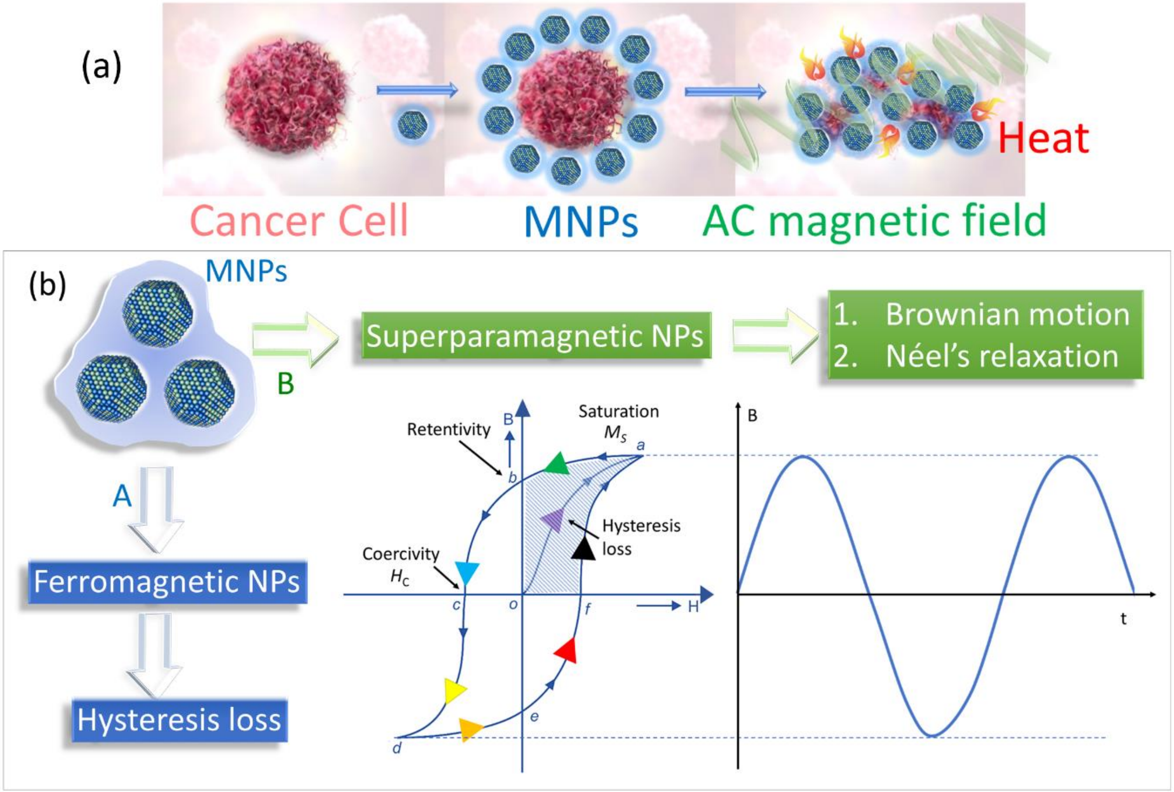

Figure 1.6: (a) Schematic of cancer cell death mechanism (apoptosis) through magnetic fluid hyperthermia based on magnetic nanoparticles (MNPs) in the presence of an alternating magnetic field. (b) Different principle of heating efficiency in ferromagnetic and superparamagnetic NPs. A representation of hysteresis loss in ferromagnetic NPs, where H is applied magnetic field, and B is magnetization of the NPs.

Magnetic nanoparticles (MNPs) have emerged as a promising tool for the treatment of cancer by hyperthermia. MNPs are utilized as an effective heating mediator, leading to the design and development of various devices for heating malignant cells. The consistent success of artificially induced hyperthermia using MNPs has propelled the field forward. In fact, the use of magnetic materials for hyperthermia was first investigated by Gilchrist in 1957.[82] Gilchrist heated various tissue samples with 20–100 nm size particles of γ-Fe_2O_3 exposed to a 1.2 MHz magnetic field, demonstrating the potential of MNPs for cancer treatment.[82] The mechanism behind cancerous cell death by using MNPs with an application of an AC magnetic field is illustrated in Figure 1.6a. If the NPs are superparamagnetic, Brownian motion and Neel relaxation drive the mechanism, whereas, if the NPs are ferromagnetic, hysteresis loss is the backbone of the mechanism. The advantage of using hyperthermia treatment with superparamagnetic NPs is that they induce extra heat to the local area by oscillating the magnetic moment inside the NPs. Compared to ferromagnetic NPs, superparamagnetic NPs have a higher specific absorption rate (SAR), making hyperthermia more efficient, and capable of efficiently destroying solid tumours at temperatures between 42-46°C.[83] However, a lower magnetic moment, less biocompatibility, and requirement of a higher magnetic field to be magnetized are challenges with superparamagnetic NPs.

Prior to injecting the MNPs at the tumour site, there is no influence of an applied field on the tumour tissues. However, once the field is applied along with MNPs, a non-equilibrium steady field is formed in the tumour, ultimately leading to the destruction of the cancerous cells. The remarkable efficacy of MNPs in hyperthermic cancer treatment a valuable tool in the fight against cancer, providing hope for more effective treatment options for patients.

1.6.1 Specific absorption rate (SAR)

Hysteresis loss in ferromagnetic NPs for hyperthermia refers to the energy dissipated by the particles when they are exposed to an alternating magnetic field. This energy is converted into heat, which can be used to induce hyperthermia in cancer cells. Under the influence of the external field, the magnetic moments of the MNPs align in the direction of the field, but only at high field magnitudes. Domains with magnetic moments that align with the field grow, while those with magnetic moments aligned in the opposite direction shrink. This process of "domain wall displacement" continues until the growing domain encloses nearly the entire volume of the material, known as saturation. In order to flip the magnetization in the particles, the reverse coercive field must be exceeded locally yielding the known magnetic macroscopic hysteresis. Figure 1.6b illustrates this process. Heat is released from the particles when an alternating field is applied. At an amplitude of at least twice of the coercive field of the particles, full reversal arises, and the maximal heat dissipation is reached. During one cycle of the magnetic field, the amount of heat (A) released by the MNPs is equal to the area of the hysteresis loop. In an alternating magnetic field, where f is frequency and $\mu_0 H_{max}$ is amplitude, the area generated is given by the applied field frequency, given that the full hysteresis is still cycled through. The amount of heat released by the ferromagnetic material through hysteresis loss is given by Equation 1.5.[83]

$$A = \int_{-H_{max}}^{+H_{max}} \mu_o \, B(H) \uparrow dH - \int_{-H_{max}}^{+H_{max}} \mu_o \, B(H) \downarrow dH \tag{1.5}$$

$$SAR = Af \tag{1.6}$$

where f denotes the frequency of the AC magnetic field, $f = \omega/2\pi$, M (ω, t) magnetization and H is the applied magnetic field. The specific absorption rate (SAR) due to heating in a magnetic field can also be calculated using SAR = $C * \Delta T/\Delta t$, where C is the specific heat capacity of the media, and ΔT is the temperature change, over a time interval Δt.[84]

Magnetite Fe_3O_4 and maghemite γ-Fe_2O_3 are deemed optimal materials for their innate biocompatibility, facile synthesis as stable aqueous magnetic fluids, and outstanding ability to serve as contrast agents in magnetic resonance imaging. However, their applicability is restricted due to their moderate heating efficiency. As higher SAR values necessitate a lower dosage, this renders SAR a crucial factor to be considered when evaluating clinical use. To overcome this limitation, the use of complex magnetic oxides can be preferred (e.g., BFO). There are multiple approaches to tailor the magnetic properties of such materials, including enhancing intrinsic properties dependent on their structure and composition, as well as optimizing extrinsic properties such as particle size through the synthesis process. By implementing these techniques, the magnetic properties of the materials can be greatly improved, paving the way for more effective and efficient biomedical applications.

In order to circumvent the use of high and potentially hazardous concentrations of MNPs, enhancing their SAR values is imperative. Achieving this objective is contingent upon manipulating various parameters, such as particle size, saturation magnetization, and effective magnetic anisotropy.

1.6.2 Magnetic anisotropy

The anisotropy of MNPs is a crucial parameter for tuning magnetic hyperthermia and is one of the main factors studied in this field. However, it is important to recognize that the heating efficiency of NPs can be either increased or decreased depending on other factors as well, in addition to anisotropy.[85]

Magnetic materials exhibit multiple forms of anisotropy, including magneto-crystalline anisotropy, surface anisotropy, shape anisotropy, exchange anisotropy, and induced anisotropy.[86–88] In MNPs, the most prominent anisotropies are shape anisotropy and magneto-crystalline anisotropy, with the former being dominant in MNPs.[89] Magneto-crystalline anisotropy is a consequence of spin-orbit interaction and energetically favours alignment of the magnetic moments along a specific crystallographic direction, referred to as the easy axis of the material.[87] The magneto-crystalline anisotropy depends on the material type, temperature, and impurities, and is independent of sample size and shape.

In contrast, shape anisotropy leads to magnetization variations depending on the nanoparticle shape [Figure 1.7]. The magnetization is more aligned along the long axis of a thin, needle-shaped sample than any of its short axes.[90]

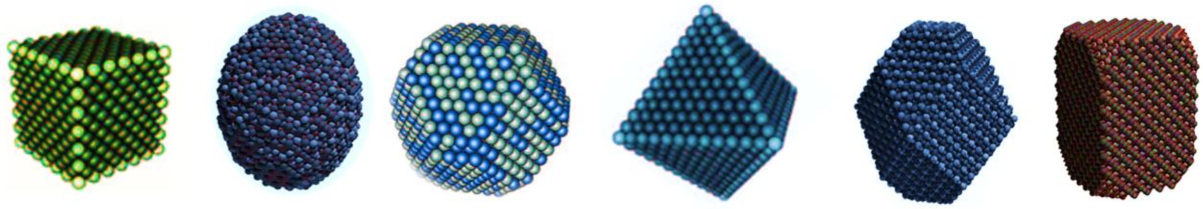

Figure 1.7: Different morphologies of magnetic nanoparticles (MNPs) which can affect magnetic anisotropy of the MNPs.

Stress anisotropy implies that magnetization might change with stress, while surface anisotropy suggests that magnetic anisotropy changes when surfaces are modified or adsorb different molecules. This highlights the crucial influence of surface structure on magnetic anisotropy. Therefore, the coating of NPs can significantly affect their magnetic anisotropies and magnetic properties, particularly due to their large surface-to-bulk atom ratio.

Although there is a linear dependence of the SAR on the saturation magnetization, reducing the size of MNPs to the nanoscale often results in a decrease in saturation magnetization, which poses a significant challenge in improving the SAR in MNPs. Modifying the morphology of the NPs, specifically the surface anisotropy, can lead to an improved magnetic response in cube-shaped Fe_2O_3 NPs, as opposed to their spherical counterparts.[90] To investigate this further, spherical and cubic exchange-coupled FeO/Fe_3O_4 NPs, with different $FeO : Fe_3O_4$ ratios were tested for hyperthermia and the results show higher values of SAR for the cubes compared to the spheres (200 vs. 135 W/g at 600 Oe and 310 kHz).[91] A recent study revealed that even for relatively large elongations, the cubic contribution to the effective anisotropy remains significant and cannot be overlooked when developing numerical and analytical models for magnetic hyperthermia.[92] These findings indicate that the saturation magnetization is not the sole factor in determining the SAR, and the heating efficiency of MNPs can be improved by tuning their effective anisotropy.

1.6.3 Biocompatibility of nanoparticles

Biocompatibility is critical in the development of MNPs for hyperthermia in vivo. MNPs are being used in the biomedical field to diagnose and treat human diseases, but their effects on the body must be understood before clinical use. Encapsulating the MNPs in biocompatible polymers/proteins that can melt and break open at 42 °C is necessary. These heat-sensitive polymers/proteins can also be loaded with chemotherapy or radiosensitizers, allowing the polymer/protein capsule to act as a carrier for the magnetic nanoparticles and drug.[83]

Current cancer treatments, like chemotherapy and radiotherapy, often come with adverse side effects, highlighting the need for new therapies with minimal side effects. MNPs-based hyperthermia has emerged as a promising solution. However, the controlled Curie temperature and colloidal stability of MNPs remain challenges. Surface functionalization strategies are needed to make highly dispersible MNPs for successful in vivo hyperthermia applications. Additionally, biocompatibility remains a significant concern as almost all studied MNPs are toxic to normal cells.

Hence, developing a colloidally stable and highly biocompatible MNPs-based hyperthermia system that does not extend the therapeutic temperature during in vivo trials is necessary.

1.7 Electrical properties of bismuth ferrite

The electrical properties of BFO, is quite interesting and unique again. BFO is a non-toxic and environmentally friendly material compared to other ferroelectric materials such as lead zirconate titanate (PZT), which is toxic and poses a risk to human health and the environment. Though BFO is a relatively new and promising piezoelectric material compared to other well-known piezoelectric materials such as quartz, lead zirconate titanate (PZT), and aluminum nitride (AlN). It has a strong ferroelectric polarization, and its high Curie temperature lending it as a high temperature piezoelectric ceramic.[93] It has a unique combination of ferroelectric, multiferroic, and piezoelectric properties that make it suitable for a wide range of applications in electronics, energy, and information storage, and sensors.

1.7.1 Piezoelectricity

Piezoelectrics (piezein is Greek word means to squeeze or press and electron=amber) are crystalline materials that become electrically polarized when subjected to mechanical stress and conversely change shape when under an applied electric field. In the year 1880, the direct piezoelectric effect was first discovered in quartz, Rochelle salt ($NaKC_4H_4O_6 \cdot H_2O$), tourmaline, and cane sugar by French physicists Pierre and Jacques Curie.[94] Converse piezoelectricity was deduced by Lippmann and confirmed by the Curie brothers in 1881. The direct piezoelectric effect is measured in unit C/N, and the converse piezoelectric effect in m/V. [Figure 1.8a]

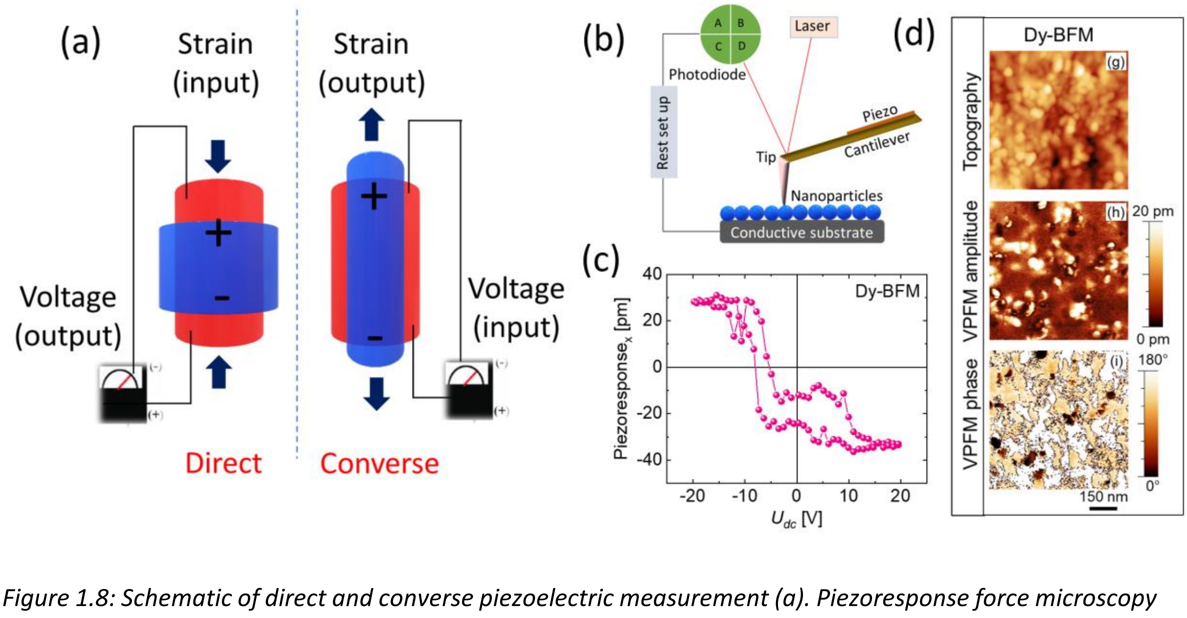

Figure 1.8: Schematic of direct and converse piezoelectric measurement (a). Piezoresponse force microscopy (PFM) set up scheme (b), piezoresponse (c), and topography, vertical PFM phase and amplitude response (d) for Dy and Mn codoped BFO NPs. [© 2022 Adv. Func. Mater., with permission][46]

Piezoelectric materials can be categorized into two main groups: inorganic and organic. Inorganic piezoelectric materials are further divided into two types, piezoelectric single crystals and polycrystals. Quartz and ZnO are notable examples of piezoelectric single crystals.[95] Polycrystalline piezoelectric such as piezoelectrics ceramics consist of multiple small crystals with random domain orientations. In order to become macroscopically piexoelectric these ferroelectric materials must be electrically poled. By applying an external electrical field on the ceramic, the domains can be made to align in the same direction, resulting in the manifestation of piezoelectricity. $BaTiO_3$, the first discovered polycrystalline piezoelectric material, has found widespread use in the production of high-quality capacitors due to its high dielectric constant (ε), and Curie temperature (T_C).[96] In order to further enhance the piezoelectric properties of inorganic piezoelectric materials, researchers have extensively studied piezoelectric solid solutions such as $Pb[Zr_xTi_{1-x}]O_3$ and $Na_xK_{1-x}NbO_3$, which exhibit excellent electrical properties exceeding these of $BaTiO_3$. Through the manipulation of stoichiometry and doping, researchers have been able to alter the local structure of these materials, thereby achieving improved piezoelectric performance.[94]

While inorganic piezoelectric materials boast superior piezoelectric properties, they are often brittle and prone to breaking during the manufacturing process. Organic piezoelectric materials, on the other hand, are typically more flexible and pliable. Prominent examples of organic piezoelectric materials include polyvinylidene fluoride (PVDF) and its copolymer poly(vinylidene-co-fluoroethylene) (P(VDF-TrFE)), which exhibit excellent sensitivity, high dent resistance, and breakdown voltage, as well as relatively low permittivity and density. Despite these advantages, the d_{33} value of PVDF remains relatively low, ranging between 20-30 pC/N.[97] Among oxides, ZnO exhibits 10-30 pC/N d_{33} value,[98] for PZT d_{33} is 225-590 pC/N,[99] for tetragonal $BaTiO_3$ 100 pC/N d_{33} value,[100] for PMN-PT d_{33} value is ~2500 pC/N,[101] and for KNN[102] d_{33} is 80 pC/N as reported in the literature.[103]

In piezoelectric materials, an electric potential (or charge displacement) is generated in response to the applied mechanical stress (direct electric field). The direct and converse piezoelectric effect can be described by the Equation 1.7, and 1.8, respectively.[104]

$$P_j = d_{jkl}X_l \ (tensor\ form), \qquad P_i = d_{ij}X_j \ (matrix\ form) \qquad (1.7)$$

$$x_{ij} = d_{ijk}E_k \ (tensor\ form), \qquad x_j = d_{ij}E_i (matrix\ form) \qquad (1.8)$$

$$d = 2\,\varepsilon_0\varepsilon_r Q P_S \qquad (1.9)$$

The polarization (P) is a vector and stress (X) is a second rank tensor, and the physical entity relating these two parameters consist of three directions. Therefore, the piezoelectricity is a polar third rank tensor [Equation 1.7]. Piezoelectric effect can be described by 6 X 3 matrix because stress tensor is symmetric ($X_{ij} = X_{ji}$).[104] For converse piezoelectric effect strain (x) is related to electric field (E). Strain is second rank tensor, and electric field is first rank tensor. The converse piezoelectric effect is a third rank tensor explained by Equation 1.8.

Under an external force, the central symmetry in the crystal is disturbed, thereby forming a piezoelectric potential, which is fundamental for piezoelectric materials to generate electricity. Equation 1.9 shows a relation between piezoelectric coefficient (*d*) and polarization (P). In order to become macroscopically piezoelectric, their ferroelectric materials must be electrically poled. The piezoelectric coefficient is proportional to the dielectric permittivity (ε). The piezoelectric effect of ferroelectrics with a centrosymmetric prototype phase is the result of the electrostriction linearized by spontaneous polarization. Hydrostatic stress is a scalar quantity. The relationship between hydrostatic piezoelectric charge coefficient (d_h) with piezoelectric coefficients for a poled ferroelectric ceramic is $d_h = -(2d_{31} + d_{33})/p$, where p is hydrostatic pressure.[105]

Poling BFO thin films has proven much easier than bulk ceramics. This is due to the poor resistivity and high coercive field of BFO ceramics. A serious obstacle for BFO ceramics is the poling process due to a high leakage current density caused by both impurity phases and electric defects. In order to overcome this obstacle, many researchers have paid much attention to modifying the preparation technologies, the formation of solid solutions, and ion-site engineering (e.g., ion substitution at the Bi and/or Fe sites). For BFO, the d_{33} value is reported around ~50-60 pm/V.[58,106] The piezoelectric properties of BFO NPs are difficult to quantify. The standard way for measuring the piezoelectric effect requires a dense, electroded sample, which cannot be achieved with NPs. Even compacted into pellets, they still have a low density and contain a large volume of voids and pores, which completely distort the internal electric field distribution inaccessible to experiment.[107] It is then difficult to apply a sufficiently strong electric field to the NPs. Extracting information on the polarization and piezoresponse of NPs from the overall response of such nanopowder-air composite is a non-trivial and error-prone task. Therefore, to study piezoelectricity in the NPs, one can use piezoresponse force microscopy (PFM) [Figure 1.8 b-d]. PFM has established itself as a reliable method for studying ferroelectric and piezoelectric properties at the nanoscale, even within individual NPs.[46,68]

Piezocatalysis is an interesting new facet of applying the piezoelectric effect. Two main strategies: one is to leverage the mechanical energy that is abundant in nature to break down and degrade organic pollutants, while the other involves converting the many chemicals and pollutants that can be found in nature into useful molecules, such as H_2 and CH_4, which can serve as fuels. To achieve these goals, researchers have approached to piezo-catalysts, which facilitate piezo-catalytic reactions combining both physical and chemical effects.

Pyroelectric materials exhibit spontaneous polarization i.e., polarization in the absence of electric field, this cannot be altered or reversed on applying an external electric field it does so in ferroelectric materials. Some of the pyroelectric materials are Tourmaline, gallium nitride, caesium nitrate ($CsNO_3$), polyvinyl fluorides, cobalt phthalocyanine, and Lithium tantalite ($LiTaO_3$). Pyroelectricity is the property of a polar crystal to produce electrical energy when it is subjected to a change of thermal energy. It is possible also to define the pyroelectric effect as the ability of crystals to generate electricity when they are dynamically heated or cooled; a pyroelectric becomes polarized positively or negatively in proportional to a *change* in temperature.[108] It looks like thermoelectric power conversion; moreover, but it is a linear one, so as per the Curie principle, a reversed effect must exist, namely "*the electrocaloric effect*", which the electrothermal energy conversion characterizes.[108]

1.7.2 Ferroelectricity

Ferroelectricity is the name in analogy to ferromagnetism due to Erwin Schrödinger (Frozen polar liquids = ferroelectric**!**).[109] Ferroelectricity was discovered by Joseph Valasek in 1921 on Rochelle salt.[110] Ferroelectric materials have a permanent polarization that can be reoriented by an applied external electric field. Ferroelectrics are named in analogy to ferromagnetic materials. There is an energy barrier between two ferroelectric states. It can be overcome by an external electric field, which tilts the energy wells and enables the transition between them. The hysteresis forms due to delay of switching while changing the wells [Figure 1.9a]. Hence, in the limit of a properly oriented single crystal, a ferroelectric phase is one in which the spontaneous polarization can be reoriented between possible equilibrium directions, which themselves are determined by the crystallography of the system by a realizable electric field. A brief summary of early breakthroughs in the ferroelectric world.

- In 1920 Joseph Valasek found ferroelectric properties in Rochelle salt, $KNaC_4H_4O_6 \cdot 4H_2O$.[110]
- 1935 KH_2PO_4 was found to be ferroelectric with a critical temperature of about 123 K by Busch and Scherrer.[111]
- 1946 ferroelectricity in $BaTiO_3$.[112]
- 1951 antiferroelectricity in $PbZrO_3$.[113]
- 1954 relaxor property in $BaTi_{1-x}Sn_xO_3$.[114]
- 1958 multiferroics in $PbFe_{0.5}Nb_{0.5}O_3$.[17]
- 1966-1970 ferroelectricity in BFO solid-solution.[35,115]
- 1971 ferroelectricity in a polymer: P(VDF).[116]
- 2003 ferroelectricity in BFO thin films.[117]

For BFO bulk ceramic ferroelectric properties were measured in 2007.[58] From group theory, there are 32 crystallographic point groups when applying the crystallographic restriction theorem in the 3-dimensional case.[118] All crystals belong to one of these 32-point groups. Since all materials belong to one of those 32-point groups possess atoms or ions with charges, the application of an electrical excitation leads to the redistribution of the charges, and the polarization is generated. The displacement of the ions is reflected macroscopically to the elastic strain. This strain is always positive and originates from the opposite shift of charged ions with different signs in the lattice. This electromechanical coupling property is called electrostriction, and the electrostrictive strain is quadratically related to the applied field. The above discussion indicates that, electrostriction applies to all crystal symmetries. Of the 32-point groups, 11-point groups are centrosymmetric. A crystal having an inversion symmetric center does not possess any polarity at a null field.

For the remaining 21-point groups which are not centrosymmetric, apart from point group (4 3 2), all of them exhibit piezoelectricity. This linear electromechanical effect is responsible for the accumulated electric charge in response to the applied mechanical stress. As a converse effect, the application of an electric field results in the change of elastic strain. This effect is also linear and called the converse piezoelectric effect. Of the remaining 20-point groups, 10 possess a spontaneous polarization along the polar axis. Since the configuration of the crystal structure is a function of temperature, this spontaneous polarization is also temperature dependent. As a result, upon heating or cooling, the spontaneous polarization will change, and a voltage can be generated. This effect is called the pyroelectric effect.

Single crystals typically form multiple domains. Under a strong external field, a single domain can be obtained. A field reversal may switch the direction of the domain, and the phenomenon is called domain switching, and a material able to do this is called a ferroelectric material. The bipolar loading can induce a 180° and 90° domain switching. The switching process generates a hysteresis shape of the field dependent polarization loop (P-E loop). The response of the polarization is non-linear and hysteretic. The application of an external field also induces strain. The strain response (S-E loop) is also non-linear and hysteretic. As $S \propto P^2$, a butterfly shape [Figure 1.9a] is formed.

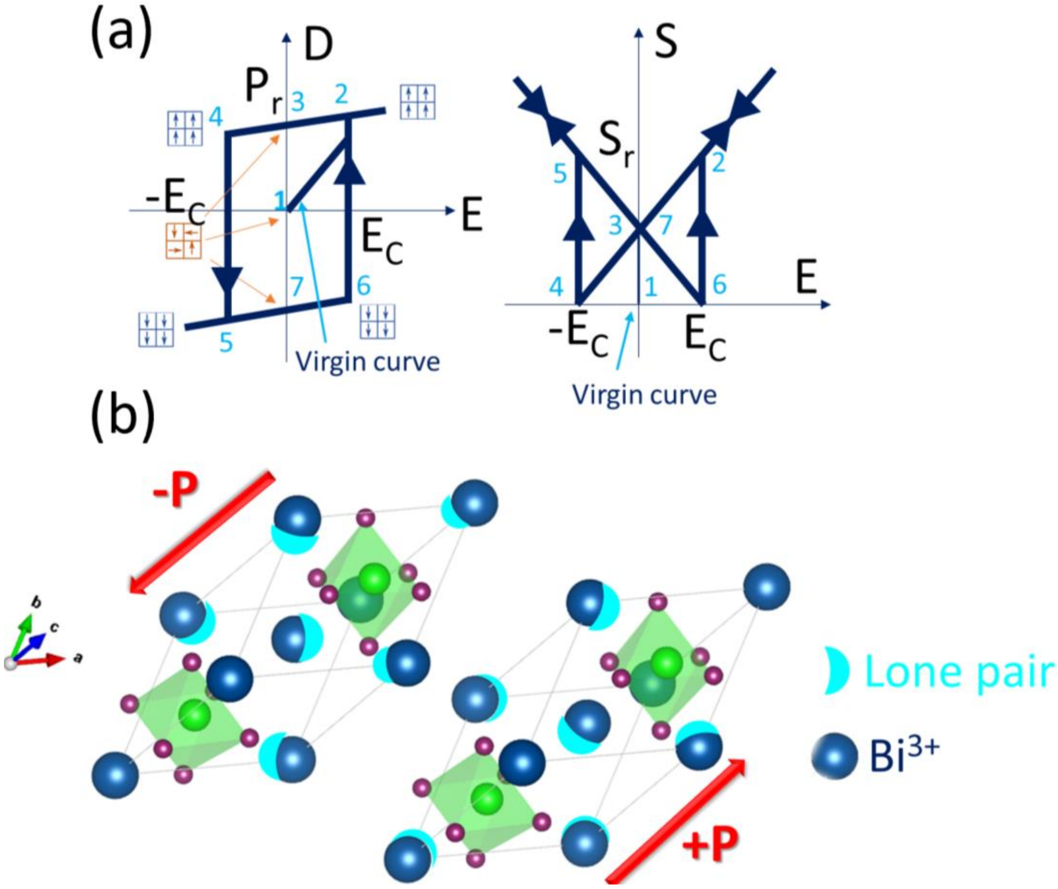

Figure 1.9: Schematic of dielectric and strain hysteresis loops of an ideal ferroelectric material under uniaxial bipolar electric filed loading (a). Schematic of lone-pair mechanism in BFO, two electrons shift away from the Bi^{3+} ion (dark blue) and towards the FeO_6 octahedra (green). This lone pair (cyan) induces a spontaneous polarization, P, along the $[111]_c$ axis.

The schematic P-E and S-E loops of an ideal ferroelectric single crystal are depicted in Figure 1.9a. The state at point 1 represents the virgin state with randomly oriented domains. Above a certain external field, a monodomain state is formed (point 2) and the polarization further increases linearly with the external field, which represents the pure dielectric response to the external field. Different from the spontaneous one, this contribution to the total polarization is reversible. When the external field is removed (point 3), the polarization for this state is called remanent polarization. Similarly, the strain at this state is called remanent strain. For a perfect single crystal, this value is usually equivalent to the spontaneous ones. If an external field is applied in the opposite direction and exceeds a specific threshold value, the polarization changes its sign (from point 4 to point 5). This critical field is referred to as the coercive field E_c . If a reverse field is applied again, the state goes back to point 2 and the whole hysteresis loop completes.

Not only the external field but also a mechanical stress (S) can induce domain switching. This effect is called ferroelastic switching. In the tetragonal phase, the domain switching can be either 90° or 180° by the electric field, while it can be only 90° switching by the mechanical loading. It implies that the polarization and strain response under the mechanical loading are also non-linear. This effect is called ferroelasticity. The schematic polarization and strain responses of an ideal ferroelectric are depicted in Figure 1.9. Above some stress threshold, the monodomain state is transferred to a multidomain state.

The Bi^{3+} ions of BFO have $6s^2$ lone pair electrons at the outer shell, [Figure 1.9b]. This causes electric dipole moments which are aligned to produce a ferroelectric polarization. This origin of ferroelectricity for BFO is quite distinct from conventional displacive ferroelectrics such as $BaTiO_3$ which have electric dipole moments arising from the displacement of one of the ions. Hybridization between e.g., an empty d orbital and the filled oxygen 2p orbital generates cation off-centering because the electronic energy can be lowered through filling the hybridized bonding state. However, the Fe^{3+} has five electrons in d orbitals and it is inevitable that the hybridization should fill not only the bonding state but also the unstable anti-bonding state. There is no reason that such off-centering happens at the expense of elastic deformation without electronic energy gain.

The *R3c* symmetry allows for weak ferromagnetism as well as for spontaneous polarization along the crystallographic $[111]_c$ direction. The two valence electrons of the Bi-ion, which do not participate in the chemical bonding, play a crucial role establishing the high ferroelectric polarizability leading to polarization values on the order of 100 $\mu C/cm^2$.[58,117] The displacement of Bi^{3+} and Fe^{3+} ions with respect to the ideal perovskite structure contributes to the electric polarization. The synthesis of large stoichiometric BFO crystals turned out to be challenging. Impurities and defects can significantly impact the magnetic and dielectric properties. For the latter, impurity-induced conductivity and, thus, the formation of Maxwell-Wagner charge relaxation is formed.

Unfortunately, the presence of a depolarizing electric field in finite-sized ferroelectrics is known to reduce their Curie temperature and polarization P. There exists a critical size below which the nanoparticle ceases to be ferroelectric.[119,120] A report suggested a critical size of 9 nm for ferroelectricity in BFO NPs.[73] While the ferroelectric properties of BFO thin films have proven useful in several applications, the utilization of spontaneous polarization in bulk BFO ceramics is hindered by leakage current and impurities. Therefore, investigating the local and macroscopic polarization of nanosized, pure (single-phase) BFO NPs is in demand. It also offers hope for their utilization in fields such as ferro-catalysis and ferro-photocatalysis.

1.8 Optical properties: An absorber of visible light

Ferroelectric materials are sensitive to temperature, pressure, electric field, strain, and chemical composition. Recently, there has been increased interest in the photo-induced properties of ferroelectrics driven by energy and environmental concerns. The intrinsic spontaneous polarization in ferroelectric materials creates an internal electric field, enabling the separation of photogenerated charge carriers. Unlike traditional semiconductor solar cells, this internal field exists throughout the entire ferroelectric domain, leading to the so-called anomalous or abnormal bulk photovoltaic effect.[121,122]

When non-centrosymmetric materials, like ferroelectrics, are uniformly illuminated with a wavelength corresponding to the absorption edge, a steady photocurrent is generated, the bulk photovoltaic effect. This phenomenon differs from the mechanism involved in p-n junctions of semiconductors. The bulk photovoltaic effect depends on the light polarization and disappears in the paraelectric phase. The non-centrosymmetry of ferroelectrics leads to a shift current being photogenerated, as the probability of the photogenerated carriers to move from k to k' momentum is different from that to move from k' to k.[122–126]

This field is ongoing, and a strong controversy regarding the existence and contribution of both mechanisms, as it is unclear whether this phenomenon exists or is related to point defects like oxygen vacancies.

BFO has garnered significant attention in recent times due to its impressive photoferroelectric properties. While the interaction of light with ferroelectrics is a well-established phenomenon, BFO has breathed new life into the field of photoferroelectrics. This is primarily due to its ability to exhibit a lower band gap of approximately 2.3 eV, which is lower than classical ferroelectrics such as $BaTiO_3$ or $PbTiO_3$ exhibiting band gaps around 3 eV.[127] BFO has been shown to demonstrate photovoltaic charge separation at ferroelectric domain walls, resulting in the production of a voltage that surpasses the band gap. This is made possible by the potential steps arising from the component of polarization perpendicular to the domain wall, which leads to a net voltage being produced at the domain wall under illumination. Thanks to the higher local electric field, BFO enables a more efficient separation of the excitons, creating a net imbalance in charge carriers near the domain walls. This, in turn, results in the observation of a net voltage across the entire sample, thereby highlighting the immense potential of BFO as a photoferroelectric material.[128–130]

BFO also demonstrates photostrictive properties.[131] In ferroelectrics, the resultant photo-induced strain arises as a superposition of photovoltaic and piezoelectric effects.[132] When light irradiates a ferroelectric, electron-hole pairs are generated, producing a voltage. These charges partially screen the polarization, and as ferroelectrics are also piezoelectric, a deformation occurs via the reverse piezoelectric effect.[133] It is noteworthy that BFO has been utilized for photo-induced strain under various wavelength excitations.[134–136] Interestingly, as the wavelength increases, the deformation value exhibits a nonlinear behaviour. Additionally, the deformation response time is also wavelength dependent.[134] The larger deformation observed in the near UV range may be attributed to the band-band transitions in BFO or impurity-defect absorption (oxygen vacancy) mechanisms. This shows the photo-effect in ferroelectrics in BFO that defects can play a crucial role in optical response. It is important to note that in these oxides, oxygen vacancies are always present, and dopants can generate even more defects.

1.8.1 Energy levels and charge transitions

In BFO Fe^{3+} ions are bonded to oxygen octahedra, Fe ions exhibit strong interactions with close oxygen ions and adjacent Fe^{3+} which cause a high spin condition for Fe^{3+} electronic structure. It is well established that three types of electronic transitions occur in the optical absorption spectra of $Fe^{3+.}$ First is the *d-d* transitions, second the ligand to metal charge transfer transitions, and third is the pair excitation resulting from the simultaneous excitation of two neighbouring Fe^{3+} cations that are magnetically coupled.

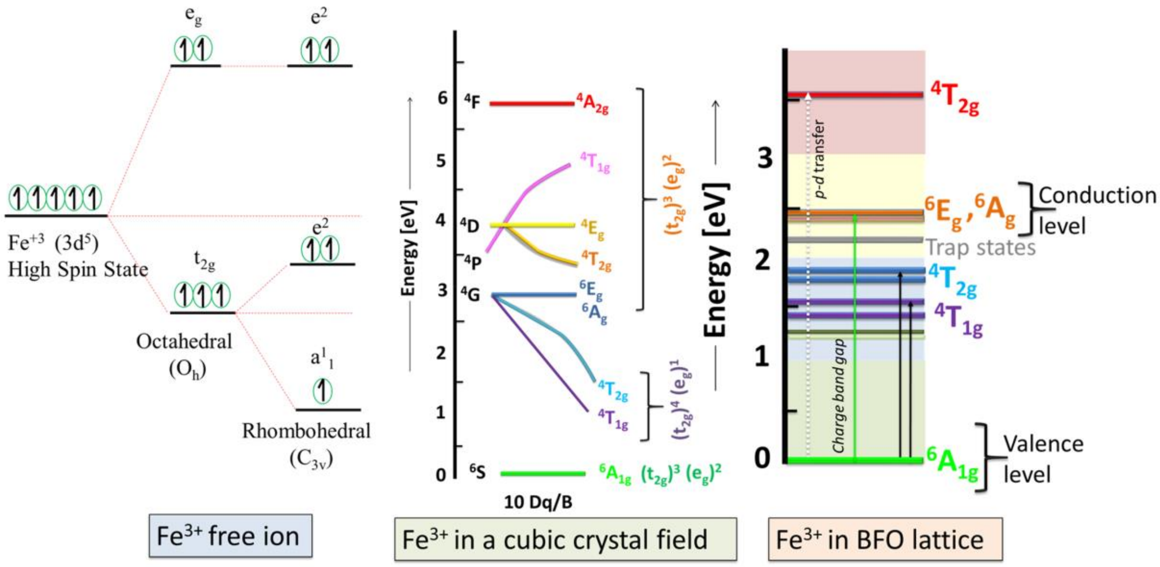

Figure 1.10: Leftmost energy level splitting shows the case of FeO_6 octahedron.[137] Middle picture is Tanabe-Sugano diagram for high-spin Fe^{3+} in octahedral coordination in ideal cubic crystal field.[137] Right most picture shows, the Fe^{3+} energy level splitting in rhombohedral BFO crystal lattice.[138]

In octahedral coordination, the Fe 3d atomic orbitals are split into two sets of orbitals labelled as t_{2g} and e_g. [Figure 1.10] The each t_{2g} and e_g orbitals are split by the exchange energy and the energy separation is the 10 Dq ligand field parameter or crystal field splitting.[137] The energies of the different states of Fe^{3+} under this ligand field as a function of 10 Dq are shown schematically in the Tanabe-Sugano diagram shown in Figure 1.10.[137] The exchange splitting results in two sets of t_{2g} and e_g orbitals, one for majority spin (spin-up or α-spin) and the other for the minority spin (spin down or β-spin) electrons. The ligand field transitions are those relating states which arise from the different possible electronic configurations of the t_{2g} and e_g orbitals. The ground $^6A_1(^6S)$ state in Figure 1.10, arises from the ground state $(t^{\alpha}_{2g})^3(e^{\alpha}_g)^2$ configuration of high-spin Fe^{3+} ions. The first possible excited state is $(t^{\alpha}_{2g})^3(e^{\alpha}_{g})^1(t^{\beta}_{2g})^1$. This configuration gives $^4T_1(^4G)$ and $^4T_2(^4G)$ states. The remaining states result from the "spin flip" configuration $(t^{\alpha}_{2g})^2(t^{\beta}_{2g})^1(e^{\alpha}_{g})^1$ and $(t^{\alpha}_{2g})^3(e^{\alpha}_{g})^1(e^{\beta}_{g})^1$.[137]

The ligand to metal charge-transfer transitions happen according to molecular orbital theory, the transitions at energy higher than most of the ligand field transitions are the ligand to metal charge-transfer transitions.[137] For BFO, since the bulk band gap is ~2.6 eV (or ~476 nm), bands above 3.0 eV (or ~400 nm) in energy were assigned to ligand to metal charge-transfer transitions.[138] However, this charge-transfer band tail may extend to lower energy (longer wavelength) regions through the magnetic coupling.[138–140]

The third type of transition, pair excitations or double exciton processes occur when an additional phenomenon resulting from the magnetic coupling of adjacent Fe^{3+} cations is the presence of absorption features corresponding to the simultaneous excitation of two Fe^{3+} centers. These features happen at energies the sum of two single-ion Fe^{3+} ligand field transitions and are named as double exciton processes. These transitions are also spin allowed i.e., if both Fe^{3+} cations are excited to a quartet ligand field state so that S_a=S_b=3/2, the pair states resulting from coupling the two Fe^{3+} cations will have S values of 0, 1, 2, and 3. Transitions to these pair states can therefore occur from the S=0, 1, 2, and 3 states in the $Fe^{3+}(^6A_1)$-$Fe^{3+}(^6A_1)$ ground state manifold.[134,137,138]

1.8.2 Optical band gap of bismuth ferrite

The fundamental band gap is defined as the energy difference between the maxima of the valence band and the minima of the conduction band as shown in Figure 1.11. It corresponds to the energy difference between the ionization potential (IP) and electron affinity (EA) of the material.[141] The band gap is also referred to as the transport gap since it represents the minimum energy necessary to create a positive charge carrier somewhere in the material (IP) minus the energy gained by adding a negative charge carrier (EA).[141] The band gap or transport gap can be estimated experimentally via a combination of ultraviolet photoelectron spectroscopy (UPS) and inverse photoemission spectroscopy (IPES).

The optical gap is the energy of the lowest electronic transition accessible via absorption of a single photon. In the excited state, the electron and hole remain electrostatically bound to one another, so optical gap is lower than fundamental band gap. The difference between the fundamental gap and the optical gap is the electron–hole pair binding energy (E_{BE}), which is different for different material. [Figure 1.11]

The band edge of an inorganic solid is located at the low energy end of the conduction band above the valence band. It is difficult to determine the band edge for transition metal oxides particularly those presenting magnetic order, because there are narrow d bands in the gap, leading to transitions implying localized charges that to some extend can be excited with infrared radiation with a finite probability. The transitions induced by these photons include the d-d transitions, pair excitation, and finally the charge transfer or optical band gap. The first two transitions mentioned previously arise from the narrow d bands.

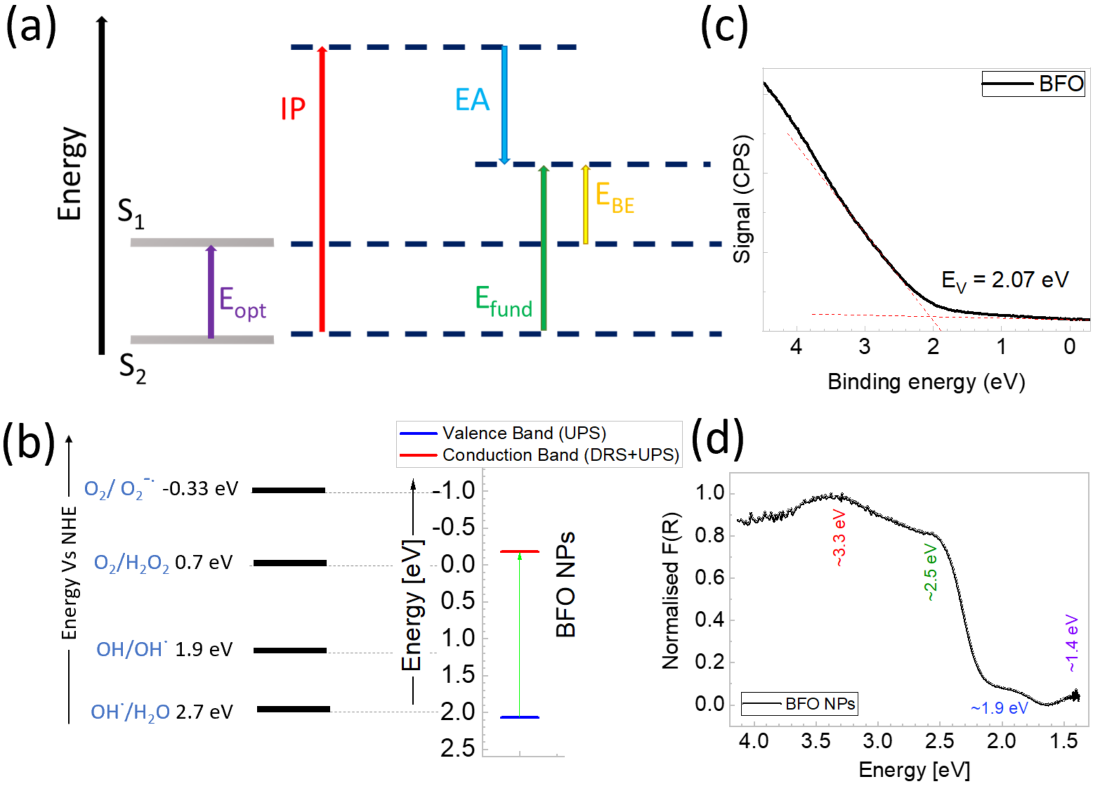

Figure 1.11: The schematic representation of band gap and optical band gap understanding (a).[141] *(b) The band gap estimation of Bismuth Ferrite nanoparticles (BFO NPs) using ultraviolet photoelectron spectrum (c) and transformed diffuse reflectance spectrum (d). [for b and d, © 2022 Adv. Func. Mater., with permission]*[46]

For the case of BFO NPss, as shown in Figure 1.11d, at least seven types of electronic transitions are observed. The crystal field levels of Fe^{3+} in BFO appear at ~1.4, 1.9 eV, the charge transition band gap appears at ~2.2 eV, the double-exciton band is found at ~2.4 eV, and ^4E_g, ^4A_g crystal field levels arise at 2.55 eV, and the transitions due to multimagnon coupling arise at ~2.8 eV, ~2.9 eV, and 3.1 eV. Two other transitions, p-d charge transfers occur at ~3.4 eV, ~4.5 eV, and (p+d)-p charge transfer happens at ~5.2 eV.[138,142]

In summary, visible light absorber BFO NPs can utilise a maximum solar light range than wider band gap materials. The defects and trap states in BFO NPs can be an interesting aspect for their effect in photocatalytic activity.

1.9 Catalysis

Catalysts play a crucial role in the production of almost every chemical product that is commercially available today. Whether it is the manufacturing of plastics, fuels, pharmaceuticals, or any other chemical product, the use of catalysts is almost always involved at some stage in the process.[143] A catalyst is a substance that accelerates a chemical reaction without being consumed in the process. It works by lowering the activation energy required for the reaction to occur, thus making the reaction happen more quickly and efficiently. In the context of chemical production, this means that catalysts can help manufacturers to produce more of a given product in a shorter amount of time, using less energy and fewer resources. The use of catalysts has become increasingly important in modern industrial processes, as it allows manufacturers to produce larger quantities of chemicals at a lower cost, while also reducing waste and improving the overall efficiency of the production process.[144]

Catalysts are also widely used in the development of new chemicals and materials, as they enable chemists to explore new reaction pathways and synthesize novel compounds that would be difficult or impossible to produce otherwise. Among the materials used as catalysts, semiconductor metal oxides are one of the most used due to their versatility and wide range of physical properties.[145]

1.9.1 Advanced oxidation processes (AOPs)

Frequently, it has been observed that certain pollutants are resistant to biological treatment due to their high chemical stability and/or strong resistance to complete mineralization. In such instances, it becomes imperative to implement reactive systems that are far more effective than those utilized in conventional purification processes.[145]

By recognizing the limitations of traditional treatment methods, we can leverage advanced reactive systems to successfully manage complex pollutants that would otherwise pose a significant threat to our environment. Only through the adoption of innovative purification techniques can we mitigate the impact of hazardous pollutants and ensure a sustainable future for generations to come.

Over the past decade, many research efforts have been devoted around the world to developing a new, more powerful, and very promising technique called Advanced Oxidation Processes (AOPs) for treating contaminants in drinking water and industrial effluents.[146] AOPs are defined as "near ambient temperature and pressure water treatment processes that involve generating hydroxyl radicals in sufficient quantity to purify water." Although it is claimed that other species are involved, the hydroxyl radical (OH•), which is unstable and quite reactive, appears to be the active species responsible for destroying contaminants in most cases.[144,147] Because OH• is unstable, it must be continuously generated "in situ" through chemical or photochemical reactions. The hydroxyl radical (OH•) is a potent, non-selective chemical oxidant that reacts very quickly with most organic compounds. It is the second strongest known oxidant after fluorine, with an oxidation potential of 2.8 V versus NHE (Normal Hydrogen Electrode). The hydroxyl radical can oxidize and mineralize almost any organic molecule, resulting in the production of inorganic ions and CO_2.[146]

In equations 1.10-1.12, the mechanisms for the oxidation of organic molecules by hydroxyl radical is the abstraction of hydrogen from organic molecules. This reaction generates organic radicals which by addition of molecular oxygen yield peroxyl radicals. These intermediates initiate thermal (chain) reactions of oxidative degradation, leading finally to carbon dioxide, water, and inorganic salts. Besides hydrogen abstraction, electron transfer to hydroxyl radicals constitutes another mechanism of oxidative degradation. Reaction combined with a subsequent proton transfer can hardly be differentiated.

$$OH^{\bullet} + RH \rightarrow H_2O + R^{\bullet} \tag{1.10}$$

$$R^{\bullet} + O_2 \rightarrow RO_2^{\bullet} \rightarrow degraded\,product \tag{1.11}$$

$$OH^{\bullet} + RX \rightarrow RX^{\bullet} \rightarrow OH^{-} \tag{1.12}$$

The reaction scheme clearly demonstrates that rate and efficiency of oxidative degradation processes, which are primarily based on the production and the reactivity of radical intermediates, depend on the energy needed in order to homolyse a given chemical bond, and to a large extent on the concentration of dissolved molecular oxygen.[144,147,148]

AOPs can be classified into two main groups: (1) Non-photochemical AOPs and (2) Photochemical AOPs. Non-photochemical AOPs include cavitation, Fenton, and Fenton like processes, ozonation at high pH, ozone/hydrogen peroxide, wet air oxidation etc.[144] Photochemical oxidation processes include (i) homogenous processes such as vacuum UV photolysis, UV/H_2O_2, UV/O_3, UV/O_3/H_2O_2, photo-Fenton, etc, and heterogeneous photocatalysis processes.[149]

1.9.2 Heterogeneous photocatalysis

Among the AOPs, heterogeneous photocatalytic process utilizing the near UV radiation to photo-excite a semiconductor catalyst in the presence of oxygen has received considerable attention as a promising method for degrading both aquatic and atmospheric organic contaminants.[148] This process involves the acceleration of photoreaction in the presence of semiconductor photocatalysts. The process is heterogeneous, because there are two active phases, solid and liquid. The heterogeneous photocatalysis is a complex sequence of reactions as shown by equations 1.13-1.21. The oxidizing pathway is not yet fully understood.

Photocatalysis differs from other AOPs because it employs low energy UV-A light, and reusable catalysts, and it does not require addition of any other strong oxidants. This process can also be carried out utilizing the near part of solar spectrum (wavelength shorter than 380 nm) what transforms it into a good option to be used at big scale. One of the major applications of heterogeneous catalysis is photocatalytic oxidation to achieve partial or total mineralisation of gas phase or liquid phase contaminants to benign substances. The oxidizing species generated in photocatalytic process are either bound hydroxyl radicals or free holes. Even though degradation begins with a partial degradation, the term photocatalytic degradation usually refers to complete photocatalytic oxidation or photo-mineralisation, essentially to CO_2, H_2O, NO_3^- , PO_4^{3-} and halide ions. The advantages of heterogeneous photocatalysis process over other conventional methods can be summarized as follows: (i) the process can be carried out under ambient condition (temperature and pressure); (ii) the process uses atmospheric oxygen as oxidant, no other expensive oxidizing chemical is required; (iii) the oxidant is strong and less selective which leads to complete mineralization of almost all organic pollutants in wastewater; (iv) this process is known as green technology because the degradation products (carbon dioxide, water and mineral acids) show moderate toxicity; (v) no residue of the original material remains and therefore no sludge requiring disposal to landfill is produced in this process; (vi) in addition, this process can be carried out at extremely low concentrations because the pollutants are strongly adsorbed on the surface of the catalyst, allowing sub part-per-million condition; (vii) the photocatalysts are cheap, non-hazardous, stable, biologically and chemically inert, insoluble under most conditions and reusable.[144,145,147,148] Summing up all these benefits and advantages, heterogeneous photocatalysis provides a cheap and effective alternative to clean water production and environmental remediation.

1.9.2.1 Photocatalysis

In the photocatalytic oxidation process, organic pollutants are destroyed in the presence of semiconductor photocatalysts (e.g., TiO_2, ZnO), an energetic light source, and an oxidizing agent such as oxygen. The first step in the heterogeneous photocatalysis of organic and inorganic compounds is the interaction of the semiconductor with light which results in the generation of electron-hole pairs in the semiconductor particles. When a semiconducting photocatalyst is illuminated with light, the energy of which is equal to or greater than the band-gap energy, light is absorbed by the semiconductor and the valence band electrons are excited to the conduction band, leaving a positive hole in the valence band.[144] [Figure 1.12 a]

The excited state conduction-band electrons and valence-band holes can then follow several pathways. The photoinduced electrons transfer to adsorbed organic or inorganic species or to the solvent resulting from the migration of electrons and holes to the semiconductor surface. The electron transfer process is more efficient, if the species are pre-adsorbed on the surface. While at the surface the semiconductor can donate electrons to reduce an electron acceptor (usually oxygen in an aerated solution) (*pathway C*), a hole can migrate to the surface where an electron from a donor species can combine with the surface hole oxidizing the donor species (*pathway D*). The probability and rate of the charge transfer processes for electrons and holes depends on the respective positions of the band edges for the conduction and valence bands and the redox potential levels of the adsorbed species. In competition with charge transfer to adsorbed species is electron and hole recombination. Recombination of the separated electron and hole can occur in the volume of the semiconductor particle (*pathway B*) or at the surface (*pathway A*) with the simultaneous release of heat.

It is generally admitted that photogenerated electrons can reduce molecular oxygen to $O_2^{\bullet-}$, which can be subsequently transformed into other chemical species, such as $HO_2^{\bullet}$, HO_2^- , H_2O_2, and possibly HO• radicals. These activated oxygen species may take part in the oxidation of the organic electron donor. On the other hand, photogenerated holes can oxidize the electron donor (also referred to as the "hole scavenger"), either via the formation of reactive species such as surface-bound HO• radicals or through direct reaction with adsorbed organic molecules. Together, these reactions can ultimately result in the complete photomineralization of the organic compounds to carbon dioxide, water, and mineral acids.[144,146,148]

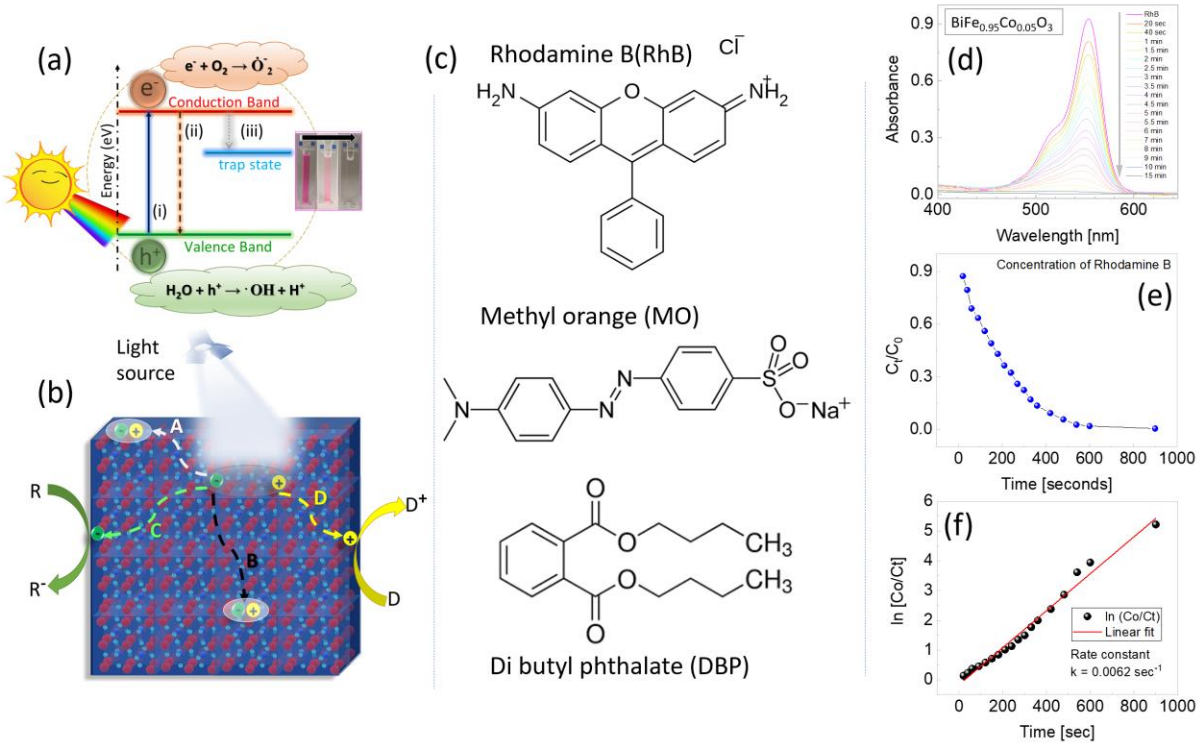

Figure 1.12: The schematic of photocatalysis © 2021 Nanoscale advances with permission (a),[150] The steps occurring during photocatalysis (b), The unwanted organic chemicals chosen to be degraded in this research via photocatalysis (c), The photodegradation of rhodamine B (RhB) dye using cobalt doped BFO NPs (d), The exponential decay of dye concentration in presence of photocatalyst (e), The reaction kinetics of first order photocatalytic reaction with rate constant (slope of the linear fit).(f)

In classical heterogeneous photocatalysis, the reaction itself occurs in the adsorbed phase and the overall process can be decomposed into these independent steps: (i) mass transfer of the reactants in the liquid phase to the surface of catalyst; (ii) adsorption of the reactants onto the photon activated catalyst surface (i.e. surface activation by photon energy occurs simultaneously in this step); (iii) photocatalysis reaction for the adsorbed phase on the catalyst surface; (iv) desorption of the products from the catalyst surface. There are two pathways through which OH radicals can be formed. The valence band hole ($^{+}h_{VB}$) can either react with the adsorbed water or the adsorbed hydroxyl groups (OH^-) on the semiconductor photocatalyst (SC) as shown by equations 1.13-1.15, respectively.[144,148]

To oxidize hydroxide ions or water, the oxidation potential for the reaction must lie above (i.e., be more negative than) the upper energy level position of the semiconductor valence band. It is generally accepted that oxygen plays an important role in photocatalysis. Oxygen can trap conduction band electrons to form the superoxide ion $O_2^{\bullet\,-}$. These superoxide ions can react with hydrogen ions (formed by water splitting), forming $HO_2^{\bullet}$. H_2O_2 could also be formed from $HO_2^{\bullet}$. The photogenerated hydrogen peroxide undergoes further decomposition to yield hydroxyl radicals.

$$SC + h\nu \rightarrow SC(e_{CB}^- + h_{VB}^+) \tag{1.13}$$

$$SC\ (h_{VB}^+) + H_2O_{ads} \rightarrow SC + HO_{ads}^{\bullet} + H^+ \tag{1.14}$$

$$SC\ (h_{VB}^+) + HO_{ads}^- \rightarrow SC + HO_{ads}^{\bullet} \tag{1.15}$$

$$SC(e_{CB}^-) + O_{2ads} \rightarrow SC + O_2^{\bullet -} \tag{1.16}$$

$$O_2^{\bullet -} + H^+ \rightarrow HO_2^{\bullet} \tag{1.17}$$

$$SC(e_{CB}^-) + O_2^{\bullet -} + 2H^+ \rightarrow H_2O_2 + SC \tag{1.18}$$

$$H_2O_2 + h\nu \rightarrow 2OH^{\bullet} \tag{1.19}$$

$$H_2O_2 + O_2^{\bullet} \rightarrow OH^{\bullet} + O_2 + OH^- \tag{1.20}$$

$$H_2O_2 + SC(e_{CB}^-) \rightarrow OH^{\bullet} + OH^- + SC \tag{1.21}$$

It should be mentioned that it takes three electrons to produce one hydroxyl radical through the above pathway, but it takes only one hole to produce a hydroxyl radical from adsorbed water or hydroxyl group. Therefore, most of the hydroxyl radicals are generated through hole reactions. Nonetheless, the presence of electron scavengers (adsorbed oxygen) is vital for prolonging the recombination and successful functioning of the photocatalysis process. The presence of oxygen prevents the recombination of electron-hole pairs, while allowing the formation of superoxide radicals.[148] On the other hand, without the presence of water molecules, the highly reactive hydroxyl radicals could not be formed and impede the photodegradation of liquid phase organics. This was evidenced from a few reports that the photocatalytic reaction cannot proceed in the absence of water molecules.[144]

The hydroxyl radical generated from the oxidation of adsorbed water where it is adsorbed as OH^- is the primary oxidant for the degradation of organic pollutants. Oxidation of organic compounds proceeds through a number of free radical reactions, producing a large number of intermediates, which in turn, undergo oxidative cleavage, ultimately resulting in the formation of carbon dioxide, water, and inorganic ions. In the photocatalytic degradation of pollutants, when the reduction process of oxygen and the oxidation of pollutants do not advance simultaneously, there is an electron accumulation in the CB, thereby causing an increase in the rate of recombination of electrons from the CB and holes from the VB.[145]

Photocalysts and their requirement for photocatalysis

The ability of a semiconductor to undergo photoinduced charge carrier transfer to adsorbed species on its surface is governed by the band energy positions of the semiconductor and the redox potentials of the adsorbed species. The energy level at the bottom of the conduction band is actually the reduction potential of photoelectrons and the energy level at the top of the valence band determines the oxidizing ability of photoholes, each value reflecting the ability of the system to promote reductions and oxidations, respectively. The flatband potential which is fixed by the nature of the material and the proton exchange equilibria, determines the energy of the two charge carriers at the interface. From a thermodynamic point of view, adsorbed couples can be reduced photocatalytically by conduction band electrons if they have redox potentials more positive than the flat band potential of the conduction band and can be oxidized by valence band holes if they have redox potentials more negative than the flatband potential of the valence band. However, the primary criteria to get a good semiconductor photocatalysts for organic compound degradation are that the redox potential of the H_2O/ $OH^{\bullet}$ ($HO^- \rightarrow OH^{\bullet} + e^-$, E_o = -2.8 V) couple lies within the band gap domain of the material and that they are stable over prolonged periods of time. An ideal photocatalyst should possess the following characteristics: (i) photoactive; (ii) can utilize visible and/or near-UV light; (iii) biologically and chemically inert; (iv) photostable (not prone to photoanodic corrosion); (v) inexpensive and (vi) non-toxic. The bulk electronic structure of the semiconductors only changes faintly with pressure and temperature, but the pH of the electrolyte used during the study influences the band edge position of the various semiconductors compared to the redox potentials for the adsorbate.[151,152]

In view of the utilization of energy (solar or UV light), semiconductors with lower band gap energy are more desired; however, the low band gap semiconductors usually suffer from serious stability problems. Such semiconductors show a tendency towards photoanodic corrosion. In the case of a p-type semiconductor, the band gaps are too small, and most suffer from serious stability problems. As a result, p-type semiconductors are rarely used in semiconductor photocatalysis. It is generally found that only n-type semiconducting oxides are stable towards photoanodic corrosion, although such semiconductors usually have so large bandgaps that they can only absorb UV light.[148] Among the semiconductors some oxide and chalcogenides have enough band gap energies to be excited by UV or visible light, and the redox potentials of the edges of the valence band and conduction band can promote a series of oxidative and reductive reaction. Nonetheless, some of the candidates do not have long term stability in aqueous media. For example, the metal sulphide semiconductors, especially cadmium sulphide

(CdS) and zinc sulphide (ZnS), are unstable since they undergo photoanodic corrosion, while hematite (α-Fe_2O_3), although absorptive in the visible region, is not a suitable semiconductor because of photocathodic corrosion. Tungsten oxide (WO_3) can also be activated in the visible region, but it is generally less photocatalytically active than TiO_2. However, TiO_2 is so far the most useful photocatalyst for widespread environmental application, owing to its outstanding optical and electronic properties, chemical stability, non-toxicity and low cost. TiO_2 exists mainly in three different crystalline forms: rutile (tetragonal), anatase (tetragonal) and brookite (orthorhombic). Rutile is the thermodynamically stable form, whereas anatase and brookite are metastable and are readily transformed to the thermodynamically stable rutile upon calcination at temperatures exceeding ~ 600 °C.

Famous photocatalysts in the market are TiO_2, Fe_2O_3, ZnO, $BiVO_4$, $BiMnO_4$, Bi_2WO_6, and Nb_2O_5, which are not ideal candidate for photocatalysis due to their wider band gap, fast recombination of charge carriers, instability, and non-selectivity.[145]

1.9.3 Piezo- and ferro- photocatalysis

The very popular TiO_2 is a wide bandgap semiconductor that absorbs ultraviolet radiation and is a prototypical photocatalyst for water oxidation and can generate oxygen. However due to its small effect on driving the hydrogen evolution reaction it is typically used with cocatalysts such as platinum to increase the rate of hydrogen production but as we know platinum is quite an expensive metal and it corrodes also.

Hindrances to improving the efficiency of photocatalytic water splitting lie in the recombination of photogenerated electron-hole pairs, as well as the back reaction of intermediate species, which serve as the rate-limiting parameters for surface redox reactions.[148] However, internal electric fields can mitigate some of these effects, inducing charge carrier separation and improving photochemical reactivity.

Ferroelectric fields can also modulate the activity of nearby catalytic layers by deforming their electronic band structures. Additionally, ferroelectrics exhibit pyroelectric and piezoelectric properties, making them potential candidates for catalysis powered not only by solar energy, but also by thermal and mechanical energies. Ferroelectric materials have already been implemented as charge sources in a variety of catalytic processes, from water splitting to the decomposition of poisonous nitrogen oxide, water remediation, disinfection, and dye degradation.[153–157] Moreover, ferroelectric materials possess distinct surface states that spur chemical activities between oppositely polarized surfaces. This allows for direct exploitation of ferroelectric materials in catalytic-driven reactions, whereby periodic modification of polarization by temperature, pressure, piezoelectricity, or electric field enables the tuning of surface chemical activity needed for the chemical reaction of interest.

The unique tunability of ferroelectric surfaces distinguishes them from typical catalytic materials with flat surfaces, which require optimum adsorbent surface interactions as determined by the Sabatier principle.[158] If the interaction is too weak, the adsorbate will not stick to the catalyst surface, and if it is too strong, the product of the reaction will not dissolve and will instead poison the surface.

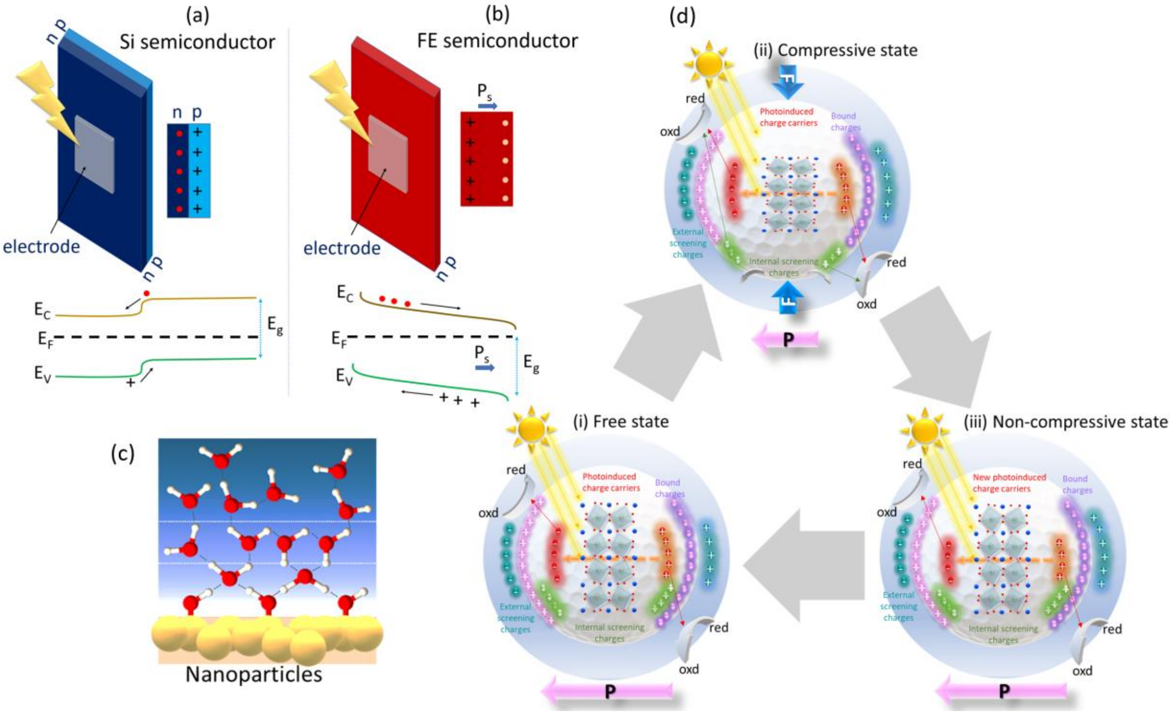

Figure 1.13: Schematic of the photovoltaic effect mechanism in a conventional semiconductor and a ferroelectric semiconductor with induced band-bending. (a-b), The adsorbed water molecules on the surface of the ferrocatalysts (c), the schematic of piezophotocatalysis in a ferrocatalyst. (d) [for d, © 2022 Advanced Functional Materials with permission][46]

This principle is graphically represented by the volcano plot [Figure 1.14d], which plots the reaction rate or activity against the heat and adsorption of reactants on the catalyst surface. However, this approach restricts the maximum activity of catalytic processes due to the competing nature of adsorption. The situation drastically changes when ferroelectric surfaces are used, because by changing the ferroelectric polarization orientation, one can cycle between states with different adsorbate-catalyst interaction strengths. This is highly beneficial since it enables one to move beyond the limitations imposed by the Sabatier principle, which is based on a single optimized interaction strength. By periodically enhancing the adsorption and desorption processes through switching the ferroelectric polarization orientation, the overall catalytic activity can be greatly improved.[157]

Kalinin et al proposed a revolutionary approach to exploring cyclic switching between polarization states in ferroelectric materials.[159] They envisioned utilizing one polarization state that exhibits strong adsorption and dissociation properties for reactant molecules while the opposite state exhibits strong desorption properties for catalytic products. In another study, Spaldin calculated the adsorption energies of water molecules on neutral and charged iron oxide and bismuth oxide-terminated bismuth ferrite surfaces.[160] The results of their study showed that water adsorption on both charged terminations proceeds by dissociation and subsequent desorption of ions, hindering the screening while it says in a molecular state in the case of neutral surfaces. This enabled them to investigate catalytic processes for water splitting through the cyclic reversal of polarization direction during which exposed charged and neutral surfaces undergo dissociative and molecular adsorption, respectively. In ferroelectric based catalysts internal and external both type of screening charges play role differently.

Internal Screening mechanism

In ferroelectrics, the internal screening of polarization can be achieved through the redistribution of mobile charge carriers and charged defects in the vicinity of surfaces and interfaces.[161] This process results in the creation of surface dipoles and subsequent band bending. For instance, when a surface has a negative bound polarization charge, electrons will be depleted, leading to the formation of a positively charged depletion region with upward bending. Conversely, surfaces with positive bound polarization charge will be screened by the accumulation of electrons, causing downward bending.[162] Moreover, ferroelectric crystal structures can contain various types of defects. One of the most common defects found in perovskite oxides are oxygen vacancies. These vacancies are present in the electronic structure of material as defect donor labels within the bandgap located below the conduction band, which results in n-type semiconductor behaviour. Importantly, ionized oxygen vacancies bear positive charges, and their location within the material can be manipulated by the application of an electric field. Therefore, they are often considered as active screening agents of ferroelectric polarization. Many studies have observed screening by oxygen vacancies using techniques such as scanning tunnelling electron microscopy and electron energy loss spectroscopy. However, it is crucial to note that oxygen vacancies have limited mobility at room temperature and therefore have a finite capacity to compensate for polarization switching in PFM experiments.

External screening by Adsorbates

Even when a ferroelectric is split into domains of opposite polarity, the depolarizing field can be further reduced by the absorption of atmospheric adsorbates. In ambient conditions, polar molecules such as hydroxide groups or ionic species that are adsorbed on the surface can modify the chemical boundary conditions and consequently influence the distribution of polarization in the bulk. Among all possible molecules available in the atmosphere, water molecules play the most critical role in the generation of screening adsorbates due to two main factors. Firstly, water is itself a dipolar molecule, which is able to align with stray ferroelectric fields. Secondly, the magnitude of stray electric field and generated surface potential produced by uncompensated polarization charges in archetypal ferroelectrics is sufficient to cause water splitting and trigger water dissociation on charged species. Thus, water plays an important role in the screening process.

Ferroelectric surfaces possess a unique characteristic wherein they can be internally screened to a certain extent by electron and hole localization from the conduction and valence bands, respectively. [163]This results in electrochemically active surfaces that can undergo reduction and oxidation reactions. Along with molecular water and hydroxyls, these electrochemical reactions lead to the formation of more complex chemical species at the solid-vapor interface.

1.9.4 Electrocatalysis

The electrolysis process principally was introduced in 1789 AD by Van Troostwijk and Deiman in Europe.[164] It is an electrochemical process of water splitting to oxygen and hydrogen induced by a minimum thermodynamic potential (theoretically 1.23 V). Nevertheless, the required operating cell voltage is significantly higher than the theoretical thermodynamic potential due to excess energy that is required to overcome the electrolyte resistance and kinetic limitations in the form of so called overpotentials.[164]

$$4H_2O + 4e^- \rightarrow 2H_2 + 4OH^- \tag{1.22}$$

$$4OH^- \rightarrow O_2 + 4e^- + 2H_2O \tag{1.23}$$

$$4H^+ + 4e^- \rightarrow 2H_2 \tag{1.24}$$

$$2H_2O \rightarrow 4H^+ + 4e^- + O_2 \tag{1.25}$$

Equations 1.22 and 1.23, show the catalytic half-cell reactions occurring in alkaline and equations 1.24 and 1.25 show is acidic media. The kinetic of both hydrogen evolution reaction (HER) and oxygen evolution reaction (OER), strongly depends on the materials used as electrocatalysts. Generally, the state-of-the-art catalysts are Pt-based and other precious metal-based oxides (Ir, Ru) for HER and OER, respectively.[165–167] In this study, the Me-N-C catalysts were investigated for water splitting reactions with different approaches to replace the precious catalysts. In the following sections, the most important steps regarding preparation of Me-N-C catalysts, possible active site formation/determination and catalyst optimization considering both reactions (HER and OER) will be discussed.

Mechanistic understanding of HER

The HER is composed of elemental reaction steps and is fundamentally described in two ways based on electrolyte solution, water reduction (alkaline) and hydronium ion reduction (acidic).

$$H_2O + e^- \rightarrow H_{ads} + 2OH^- \tag{1.26}$$

$$H_2O + H_{ads} + e^- \rightarrow H_2 \tag{1.27}$$

$$H_{ads} + H_{ads} \rightarrow H_2 \tag{1.28}$$

$$\eta = a + b\,(\log j) \tag{1.29}$$

The Volmer step represents the initial step for the hydrogen production and describes the adsorption of hydrogen on the electrodes surface (equation 1.26).[168,169] Thereafter, the reaction path might involve the Heyrovsky or Tafel step for H_{ads} recombination and H_2 desorption (equation 1.27 and 1.28).[168,169] In order to investigate the reaction mechanism, several techniques can be applied such as Tafel analysis, AC impedance spectroscopy and potential step charging.[170,171] Tafel analysis results in two important parameters, namely exchange current density and Tafel slope based upon the equation 1.29. The term η is the overpotential, which is the difference between the formal electrode potential of the reaction and the standard potential. Empirically the equation is reported as Tafel relation, where the Tafel slope can be obtained by plotting overpotential (η) with log(j).[172]

The hydrogen evolution reaction includes adsorption and desorption of hydrogen atoms on the active site. Therefore, a suitable catalyst should bond to the reaction intermediates neither too strong nor too weak, following on the Sabatier's principle.[158] The free energy of hydrogen adsorption (ΔGH) is defined as an appropriate descriptor for catalytic activities. The influence of the adsorption energy on the reaction rate can be expressed with a volcano plot, as a function of the exchange current density (as an activity descriptor) obtained from Tafel slope extrapolation. It should be noted that these fundamental studies were reported for single crystal metals in the steady-state conditions.

1.9.4.1 Active sites in electrocatalysis

The concept of "active sites" in heterogeneous catalysis is attributed to Taylor.[173] He suggested that the concentration of sites, where rate-determining catalytic reaction steps occur is much smaller than the total concentration of available surface sites. The correlation of catalyst surface structure with rates of different reactions indicated that the nature of the active site where bond breaking occurs, for example, is different for different chemical bonds. H_2 may dissociate at a single metal atom, or at step and kink sites on metal surfaces while it may not readily dissociate on a smooth, highly coordinated (111) crystal face of platinum.[174]

Paul Sabatier (1854–1941)[175] stated that, in order for a catalyst (in his case, often a "finely divided metal") to work, the adsorbent should neither be adsorbed too strongly nor too weakly, (1912 Nobel Prize in Chemistry). Linus Pauling (1901–1994) added that the catalyst (in his case, an enzyme) must bind the transition state more tightly than the substrate. Yet, before we begin to analyse the active site in a bottom-up manner, we must be aware of the multidimensional factors across multiple scales that can contribute to the observed activity of the 'active site'. Heterogeneous catalysts often involve porosity on the micrometre to nanometre scale and are subject to phase and morphological transformations over a huge time range from as long as years to as short as sub-milliseconds.

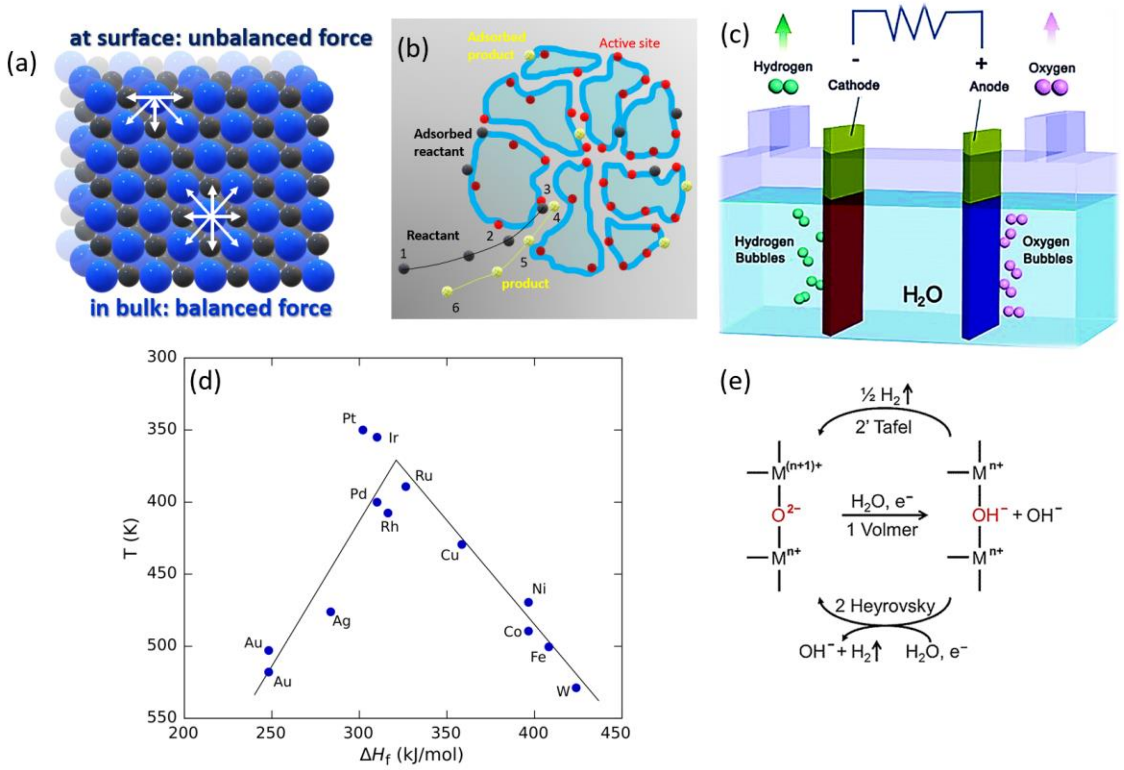

Figure 1.14: The schematic of difference between the surface and the bulk of nanoparticles where in the former forces are unbalanced which makes the surface highly active (a). The scheme for the presence of a limited number of active sites on the surface of catalysts (b). The schematic representation of hydrogen evolution reaction (c) [© 2015 Chem. Soc. Rev., with permission] [176] *, The volcano plot from the Sabatier principle (for the decomposition of formic acid on transition metals) (d)*[158]*, and the mechanisms involved in hydrogen evolution reaction (e).*

Surfaces reconstruct, while reactants and intermediates can be locally depleted. To define an active site in heterogeneous catalysis is to understand these complexities and their dynamic variability in various reaction environments, be they liquid phase or gas phase, and as a function of reaction temperature and pressure. Hugh Stott Taylor (1890–1974) was one of the first to allude to this complexity and variability in active sites.[177,178] He realized that the entire surface of a metal nanoparticle did not participate in a catalytic reaction but, rather, certain active centres. In doing so, he defined what is now termed the ‘Taylor ratio’, which relates the fraction of active sites to the total exposed surface, and is, hence, always less than 1.[179] There are many different kinds of heterogeneous catalysts, and they can contain many different types of surfaces, and, hence, also active sites. Bronsted acid (proton donating) and Lewis’s acid (electron withdrawing) are the sites that lead to catalytic activity in solid acid catalysts. The formation or breaking of a covalent bond is often involved in these two types of catalysis, and these two types of active sites are intimately linked.[173]

It is important to note that the active site can technically be located at a single atom for supported metal nanoparticles, for solid acids and for atomically dispersed catalysts. This final type of active sites is often also termed single-atom catalysts, a term that is somewhat under scrutiny, but refers to heterogeneous catalysts with atomically dispersed metal atoms.[173,180,181] Nevertheless, the workings of an active site would be very different were it not surrounded by other atoms; the same 'active' atomic site may even be completely inactive, depending on the geometrical environment. This fact is externalized in different ways for the different classes of catalysts as, inherently, different types of bonds and length scales and, thus, geometries are involved in the different classes. Geometric and electronic effects on the active site are closely correlated but can be separated based on the Bronsted–Evans–Polanyi relationships.[173]

Catalysis exhibits a fascinating phenomenon known as structure sensitivity, where not all atoms in a catalytic nanoparticle have the same catalytic activity. Michel Boudart observed that reactions can either be 'facile' or 'demanding,' depending on whether the turnover frequency (TOF) is independent or dependent on nanoparticle size.[147] This can be explained by the preferential cleavage of σ-bonds at highly uncoordinated atoms and preferential cleavage of π-bonds at defect sites. The TOF can vary depending on the class of reaction and the size of the nanoparticle. The assumption that all exposed surface area is equally active is clearly erroneous, and there is still much to be explained in this field. The Langmuir adsorption isotherm and the Hinshelwood kinetic formalism, based on ideal surfaces with equivalent adsorption sites and randomly mixed adsorbates that do not interact, are still used to describe catalytic reactions, but it is becoming increasingly clear that this picture is much more complex than previously thought.[147,182]

Throughout the history of research aimed at identifying and comprehending the active site in heterogeneous catalysis, two main schools of thought have emerged. The first is the Irving Langmuir (1881-1957) school, which relies on the assumption of a continuous monolayer of adsorbate molecules surrounding a homogeneous solid surface. Langmuir's school is the main driver of surface science and assumes a 'polyocracy' of equivalent surface sites.[182] In contrast, the Hugh Stott Taylor (1890-1974) school recognizes the higher degree of complexity involved in surfaces influenced by crystalline anisotropy, surface defects, and various surface compositions. Taylor's active sites are 'oligarchs,' with only a few dominant sites and the rest of the surface covered with spectator species.[173] These two schools of thought, while differing, are not necessarily opposing and have allowed the scientific community to group together technical developments and increase our understanding of the active site. However, neither school provides a complete picture of the complexity involved. Moving forward, it is necessary to develop new concepts in catalysis that consider the limitations of both schools of thought.

1.10 Doping and Defects

Single point defects refer to the presence of impurities, vacancies, or interstitial atoms at a single lattice site in the crystal structure.[183] These defects can affect the local electric field and alter the polarization of the material. The presence of single point defects in materials can have significant effects on their properties, particularly their ferroelectric and magnetic behaviors. Specifically, cation anti-site defects have been found to induce polar displacements in $SrTiO_3$, resulting in off-centering within the coordination polyhedron due to a bonding optimization of cations occupying too large sites. Similar effects have been observed in $EuBaTi_2O_6$, where oxygen vacancies lead to Ti off-centering and the emergence of ferroelectric-ferromagnetic multiferroic properties.[183] Jahn-Teller distortions in perovskite oxides have also been shown to induce polar structures around defects. For example, stoichiometric $LaMnO_3$ exhibits a cooperative Jahn-Teller distortion that is altered by oxygen vacancies, leading to a net polarization around the defect.[184]

The band gap energy can also be affected by defects and oxygen vacancies, which can cause a shift in the energy levels and modify the electronic properties of the material. For example, the presence of oxygen vacancies can create additional energy levels in the band structure of BFO, leading to a decrease in the band gap energy and an increase in the absorption of visible light. Transition-metal defects of groups VII through XI (except Ag) can introduce deep impurity levels in the band gap region, which enables band gap tuning for optical applications.

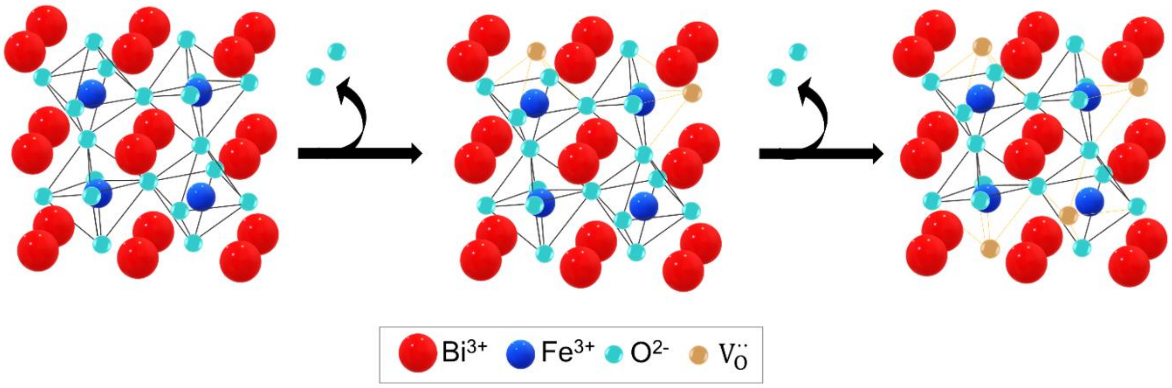

Figure 1.15: Creation of oxygen vacancies in BFO NPs upon doping aliovalent ions. The type of dopant decides number of oxygen vacancies in BFO NPs. In spite of oxygen vacancies, the crustal structure of BFO retains till at least 5 mol% dopant concentration.

In addition to changes in the band gap energy, defects and oxygen vacancies can also affect other light absorption and emission features of BFO. For instance, the presence of oxygen vacancies can lead to the formation of localized states within the band gap, which can trap excitons and cause a decrease in the luminescence efficiency. Furthermore, defects can also affect the radiative recombination rates, which can alter the emission spectrum of the material. In conclusion, defects and oxygen vacancies play a crucial role in determining the optical properties of BFO.

Ionic engineering or doping or substitution of host from a dopant ion is a classic way to alter the properties of pristine material based on distortion in crystal structure and creation of defects. A huge number of doping studies have already been carried out in BFO.[185,186] Doping of BFO often gives a beneficial effect on properties, such as an increase in dielectric constant, the decrease in the leakage current and the destruction of the space modulated spin structure. Rare earth cations are considered the most suitable substitutes for Bi^{3+} ions as they can easily be accommodated in the structure. Partial substitution of Bi^{3+} ions by lanthanides improve the ferroelectric properties and magnetization of BFO. Aside substitution results in a canted spin cycloid and reportedly increases magneto-electric interaction.

Perovskites are known to be structurally rather flexible, accepting tolerance factors in a range of roughly $0.75 < t < 1$. Therefore, the tolerance factor for BFO should be within t = 0.94–0.99. The BFO tolerance factor smaller than one means that ion sizes different from Fe^{+3} and Bi^{+3} are not necessarily destabilizing to the structure and could, to some extent, even be favourable. The effect on tolerance factor upon co-doping in BFO NPs, is discussed in Chapter 4. Once the correct oxidation states are assigned, the site preference between A- and B-site substitution in BFO can be reliably estimated from differences in the ionic radii between targeted host and dopant ions. Highly oxidized cations in oxidation states of +3 and above prefer the B site for most of the periodic table until the sixth period, i.e., up to cations that are almost as large as Bi^{+3} itself. For lower oxidation states, B-site preference is limited to a few very light elements (Li, Be, and Mg). However, the fact that metals in low oxidation states can favour the B site at all might be surprising and against common perception, e.g., the (small) B-site preference of Li^+.[185,186] The fact that alkaline-earth metal +2 doping results in a smaller lattice compared to alkali metal +1 doping within the same period.[185,186] On the other hand, there are secondary effects due to oxidation (p-type doping) or reduction (n-type doping) of iron centers that significantly change the oxygen octahedra. As a result, the observed lattice relaxation cannot be directly deduced from ionic radii differences. Na^+ exhibits the smallest mismatch of all alkali metals on the A site, however, K^+ and Rb^+ show smaller deviation from the pristine lattice volume.

For alkali and alkaline-earth metals, the oxidation states are +1 and +2, respectively. Consequently, we obtain desired p-type doped semiconductors with one and two holes in the BFO band structure upon such doping. Alkali and alkaline-earth metals as the elements that are commonly used to dope semiconductors with holes. When small amounts of Zn, Ag, or Pb are added as dopants to BFO, they can also create "holes" in the material, which leads to the creation of p-type doped semiconductors.[185,186]

Usually oxygen vacancies create n-type doping as shown in Figure 1.15. On the other hand, cation vacancies create p-type doping. In literature, p-type doping by substitutional cation doping is challenging and has so far only been reported for Ca^{+2} and Ba^{+2}. The different possibilities with respect to doping site and oxidation state allow us to tune the magnetism that is introduced for each doping type. p-type doping can be accompanied by 1 μB to 4 μB per dopant. Isovalent doping was observed with resulting magnetic moments ranging from 0 μB to 5 μB. Finally, n-type doping can be accompanied by 4 μB to 6 μB per dopant (dopant per unit cell).[187]

The Bi-site substitutions by ions with smaller ionic radius would induce more buckling in the Fe–O–Fe bond angle accompanying a smaller tolerance factor which can lead to a more insulating character. Large deviations in the tolerance factor from “1” by substitutions of too small Bi-site ions would make the chemical structure unstable. Since most lanthanide rare-earth trivalent ions have a smaller ionic radius than the Bi^{3+} ion, the substitutions are expected to bring about a more insulating behaviour in BFO. Experimental estimation of the bond angle bending can be made through detection of a superlattice peak indicative of the extent of cooperative tilt of antiferrodistortive octahedra.

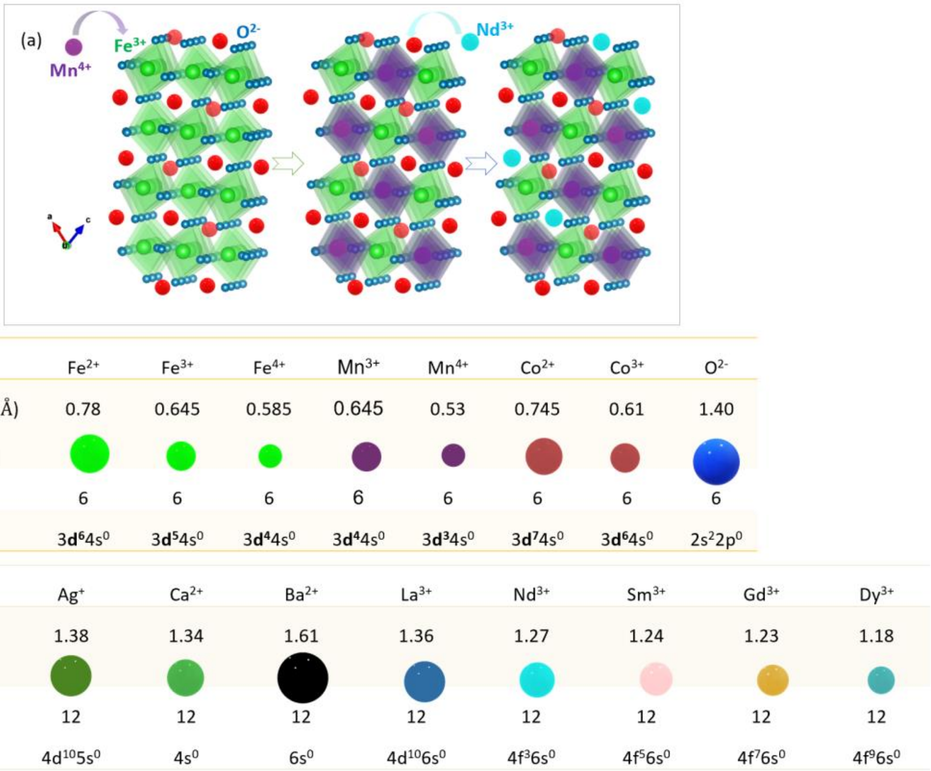

(b) Ions	Fe^{2+}	Fe^{3+}	Fe^{4+}	Mn^{3+}	Mn^{4+}	Co^{2+}	Co^{3+}	O^{2-}
Ionic radius (Å)	0.78	0.645	0.585	0.645	0.53	0.745	0.61	1.40
[High spin]	●	●	●	●	●	●	●	●
C. N.	6	6	6	6	6	6	6	6
O. E. C.	$3d^64s^0$	$3d^54s^0$	$3d^44s^0$	$3d^44s^0$	$3d^34s^0$	$3d^74s^0$	$3d^64s^0$	$2s^22p^0$

Ions (c)	Bi^{3+}	Ag^{+}	Ca^{2+}	Ba^{2+}	La^{3+}	Nd^{3+}	Sm^{3+}	Gd^{3+}	Dy^{3+}
Ionic radius (Å)	1.45	1.38	1.34	1.61	1.36	1.27	1.24	1.23	1.18
	●	●	●	●	●	●	●	●	●
C. N.	12	12	12	12	12	12	12	12	12
O. E. C.	$6s^26p^0$	$4d^{10}5s^0$	$4s^0$	$6s^0$	$4d^{10}6s^0$	$4f^36s^0$	$4f^56s^0$	$4f^76s^0$	$4f^96s^0$

Figure 1.16: Scheme for Mn doping at Fe-site, and further co-doping with trivalent Nd ion at Bi-site (a). The ionic radii of dopants for Fe-site as per the co-ordination number (C. N.), and their outermost electronic configuration (O. E. C.) (b). The ionic radii of dopants at Bi-site as per their coordination number, and their outermost electronic configuration (c).

1.10.1 Kröger-Vink notation

The Kröger-Vink notation was initially introduced by Helmut Kröger and Frank Albert Vink in 1955 to describe the occurrence of point defects within crystal structures.[188] Point defects represent deviations from the perfect crystal lattice structure, resulting from either the presence of extra atoms (interstitials) or missing atoms (vacancies). The Kröger-Vink notation presents a straightforward approach to symbolize point defects in crystals. It uses the host cation or anion symbol, followed by the defect symbol and a corresponding subscript that indicates the number of defects. For instance, a single cation vacancy could be presented as "M_{vac}," where "M" denotes the host cation and "vac" represents a vacancy.

In an oxide the metal ions on the regular lattice positions are thus written M_M, where the subscript thus describes the type of structure site which is occupied. Correspondingly, the oxide ions on normal lattice sites are written O_O. These are not defects, they are the ideal structural elements. The native point defects in an oxide include M and O vacancies and M and O interstitial atoms or ions. Vacancies in are denoted by “V” with a subscript M or O referring to vacant metal or oxygen sites, respectively: V_O oxygen vacancy, V_M metal vacancy, Interstitial sites are described with a subscript "i". Interstitials are thus written O_i to an oxygen interstitial, and M_i for metal interstitial.

Charge notation is done like this, for positive: point (•), negative: dash (′), and for neutral: cross (**x**). A system can be represented by S_P^C, where S is the species, P is position in the crystal, and C is the charge relative to the perfect crystal. The effective charge of a species is the actual charge of the species minus the actual charge that the ideal perfect reference structure would have had in the same structural element.

Using Kröger-Vink notation it is possible to estimate on substituting Bi^{3+} with divalent cation like Ca^{2+} ions, point defects with an effective negative charge, $2\mathrm{Ca}_{\mathrm{Bi}}^{'}$ are created. In order to preserve overall charge neutrality, these defects are balanced by defects of effective positive charge which are likely to be oxygen vacancies. An alternative charge compensation possibility involving creation of interstitial Ca ions, $\mathrm{Ca}_{\mathrm{i}}^{\bullet\bullet}$ is considered unlikely in the perovskite structure of BFO.

Based on Kröger-Vink notation, let's understand the creation of vacancies in doped BFO. When Mn^{4+} is a dopant at the Fe site, this would enhance the conductivity of BFO, due to the generation of electrons for overall charge balance, as shown in Eq. 1.30.

$$MnO_2 + Bi_2O_3 \rightarrow Mn_{Fe}^{\cdot} + e^{'} + Bi_{Bi}^{x} + 5O_O^{x} \tag{1.30}$$

$$Ag_2O + Fe_2O_3 \rightarrow 2Ag_{Bi}^{''} + 2V_O^{\cdot\cdot} + 2Fe_{Fe}^{x} + 4O_O^{x} \tag{1.31}$$

$$2CaO + Fe_2O_3 \rightarrow 2Ca_{Bi}^{'} + V_O^{\cdot\cdot} + 2Fe_{Fe}^{x} + 5O_O^{x} \tag{1.32}$$

$$La_2O_3 + Fe_2O_3 \rightarrow 2La_{Bi}^{x} + 2Fe_{Fe}^{x} + 6O_O^{x} \tag{1.33}$$

Upon doping of the monovalent ion Ag^{+} and divalent ion Ca^{2+} at the Bi site, oxygen vacancies are created to maintain overall charge neutrality in the doped composition, as shown in Eq. 1.31 and Eq. 1.32. However, doping with trivalent La^{3+} does not generate oxygen vacancies or charges, as shown in Eq. 1.33. This clearly shows the alteration of oxygen vacancy concentration upon multivalent doping in BFO NPs, which can induce several functionalities in the system.

The effect of oxygen vacancy concentration caused by such aliovalent dopants can bring new functionalities in BFO NPs.

1.10.2 Nanoparticles and graphene oxide (GO) composite

Graphene is a carbon allotrope comprising of a densely packed atomically thin layer of sp^2 hybridized carbon atoms in a honeycomb crystal lattice. This precisely two-dimensional material exhibits unique high crystal and electronic quality and has emerged as a promising new nanomaterial for a variety of exciting applications despite its short history. The history of graphene oxide (GO) extends over many decades, even back to the earliest studies involving the chemistry of graphite. GO has been mainly produced by different variations of Brodie, Staudenmaier, and Hummer’s methods that involve the oxidation of graphite in the presence of strong acids (nitric acid or its mixture with sulfuric acid) and oxidants ($KMnO_4$, $KClO_3$, $NaNO_3$).[189]

The oxygen functionalities in the basal plane of GO alter the van der Waals interactions between the layers and render them hydrophilic, thus greatly facilitating the hydration and exfoliation of GO in aqueous media. Moreover, in a recent study of the surface charge (zeta potential) of the as-prepared GO sheets, it has been shown that GO sheets acquire negative charges when dispersed in water, apparently because of the dissociation of carboxylic acid and phenolic hydroxyl groups.[190,191] As a result, GO readily forms stable colloidal dispersions in water, which is attributed to both the electrostatic repulsion and hydrophilicity of GO sheets.[191] Thus, complete exfoliation of GO can be achieved by sonication and by stirring the water–GO mixture for a sufficient time, to produce aqueous suspensions of graphene oxide sheets.

The binding or loading of metal and metal oxide NPs onto graphene for the preparation of graphene-based nanocomposites is generally realized in two different ways: post immobilization (ex situ hybridization) or in situ binding (in situ crystallization). Post immobilization involves mixing separate solutions of graphene nanosheets and pre-synthesized NPs. Before mixing, the NPs and/or graphene sheets are surface functionalized to enhance the processability of the resulting products. The conjugated graphene sheets can readily be functionalized by non-covalent p–p stacking or covalent C–C coupling reactions.[190,191] The functionalization of graphene and/or NPs significantly enhances their solubility and hence broadens the opportunities for the preparation of graphene-based composites. However, post immobilization may suffer from low density and non-uniform coverage of nanostructures by graphene sheets.

GO has unique properties that can enhance the performance of metal oxide in catalysis. For instance, GO is highly conductive, allowing for efficient electron transfer between the metal oxide and the reaction intermediates. This improved electron transfer can facilitate the activation of reactants and intermediates, leading to improved catalytic activity. Furthermore, GO exhibits a high surface area and can act as a support for the metal oxide/perovskite NPs, providing a stable and well-dispersed catalyst. The presence of GO in the nanocomposite can also improve the adsorption/desorption of reactants, leading to enhanced selectivity towards specific reactions.

2 Materials and Techniques

2.1 Materials

For the synthesis of BFO NPs, bismuth nitrate $Bi(NO_3)_3{\cdot}5H_2O$ (≥ 98%), iron nitrate $Fe(NO_3)_3{\cdot}9H_2O$ (≥ 98%), tartaric acid $C_4H_6O_6$ (≥ 99%), and nitric acid HNO_3 (65%) from Sigma Aldrich were used. For doped-BFO NPs, manganese acetate $Mn(CH_3COO)_2{\cdot}4H_2O$ (≥ 99%), cobalt nitrate $Co(NO_3)_2.6H_2O$ (99.999%), and barium hydroxide $Ba(OH)_2{\cdot}8H_2O$ (99.995 %), and calcium nitrate $Ca(NO_3)_2{\cdot}4H_2O$ (≥ 99%), and silver nitrate $AgNO_3$ (≥ 99%), and lanthanum nitrate $La(NO_3)_3.6H_2O$ (99.999%), and neodymium nitrate $Nd(NO_3)_3{\cdot}6H_2O$ (≥ 99%), and gadolinium nitrate $Gd(NO_3)_3{\cdot}6H_2O$ (99.9 %), and samarium nitrate $Sm(NO_3)_3{\cdot}xH_2O$ (99.9%), and dysprosium nitrate $Dy(NO_3)_3{\cdot}xH_2O$ (99.9%), from Sigma Aldrich were used.

The single doped and co-doped BFO NPs are synthesized using “modified sol-gel Pechini method”. The synthesis procedure is explained in Chapter 3.

Table 2.1: Abbreviations are used for the BFO NPs under this study.

Chemical formula of NPs	Given short names of NPs
$BiFeO_3$	BFO
$BiFe_{0.95}Mn_{0.05}O_3$	BFM
$BiFe_{0.95}Co_{0.05}O_3$	BFC
$Bi_{0.95}Ba_{0.05}FeO_3$	Ba-BFO
$Bi_{0.95}Ag_{0.05}Fe_{0.95}Mn_{0.05}O_3$	Ag-BFM
$Bi_{0.95}Ba_{0.05}Fe_{0.95}Mn_{0.05}O_3$	Ba-BFM
$Bi_{0.95}Ca_{0.05}Fe_{0.95}Mn_{0.05}O_3$	Ca-BFM
$Bi_{0.95}La_{0.05}Fe_{0.95}Mn_{0.05}O_3$	La-BFM
$Bi_{0.95}Nd_{0.05}Fe_{0.95}Mn_{0.05}O_3$	Nd-BFM
$Bi_{0.95}Sm_{0.05}Fe_{0.95}Mn_{0.05}O_3$	Sm-BFM
$Bi_{0.95}Gd_{0.05}Fe_{0.95}Mn_{0.05}O_3$	Gd-BFM
$Bi_{0.95}Dy_{0.05}Fe_{0.95}Mn_{0.05}O_3$	Dy-BFM
$Bi_{0.99}Ba_{0.01}Fe_{0.95}Mn_{0.05}O_3$	1BBFM
$Bi_{0.98}Ba_{0.02}Fe_{0.95}Mn_{0.05}O_3$	2BBFM
$Bi_{0.97}Ba_{0.03}Fe_{0.95}Mn_{0.05}O_3$	3BBFM
$Bi_{0.95}Ba_{0.05}Fe_{0.95}Mn_{0.05}O_3$	5BBFM

2.2 Photocatalytic set up

Photocatalytic (PC) procedure for organic dyes[a]

“A black box was made, to avoid any extra source of light other than the main light source (halogen lamp) as shown in Figure 2.1a. 10^{-5} M of methyl orange (MO) and rhodamine B (RhB) aqueous suspensions were prepared for their photodegradation. To establish an adsorption-desorption equilibrium between the dye and the photocatalyst, 50 ml of organic dye with 0.025 g of NPs were placed into a jacketed beaker in the dark for 30 minutes. For a well dispersed dye solution, 9 minutes ultrasonication was applied in the dark. Dye degradation was carried out under the irradiation of a halogen lamp (250-850 nm, LOT-Oriel) in a dark chamber. During PC experiments, continuous magnetic stirring of the NPs was performed to avoid their settling. **”** [a]

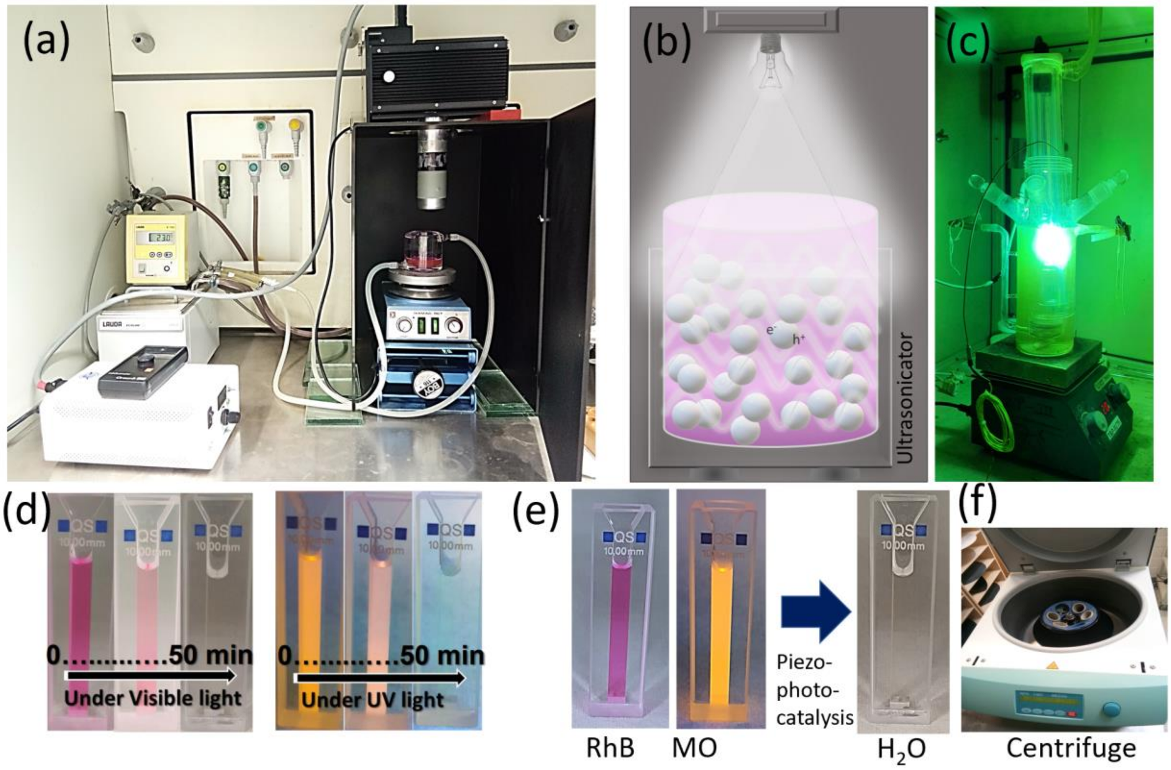

Figure 2.1: The UDEMAT built photocatalytic set up kept inside the fume hood, with UV-Visible light source and UV cut off filter (a). The schematic representation of piezo-photocatalysis happens under ultrasonication conditions (b). UV-reactor for photocatalysis of phthalate (c). The pink colored Rhodamine B (RhB) dye degradation and orange colored Methyl Orange (MO) dye photodegradation using 1BBFM as photocatalyst (d). The complete photodegradation of both dyes under piezo-photocatalytic condition (e). The centrifugation device used to separate NPs with dye solution (f)

For the PC in an acidic medium, the pH of the dispersion (dye + NPs) was adjusted to 2.2 by adding a few drops of 2N HNO_3. To keep a constant temperature (298 K) during PC and avoid thermal catalytic effects, a continuous water flow was maintained around the jacketed

---

[a] This paragraph is based on (Dubey et al, Nanoscale Advances, 2021, http://doi.org/10.1039/d1na00420d)

beaker. To study the degradation of the dye, 1 ml solution was taken every 5 minutes and centrifuged using a Hettich Zentrifugen Universal 320 R centrifuge at 9000 RPM for 10 minutes in the dark to separate the NPs [Figure 2.1f]. Afterwards, absorption measurements were performed on the centrifuged solutions. After the complete degradation of the dye (colourless solution; Figure 2.1d), the NPs were conveniently separated with the help of magnets under the PC vessel and used for the next cycles of PC. We checked the stability of NPs after Photocatalytic reaction, using XRD and TEM and found that the NPs can be used for at least three next PC cycles.

Piezo-photocatalysis (PPC) procedure[b]

"For piezo-photocatalytic reaction we used an ultrasonic (US) condition as shown in the schematic of Figure 2.1b. An ultrasonicator of 480 W, 40 kHz (Palssonic, Allpax Germany) was used for performing PC under ultrasonic excitation. It has a 190 x 100 x 55 mm basket, with a soundproof V2A stainless steel construction, and 2 liters net volume capacity. An ultrasonic generator generates electrical high-frequency energy, which is converted into mechanical vibrations by piezoelectric oscillating systems and released into the liquid via the bottom of the tub. "Cavitation" occurs, the formation of millions of tiny vacuum bubbles, which implode during the pressure phase. Highly effective pressure surges onto surface of the sample.

For the PPC, all the other photocatalytic conditions were kept as before (PC), and we could observe complete degradation of the dyes in PPC conditions as shown in Figure 2.1e.**"** [b]

Photocatalytic procedure for Phthalate

A quartz photoreactor was used for photodegradation under the illumination of a 125 W mercury lamp [Figure 2.1c]. All the samples were centrifuged at 3500 rpm for 15 minutes. After the centrifugation, 600 mL supernatant was taken and acidified to pH of 3 using 3 % sulfuric acid. It was then extracted with a solid phase extraction (SPE) cartridge (Water Oasis HLB, 200 mg/6 mL), which had been sequentially preconditioned with 3 mL ether, 3 mL methanol (99.9 % HPLC purity, Merck), and 3 mL distilled water. After the supernatant passed through the cartridges at a flow rate of 1-2 mL/min, the cartridges were then washed using 3 mL methanol/water (5:95 v/v), and vacuumed for 30 sec, and dried under nitrogen flow for 5 min. The chemicals retained on the cartridges were eluted with 6 mL of methanol/ether (10:90 v/v). The eluents were evaporated to dryness at 50 °C with a gentle flow of nitrogen. The results phthalates residue was further dissolve in 1 mL of mixture of n-hexane and methanol (60:40 ratio) for further analysis in GC-MS.

The extracted product was studied using gas chromatography (GC) (Agilent GC-7890 B) with flame ionization detector (FID) and the thermal conductivity detector (TCD) and He carrier gas.

---

[b] This paragraph is based on (Dubey et al, Advanced Functional Materials 2022, https://doi.org/10.1002/adfm.202207105)

2.3 Structural characterization

The structure of BFO and doped BFO NPs are explored using XRD, SEM, TEM, BET-BJH based nitrogen physisorption, XPS, and EXAFS.

2.3.1 X-ray diffraction (XRD)

XRD is one of the most commonly used techniques in the field of materials science. It provides quantitative information on crystal structure and defects averaged over volumes from about 10^{-3} cm^3 to a few cm^3. Electron microscopy probes volumes of many orders of magnitude smaller than XRD (10^{-19}-10^{-17} cm^3).

Bragg diffraction results from the interference phenomena between a periodic lattice of atoms with waves of a suitable wavelength (Cu Kα radiation of wavelength 1.54 ± 0.09 Å; with monochromatic resolution of 0.09 Å. Bragg's law (introduced by Sir W.H. Bragg and his son Sir W.L. Bragg) relates the periodically re-occurring distances of lattice planes (d-spacings) to the wavelength λ and the Bragg angle θ (n is an integer number) as shown in Figure 2.2a.

The approximate resolution function of the two-axis diffractometer [Figure 2.2b] can be calculated using Caglioti's relation.[192] The full width at half maximum (FWHM; *H*) of Bragg's reflections varies with the scattering angle 2θ, following the expression.

$$H^2 = W + V\, tan\theta + U tan^2\theta \tag{2.1}$$

The parameters U, V, and W can be written in terms of angular divergence of the incoming radiation to the monochromator (α_1), the angular aperture of a monochromator to sample collimator (α_2), the collimation between sample and detector (α_3), and the take-off angle of the monochromator ($2\theta_m$) and its mosaicity (β) i.e., a measure of the spread of crystal plane orientations. The Caglioti-Paoletti-Ricci equations for the U, V, and W parameters are the following.

$$U = 4\,(\alpha_1^2\alpha_2^2 + \alpha_1^2\beta^2 + \alpha_2^2\beta^2)/[tan^2\theta_m(\alpha_1^2 + \alpha_2^2 + 4\beta^2)] \tag{2.2}$$

$$V = -\,4\,\alpha_2^2(\alpha_1^2 + 2\beta^2)/[tan\theta_m(\alpha_1^2 + \alpha_2^2 + 4\beta^2)] \tag{2.3}$$

$$W = (\alpha_1^2\alpha_2^2 + \alpha_1^2\alpha_3^2 + \alpha_2^2\alpha_3^2 + 4\beta^2(\alpha_2^2 + \alpha_3^2))/(\alpha_1^2 + \alpha_2^2 + 4\beta^2) \tag{2.4}$$

$$tan\theta = -\frac{V}{2U} = \alpha_2^2(\alpha_1^2 + 2\beta^2)tan\theta_m/2(\alpha_1^2\alpha_2^2 + \alpha_1^2\beta^2 + \alpha_2^2\beta^2) \approx tan\theta_m \tag{2.5}$$

The best resolution conditions can be obtained with $\alpha_2 = 2\beta > \alpha_1 \sim \alpha_3$.

Theoretically, ideal Bragg diffraction should yield infinitely sharp reflections, a single exact wavelength diffracted at lattice planes with an exactly defined d-spacing would fulfill Bragg's law only for an exactly defined angle. However, neither the experimental setup nor the investigated sample are ideal. All imperfections of the experiment and the sample will contribute to some softening off Bragg's law, resulting in noticeable broadening of the observed peak profiles. Perfect periodicity would mean infinite crystals. As real crystals are finite, the periodicity stops at a certain point. The smaller the crystal, the smaller the number of periods, and thus the less perfect the Bragg diffraction (like the case of NPs). There are also instrument-related broadening effects, which generate the instrumental profile, while the description of the instrumental profile as a function of the diffraction angle is known as the instrument function. The device is calibrated with a reference sample like SRM 660a.

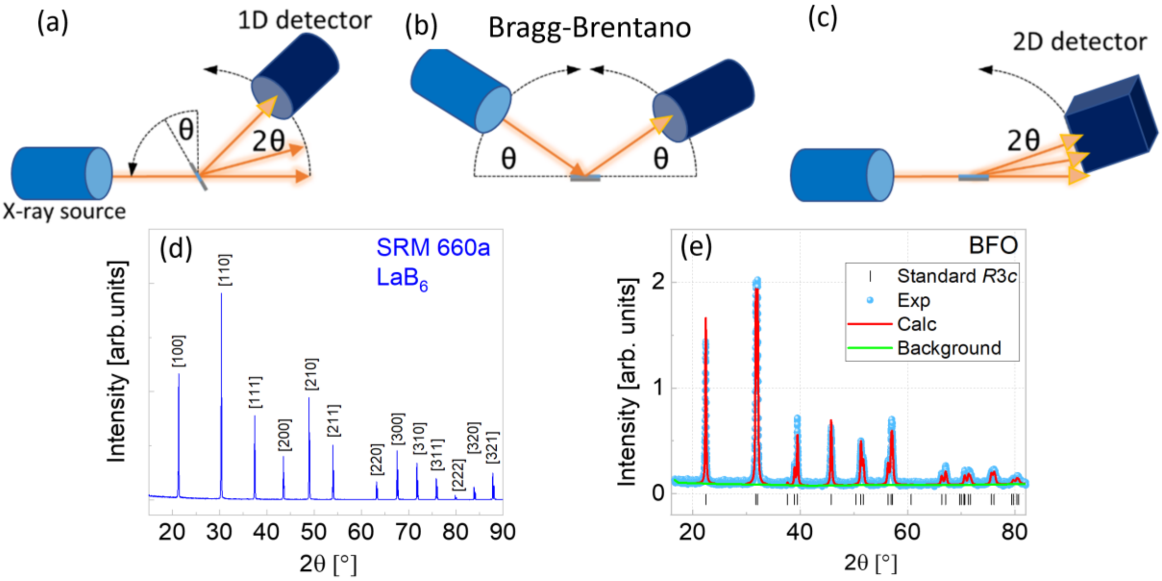

Figure 2.2: Different possible geometries in XRD device (PANalytical EMPYREAN) Debye-Scherrer (a), Bragg-Brentano (b), and grazing incidence diffraction (c). XRD diffractogram of the standard reference material SRM 660a LaB_6 measured at room temperature (d). Rietveld fitted XRD diffractogram of BFO NPs using the High-Score program from PANalytical (e).

Reference SRM-660a (LaB_6) for XRD analysis?

Lanthanum Hexaboride is a material commonly used as a calibration standard for XRD instruments because it has a well-defined and known crystal structure. The diffraction pattern of LaB_6 is very sharp, see Figure 2.2c. It is recorded before any XRD measurement of NPs. This helps to ensure the accuracy and precision of the XRD measurements. So errors or drifts in the instrument can be detected and corrected. Additionally, the use of LaB_6 as a calibration standard allows for the comparison of XRD results obtained from different instruments or laboratories, as long as they have been calibrated using the same standard material. The choice of LaB_6 (or SRM 660a) as a calibration standard for XRD is based on several scientific reasons. Firstly, LaB_6 has a well-defined crystal structure, which is a simple cubic lattice with a lattice constant of 4.156 Å. The crystal structure of LaB_6 is relatively easy to model and it is well-suited for testing the accuracy and precision of XRD instruments. Secondly, LaB_6 has a high melting point (2210 °C) and is chemically stable, which makes it a suitable standard for high-temperature XRD measurements. This is important for the analysis of materials that are stable at high temperatures, such as ceramics and metals. Thirdly, LaB_6 produces a low background signal in XRD measurements. This makes it easier to detect and measure the diffraction peaks from the sample being analysed.

Rietveld fitting of XRD diffractograms

In 1969, Hugo Rietveld published article on nowadays called "Rietveld refinement method".[193] As a result, in the last 50 years, we have witnessed a true revolution in the application of powder diffraction in crystallographic research. The Rietveld refinement is a mathematical technique, for the analysis and evaluation of powder diffraction data.

Using a theoretical line profile with the similar structure as the measured sample, which serves as a reference, a theoretical powder diffraction diagram is created and iteratively compared to the measured data. The comparison is based on the least square method. The Rietveld analysis consists of two segments, (a) the profile and (b) structure fitting combined with the background adjustment. Certain functions are available for the shape fitting, a linear combination of a Gauss and Lorentz function is commonly used, the Pseudo-Voigt function. Simultaneously, it is possible to determine changes of the unit cell parameters, such as lattice parameters, atomic position, thermal displacement, or occupation. The Rietveld analysis makes it also possible to determine the composition of multi-phased materials due to the use of integral intensities. Important for the profile functions are the integral intensities of the k reflection I_k, the reflex position $2\theta_k$ and the FWHM.

The FWHM is described by Caglioti equation (Equation 2.1) as such, where W parameter is the variation of principle half width coefficient, and U, and V, parameters are variation of two other half width coefficients. During the refinement, the parameters U, V, and W are used to fit the profile. The quality of a Rietveld refinement is evaluated according to the agreement of the observed values $y_i(obs)$ with the calculated values $y_i(calc)$ and is given by residual values (R-values). The value R_{wp} (weighted R-value) indicates the mean deviation of the calculated data to the observed diffraction pattern and is minimized during the refinement.

$$R_{wp}^2 = \frac{\Sigma w_i\, (y_i(obs) - y_i(calc)^2}{\Sigma w_i(y_i(obs)^2)} \tag{2.6}$$

Where, w_i is the weighting factor, $y_i(obs)$ is the measured intensity, and $y_i(calc)$ is the calculated intensity. Ideally this value is zero, which can never be achieved due to the signal to noise ratio, thus the R_{exp} value is calculated, indicating the best possible value and the accuracy of the measurement.

$$R_{exp}^2 = \frac{N - P + C}{\Sigma w_i(y_i(obs)^2)} \tag{2.7}$$

N is the number of measured points, P is the number of parameters, and C is the number of parameters linked. The value R_{Bragg} is calculated from the intensities of the n reflections that are present in the pattern.

$$R_{Bragg}^2 = \frac{\Sigma(I_n\,(obs) - I_n\,(calc)\,)}{\Sigma I_n(obs)} \tag{2.8}$$

$I_n(obs)$ is the measured integral intensity of the nth reflection, $I_n(calc)$ is the calculated integral intensity of the n reflection The goodness of fit *GOF* is formed by the ratio of the two former R-values R_{wp} and R_{exp}. In the ideal case *GOF* should approach a value of 1.

$$GOF = {R_{wp}}/{R_{exp}} \tag{2.9}$$

While doing Rietveld refinement one should know these terms of the material. The Site Occupancy Factor (SOF) indicates what a fraction of a site is occupied by a specific atom. The Wyckoff site notation is a shortcut to indicate the type of site that the atoms occupy in the crystal. each letter in the Wyckoff notation specifies a different combination of symmetry elements of a site. The number in the Wyckoff notation indicates the number of atoms put into the unit cell if the atom is on that site. For example, for BFO the Wyckoff sites are Bi (6a), Fe (6a), and O (18b).

Since the sample-related contribution to the peak profile contains information about the sample imperfections, like crystallite size, microstrain, stacking faults and other defects, a careful peak profile analysis should yield information about the nature and amount of such defects in the sample. However, as the peak profile results from the convolution of all effects mentioned above, the extraction of a single quantity from the total peak profile is intrinsically difficult. The sample related contribution to the diffraction peak profiles is often described by the Pseudo-Voigt function a convolution of a Gauss and a Lorentz function. Pseudo-Voigt functions are easier to handle and represent a very good approximation to Voigt functions. Simple Gauss and Lorentz functions may also occur but can be considered as boundary cases of Voigt or Pseudo-Voigt functions. Another related function which somewhat came out of trend is the Pearson-VII function. Empirically, peaks profiles may also have super-Lorentzian line shapes, which can be approximated by the superposition of two or more Lorentz functions. All of the above functions have some properties in common: they are symmetric, and they do not have a defined cut-off, but drop asymptotically towards zero on both flanks. Thus, a perfectly complete integration would have to be performed over an infinite interval. The drop-off behaviour of peak-shape functions has implications for practical aspects like peak overlap, correlation between reflection and background shapes, and determination of peak widths.

Size and strain broadening

There are many different methods proposed to extract crystallite size and microstrain information from XRD patterns. Methods which extract the size broadening by Fourier-deconvolution (e.g., the Warren-Averbach method) give area weighted mean size values. Methods which are based on peak width analysis, like the Scherrer method, the Williamson-Hall method or the Double-Voigt approach, yield volume weighted mean size values.

In 1918, Scherrer published an article (in German) in which he related the width of XRD peaks to the size of crystalline particles [Equation 2.12].[194] It involves several aspects: Averaging of the column lengths within the crystallites depending on the shape and averaging between different crystallites depending on the size distribution. Crystallite size broadening is proportional to 1/cosθ. The reasonable grain size should be less than 200 nm, and considered to be 11.9 % of the extinction length.[195]

Lattice strain or microstrain is a local deviation of d-spacings from the average value caused by local disordering. The origin may be reduced crystallite size, point defects, or substitution with different atoms (doping). These effects cause the contraction or expansion of d spacing. The forces of compression and expansion are balanced, and thus results in diffraction peak broadening (a distribution of strain) instead of a peak shift. Macroscopic stress applied on a material, typically causes peak shifts. In polycrystalline material the projection of external strain on local strain may also cause line broadening.

While both size and strain broadening affect the width of diffraction peaks, they show a different angular dependence of the peak width. The integral breadth of the strain-related diffraction peak broadening is proportional to tanθ. The widening of the Bragg peaks follows Equation 2.10, where ε is the microstrain.

$$\beta_{total} = \beta_{strain} + \beta_{size} \tag{2.10}$$

$$\beta_{total} = [4\ \varepsilon \tan\theta + (K\lambda/L\cdot\cos\theta)]\cdot\cos\theta \tag{2.11}$$

$$\beta_{size} = K\lambda/L\cdot\cos\theta \tag{2.12}$$

K is set to 1.0 for integral breadth. The Williamson-Hall analysis is based on the sum of both kinds of broadening. Plotting β_{tot}*cosθ versus 4sinθ allows separating and getting a measurement of both the size and micro-strain effect: the micro strain is obtained by the slope of the plot and the crystallite size is obtained by the intercept at sinθ = 0. The FWHM, β, was corrected for instrumental broadening using the of standard SRM 660a with identical X-ray optics.

In 1953, Williamson and Hall proposed a method in which the integral breadth of all diffraction peaks (corrected for instrumental broadening) is plotted. The Williamson-Hall Plot assumes that both size and strain broadening are Lorentzian, and the integral breadths of both components are additive [Equation 2.13]. β represents the sample related integral breadth, λ the wavelength, θ the Bragg angle, D the volume weighted mean domain size, “e” is a measure for the microstrain distribution and d* = 1/d the reciprocal lattice spacing. By plotting β* versus d*, fitting the data points with a straight line yield the crystallite size from the intercept and the microstrain from the slope of the line.

$$\beta^* = \frac{\beta\ cos\theta}{\lambda} = \frac{1}{D} + 2\ e\ d^* \tag{2.13}$$

The derivation of the Williamson-Hall method explicitly assumes purely Lorentzian broadening, which is often not fulfilled in reality. A severe limitation comes from the fact that the individual peak widths have to be accessible, i.e., the method will fail in the case of extensive peak overlap. Theoretically, pure size broadening will give a horizontal line (no slope), while pure strain broadening will yield a line through the origin (no intercept). In the case of anisotropic line broadening, i.e., size and/or strain effects which are a function of the direction in the crystal lattice, the data points of the different reflections will not fall onto a line. In this case, families of higher order reflections representing common directions in the crystal (e.g., 00*l* etc.) have to be analysed separately. Unfortunately, families with more then two members and well resolved (non-overlapping) diffraction peaks are rarely available.

We have utilised the **Double-Voigt approach** for the estimation of the average crystallite size and the strain distribution in NPs. In the double-Voigt approach, both size and strain broadening are modelled by Voigt functions. The lattice strain is defined in terms of physically credible mean-square strain average over a distance in the diffracting domains. Thus, there is no general limitation to the components being purely Gaussian or Lorentzian. The differentiation of size and strain again relies on their different angular dependence. In the framework of convolutional whole powder pattern fitting, in which all contributions (including instrumental functions) are convoluted with each other, this concept couples the shapes and widths of all peaks belonging to the same phase to each other. Thus, peak overlap becomes much less of an issue, and a good fit resolves size and strain from the pattern. If a good fit over the whole pattern is not achieved, then often the underlying assumption of isotropy is not fulfilled. In this case, peak widths are additionally a function of the crystal direction, not only the diffraction angle.

Experimental conditions

XRD at ambient temperature was performed with Cu Kα radiation in Bragg-Brentano geometry. The crystalline phase and lattice parameters of all NPs were studied by powder XRD using a Panalytical Empyrean (Cu Kα radiation) diffractometer over a 2θ range of 10° to 80° with a step size of 0.026°. For measurement, the powders were placed on a standard sample holder as a thin flat layer and measured in reflection mode (Bragg-Brentano geometry). The background parameters, zero shift and detector shifts, lattice parameters and atomic coordinates for the host and the doping atoms, profile parameters (crystallite size, and strain parameters) were fitted simultaneously using the Rietveld refinement procedure realized in the High Score Plus software. The background intensity was accounted for using a Chebychev polynomial of the minimum order to account for the curvature.

Rietveld Fitting steps

Sample displacements were refined, while zero errors were fixed. Afterwards, the peak shapes were refined. The peak profile function giving the best fit to the experimentally observed data was chosen and kept for all patterns within a series of patterns with varying composition, temperature, or crystallite size. Refinements of diffraction patterns within the space group no. 161 (R3c) were done in the hexagonal setting with the Bi cation in origin. Lattice parameters, background, displacement, and peak profile parameters were allowed to converge before atomic positions were added to the refinement. Systematically, the position parameters of the heaviest atom in the unit cell were refined to convergence before subsequently adding lighter atoms to the refinement. Isotropic thermal displacement parameters were added to the refinement after convergence of atomic positions, and finally anisotropic thermal displacement parameters. Dopant occupancies in the *R3c* phase were subsequently added to the refinement after convergence of the thermal displacement parameters. Lattice parameters, background, displacement, and peak profile parameters were allowed to converge before atomic position were added to the refinement. Systematically, the position parameters of the heaviest atom in the unit cell were refined to convergence before subsequently adding lighter atoms to the refinement. Isotropic thermal displacement parameters were added to the refinement after convergence of atomic position, and finally the anisotropic thermal displacement parameters. For example, Rietveld fitted XRD diffractogram of BFO NPs is shown in Figure 2.2d.

2.3.2 Electron microscopy

Scanning Electron Microscopy (TEM)

SEM is utilized to image the sample surface through detecting different signals generated from the impact of focused highly energetic electrons (primary electrons) at the sample surface. These electrons have very short wavelength (λ) which can vary as per the applied high voltage. SEM is an electronic and optical system which consists of the following components: (i) Electron gun (ii) Vacuum (iii) Column: condenser lens, scanning coil, objective lens, stigmator, sample holder and detector as shown in Figure 2.3c.

Working Principle

An SEM operates on the principle that primary electrons produced and emitted from the electron gun are accelerated applying high energy in the range of 1-40 keV. These emitted electrons are then focused and confined to a monochromatic beam with a diameter of 100 nm or less using magnetic field lenses and metal slits within a vacuumed column. The confined primary electrons are then scanned across the sample surface by the corresponding magnetic field scanning coils in a raster pattern. To obtain high resolution, the basic requirement for an SEM is to operate under vacuum to avoid electron interactions with gas molecules.

When the primary electron beam hits the sample surface, it interacts with the near-surface area of the sample to a certain depth. The impinging electrons have substantial kinetic energy, which they lose inside the sample by generating several signals from the interactions with the specimen. These signals include elastic and inelastic scattering of the electrons. Inelastic interactions are those in which transfer of energy from the beam electron to the specimen atom takes place thus results in the potential ejection of an electron from that atom as secondary electron (SE). [Figure 2.3a] Usually have energy less than 50 eV. The vacancy created by the emission of a SE is filled from a higher-level orbital, and an X-ray characteristic of that energy transition is produced. Elastic interactions are those interactions that take place between the primary electrons and electric field of the specimen atom, and due to these interactions, the direction of the primary electrons' changes without a change in the energy of the primary electron (less than 1 eV). These elastically scattered electrons deflect back out of the specimen, are called back scattered electrons (BSEs). The BSEs maintain a minimum of 50 % of the total incident beam energy. Since heavy elements scatter electrons back more strongly than light elements, they appear brighter in the images. BSE are also used to detect contrast between areas with different chemical compositions.

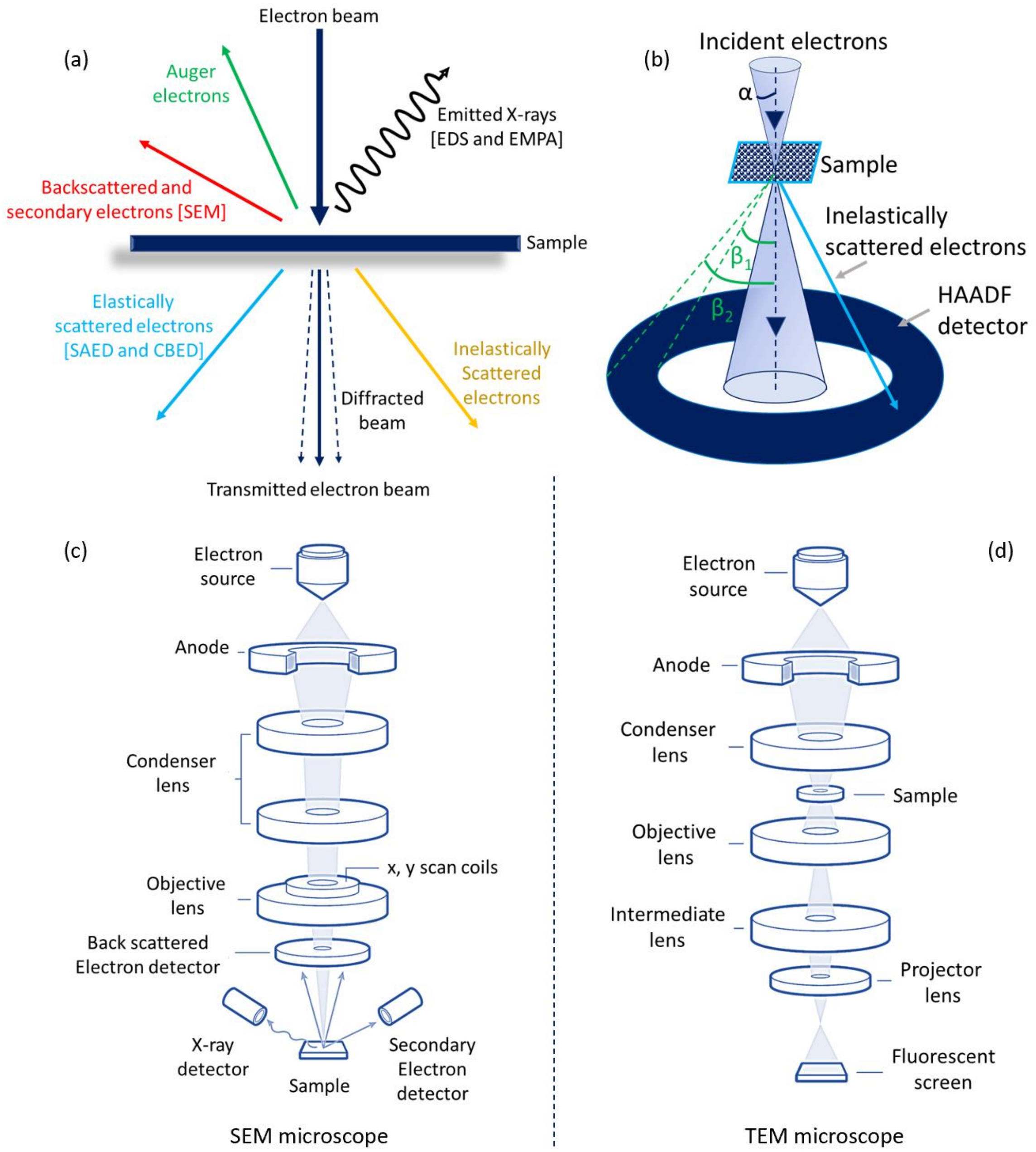

Figure 2.3: Various signals produced from sample and electron beam interaction (a). The relationship between the convergence semi-angle of the incident electron beam and acceptance semi-angles of the detector for HAADF-STEM. Where, $\beta_1 = \sim 50$ mrad and $\beta_2 = \sim 200$ mrad, detecting inelastically scattered electrons at high angles and convergence semi-angle α is ∼25 mrad for a 200 kV Cs-corrected TEM (b). The schematic of SEM and TEM microscopes in (c) and (d), respectively.[196]

The scattering of electrons and interaction volume depends on the atomic number, concentration of atoms of the analysed sample and the incoming electron energy. Increasing the accelerating voltage will increase the interaction volume. If the concentration of atoms and atomic number of the element is high, then the interaction volume will be low. The angle of the incident electron beam also plays an important role in the interaction volume. Materials having higher atomic number absorb or stop more electrons and will thus generate smaller interaction volume. Similarly, if high voltages are applied, the electrons and will penetrate farther into the sample and generate a larger interaction volume. The greater the angle of incidence (further from normal), the smaller will be the interaction volume. According to the detected signal, different information about the sample can be obtained. SEs provide information about sample morphology and topography, while BSEs are used for demonstrating the contrasts in the multiphase sample composition. X-rays are generated by the inflexible impacts of the incident electrons with the electrons available in sample atoms. SEM is non-destructive.

Experimental conditions

An ESEM Quanta 400 FEG, FEI instrument was used to study the shape and morphology of the NPs. The atomic composition of the NPs was estimated by energy dispersive X-ray spectroscopy (EDXS) using an Analytical SEM device (EDS, energy resolution < 132 eV for Mn Kα, detector area 10 mm^2).

Transmission Electron Microscopy (TEM)

In TEM microscope the resolution limit can go down to ~ 0.15 nm. For TEM measurements the sample should be thinner than 500 nm. TEM is ideal for investigating thin foils, thin edges, and NPs. In this method, electrons pass through the specimen, and the resulting image is formed on a fluorescent screen, either by utilizing the transmitted beam or the diffracted beam. The specimen is positioned between the condensing lens and the objective lens (Figure 2.3d). To enhance image contrast, a magnetic objective lens is positioned to block the high angle diffracted beam. An aperture is used to eliminate the diffracted beam entirely. Magnetic projector lens is placed above the fluorescent screen to achieve higher magnification of the image. The image can be recorded using a fluorescent screen or a charged coupled device (CCD).

The bright field image is purely due to elastic scattering, specifically the transmitted beam alone as shown in Figure 2.4. The aperture is utilized to selectively choose the unscattered (transmitted) electrons, while blocking the scattered electrons. In bright-field TEM images, areas with crystalline or high mass density appear dark, allowing for precise visualization of the structure under study. Bright-field images are the most commonly acquired images in TEM. In dark-field TEM the diffracted electrons are selectively chosen while the undiffracted electrons are excluded by the aperture [Figure 2.4b]. Consequently, the area around the sample being examined appears light instead of dark. Although dark-field TEM is less commonly employed than bright-field TEM, it can offer distinct advantages in certain cases. By selectively imaging the diffracted electrons using the aperture, crystalline structures can be more easily visualized, including features such as the crystal lattice, crystal defects, dislocations, stacking faults, and particle/grain size.

Energy-Dispersive X-ray Spectroscopy (EDX)

When inelastic transition occurs, electrons from inner shells can be knocked out. This results a transition from higher levels to the core level with the emission of X-rays. The energy of these characteristic X-rays represents the chemical nature of the material. The emission spectrum of the X-ray is relatively easy to analyse than the counterpart energy loss in EELS. X-ray energy-dispersive detectors are available commercially which can collect the X-ray signals and display them in the form of spectrum. The electron energy for EDX in the TEM is set to 200 keV.

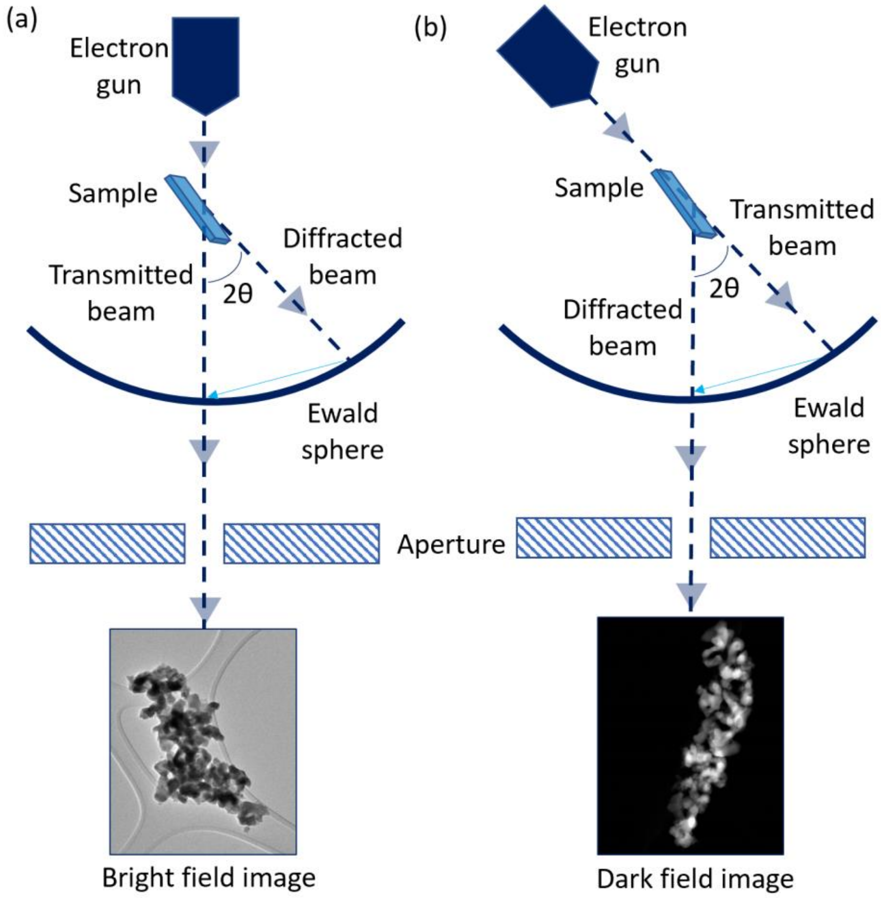

Figure 2.4: Electron beam schematics for bright field and dark field imaging in TEM.

Scanning Transmission Electron Microscopy (STEM)

In scanning TEM, the widespread beam is transformed into focused beam and acts as an optical probe that can be scanned over the sample. The STEM mode is often operated in dark-field imaging mode. The STEM mode is useful for microanalysis, and contrast, as in this mode, it depends solely on atomic number. All types of signals, i.e., elastic, inelastic, scattered, and unscattered, are emitted and detected using an annular detector position below the sample as shown in Figure 2.3b. That’s why this mode is also named high-angle annular dark-field scanning transmission electron microscopy (HAADF-STEM). The STEM mode is efficient for energy-dispersive spectroscopy (EDS) analysis at the nanoscale. The STEM technique is similar to SEM, except that the specimen is much thinner, and we collect the transmitted electrons rather than the reflected electrons.

Selected Area Electron Diffraction (SAED)

In diffraction mode, the intermediate lens is focused in the back focal plane of the objective lens, allowing both transmitted and diffracted beams to be imaged. An aperture is then introduced in the image plane of the objective lens, which enables the acquisition of diffraction patterns from selected areas of the sample, giving rise to the term "selected area electron diffraction" (SAED). To obtain a diffraction pattern, the first step is to examine the sample in image mode and locate the specific part or group of NPs of interest. The beam is then fully spread so that the maximum number of electrons remain parallel to the sample. Next, an intermediate aperture is inserted and fixed at the specific feature of interest. By switching from imaging to diffraction mode, a diffraction pattern in the form of spots or circles can be observed on the viewing screen. To avoid damage to the camera, a beam stopper is introduced in the path of the diffracted beam during observation. The obtained diffraction patterns can then be analysed and indexed based on their d-spacing, providing information about the crystal structure and orientation of the sample.

The emergence of the diffraction spots can be understood by constructing the Ewald sphere which provides lattice planes for a particular wavelength of incident radiations. The spots apparent on the diffraction pattern belong to the nodes of the reciprocal lattice intercepted by the Ewald sphere. The radius of this hypothetical sphere is inversely proportional to the wavelength of the incident beam. Due to this reason, electron (λ_e; ~3.88 pm at 100 keV, ~2.74 pm at 200 keV, and ~2.24 pm at 300 keV) diffraction becomes more prominent than X-ray ($\lambda_{X\text{-rays}}$; ~0.1 nm) diffraction where fewer nodes are observed at the tangent of the Ewald sphere. This phenomenon is further enhanced by introducing the diffraction volumes so that spots remain visible even when the Bragg condition is not completely fulfilled. The diffraction pattern depends mainly on the orientation of the NPs in the sample. In the case of a monocrystalline sample, distinct diffraction spots which correspond to specific planes can be observed, but the condition is that all parts of the samples selected by the aperture should align with the electron beam. But in case of NPs, they can all be oriented in different directions. As a result, the distance from the direct beam remains the same for spots, but the angle is changed for every nanoparticle. Finally bright circles are obtained in place of spots. Similarly, for polycrystalline materials, circles are obtained. Each circle corresponds to specific planes that can be determined from the d spacing.

$$d_{\mathrm{hkl}} = L\,\lambda / R_{\mathrm{hkl}} \qquad (2.14)$$

L is the camera length, λ the wavelength of the electrons. L·λ is called the camera constant and has units Å cm. R_{hkl}, is the distance of the spot or circle from the direct beam. If the nanocrystals are relatively small and well-ordered, they can exhibit spot-like patterns in SAED, indicating a single-crystal-like behaviour. However, if the nanocrystals are larger and randomly oriented, or if the sample contains a mixture of differently oriented nanocrystals, the diffraction pattern will appear more like circles, reflecting the polycrystalline nature.

Experimental conditions

The size and crystallinity of the NPs were analyzed by high-resolution TEM on a JEOL JEM-2200FS microscope using 200 kV acceleration voltage and a probe side aberration corrector. The atomic composition of the NPs was estimated by EDX and HAADF using an analytical SEM device (EDX, energy resolution < 132 eV for Mn Kα, detector area 10 mm^2). Gatan and ImageJ software were used to do image and profile analysis.

2.3.3 Nitrogen physisorption measurements

Specific surface area (SSA) is undoubtedly the most meaningful morphological characteristic of NPs in applications related to adsorbents, and catalysts. Pores of less than 2 nm are classified as micropores, while mesopores lie between 2 to 50 nm, and macropores exceed 50 nm in diameter.[197] At temperatures below 100 K, van der Waals forces govern the interaction between gas molecules and surfaces with heat of adsorption lower than 4 $kJ \cdot mol^{-1}$. These forces lead to the reversible physisorption of gas molecules on material surface in multiple layers. Chemisorption, on the other hand, is a different process, occurring in a monolayer irreversibly with higher heat of sorption. Brunauer et. al. extended the Langmuir theory of monolayer adsorption to include multiple layers for which only adjacent layers of gas molecules interact to calculate the surface area, S_{BET}.[198] Barrett et. al. introduced the Kelvin equation to calculate the pore size distribution, the Barrett-Joyner-Halenda (BJH) method.[199] The Brunauer–Emmett–Teller (BET) and the Barrett–Joyner–Halenda (BJH) methods determine the for surface area and pore size distributions, respectively.[198] BET name is based on three scientists Stephen Brunauer, Paul Hugh Emmett, and Edward Teller. Using physisorption (N_2, Ar, Kr), one can determine the surface area, pore volume, and pore size distribution. Low pressure mercury porosimetry can be applied to measure macropores (14 µm-200 µm). High pressure Hg porosimetry measures pore diameters as low as 3 nm (mesopores).

The two major components of N_2 physisorption analysers are the degassing and adsorption stations (Figure 2.5). The first step in the process is to calibrate a quartz cell used for gas adsorption. This cell is evacuated under high vacuum (10^{-3} to 10^{-8} mbar) at 300 °C for 2 hours (degassing), followed by a complete adsorption cycle in the empty cell at 77 K. The cell is then loaded with 50-150 mg of sample and connected to the degassing station. Degassing the sample is to remove physically adsorbed water and volatiles that accumulated during storage. For thermally sensitive solids, mild degassing temperatures are used, and for mechanically fragile porous materials, a stream of inert gas is introduced instead of vacuum, using the adsorbate path (ADS) connected to the degassing station (Figure 2.5). After degassing, the cell is transferred to the adsorption station and evacuated. The adsorption cycle is performed by incremental introduction of adsorbate gas using the calibration volume (CAL) connected to the adsorption station. The difference between the measured pressure and that of the empty cell correlates with the number of moles of adsorbed nitrogen. Nitrogen is the preferred gas adsorbate because it is inert, available in high purity, inexpensive, and interacts with most solids. During measurement, the cell is maintained at liquid nitrogen boiling point using a Dewar flask filled with liquid nitrogen.

Working Principle

The relative pressure is calculated by subtracting the free space of sample tube, which is the volume of sample tube not occupied by sample, from the total volume of the gas dosed to the sample. The increment data set consists of data points, where each data point is processed by calculating the volume adsorbed and measuring the sample pressure divided by the saturation vapor pressure. The relative pressure is plotted as abscissa axis.

The BET theory assumes that the adsorption energy is independent of the adsorption sites and gas molecules interact only in the vertical direction, lateral interactions between adjacent adsorbed molecules being negligible. Physisorption of the first adsorbate layer is shown Equation 2.15.

$$\frac{x}{W\,(1-x)} = \frac{1}{C * W_{ml}} + \frac{C-1}{C * W_{ml}}\,x \tag{2.15}$$

W is the mass adsorbed at relative vapour pressure, $x = P/P_0$ (P and P_0 are the actual and saturated vapour pressures of the adsorbate); W_{ml} is the required mass of adsorbate forming a complete monolayer adsorbed on a given sample. C is a constant expressing the differences in the heat of adsorption of the first and second or higher layers and depends on temperature and on the heat of adsorption of the first layer (E_1). For higher layers (E_L) equals the latent heat of condensation.

$$C = \exp\left(\frac{E_1 - E_L}{RT}\right) \tag{2.16}$$

For type III and V isotherms, C = 1. From Equation 2.16, a plot of $x/W(1-x)$ versus x gives a straight line with an intercept at $\beta_0 = 1/(C \cdot W_{ml})$ and a slope of $\beta_1 = (C-1)/(C \cdot W_{ml})$. The mass of gas that forms a monolayer, W_{ml}, can be obtained using Equations 2.17 and 2.18.

$$\frac{1}{W_{ml}} = \beta_0 + \beta_1 \tag{2.17}$$

The specific surface area, SSA, is as follows.

$$SSA = \frac{W_{ml}}{M * m} * N * A \tag{2.18}$$

M is the nitrogen molar mass; m it the sample mass; A the nitrogen molecular cross-sectional area (0.162 nm^2); and N is Avogadro's number. For BFO NPs SSA was calculated using the BET-plot shown in Figure 2.5d.

Nitrogen physisorption isotherms are categorized into six types as shown in Figure 2.5b. *Type I* corresponds to monomolecular adsorption postulated by Langmuir. The volume of the gas adsorbed approaches a limiting value (enough for monomolecular layer). The examples are furnished by adsorption of N_2 or H_2 on charcoal at temperature close to -180 °C. *Type II* and *III*, show large deviation from Langmuir model. The adsorption keeps on increasing with increase in gas pressure, which attributes to formation of additional layers of physically adsorbed gas molecules. Example of *type II* is adsorption of N_2 on an iron or a platinum catalyst at -195 °C. *Type III* is found for adsorption of bromine on silica or alumina gel at 80 °C. In *type IV* and *V* the condensation of gases occur in the minute capillary pores of the adsorbent at pressures even below the saturation pressure of the gas. Example of *type IV* is adsorption of benzene on silica gel at 50 °C. The adsorption of water vapour on activated carbon at 100 °C, represents *type V* isotherm.

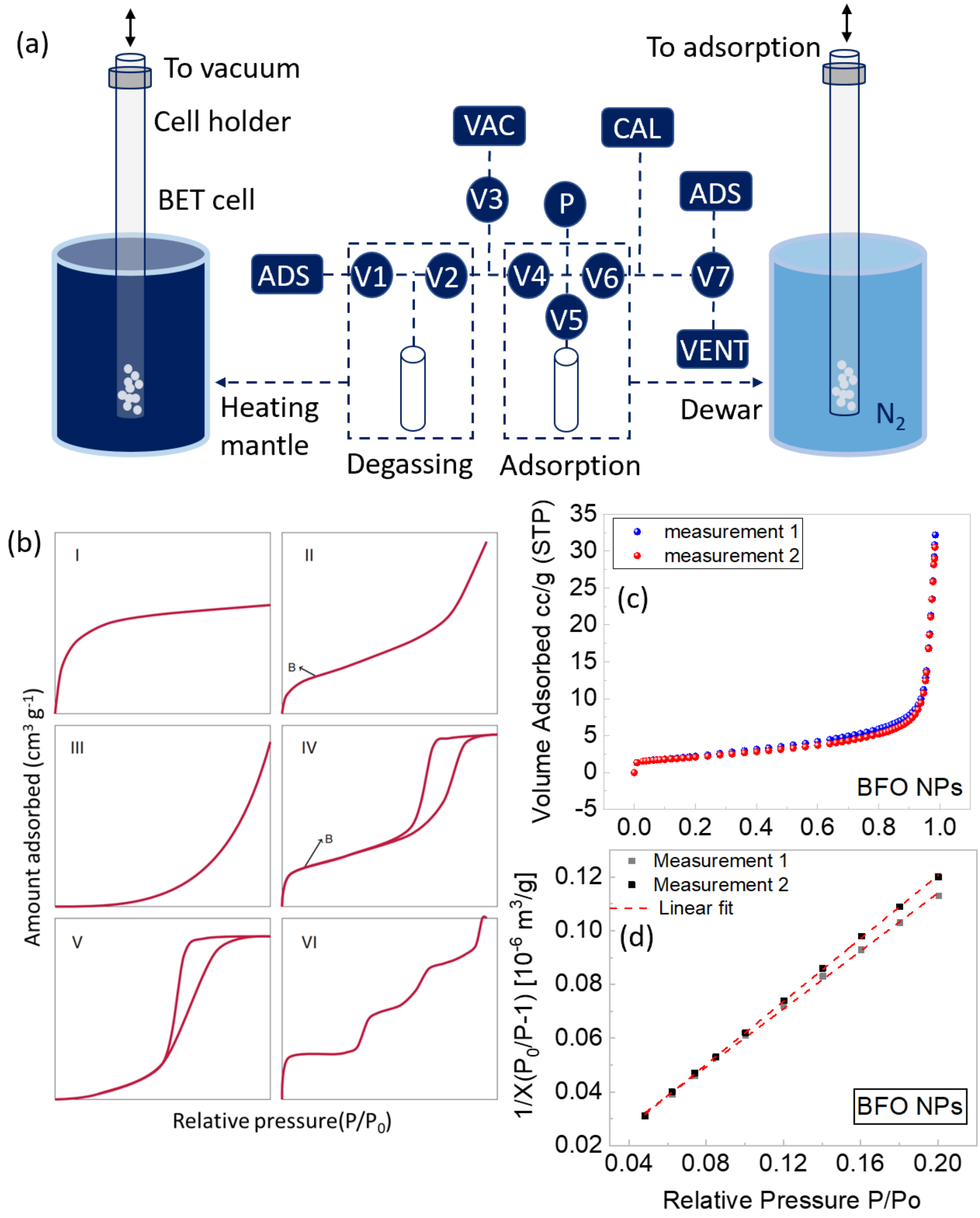

Figure 2.5: Gas physisorption apparatus (a) to obtain adsorption-desorption isotherm (VAC: vacuum, CAL: calibration, ADS: adsorbate, P: pressure gauge, V1-V7: valves). Six types of nitrogen adsorption-desorption isotherms (b). For BFO NPs, the isotherm (c), and the surface area plot (d).

The *Type VI* isotherm represents stepwise multilayer adsorption on a uniform non-porous surface. The step height represents the monolayer capacity for each adsorbed layer. Example of *type IV*, argon or krypton on graphitised carbon blacks at liquid nitrogen temperature.[200] In Figure 2.5c, representative isotherm of BFO NPs is shown, which is most likely *type II* due to a broader distribution of the macroporous structure.

The BJH method allows to estimate the pore size distribution (PSD) based on physisorption equilibrium isotherms. The BJH theory implements two fundamental assumptions: first the shape of pore is cylindrical, and second the adsorbed amount results from both physical adsorption on the pore walls and capillary condensation in mesopores. BJH thus considers the radius of a pore as the sum of the multilayer thickness (t) and the meniscus radius obtained from the Kelvin equation.

$$ln\frac{P}{(P_0)} = \frac{2\gamma V_M}{rRT} \tag{2.19}$$

P/P_0 is the relative pressure in equilibrium with a meniscus; γ is the surface tension of the adsorbate in liquid form; V_M is the molar volume of the liquid; R is the universal gas constant; r is the radius of the meniscus formed in the mesopore; and T is temperature.

BJH calculates the change in the thickness of the adsorbed film from the decrease of relative pressure in the desorption branch. Each decrement is considered to result from evacuation of the largest pores from the capillary condensate, as well as a reduction in thickness of the physically adsorbed layer. This theory yields a particular equation correlating pore volume and radius, which is solved by numerical iteration.

Experimental conditions

Foe BET-BJH measurements we utilised Beckman Coulter SA 3100 analyser. Compressed nitrogen gas was used as adsorbate. It uses the static fully equilibrated volumetric method. The samples were degassed under vacuum at room temperature for 24 h before the adsorption tests.

2.3.4 X-ray photoelectron spectroscopy (XPS)

Working Principle

XPS also known as Electron Spectroscopy for Chemical Analysis (ESCA), is used to determine quantitatively atomic composition and chemistry. XPS is based on the photoelectric effect, first discovered by Heinrich Hertz in 1887. He noticed that electrons are emitted from surfaces when irradiated with light. Albert Einstein more formally described the concept in 1905 and was awarded the Nobel Prize in physics in 1921 for this work. Photoemission from X-ray irradiation was first observed by Robinson and Rawlinson in 1914, and the first application of photoemission as an analysis method was presented by Steinhardt and Serfass in 1951.[201] XPS instrument contains an X-ray source, a sample stage, extraction lenses, analyser, and detector housed in an ultra-high vacuum environment as developed by Kai Siegbahn in the 1950s and 60s. A schematic diagram of an XPS system is shown in Figure 2.6.

In XPS, the sample is irradiated with soft X-rays (energies lower than ∼6 keV) and the kinetic energy of the emitted electrons is analysed. The emitted photoelectron is the result of complete transfer of the X-ray energy to a core level electron. The energy of the X-ray (hv) is equal to the binding energy (BE) of the electron, plus the kinetic energy (KE) of the electron that is emitted, plus the spectrometer work function (Φ_{sp}), a constant value. The binding energy of an electron is a material property and is independent of the X-ray source.

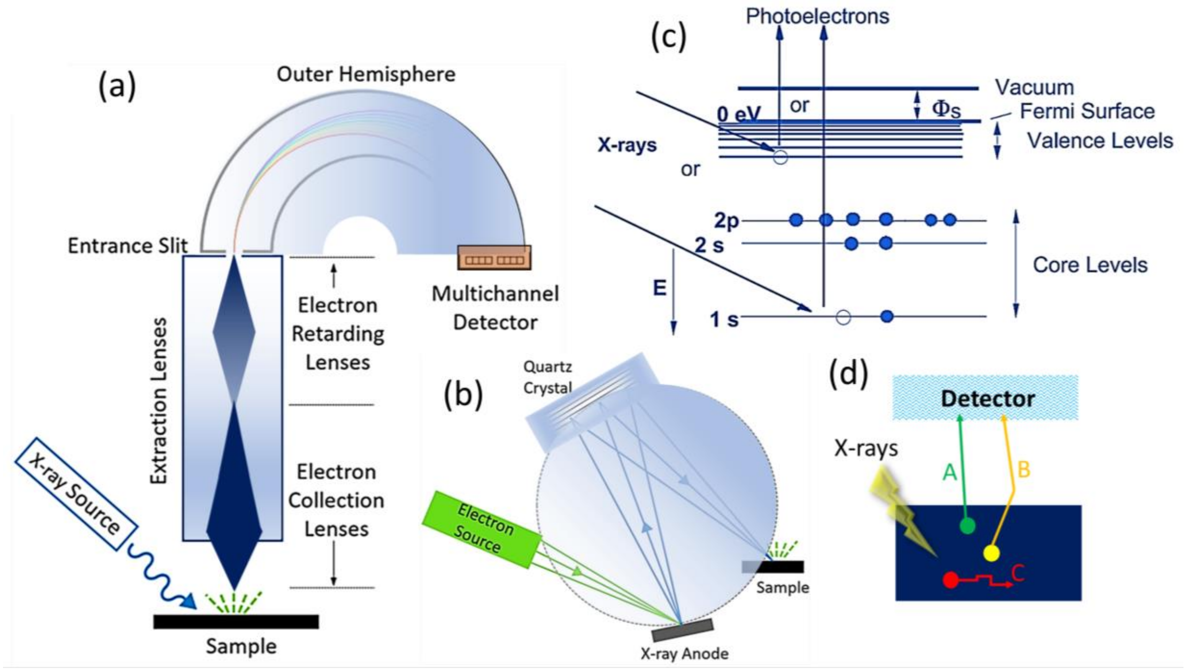

Figure 2.6: Schematic of XPS instrumentation represents the major components of an (a) XPS instrument and (b) monochromator. The schematic of ejection of photoelectron (c). A schematic of interaction of emitted electrons with the sample in different ways depending on the depth at which they are generated (d).

The photoelectron binding energy is measured with respect to the sample Fermi level (not the vacuum level) which is the reason that Φ_{sp} is included as shown in Figure 2.5c.

$$h\nu = E_K + E_b + \phi_{sp} \qquad (2.20)$$

Photoelectron peaks are notated by the element and orbital from which they were ejected. For example, “O 1s” describes electrons emitted from the 1s orbital of an oxygen atom. The loss of the XPS core electron results in a core “hole.” This excited ionized state will relax by filling the hole with an electron from a valence orbital. This relaxation process releases energy in one of the two competing processes: X-ray fluorescence or the emission of an Auger electron, where Auger electrons are detected and used in XPS for quantitative analysis. The kinetic energy of the Auger electron depends on the binding energies of specific orbitals in the atom from which it originated.

An important advantage of XPS over other techniques is the ability to determine the chemical environment of the atoms present in a sample. This chemical environment, including factors like nearest neighbours and the oxidation state of the element, affects the binding energy of the photoelectron peaks (and the Auger peaks). In the case of C 1s, the binding energy is dependent on the electronegativity of the nearest neighbour elements. As the neighbouring atom becomes more electronegative, the binding energy of C 1s electron increases. For most transition metals, the binding energy is primarily affected by the oxidation state of the metal. If an atom has already lost some electron density and exhibits a positive charge, it will be more difficult to remove an electron from that atom, and the binding energy will be higher.

XPS is surface sensitive method, which can be explained by Figure 2.6d, where the X-rays that irradiate the sample can penetrate quite deeply (a few µm) into the sample. Electrons generated this deep in the sample will encounter many inelastic collisions (collisions that involve the loss of energy) and will eventually lose all their energy before escaping from the sample. The electrons labelled “C” represent these deeply generated electrons. Electrons generated nearer to the surface may have only one or two inelastic collisions before escaping from the sample and reaching the detector. These electrons leave the sample with less kinetic energy than expected, because they have lost some random amount of energy on their way to the detector. These electrons are labelled as “B”; they contribute to the vertical step in the background signal that accompanies any large photoelectron or Auger electron peak. The background contribution from the C 1s peaks is shaded in orange, and similar background contributions are made by the O 1s and O Auger peaks. Only the electrons that escape the surface without any inelastic collisions will contribute to the characteristic photoelectron peaks that we use in XPS analysis. These are labelled “A” in Figure 2.6d.

The surface sensitivity of XPS is determined by how deep an electron can be generated and still escape without inelastically scattering. Beer’s law describes the intensity, I, of electrons emitted from a sample at depths deeper than d, where I_0 represents the total number of electrons generated from the sample.

$$I = I_0 \exp(-d/\lambda) \tag{2.21}$$

The term λ is the attenuation length of the electron, which will depend on the energy of the electron and the material through which it is traveling.

Experimental conditions

XPS measurements were performed on a VersaProbe II System by UlvacPhi. A monochromatized Ag-Kα source was used with a beam diameter of 100 µm. The NPs were dropcast onto a conductive Si-wafer for the measurements. For data analysis a Shirley background was used.

In Shirley background method, the background intensity at any given binding energy is proportional to the intensity of the total peak area above the background in the lower binding energy peak range.[202] The precise way of fitting depends on the element. In the case of carbon, the Gaussian-Lorentzian curve is representative for one specific species (the same applies for oxygen and silicon).

2.3.5 Extended X-ray absorption fine structure (EXAFS)

XAFS is the modulation of the X-ray absorption probability of an atom due to the chemical and physical state of the atom. XAFS spectra are especially sensitive to the formal oxidation state, coordination chemistry, and the distances, coordination number and species of the atoms immediately surrounding the selected element. As all atoms have core level electrons, XAFS spectra can be measured for essentially every element on the periodic table. Importantly, crystallinity is not required for XAFS measurements, making it one of the few structural probes available for nanocrystalline and highly disordered materials, including solutions and amorphous materials. XAFS is not inherently surface-sensitive unlike XPS, because electron absorption in involved in former case.

The X-ray absorption spectrum is typically divided into two regimes: X-ray absorption near-edge spectroscopy (XANES) and extended X-ray absorption fine-structure spectroscopy (EXAFS) as shown in Figure 2.7d. Though the two have the same physical origin, this distinction is convenient for the interpretation. XANES is strongly sensitive to formal oxidation state and coordination chemistry of the absorbing atom, (e.g., octahedral or tetrahedral coordination) while the EXAFS is used to determine the distances, coordination number, and species of the neighbours of the absorbing atom.

X-rays have energies ranging from ~ 500 eV to 500 keV, or wavelengths from ~ 25 Å to 0.25 Å. In this energy regime, light is absorbed by all matter through the photo-electric effect. In this process, an X-ray photon is absorbed by an electron in a tightly bound quantum core level (such as the 1s or 2p level) of an atom as shown in Figure 2.7a-c. In order for a particular electronic core level to participate in the absorption, the binding energy of this core level must be less than the energy of the incident X-ray. If the binding energy is greater than the energy of the X-ray, the bound electron will not be perturbed from the well-defined quantum state and will not absorb the X-ray. If the binding energy of the electron is less than that of the X-ray, the electron may be removed from its quantum level. In this case, the X-ray is destroyed (i.e., absorbed) and any energy in excess of the electronic binding energy is given to the photo-electron that is ejected from the atom. In the hard X-ray regime (> 2 keV), X-ray fluorescence is more likely to occur than Auger emission.

In the process of X-ray absorption, the absorption coefficient (μ) gives the probability that X-rays will be absorbed according to Beer's Law Equation 2.22.

$$I = I_0 e^{-\mu t} \tag{2.22}$$

Where, I_0 is the x-ray intensity incident on a sample, t is the sample thickness, and I is the intensity transmitted through the sample. At most X-ray energies, the absorption coefficient μ is a smooth function of energy, with a value that depends on the sample density ρ, the atomic number Z, atomic mass A, and the x-ray energy E roughly as equation 2.23.

$$\mu = {}^{\rho Z^4}\!/_{AE^3} \tag{2.23}$$

Due to the Z^4 dependence, the absorption coefficient for O, Ca, Fe, and Pb are very different spanning several orders of magnitude, so that good contrast between different materials can be achieved for nearly any sample thickness and concentrations by adjusting the x-ray energy. When the incident x-ray has an energy equal to that of the binding energy of a core-level electron, there is a sharp rise in absorption. The absorption edge corresponding to the promotion of this core level to the continuum is shown in Figure 2.7d.

An XAFS measurement is simply a measure of the energy dependence of μ at and above the binding energy of a known core level of a known atomic species, for example the XAFS spectra of BFO NPs are shown in Figure 2.7e. Since every atom has core-level electrons with well-defined binding energies, we can select the element to probe by tuning the X-ray energy to an appropriate absorption edge. Following an absorption event, the atom is in an excited state, with one of the core electron levels left empty (a so-called core hole), and a photo-electron. The excited state will decay typically within a few femtoseconds of the absorption event. There are two main mechanisms for the decay of the excited atomic state following an X-ray absorption event. The first of these is x-ray fluorescence in which a higher energy electron core-level electron fills the deeper core hole, ejecting an x-ray of well-defined energy. The fluorescence energies emitted in this way are characteristic of the atom and can be used to identify the atoms in a system, and to quantify their concentrations. For example, an L shell electron dropping into the K level gives the Kα fluorescence line.

XAFS can be measured either in transmission or fluorescence geometries. The geometry for Auger measurements is typically the same as for fluorescence. One can measure the energy dependence of the absorption coefficient μ(E) either in transmission as shown in Equation 2.24 or in X-ray fluorescence (or Auger emission) as shown in Equation 2.25.

$$\mu(E) = \log\left(I_0/I\right) \tag{2.24}$$

$$\mu(E) \propto \log\left(I_f/I\right) \tag{2.25}$$

where I_f is the monitored intensity of a fluorescence line (or, again, electron emission) associated with the absorption process.

For EXAFS, one is interested in the oscillations well above the absorption edge. The EXAFS fine-structure function χ(E), as defined in Equation 2.26.[203]

$$\chi(E) = {\mu(E) - \mu_0(E)}\Big/{\Delta\mu_0(E)} \tag{2.26}$$

μ(E) is the measured absorption coefficient, $\mu_0(E)$ is a smooth background function representing the absorption of an isolated atom, and $\Delta\mu_0$ is the measured jump in the absorption μ(E) at the threshold energy E_0. As we will see below, EXAFS is best understood in terms of the wave behaviour of the photo-electron created in the absorption process. Because of this, it is common to convert the x-ray energy to k, the wave number of the photo-electron, which has dimensions of 1/distance and is defined by equation 2.27.

$$k = \sqrt{{2m(E - E_0)}\Big/{\hbar^2}} \tag{2.27}$$

where E_0 is the absorption edge energy and m is the of the free electron mass. The primary information for EXAFS is χ(k), the oscillations as a function of photo-electron wave number. χ(k) is often referred to simply as "the EXAFS".

The different frequencies apparent in the oscillations in χ(k) correspond to different near-neighbours coordination shells which can be described and modelled according to the EXAFS superposition equation.[203]

$$\chi(k) = \sum_j \frac{N_j f_j(k) e^{-2k^2\sigma_j^2}}{kR_j^2} sin\big(2kR_j + \delta_j(k)\big) \tag{2.28}$$

f(k) and δ(k) are the scattering properties of the atoms neighbouring the excited atom, N is the number of neighbouring atoms, R is the distance to the neighbouring atom, and σ^2 is the disorder in the neighbour distance. Though somewhat complicated, the EXAFS equation allows us to determine N, R, and σ^2 knowing the scattering amplitude f(k) and phase-shift δ(k). Furthermore, since these scattering factors depend on the Z of the neighbouring atom, EXAFS is also sensitive to the atomic species of the neighbouring atom.

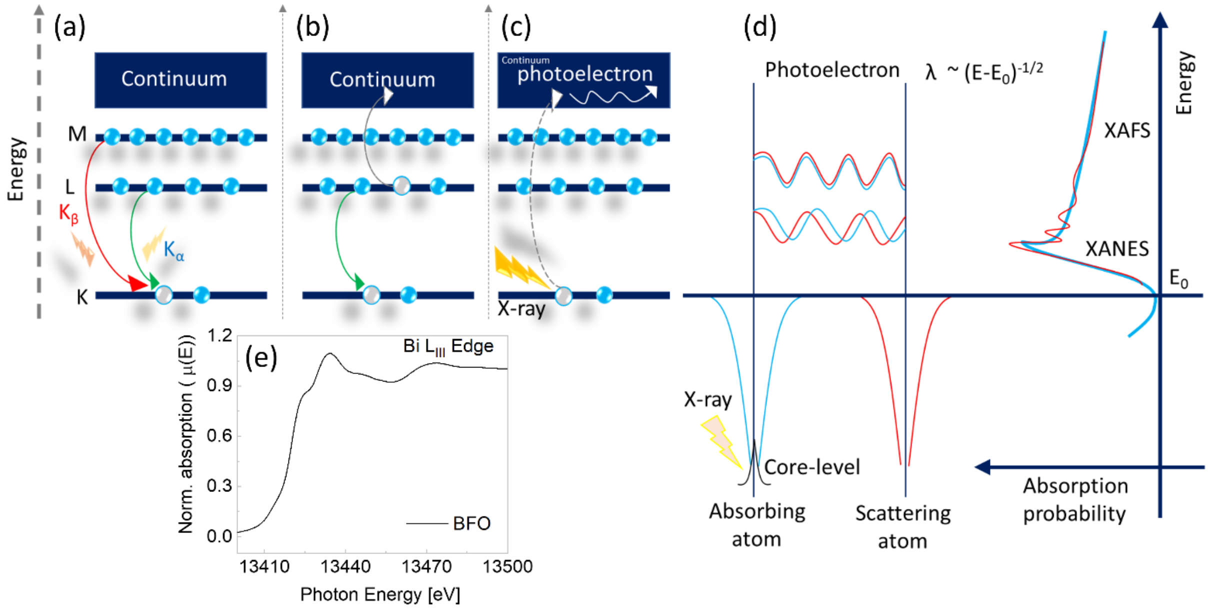

Figure 2.7: Decay of the excited state, X-ray fluorescence (a) and the Auger effect (b). In both cases, the probability of emission (X-ray or electron) is directly proportional to the absorption probability. The photoelectric effect, in which an x-ray is absorbed, and a core-level electron is promoted out of the atom (c). XAFS occurs because the photo-electron can scatter from a neighbouring atom. The scattered photo-electron can return to the absorbing atom, modulating the amplitude of the photo-electron wave-function at the absorbing atom. This in turn modulates the absorption coefficient μ(E), causing the EXAFS (d).

Experimental conditions

EXAFS spectra for Bi L_{III} absorption edges (13.4186 keV) were recorded in transmission at the BAMline at the Helmholtz-Zentrum Berlin (BESSY II, Berlin, Germany)[204] with horizontally polarized hard X-rays from a 7 T shifter at room temperature in air. The signal from the upstream ionization chamber is filled with xenon for the normalization of the X-ray incoming intensity. Powders were mixed with hexagonal BN powder to get correct transmission and pressed between 50 µm thick Kapton foils in pellets of 1 mm thick for measurement. As reference, X-ray absorption spectrum of pure Bi foil was recorded at the same absorption edge. EXAFS spectra at the Fe and Mn K-edges (7.1120 and 6.5390 keV, respectively) were recorded in the fluorescence mode (TFY) at the same beamline. A four-element energy dispersive detector was used to collect the fluorescence signal in a similar way as in.[205] As references, X-ray absorption spectra of pure Fe and Mn foils were recorded at the same absorption edges by TFY.

Typically, for each sample and each absorption edge, 2 to 3 measurements were performed and further averaged to improve statistics. Data evaluation, analysis and simulation have been performed using the IFEFFIT software.[206,207]

2.4 Optical characterization

The optical characterization of BFO and doped BFO NPs were performed using DRS, PL, trPL, transient absorption, Raman, IR, and UPS.

2.4.1 Diffuse reflectance spectroscopy (DRS)

The diffuse reflection method is used to measure powder samples with a UV-VIS spectrophotometer. It involves using an integrating sphere to collect and measure the diffuse reflected light. In diffuse reflectance measurements, diffuse reflectance is proportional to concentration and the absorption coefficient when converted by Kubelka-Munk transformation, in the same way that transmittance is proportional to concentration and the absorption coefficient when converted to absorbance.

When monochromatic light passes through a sample, the ratio between the intensity of the incident light beam (I_0) and the intensity of the transmitted light beam through the sample (I_t) is referred to as the transmittance (t). The percent transmittance (%T) indicates transmittance as a percentage [Equation 2.29].

$$T(\%) = {}^{I_T}\!/_{I_0} \cdot (100) \tag{2.29}$$

Given a sample absorption coefficient ε, sample concentration c, and length (optical path length) ℓ, I_0 and I_t are related by Equation 2.30.

$$I_t = I_0 \cdot (10^{-\varepsilon c l}) \tag{2.30}$$

The absorbance (A) value indicates the level of light absorption. It is expressed by Equation 2.31, which represents the negative common logarithm of transmittance.

$$A = -log\ ({}^{I_T}\!/_{I_0}) \tag{2.31}$$

Absorbance is the multiplicative product of the absorption coefficient (ε), concentration (c), and optical path length (ℓ). This relationship is referred to as the Lambert-Beer Law.

The absorbance can be normalised to the path length of the light through the material (or thickness of film) producing the absorption coefficient “α” [Equation 2.32].

$$\alpha(cm^{-1}) = \ln(10)\varepsilon c \tag{2.31}$$

The optical path is different when measuring the diffuse reflectance of powder samples. A diagram of light shining onto a powder sample is shown in Figure 2.8. Two types of light are reflected from powder samples, specular reflected light that is reflected from the sample surface and diffuse reflected light that is emitted out of the surface after penetration and repeated refraction, transmission, and scattering inside the sample. Powder sample measurements detect reflected light that is a mixture of specular and diffuse reflected light.

However, if the particle size in the sample is sufficiently small, the effect of specular reflected light is not large. Because diffuse reflected light repeatedly passes through the sample before exiting the surface, it results in a similar absorption spectrum as transmittance measurements. However, the direction and distance the light travels is different, so the Lambert-Beer Law used for transmittance measurements cannot be used. The absorption of diffuse reflected light was analysed by Kubelka and Munk.[208] Paul Kubelka and Franz Munk proposed a theoretical approach to study how the colour of a substrate is changed after the application of a paint layer with certain composition and thickness. At present, the K-M model is commonly used to analyse DRS results and estimate the optical band gap energy (or simply the band gap) of semiconductor materials. Kubelka and Munk suggested that the absorption and scattering are first order phenomena.[208]

As per the K-M model, system must have a cylindrical geometry with a flat area A and a thickness L, so the boundaries' effects are nominal. The incident light has intensity I and the reflected portion has intensity *J*, which allows to define a dimensionless quantity, the reflectance (R = *J*/*I*). Naturally, R depends on L and the absorption and scattering properties of the medium. When considering a sample with semi-infinite thickness (L→ ∞), the K-M model written as Equation 2.32.

$$f(r_\infty) = {(1 - R_\infty)^2}/{2R_\infty} = {K}/{S} \tag{2.32}$$

(R_∞) is referred to as the Kubelka-Munk function, where R_∞ is the absolute reflectance of the sample, K is the absorption coefficient, and S is the scattering coefficient. The scattering coefficient varies depending on the size and density of the particles. For actual measurements, the absolute reflectance is difficult to determine. Therefore, barium sulfate with an absorption coefficient K that is close to zero in the measurement range (i.e., with an R_∞ value close to 1) is used as a standard powder and then the relative reflectance is measured. Typically, an integrating sphere attachment is used to measure the relative diffuse reflectance values of a powder sample required for the Kubelka-Munk transformation. Figure 2.8, shows an example of an integrating sphere attachment. Diffuse reflectance is measured by placing the measurement sample next to the reflectance measurement window on the side of the integrating sphere. The sample is placed in a powder sample holder. Barium sulphate ($BaSO_4$) is used as standard and also to correct the baseline.

The Kubelka-Munk transformation for DRS measurements yields values that are proportional to the concentration and the absorption coefficient. This can be utilized for various applications such as for the quantification of samples that cannot be prepared as a solution. However, using the Kubelka-Munk transformation involves an additional scattering coefficient, which can cause the resulting values to vary depending on the particle size and density. Therefore, to ensure accurate quantitative values, the scattering coefficient must be constant.

Tauc and Cody Model for optical band gap estimation

For the estimation of the optical band gap based on the K-M plot and the absorbance plots of semiconductors, there are two widely used methods, one is the Tauc model, and another one is Cody plot.[209,210] The theoretical foundation of the Tauc plot extrapolation[209] is based on the energy dependence of the above-band-gap absorption, which appears either as a squared relation (direct-allowed-transition dominated) or a square-root relation (indirect-allowed-transition dominated).[209,211]

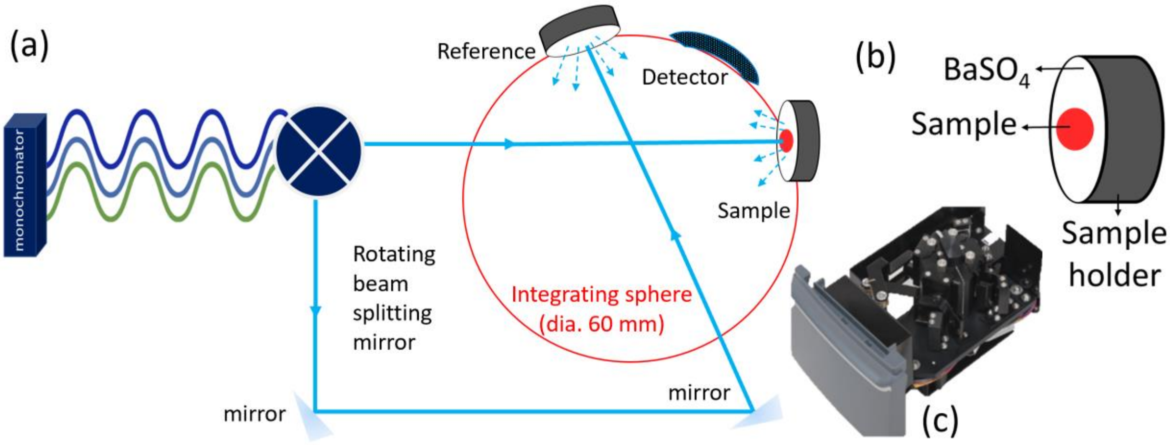

Figure 2.8: the schematic of DRS measurements within integration sphere (a). Sample with standard Barium sulphate for relative diffuse reflectance measurement (b). Integrating sphere attachment (ISR-2600 Plus) (c).

For the crystalline semiconductors, the momentum matrix element is independent of the photon energy, $\hbar\omega$. As a consequence, assuming square-root distributions of valence-band and conduction-band band states, for sufficiently large values of $\hbar\omega$, the imaginary part of the dielectric function is.

$$\varepsilon_2(\hbar\omega) \propto \frac{(\hbar\omega - E_g)^2}{(\hbar\omega)^2} \tag{2.33}$$

Where, E_g provides the energy difference between the two band edges. The optical absorption coefficient α can be described by Equation 2.34.

$$\alpha(\hbar\omega) = \frac{\omega}{n\ (\hbar\omega)\mathrm{c}}\varepsilon_2(\hbar\omega) \tag{2.34}$$

n($\hbar\omega$) signifies the spectral dependence of the refractive index, and c is the speed of light in vacuum. Assuming that n($\hbar\omega$) is independent of photon energy ($\hbar\omega$), the absorption coefficient can be written as Equation 2.35.

$$\alpha(\hbar\omega) \propto \frac{(\hbar\omega - E_g)^2}{(\hbar\omega)} \tag{2.35}$$

This yields a linear [equation 2.36] extrapolation to the abscissa-axis which will provide the optical band gap E_g.

$$\sqrt{\alpha(\hbar\omega)} \propto (\hbar\omega - E_g) \tag{2.36}$$

The Cody model uses a dipole matrix element that is independent of the photon energy $\hbar\omega$, and not the momentum matrix element. Cody et al argue for square-root distributions of valence-band and conduction-band states, for sufficiently large values of $\hbar\omega$, that the imaginary part of the dielectric function is.

$$\varepsilon_2(\hbar\omega) \propto (\hbar\omega - E_g)^2 \tag{2.37}$$

Upon assuming that n($\hbar\omega$) is independent of the photon energy ($\hbar\omega$), the optical absorption coefficient is written as.

$$\alpha(\hbar\omega) \propto \hbar\omega(\hbar\omega - E_g)^2 \tag{2.38}$$

From equation 2.38, there is a linear extrapolation of the spectral dependence [Equation 2.39] to the abscissa axis which yield the optical gap measure E_g.

$$\sqrt{\alpha/(\hbar\omega)} \propto (\hbar\omega - E_g) \tag{2.39}$$

Hence general equations for optical band gap estimation from Tauc [Equation 2.40] and Cody [Equation 2.41] models can be written as following.

$$(\hbar v\alpha)^{1/n} \propto (\hbar\omega - E_g) \tag{2.40}$$

$$(\alpha/\hbar v)^{1/n} \propto (\hbar\omega - E_g) \tag{2.41}$$

Where, for direct allowed transition n =1/2, for direct forbidden transition, n =3/2, for indirect allowed transition n= 2, and for indirect forbidden transition n = 3.

The acquired diffuse reflectance spectrum can be converted to the K-M function $f(r_\infty)$ as discussed previously. The $f(r_\infty)$ is proportional to the optical absorption coefficient α,[212] and hence $f(r_\infty)$ can be replaced with α in Equations 2.40, and 2.41 for estimation of optical band gap using DRS spectrum of a powder sample.[211]

Experimental conditions

Diffuse reflectance spectra (DRS) of the NPs were collected using a UV-Vis spectrometer Shimadzu 2600 in the wavelength range 300-900 nm. The NP-powder was pressed and then measured inside an integrating sphere in reflectance mode. Barium sulfate was used as a reference and the baseline was corrected before recording each spectrum. Transmission spectra of diluted NPs and NPs drop-cast onto quartz substrates were recorded using a Shimadzu UV-2550 spectrometer equipped with an integrating sphere in transmission geometry.

2.4.2 Emission spectroscopy

The excitation and recombination of the electronic transition are shown in Figure 2.9i using Jablonski diagram. Photoluminescence is when light energy, or photons, stimulate the emission of a photon. Fluorescence is a type of photoluminescence caused by photons exciting a molecule, raising it to an electronic excited state. The excited state undergoes rapid thermal energy loss to the environment through vibrations, and then a photon is emitted from the lowest-lying singlet excited state. This process of photon emission competes for other non-radiative processes including energy transfer and heat loss. Both phosphorescence and fluorescence are forms of photoluminescence, photo stimulated light emission. The key difference between phosphorescence and fluorescence is that the photoluminescence occurs via absorbing and emitting photons having equal wavelengths whereas fluorescence occurs via emitting a longer wavelength than the absorbed wavelength.

Charge carrier recombination

Charge carrier recombination describes various processes of electron-hole pair annihilation inside a semiconductor. Fundamentally, charge carriers in semiconductors can recombine by releasing the excess energy either by emitting photons (radiatively) or releasing phonons (non-radiatively). While radiative recombination processes are unavoidable from a thermodynamic point of view, suppression of non-radiative and defect-related recombination has to studied in order to understand their impact in overall catalytic activity or other semiconductor properties. Radiative recombination occurs when the excited electron and hole recombine and emit a photon of light, it can observed in luminescence spectrum. Time-resolved photoluminescence (TRPL) technique can be used to detect radiative charge carrier recombination.

The excitation energy is dissipated during nonradiative recombination as phonons instead of photons, non-radiative recombination processes cannot be directly observed in luminescence spectra. The respective recombination rate increases with increasing temperature, decreasing band gap and an increasing concentration of deep states, respectively. As these states typically arise from impurity atoms and defects, a suppressed recombination rate is an indicator for a rather defect-free semiconductor material. Transient absorption spectroscopy (TAS) measures the change in absorption of the material as the charge carriers recombine, providing information about the energy levels involved in the recombination process.

The time resolved photoluminescence decay kinetics of NPs can be calculated using a TRPL decay graph. The decay kinetics can be fitted by a mono-, bi- or tri- exponential decay function, explaining the type of decay components. For example, for bi-exponential decay, $\mathrm{I} = \mathrm{A}_1\exp(-\mathrm{t}/\tau_1) + \mathrm{A}_2\exp(-\mathrm{t}/\tau_2)$. The average lifetime of charge carriers is,

$$\text{Average } \tau = \frac{[(A_1 \cdot \tau_1^2) + (A_2 \cdot \tau_2^2)]}{[(A_1 \cdot \tau_1) + (A_2 \cdot \tau_2)]} \tag{2.42}$$

To understand the charge carrier dynamics, one can utilise TAS. In TAS measurements, to pump, i.e., to excite a molecular ensemble to a state above the ground state at an exactly defined moment in time.[213] Subsequently, the excited-state dynamics are probed at different delay times τ between the pump and the probe occurrences. A large variety of experiments for preparing excited-state populations or reactive intermediates and suitable probing methods can be employed. The pump triggers the population of the excited state in the sample can either be irradiation of the sample with a laser pulse to transfer energy into the initial equilibrium system.[214]

Hence, a pump light pulse excites the sample and a weak probe pulse delayed by Δt (delay time between pump and probe) analyses the resulting mixture of ground state absorption (GSA) and excited state absorption (ESA) as shown in Figure 2.9. The pump (488 nm, 280 nJ) induced transient absorption signal ΔOD (t, λ) (optical density), is measured with a continuum probe in the range of 400-850 nm. The TAS setup and the method have been described elsewhere.[215,216,217,218] Briefly, TA spectra are recorded with 16 forward and backward pump-probe scans, with 1 ps steps. The TA signal consists of three contributions: negative bleach, negative stimulated emission (SE), and positive ESA. The spectra are measured at a pump energy of 280 nJ. Here, a negative bleach signal can be traced from 415 to 450 nm (before the scattering starts) while ESA extends from 550 to 830 nm. Band integrals taken over these regions give the ground-state recovery and the excited-state evolution.

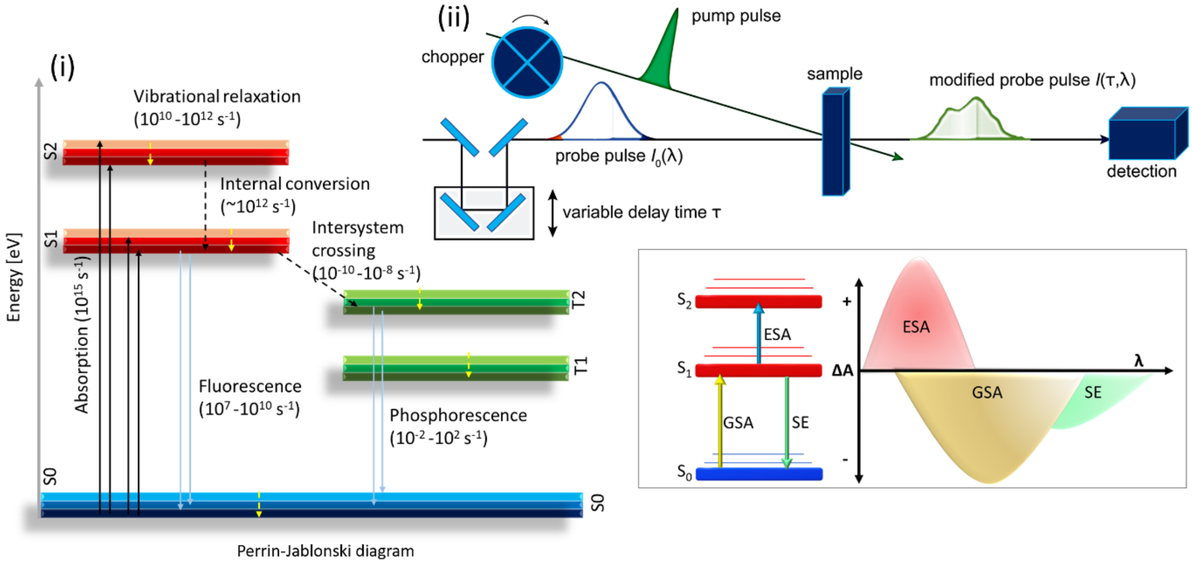

Figure 2.9: Schematic of electronic transition and emission based on Perrin-Jablonski diagram (i). The schematic of transient absorption (TA) pump–probe experiment to measure photoinduced molecular dynamics. Here an optical pump pulse excites the molecular sample whereas a temporally delayed probe pulse measures the pump-induced change in the sample's absorbance. So, the wavelength-dependent intensity of the probe spectra has to be measured with and without the pump interaction.[213] Bottom image: schematic of three main electronic contributions in TA signal, ground state absorption (GSA), excited state absorption (ESA), and stimulated emission (SE).

In a TAS spectrum, the absorption band shows a negative sharp GSA feature that is due to bleaching of the ground state,[215,216] due to excitation by the higher intensity pump source. The ESA spectral intensity decreases with increased delay time due to less population of the excited state. The ESA decay region can be fitted using exponential functions. Fitting the bleaching kinetics can also be fitted using exponential functions. For example, the bi-exponential decay fit for the change in absorbance is.

$$\Delta A(\tau) = A_1 e^{-t/\tau_1} + A_2 e^{-t/\tau_2} \tag{2.43}$$

A is absorbance, t is time, and A_1, A_2, are the pre-exponential factors corresponding to the exponential decays with lifetimes of τ_1, and τ_2, respectively. There can be two or more types of components with shorter and longer decay times. The average lifetime can also be calculated using.

$$\text{Average } \tau = \frac{[(A_1 * \tau_1) + (A_2 * \tau_2)]}{[A_1 + A_2]} \tag{2.44}$$

The shorter decay lifetimes are attributed to the presence of trap-states, which introduce additional pathways for non-radiative recombination of charge carriers.

Experimental conditions

To measure the emission spectra, a Varian Cary Eclipse Fluorescence spectrophotometer was used. A 450 nm laser excitation source was used. The emission spectra were collected in the range from 550-650 nm. A stable dispersion of NPs was prepared in ethanol (optical grade) and a baseline was obtained by measuring pure ethanol. The samples were dissolved in optical grade ethanol and treated in an ultrasonic bath for 10 minutes. The concentration of all types of NPs were kept the same during the PL measurements.

Temperature-resolved PL measurements were conducted inside a CryoMech PT-403 closed-cycle cryostat under high vacuum (< 10^{-5} mbar). The samples were excited with the filtered 325 nm line of a Kimmon IK-series He-Cd laser. Luminescence spectra were collected using a fused-silica lens system and dispersed using a Horiba iHR320 grating monochromator before being recorded by a Horiba Symphony I CCD camera. Samples were dissolved in optical grade ethanol and treated in an ultrasonic bath for 30 minutes. 20 µL of the dispersion were then drop-cast onto a cleaned Si substrate and dried at room temperature. A reference sample was prepared by drop-casting 20 µL of ethanol on an identical Si substrate.

2.4.3 Infra-red spectroscopy (IR)

Working Principle

IR spectroscopy deals with the absorption of infrared light at characteristic frequencies. Fourier transform infrared (FTIR) spectrometer separate the frequencies instead of any dispersive elements like grating or prism. The advantages of using a FTIR over an IR spectrometer are high throughput, simultaneous measurement of all frequencies (multiplex advantage), mechanical simplicity (very few moving parts), and internal calibration with the He-Ne laser.

The main components of an FTIR spectrometer are the infrared source, an interferometer, and an infrared detector (Figure 2.10). The interferometer essentially consists of a titled beam splitter, and movable mirrors. If a collimated beam of monochromatic light of wavenumber $\nu = 1/\lambda$, is made to fall onto an ideal beam splitter, 50% of the incident radiation will be reflected to one of the mirrors while 50% will be transmitted to the other mirror. The two beams reflected from the fixed and movable mirrors and return to the beam splitter where they recombine and interfere. Finally, this light interacts with the sample after which it is measured by the detector. It detects the intensity of light as a function of path difference, δ (also known as retardation), introduced by the movable mirror. The resulting pattern is known as an interferogram ($I(\delta)$). The resolution for an FTIR instrument is given by the inverse of the maximum path difference introduced by the movable mirror. For instance, a path difference of 10 cm will result in a resolution of 0.1 cm^{-1}.

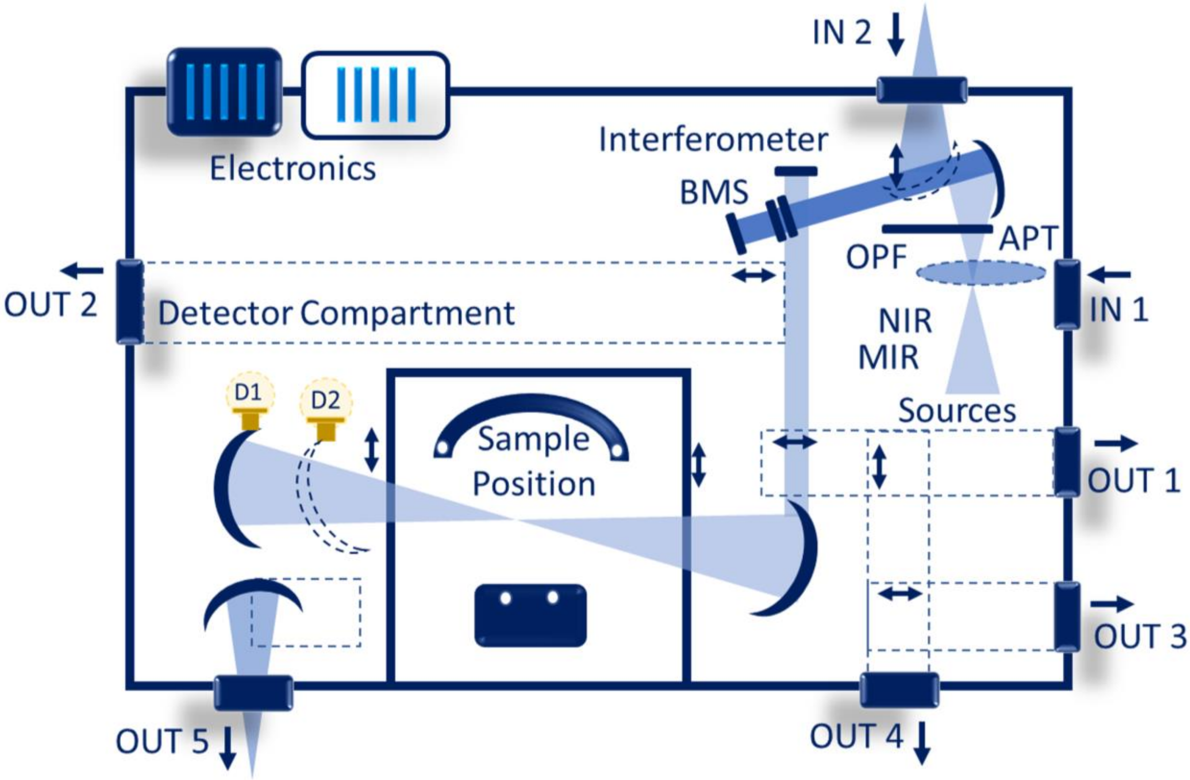

Figure 2.10: Optical beam path of the standard spectrometer configuration of Vertex 70. D1: standard detector, D2: optional detector, BMS: beam-splitter, APT: aperture wheel, OPF: optical filter wheel with filter diameter 25 mm, IN1 and IN2: IR beam inlet port 1 and 2, Out1 to out 5: IR beam outlets.

Experimental conditions

IR measurements were performed on a Bruker Vertex 70 FT−IR spectrometer operated with a liquid nitrogen cooled mercury−cadmium−telluride (MCT) detector (Bruker Optics, Germany) and along with an ATR accessory (ConcentratIR2, Harrick Scientific, U.S.A.) comprising a diamond ATR waveguide (10 internal reflections). IR spectra (4000−600 cm^{-1}) were recorded at a resolution of 2 cm^{-1} averaging of 100 spectral scans and processed utilizing the OPUS 7.2 software package (Bruker Optics, Germany). The spectral resolution 0.4 cm^{-1} was kept for all measurements.

2.4.4 Raman spectroscopy

In 1928, the Indian scholar C. V. Raman discovered that when monochromatic light of a fixed frequency is incident on a medium, two scattering processes occur simultaneously: one is Rayleigh scattering with constant frequency, which is caused by elastic collisions between the incident photons and matter, and the other is frequency-changing Raman scattering, which is caused by an energy exchange that occurs when the incident photons collide with matter, causing a change in the molecule vibrational or rotational energy levels.[219]

Raman spectroscopy is based on inelastic scattering of a monochromatic light by the sample. When light of frequency ν_0 is incident on a solid, most of it is scattered at the same frequency (elastic scattering), while a small fraction gets scattered inelastically with frequencies $\nu_0 \pm \nu_m$, where ν_m are the characteristic vibrational frequencies of the solid or molecule. The quantum mechanical description of Raman scattering is shown in Figure 2.11a. The sample goes from ground state to a virtual state when an incident radiation of frequency ν_0 is made to fall onto the sample and returns to the ground state by emitting radiation of the same frequency as the incident frequency (Rayleigh scattering) or of a lower frequency by returning to a vibrational excited state (Stokes scattering). On the other hand, the sample may also go from an excited state to a virtual state by interacting with the laser light and then return to the ground state by emitting a light of higher frequency (anti stokes scattering). [Figure 2.11b]

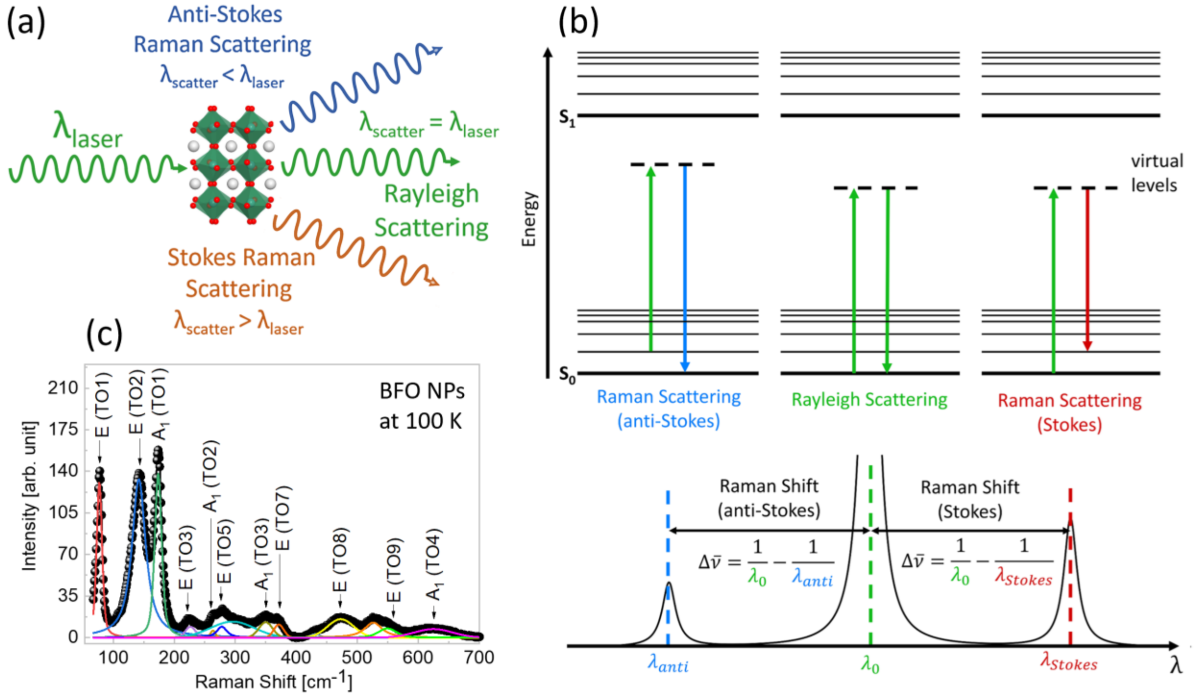

Figure 2.11: Types of scattering processes that can occur when light interacts with a molecule (a). Jablonski Diagram showing the origin of Rayleigh, Stokes, and Anti-Stokes Raman Scatter (b). Raman Spectra of BFO NPs measured using a 533 nm laser at 100 K, indexed with 13 active Raman modes of R3c BFO (c).

The Raman peaks occur due to the vibrational modes of the molecules. When a molecule absorbs a photon of light, it can undergo a change in its vibrational energy, which leads to the Raman scattering. The Raman peaks correspond to the energies of the vibrational modes of the molecule, and the intensity of each peak is related to the strength of the interaction between the light and the number of molecules/atomic sites that have the corresponding vibrational mode. The positions and intensities of the Raman peaks are therefore characteristic of the chemical and physical properties of the sample and can be used for identification and characterization of materials. For BFO NPs, and Ba and Mn doped BFO NPs, the Raman spectra measured using a 533 nm laser are shown in Figure 2.11c.

A schematic of the Raman spectrometer is shown in Figure 2.12. The laser beam passes through a holographic filter, which makes the beam pure plane wave and then reaches the sample surface with the help of a combination of lenses, mirrors, and a beam splitter. The back scattered laser light passes through optical filters, which filters out the predominant Rayleigh scattering (99.999 %) and allows Raman (stokes and anti stokes lines) scattered signals to pass. Finally, the Raman signal is measured by charge coupled device (CCD) detectors.

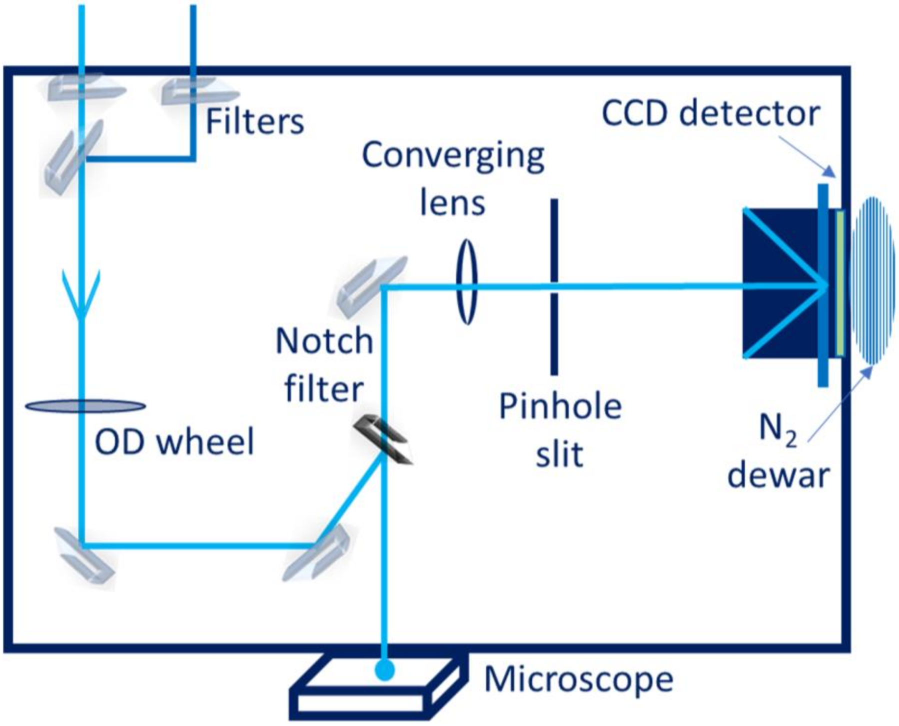

Figure 2.12: Schematic diagram of the internal optics of the Raman spectrometer (LABRAM HR 800).

Experimental conditions

Raman measurements were performed in a back-scattering geometry using a LABRAM Horiba Jobin–Yvon spectrometer (He–Ne laser, 632.8 nm) in backscattering geometry. Scattered photons with wavenumber from 50 to 1000 cm^{-1} were selected using an edge band pass filter. The temperature was controlled by using Linkam heating stage (80 K-870 K) placed under the Raman microscope. Typical optical magnification was attained using a x 10 objective lens having a numerical aperture of 0.25, to obtain a signal averaged within different grains. The sample was carefully deposited on the heating plate and then the laser was focused on it. After the temperature was stabilized, the beam focusing was again adjusted to obtain the maximum intensity, and suitable testing time was set.The laser power was not harmful to the sample by any heating process and an objective lens of 10 times magnification was used. The deconvolution was done by Lorentzian and Gaussian schemes.

2.4.5 Ultraviolet photoelectron spectroscopy (UPS)

UPS functions on the same principles as XPS. The difference between the two techniques lies in the fact that UPS utilizes ionizing radiation with energies of tens of electron volts to induce the photoelectric effect, instead of using photons with energies greater than 1 keV as in XPS. UPS uses vacuum UV radiation (with a photon energy of 10-45 eV) to examine electrons in valence levels. Ultraviolet photons are produced in the laboratory setting using a gas discharge lamp that is typically filled with helium, although other gases like argon and neon can used. The photons emitted by helium have energies of 21.2 eV (He I) and 40.8 eV (He II). Since lower energy photons are used, most core level photoemissions are not accessible using UPS. Therefore, spectral acquisition is limited to the valence band region as shown in Figure 2.13. There are two types of experiments that are performed using UPS, valence band acquisition and electronic work function (ϕ) measurement. Many of the molecular orbitals from which valence band photoelectron signal originates possess a high degree of hybridization. Therefore, the shifts in peak binding energy are far more varied and subtle than those observed for core level photoemission peaks. For this reason, valence band spectra are predominantly used for material characterization through spectral fingerprinting.

Different electronic transitions and states can be probed by using different photon energies. UPS exhibits greater surface sensitivity than XPS. The inherent surface sensitivity of XPS is due to the short inelastic mean free path of free electrons within a solid, with the "information depth" from which more than 99 % of a photoemission signal originates conventionally being defined at 3 mean free path lengths from the surface, which in XPS is often quoted as 10 nm as shown in Figure 2.13a. This is an approximation as the inelastic mean free path of an electron is determined by the material properties of the solid media through which it is traveling and its kinetic energy, with electrons of lower kinetic energy having shorter path lengths. The lower incident photon energies used in UPS emit photoelectrons of much lower kinetic energies than those measured in XPS. This gives UPS an approximate information depth of 2-3 nm.

The difference between the Fermi level and vacuum level is referred to as the electronic work function (ϕ). As a surface property, the work function is strongly influenced by variation in composition or structure at the surface, such as atmospheric contamination. The electronic work function is acquired spectroscopically by measuring the difference between the Fermi Level and the cut-off of the "tail" at the low kinetic energy end of the spectrum, also known as spectrum width, and subtracting this value from the incident photon energy. This value can also be measured using X-ray incident radiation. However, UPS allows for work function calculation from a single spectrum. When measuring the electronic work function using photoelectron spectroscopy, it is necessary to apply a small bias of typically 5-10 volts to the sample surface. This is done to deconvolute the true work function of the surface from the internal work function of the spectrometer. [Figure 2.13b]

High binding energy cut off (HBEC) refers to a threshold value of the binding energy (E_B) that is used to limit the energy range of a particular spectroscopic technique. This threshold is typically set to exclude signals from higher binding energy states, which are often associated with surface contaminants or other extraneous species that may interfere with the analysis of the sample of interest. The HBEC can be determined from UPS spectra by identifying the energy range over which the signal-to-noise ratio drops off significantly. In general, this cut-off is set to a value that excludes any signals that are not directly related to the sample being analysed, while still allowing for the detection of all relevant signals associated with the sample. To determine HBEC, one typically examines the energy range at which the signal intensity drops below a certain threshold or becomes indistinguishable from the background noise.

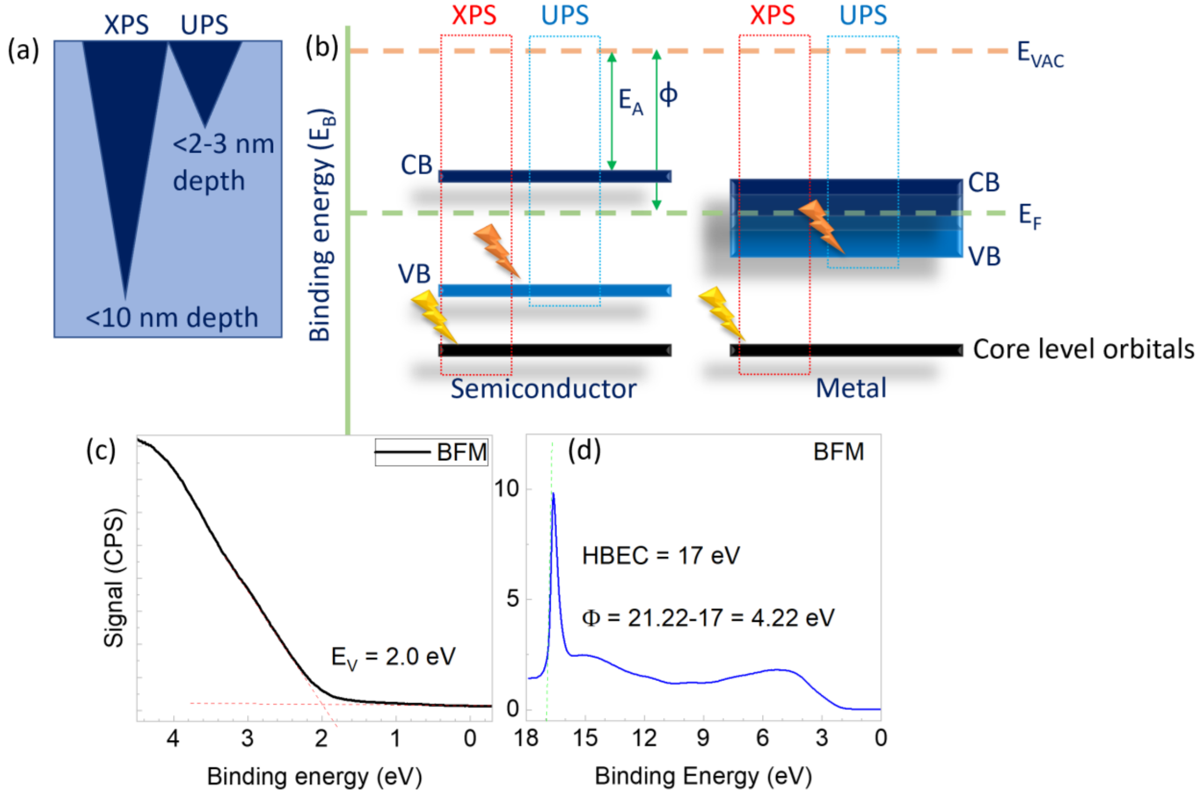

Figure 2.13: The information depth of a material from XPS and UPS (a). Energy level diagram summarizing XPS and UPS differences in semiconductor and in metals (b). The UPS spectrum of Mn doped BFO NPs (BFM) for estimation of valence band edge and work function φ (c-d).

Experimental conditions

UPS measurements were performed on a VersaProbe II System by UlvacPhi. For XPS we used a monochromatized Ag-K_α source with a beam diameter of 100 µm. For UPS we used He I light at 21.22 eV from a He discharge source. To measure the HBEC a negative voltage was applied to overcome the work-function of the analyzer. The NPs were dropcast onto a conductive Si-wafer for the measurements. For data analysis a Shirley background was used. The precise way of fitting depends on the element that is being fitted. In the case of carbon, a Gaussian-Lorentzian curve is representative for one specific species (the same goes for oxygen and silicon).

2.5 Magnetic characterization

VSM (Vibrating Sample Magnetometer) and Mössbauer spectroscopy are two different experimental techniques that can provide complementary information about the magnetic properties of materials. VSM is a common technique used to measure the magnetic properties of materials, such as magnetic moment, magnetic anisotropy, and coercivity. It works by subjecting a sample to a magnetic field while vibrating it and measuring the response of the sample to the field. VSM is particularly useful for measuring macroscopic magnetic properties of bulk materials. Mössbauer spectroscopy, on the other hand, is a technique used to study the hyperfine structure of certain atomic nuclei, such as Fe_{57}. It can provide information about the electronic and magnetic environments of these nuclei in a material. Mössbauer spectroscopy is particularly useful for studying the local magnetic properties of specific atoms in a material.

2.5.1 Vibrating sample magnetometer (VSM)

Working principle

VSM is based on Faraday's law of electromagnetic induction. A schematic for VSM is shown in Figure 2.14a. When a magnetic field is applied to a sample, the magnetic moments of the sample align with the applied field. In VSM the sample is attached to a nonmagnetic rod, which is oscillates or vibrates in a gap between (pairs of) fixed coils (pick-up coils). The stray magnetic field arising from the magnetized sample moves together with the sample, thus producing a varying magnetic flux in the coils. The way to read the magnetic moment of the sample consists in tracking the voltage generated by this varying magnetic flux in the coils, which is proportional to the magnetic moment. The absolute scale of magnetization and the corresponding voltage calibration is done by means of a reference sample. The sample vibrates with frequency ω, such that the signal of interest has also this frequency, being characterized by an amplitude A in the pick-up coils (magnetic induction). The signal from the pick-up coils can be interfered by external sources of electromagnetic radiation (50 Hz). The measured signal is multiplied with the reference signal (ω_1) defined by the vibration driving the sample, where a certain phase difference ϕ may exist.

For the highest resolution a superconducting quantum interference device (SQUID) can be used, consists of two superconductors separated by thin insulating layers to form two parallel Josephson junctions. The device may be configured as a magnetometer to detect extremely weak magnetic fields. SQUID sensitivity can be up to 10^{-14} T.

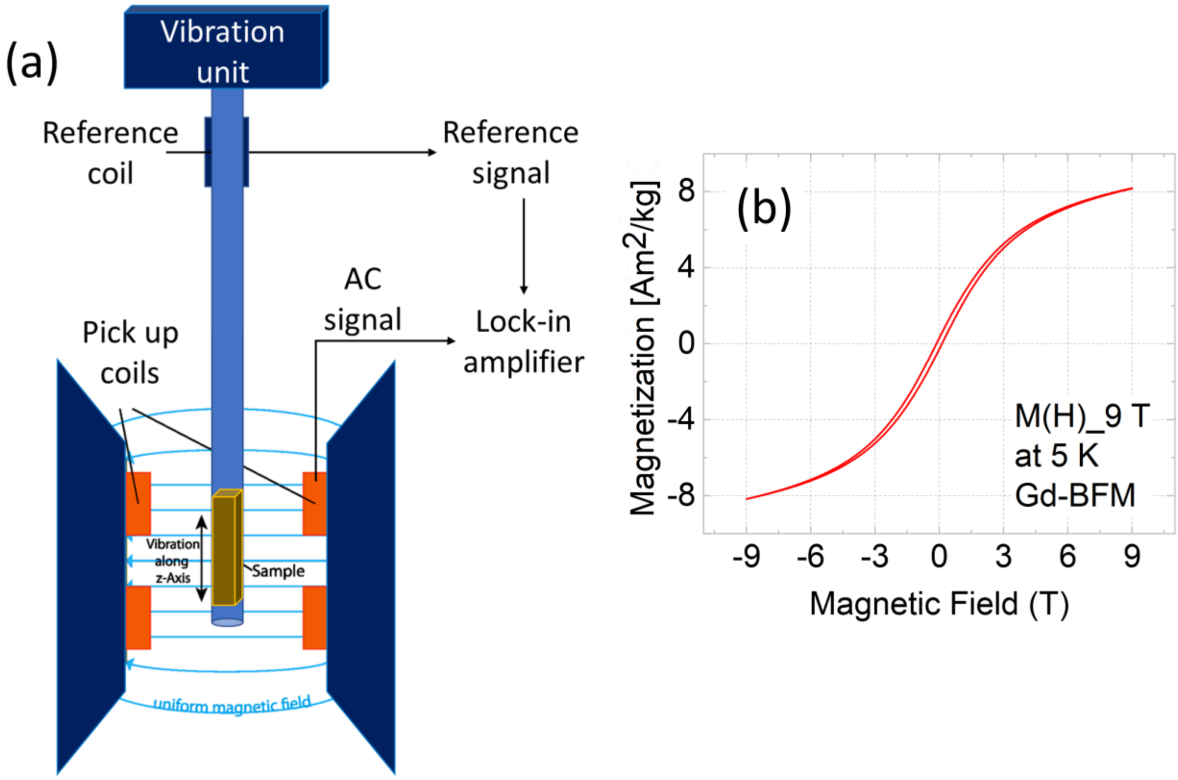

Figure 2.14: (a) The schematic of VSM device, the sample is placed inside the measurement space between the pickup coil and the superconducting solenoid magnet. (b) The magnetic hysteresis loop of Gd doped BFM NPs at 5 K.

Experimental conditions

Magnetic measurements were performed using the vibrating sample magnetometer (VSM) option of a Quantum Design PPMS DynaCool at 300 K and at 5 K up to a maximum magnetic field of 9 T. Foremost a 9 T *M*(*H*) sweep at 300 K was recorded, followed by the 300-900 K *M*(*T*) sweep at 0.1 T, and lastly another *M*(*H*) sweep at 300 K. All samples were measured at 5 K/min rate for *M-T* plots.

The NPs were pressed into 3 mm discs prior to weighting and then glued onto a ceramic heater with the help of a cement (Zircar AL-CEM). The high temperature *M*(*T*) measurements were performed in high vacuum (below 10^{-5} mbar), while the sample space being repeatedly purged with, He before pumping down.

2.5.2 Hyperthermia tests

The magnetic nanoparticles (MNPs) are exposed to an alternating magnetic field (AMF), which causes them to move and generate heat via hysteresis and relaxation losses. The heat is then dispersed within the tumour cells, causing them to undergo thermal damage. Importantly, the magnetic field used in MH is designed to only affect the MNPs and not the surrounding healthy tissues. This selective heating ability allows for the delivery of higher temperatures to the cancerous cells, without damaging the normal cells. The detailed explanation of hyperthermia principle has been discussed in Chapter 1 Foundation.

Experimental conditions

The experiments were carried out using a 4.2 kW Ambrell Easyheat Li3542 system with a frequency of the AC magnetic field of 310 kHz. The NPs were dispersed into both water and agar media. Agar was used because it roughly has the same viscosity as the cells. 1 mg/ml and 3 mg/ml concentrations of NPs were used for the testing at two different AC fields of 60 mT and 80 mT.

2.5.3 Mössbauer spectroscopy

Mössbauer spectroscopy is an element-specific, non-destructive measurement method that utilizes the resonant emission and absorption of γ-rays to probe extremely small nuclear energy changes in the range of a few neV. It is named after Rudolf L. Mössbauer, who discovered this effect while working on his dissertation. After his first observation of this effect, an experimental proof was obtained in 1958, for which he received the Nobel Prize in physics in 1961, together with Robert Hofstaedter. In this work, we only deal with ^{57}Fe Mössbauer spectroscopy.

The source material consists of ^{57}Co embedded in Rh, with the according nuclear transitions shown in Figure 2.15h. ^{57}Co, which has a half-life of 270 days, decays into an excited I=5/2 state of 136 keV via electron capture and can further decay to the I = 1/2 ground state after an 8.7 ns half-life via two routes. One of those routes goes through an intermediate I = 3/2 state of 14.41 keV with a 97.8 ns half-life. This transition leads to the emission of the 14.41 keV γ-photons that we are interested in, with the mentioned half-life leading to a natural line width of ca. 5 neV, as it follows from the time-energy uncertainty equation.

There are several different methods that can be utilized to obtain Mössbauer spectra. The by far most common one is referred to as the transmission geometry, with a sample being placed between the γ-ray source and the detector, enabling the measurement of transmission spectra that show characteristic negative peaks at energies where resonant absorption takes place. The schematic in transmission geometry measurement setup is shown in Figure 2.15f.

In Mössbauer spectroscopy, the transfer of momentum refers to the exchange of momentum between a nucleus and a gamma-ray photon during the emission or absorption of the photon by the nucleus. During emission, the nucleus loses momentum equal to that of the emitted photon, resulting in recoil of the nucleus in the opposite direction. In contrast, during absorption, the nucleus gains momentum equal to that of the absorbed photon, resulting in recoil of the nucleus in the same direction as the incident photon. [Figure 2.15g] This transfer of momentum is important in Mössbauer spectroscopy as it affects the energy and shape of the spectral lines, which can provide information about the properties of the material being studied. By carefully controlling the recoil velocity of the nucleus, researchers can minimize the broadening of spectral lines and obtain more precise measurements of the hyperfine interactions.

Hyperfine interactions in Mössbauer spectroscopy arise due to the interaction between a nucleus and its surrounding electronic environment. [Figure 2.15a-e]

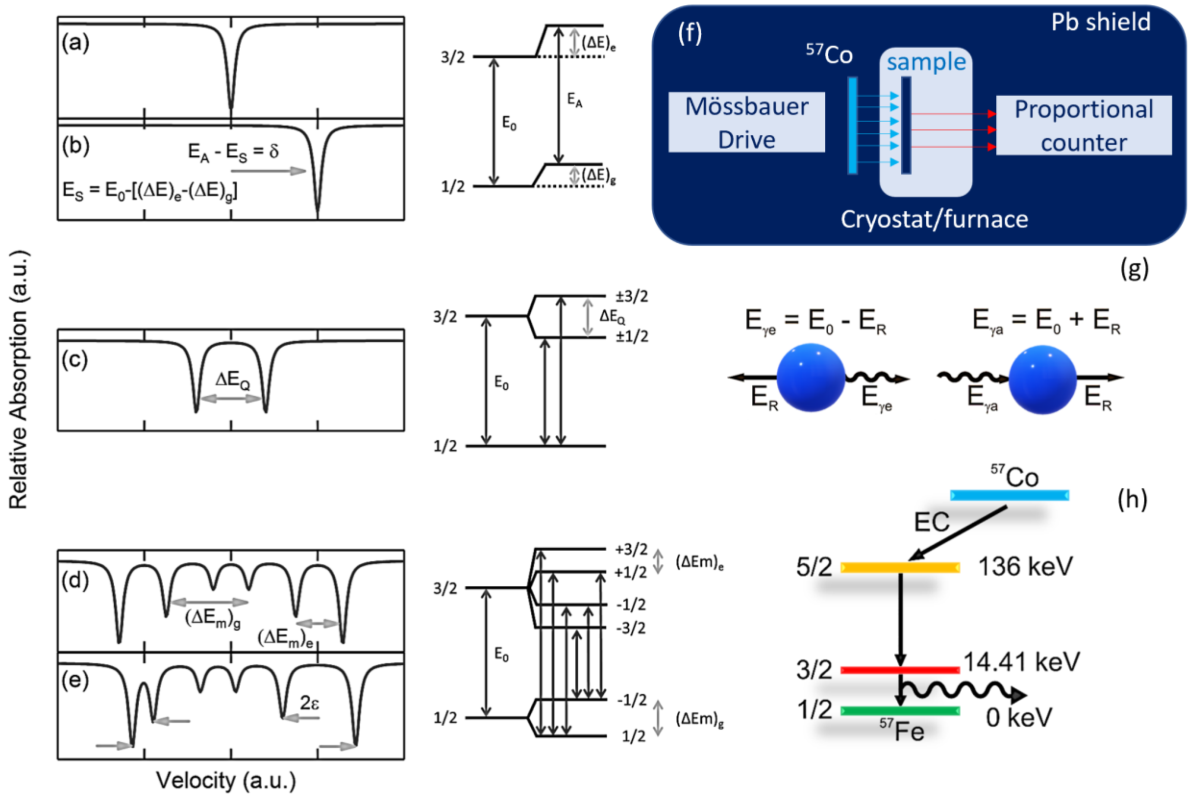

Figure 2.15: Schematic representation of the effect of hyperfine interactions on Mössbauer spectra. No-interaction (a), electric monopole interaction (b), electric quadrupole (splitting) interaction (c), magnetic dipole interaction (d) and magnetic dipole interaction under the influence of electric quadrupole (shift) interaction (e). Schematic of set up in transmission geometry, with the sample placed in furnace or cryostat for high or low temperature measurements, respectively (f). Schematic representation of the transfer of momentum during the emission (left) and absorption (right) of a γ-quantum by a nucleus (g). Decay scheme of ^{57}Co to ^{57}Fe and associated emission of the 14.41 keV γ-photon used for Mössbauer spectroscopy (h).

This results in the splitting of energy levels of the nucleus, which can be observed in Mössbauer spectra. Magnetic and electric hyperfine interactions provide insights into the local structure, bonding, and magnetic properties of materials. Electric monopole interaction does not cause any hyperfine splitting as it does not interact with the nuclear magnetic moment. Electric quadrupole interaction causes a small splitting of the energy levels due to the interaction between the electric field gradient at the nucleus and the electric quadrupole moment of the nucleus. Magnetic dipole interaction causes larger splitting of the energy levels due to the interaction between the nuclear magnetic moment and the magnetic moment of the surrounding electrons. The magnetic dipole interaction under the influence of electric quadrupole interaction causes both splitting and shifting of the energy levels. This is because the electric quadrupole interaction changes the symmetry of the electronic environment, which in turn affects the magnetic dipole interaction. The combined effect of electric quadrupole and magnetic dipole interactions can result in complex hyperfine splitting patterns that provide valuable information about the electronic environment surrounding the nucleus in a solid-state system. [Figure 2.15a-e]

In Mössbauer spectroscopy, a radioactive ^{57}Co source is attached to a Mössbauer drive that is an electromechanical linear motor. This device is capable of moving the source back and forth in various modes. During the early days of Mössbauer spectroscopy, these drives were often assembled using low-frequency speakers. However, contemporary laboratories use commercially available units such as Mössbauer Velocity Transducers manufactured by WissEl. The type of modulation used in Mössbauer spectroscopy causes the energy axis to be labeled in terms of velocity rather than energy. It is crucial to consider the mode of motion employed since a physical oscillator would generally move sinusoidally. However, this would result in an excessive number of data points being recorded in the two outer regions of the spectrum, which are primarily composed of background noise. This would lead to fewer data points being recorded in the region containing the absorption peaks, resulting in a longer data acquisition time.

Experimental conditions

The sample preparation, in the case of the BFO powder samples, must take into account the high amount of non-resonant absorption caused by Bi, which is a high-Z element like the Pb used for radiation shielding. In order to have sufficient sample volume without absorbing too much radiation non-resonantly, the sample material was mixed with chemically inert boron nitride (BN), with the optimum ratio having been determined experimentally before the series of measurements were performed.

Mössbauer spectra of all doped and pristine BFO NPs samples were recorded in transmission geometry at 300 K and 80 K using a nitrogen bath cryostat. Approximately 20 mg/cm^2 of NP powder were used for the experiments, to guarantee sufficient spectral intensity. We have used ^{57}Co (Rh), as a source material, mounted in a WissEL. Mössbauer velocity transducer was operating in the constant acceleration mode.

2.6 Electrical and analytical characterization

The electrical and analytical characterization of doped BFO and undoped BFO NPs were examined and studied using PFM, EIS and GC-MS techniques.

2.6.1 Piezoresponse force microscopy (PFM)

In rhombohedral BFO, there are three possible switching of ferroelectric domains, which are at an angle 71°, 109° and 180° with the polarization direction along $[111]_{pc}$ as shown in the Figure 2.16.[220] The applied electrical energy needs to overcome the energy barrier associated with the polarization and stress energy of the ferroelectric domain and its surrounding domains. The domain with larger switching angle requires ample amount of electrical energy for switching as the polarization vector undergoes a larger rotation. Whereas the smaller switching angle domain needs lesser amount of electrical energy as the polarization vector rotates through a smaller angle. However, in polycrystalline NPs, the ferroelectric domains are randomly oriented.

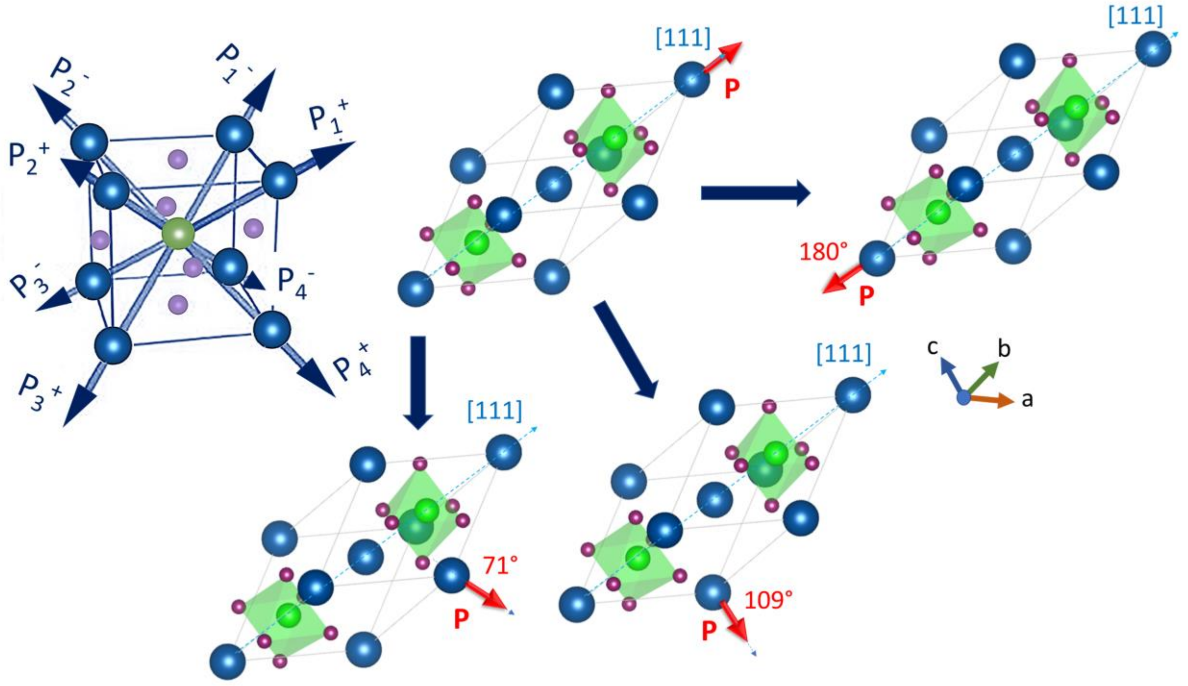

Figure 2.16: The polarization vectors in pseudo-cubic unit cell of BFO. Schematic of 71°, 109° and 180° domain switching in rhombohedral bulk BFO.

The standard way for measuring ferroelectricity and the piezoelectric effect requires a dense, electroded sample, which cannot be achieved with NPs. Even compacted into pellets, they still have a low density and contain a large volume of voids and pores, which completely distort the internal electric field distribution inaccessible to experiment. It is then difficult to apply a sufficiently strong electric field to the NPs. Extracting information on the polarization and piezoresponse of NPs from the overall response of such nanopowder-air composite is a nontrivial and error-prone task. Therefore, to confirm the ferroelectricity in the NPs under study, we used PFM. PFM has established itself as a reliable method for studying ferroelectric and piezoelectric properties at the nanoscale, even within individual NPs.

Working Principle

The PFM device mainly consist of a function generator, a lock-in amplifier, and a conductive tip. [Figure 2.17] The function generator generates an alternating voltage Vac, which is applied onto the sample's surface via conductive probe (tip). The tip works as a top electrode. The voltage applied to the tip contains *dc* and *ac* components as shown in Equation 2.45.

$$V = V_{dc} + V_{ac} \cdot cos(wt) \tag{2.45}$$

In converse piezoelectric effect, the electric field induces a deformation of the sample surface, which causes a deflection in the cantilever. This deformation is tracked by four quadrant photodetector that records the alteration in relative position of the laser beam.[221] Such deformation is due to two contributions one is electrochemical response and electrostatic force. The electrochemical response is due to converse piezoelectric and the electrostrictive effect whereas, the electrostatic force forms between surface of sample and the tip. Electrochemical response can be defined by Equation 2.46. The first term reflects the converse piezoelectric signal and second term correspond to electrostrictive component of the electrochemical response. The electrostrictive part is usually small in comparison to the converse piezoelectric component in absence of a *dc* field.[221]

$$\Delta z = d_{33}V + \frac{M_{333}}{t}V^2 \tag{2.46}$$

V is the bias voltage, t is the sample thickness and d_{33} is the piezoelectric coefficient, and M_{333} is the electrostrictive constant. The first harmonic signal Δz_{ω} and second harmonic signal $\Delta z_{2\omega}$are described by Equations 2.47, 2.48, respectively.

$$\Delta z_{\omega} = (d_{33}V_{ac} + 2\frac{M_{333}}{t}V_{dc}V_{ac})\ \cos(\omega t) \tag{2.47}$$

$$\Delta z_{2\omega} = \left(\frac{1}{2}\frac{M_{333}}{t}V_{ac}^2\right)\cos(2\omega t) \tag{2.48}$$

The piezoresponse amplitude is given by the amplitude of the first harmonic response i.e., A_{ω}.

The contrast in PFM image is due to the relative orientation of spontaneous polarization P, and the vector of the applied electric field E which determines sign of the converse piezoelectric signal. This signal will be positive when E and P vectors are parallel and with same polarity. A positive signal reflects the local expansion of the piezoelectric surface of sample. However, the piezoelectric sample will contract when P and E vectors are antiparallel to each other. PFM spectroscopy can be used for investigating local polarization switching on the nanoscale at the surface of a sample. This involves applying a sequence of dc voltage pulses to the sample surface using a conductive tip, while simultaneously measuring the local piezoresponse with an overlaid ac voltage. [Figure 2.17b] The resulting hysteresis loop in the

PFM measurement reflects the bias-induced domain switching that occurs in the region of the sample beneath the PFM tip [Figure 2.17c].

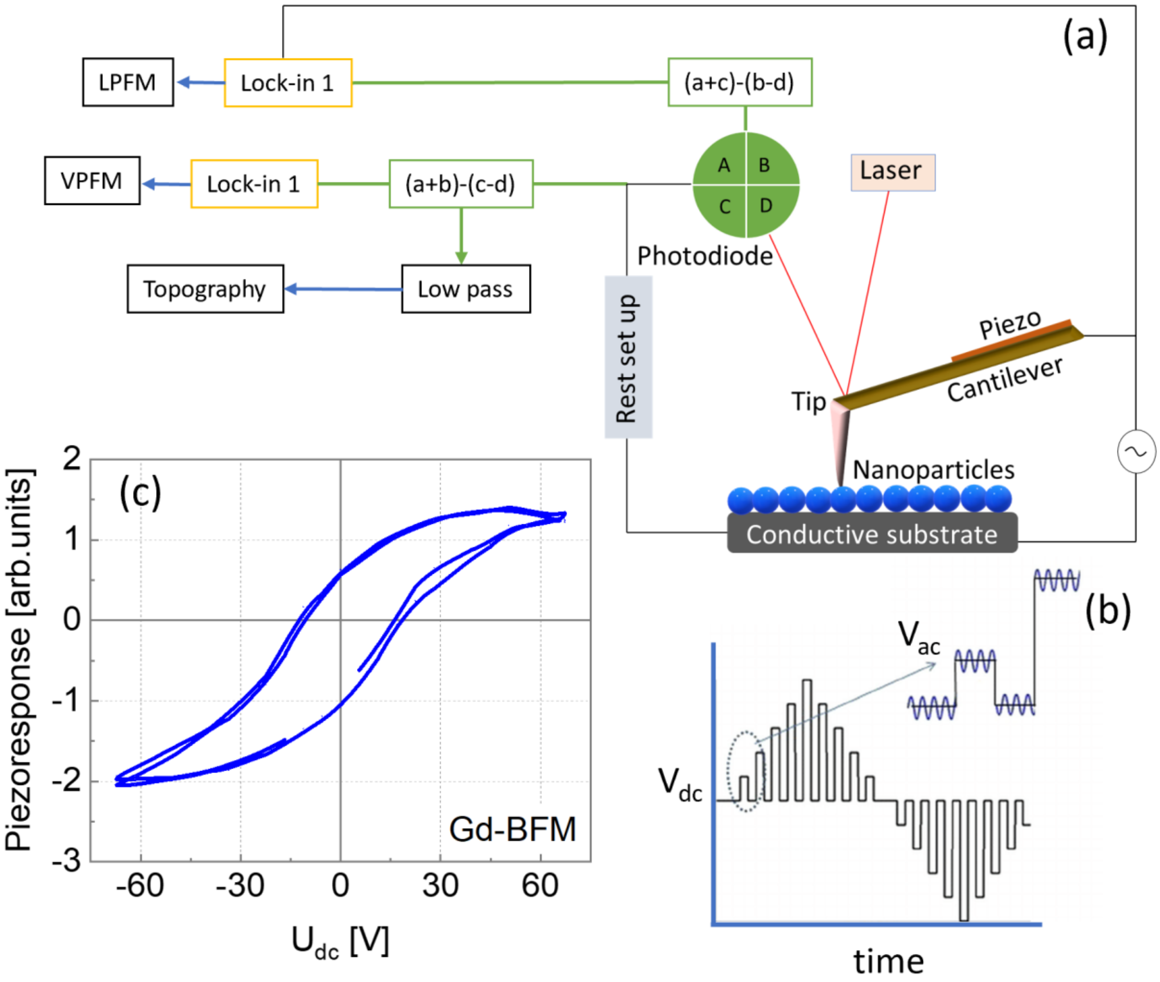

Figure 2.17: Schematic of piezoresponse force microscope (a). In PFM spectroscopy, the schematic representation of applied Bias waveform to the tip (b). Local hysteresis loop of Gd-BFM NPs (c)

Experimental conditions

To address the ferroelectric properties of the NPs, PFM measurements were performed using a commercial scanning probe microscope MFP-3D (Asylum Research). Pt/Cr coated cantilevers Multi 75E-G (Budget Sensors) with a spring constant of 3 N/m were used. PFM measurements were conducted at a probing voltage amplitude of U_{ac} = 5 V and a frequency f = 50 kHz. The NPs were drop cast onto a conductive carbon tape for the PFM measurements. The dropcasted NPs were dried in a desiccator over night before PFM measurements.

2.6.2 Electrochemical impedance spectroscopy (EIS)

The EIS technique is based on the excitation of an electrochemical system by a sinusoidal signal. This technique is very useful for both the evaluation of the heterogeneous charge transfer parameters and the investigation of the double layer structure in electrochemical set up. Electrochemical experiments range from simple potentiostatic (chronoamperometry), to cyclic voltammetry (potentiodynamic), to complex AC techniques such as impedance spectroscopy.

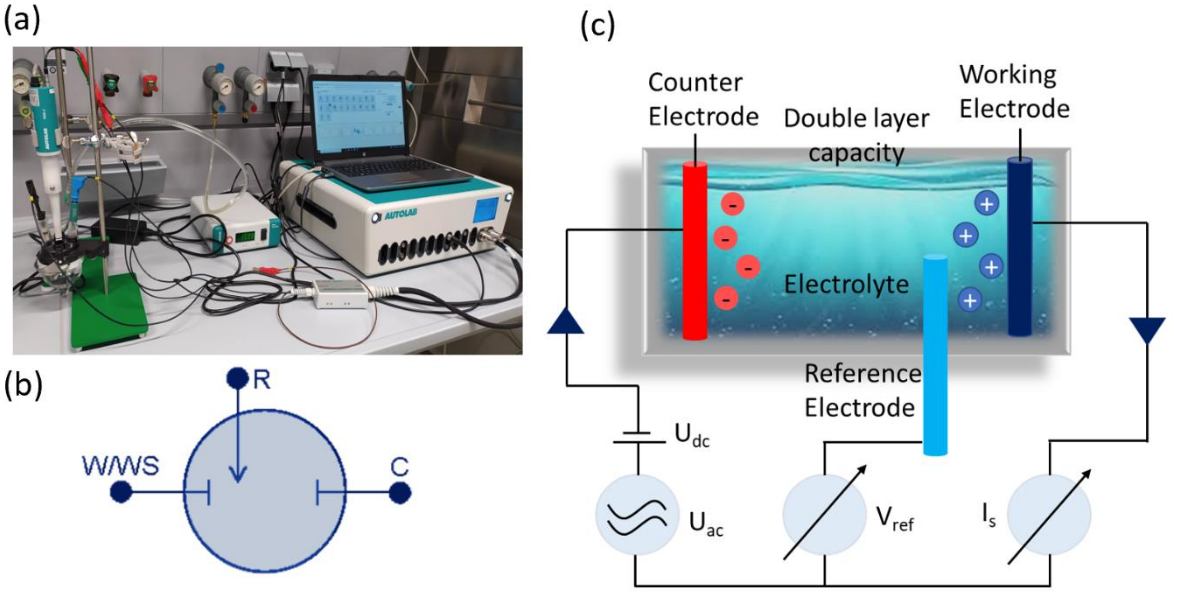

Figure 2.18: The electrochemical set up in the laboratory (a), and schematic of principle set-up of a three-electrode electrochemical cell for impedance measurement (b). The schematic of electrical circuit during electrochemical measurement (c).

The electrodes are (semi-)conductive solid that interfaces with an electrolyte solution. The common designations are: Working, Reference and Counter (or Auxiliary) electrode. *Working electrode* is the designation for the electrode being studied. In corrosion experiments, this is probably the material that is corroding. In physical-electrochemistry experiments, this is most often an inert material, commonly gold, platinum or carbon, which passes current to other species without being affected by that current. The *Counter* or *Auxiliary* electrode is the electrode in the cell that completes the current path. All electrochemistry experiments (with non-zero current) must have a working–counter pair. In most experiments the Counter is the current source/sink and so relatively inert materials like graphite or platinum are ideal, though not necessary. In some experiments the counter electrode is part of the study, so the material composition and setup vary accordingly. *Reference electrodes* are, as their name suggests, electrodes that serve as experimental reference points. Specifically, they are a reference for the potential measurements. Reference electrodes should, therefore, hold a constant potential during testing, ideally on an absolute scale. This is accomplished by first having little or, ideally, no current flow through them, and second by being "well-poised," which means that even if some current does flow it does not affect the potential. While many electrodes could be well-poised, there are several that are very commonly used and commercially available for example, Ag/AgCl, saturated calomel, Hg/HgO, $Hg/HgSO_4$, and $Cu/CuSO_4$. There are other couples that are often referenced but are not typically used today, such as the normal hydrogen electrode (NHE).

In three electrode mode, the Reference lead is separated from the Counter and connected to a third electrode. This electrode is most often positioned so that it is measuring a point very close to the working electrode (which has both Working and Working Sense leads attached). [Figure 2.18b]

In EIS, a sinusoidal perturbation around a constant current (or potential) is applied to the electrochemical system, but the amplitude of the perturbation is small enough to assume a linear behaviour of the system.

$$I_{WE} = I + i_a \sin(2\pi f t) \tag{2.49}$$

$$E_{WE} = E + V_a \sin(2\pi f t + \varphi) \tag{2.50}$$

$$Z_{tot}(\omega) = Z_{Re}(\omega) + iZ_{Im}(\omega) \tag{2.51}$$

I_{WE} is the applied alternating current signal, i_a is the current amplitude, f is the frequency of the applied probing signal and t is time. The potential (or current) responses of the system subjected to the perturbations in the steady-state can be observed. In Equation 2.50. E_{WE} is the potential measured at time t, Va is the potential amplitude, Φ is a phase angle between the two phasors (the potential and the current). The obtained response follows at the same frequency, but at a different phase. The measured ratio of the perturbing signal and the response is the impedance of the system. The corresponding value depends on the frequency, f. Effectively, the phase angle, Φ, varies with the probing signal frequency, f . At different angular frequencies, ω (ω = $2\pi f$), the overall system impedance, $ZTol(\omega)$, can be written as in Equation 2.51, where $ZRe(\omega)$ is the real component of the impedance and $ZIm(\omega)$ is the corresponding imaginary component. Using an equivalent circuit to analyse the EIS data can give a lot of information about the system, the reaction parameters, the interfacial capacitance and the mass transport parameters. In EIS, plots of $-ZIm(\omega)$ as a function of the real component, $ZRe(\omega)$, are very often used. [Figure 2.19c]

Equivalent circuits can comprise different elements such as resistors (R), capacitors (C) inductors (L) and specific electrochemical elements, which are connected in series and/or parallel. [Figure 2.18d-e] The actual equivalent circuit and the value of each element can be fitted to the EIS data.

Cyclic voltammetry (CV) is one of the most widely used techniques to acquire quantitative information about electrochemical reactions. In this method, a triangular potential waveform is applied to the electrode one or several times, and the current-potential curves are recorded. A typical cyclic voltammogram is a plot showing the dependence of the measured current on the applied potential. [Figure 2.19a-b] The CV method has been widely used in the investigation of adsorption processes, heterogeneous electron transfer reactions and redox processes. It can provide information about the properties and mechanisms of electrochemical reactions and kinetic parameters of these reactions. It can be employed to determine reactant concentration, coverages of adsorbates on the electrode surface, the electrochemically active surface area of the electrode and several kinetic parameters such as electrode reaction rate constant, exchange current density and reaction transfer coefficient. Its application can be divided into two main types, as described below: 1. Reaction reversibility. The height and symmetry of the oxidation and reduction waves of the obtained

CV can often be used to judge about the reaction reversibility. 2. Reaction mechanism. Information about electrochemical adsorption phenomena, electrochemical reactions and electrochemical-chemical coupling reactions can be obtained from CV. It is useful for studying the redox mechanism of organic compounds, organometallic compounds, and biological materials.

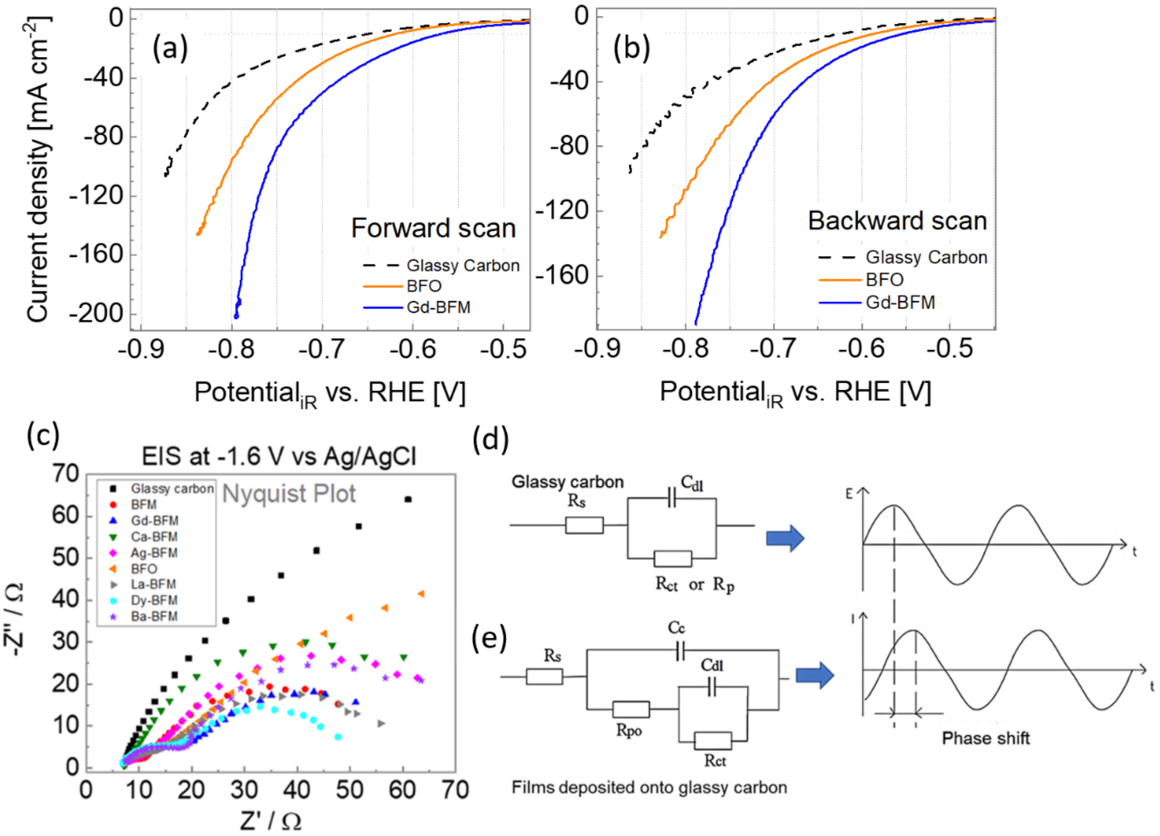

Figure 2.19: An example of cyclic voltammetry curve in its forward and backward scans (a-b). The EIS spectrum (c), and the fitted electrochemical equivalent circuit (d-e). [measured by Dr. Ignacio S. Moltó]

Experimental conditions

Preparation of the catalytic ink

5 mg of the catalyst (BFO/doped-BFO NPs) dispersed in 490 µL ethanol absolute. The mixture of 490 µL ultrapurewater and 20 µL of a 5 wt % Nafion were sonicated for 1 minute to obtain a proper dispersion.

Pretreatment of the glassy carbon

The glassy carbon (GC) disk in a Teflon sheath is first polished with polishing paper of different grit size of abrasive particles (3 µm, 1 µm and 0.3 µm), using ethanol absolute as lubricant. Second, the GC is polished by suspension of alumina slurry of 0.05 µm particle size in water for 5 minutes. Afterwards, the glassy carbon is sonicated in a mixture of ultrapure water and ethanol absolute to remove the remaining alumina and dried under a nitrogen stream.

Preparation of the working electrode

Working electrodes are prepared by drop-coating of the catalytic ink onto the surface of the glassy carbon to create a homogeneous film. For that, 4.5 µL of the ink dispersion are drop-casted onto the glassy carbon and let to dry at room temperature. The catalyst loading is always 0.2 mg/cm^2.

Freshly prepared 1 M KOH electrolyte solution was used as alkaline medium. It was purified using a cation-exchange resin (Chelex 100 sodium form C7901-50G, Sigma-Aldrich). This solution is used for both electrode compartments. Electrochemical measurements were conducted with Rotating Disc Electrode (Autolab RDE-2 rotator and motor controller) and a potentiostat/galvanostat (Autolab PGSTAT203N). The software NOVA 2.1.4. was used for data acquisition. The electrochemical glass cell with a three-electrode standard configuration was used. It consists of a counter electrode, and Pt coil separated from the cathode compartment by a glass frit. Double junction AgCl/Ag (3 M KCl) reference electrode and working electrode: a film of the material to study is deposited on a GC disk of 0.1134 cm^2 of area. All measurements were carried out at room temperature and ambient pressure.

Parameters of electrochemical measurements.

1. Open circuit potential (OCP) determination. OCP measured during 60 s.
2. EIS at OCP. From 100 kHz to 10 Hz. Amplitude of 10 mV$_{RMS}$.
3. CV from -1 to -2 V vs. Ag/AgCl 3M KCl (HER)

During the measurements the scan rate was 5 mV/s, 3500 rpm – LSV. This procedure is conducted in Ar- saturated solutions. Before the experiment, the corresponding gas (pure) is bubbled into the solution for 25 min. During the measurements a stream of the same gas is flowed over the solution (headspace of the cell). The electrochemical response of the glassy carbon current collector is continuosly registered to verify the activity of the deposited catalyst.

2.6.3 Gas chromatography and mass spectrometry (GCMS)

GCMS device consists of two very different analytical techniques GC and MS. Usually, the analytical instrument contains a gas chromatograph that is hyphenated via a heat transfer line to the mass spectrometer, and the two techniques take place in series. However, some specialized and usually miniaturized or portable instruments contain the whole GC-MS system within a single box. [Figure 2.20a]

GC is a separation technique for chemical components of a sample mixture. It detects their presence or absence and/or how much is present. GC detectors are limited in the information that they give. This is usually two-dimensional giving the retention time on the analytical column and the detector response. Retention time (RT) is a measure of the time taken for a solute to pass through a chromatography column. [Figure 2.20d] It is calculated as the time from injection to detection. Identification is based on comparison of the retention time of the peaks in a sample to those from standards of known compounds analyzed using the same method. However, GC alone cannot be used for the identification of unknowns, which is where hyphenation to an MS works very well. MS can be used as a sole detector, or the column effluent can be transferred between the MS and GC detectors.

MS is an analytical technique that measures the mass-to-charge ratio (m/z) of charged particles and therefore can be used to determine the molecular weight and elemental composition, as well as the chemical structures of molecules. Data from a GC-MS is three-dimensional, providing mass spectra that can be used for identity confirmation or to identify unknown compounds plus the chromatogram that can be used for qualitative and quantitative analysis. The sample mixture is first separated by the GC before the analyte molecules are eluted into the MS for detection. They are transported by a carrier gas, which continuously flows through the GC and into the MS, where it is evacuated by the vacuum system. The sample is first introduced into the GC manually or by an autosampler and enters the carrier gas via the GC inlet. If the sample is in the liquid form, it is vaporized in the heated GC inlet and the sample vapor is transferred to the analytical column. [Figure 2.20a]

The sample components, the “analytes”, are separated by their differences in partitioning between the mobile phase (carrier gas) and the liquid stationary phase (held within the column), or for more volatile gases their adsorption by a solid stationary phase. In GC-MS analyses, a liquid stationary phase held within a narrow (0.1-0.25 mm internal diameter) and short column is most common. After separation, which for GC-MS analyses doesn’t require total baseline resolution unless the analytes are isomers, the neutral molecules elute through a heated transfer line into the mass spectrometer. [Figure 2.20a]

Within the mass spectrometer, the neutral molecules are first ionized most commonly by electron ionization (EI). In EI, an electron, produced by a filament, is accelerated with 70 electron volts (eV) and knocks an electron out of the molecule to produce a molecular ion that is a radical cation. This high energy ionization can result in an unstable molecular ion and excess energy can be lost through fragmentation. Bond breakages can lead to the loss of a radical or neutral molecule and molecular rearrangements can also occur. This all results in a, sometimes very large, number of ions of different masses, the heaviest being the molecular ion with fragment ions of various lower masses, depending on; The molecular formula, the molecular structure of the analyte, where bond breakage has occurred, and which part has retained the charge. The next step is to separate the ions of different masses, which is achieved based on their m/z by the mass analyzer.

Mass resolution is the ability of the mass analyzer to separate ions with very small differences in m/z. [Figure 2.20b-c] Unit mass resolution instruments can only separate nominal masses or those down to a single decimal place, whereas high mass resolution (HRMS) instruments can separate them to four or five decimal places. The most common type of unit mass instrument is the quadrupole which is a scanning instrument and varies the voltage to allow only ions of a certain m/z to have a stable trajectory through the four poles to reach the ion detector. The representative mass spectrum of dibutyl phthalate (DBP) is shown in Figure 2.20b, where the peaks correspond to m/z of fragmentation of DBP.

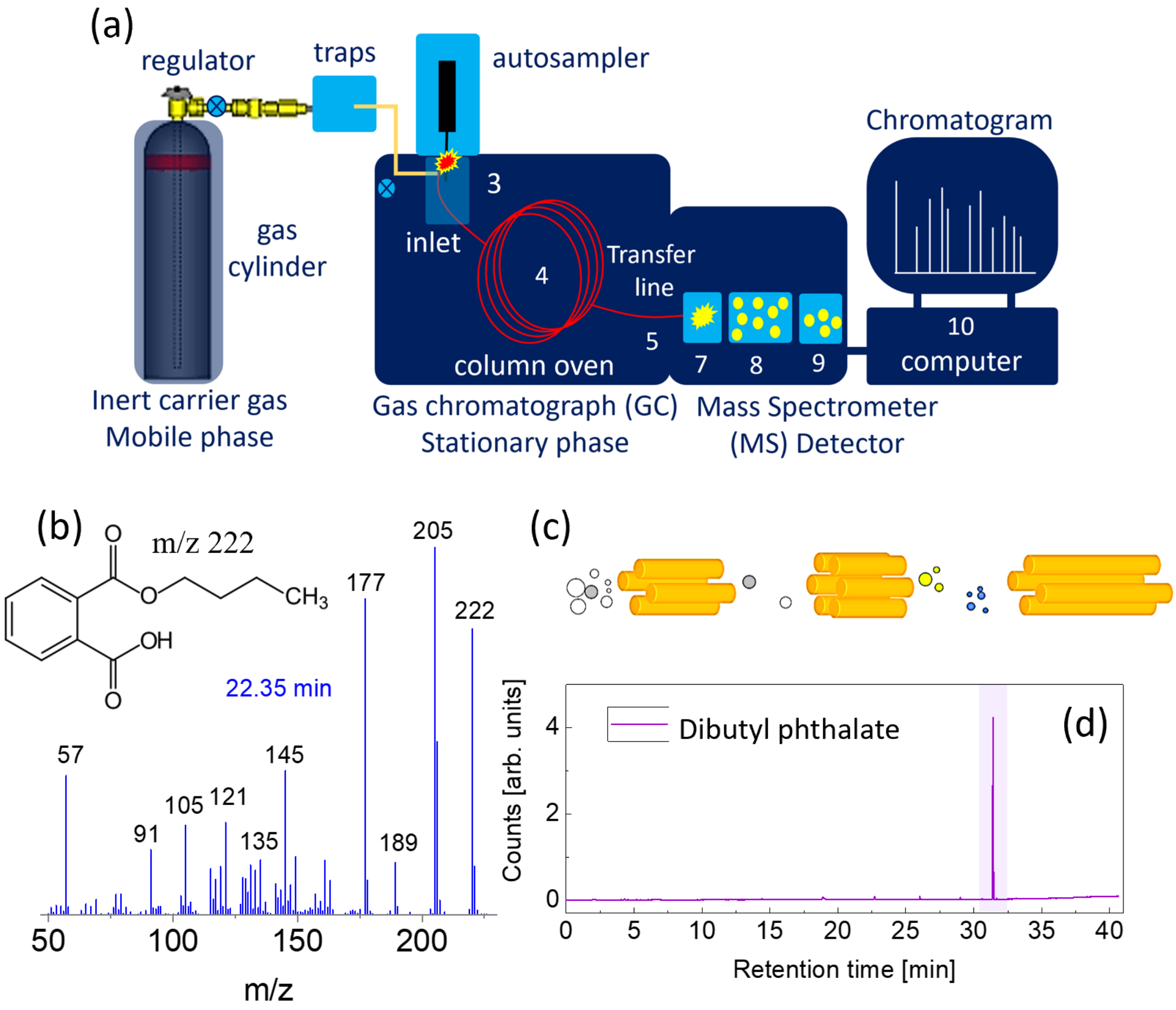

Figure 2.20: (a) A simplified diagram of a gas chromatograph–mass spectrometer. (b) A mass spectrum of dibutyl phthalate (DBP). (c) The ionization in a triple quadrupole MS/MS instrument in multiple reaction monitoring (MRM) mode. (d) Total ion chromatogram (TIC) output from a GC-MS of DBP.

Experimental conditions

Quantification of phthalates was done using a Varian 450 GC coupled to a Varian 240 MS (Agilent Technologies, Avondale, PA, USA) and equipped with a capillary column (30 m × 0.25 mm ID, 0.25 mm film thickness, factor four, Varian Technologies) for chromatographic separation. The transfer line and the ion source temperatures were 280 °C and 230 °C, respectively. The column temperature initiated from 60 °C to 250 °C at a rate of 6 °C/min, held for 1 minute, and finally ramped up to 280 °C and held for 2 minutes. The acquisition continued for 55 minutes in the scan mode for a selective ion range of 40 to 500. Helium (98 % purity) was the carrier gas with a flowrate of 0.8 mL/min. Prepared samples of 5.0 mL were injected in split less mode with an injector temperature of 250 °C.

Synthesis Routes of BFO Nanoparticles

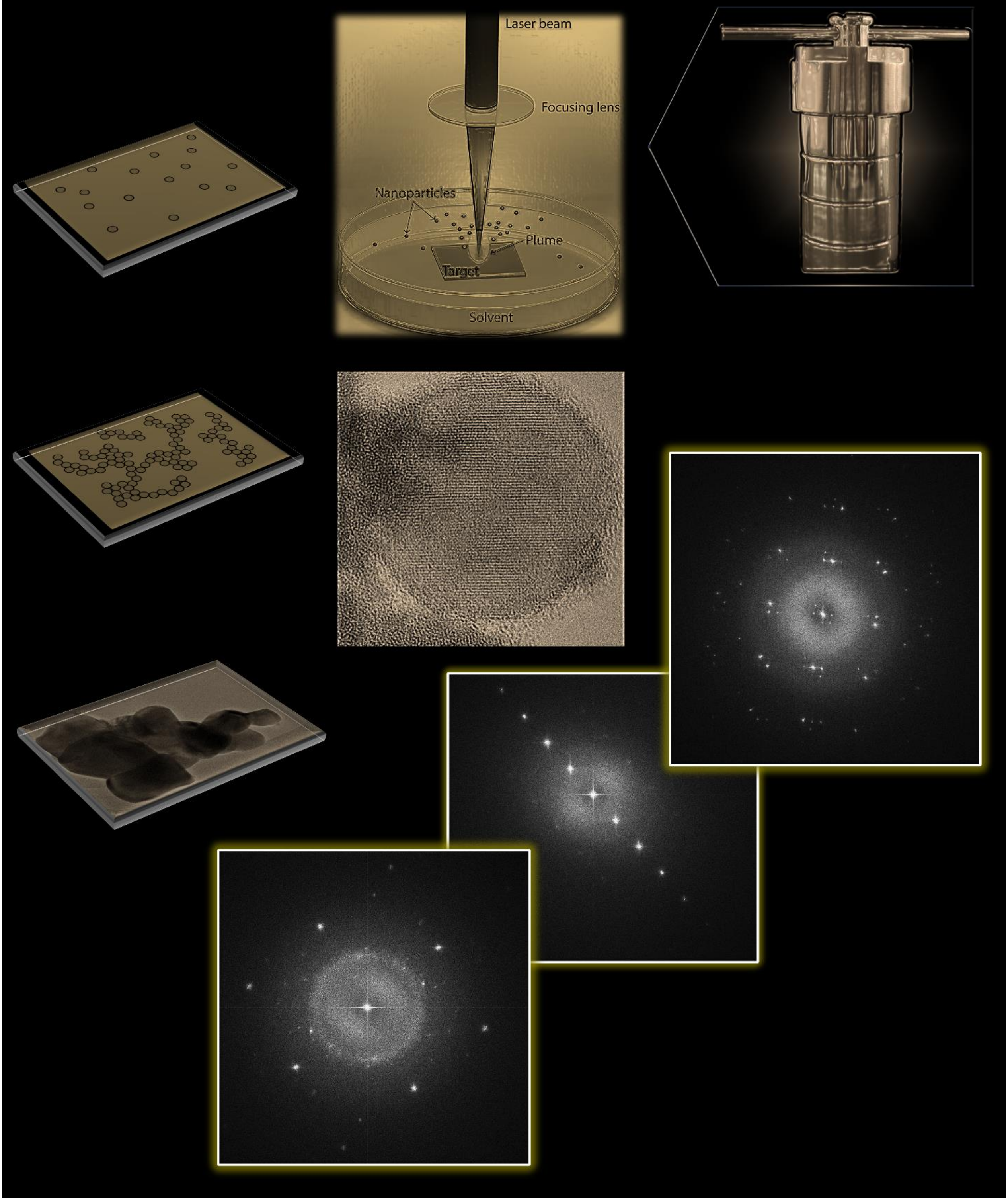

3. Synthesis routes for BFO nanoparticles

3.1 Introduction

"A nanoparticle is a small particle that ranges between 1 to 100 nanometres in size. Undetectable by the human eye, nanoparticles can exhibit significantly different physical and chemical properties to their larger material counterparts."[222] *– European Commission*

NPs are generally formed by two different processes. Based on coarser particles, the **top-down** process leads to smaller particles mainly by mechanical comminution.[223] In **bottom-up** processes, nanosized particles are formed by gas phase or liquid-phase reactions.[223] The fundamental difference between the two processes lies in their approach to sample formation. The top-down method generally produces crystalline samples, including small single crystals or polycrystalline material, obtained from a previously formed starting material through thermodynamic means. On the other hand, the bottom-up approach leads to the formation of small particles from crystalline areas that deviate from the ideal lattice, resulting in defect structures. These structures are typically often "kinetic" products, where the products do not have enough time for ideal crystal growth, leading to a defect structure.[224] The structures resulting from the bottom-up approach are classified according to their geometry as 0-dimensional defects such as non-stoichiometry, 1-dimensional defects such as dislocations, 2-dimensional defects such as grain boundaries, and 3-dimensional defects like pores. Additionally, bottom-up processes may also form molecular structures resulting in clusters. Clusters are units consisting of several atoms or compounds whose physicochemical properties depend on the size of the clusters.

As a semiconductor with an absorption edge in the visible region, BFO NPs are potential candidates for photocatalytic and electrocatalytic applications. For surface-based reactions on BFO NPs, it is important to quantify the remaining nitrate groups or other anions that could be adsorbed onto the surface of the NPs, potentially changing their surface activity. This activity is highly dependent on available active sites.[182] Additionally, impurities or amorphous phases could modify the electron-hole recombination kinetics, which can affect the photocatalytic efficiency of BFO.[46,150] Therefore, developing methods to synthesize high-purity, single-phase BFO NPs is highly desirable.

In the field of catalysis, it is generally considered desirable to have a narrow size distribution of NPs. This is because NPs with a narrow size distribution tend to have the appropriate surface available for catalysis, which can lead to improved catalytic performance. Additionally, having a narrow size distribution can also provide better control over the catalytic properties of the NPs.[225] One of the advantages of NPs with a narrow size distribution is that they can exhibit improved selectivity due to the uniformity of the active sites.[182] When NPs have a narrow size distribution, the size of the catalytic sites is more uniform, which can lead to more consistent catalytic performance. This is particularly important for reactions that require high selectivity, where even small variations in number of active sites can have a significant impact on the outcome of the reaction. In contrast, NPs with a broad size distribution can have a lower surface area per unit volume, which can reduce the number of active sites available for catalytic reactions. Furthermore, NPs with a broad size distribution can exhibit lower selectivity due to the variation in the size of the catalytic sites.

In this chapter, we will explore the various techniques including top-down (laser ablation) and bottom-up (hydrothermal and sol-gel), for synthesizing BFO NPs with diverse morphologies. It is widely recognized that the size, shape, and crystal structure of a photocatalyst play critical roles in determining the photocatalytic activity.[147] To this end, researchers have employed a range of methods, including the sol-gel method, hydrothermal method, microwave hydrothermal method, laser fragmentation, and others to produce BFO NPs with specific morphologies.[186] In the following sections, we delve into the details of the sol-gel, hydrothermal, and pulsed laser ablation in liquid routes.

The classic sol-gel method was developed earlier in the 1800s for the synthesis of NPs than the hydrothermal method in the 1950s. The sol-gel method was originally used for the synthesis of glass and ceramics, while the hydrothermal method was first used for the synthesis of inorganic crystals. However, both methods have since been adapted for the synthesis of a wide range of inorganic materials, including NPs.[226,227] In literature there are other methods reported for synthesizing BFO NPs, in addition to the sol-gel and hydrothermal methods.[228] Each of these methods has its own advantages and disadvantages, and the choice of method will depend on the specific application and desired properties of the NPs.[229] Factors such as particle size, shape, crystallinity, purity, and reproducibility will need to be considered in selecting an appropriate synthesis method.

Many synthesis routes for the synthesis of BFO NPs have been reported in the literature [Table 1].[230] The co-precipitation method involves dissolving bismuth and iron salts in a solvent, followed by the addition of a precipitating agent to form BFO NPs.[231] The spray pyrolysis method involves spraying an aerosol of bismuth and iron precursors onto a hot substrate, which decomposes to form BFO NPs.[232] However, this method can result in secondary phases if not carefully controlled and can generate significant waste. Microwave-assisted synthesis involves using microwave radiation to heat a solution of bismuth and iron precursors, which promotes the formation of BFO NPs.[233] This method is relatively eco-friendly and cost-effective, producing NPs with a relatively narrow size distribution and high purity. However, achieving a single-phase BFO formation can be challenging, and the reproducibility can be affected by variations in the microwave conditions. The solid-state reaction method involves grinding bismuth and iron oxides together and heating them to high temperatures to form BFO NPs.[234] This method is relatively cost-effective and reproducible, producing single-phase BFO NPs. However, achieving a narrow size distribution can be challenging, and the process can be more energy-intensive compared to other methods.

A recently reported method is *Pulsed Laser fragmentation*.[235] It involves irradiating a liquid jet with a laser to perform the fragmentation of colloidal submicron-sized BFO particles (educt powder), resulting in the synthesis of smaller-sized BFO NPs. This treatment is capable of achieving a size reduction from 450 nm to below 10 nm. The primary purpose of this method is to reduce the particle size of already synthesized larger NPs.

Table 1: A comparative study of synthesized BFO NPs by different synthesis routes.

Chemicals used	**Method**	**Particle size**	**Final product**	**Reference**
[$Bi(NO_3)_3•5H_2O$] [$Fe(NO_3)_3•9H_2O$] 50 mL DI H_2O 5 M NaOH (pH 10) H_2O_2	Hydrothermal	Up to 100 nm	BFO NPs with small amount of impurity	[236]
[$Bi(NO_3)_3•5H_2O$] [$Fe(NO_3)_3•9H_2O$] HNO_3 6 M KOH	Hydrothermal	20 nm – 1 µm	Single phase BFO NPs	[237]
$Bi(NO_3)_3•5H_2O$ $Fe(NO_3)_3•9H_2O$ CTAB as surfactant 9 M KOH	Microwave hydrothermal	10 µm	BFO NPs Impurity: $Bi_2Fe_4O_9$ NPs	[238]
$Bi(NO_3)_3•5H_2O$ 36 mL (EG, $HOCH_2CH_2OH$) $Fe(NO_3)_3•9H_2O$	Sol-gel rapid calcination	35 nm	Single phase BFO NPs	[239]
$Fe(NO_3)_3•9H_2O$ $Bi(NO_3)_3•5H_2O$ $C_3H_8O_2$ HNO_3 Citric acid [$C_6H_8O_7$] Polyethylene glycol	Sol-gel	80 nm – 120 nm	Single phase BFO NPs	[74]
$Bi(NO_3)_3•5H_2O$ $Fe(NO_3)_3•9H_2O$ HNO_3 (2 pH) 30 wt% NH_4OH	Sonochemical	32 – 38 nm	Single phase BFO NPs	[240]
$Fe(NO_3)_3•9H_2O$ $Bi(NO_3)_3•5H_2O$ 20 mL HNO_3 (68 %) 10 g $C_6H_8O_7$	Wet chemical-Pechini Method	4 – 30 nm	Single phase BFO NPs	[241]
BFO (450 nm) colloidal solution (Sol-gel synthesized)	Laser fragmentation	Below 10 nm	$BiFeO_3$ NPs $Bi_2O_2CO_3$ NPs	[242]
0.1 M $Bi(NO_3)_3$ 0.1 M $Fe(NO_3)_3$ 2 N HNO_3 Oxalic acid	Ferrioxalate precursor (Low temperature)	11 – 22 nm	Single phase BFO NPs	[243]

Pulsed laser ablation in liquid (PLAL) is another modern method for synthesis of high quality of NPs.[244] The PLAL method for synthesizing NPs from a bulk target sample was first reported in 1994 by Takami and co-workers. They used a pulsed Nd:YAG laser to ablate a metal target in a liquid medium to produce NPs of that metal. Since then, PLAL has been extensively studied and developed as a versatile and effective method for synthesizing a wide range of NPs including oxides with various sizes, shapes, and compositions.[245,246] The PLAL method is a simple, versatile, and environmentally friendly approach to synthesizing NPs with precise control over their size and shape. PLAL produces high-purity NPs without requiring additional purification steps and can be easily scaled up for large-scale production. It can be performed in various solvents, making it a popular and widely used approach in the field of NP synthesis.

In summary, the "best" method for synthesizing BFO NPs will depend on the specific requirements and constraints of the application, and a trade-off between various factors such as eco-friendliness, cost, size distribution, reproducibility, and phase purity may be necessary.

The crystal structure of BFO is rhombohedral, which means that its three axes are equal in length and intersect at non-90° angles. As crystal structure affects the surface energy of the material, which influence the way in which particles agglomerate or form aggregates. If the crystal structure has a high surface energy, particles may be more likely to form aggregates, resulting in a larger overall particle size and potentially a more irregular shape. Conversely, if the crystal structure has a lower surface energy, particles may be more likely to exist as discrete particles, resulting in a smaller overall particle size and potentially a more uniform shape.

When growing nano-sized particles of BFO, the shape of the resulting particles will depend on the specific growth conditions and the synthesis method used. However, based on previous studies, it is expected that the particles will be roughly equiaxed, with no significant elongation in any one direction.[223,247] Sol-gel synthesized BFO NPs using citric acid based chelating agent were found to be roughly spherical with an average size of 60-80 nm.[248] Hydrothermally synthesized BFO NPs using surfactant were found to be roughly spherical with an average size of 50-80 nm.[249] In 2013, Escobar et al, reported distorted spherical morphology of BFO NPs synthesized by the sol-gel method.[250]

The presence of oxygen vacancies in a crystal lattice can significantly affect the nucleation and growth of NPs resulting in variations in their shapes and sizes. Oxygen vacancies can also create surface defects, altering the surface energy of the material, which in turn affects the surface reactivity and crystal lattice stability. The formation of oxygen vacancies can generate local electric fields, causing the migration of surface atoms and the creation of surface defects.[247,251–254]

3.2 Hydrothermal method

The hydrothermal synthesis method has a long history, dating back to the early 19th century, when scientists first discovered the phenomenon of hydrothermal mineral growth in geothermal systems. However, it was not until the mid-20th century that the hydrothermal method was developed and widely used for the synthesis of inorganic NPs and crystals. There is no unanimity about the definition of hydrothermal. The term hydrothermal usually refers to any heterogeneous reaction in the presence of aqueous solvents or mineralizers under high pressure and temperature conditions to dissolve and recrystallize materials that are relatively insoluble under ordinary conditions. Morey and Niggli in 1913 defined it as "In the hydrothermal method the components are subjected to the action of water, at temperatures generally near though often considerably, above the critical temperature of water (~370 °C) in closed bombs, and therefore, under the corresponding high pressures developed by such solutions."[255] After this definition many more came to explain hydrothermal concisely, one of them is "Any heterogeneous chemical reaction in the presence of a solvent (whether aqueous or nonaqueous) above room temperature and at pressure greater than 1 atm in a closed system." [255]

Since then hydrothermal synthesis has emerged as a highly effective method for the preparation of high-quality crystals in water under high pressure and at temperatures exceeding the boiling point of water.[255,256] With its facile route, this approach offers control through simple adjustments of solvent types, temperature, and pressure on the ionic reaction equilibria.[255,256]

The synthesis of BFO NPs using hydrothermal methods involves dissolving bismuth and iron nitrates in deionized water to create the precursor, which is subsequently transformed into $Fe(OH)_3$ and $Bi(OH)_3$ precipitates with the addition of mineralizing agents such as KOH. Further addition of the hydroxide mineralizer (KOH) causes $Fe(OH)_3$ and $Bi(OH)_3$ to dissolve and react during the hydrothermal stage at a particular temperature and pressure (autogenous) in a steel or Teflon pressure vessel known as an autoclave. This super-saturated process drives BFO precipitates, yielding single phase NPs.[257,258]

The key parameters temperature, pH value, and mineralizer determine the morphology, size, and properties of the synthesized nanomaterials. Temperature is a critical parameter that can modify the size and shape of the NPs.[256] The pH value is essential in tuning the ionization equilibrium conditions, which control the morphology and size of the desired materials.[256] The mineralizer acts as a catalyst to aid the formation of seed crystals and controls the dissolution, nucleation, and crystallization of the metal oxide under hydrothermal conditions. The viscosity of the solvent and the autogenous pressure value also impact the morphology and properties of the nanomaterials.[256,226]

There are several advantages to use the hydrothermal synthesis method for NPs production. Firstly, this method allows for a controlled synthesis of NPs with specific size, morphology, and crystal structure, which can be tailored to meet the desired application. Additionally, the hydrothermal synthesis method typically yields high product yields with a relatively simple experimental setup, making it an attractive option for many researchers. Moreover, this method is environmentally friendly compared to other synthesis methods. Lastly, a wide range of precursor materials can be used in the hydrothermal synthesis method, providing flexibility in NPs design. [226]

However, there are also some limitations associated with this method. The hydrothermal synthesis process requires high temperatures and pressures, which can limit the scalability of the method. Furthermore, long reaction times are often needed, particularly when synthesizing larger particles, which can be a time-consuming process. Additionally, the method can be sensitive to impurities in the starting materials, which can affect the quality and yield of the final product.[226,257]

Despite some disadvantages such as the need for an expensive autoclave and the inability to perform in situ analysis of the growing crystals due to the harsh reaction environment, the hydrothermal process offers significant potential to produce well-crystallized nanopowders with controlled morphology. Furthermore, this method can synthesize nanocrystalline or microcrystalline materials at much lower temperatures compared to the sol-gel method, providing distinct advantages in the field of materials science.

3.2.1 Hydrothermally synthesized BFO NPs

Synthesis steps

BFO NPs were synthesized from an equimolar mixture of $Bi(NO_3)_3 \bullet 5H_2O$ (0.01 mol) and $Fe(NO_3)_3 \bullet 9H_2O$ (0.01 mol) dissolved in 25 mL of water each, using KOH as the mineralizer. The mixture was ultrasonically dispersed for 15 minutes and then transferred into a 120 mL teflon-lined autoclave. The final concentration of KOH in the dispersion was 10 M for 50 ml of dispersion. For hydrothermal treatment, the autoclave was sealed and heated at 200 °C for 3 hours without shaking or stirring, then cooled to room temperature naturally. The final products were collected by centrifugation, rinsed with 10 % acetic acid, and further washed with distilled water and ethanol. They were then dried at 70 °C for 4 hours before further characterization. The scheme is shown in Figure 3.1. The hydrothermal method for the synthesis of BFO NPs can be described by the following chemical reactions.

$$Bi(NO_3)_3 \bullet 5H_2O + Fe(NO_3)_3 \bullet 9H_2O + 6\ KOH \rightarrow BiFeO_3 + 6\ KNO_3 + 17\ H_2O$$

The reaction takes place in an autoclave (sealed vessel) under high temperature and pressure conditions 200 °C typically at pressures up to 10 MPa. As the temperature and pressure increase, the solubility of the precursors in the solvent decreases, leading to the formation of small clusters of BFO nuclei. The formation of these nuclei is a nucleation process, where the precursors react with each other to form small particles of the desired product. In the second step, the BFO nuclei grow into larger NPs reacting with available precursors in the reaction vessel. The growth process occurs through the adsorption of additional precursor ions onto the surface of the nuclei, followed by a crystallization step that incorporates the additional ions into the crystal structure. The reaction is terminated after 3h for the desired particle size.

The obtained BFO NPs are separated from the reaction mixture through a washing and drying processes.

3.2.2 Results and discussion

The hydrothermally synthesized BFO NPs, were structurally characterized using XRD, EDX, and TEM. Figure 3.1a, shows the XRD pattern of hydrothermally synthesized BFO NPs. The red vertical lines represent the reference pattern of the *R3c* crystal structure (ICSD: 417304). It is evident that BFO NPs consist of a single phase with *R3c* (rhombohedral) crystal symmetry. There is no impurity above the XRD detection limit.

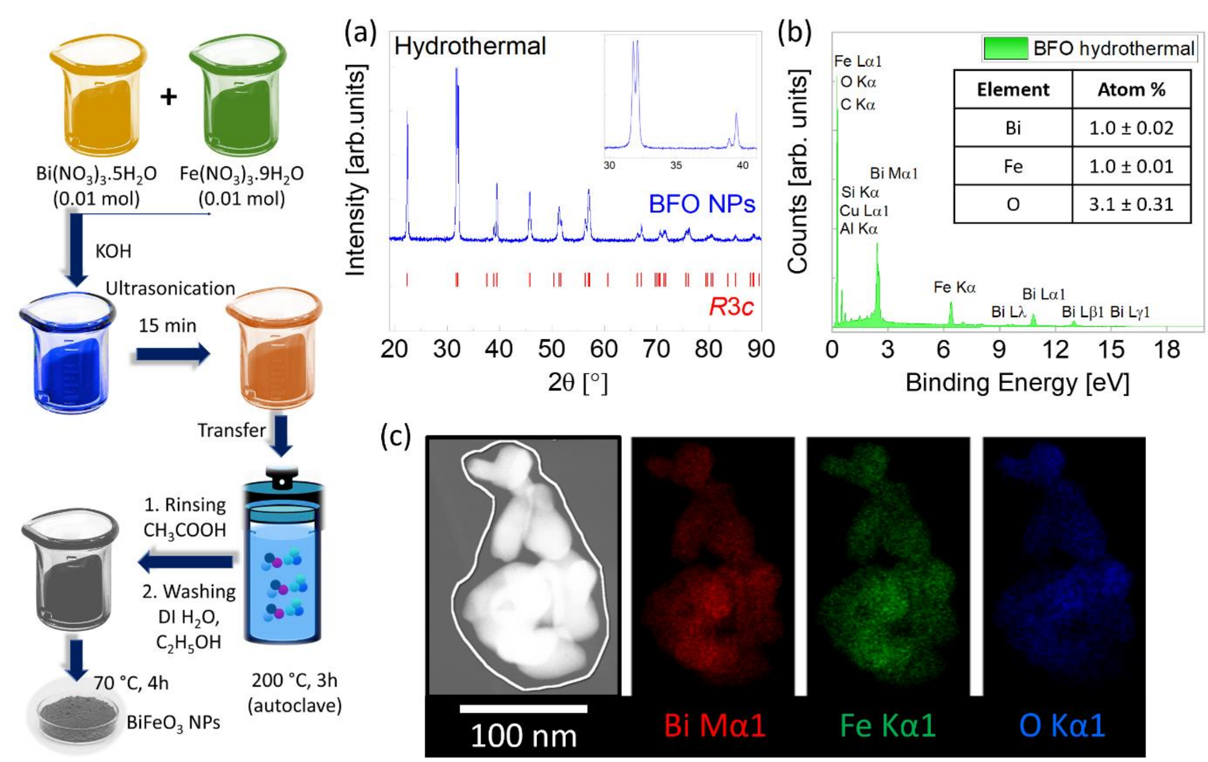

Element	Atom %
Bi	1.0 ± 0.02
Fe	1.0 ± 0.01
O	3.1 ± 0.31

Figure 3.1: Scheme of hydrothermal method for synthesis of BFO NPs on the left. XRD diffractogram of BFO NPs synthesized by hydrothermal method, the inset shows the splitting of peaks in 2ϑ range 30-41° (a). EDX profile of BFO NPs where inset shows the relative atomic percentage present (b). The HAADF images for Bi, Fe and O elemental distribution for a selected group of agglomerated BFO NPs (c).

EDX was performed to further confirm the purity of NPs, as shown in Figure 3.1b. From the EDX result we find that there is similar relative atomic stoichiometry as for BFO i.e., 1:1:3, which supports the formation of BFO NPs. The distribution of elements in BFO NPs shown in Figure 3.1c also tells that no impurities are formed. The HAADF images show that there is a homogeneous distribution of elements in a nanoparticle, which supports the single-phase formation of BFO NPs. The morphology of hydrothermally synthesized BFO NPs is shown in the TEM image in Figure 3.2. We observe that BFO NPs are of average particle size 47 ± 9 nm. BFO NPs have irregular shape with broad size distribution. Nevertheless, from the HRTEM image [Figure 3.2b] a high crystallinity of the NPs is observed. The (012) crystalline planes of rhombohedral BFO NPs are confirmed by the SAED image shown in Figure 3.2 c.

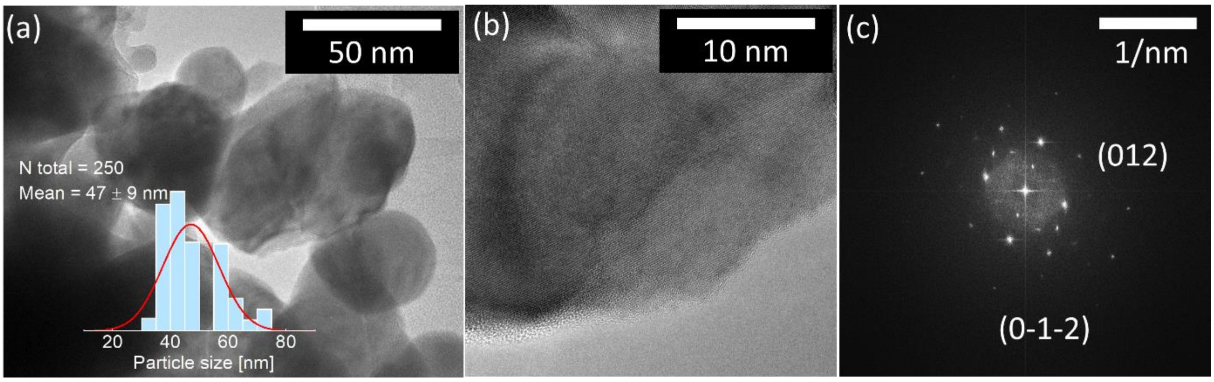

Figure 3.2: TEM image of hydrothermal-synthesized BFO NPs (a) with particle size distribution histogram. High resolution TEM image (b), and SAED pattern of crystalline nanoparticle shown in (c).

Hence, optimizing the conditions of the hydrothermal method for the synthesis of single-phase BFO NPs results in a broad size distribution and irregular shape. What can be reasons?

Ostwald ripening can be one of the reasons, where the larger particles grow at the expense of smaller ones.[259–261] In a solution containing NPs, the NPs are constantly colliding and interacting with each other. At the same time, the NPs are also in contact with the surrounding solvent or solution. Because smaller NPs have a larger surface area-to-volume ratio, they tend to dissolve more easily in the solvent than larger NPs. As a result, the smaller NPs release atoms or molecules into the surrounding solution, which can then be taken up by larger NPs. Over time, this process causes the larger NPs to grow at the expense of the smaller ones, leading to a gradual increase in the average size of the NPs in the solution. This process is known as Ostwald ripening, named after the German chemist Wilhelm Ostwald, who first described it in 1896.[261–263] Ostwald ripening can lead to a broad size distribution and a loss of control over the final product.[263] During the hydrothermal reaction, the precursor ions interact with each other and with the solvent, leading to the formation of nuclei. As the reaction proceeds, these nuclei grow by the addition of precursor ions. The growth rate of these nuclei depends on several factors, including the concentration of precursor ions, temperature, and pressure. However, the formation of irregular shaped NPs can occur due to the non-uniform growth of these nuclei. The non-uniform growth can occur due to several reasons, including the presence of impurities, the distribution of precursor ions, and the local variations in the temperature inside the reaction vessel. An unequal distribution of the reactants leads to regions with different concentrations of reactants. As a result, the growth of nuclei in these regions can be different, leading to non-uniform sizes or variations in the rate of nucleation and growth of the NPs.

3.3 Sol-gel methodology

The "sol-gel" method is based on the transformation of a solution or "sol" of precursor molecules into a solid or "gel" network through a series of chemical reactions, often involving hydrolysis and condensation.[248] The sol-gel process was first discovered and studied in the early 20th century by two French scientists, Gustave Bernal and Eugene Pochet, who observed the gelation of colloidal silica particles in a solution of tetraethyl orthosilicate (TEOS).[248]

However, it was not until the 1950s and 60s that the sol-gel method began to be recognized as a powerful tool for materials synthesis, especially in the field of glass science.[264] In 1953, Kistler reported the synthesis of porous silica glasses using the sol-gel process, and later, in 1969, Stookey developed a method for producing a transparent, colourless glass-ceramic material called "Fotoceram." This material was made by using the sol-gel process to convert a liquid solution of titania and alumina precursors into a glass-ceramic composite with high thermal stability and transparency.[260]

In the 1950s and 1960s, especially for applications in an industrial scale, the conventional method of preparing powder formulations used in the manufacture of ceramic materials required the calcinations of a mechanically ground mixture of metal oxides and carbonates in definite proportions.[227] However, the milling and grinding, normally employed to obtain a mixture in a fine state of subdivision, introduces contaminates from abrasive materials.[248] These contaminants have a detrimental effect on the electrical properties and introduce a variance into each batch of powder prepared. The solid-state reaction, a diffusion-controlled process, requires intimacy of reacting species and a uniform distribution of each species to obtain a completely reacted and uniform product. The mechanically ground mixture requires prolonged calcinations at high temperatures under accurate control of the atmosphere. Such prolonged calcination promotes crystallite growth which is undesirable in the fabrication of dense fine-grained ceramics. Moreover, it is extremely difficult to prepare dielectric films composed of two or more chemically combined oxides by conventional evaporation techniques. This requires the difficult art of controlling the rate of deposition of metal oxides from the vapor phase onto a substrate enclosed in an evacuated chamber. The high temperature and high vacuum required to vaporize the oxides cause variations in oxidation states and contamination from metal vapours. For these reasons a process eliminating the cumbersome apparatus and tedious techniques was needed.[260,261,264]

With traditional sol–gel methods, the particles are part of a gel structure, while in the Pechini method, the metal cations are trapped in the polymer gel.[227] This reduces the ability to grow controlled shapes and involves the formation of hard crystallite agglomerates. The size of the final product is controlled, to an extent, by the sintering process and the initial concentration of metals in the gel.

3.3.1 Pechini method

The Pechhni synthesis method was named after the American researcher Dr. Maggio Pechini.[265] The year was 1967, and the scientific community was abuzz with the proposed Pechini method.[265] This method offered a new way of depositing dielectric films of titanates and niobates of lead and alkaline-earth elements in the production of capacitors. At the heart of this method was a novel approach to the synthesis of complex oxides. By carefully controlling the chemical reactions between metal salts and organic acids, researchers were able to produce finely dispersed oxide materials with a high degree of homogeneity. Over time, the Pechini method proved to be more than just a game-changer in the production of capacitors. Its versatility and adaptability allowed scientists to customize the process for the in-lab synthesis of multicomponent oxide materials.[266] This opened up a world of possibilities for the development of new materials with unique and desirable properties.

Pechini patented this method for making powders consisting of Ti, Nb or Zr.[265] This method resulted in nanosized particles due to the solution undergoing a poly-esterfication leading to a viscous resin, at temperatures relatively low compared to other synthesis method such as solid-state.[227,266] By adjusting the calcining temperature, one is able to control the size of the particles or crystallites in the calcined powder. A powder calcined at a lower temperature will consist of particles smaller than those calcined at a higher temperature. Selbach measured the crystallite sizes of BFO powder prepared by Pechini synthesis with different carboxylic acid with or without ethylene glycol (EG) calcined at different temperatures and found a strong dependence between size and temperature.[73]

3.3.2 Modified sol-gel Pechini method

Synthesis of single phase BFO NPs was achieved in 2007, however, the contaminant produced by decomposition of the precursor was still present in final product.[240] Ghosh et al. synthesized nanosized BFO using a soft chemical route with tartaric acid as a template material and nitric acid as an oxidizing agent.[62] However, the crystallinity of the resulting BFO NPs was unsatisfactory and the existence of an impure Bi_2O_3 amorphous phase in the host at low temperature product of 400 °C was evident. To deal with the issues mentioned above, we altered the reaction parameters so that the crystallinity of BFO NPs can be improved without compromising with its single phase.

“We synthesized BFO NPs by a modified wet chemical Pechini route, followed by the auto combustion method. For the synthesis, 0.01 mol of Bismuth nitrate and Iron nitrate were dissolved in 25 mL of 2 N HNO_3 with 0.02 mol of tartaric acid as a chelating agent. Nitric acid is used as an oxidizing agent, which also leaches out impurity phases by discerningly dissolving some elements. It also prevents the hydrolysis of Bismuth nitrate.[10] Afterward, the solution was kept under continuous magnetic stirring at room temperature for at least 2 h. The tartaric acid form chelate compound with Bi^{3+} and Fe^{3+} ions shown in Figure 3.3. We optimised the crystallization temperature for the chelating agent tartaric acid, a lower crystallization temperature of 403 K is best for fabricating the xerogel precursor completely. The obtained cloudy yellow coloured sol was heated up to 403 K and kept at this temperature for 10 h. The resulting brownish-yellow fluffy xerogel was collected and crushed in a mortar to obtain a fine amorphous powder, followed by a calcination process at 798 K for 1 h with 3 K/min heating and cooling rates to obtain the final BFO NPs. For doping, we followed the same route shown in Figure 3.3, using the same reaction parameters with dopant precursors added to the primary solution in the corresponding molar percentages.**”**[c]

In the sol-gel process for the synthesis of BFO NPs, the nucleation and growth of the NPs involves the hydrolysis of the precursors, precipitation, and calcination. The process starts

---

[c] This paragraph is based on (Dubey et al Journal of Physical Chemistry C 2022, https://doi.org/10.1021/acs.jpcc.0c05778)

with the hydrolysis of the precursor compounds, such as bismuth nitrate and iron nitrate, in the presence of a solvent (H_2O). This leads to the formation of bismuth hydroxide and iron hydroxide.

$$Bi(NO_3)_3 + 3H_2O \rightarrow Bi(OH)_3 + 3HNO_3$$

$$Fe(NO_3)_3 + 3H_2O \rightarrow Fe(OH)_3 + 3HNO_3$$

$$Bi(OH)_3 + Fe(OH)_3 \rightarrow BiFeO_3 + 3H_2O$$

The hydroxide formed in the hydrolysis step undergo condensation to form larger molecular clusters.

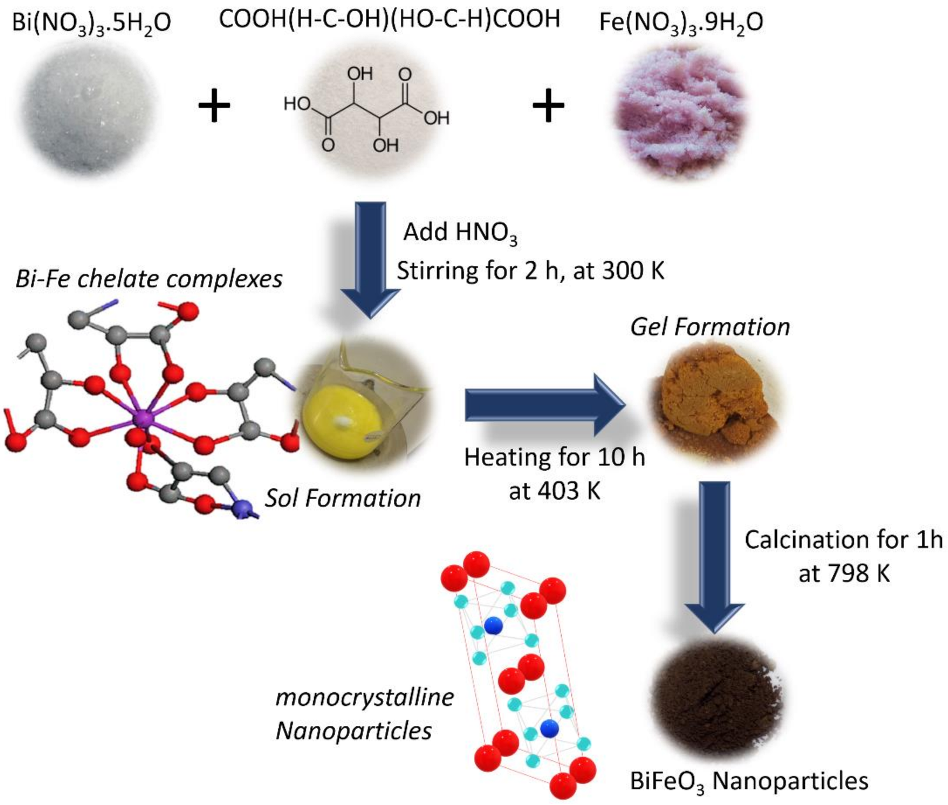

Figure 3.3: Scheme of an optimised and modified sol-gel Pechini method for synthesis of Bismuth Ferrite ($BiFeO_3$) nanoparticles.

These clusters can then aggregate to form the nuclei or small crystalline clusters of $BiFeO_3$. During the precipitation step, the bismuth nitrate, iron nitrate, and tartaric acid are dissolved in distilled water, and nitric acid is added to adjust the pH of the solution to around 2.5 - 3. Tartaric acid acts as a chelating agent and forms a complex with the metal ions (Bi^{3+} and Fe^{3+}) through its carboxylic acid groups. The two carboxylic acid groups in tartaric acid coordinate with the metal ions, forming a chelating ring structure that stabilizes the complex and prevents the metal ions from precipitating out of solution. The chelating ability of tartaric acid arises from its ability to bind metal ions through its carboxylic acid groups. The carboxylic acid groups of tartaric acid act as ligands, which are molecules or ions that bind to a central metal ion. In this case, the metal ions are Bi^{3+} and Fe^{3+}. The chelate forms by coordinating with the metal ions in the solution, effectively trapping them in a ring structure that prevents them from reacting further. The chemical equation for the precipitation step is the following.

$$\mathrm{Bi(NO_3)_3 + Fe(NO_3)_3 + C_4H_6O_6 + 4\ HNO_3 \rightarrow BiFeO_3 + 4\ NO_2 \uparrow + 4CO_2 \uparrow + 10\ H_2O}$$

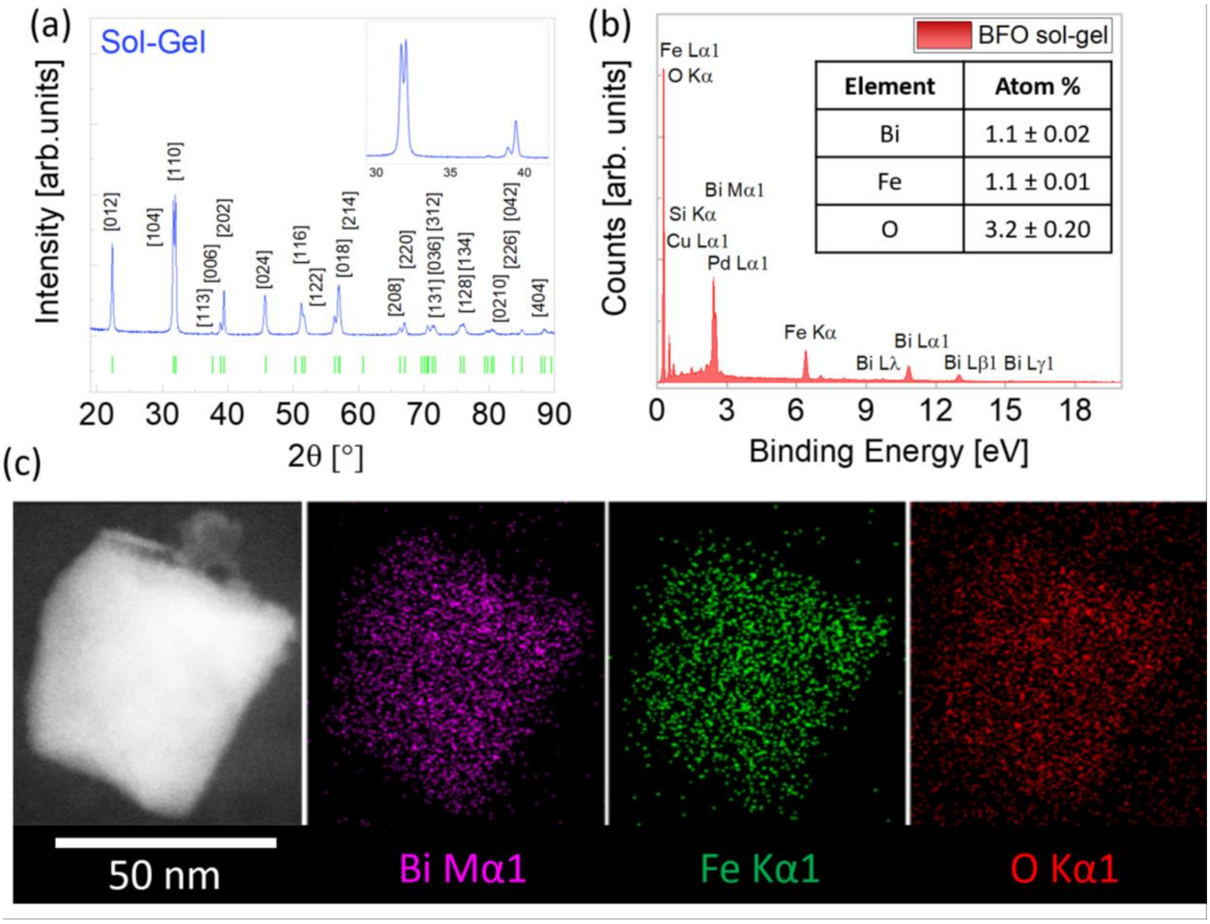

Element	Atom %
Bi	1.1 ± 0.02
Fe	1.1 ± 0.01
O	3.2 ± 0.20

Figure 3.4: XRD diffractogram of BFO NPs synthesized by the sol-gel method, the inset shows the splitting of peaks in the 2ϑ range 30-41° (a). EDX profile of BFO NPs where inset shows the relative atomic percentage present (b). The HAADF images for Bi, Fe and O elemental distributions in an individual BFO nanoparticle.

The bismuth ferrite precipitate is formed due to the reaction between the chelated complex and nitric acid. The nitric acid reacts with the metal ions and breaks the chelating ring structure, resulting in the formation of bismuth ferrite precipitate. Nitric acid also helps to dissolve the metal salts in water by protonating them, which makes them more soluble and readily available for reaction. During calcination, the tartaric acid decomposes and burns off leaving behind the pure bismuth ferrite powder. The growth of NPs can occur through different mechanisms, including oriented attachment, Ostwald ripening, or agglomeration depending on the specific conditions used. In this case, oriented attachment is the most plausible growth mechanism as confirmed by TEM images in Figure 3.5. In the diffusion stage, the smaller NPs diffuse through the solution and come into contact with the larger NPs. The larger NPs have a lower surface energy and are more stable than the smaller NPs. No chemical reaction occurs in this stage.

The obtained BFO NPs were characterized to check their phase purity, crystallinity and elemental composition as discussed in the next section. For simple terminology and to address the comparison among different synthesis routes, we will be using the term “sol-gel” even for our “*modified sol-gel Pechini method route*”.

3.3.3 Results and discussion

In Figure 3.4a, the XRD diffractogram of BFO NPs synthesized by the modified sol-gel method is shown. The XRD pattern unveils the $R3c$ crystal structure, without any secondary phase. The XRD peaks are well matched and indexed with reference $R3c$ pattern (space group 161, ICSD: 417304). The characteristic set of peaks at ~32 degrees for rhombohedral symmetry of bulk BFO, is merged for sol-gel synthesized BFO NPs due to the reduced crystallite size and larger microstrain.

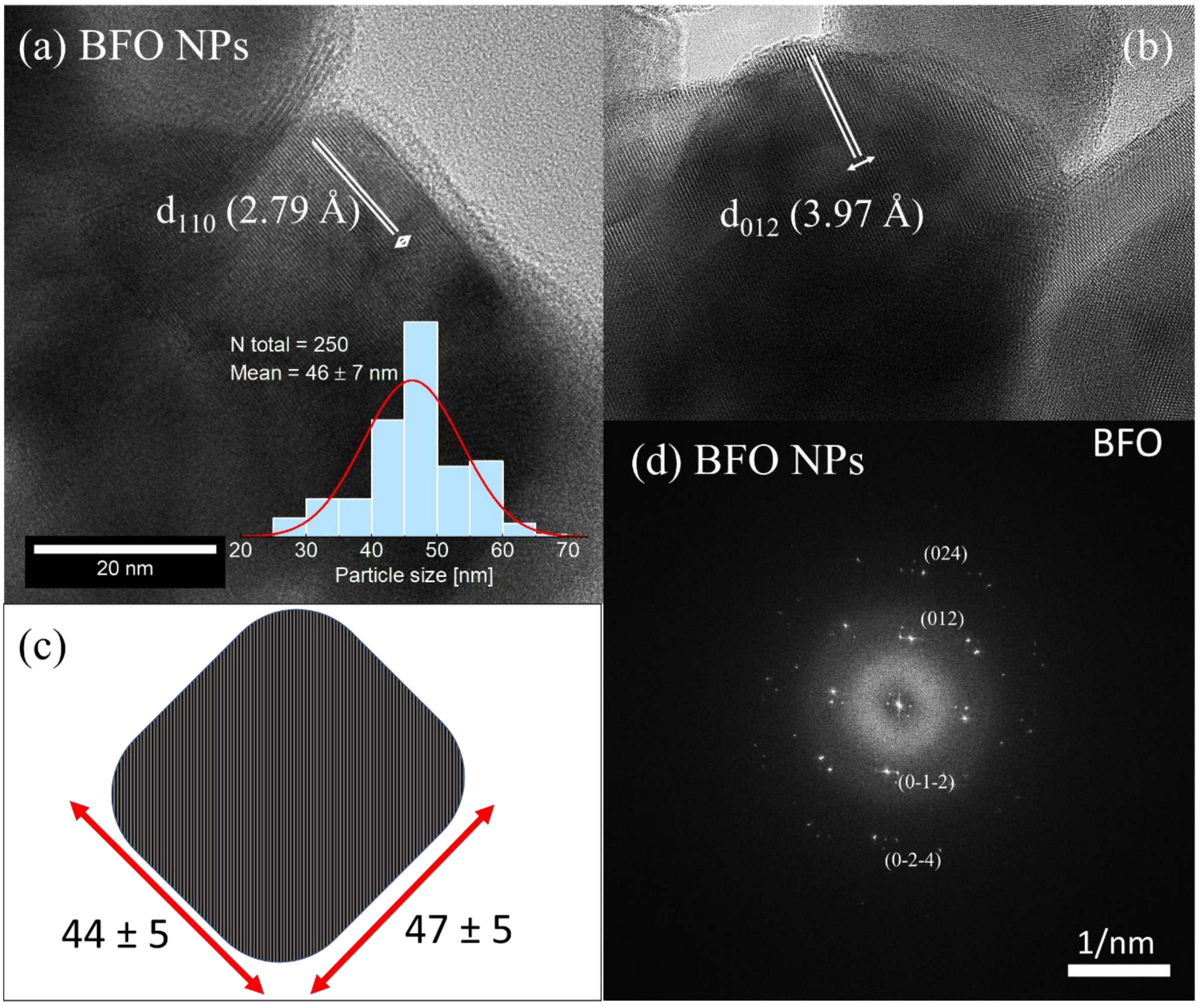

Figure 3.5: High resolution TEM image of sol-gel synthesized BFO NPs (a-b) scale bar 20 nm. The schematic of individual BFO NPs based on the obtained TEM image (c), and selected area electron diffraction pattern of BFO NPs. (d)

The EDX pattern in Figure 3.4b shows the elemental atomic percentage relative ratio in BFO NPs, which is 1:1:3 for Bi:Fe:O confirming the phase purity of NPs. We were able to image a single nanoparticle of BFO, and upon HAADF mapping, all the elements are found to be homogeneously distributed as shown in Figure 3.4c. From the TEM image of NPs [Figure 3.5] we observe that sol-gel synthesized BFO NPs consist of a cuboidal shape with two different length and breadth [Figure 3.5c]. The HRTEM image, confirms the high crystallinity of these NPs, where the SAED pattern represents the (012) lattice planes of these nanocrystals.

The microstructural characteristics of the NPs were further analysed with the help of HR-TEM and SAED patterns. Figure 3.5 depicts that the interplanar spacing is about 0.27 and 0.39 nm, which corresponds to the (012) crystallographic plane of BFO with R3c symmetry as shown in Figure 3.5d. The SAED patterns of BFO in Figure 3.5d also depicts the formation of NPs in crystalline form. The HR-TEM images also indicate the variation in the domain structure of the samples. In addition, we observe that cuboidal BFO NPs agglomerate with each other from edge to edge. This shows that edges of NPs are quite active and prone to react with the environment.

3.4 Pulsed laser ablation in liquid (PLAL) method

History

Initially, the laser ablation method was used to carve or modify the surface of a target material. However, the removed particles were insignificant and treated like waste.[267] The laser beam ability to focus on the target surface in a liquid environment allowed direct dispersion of the products or ablated materials in the solvent. A liquid medium was chosen during laser ablation instead of other media like gas because it is safer. There are no dust or gaseous pollutants released into the surrounding atmosphere thereby preventing harmful health effects like respiratory diseases.[267] Additionally, using liquid as a medium could control not only the surface quality but also the ablation efficiency.[268,269] Synthesizing NPs or colloids in a liquid environment by using a target dipped into a liquid medium has several advantages including minimizing the temperature rise on the target, maintaining the target surface clean, keeping vapor and plasma contained in a confined liquid environment, and increasing shock intensity on the target surface.[268,270,271]

Plasma and Bubble Dynamics

During the PLAL process in a set up like shown in Figure 3.6, three main steps take place: generation of a plasma, formation of a cavitation bubble, and dispersion of the NPs into the liquid phase. Plasma containing ablated NPs are formed from the target surface when a laser intensity greater than 10^9 W/cm^2 is irradiated onto the solid target as illustrated in [Figure 3.6d]. The generated plasma is made up of strongly ionized, atomic or molecular species with a high density. However, this also depends on the value of laser pulse energy being used.[268]

The thermodynamic properties and chemical composition inside the bubble are essential. During the initial stage of the cavitation bubble formation a chemical reaction occurs. The rapid cooling plasma causes the development of a vapor layer inside the cavitation bubble, and this vapor surrounds the area that initially contains liquid matter such as atom clusters, primary particles, and secondary particles.[272] The relationship between the chemical composition of liquid-vapor near the bubble boundaries and the target surface does not affect the bubble dynamics. Additionally, it is not influenced by the viscosity or the surface tension of the liquid.[272] It has been shown that no thermal energy is transferred between vapor and liquid after the first plasma stage, and even during the first oscillation, the number of molecules within the bubble does not vary substantially.[273]

Kim et al. showed that the lifetime of plasma increases with laser energy by using the time-resolved imaging.[274] They also revealed that increasing the laser power would result in bigger size of laser induced bubbles.[275] Furthermore, adding electrolytes like NaCl could also make the plasma lifetime longer due to the enhanced Bremsstrahlung that is emitted from the electrolyte.[275] The word Bremsstrahlung comes from German word *bremsen* "to break" and *Strahlung* "radiation" which generally give the full definition "breaking radiation" that means, when a charged particle is deflected by magnetic fields or another charged particle, and electromagnetic radiation gets emitted.[276]

In the next stage, which is the plasma decay phase, energy is transferred to the surrounding liquid by a shockwave as shown in Figure 3.6e, resulting in a layer of liquid- vapor. This vapour layer has similar volume as plasma. The formation of this shockwave is due to the fast expansion of the plasma that is compressing the surrounding liquid. After around 1 µs from the first shockwave, a second shockwave that is parallel to the target is generated. This second shockwave is generated at speed of 1500 m/s in water,[277] while 1200 m/s in the acetone[278] and expands in an anisotropic manner in both parallel and perpendicular directions to the surface of the target.

In the second main stage, an oscillating cavitation bubble is created during the plasma cooling phase, when heat from the plasma releases to the surrounding (Figure 3.6 e). This oscillating bubble mainly consist of vapour from the liquid and ablated products.[267] Later, this perfect hemisphere cavitation bubble expands at 0.1% of lifetime until it comes maximum height at approximately 20% of its lifetime and soon after, it collapses.[279] The expansion of the bubble occurs when the pressure of bubble continuously decreases, and it collapses when the pressure becomes lower than the surrounding liquid pressure. The shape of bubble does not change significantly from growth until shrinking period, maintaining to have a distinct hemispherical shape. The shrinking of the first cavitation bubble starts at almost 50% of the lifetime until it fully collapses (Figure 3.6), followed by full expansion of a second bubble at 60% of lifetime and at 80% of the lifetime, the second bubble shrinks. This second bubble finally collapses at around 90% - 100% of its lifetime.[268]

Fluence primarily influences the lifetime and volume of the cavitation bubble.[277] In addition, this cavitation bubble could also grow large with the compressibility of the liquid[280] and decreases with the density of the liquid.[281] Generally, it is expect that particles agglomerate more as the size of the cavitation increases (higher fluence). Nonetheless, Tomko's group made known that they got smaller and homogenous particles when they increase the fluence.[282]

As per the above explanation, target experiences a local high temperature and high pressure, however it is mostly an estimation and further experiments and theoretical calculations are required to unveil the local conditions onto the surface of target during PLAL.[268] This high temperature and pressure condition is however only relevant to the first plasma and for final collapse stage but not to the cavitation bubble.[283,268] Some researchers have reported that high-temperature, high pressure, and rapid cooling time of plasma provide an ideal thermodynamic condition for the formation of NPs.[284,285,286,287,288] During the expansion and shrinking process of cavitation bubble, temperature and pressure values change. De Giacomo et al have reported that the high initial pressure (> 10^5 atm) of cavitation bubble gradually decreases due to the fast expansion of gas bubble in liquid and it finally collapses when the pressure is lower than the surrounding liquid. It results in a decrease of the initial temperature of the cavitation bubble from more than 1000 K to hundreds of Kelvin.[283] Plasma spectroscopy can be useful to determine the occurrence and understanding of the chemical reaction for the synthesis of possible LAL products. NPs formation can happen from the condensation of clusters of material vapor with the assumption that there is no presence of any chemical reaction inside the cavitation bubble as demonstrated by Zhigilei's group.[289]

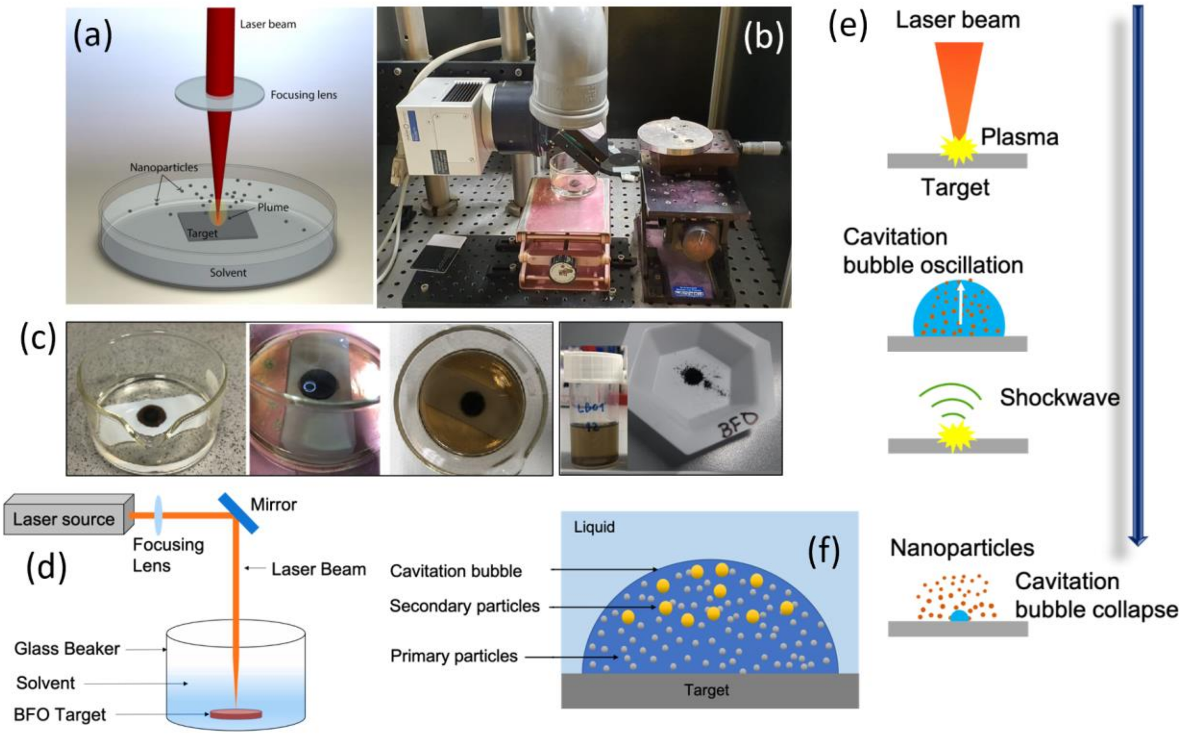

Figure 3.6: Schematic of laser ablation in liquid for the synthesis of nanoparticles (NPs) (a, and d), the real lab set up, where beaker is kept on a pink coloured stand to set the optimum height from the laser source (b), The production of NPs: when the laser hits the bulk target, the transparent acetone (liquid) changes its colour to brown due to the presence of BFO NPs, which are finally dried and collected. The proposed mechanism of the generation of NPs using PLAL method (e), and the formation of cavitation bubbles (f).

Primary particles that are less than 10 nm in size are distributed evenly from right above the target to the very top of the bubble. Secondary particles which are larger than primary particles, normally have sizes more than 40 nm or agglomerates are densely concentrated at the center and upper parts of bubble[268] Figure 3.6f. There is no evidence of dispersion of these particles into the liquid before bubble collapses. Furthermore, these secondary particles increase their size from approximately 40 nm to more than 60 nm after the collapse of the first bubble. It is suggested that a perfect condition for the crystallization of NPs is from the plasma-heated supercritical water phase and cold bubble vapor.[268] However, more studies related to this subject need to be done in the future since this is still not fully understood yet.

Although it remains difficult to understand, a bimodal size distribution of primary and secondary particles usually found after LAL.[272,290] One of the possibilities of this phenomenon can related to the distribution of beam intensity on the target surface during LAL.[291] The ablation area with the highest fluence regime is usually found at the center spot and a lower-fluence regime at the outermost spot. These two spots determine the size of the ablated NPs as primary or secondary particles.

Optimization of reaction parameters

During PLAL, factors such as target material, liquid properties, and processing time have a big impact on the size, morphology, purity, productivity, stability, and dispersion of the ablated NPs. These factors affect the formation of byproducts.[268] Metals and oxides are often used to synthesize NPs via PLAL. Carbides, nitrides, and sulfides also have been successfully synthesized by this method.[267] Unlike for oxides, metal ablated NPs consist of mixture of defect-rich crystal phases and this not favorable as it is hard to reproduce. Generally, noble materials like Ag and Au are easy to handle, since almost no oxidation occurs producing purely monophasic crystals.[268] Apart from material composition, shape of material also gives significant effect to the characteristic of the NPs. Bulk targets and thick films are often used in PLAL. Long ablation time can be performed using bulk targets and a high ablation rate can be achieved. Regardless of having these advantages, more uniform NPs can be produced with film targets. However, film targets are harder to deal with since they are very thin.[268]

Liquids such as distilled or deionized water are typically used in PLAL for NPs synthesis. Streubel et al reported that 30% concentration of oxidation took place for Pt (Pt to Pt^{2+} and Pt^{4+}) during LAL.[292] Instead of using water for materials that are sensitive to oxidation, organic solvent like acetone, ethanol or propanol can also be used to avoid oxidized metallic particles.[267] Increasing liquid layer thickness from target surface may minimize the NPs size as “laser fragmentation in liquids” (LFL) may happen simultaneously.[268] Generally, LFL is a great method to reduce the particle size compared to other laser synthesis methods like LAL and “laser melting in liquids” (LML) methods. The only difference between LAL and LFL is, instead of a solid target, colloids are irradiated with laser beam in LFL. [242,268] However, higher productivity can be achieved by minimizing the liquid layer above target.[293] Furthermore, high viscosity liquids are prone to have lower particle aggregation and can produce smaller particles.[268] Oseguera-Galindo et al. proved that smaller Ag NPs are generated with using propanol (1.94 mPa·s) compared to ethanol (1.07 mPa·s) and acetone (0.31 mPa·s).[294]

In PLAL, long time processing may cause a high concentration of NPs, but too long time processing leads to particles aggregation.[268] Hence, knowing the optimized time is crucial when performing LAL also depending on other laser parameters such as laser fluence, wavelength, frequency and pulse duration. Getting too high concentration also triggers LFL process and when this happens, reproduction may become a problem because of the unstable method. Additionally, increasing the processing time may also increase the temperature of the liquid. Although with ultrashort pulses, the cumulative heat in the laser-irradiated area after each pulse tends to flow to the surrounding liquid.[295]

3.4.1 Bulk BFO target synthesis: Mechanochemical activated assisted (MAA) method

For a bulk BFO target it was required to have a material which is phase pure and with narrow size distribution. The bulk target for laser ablation was prepared by the mechanochemical activated assisted (MAA) route. For synthesizing the BFO target, Bi_2O_3, and Fe_2O_3 were ground separately with absolute ethanol and yttria-stabilized zirconia (YSZ) milling balls (ball diameter 3 mm). The stoichiometric amounts of Bi_2O_3, and Fe_2O_3 were mixed with ethanol and the mixture was milled for 4 h in a planetary mill (Retsch) at 200 min^{-1} for homogenization of the precursors. Afterwards, the powder was dried at 120 °C. For the activation step, the dried powder was again high energy planetary ball milled (Fritsch) for 40 h with tungsten carbide balls, 1:1 ratio of mixture with balls. The milled mixture was periodically taken out of the vial to analyse using X-ray diffraction. The activated powder was dried and pressed uniaxially at 50 MPa into pellet and then isostatically at 300 MPa. It was sintered at 760 °C, 5 K/min for 4 h in air. The steps of MAA method are represented in Figure 3.7 e.

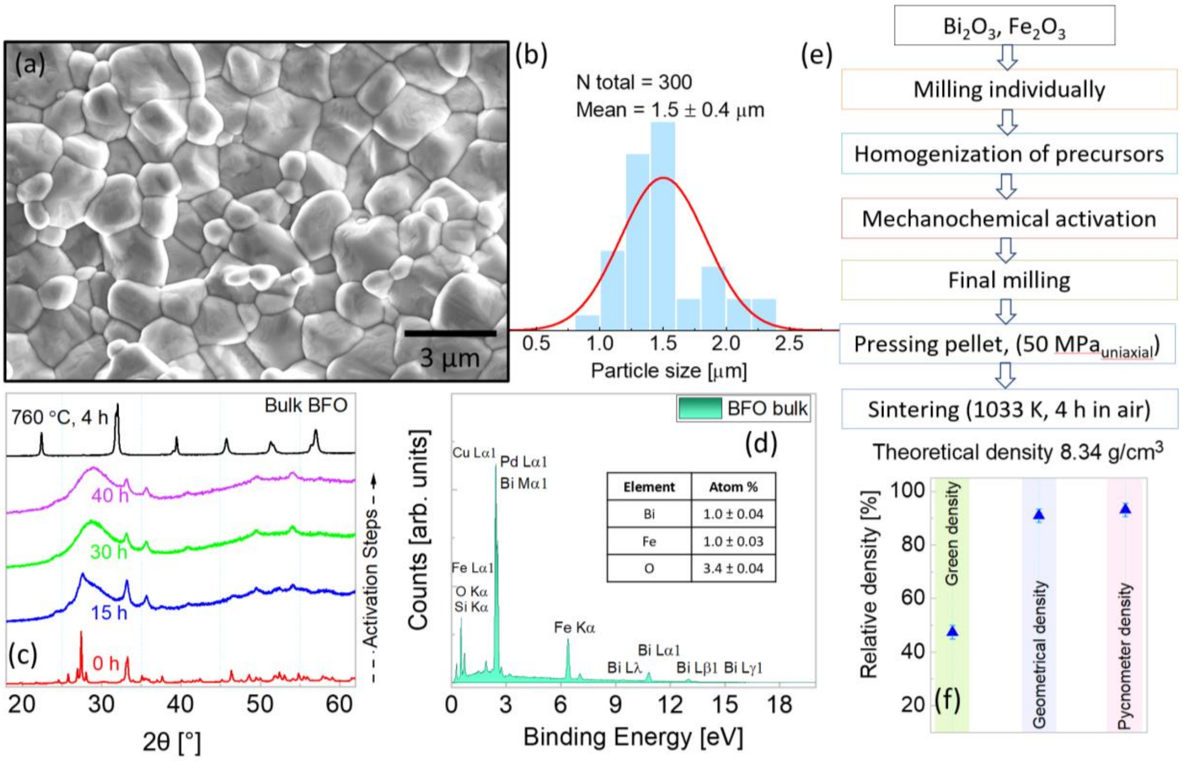

Figure 3.7: Mechanochemical-activated-assisted-method for synthesis of bulk-BFO target. SEM image (a), grain size distribution (b), XRD diffractograms of each activation step of mixture of precursors by milling and the final sintering step (c), The EDX pattern of the final sintered bulk BFO target (d), Scheme of the MAA method (e), and the density trend from the green body to the sintered pellet and comparison with pycnometer-based density with respect to the theoretical density of BFO (8.34 g/cc).

The density of the green body was around 50 % with respect to the theoretical density of BFO 8.34 g/cc. After sintering the geometrical and pycnometer-based density were found to be around 90 % of the theoretical density as shown in Figure 3.7 f.

From Figure 3.7c, the XRD peaks at 0 h of milling represent the individual precursors i.e., Bi_2O_3, and Fe_2O_3. Upon milling the mixture of precursors for 15 h, the peaks of the individual precursors disappear. New peaks represent the crystallinity of the mixture and the formation of new chemical bonds. The XRD diffractograms of the activation step of the mixed precursors show good mixing and the reaction which is activated at these milling conditions.

After complete activation by 40 h of high-speed milling, the sintering of the pressed pellet was done at 760 °C for 4 h. This is the advantage of this method, which removes the step of calcination and so avoids the impurity formation chances in BFO. The XRD diffractogram of the sintered pellet is shown in Figure 3.7 c, where a single-phase of BFO is confirmed with its *R*3*c* crystal symmetry. Further confirmation was done by EDX mapping from different areas of the pellet as shown in Figure 3.7 d, where the elemental ratio fits the stochiometric composition of BFO. The grain size and density were studied by SEM images shown in Figure 3.7 a-b. The BFO bulk target is a compact pellet with no holes or cracks. The average grain size is larger than 2 µm.

3.4.2 Results and discussion for PLAL synthesized BFO NPs

The MAA synthesised bulk BFO target was kept in a beaker filled with acetone. As shown in Figure 3.6 c and d. We have used MAA synthesized bulk BFO target for synthesis of colloidal NPs by means of PLAL. This technique has been conducted by using Nd:YAG (Rofin Powerline E20) laser source. The laser was operated with parameters as shown in Table 2. We could change current and frequency of laser for parameter variation of laser fluence. Each target was placed horizontally into glass beaker filled with acetone and its surface was irradiated by a laser source perpendicularly.

About 20 experiments on BFO target were performed in this study by varying laser parameters such as frequency, current, time, and volume and type of solvents until optimum parameters were achieved Table 3. A power sensor and power meter devices were used to determine value of laser power. Laser beam was irradiated onto the sensor and light from laser was first converted to heat. The heat flows through the sensor were then converted to an electrical signal which can measured and read by the meter. To get a very precise power value, laser was allowed to hit the sensor for at least 20 seconds.

Upon irradiation of laser beam, the solution was gradually turned into brown from colourless. At least seven runs of each target were carried out to get enough products for characterization of NPs. Different spots on the target surface were ablated during each run. Total mass of NPs released in the acetone solution was measured from the weight loss of target after laser ablation process.

The optimised parameters for BFO NPs synthesis are shown in Table 3. Figure 3.8 shows the results of structural characterization of laser ablated BFO NPs. The XRD diffractogram indicates the phase purity of BFO NPs. As the characteristic doublet peak of bulk BFO at ~32° is completely merged, the crystal structure is distorted due to the small crystallite size and increased microstrain. However, the average crystal symmetry remains *R3c*.

Table 2: General parameters for PLAL method

General Parameter	Value
Wavelength (nm)	1064
Goodness of beam	1.3
Pulse length (nm)	5
Raw beam diameter (μm)	4800
Focal length (mm)	10
Stage height (cm)	10.85
Beam incidence angle (°)	0

The EDX mapping of the laser-ablated BFO NPs shows high phase purity, with expected elemental stoichiometry. The HAADF images of the NPs also demonstrate a homogeneous distribution of the elements within them.

Table 3: The optimised laser parameters for synthesis of BFO NPs from its bulk target.

Optimised Parameter	Values
Laser Power (W)	5.5
Frequency (kHz)	10
Pulse energy (μJ)	550
Current (A)	36
Maximum fluence (J/cm²)	2.7
Solvent	Acetone
Volume of solvent (ml)	15
Ablation time (min)	3

The average particle size of the BFO NPs is confirmed by HR-TEM images, where we observe NPs with an average size of 22 nm, exhibiting high crystallinity and a spherical morphology. The spherical NPs are often the most thermodynamically stable configuration because they have the lowest surface area-to-volume ratio, which minimizes the surface energy of the particle. This can be explained by the interplay between various forces that act on the NPs during its nucleation and growth. One of the most important forces that influences the shape of a NPs is surface tension. Surface tension is a force that acts to minimize the surface area of a liquid or solid and so of NPs. A sphere is the shape that minimizes surface area for a given volume, making it the most stable shape. Other forces, such as electrostatic interactions and van der Waals forces, can also play a role in promoting or inhibiting certain types of growth.

For example, if the surface of the NPs is charged, electrostatic repulsion between particles can prevent growth in certain directions, leading to a more spherical shape. Similarly, van der Waals forces, which are attractive forces between particles, can promote growth in certain directions and influence the final shape of the NPs.

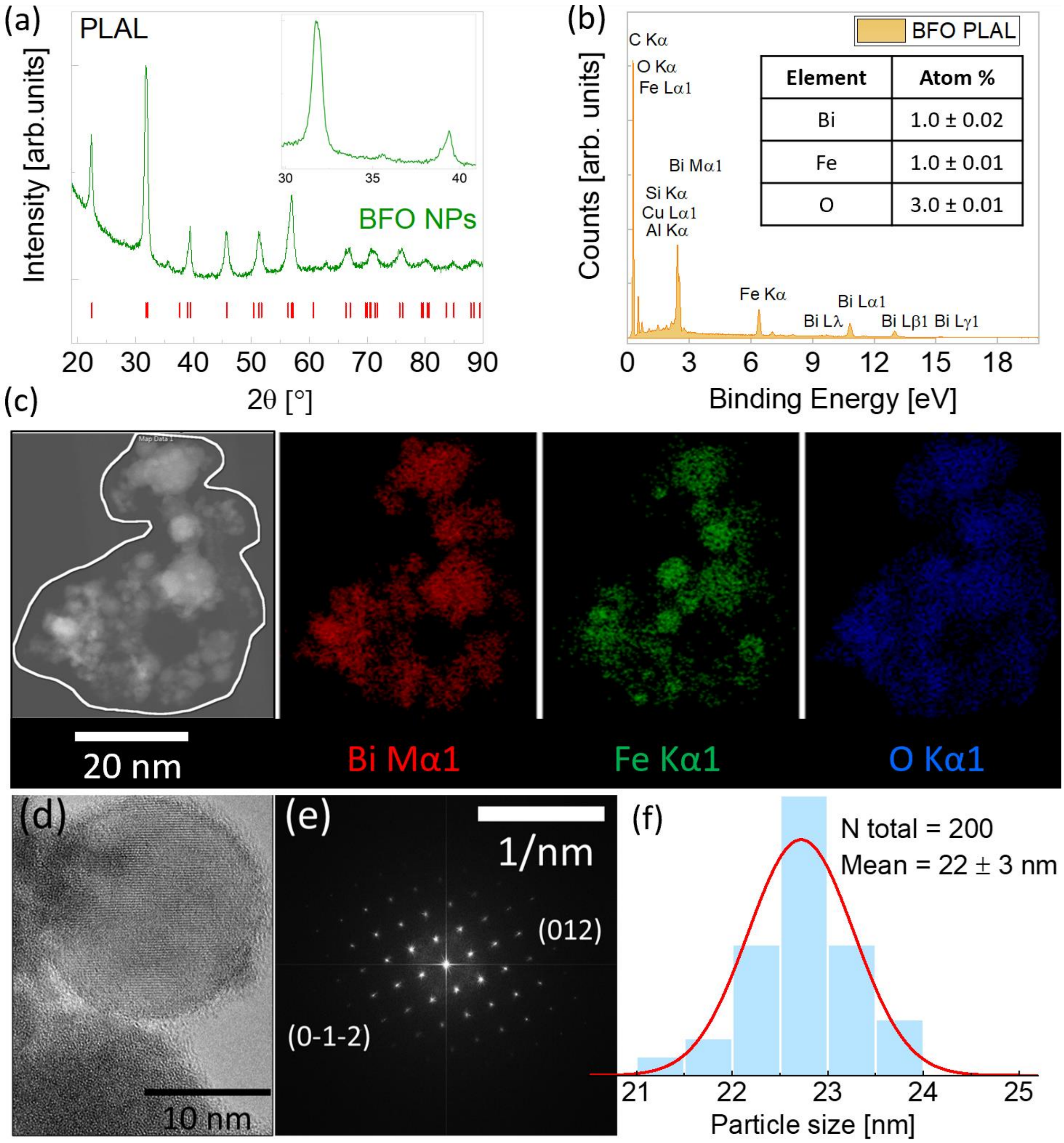

Figure 3.8: XRD diffractogram of BFO NPs synthesized by pulsed laser ablation (PLAL) method, the inset shows the splitting of peaks in 2ϑ range 30-41° (a). EDX profile of BFO NPs. The inset shows the relative atomic percentage present (b). The HAADF images for Bi, Fe and O elemental distribution for a selected group of agglomerated BFO NPs. The HR-TEM image of individual BFO NPs (d) and its SAED pattern (e). The particle size distribution of laser ablated BFO NPs (f).

The drawback of this method is the double work of synthesizing bulk targets for each composition from which we want to obtain NPs. Synthesizing phase-pure bulk targets with high density and narrow size distribution is a time-consuming task. Additionally, in this method, the reaction parameters need to be optimized for each type of composition. For example, when we synthesize Ba and Mn single- and co-doped BFO NPs, we had to optimize the reaction parameters for each composition, which was different from only synthesizing BFO NPs.[296]

3.5 Strategic selection of synthesis route for doping

Comparing the methods for synthesizing single-phase BFO NPs is difficult, but a strategy can be chosen. All three methods successfully produce single phase BFO NPs based on our optimized reaction parameters. The sol-gel method produces NPs with cuboidal morphology, while the hydrothermal method produces irregularly shaped NPs. The PLAL method, on the other hand, produces quite spherical NPs. Therefore, the choice of method can result in different morphologies of the BFO NPs, each with their own unique functionalities depending on the active facet sides.

A quick comparison of the XRD diffractograms of BFO NPs synthesized from these three different methods is shown in Figure 3.9. The characteristic peak at 32 degrees is highly merged for the case of laser ablated BFO NPs and least merged for the hydrothermal-based method. This merging indicates lattice distortion due to reduced crystallite size and increased microstrain in these NPs. Hence, the ~46 nm sized sol-gel synthesized BFO NPs are interesting in terms of being closer to the lattice structure of bulk BFO, with a size less than 50 nm. Nevertheless, the PLAL synthesized BFO NPs are also fascinating to study due to the changes in properties of BFO NPs with such reduced size of spherical morphology.

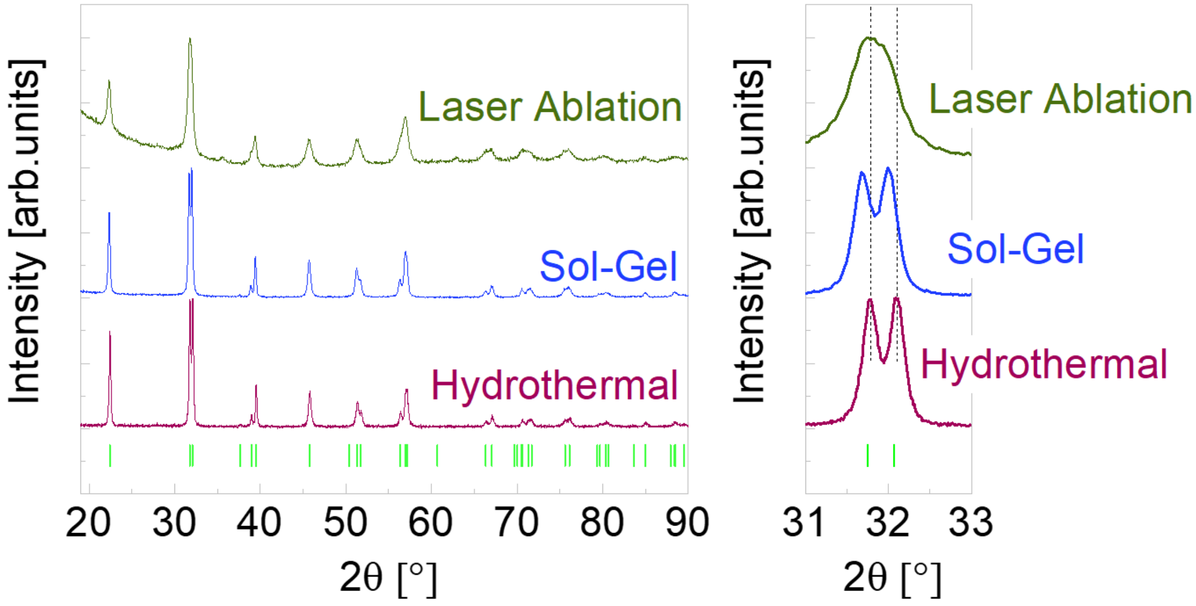

Figure 3.9: The XRD diffractograms of BFO NPs synthesized by laser ablation, sol-gel, and hydrothermal methods.

There are pros and cons associated with each method. In the case of the hydrothermal method, there is a large distribution of particle size. Conversely, with PLAL, a target material is always required, which can make it a long process to fabricate NPs, especially for the case of doped BFO NPs. However, this is also an advantage because once a bulk target is obtained, a lot of NPs can be produced without worrying about stoichiometry. Nonetheless, the reproducibility of similar NPs must be checked upon changing the batch of bulk targets. Especially for doping purposes, which is the main agenda of our research, the sol-gel method is more practical than PLAL since we do not need to make a doped bulk target for each composition. We can start with precursors and produce several doped BFO NPs via this bottom-up approach. However, the tendency of sol-gel synthesized and hydrothermally synthesized BFO NPs to form agglomerates can clearly be seen in TEM images. Agglomeration is less for the case of laser ablated BFO NPs, due to effect of the solvent (acetone) to reduce agglomeration. Nevertheless, it is easier to optimize the method for doped compositions in sol-gel rather than doping in hydrothermal, depending on the dopant sensitivity. Some dopants are highly reactive for hydrothermal reactions and should not be kept under such high pressure. For further doping in BFO NPs, we opted for the sol-gel method based on the following agreements.

Precise control over particle size and shape

The sol-gel method provides greater control over the size, shape, and surface properties of the NPs. This is because the sol-gel process allows for easier control over the nucleation and growth of particles by adjusting the precursor concentration, solvent composition, and other reaction parameters.

More versatile

The sol-gel method is more versatile than the other methods in terms of the range of precursor materials that can be used. For example, the sol-gel method can use a wider range of organic and inorganic precursors, while the hydrothermal method is typically limited to inorganic precursors.

Homogeneous particle distribution

The PLAL method is best in this respect. The sol-gel method can provide a more homogeneous distribution of NPs in the final product, compared to the hydrothermal method. This is because the sol-gel process typically involves a homogeneous distribution of precursors in a liquid solution, which promotes uniform particle growth.

Simplified equipment requirements

The sol-gel method requires less specialized equipment than the other methods. For example, a sol-gel reaction can be carried out in a simple glassware setup, while the hydrothermal method requires specialized high-pressure reactors, and for laser ablation we must include target synthesis milling machine/jars and a fancy laser set up.

Overall, the sol-gel method offers several advantages over the other methods for the synthesis of BFO NPs, particularly in terms of particle size and shape control, reaction temperature, versatility, and equipment requirements.

3.6 Synthesis of BFO and Graphene Oxide (GO) nanocomposite

The modified Pechini method was used to obtain BFO NPs, which were then decorated onto GO nanosheets to increase the total surface area. The following methodology was applied.

Synthesis of Graphene oxide (GO)

The GO was synthesized by a "modified Hammer's method".[297] 378 ml of 1 M sulfuric acid (H_2SO_4) and 42 ml of 1 M phosphoric acid (H_3PO_4) (volume ratio 9:1) were mixed and stirred for several minutes. Then 3 g of graphite powder was added into mixing solution under stirring. 18 g of potassium permanganate ($KMnO_4$) were added slowly into the solution. This mixture was stirred for 6 hours until the solution became dark green. To eliminate excess $KMnO_4$, 6 ml of hydrogen peroxide (H_2O_2) were dropped slowly and stirred for 10 minutes. An exothermic reaction occurred, and the beaker was let it to cool down. 10 ml of hydrochloric acid (HCl) and 30 ml of deionized water (DI) were added and centrifuged at 9000 rpm for 10 minutes. Then, the supernatant was decanted. The residuals were then rewashed with 5% HCl, DI water and ethanol for 3 times. The washed GO solution was dried at 50°C for 24 hours in an oven to produce the sheet form of GO.

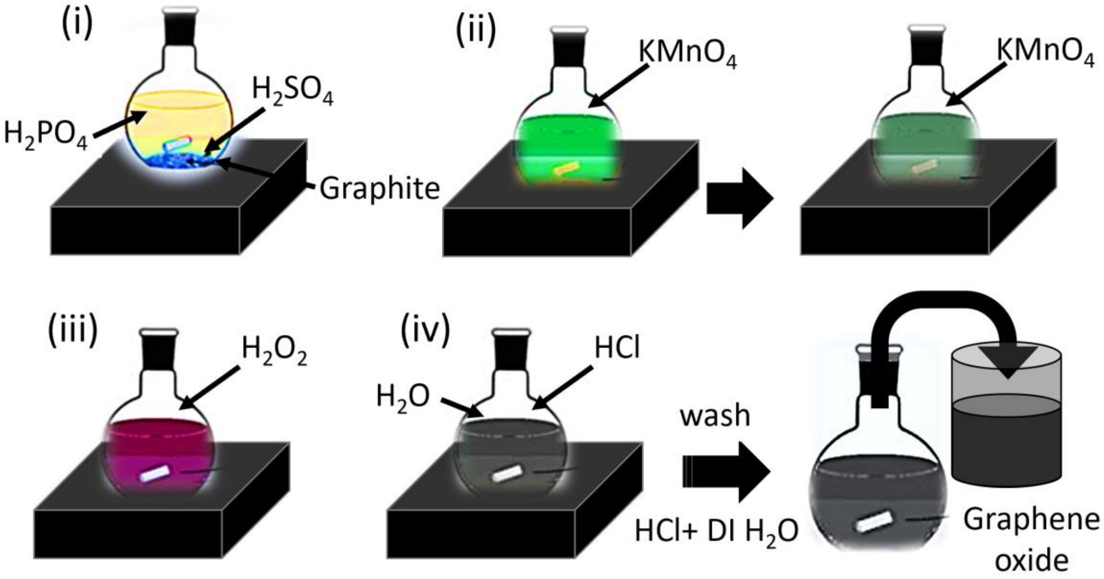

Figure 3.10: Schematic of synthesis of graphene oxide by modified Hummers' method.

Synthesis of doped-BFO+GO nanocomposite

For the functionalisation of BFO NPs, GO and sol-gel synthesized BFO NPs (1:1 molar ratio) were ground together using a mortar and pestle for 15 minutes. The powder was dispersed in DI water and sonicated for 30 minutes at 300 K to obtain a blackish suspension. Afterwards, the dispersion was kept for gelation at 423 K. The dried black aerogel was crushed and further washed with DI water and ethanol several times to remove unwanted impurities. Afterwards, it was dried in a vacuum oven at 333 K for 10 h. For doped-BFO NPs the same procedure was applied.

3.7 Conclusions

In this chapter, we conclude that the synthesis of phase-pure BFO NPs is achievable using any of three methods: hydrothermal, wet chemical modified Pechini method, and pulsed laser ablation in liquid. The morphology and size of NPs can be controlled based on the reaction parameters in all of these methods. The hydrothermal method yields more irregular shaped BFO NPs, while the modified sol-gel Pechini method provides cuboidal morphology. The PLAL method gives a spherical shape of the BFO NPs. The narrowest size distribution is found for the PLAL method. However, in terms of being less time-consuming, easy, eco-friendly, and reproducible, the modified Pechini method is the best for synthesizing various doped BFO NPs, because one can easily control the parameters and optimize the reaction to synthesize high-quality NPs.

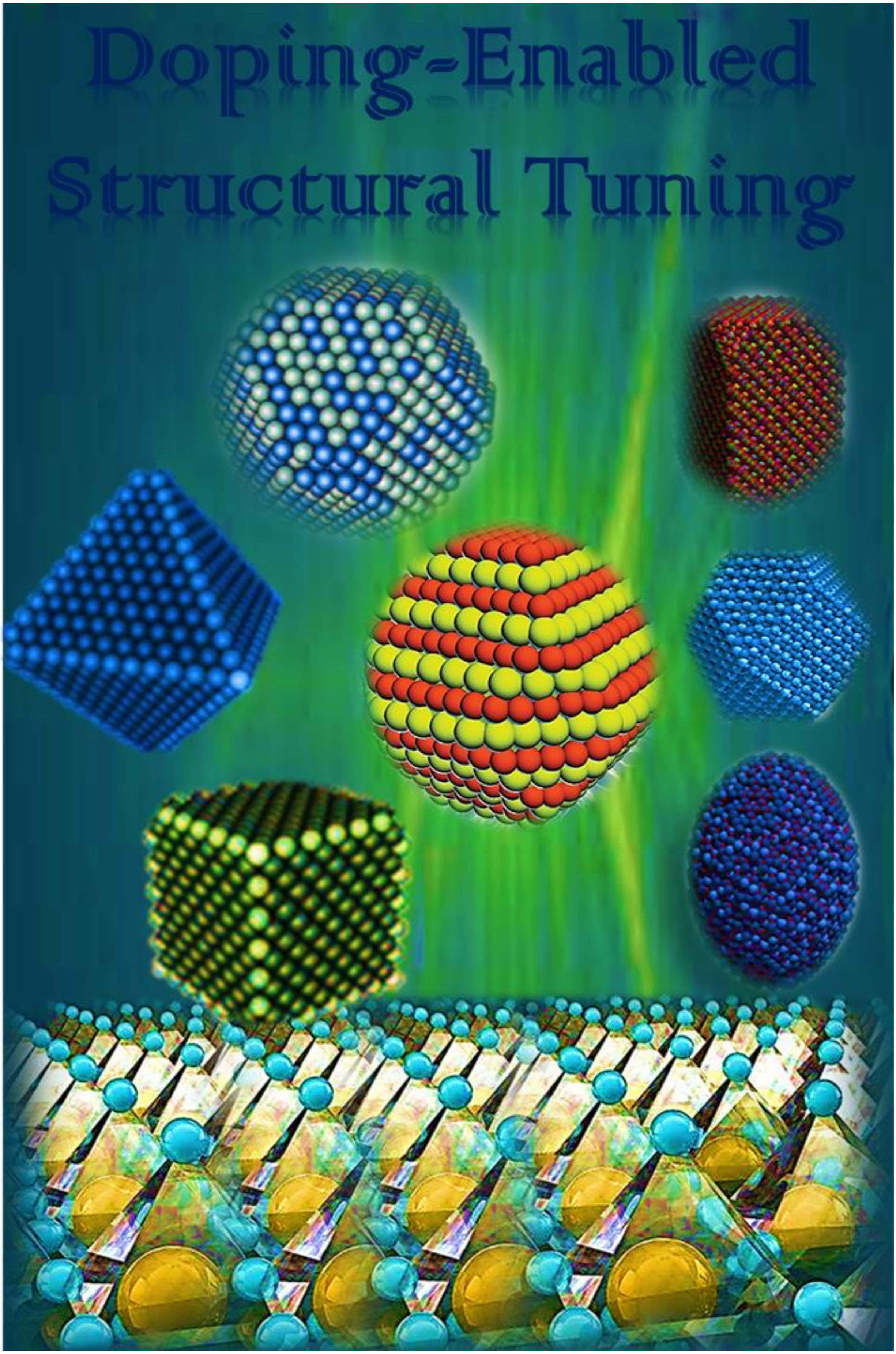
Doping-Enabled
Structural Tuning

4 Doping-enabled structural tuning

4.1 Introduction

In this chapter, we explore the doping in BFO NPs, with the aim to alter the electronic, optical, and magnetic properties of the NPs. The size and charge of the dopant ion influences the degree of substitution and the stability of the resulting solid solution, leading to changes in crystal symmetry, morphology, and structure. Different dopant atoms can cause lattice distortion, leading to the formation of different crystal phases. The changes in crystal symmetry can have a profound effect on the electronic, optical, and magnetic properties of the NPs.

Doping can also alter the morphology of NPs, leading to changes in their shape, size, and surface area. By influencing nucleation and growth kinetics, dopants can promote the formation of smaller NPs with higher surface area and improved photocatalytic activity. Conversely, dopants can also lead to the formation of larger or smaller NPs, depending on their type and concentration. Additionally, the introduction of aliovalent dopants can create point defects in the crystal lattice, leading to changes in the electronic and magnetic properties of the NPs.

4.2 Rational dopant selection for controlled crystal distortion

The selection of dopants in a material is typically based on the desired changes in the material properties. Factors that characterize a dopant are its size, outermost electronic configuration, and the valency. The foremost factor is the ionic radius as shown in Table 4.1 and 4.2. Usually, the size of a dopant atom should be similar to the host material atoms, or at least not differ too much. If the dopant is too large, it can cause lattice distortion or strain, leading to defects and altered material performance. Similarly, if it is much too small. The outermost electronic configuration of the dopant affects its ability to donate or accept electrons and alter the electronic properties of the material. Therefore, we have chosen dopants with different outermost orbitals namely *s (Ba, Ca)*, *d (Ag, Mn)* and *f (La, Nd, Sm, Gd, Dy)*. The dopant valency also affects the electrical and optical properties of the material. Doping with aliovalent ions in a semiconductor can create n-type or p-type conductivity. Therefore, we have compared the properties of mono- (Ag^+), di- (Ca^{2+}, Ba^{2+}), tri-valent (La^{3+}, Dy^{3+}) cation doped BFO NPs. The dopant should be chemically compatible with the host material to avoid reactions that could damage the material or alter its properties. The dopant concentration become an important control parameter. Too high of a concentration can lead to clustering, yielding extended defects with often uncontrollable properties, while too low of a concentration may prove to be ineffective overall. We varied the concentration of Ba from 1 to 5 mol % to study the role of divalent dopant ion onto structural properties of BFO NPs.

5 mol % Mn at the Fe-site has chosen as dopant, as Mn is magnetic in nature and Mn is not a rare earth element; Mn can directly affect the magnetic superexchange interaction via Fe^{3+}-

O-Mn^{4+} bonding in BFO NPs. At $_{26}$Fe-site ([Ar $3d^64s^2$]) we opted magnetic $_{25}$Mn: [Ar]$3d^54s^2$ and $_{27}$Co: [Ar]$3d^74s^2$. Where, high spin Mn^{4+}=[Ar]$3d^34s^0$ has magnetic moment of 3.87 μ_B/Mn,[298] and high spin Co^{3+} = (Ar)$4s^03d^6$ has calculated magnetic moment of 4.9 μ_B/Co and experimentally often a μ_{eff} of 5.4 μ_B/Co.[299] For high spin Fe^{3+} = $3d^54s^0$ (t_{2g}^3 e_g^2,) the calculated magnetic moment is √35 = 5.92 μ_B/Fe, and for high spin Fe^{2+} = $3d^64s^0$ ($t_{2g}^4e_g^2$), √24 = 4.90 μ_B/Fe.[298]

Table 4.1: The plausible ions at Fe-site in BFO NPs. The blue highlighted ones are confirmed by XPS measurements. The ionic radii is based on Scherrer's calculations.

Ions	Fe^{2+}	Fe^{3+}	Fe^{4+}	Mn^{3+}	Mn^{4+}	Co^{2+}	Co^{3+}	O^{2-}
Ionic radius (Å) [High spin]	0.78	0.645	0.585	0.645	0.53	0.745	0.61	1.40
C. N.	6	6	6	6	6	6	6	6
O. E. C.	$3d^64s^0$	$3d^54s^0$	$3d^44s^0$	$3d^44s^0$	$3d^34s^0$	$3d^74s^0$	$3d^64s^0$	$2s^22p^0$

Ba is one of the most effective non-magnetic, divalent *p*-type dopants. It is suitable for A site doping as per size and thermodynamics. It prevents Bi vacancies in the BFO system via replacing its site. Experimentally, Ba is easily incorporable among alkaline earth metals, and it also causes hole formation in BFO and hence makes it a *p*-type semiconductor. The inspiration of doping larger sized Ba than Bi also comes from the magnetic behaviour of the $BaFeO_x$ systems.[300] Ba and Ca are non-magnetic elements, which are examined to study the changes in the magnetization of BFO NPs via strain engineering.

Table 4.2: The dopants at Bi-site in BFO NPs, the ionic radii is based on Scherrer's calculation.[194]

Ions	Bi^{3+}	Ag^+	Ca^{2+}	Ba^{2+}	La^{3+}	Nd^{3+}	Sm^{3+}	Gd^{3+}	Dy^{3+}
Ionic radius (Å)	1.45	1.38	1.34	1.61	1.36	1.27	1.24	1.23	1.18
C. N.	12	12	12	12	12	12	12	12	12
O. E. C.	$6s^26p^0$	$4d^{10}5s^0$	$4s^0$	$6s^0$	$4d^{10}6s^0$	$4f^36s^0$	$4f^56s^0$	$4f^76s^0$	$4f^96s^0$

Ag^+ is a good monovalent dopant for the substitution of Bi. It increases the oxygen vacancy concentration in the lattice leading to an increase in the electrical conductivity of the material. Ag doping can also lead to the formation of Ag-Bi-O bonds, which can enhance the stability of the material and prevent the formation of secondary phases. The smaller size of Ag compared to Bi can lead to lattice distortion, which can modify the ferroelectric properties of the material and enhance its piezoelectric response.[46] Ag doping can also improve the photocatalytic activity of BFO, making it a promising material for various applications such as water splitting and gas sensors.[301–303]

When rare earth (RE) elements are doped into BFO, they substitute the Bi^{3+} ion due to their similar ionic radii. The electronic structure of rare earth elements is characterized by their non-filled (La^{3+}), partially-filled (Nd^{3+}, Sm^{3+}), and half-filled (Gd^{3+}) and more than half-filled (Dy^{3+}) 4*f* orbitals. Lanthanides have partially filled *f*-orbitals that can strongly interact with the surrounding oxygen ions in the crystal lattice. This interaction can lead to a distortion in the local crystal structure and a reduction in the oxygen content. Lanthanide cations interact with oxygen ions in the lattice and pull them away from their lattice positions, causing structural distortion.[304,305]

**All the doped BFO NPs are synthesized using "modified sol-gel Pechini" methodology explained in previous synthesis chapter 3.*

4.2.1 Tolerance factor

The tolerance factor can provide an estimation of impact on the crystal structure and properties of perovskite materials like BFO. Even a small change in the tolerance factor can result in a change in the symmetry of the crystal structure, which in turn can affect the electronic, magnetic, and optical properties of the material.

If the tolerance factor of BFO decreases, this generally leads to a distortion of the crystal structure and a shift towards lower symmetry structures, such as tetragonal or orthorhombic. If the tolerance factor of BFO increases, the crystal structure can become more symmetric and approach a cubic structure.

For the stability of the perovskite structure, the Goldschmidt's tolerance factor[45], (*t*) was determined by.

$$t = \frac{[(1-x)r_{Bi} + xr_A] + r_O}{\sqrt{2}[\{(1-y)r_{Fe} + yr_B\} + r_O]} \tag{4.1}$$

'*r*' is an effective ionic radius of the respective element[47] for the corresponding coordination number as shown in Tables 4.1 and 4.2. "r_A" and "r_B" are the radii of the dopants at Bi- and Fe-sites, respectively. The tolerance factor is plotted in Figure 4.1.

Upon single doping of 5 mol% in BFO NPs, we observed that Mn doping increased the tolerance factor due to its smaller size than Fe. Ba doping at the Bi-site also increased the *t* value, but still less than BFM NPs. Cobalt doping showed the least increase in the *t* value due to its similar size as Fe^{3+}. Upon co-doping of 1 to 5 mol % of Ba into BFM NPs, the *t* value increased up to ~0.991 for 5BBFM NPs, indicating lesser deformation of the oxygen octahedral.

Among lanthanide doped BFM NPs, we observed a non-linear trend in the *t* value. Compared to BFM NPs, the *t* value was almost similar to Nd-doped BFM NPs, while for others, the *t* value decreased, with the most significant decrement for Dy-BFM NPs. The reduction in *t* value could lead to larger octahedral distortion in the crystal lattice.

The trend of the tolerance factor *(t)* among the mono-, di-, and tri-valent cation-doped BFM NPs, is plotted in Figure 4.1. We observe that *t* reduces upon Ag, Ca, La, and Dy doping due to the smaller ionic radius of these ions. For 5 mol% Ba-doped BFM NPs, the *t* value was higher than BFM [Figure 4.1], due to the larger ionic radius of the divalent Ba.

These calculations suggest that the octahedral distortion could be greater for lanthanide-doped BFM NPs and mono-, di-, and tri-valent cation (Ag^{+}, Ca^{2+}, La^{3+}, Dy^{3+}) doped BFM NPs, except for Ba-doped BFM NPs (5BBFM). Since the alteration in the tolerance factor depends upon the ionic radius of dopants, it is necessary to investigate the oxidation state of dopants and hosts.

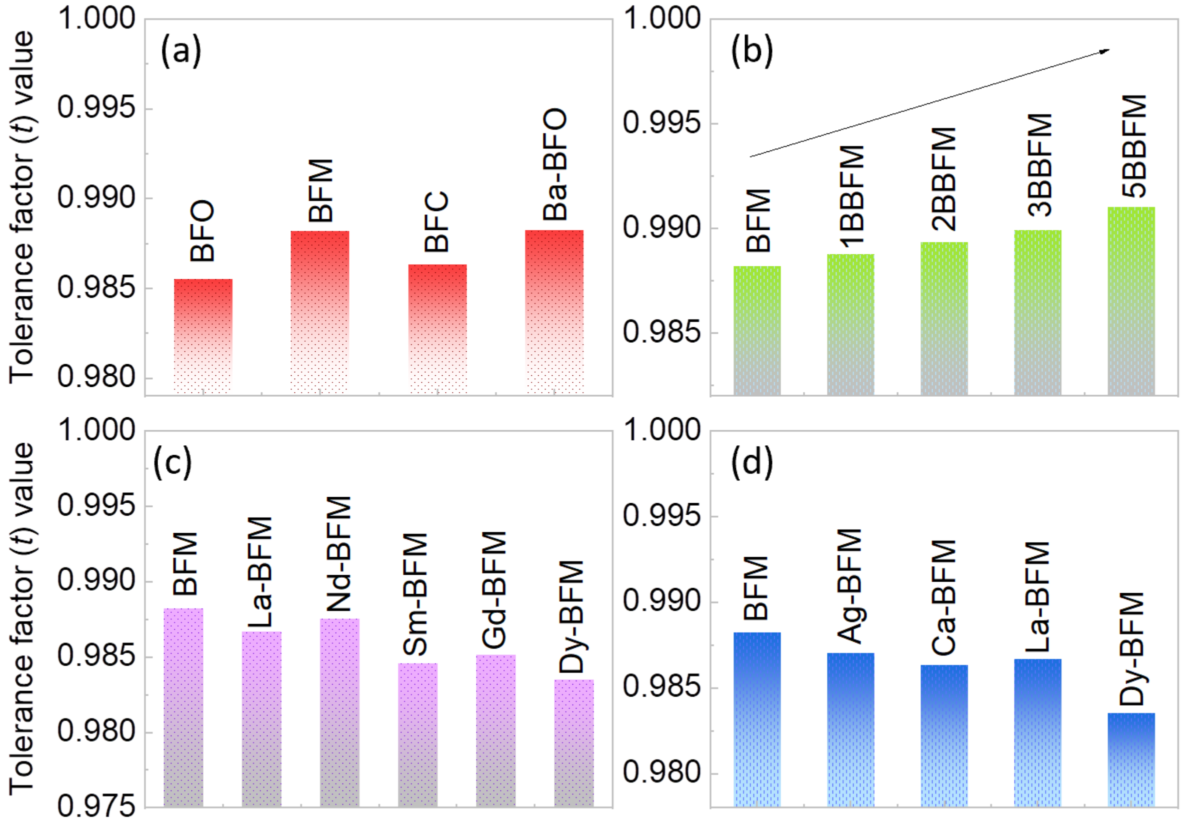

Figure 4.1: The calculated tolerance factor values of undoped and doped BFO NPs. Single doped BFO NPs (a). Ba doped BFM NPs (b). Rare-earth-lanthanide doped BFM NPs (c). mono-,di-, and tri-valent cation doped BFM NPs (d).

4.3 Elemental analysis of host and doping elements

The presence of doping and host elements in doped and undoped BFO NPs are confirmed by EDX. In Figure 4.2, a few representative EDX spectra of doped BFM NPs are shown. The expected starting molar stoichiometry (5 mol %) of doping and host elements are found in all doped BFO NPs. As during EDX measurements, the electron depth is from 2-10 µm, so the presence of dopants is confirmed.

The distribution of doped elements throughout of individual particle is important in terms of understanding of defects and active sites on the surface for catalysis. In Figure 4.3, the HAADF images of doped BFM NPs are shown. The bunch of agglomerated NPs were chosen to capture the elemental distribution in dark field imaging mode, where the overlay of all elements show that Mn is present in all particles. From the individual elemental distribution images, it is quite obvious that Mn is homogeneously distributed in BFO NPs.

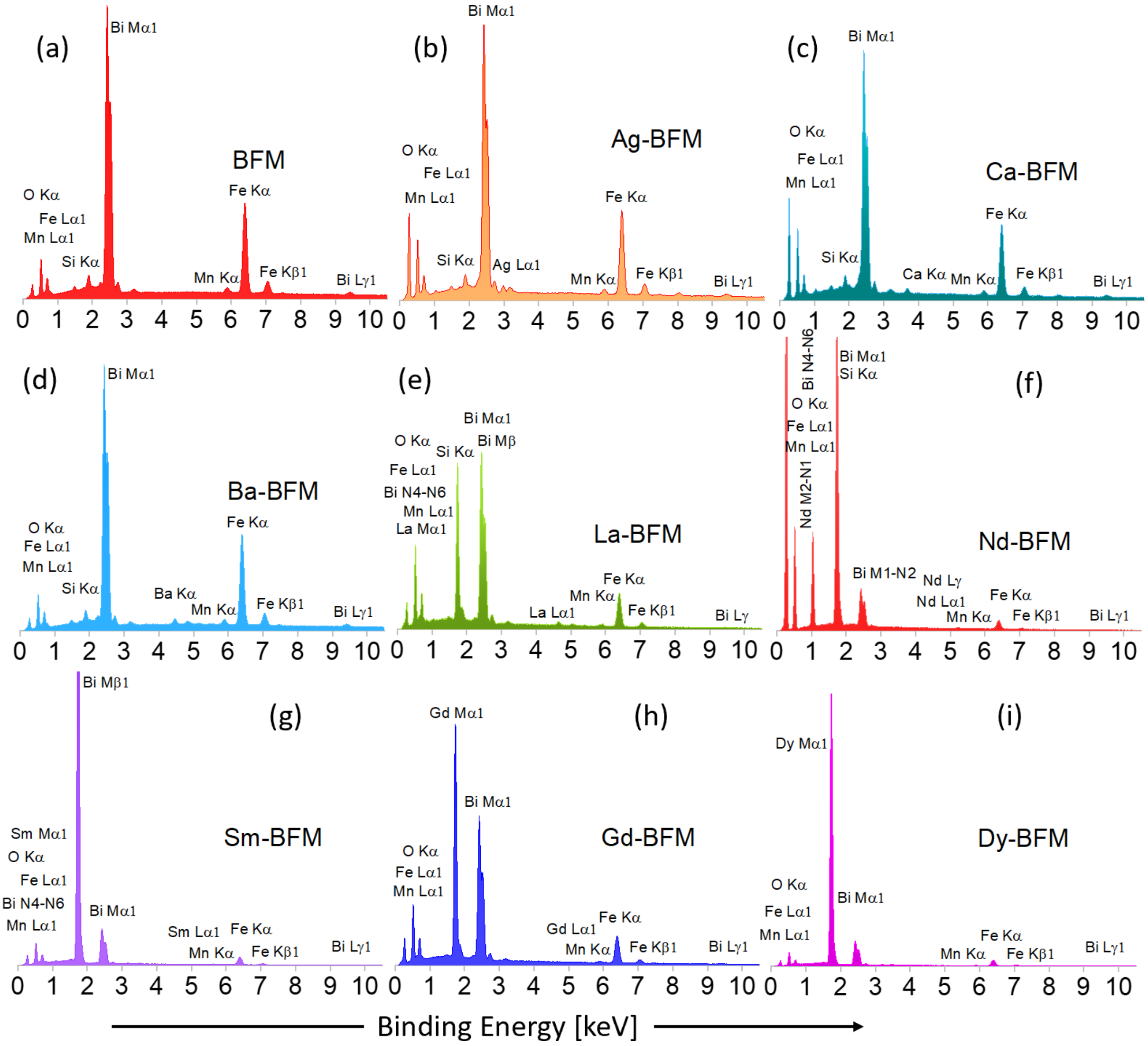

Figure 4.2: EDX spectra of BFM and doped BFM NPs. [measured by Dr. Markus Heidelmann]

When the dopants are not uniformly distributed throughout a NP, these variations in the dopant concentration change the electronic properties of the material locally. For example, if the dopants are concentrated in one part of a NP, the Fermi level varies which affects the charge carrier density and the electronic band structure. This can overall impact the optical and electronic properties of the NP, such as its absorption spectrum, plasmon resonance, and photocatalytic activity. A non-homogeneous dopant distribution can also have an impact on catalytic activity of the NPs. If the dopants are concentrated in one part of the NP, the surface chemistry and reactivity vary locally. This can impact the NP ability to catalyse reactions and may lead to non-uniform catalytic activity across the NP surface, which must be considered in the design of chemical reaction.

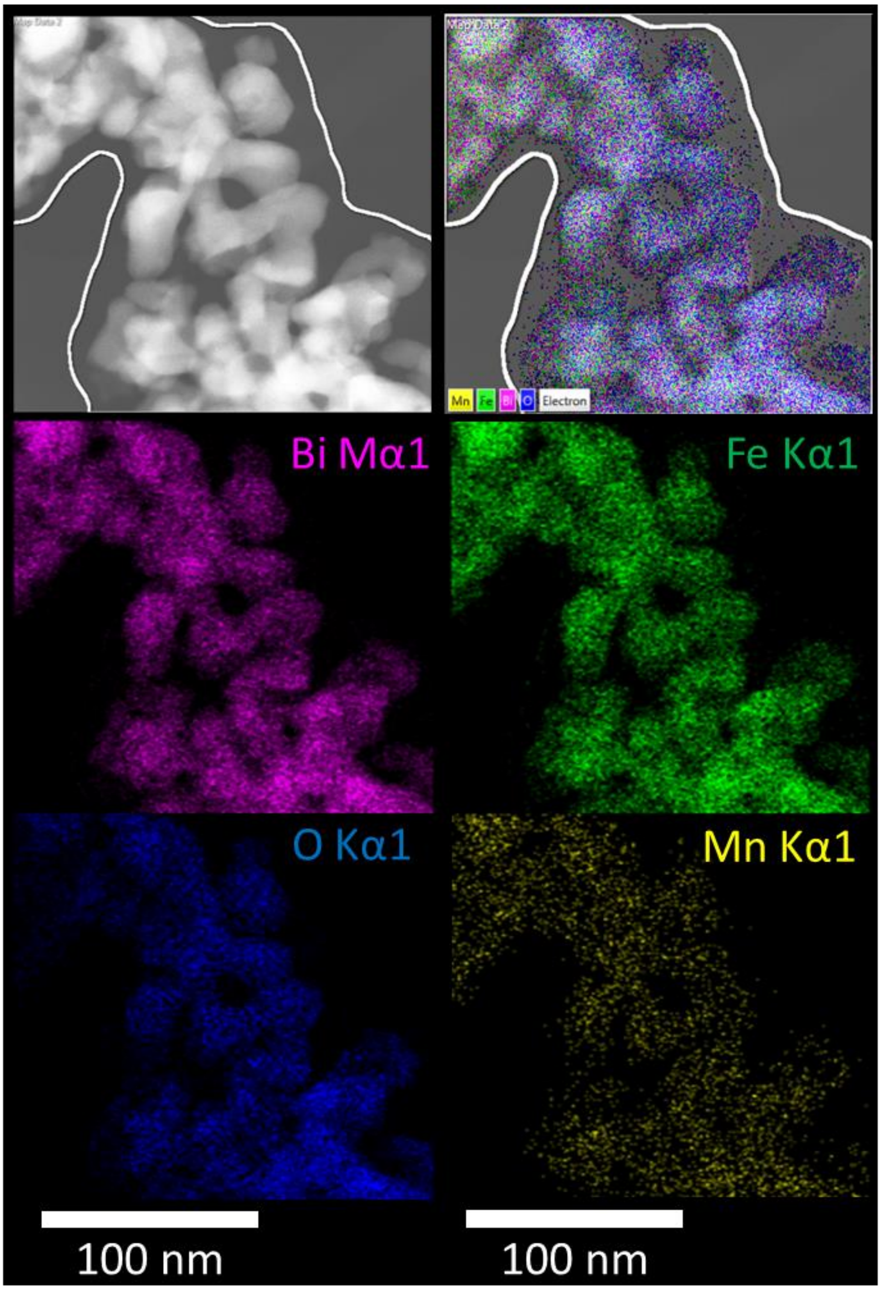

Figure 4.3: Exemplary HAADF image of BFM NPs in dark-field imaging mode. The particles are shown in the top left image, the overlay of all elements in the top right image. The individual elemental distributions are shown in different colours. [measured by Dr. Markus Heidelmann]

Homogeneous distribution of dopants in a material has several advantages in terms of its properties. It leads to uniform electrical properties throughout the material, such as uniform carrier concentration and resistivity. Homogeneous doping can also lead to uniform optical properties, such as consistent absorption and emission spectra. This is particularly important for catalysis and optoelectronic devices such as solar cells and LEDs, where uniform absorption and emission properties are critical for device efficiency. Homogeneous doping can also improve the thermal conductivity of the material, which is important for heat dissipation in electronic devices.[306]

4.3.1 Oxidation states of host and doping elements

**All XPs spectra are measured by Dr. Ulrich Hagemann.*

After confirming the presence of dopants, the valence states of the doping elements are the most interesting information to be known. Heterovalent dopants can cause charge compensation to the system for overall electrochemical neutrality, either by altering the oxidation states of the Fe-site cations or by creating oxygen or Bi-site cation vacancies. Therefore, we utilized XPS to determine the elemental composition and oxidation states of the host and doping elements in both doped and undoped NPs.

This can provide quantitative information about the elemental composition of the sample by measuring the binding energies of the different elements present. XPS provides information about the types of chemical bonds present in the material, such as metal-oxygen or metal-metal bonding and the oxidation state.

From the XPS spectra of BFO NPs, we found that Fe has expected oxidation state of +3 and Bi +3 as well as shown in Figure 4.5 and 4.6. For single doped (Mn, Ba, Co) BFO NPs, the XPS spectra are shown in Figure 4.4.

The determination of the Fe and Mn oxidation states is based on the work of Biesinger et. al[307]. From the 2p XPS spectrum of BFM NPs, Mn on the surface is present in its +4 and +3 states confirmed by 2p XPS spectra of Mn [Figure 4.4a]. However, from XANES data Mn is present in +4 state in the bulk of the BFM NPs.[46] This information manifests the difference of surface and bulk in the NPs, especially the presence of the Jahn-Teller cation (Mn^{3+}) can lead to new active sites in BFM NPs. In the synthesis route, Mn^{+2} may get oxidized to Mn^{+3} or Mn^{+4} by the oxidizing agent (nitric acid). Hence the peak deconvolution of the Mn 2p signal unveils that the BFM contains both Mn^{+3} and Mn^{+4} on the surface of the NPs.

For Ba 3d XPS spectra we observe a peak at ~779 eV and at ~795 eV attributed to $3d_{5/2}$ and $3d_{3/2}$, respectively, which corresponds to the Ba^{+2} oxidation state, as confirmed from Figure 4.4b. In the cobalt doped BFO NPs at Fe-site, we observe $3p_{3/2}$ and $3p_{1/2}$ peaks corresponding to the +3 oxidation state of cobalt as shown in the 3p XPS spectrum in Figure 4.4c.

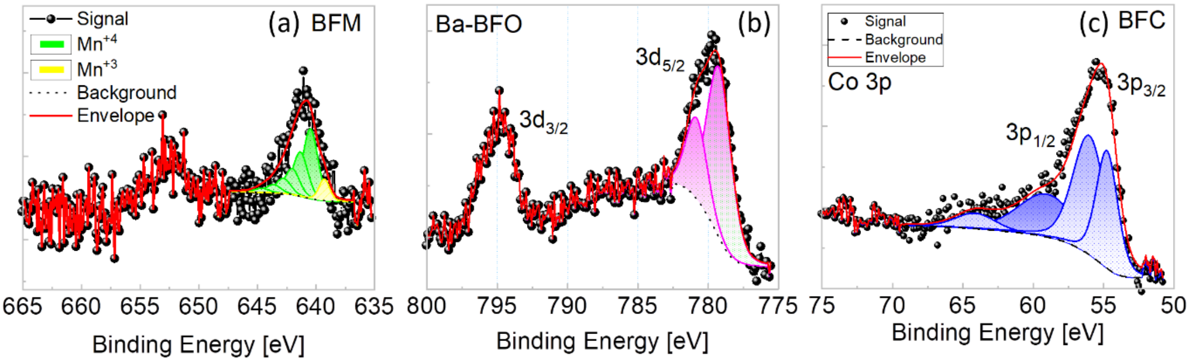

Figure 4.4: XPS spectrum of Mn 2p of BFM NPs (a), Ba 3d of Ba-BFO NPs (b), and Co 3p of BFC NPs (c).

As aliovalent doping can alter the oxidation state of Fe, it is crucial to examine Fe XPS spectra for doped NPs. The Fe 2p XPS spectra for single-doped and undoped BFO are shown in Figure

4.5. We observe that only Ba doping raise the concentration of Fe^{2+} ion, whereas Mn and Co doped NPs have mostly Fe^{3+} state on their surface. The two defined Fe $2p_{3/2}$ and $2p_{1/2}$ peaks are evident[308] with the presence of a characteristic satellite peak of Fe $2p_{3/2}$ at 718 ± 0.3 eV, which is found to be a distinct peak instead of a 'shoulder peak'[309]. The satellite peak originates from the motion of 3d electrons to vacant 4s orbitals during the ejection of electrons from the 2p shell, the so-called 'shake-up transition'[310]. The $2p_{3/2}$ peak is broad which could be due to spin-orbit interaction between 2p holes and unpaired 3d electrons of Fe^{+3} present in the t_{2g} and e_g levels[311]. The binding energy difference between the Fe $2p_{3/2}$ main peak and the satellite peak is approximately 8 eV, as shown by the green rectangle, which confirms the presence of Fe^{+3} in all studied samples[312]. However, we cannot exclude the presence of ~ 9 % ± 3 % Fe^{+2} at the surface of the Ba doped NPs.

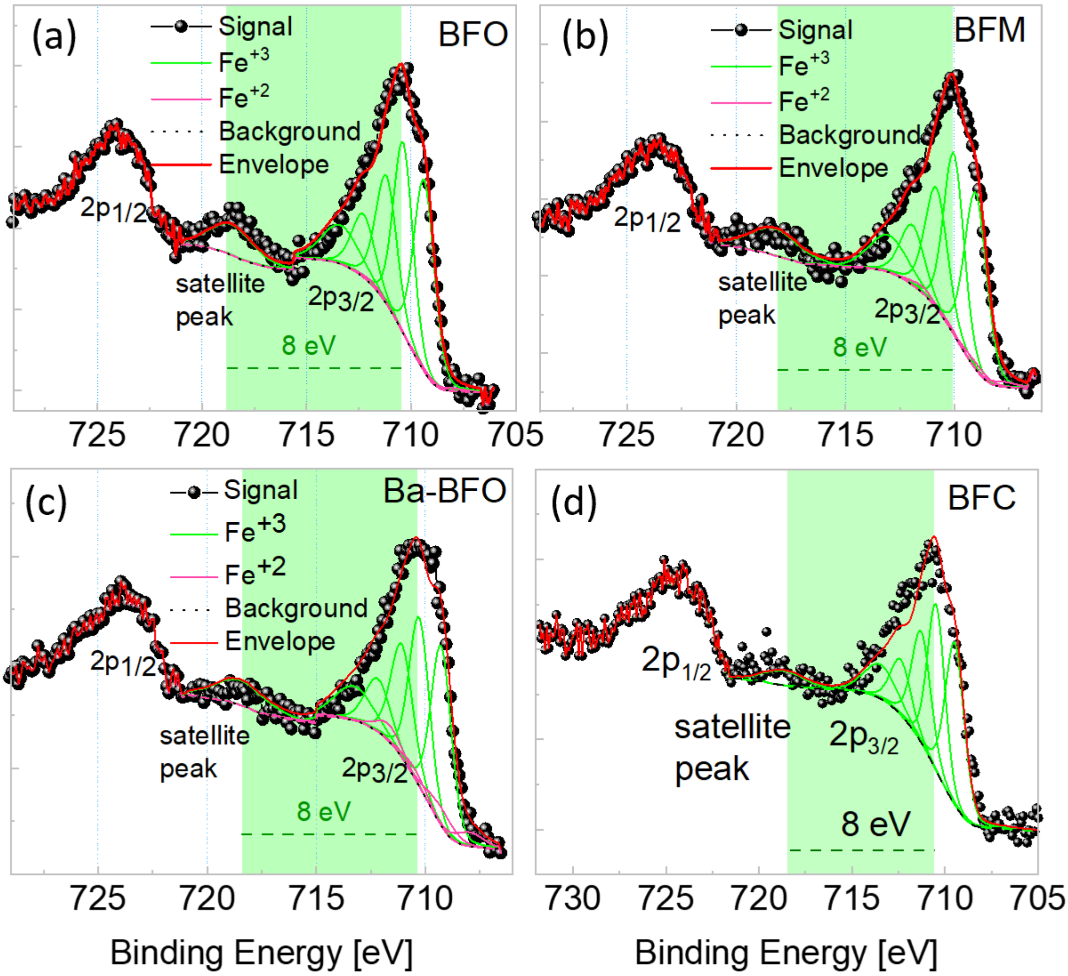

Figure 4.5: XPS spectra of Fe 2p of BFO and single-doped BFO NPs.

The 4*f* Bi spectra of single doped and undoped BFO NPs are shown in Figure 4.6. The spectrum contains a Bi 4*f* doublet that corresponds to the Bi-O bonds. The peaks at ~ 158.5 eV and ~ 164 eV correspond to the binding energies of $4f_{7/2}$ and $4f_{5/2}$ of Bi^{+3}, respectively[313]. The moderate chemical shift and changes in peak area of the $4f_{7/2}$ and $4f_{5/2}$ peaks are due to a variation in the electronegativity of Bi (2.02), Ba (0.89), Fe (1.83), Mn (1.55), Co (1.88) and O (3.44) indicating that dopants are present in the crystal lattice and have involved in the chemical bonding with Bi and oxygen, which cause the shift in respective binding energies.[314]

Thus, the XPS spectra analysis reveals that Bi^{+3} and Fe^{+3} are present in the pristine BFO NPs.

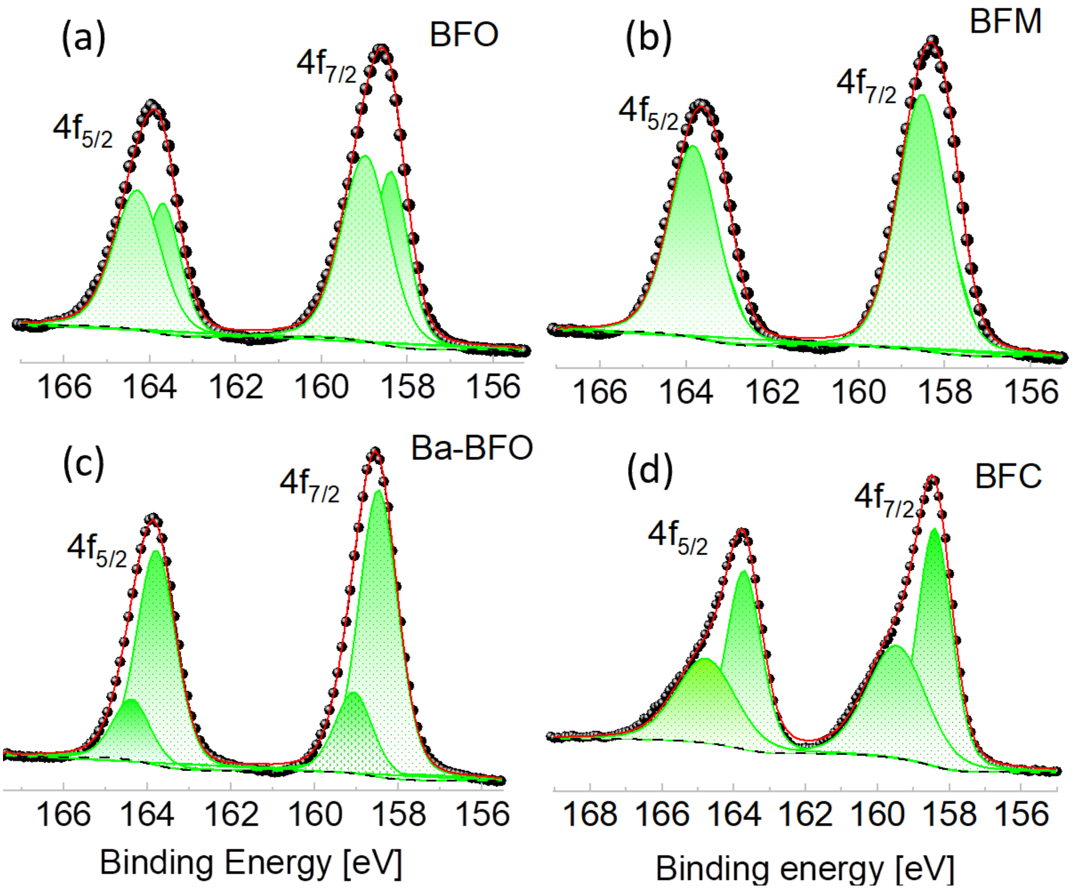

Figure 4.6: Bi 4f XPS spectra of BFO NPs (a), BFM NPs (b), Ba-BFO NPs (c), and BFC NPs (d).

Role of Ba doping into BFM NPs

As per the Mn 2p signal, BFM NPs contain both Mn^{+3} and Mn^{+4} on the surface of the NPs, while doping by Ba from 1 to 5 mol % causes a dominance of Mn^{4+} over Mn^{+3}.[10] This can be due to the charge compensation effect which is also supported by the Raman spectra analysis as discussed in the "Chapter 6 Optical". In the Raman spectra one observes the signal from the Jahn Teller cation (Mn^{3+}). For the Ba 3d XPS spectra there is a peak at ~779 eV, which is attributed to the Ba^{+2} oxidation state in all Ba doped BFM NPs. However there was no large shift (< 1 eV) of this peak with increasing the amount of Ba up to 5 mol%.[10] The XPS spectra analysis reveals that in Ba doped BFM NPs, Bi^{+3} and Fe^{+3} are present, and mostly Mn^{+4} was confirmed. However, the presence of ~10 % Mn^{+3} onto the surface cannot be ignored as the signal to noise ratio is not well resolved for just 5 mol % Mn content.[10]

Influence of mono-, di-, and tri-valent (MDT) dopants in BFM NPs

Oxygen is in -2 oxidation state for all NPs as confirmed by 1*s* oxygen XPS spectra of each doped and undoped NPs.[10,46,315] The presence of dopants was again confirmed by their XPS spectra as shown in Figure 4.7. The 3d XPS spectra of the Ag ion in Ag-BFM NPs, shows two peaks corresponding to $3d_{3/2}$ and $3d_{5/2}$, which matches well with the +1 oxidation state of Ag.[316] The divalent Ca doping into BFM NPs was confirmed by the 2p XPS spectra of Ca as shown in Figure 4.7b. The two peaks are attributed to $2p_{3/2}$ and $2p_{1/2}$ which confirms the +2 oxidation state of

Ca in Ca-BFM NPs. Similarly, we found +2 oxidation state of Ba in Ba-BFM NPs, as shown in 3d XPS spectra of Ba.

In the case of trivalent cations, their individual 3d XPS spectrum confirms the +3 oxidation state for La, Nd, and Sm, Gd, and Dy. The peak assignment of all of them has been done after peak deconvolution as shown in Figure 4.7 d-h.

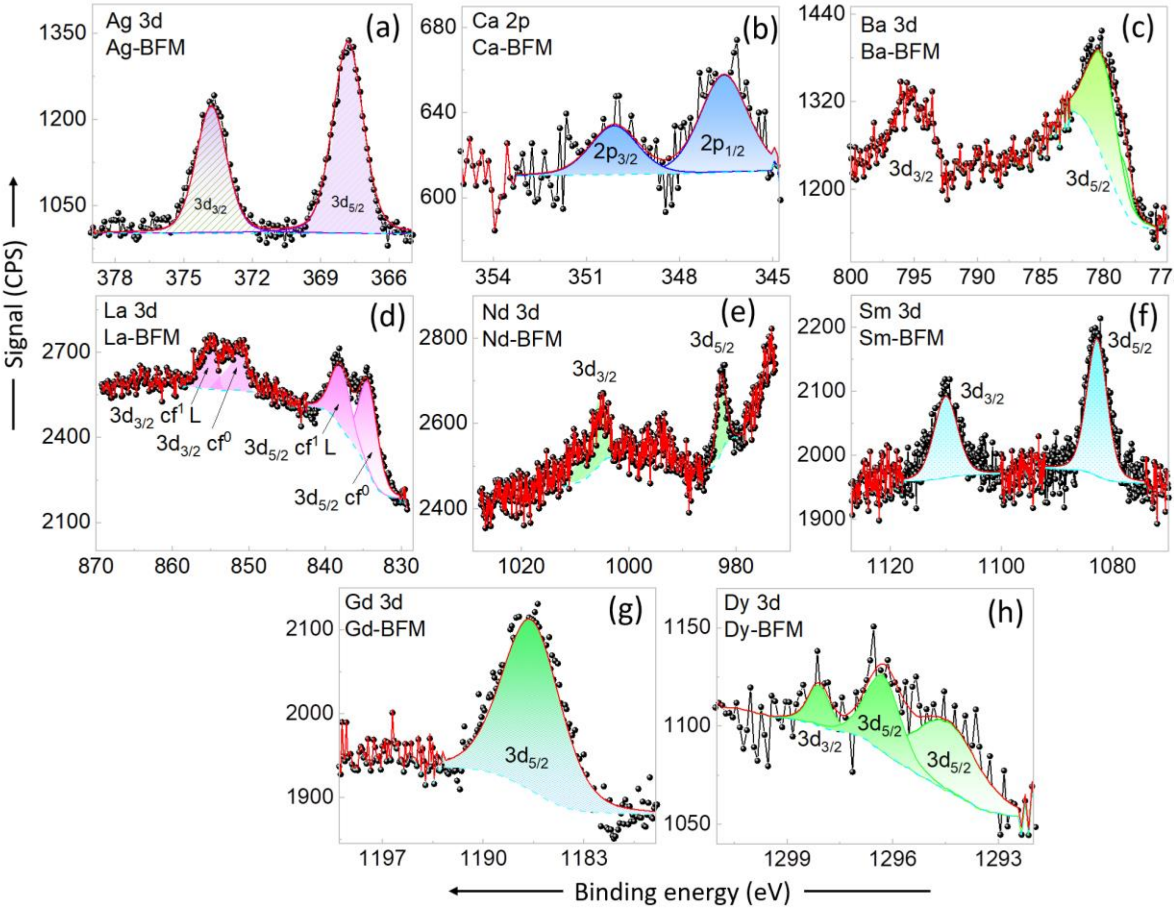

Figure 4.7: The XPS spectra of dopants Ag (a), Ca (b), Ba (c), and La (d), and Nd (e), and Sm (f), and Gd (g), and Dy (f).

The Mn 2p XPS spectra for all doped BFM NPs are shown in Figure 4.8. The doping of cations at the Bi site in BFM NPs causes a slight shift in peak position of the 2p Mn peak and also the peak area (written in brackets in the graph) changes quite a lot especially for Dy-BFM and Ba-BFM. Such changes manifest the chemical bonding of these dopants into the crystal lattice and so attribute to their effect on the Mn binding energy.

The doping of Ag in the BFM NPs retains the presence of Jahn-Teller cation (Mn^{3+}) on the surface as shown by the yellow peak, but with a reduced peak area compared to BFM NPs. For Ca doped BFM NPs, the Jahn-Teller peak reduces slightly, moreover for Ba doping into BFM NPs the Mn^{3+} peak reduces further. This shows that mono- and di-valent cation doped BFM NPs have Jahn-Teller cation at the surface with different concentration. Whereas, for the case of tri-valent cation doped BFM NPs, we could observe only the presence of Mn^{4+}, which is unexpected but interesting, however the signal to noise ratio of Mn 2p spectra is less. Therefore, we cannot fully confirm whether there is no Jahn-Teller cation for trivalent doped

BFM NPs. Raman spectra have to be studied for confirmation of Jahn Teller cation in lanthanide doped BFM NPs.

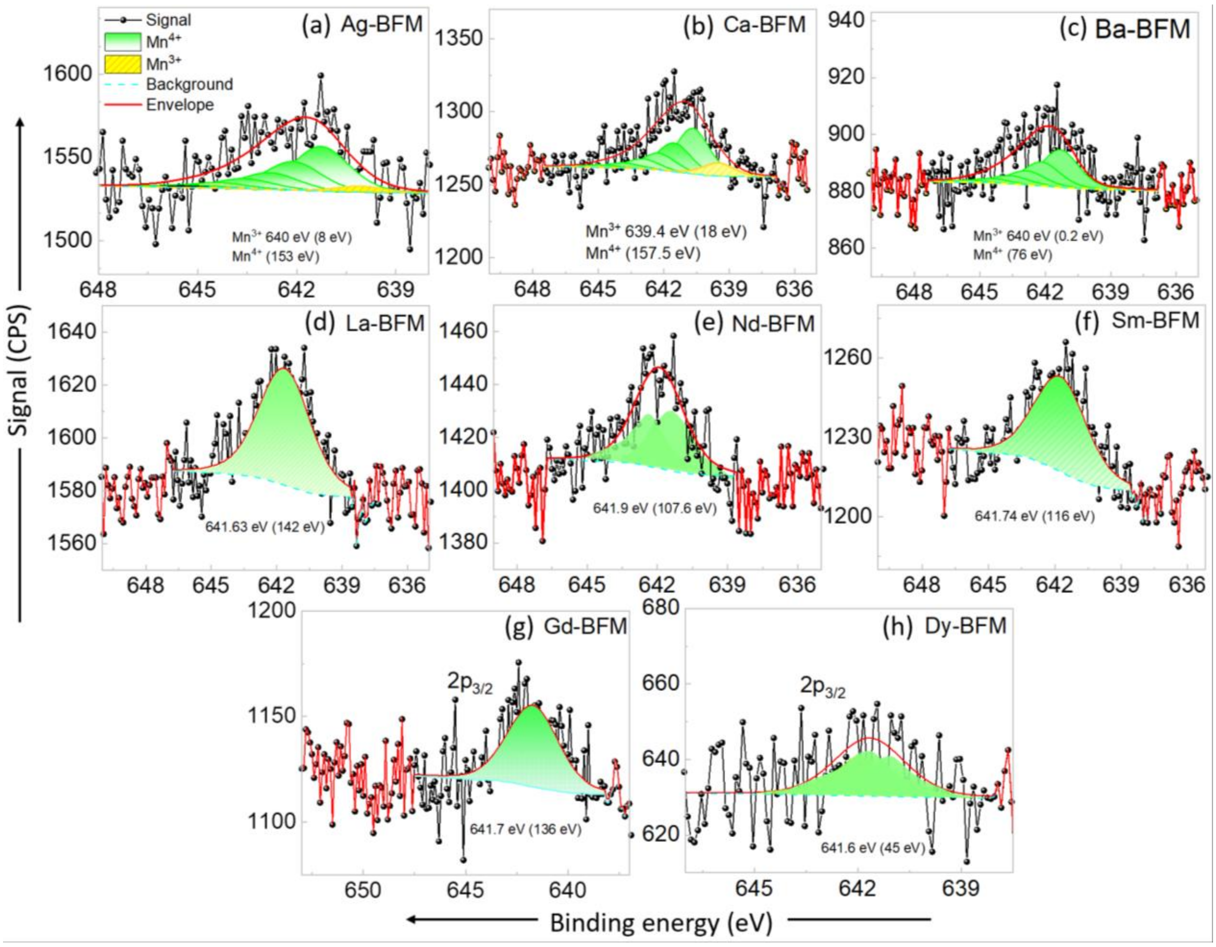

Figure 4.8: Mn 2p XPS spectra of doped BFM NPs, the peak position is mentioned at the bottom of the peak at ~642 eV, and in brackets the peak area is given. The green peaks belong to Mn^{4+} and the yellow peak correspond to the Mn^{3+} valence state.

The difference between the XPS and XANES results is related to their sensitivity to the surface and bulk states, respectively. The representative XANES spectra for doped BFM NPs are shown in Figure 4.9. The Bi-L_{III} near edge spectra consist of two main features B1 and B2, where B1 is the first inflection point of the spectrum and shows the absorption edge energy value corresponding to the $2p^{3/2} \rightarrow 6d$ transition.317 All spectra correspond to the Bi^{3+} state. We observe three features in the Fe-K edge spectra: A1, A2, and A3. The pre-edge A1 feature is attributed to the O-1s to Fe-3d quadrupole forbidden transition, A2 corresponds to the O-2p to Fe-3d ligand to metal transition, and A3 is due to the O-1s to Fe-4p dipole allowed transition.317 The change in intensity shows the alteration in electron density and hybridization between metal Fe (3d) and ligand O (2p). There is a significant difference in intensity found for absorption edges of Dy-BFM from the others.

From the XANES data of the Mn-K edge spectra, we found that only the 4+ state of Mn is present in all samples [Figure 4.9]. So, most of the Mn is in the 4+ state, but a small percentage of Mn is also present in the 3+ form at the surface of the NPs due to the termination of bonding chains at the surface which causes lower oxidation states of the ions.

The Fe-3*p* spectra of Dy-BFM manifest the 3+ state of Fe for the other doped BFM NPs.[46] The X-ray absorption near edge structure (XANES) spectra of the Fe K-edge also manifest the presence of Fe 3+ and 2+ states [Figure 4.9]. However, from the Fe-2*p* spectrum of Ag-BFM, we find that the 3+ state is in majority over the 2+ state (7±5 %) of Fe.[46]

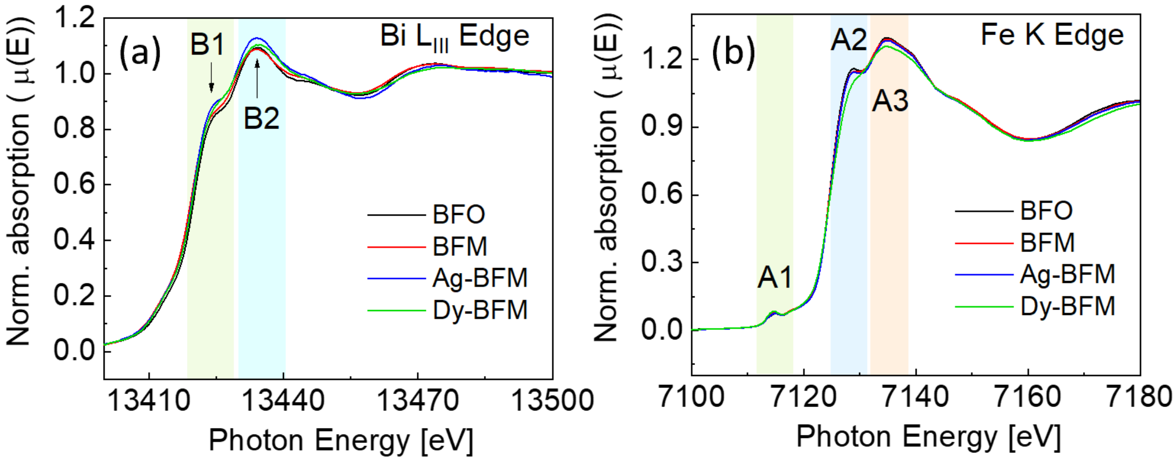

Figure 4.9: XANES spectra of Ag, Ba, Dy, and Mn codoped and undoped BiFeO3 NPs: Bi LIII-absorption edges (a) and Fe K-absorption edges (b).

Even if Mn is completely in the 4+ state, its concentration is not high enough to compensate for the charge imbalance in Ag-BFM caused by the replacement of Bi^{3+} by Ag^{+}. The overall electric neutrality can be kept by formation of oxygen vacancies as shown by the following defect equation in the Kröger-Vink notation.

$$Ag_2O + 2Bi_{Bi}^{x} \rightarrow 2Ag_{Bi}^{\prime\prime} + 2V_{O}^{\cdot\cdot} + Bi_2O_3 \tag{4.2}$$

For Ca-BFM, the 4+ state of Mn maintains charge balance, which has also been found for other divalent, i.e., Ba, doped BFM NPs.[10] For Dy-BFM NPs, the excessive positive charge due to the presence of Mn^{4+} can be compensated via creation of cation vacancies, similar for other trivalent cation doped BFM NPs. Both substitutional atoms and vacancies as a result of MDT doping could affect the crystal structure of NPs. This analysis is for the surface of the NPs as XPS largely unveils the surface chemistry rather than bulk.

4.3.2 Estimation of oxygen vacancies in doped BFO NPs

Oxygen vacancies are created when one or more oxygen atoms are missing from the lattice of a material. These vacancies can affect the chemical and physical properties of the material. For quantitative characterization of the oxygen vacancy, still there is no single proper technique. Normally, due to the lack of oxygen at the lattice sites, the structure of lattice is expected to reorganize to decrease the energy of the system. Using this information, the oxygen void existed on the surface can be detected by scanning tunnelling microscopy (STM), and the structural change can be detected by the neutron diffraction (ND). Moreover, the loss of oxygen can also lead to the electron distribution change, which leads to the change of the binding energy and peak intensities in the XPS.

The O1s spectrum in XPS can be used to identify the chemical environment of the oxygen atoms in the sample, including rough estimation of oxygen vacancies. Usually, the O 1s XPS signal can be deconvoluted into lattice bonded oxygen and vacancy oxygen.[318] In Fe_2O_3 the peak attributed to oxygen vacancies increased with the prolongation of N_2 treatment, suggesting an increase amount of oxygen vacancy.[319] In addition, the carrier concentration can also be tailored by the compensated charge of oxygen vacancies in the system. The intensity and binding energy of the oxygen vacancy component can be used to estimate the concentration of oxygen vacancies in the sample; however, the binding energy of surface absorbed oxygen species overlap with the information about oxygen vacancy which makes difficult to quantify the oxygen vacancies using only XPS.[318]

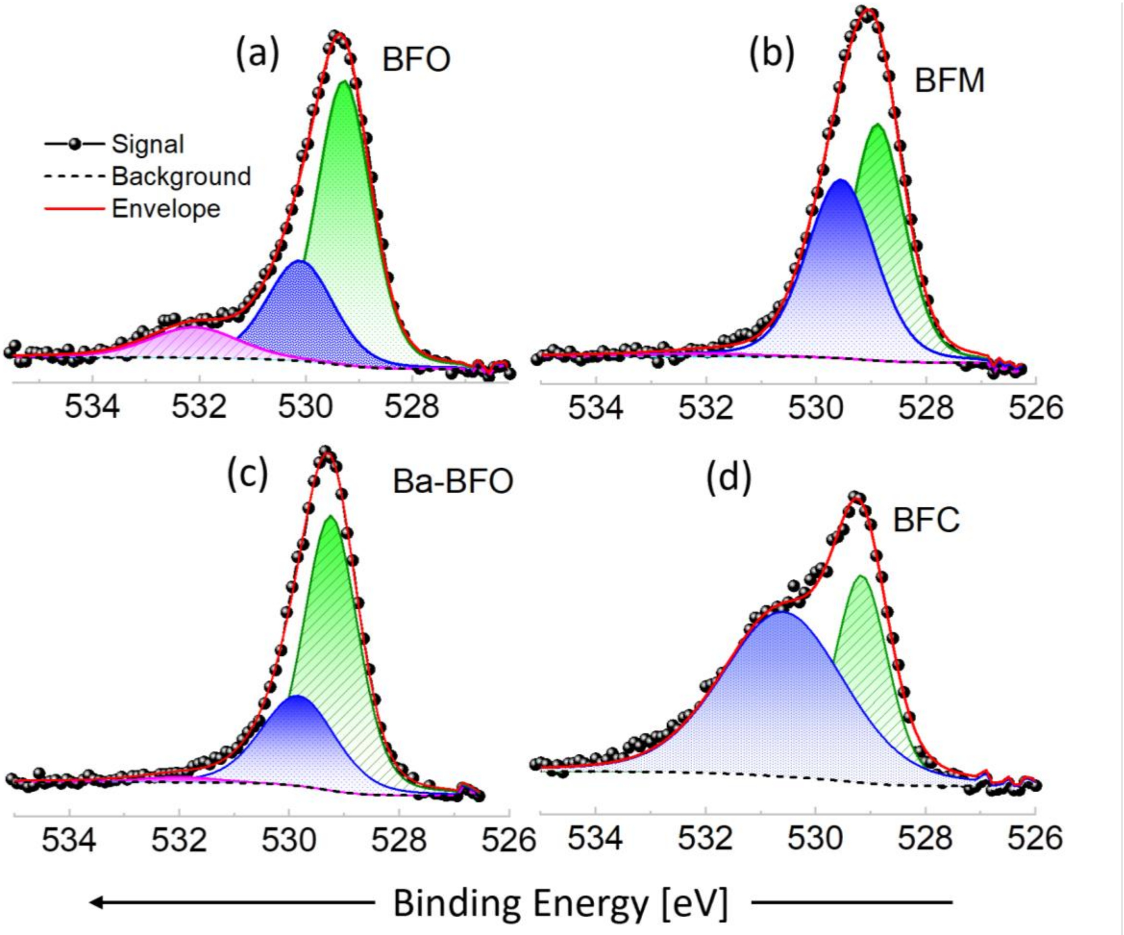

Figure 4.10: The O 1s XPS spectra of BFO (a), BFM (b), Ba-BFO (c), and BFC (d).

Other techniques, such as Raman spectroscopy or positron annihilation spectroscopy, can also be used in conjunction with XPS to confirm the presence of oxygen vacancies and provide more detailed information about their distribution and concentration.

In Figure 4.10, the O 1s XPS spectra of BFO and single doped BFO is shown. For BFO NPs, the O 1s spectra has peak at ~529 eV belongs to Bi-O bonding (green), and peak at ~530 eV attributes to Fe-O bonding (blue), whereas the peak at 532 eV (pink) corresponds to surface adsorbed oxygen and the presence of oxygen vacancies. Upon 5 mol % Mn doping the peak area corresponding to the Fe-O binding energy has increased. Such a change can be due to the presence of Mn-O bonds. Similarly, upon Co doping in BFO NPs at the Fe site, the blue peak area increases which can be due to presence of Co-O bonding. Nevertheless, upon Ba doping in BFO at the Bi-site, the blue peak area reduces and the green peak corresponding to Bi-O increases which manifests the influence of Ba doping into BFO NPs. Interestingly, upon single doping of Mn or Co or Ba, there is almost no peak corresponding to surface adsorbed oxygen, except for Ba-BFO case where we observe a little peak in that area, which may be due to charge imbalance due to divalent Ba at the Bi-site creating oxygen vacancies in the system.

Table 4.3: Peak position, FWHM and Peak area in eV for O 1s spectra of single-doped BFO NPs are listed in eV.

Material	**O 1s peak 1 (eV) [Surface O]**		**O 1s peak 2 (eV) [Fe-O]**		**O 1s peak 3 (eV) [Bi-O]**	
	FWHM (eV)	Area (eV)	FWHM (eV)	Area (eV)	FWHM (eV)	Area (eV)
BFO	**532**		**530**		**529.3**	
	2	518	1.5	1275	1.2	2945
BFM	**-**		**529.5**		**529**	
	-	-	1.5	2344	1.2	2457
BFC	**-**		**530.6**		**529.2**	
	-	-	2.6	2944	1.1	1602
Ba-BFO	**532**		**529.8**		**529**	
	1.6	87	1.6	1473	1.2	3277

The O 1s XPS spectra of further mono-, di-, and tri- valent cation doped at the Bi-site in BFM NPs are shown in Figure 4.11. The XPS spectra of Ag-BFM, Ba-BFM, Gd-BFM, and Dy-BFM reveal a peak related to surface adsorbed oxygen at ~532 eV. The highest area under the peak is observed for Dy-BFM NPs, followed by Gd-BFM NPs. The reason for Dy being the most reactive of all trivalent dopants and leading to the oxygen vacancy peak is due to its high reactivity towards surface available oxygen-containing groups such as carboxylates, which can be explained by its well-known activity towards air and moisture.[320] This suggests that Dy on the surface can be an active site in Dy-BFM NPs, making it highly beneficial for catalytic purposes. Furthermore, the C 1s XPS spectra of Dy-BFM also show the presence of carbonates and bicarbonates.[46] Interestingly, Ba doping in BFM NPs results in a peak at 534 eV, which is attributed to the C-OH bonding. This indicates that Ba doping activates the surface of BFM NPs and makes it prone to adsorption of –OH groups more than any other NPs.

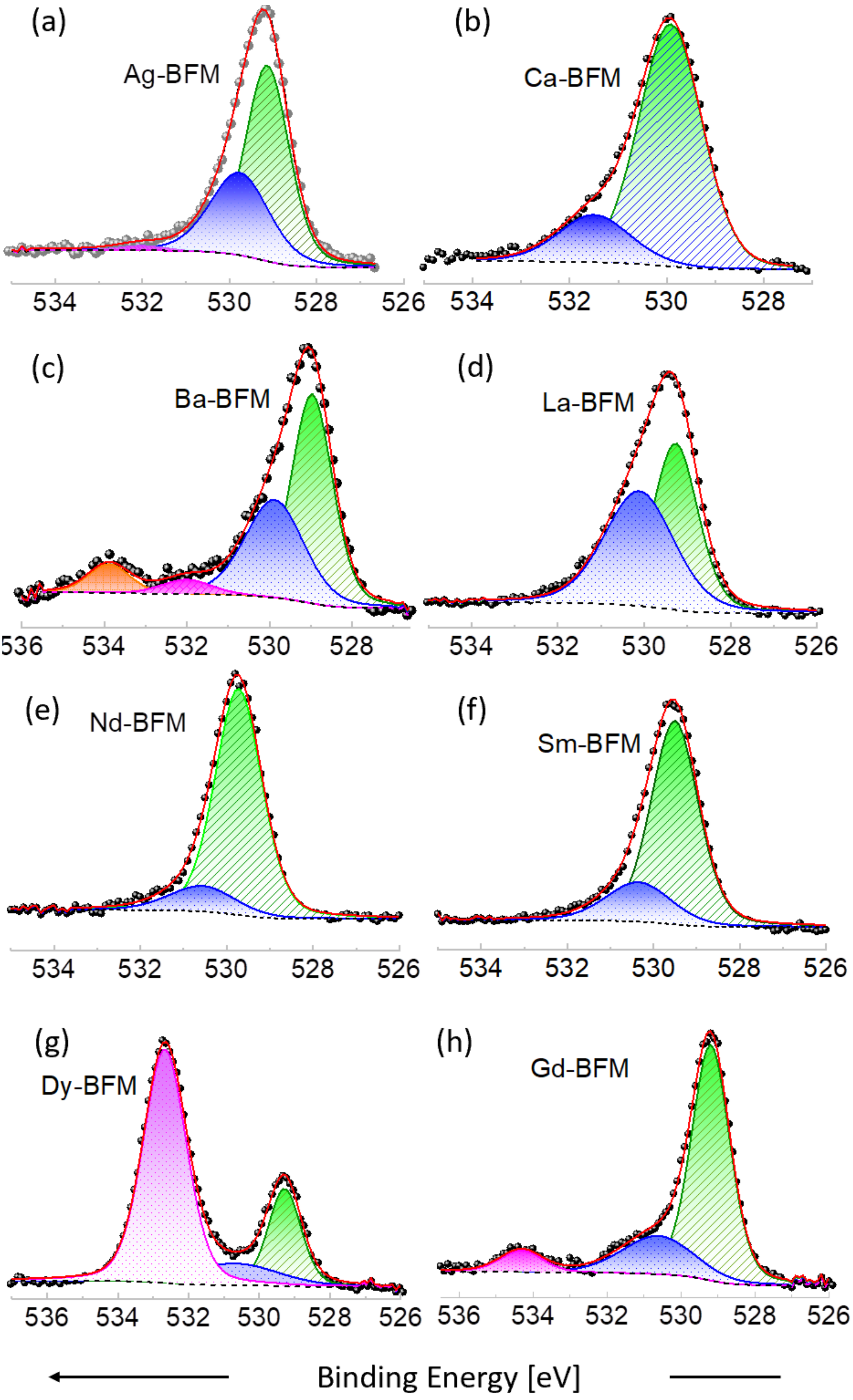

Figure 4.11: The O 1s XPS spectra of Ag-BFM (a), Ca-BFM (b), Ba-BFM (c), La-BFM (d), Nd-BFM (e), Sm-BFM (f), Dy-BFM (g), Gd-BFM NPs (h).

Table 4.4: Peak position, FWHM and peak area in eV for O 1s spectra of doped BFM NPs.

<table>
<tr><th rowspan="2">Material</th><th colspan="4">O 1s peak 1 (eV)</th><th colspan="2">O 1s peak 2 (eV)</th><th colspan="2">O 1s peak 3 (eV)</th></tr>
<tr><th colspan="2">FWHM (eV)</th><th colspan="2">Area (eV)</th><th>FWHM (eV)</th><th>Area (eV)</th><th>FWHM (eV)</th><th>Area (eV)</th></tr>
<tr><td rowspan="2">BFM</td><td colspan="4">-</td><td colspan="2">529.5</td><td colspan="2">529</td></tr>
<tr><td colspan="2">-</td><td colspan="2">-</td><td>1.47</td><td>2344</td><td>1.16</td><td>2457</td></tr>
<tr><td rowspan="2">Ag-BFM</td><td colspan="4">532</td><td colspan="2">529.7</td><td colspan="2">529.13</td></tr>
<tr><td colspan="2">1.28</td><td colspan="2">67.6</td><td>1.59</td><td>1339</td><td>1.18</td><td>2352</td></tr>
<tr><td rowspan="2">Ca-BFM</td><td colspan="4">-</td><td colspan="2">531.5</td><td colspan="2">529.9</td></tr>
<tr><td colspan="2">-</td><td colspan="2">-</td><td>1.72</td><td>767.5</td><td>1.57</td><td>3443.22</td></tr>
<tr><td rowspan="2">Ba-BFM</td><td colspan="2">534</td><td colspan="2">532</td><td colspan="2">529.8</td><td colspan="2">528.9</td></tr>
<tr><td>1.19</td><td>182</td><td>1.42</td><td>108</td><td>1.67</td><td>871</td><td>1.17</td><td>1311</td></tr>
<tr><td rowspan="2">La-BFM</td><td colspan="4">-</td><td colspan="2">530</td><td colspan="2">529.7</td></tr>
<tr><td colspan="2">-</td><td colspan="2">-</td><td>1.9</td><td>2244</td><td>1.23</td><td>2110</td></tr>
<tr><td rowspan="2">Nd-BFM</td><td colspan="4">-</td><td colspan="2">530.6</td><td colspan="2">529.7</td></tr>
<tr><td colspan="2">-</td><td colspan="2">-</td><td>1.8</td><td>528</td><td>1.28</td><td>3309</td></tr>
<tr><td rowspan="2">Sm-BFM</td><td colspan="4">-</td><td colspan="2">530.5</td><td colspan="2">529.5</td></tr>
<tr><td colspan="2">-</td><td colspan="2">-</td><td>1.8</td><td>684</td><td>1.3</td><td>2555</td></tr>
<tr><td rowspan="2">Gd-BFM</td><td colspan="4">534.2</td><td colspan="2">530.6</td><td colspan="2">529.2</td></tr>
<tr><td colspan="2">1.35</td><td colspan="2">235</td><td>2.3</td><td>701</td><td>1.2</td><td>2323</td></tr>
<tr><td rowspan="2">Dy-BFM</td><td colspan="4">532.7</td><td colspan="2">530.7</td><td colspan="2">529.3</td></tr>
<tr><td colspan="2">1.44</td><td colspan="2">2559</td><td>3</td><td>495</td><td>1.1</td><td>814</td></tr>
</table>

Role of aliovalent doping amount

The effect of the doping amount on the oxygen vacancies in BFM NPs has been studied by doping 1, 2, 3, and 5 mol % of Ba in BFM NPs. The O 1s XPS spectra are presented in Figure 4.12. Comparative to the O 1s XPS spectra of BFM (Figure 4.10), 1 mol % Ba doping creates a certain amount of vacancies, which corresponds to the peak at 532 eV, as shown in Table 4.5.

In addition, the 1BBFM NPs also exhibit new active sites in terms of Ba^{2+} ions onto the surface of NPs which adsorb -OH groups and provide a peak at ~535 eV. This indicates that only 1 mol % doping can alter the active sites and surface reactivity of NPs.

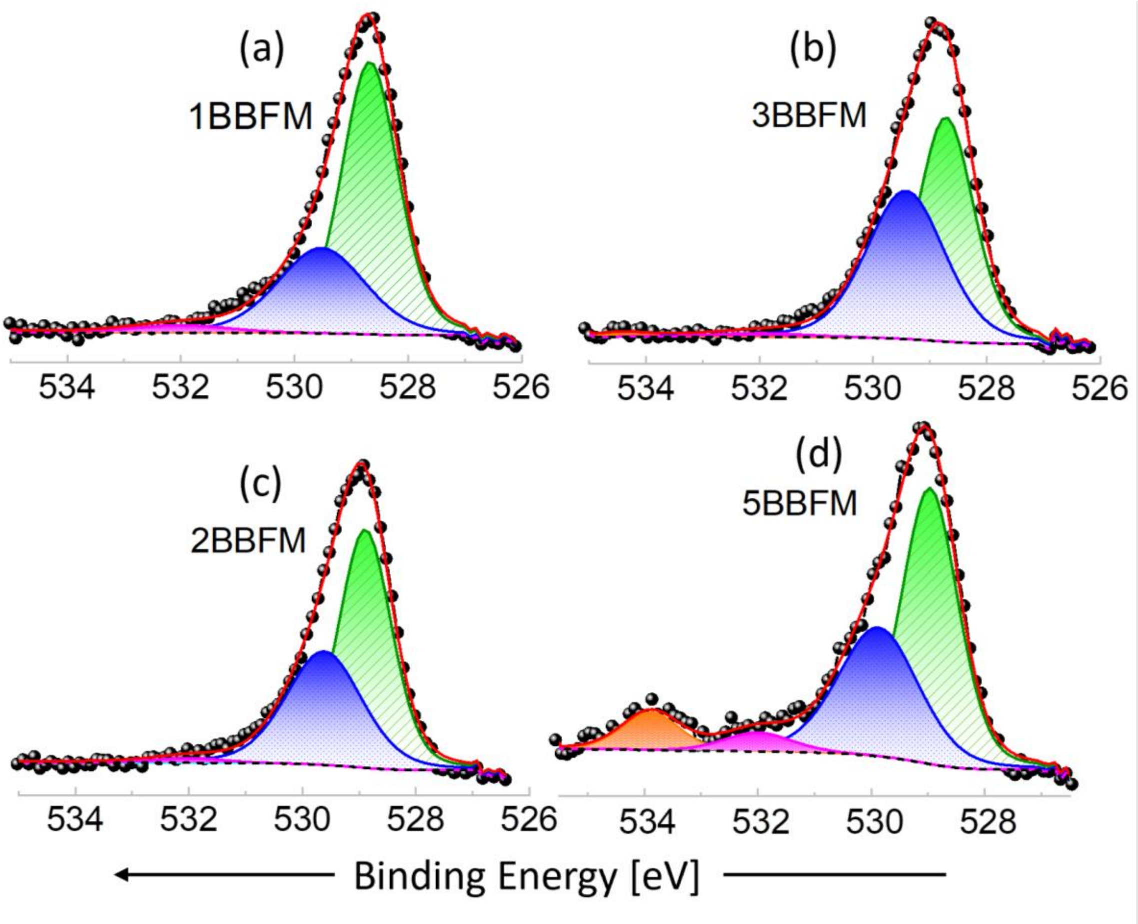

Figure 4.12: The O 1s XPS spectra of 1BBFM (a), 2BBFM (b), 3BBFM (c), and 5BBFM (d).

Upon further doping of 2 mol % Ba, it is observed that the area of the peak corresponding to oxygen vacancies reduced, and there is also no peak related to -OH group adsorption. Interestingly, for 3BBFM NPs, both peaks related to oxygen vacancies and -OH group adsorption are observed, and for 5 BBFM, as previously mentioned, an increment in peak intensities at 534 and 532 eV is found.

These results clearly show how the amount of aliovalent doping can alter the surface available active sites and create a number of vacancies and defects, which cause adsorption of -OH groups and oxygen molecules.

Table 4.5: Peak position, FWHM and peak area in eV for O 1s spectra of Ba doped BFM NPs.

<table>
<tr><th rowspan="2">Material</th><th colspan="4">O 1s peak 1 (eV)</th><th colspan="2">O 1s peak 2 (eV)</th><th colspan="2">O 1s peak 3 (eV)</th></tr>
<tr><td colspan="2">FWHM (eV)</td><td colspan="2">Area (eV)</td><td>FWHM (eV)</td><td>Area (eV)</td><td>FWHM (eV)</td><td>Area (eV)</td></tr>
<tr><td rowspan="2">BFM</td><td colspan="4">-</td><td colspan="2">529.5</td><td colspan="2">529</td></tr>
<tr><td colspan="2">-</td><td colspan="2">-</td><td>1.47</td><td>2344</td><td>1.16</td><td>2457</td></tr>
<tr><td rowspan="2">1BBFM</td><td colspan="2">535</td><td colspan="2">532</td><td colspan="2">529.5</td><td colspan="2">528.7</td></tr>
<tr><td>1</td><td>15</td><td>2</td><td>108</td><td>1.82</td><td>1120</td><td>1.17</td><td>2306</td></tr>
<tr><td rowspan="2">2BBFM</td><td colspan="4">532</td><td colspan="2">529.6</td><td colspan="2">528.8</td></tr>
<tr><td colspan="2">1.4</td><td colspan="2">58</td><td>1.6</td><td>1548</td><td>1.1</td><td>2260</td></tr>
<tr><td rowspan="2">3BBFM</td><td colspan="2">534.4</td><td colspan="2">532</td><td colspan="2">529.4</td><td colspan="2">528.7</td></tr>
<tr><td>1</td><td>32</td><td>2</td><td>61</td><td>1.62</td><td>1981</td><td>1.2</td><td>2146</td></tr>
<tr><td rowspan="2">5BBFM</td><td colspan="2">534</td><td colspan="2">532</td><td colspan="2">529.8</td><td colspan="2">528.9</td></tr>
<tr><td>1.19</td><td>182</td><td>1.42</td><td>108</td><td>1.67</td><td>871</td><td>1.17</td><td>1311</td></tr>
</table>

However, it is important to note that the accuracy and precision of the quantitative oxygen vacancy values obtained using XPS will depend on various factors, including the instrument setup, data analysis methods, and calibration procedures. Therefore, it is recommended to perform XPS measurements under consistent experimental conditions and validate the results using other techniques if possible.

4.4 Distortions in the crystal structure

4.4.1 Crystal symmetry and lattice parameters

To unveil the crystal structure of doped BFO NPs, the XRD diffractograms were analysed. The diffractograms are shown in Figure 4.13, where their XRD pattern matches quite well with the *R3c* rhombohedral phase of BFO.

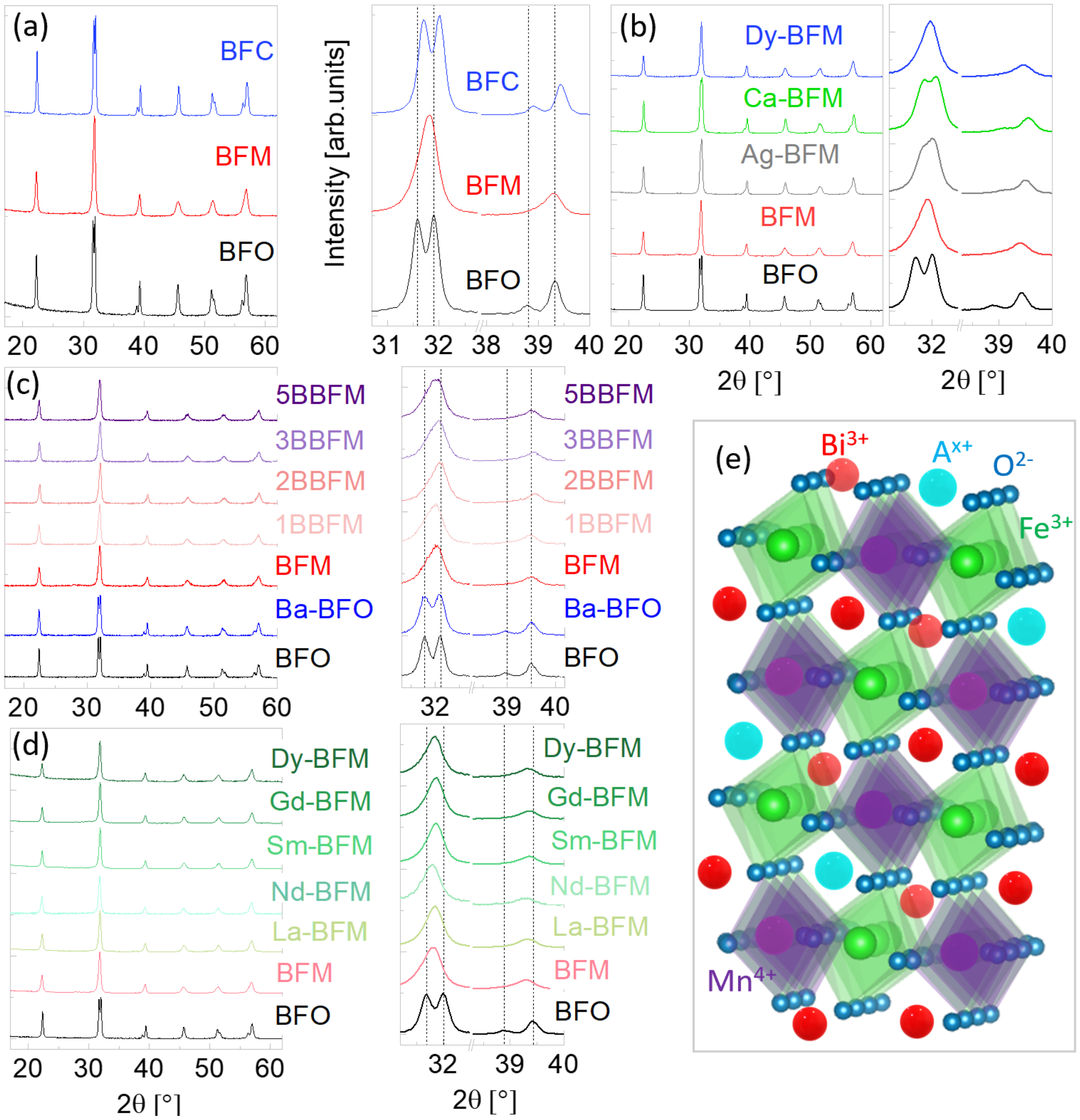

Figure 4.13: XRD diffractograms of all doped and undoped BFO NPs. Mn and Co single doped BFO NPs (a) with zoomed peaks 31-40° in right side graph. The mono-, di-, and tri-valent cation doped BFM NPs (b). The Ba doped BFM NPs along with only Ba doped BFO NPs (c). The rare earth lanthanide doped BFM NPs (d). The colourful representation of crystal structure of co-doped BFO NPs, with octahedral tilts due to doping at Bi and Fe sites (e).

The slight shift in XRD peaks represent the effect of aliovalent doping which causes the distortion in lattice parameters that is responsible for shift in 2-theta values due to size mismatch. The Bragg diffraction peaks match well with ICSD database no. 417304 for space group *R3c* (in the hexagonal representation: *R*3*cH*) for all doped and undoped BFO NPs, which means that up to 5 mol % doping all NPs exhibit rhombohedral crystal structure, there is no structural phase transition for this doping concentration. We have not found any parasitic phase in XRD diffractograms for both pristine BFO and Ba and Mn co-doped BFO NPs

The obtained XRD spectra were fitted using Rietveld refinement method as explained in previous chapter. The equations 4.2 and 4.3 were used for the conversion from hexagonal to rhombohedral lattice parameters and vice-versa.[321]

$$\alpha_{rh} = 2arcsin[\frac{3a_{hex}}{2\sqrt{3a_{hex}^2 + c_{hex}^2}}] \qquad (4.2)$$

$$a_{rh} = \frac{a_{hex}}{2sin(^{\alpha_{rh}}/_{2})} \qquad (4.3)$$

Effect of Single doping in BFO NPs

For 5 mol % single doped BFO NPs, the XRD diffractograms are plotted in Figure 4.13. Splitting of the (104) and (110) peaks at ~32 degrees for pristine BFO reflects the rhombohedral distortion of the unit cell [Figure 4.13e]. This splitting decreases after 5 % Mn doping merging the characteristic peak (*R*3*c*) at ~32 degrees. However, for cobalt and Ba doped BFO NPs, there is less merging of peaks than Mn as shown in Figure 4.13a-c. As similar trend is found for the peak at ~39.5 degrees, that Mn doping merges the three peaks mostly among single-doped BFO NPs.

To analyze this distortion in more detail, we performed a Rietveld refinement of the XRD-diffractograms, as shown in Appendix. The refinement for lattice parameters is plotted in Figure 4.14 and Figure 4.16. Ba doping and Mn doping increases the lattice parameter a_{hex}, whereas Co doping has no large effect on a_{hex}. The lattice parameter c_{hex} reduces upon Mn and Co doping but increases for Ba doping. From the hexagonal unit cell volume (UCV) trend shown in Figure 4.16, the UCV is largest for Ba-BFO followed by BFM and BFC NPs. The increase in hexagonal unit cell volume is due to the increment in lattice parameters caused by larger sized dopant (Ba^{2+}). This would require changes in other aspects of the crystal structure, such as the atomic positions or the degree of distortion of the unit cell. Overall, due to single doping in BFO NPs the UCV increases.

The alteration in UCV not only depends upon the lattice parameters even the atoms in the crystal structure can rearrange in a way that creates more space between them. This causes an increment in UCV despite the decrease in the lattice parameters. Additionally, if the hexagonal unit cell undergoes a distortion, such as becoming more rhombohedral, the UCV could also increase even if both lattice parameters decrease. Therefore, one should compare the lattice parameter results in the rhombohedral crystal structure as well. Using equations 4.2 and 4.3, the calculated a_{rh} and α_{rh} and plotted then into Figure 4.15. For single doped BFO

NPs, we observe that a_{rh} is largest for Ba doping and least for Co doping even less than the BFO NPs, similar as for the hexagonal unit cell.

Doping in BFM NPs

From Figure 4.13b, it can be seen that MDT doping into BFM NPs results in merging /demerging of XRD peaks at 2θ ~32 degrees. Dy and Ag dopings retain the merged peak at ~32 degrees, however Ca doping demerges it. To compare the distortion, the lattice parameters for MDT doped BFM NPs are plotted in Figure 4.14c, 4.16b. As compared to BFM NPs, Ca doping does not significantly alter the hexagonal lattice parameters, but Dy and Ag do. The hexagonal UCV is smallest for Ag-BFM NPs and largest for Ca-BFM NPs among the MDT doped NPs. Moreover, the rhombohedral lattice parameter a_{rh} is largest for Ca doping, and the angle α_{rh} is largest for Dy-BFM NPs as shown in Figure 4.15.

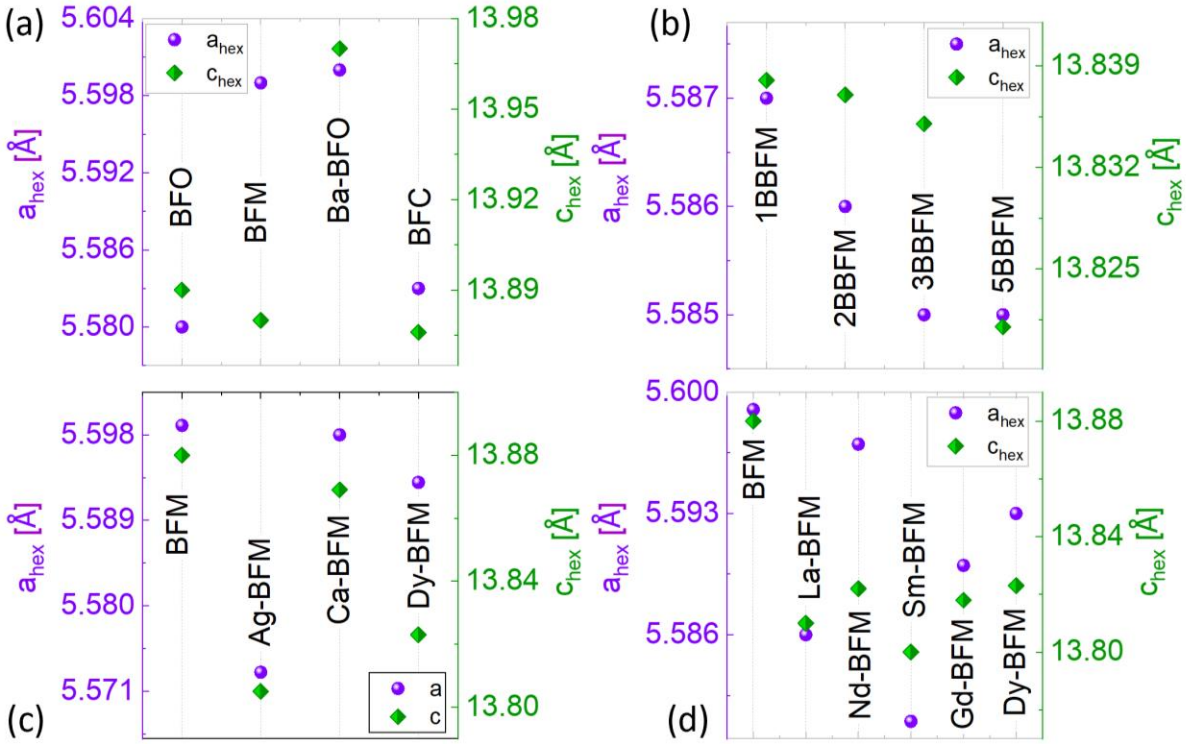

Figure 4.14: The trend of lattice parameters in hexagonal crystal structure representation of BFO. (a) single doped BFO NPs. (b) Ba doped BFM NPs. (c) mono-, di-, tri-valent cation doped BFM NPs. (d) comparison of rare earth-lanthanide doped BFM NPs. [Error bars are the size of symbols]

Ba-Doping amount in BFM NPs

The X-ray diffractograms for the $Bi_{1-x}Ba_xFe_{0.95}Mn_{0.05}O_3$ (x = 0.00, 0.01, 0.02, 0.03, 0.05) samples are shown in Figure 4.13c. The merged peaks at ~32 degree and at ~39 degree become broader upon Ba doping, which can be due to combined effect of increased microstrain and reduced crystallite size. The variation of the lattice parameters is represented in Figure 4.14b. Doping by 1% Ba results in reducing the hexagonal lattice parameters and it keeps reducing upon further doping of Ba up to 5 mol %. The hexagonal UCV also follows the same trend as shown in Figure 4.16d, where Ba doping into BFM causes reduction in UCV. Such a counterintuitive decreasing of the unit cell by introducing of larger Ba^{2+} cation in the sites of Bi^{3+} is most probably caused by creation of oxygen vacancies to compensate the charge disparity.

Figure 4.15 shows variation of the rhombohedral lattice parameters (a_{rh} and α_{rh}) with respect to the Ba doping into BFM NPs. One can see that a_{rh} decreases and α_{rh} increases upon Ba doping from 1 to 5 mol % into BFM. The reduction of a_{rh} and increase of α_{rh} manifests the crystal distortion of rhombohedral crystal lattice due to larger sized Ba doping into BFM. The unexpected trend can be due to the presence of oxygen vacancies or other defects.

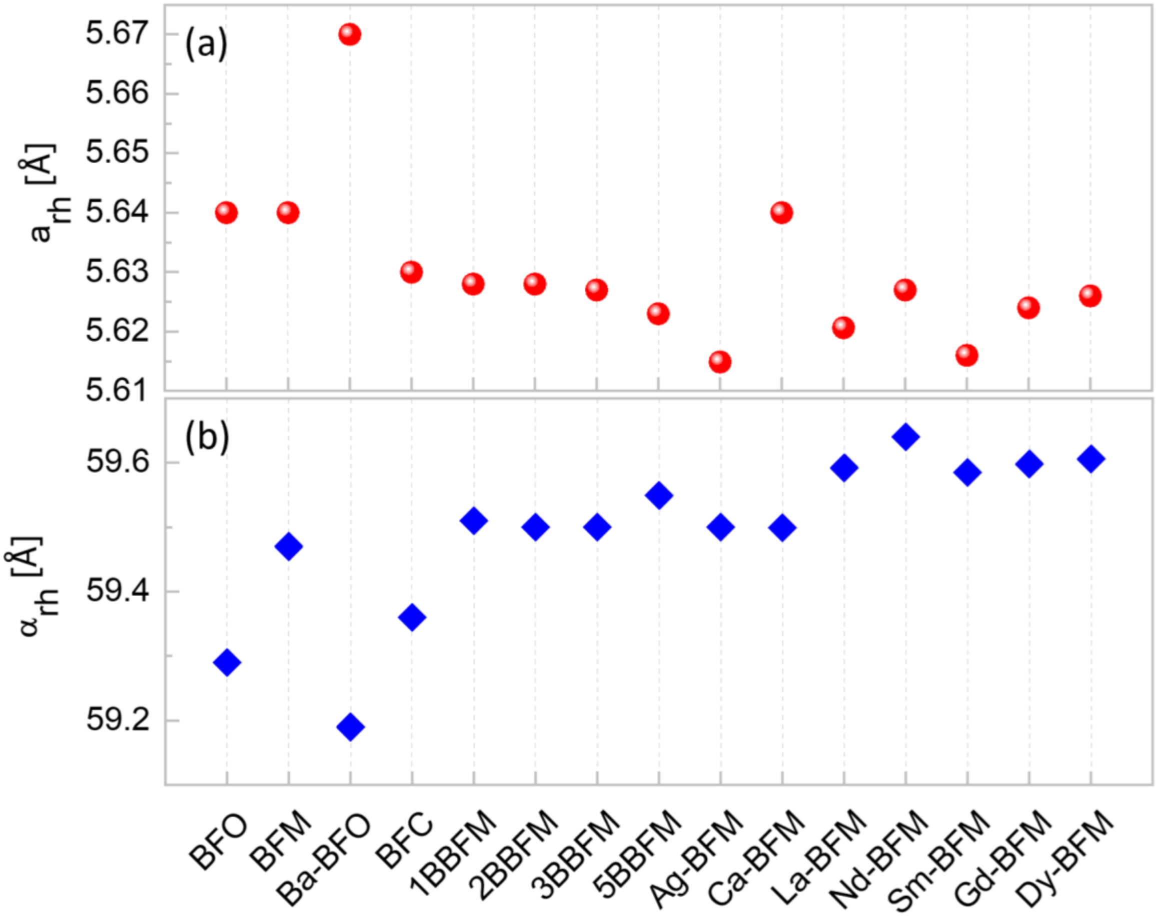

Figure 4.15: The rhombohedral lattice parameter of doped and undoped BFO NPs (a). The rhombohedral angle in doped and undoped BFO NPs (b). [Error bars are the size of symbols]

Rare-earth (RE) doping in BFM NPs

The XRD diffractograms are shown in Figure 4.13. The RE dopants do not demerge the peaks of BFM NPs, however the broadening in XPD peaks is observable upon RE doping. The lattice parameter trend is shown in Figure 4.14d, where La doping reduces both hexagonal lattice parameters, and Nd mostly reduces c_{hex} rather than both. There is a reduction in a_{hex} till Sm doping, but then a_{hex} value starts to increase for Gd and Dy. A similar trend is observed for c_{hex} as well. Overall, the lattice parameters of RE-doped BFM NPs are less than BFM itself. In rhombohedral lattice parameter a_{rh} is also less for RE-doped BFM NPs, however, among RE-doped ones, Nd has the largest a_{rh} value, which means the lattice is elongated for Nd-BFM NPs [Figure 4.15a]. The rhombohedral angle is also largest for Nd-BFM among all NPs [Figure 4.15b].

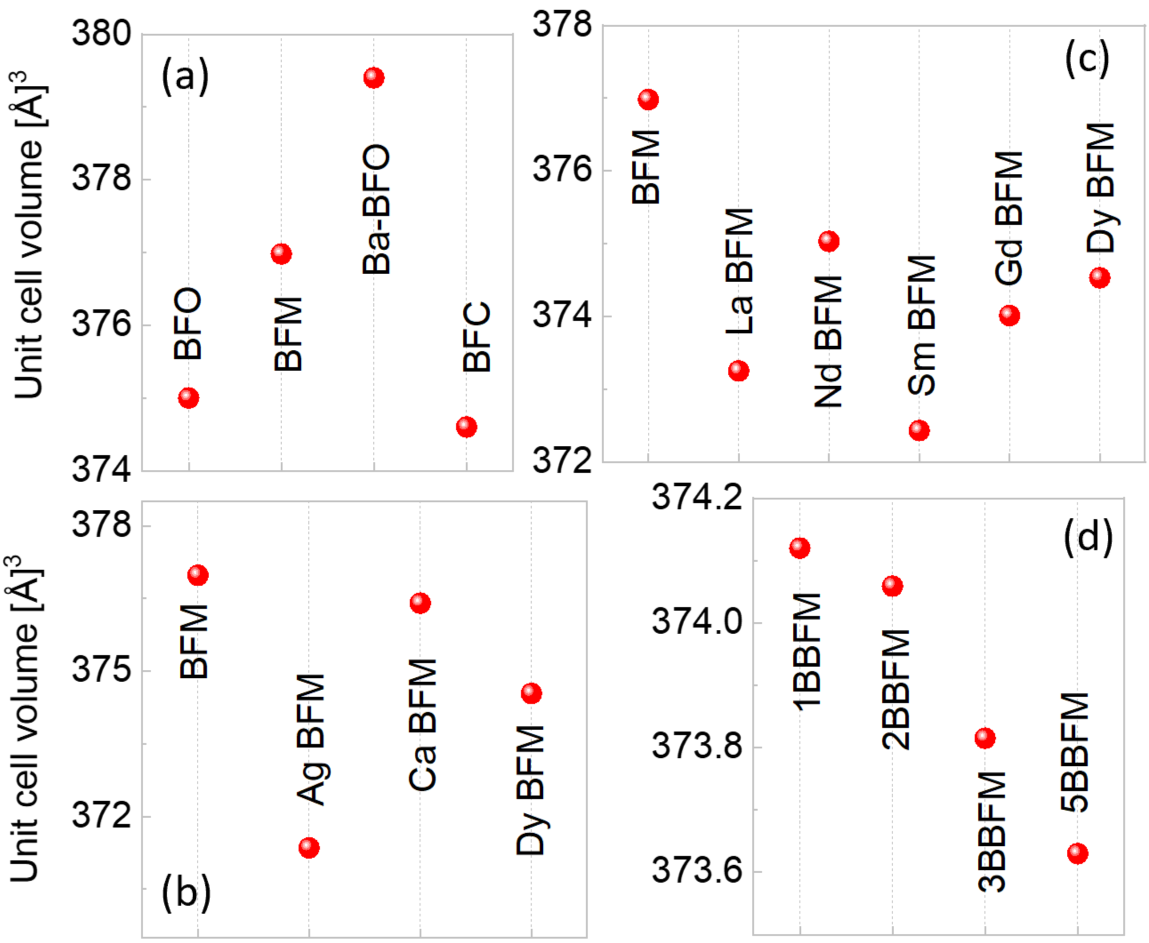

Figure 4.16: Unit cell volume in hexagonal crystal structure representation of BFO. (a) single-doped BFO NPs. (b) Lanthanide-doped BFM NPs. (c) mono-, di-, and tri-valent cation doped BFM NPs. (d) Ba doped BFM NPs.

4.4.2 Crystallite size and microstrain

The resultant XRD peak broadening in doped BFO NPs is due to a combine effect of reduced crystallite size and increased microstrain.[10,322] In addition, the ionic size disparity also contributes to the overall strain in the lattice of the nanocrystal. The trend of crystallite size and microstrain are plotted in Figure 4.17. In single-doped BFO NPs, Ba-BFO has a larger crystallite size than BFO, whereas BFM and BFC have smaller size than BFO, and BFC has smallest crystallite size (~25 nm) among all [Figure 4.17a]. Similarly, the Ba-BFO has the smallest microstrain and BFC has largest microstrain, which is expected as crystallite is usually inversely proportional to microstrain in NPs.

Doping of Ba from 1 to 5 mol % into BFM causes reduction in crystallite size as shown in Figure 4.17b. Interestingly, 1 % Ba increases the crystallite size up to ~31.5 nm, and upon further Ba doping reduces the crystallite size up to 28 nm for 5BBFM NPs. The microstrain is found to have inverse proportional trend with Ba doped BFM NPs. The largest microstrain is observed in 5BBFM.

The crystallite size reduces upon MDT doping as shown in Figure 4.17c, where the smallest crystallite size and highest microstrain value are observed for Ag-BFM. Among the MDT-BFM

NPs, Ca-BFM has the largest crystallite size. Nevertheless, all MDT-doped BFM NPs have smaller crystallite size than BFM itself.

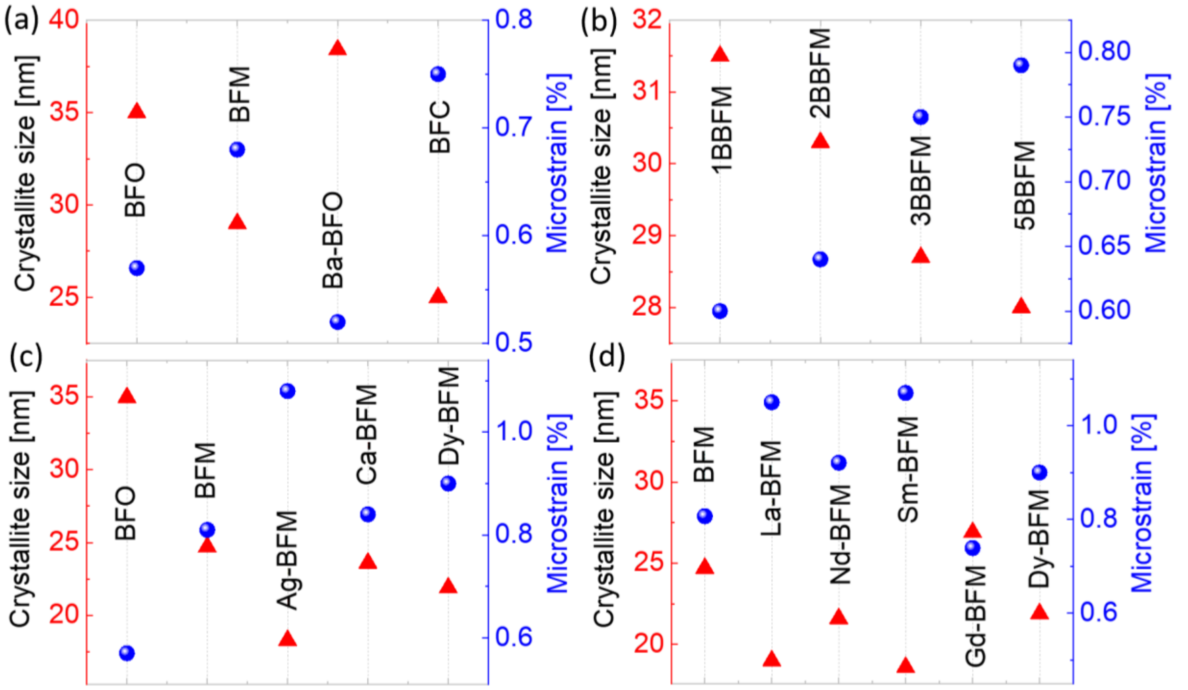

Figure 4.17: Crystallite and microstrain trend with respect to single doped BFO NPs (a), Ba doped BFM NPs (b), mono-, di-, and tri-valent cation doped BFM NPs (c), and lanthanide rare earth doped BFM NPs (d).

The crystallite size for RE-doped BFM NPs is shown in Figure 4.17d, where La and Sm doping have the smallest crystallite size (~18 nm) among the RE-doped ones. The Gd doped one has the largest crystallite size. The microstrain follows the inverse trend of crystallite size, and hence Sm-BFM has largest microstrain followed by La-BFM NPs.

There is a non-linear trend of crystallite size in RE-doped BFM NPs with respect to their atomic numbers, which can be due to defects and influence of oxygen vacancies in these NPs. As Dy is found to have a large amount of surface adsorbed oxygen species which are related to oxygen vacancies and defects, one can connect this with the alteration in crystallite size of doped BFM NPs. When oxygen vacancies are present in a material, they can cause lattice strain. This is because neighbouring atoms will try to occupy the empty sites left by the missing oxygen atoms, leading to distortions in the lattice structure. The lattice strain can create areas of higher energy in the material, which impedes crystal growth and can result in the formation of smaller crystallites.[323]

Furthermore, oxygen vacancies in large amount can lead to the formation of extended defects, such as dislocations and stacking faults, which can also hinder crystal growth and promote the formation of smaller crystallites. These defects act as barriers to crystal growth, which limits the size of the crystallites that can form. There are several factors, the ionic radii of the dopants, the valency to have charge compensation, and then defects like oxygen vacancies present in the system which all together lead to certain crystallite size and developed microstrain on doped NPs.

4.4.3 Bond angles and bond lengths

In BFO, both BiO_{12} the cuboctahedron, and the FeO_6 octahedron are found to undergo structural modifications upon dopants size alteration. BiO_{12} can undergo a large and unsystematic distortion due to the loss of the $6s^2$ lone pair electrons.

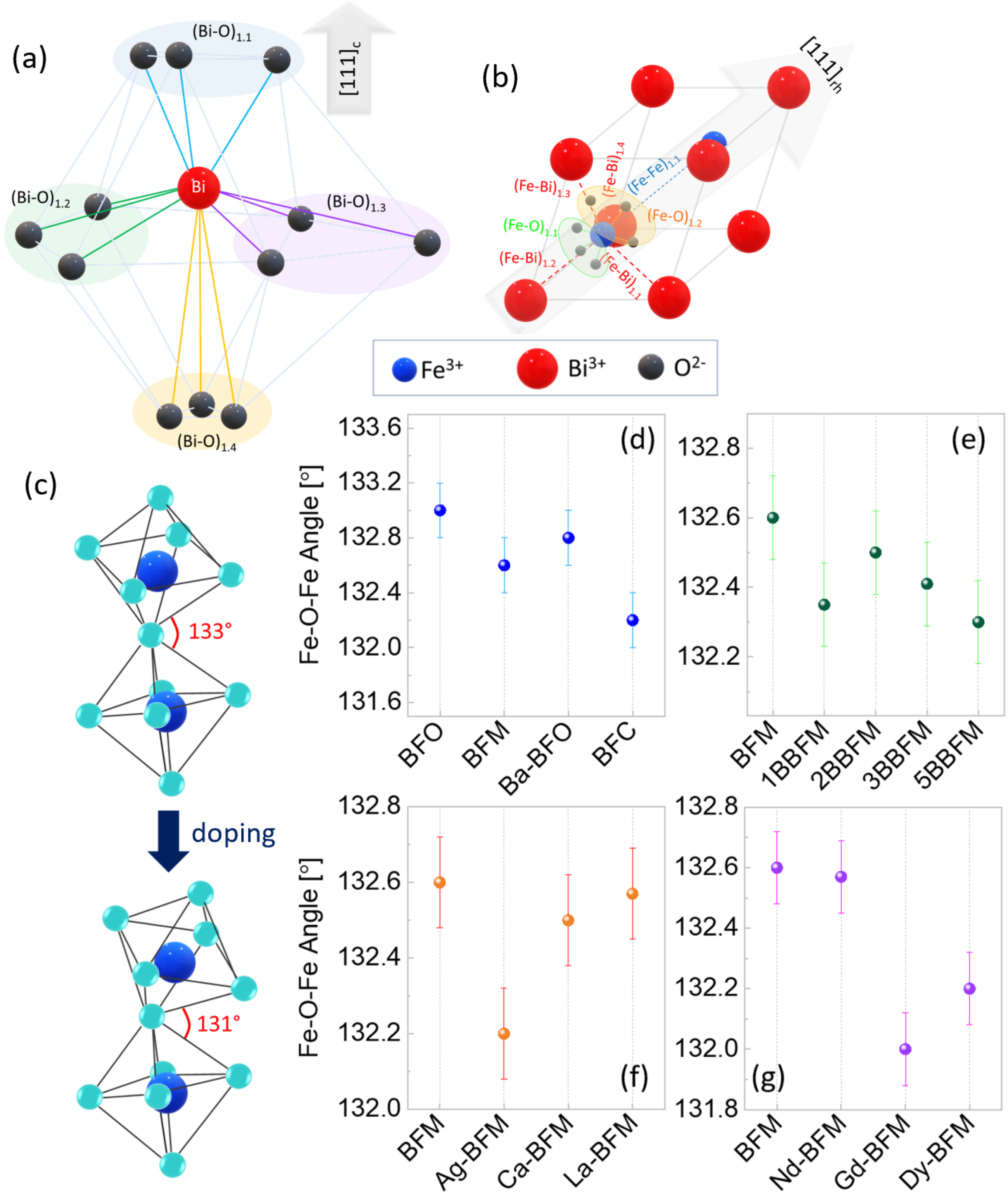

Figure 4.18: Bi-cuboctahedron schematic in rhombohedral BFO NPs (a), where four groups of oxygen atoms are being represented in different colours based on Bi-O bond distances. Schematic of Fe-O, Fe-Bi, and Fe-Fe bond distances in the unit cell of BFO (b). The Fe-O-Fe bond angle in neighbouring FeO_6 octahedra of BFO NPs (c). The alteration in Fe-O-Fe bond angles upon doping in BFO NPs are shown in (d-g).

The Fe-O-Fe bond angle is quite important in terms of magnetic properties of BFO, where 133° is said to be a critical angle, below which an antiferromagnetic to ferromagnetic transition occurs as shown in Figure 4.18c,[324,325] because the oxygen atoms are a link between BiO_{12} cuboctahedron, and the FeO_6 octahedron. So, the Fe-O-Fe angle can be altered by doping larger or bigger sized ions, at Bi-site. The long-range superexchange Fe–O–Fe (154.8°) configuration of bulk BFO leads to antiferromagnetism.[326] However, the role of local disorder cannot be ignored which can cause distortion in superexchange interaction and leads to local ferromagnetism.

The calculated Fe-O-Fe bond angles based on Rietveld refinement are shown in Figure 4.18d-g. For pristine BFO NPs, we have found a band angle in the range of ~132.9° with error bars as shown in Figure 4.18d, this angle value manifests that ~35 nm crystallite size BFO NPs could show ferromagnetism which will be discussed in “Chapter 5 Magnetism”. Further single doping in BFO NPs reduces the Fe-O-Fe bond angle largest for cobalt doping and least for Ba doping. This can be one of the reasons for higher maximum magnetization of BFC NPs than Ba-BFO NPs (Figure 5.2). The effect of Ba doping on the Fe-O-Fe bond angle is shown in Figure 4.18e, where the bond angle a bit reduced in 1BBFM, but for 2 BBFM it increases again and upon further doping of Ba leads to linearly reduction of the bond angle. Such trend can be due to presence of oxygen vacancies in Ba-doped BFM NPs.

For the non-magnetic MDT ion doped BFM NPs, the Fe-O-Fe bond angles are shown in Figure 4.18f. Ag doping reduces the bond angle down to 132.2°, Ca and La doping have higher band angles than Ag-BFM. This shows that the smaller size and charge imbalance due to the monovalent cation (Ag^+) causes large structural changes. This leads to a higher magnetization among the MDT doped BFM NPs as shown in Figure 5.4.

For the magnetic rare-earth doped BFM NPs the Fe-O-Fe bond angles are plotted in Figure 4.18g. Gd doped NPs has the least bond angle value (132°) after Dy doping. Nd doping generates a slight reduction in Fe-O-Fe bond angle as compared to BFM itself. The reduction of band angle by up to 1-2° can cause increase in magnetization as shown in Figure 5.8. The obtained Fe-O-Fe bond angles from XRD data analysis are average information, not local information.

In the bulk BFO crystal structure, a distorted cuboctahedron arrangement is observed, wherein six oxygen atoms are located in a plane perpendicular to the polar axis $[111]_c$. These six oxygen atoms form a hexagon with bismuth (Bi) located at the top, slightly displaced from the center. Additionally, three oxygen atoms are located in the plane below the hexagon and three oxygen atoms are located in the plane above it, forming a triangular base. Four Bi-O bond groups can be categorized from shortest to longest distances as follows: $(1.1)_3$, $(1.2)_3$, $(1.3)_3$, and $(1.4)_3$.[327] These groups are represented with different colours to distinguish them as shown in Figure 4.18a. The Fe-Bi bond distances are also categorized into as shown in Figure 4.18b.

As we learnt in the previous chapter, EXAFS gives information about the interatomic distances, near neighbour coordination numbers, and lattice dynamics and XANES gives information about the valence state, energy bandwidth and bond angles.

The alteration of Bi-O bond and Bi-Fe bond distances upon doping BFM/BFO NPs are shown in Figure 4.19a-b. After deconvoluting the peaks from EXAFS spectra, we have calculated the Bi-O bond distances and also the relatively altered Fe-O, Fe-Bi and Fe-Fe bond distances. Within the first coordination shell, out of the four different Bi-O bonds the Bi-O $(1.1)_3$, Bi-O $(1.2)_3$ bond distances are zoomed in and shown in the right side of Figure 4.19. Upon Mn doping into BFO NPs there is not a big change in the four Bi-O distances, except a slight decrease of $(Bi\text{-}O)_{1.2}$ and $(Bi\text{-}O)_{1.3}$. This shows that doping by Mn does not alter the Bi-O distances significantly so there is no big effect on the polarization of BFO NPs into which Mn is incorporated. Whereas the Fe-O bond distances in one unit cell i.e., Fe-O $(1.1)_3$, and Fe-O $(1.2)_3$ decrease and increase, respectively, due to Mn-doping. This might be one of the major factors influencing the magnetic properties of BFM NPs, which is discussed in the “Magnetic chapter”.

Gd doping reduces the longer Bi-O bonds, whereas the Dy further reduces the longer Bi-O bonds. Similarly, Nd, Sm and La all three largely reduce the longer Bi-O bonds. The smaller Bi-O bonds are influenced non-linearly by RE-doping as can be seen in zoom-in graphs. Gd doping increases the $(1.1)_3$ bond distance as compared to BFM and BFO NPs, Dy also has slightly increased this particular bond, but it is still smaller than for pristine BFO NPs. The most reduction in this bond is generated by Nd-doping and also Sm-doping after La-doping. Interestingly, the $(1.2)_3$ Bi-O bond becomes shortest for the case of Gd-BFM, and longest for Dy-BFM NPs. As compared to BFM NPs La, Nd, and Sm have slightly reduced this bond distance. Relative to Bi-O bond distances, the Bi-Fe bond distances also get affected as can be seen in Figure 4.19a. This leads to lots of complex crystal structure modifications in the core level of these doped NPs. So, one can anticipate how complicated it could be to study the crystal structure at surface of these NPs. The crystal structure at surface can be studied by using Low energy electron diffraction (LEED). In LEED, the surface of a NPs is bombarded with low energy electrons which diffract off the surface. The diffraction depends on the crystallographic properties of the surface. This technique enables the surface structure, overlayer structure, lattice type, unit cell, point defects, bonding and the surface processes of a NPs to be determined.

Upon monovalent Ag doping into BFM NPs, the shorter Bi-O distances (Bi-O $(1.1)_3$ and $(1.2)_3$) slightly increase by 1 and 2 % with respect to BFO NPs, however the longer Bi-O distances (Bi-O $(1.3)_3$ and $(1.4)_3$) significantly decrease to 19% and 8% to BFO NPs, which alters the distorted-cuboctahedron and corresponds to an increment in polarization. Divalent Ca-doping into BFM NPs results in a decrement of all four Bi-O bond distances, 3%, 6%, 21%, and 18 % from the shortest to the longest, respectively. This makes the distorted cuboctahedron a bit more symmetrical and could bring Bi into the plane of the hexagon, which can explain the lower polarization for divalent cation doped BFM NPs. Similar results are also observed by us for Ba-doped BFM NPs. For trivalent Dy-doped BFM NPs, the bond distances change similar to the mono-valent case, however, here is a slight decrement of 0.5% for $(1.1)_3$, an increment of 2% for $(1.2)_3$, and again decrements of 17% and 7% for $(1.3)_3$, and $(1.4)_3$ distances, respectively. Changes in the crystal structure via the Bi-O bond distance may explain a higher piezoresponse in Ag-BFM NPs and Dy-BFM NPs and lower piezoresponse in Ca-BFM NPs as will be discussed in the “Catalysis Chapter 7”.

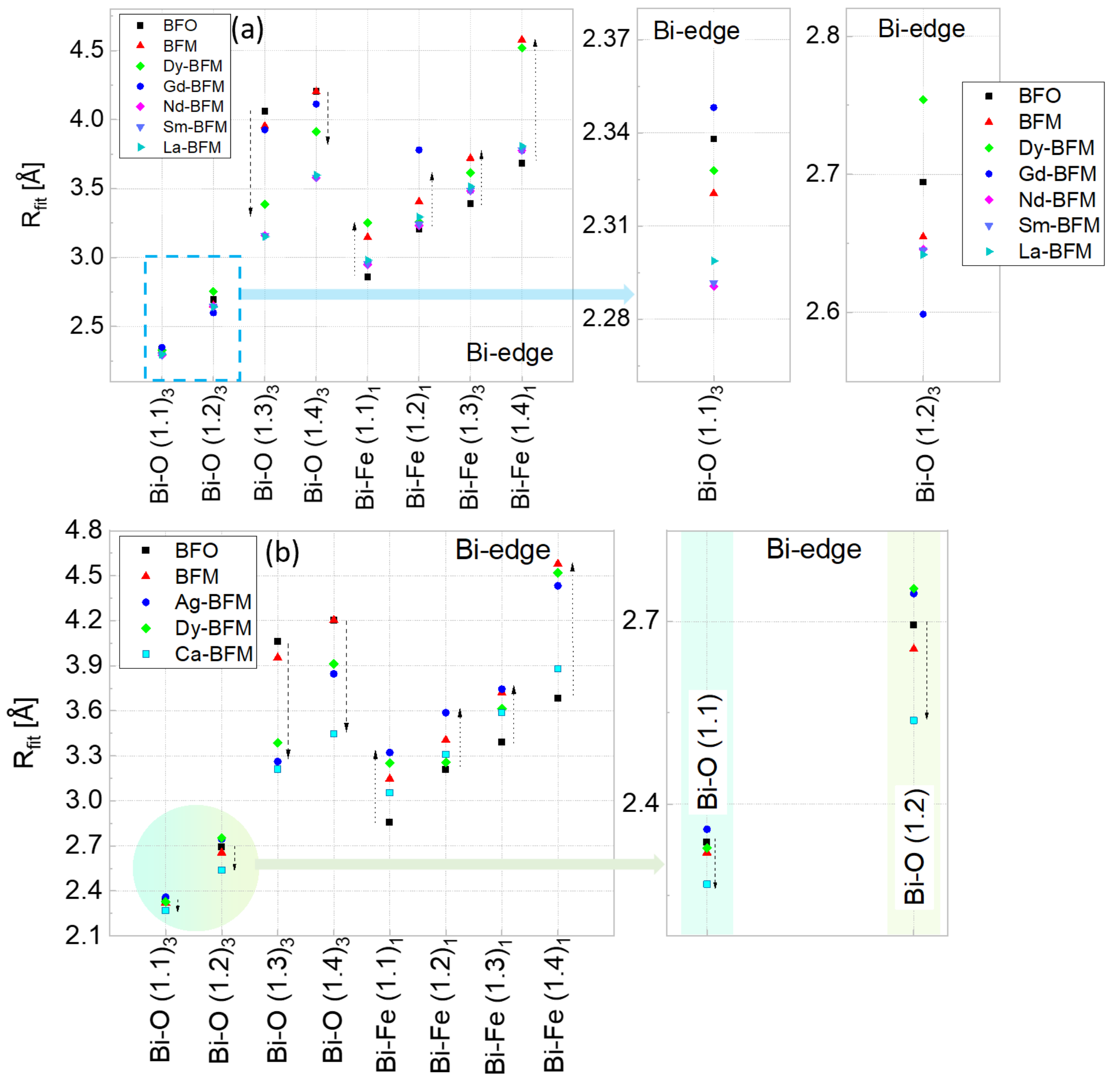

Figure 4.19: Bond length of Bi-O in doped BFO NPs calculated by EXAFS spectra. (a) for Lanthanide doped BFM NPs. (b) mono-, di-, and tri-valent cation doped BFM NPs. [Error bars are within the size of symbols]

The changes in the Fe-O bond distances are relative changes. The change in magnetic properties of MDT-doped BFM NPs will be discussed in “Magnetic Chapter 5”. These results show that divalent cations affect the crystal symmetry in a different way than monovalent and trivalent cations do. Thus, different types of dopants can be chosen for optimizing the required physical properties of BFO NPs.

These XRD and EXAFS results reveal: (i) Smaller Fe–O–Fe bond angles, which may lead to ferromagnetic configuration in doped NPs. (ii) Changes in Bi-Fe bond distances affected by distortion in BiO_{12} cuboctahedron due to doping (iii) distinct amount of BiO_{12} distortion due to doping, locally. These local units develop local ferromagnetism, which disrupts long-range antiferromagnetic order. In summary, we experimentally demonstrate the route to local and average ferromagnetism in doped BFO originating from a BiO_{12} distortion and reduced Fe–O–Fe (<133°) angle.

4.5 Morphology and Surface area of NPs

To probe the morphology and surface area of doped BFO NPs, we have utilised TEM, SEM, HR TEM, and BET-BJH. For the techniques see chapter 2 “Materials and Techniques”.

4.5.1 Particle size determination

From the previous chapter, we know that modified sol-gel synthesized BFO NPs acquire a rectangular shape with particle size of ~46 nm [Figure 3.5]. Upon Mn doping, the particle size reduces down to ~35 nm. Not only the morphology of the BFM NPs is not more rectangular, but they also even appear a more spherical as shown in Figure 4.20a. Further doping of MDT ions into BFM NPs, leads to reduction in particle size and changes in the morphology from elliptical (~18 nm) to distorted ellipse (~25 nm) to distorted pentagonal (~22 nm) for Ag, Ca and Dy doping respectively. The elemental distributions of the dopants and host elements are shown on the right side of Figure 4.20, which confirms that these dopants are homogeneously distributed within the particles.

The role of the amount of doping on the morphological properties of BFM NPs is shown in Figure 4.21. Doping by 1% Ba already causes changes in the morphology and provides more facets to the BFM NPs. The 1BBFM NPs is quite crystalline as shown in SAED and HRTEM image in Figure 4.21a. The particle size increases up to 40 nm due to 1% Ba doping, which can be due to larger sized Ba (1.61 Å) ion than Bi (1.45 Å). For 1BBFM NPs the photocatalytic properties are more interesting among Ba-doped BFM NPs as will be discussed in chapter 7 “Catalysis”, therefore we explored the size distribution from many different batches of this composition and found to have narrow size distribution and high reproducibility of the morphology and the size all the time as shown in Figure 4.22.

Further addition of Ba into BFM changes the overall morphology of particles, 2% Ba makes it more cuboidal with longer edges, and 3 % Ba reduces the longer edge making the particle more symmetrical, whereas 5% Ba doping results more octahedral particles with many facets but more symmetrical. We have defined the shape of Ba-doped BFM NPs based on images from different areas and have drawn a schematic shown on the right side of Figure 4.21. The addition of further Ba into BFM NPs causes a size reduction 5BBFM has the smallest size ~36 nm. The distribution of Ba and other elements in 5BBFM NPs are shown on the left side of Figure 4.21, where all elements are found to be homogeneously distributed.

The contradictory behaviour of size reduction upon larger ion (Ba^{2+}) doping can be due to presence of oxygen vacancies. Furthermore, the introduction of larger size dopants can promote the formation of new particles. The larger dopant atoms can act as nucleation sites, facilitating the formation of new nuclei and leading to the formation of smaller NPs. This enhanced nucleation may result in particle size reduction in the pristine NPs. Larger size dopants can potentially increase the rate of reaction, leading to faster nucleation and growth of NPs. This increased reaction rate can result in smaller particle sizes due to limited growth time before the reaction is terminated or quenched.

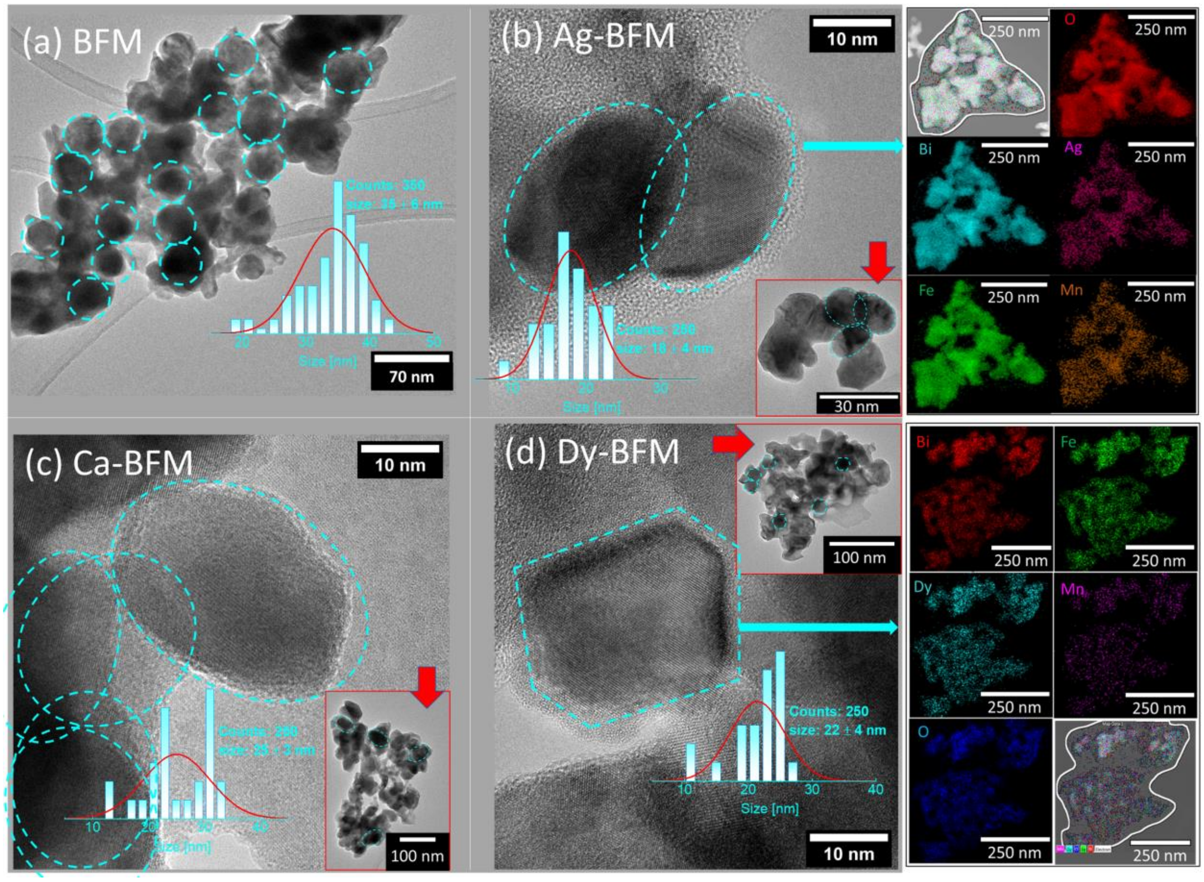

Figure 4.20: TEM image of BFM NPs (a). TEM images of Ag-BFM, Ca-BFM and Dy-BFM (b-d) respectively. In right side HAADF images of elements in Ag-BFM and Dy-BFM NPs. [© 2022 Advanced Functional Materials] [46]

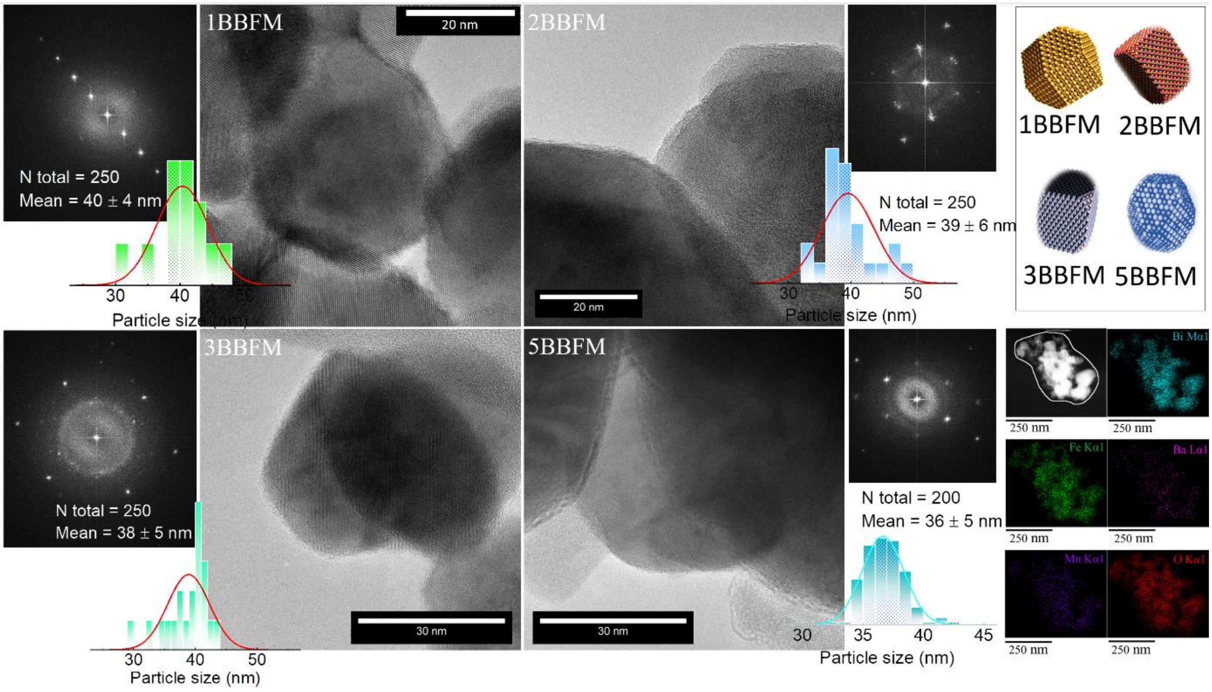

Figure 4.21: HR- TEM images of 1 to 5 mol % Ba doped BFM NPs, along with SAED pattern and the particle size distribution statistics.

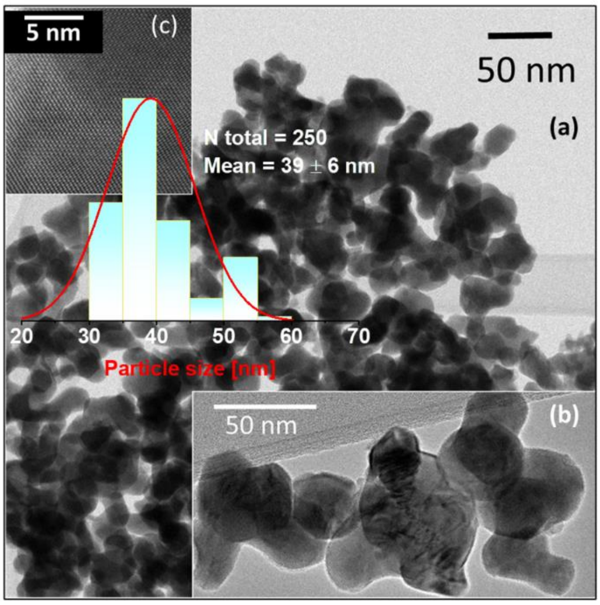

Figure 4.22: TEM images of 1BBFM NPs are shown in (a) and (b). The HR-TEM at 5 nm scale bar for 1BBFM (c). [© 2021 Nanoscale Advances] [150]

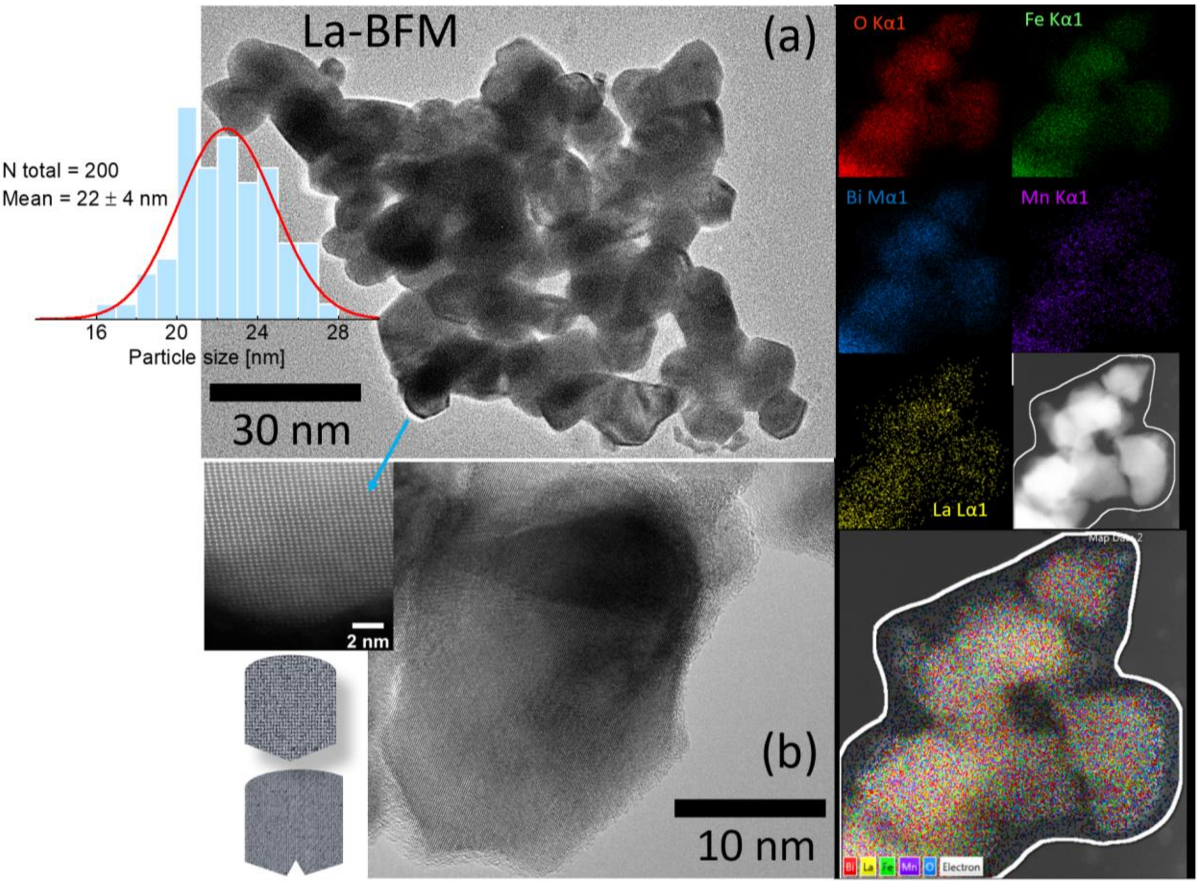

Figure 4.23: High-resolution TEM image of La-BFM NPs on the left side, the STEM image of edge of NPs. In the bottom graph the particle size distribution is shown from different areas. HAADF images for elemental distribution on the right side of image with an overlay.

The trivalent lanthanide doped BFM NPs were also studied under TEM to unveil the morphology and particle size distribution.

The TEM images of La doped BFM NPs are shown in Figure 4.23, where most of La doped BFM NPs have rectangular shape with triangular edges and that also split in some NPs as shown by schematics. La-BFM has an average particle size of ~22 nm, with a broader particle size distribution due to non-equal length and breadth. From the HAADF and dark field images of La-BFM NPs, the elements are quite homogeneously distributed within the selected particles.

The TEM images of Nd-BFM NPs are shown in Figure 4.24, where we observe that this dopant causes an irregular elliptical morphology to the NPs, where all ellipses are not of equal major and minor axes. The average particle size distribution is not narrow due to the irregular shape. Nd-BFM NPs are ~22 nm bigger in size, and the Nd dopant has been distributed evenly in the chosen set of particles.

The Sm doped BFM NPs consist of irregular octahedron morphology as shown by the schematic in Figure 4.25. The particles are crystalline as shown by the STEM image of one of the marked particles. Sm and other elements are found to be homogeneously distributed in the particles as shown in the selected agglomerate of ~25 particles. The average particle size of Sm-BFM NPs is 20 nm, which is slightly smaller than the La-BFM and Nd-BFM NPs. Among these NPs one can see the changes in the morphology just by doping La, Nd and Sm.

The Gd-doped BFM NPs have more regular rectangular morphology as compared to La-BFM. The TEM images of Gd-BFM are shown in Figure 4.26. The high crystallinity of the Gd-BFM confirmed by STEM image shown for the marked nanoparticle. The average particle size is bigger than for Sm-BFM, and also bigger than for La-BFM and Nd-BFM NPs. This can be due to different nucleation and growth mechanism for Gd doped BFM NPs than other RE-doped BFM NPs, as Gd^{3+} is the only ion with half-filled *f*-orbital among the selected RE-dopants.

The elemental distribution of Gd and other elements is confirmed by HADDF images shown on right side of Figure 4.26.

Hence, upon doping rare-earth dopants into BFM NPs, there is no large difference between the average particle sizes, but the morphology definitely changes upon different lanthanide doping as shown in quick comparison in Figure 4.27. The change in morphology can be due to different nucleation and growth mechanisms, among the synthesis of other doped BFM NPs. In addition, the presence of oxygen vacancies can lead to a deformation of the morphology and can also cause more irregular shapes. The facets of these NPs can be quite useful in terms of catalytic applications. In the context of NPs, a crystal facet refers to the exposed surface of a nanoparticle crystal that is characterized by a specific set of crystallographic planes. A crystal facet is a flat, well-defined, and geometrically regular surface that is formed during the growth of NPs as they arrange themselves in a crystalline structure. The arrangement of atoms or molecules on the crystal facets of nanoparticles determines their surface properties, such as reactivity, stability, and surface energy. Different crystal facets may have different chemical, physical, and electronic properties, which can influence the behaviour of NPs in various applications, including catalysis, sensing, drug delivery, and electronics.

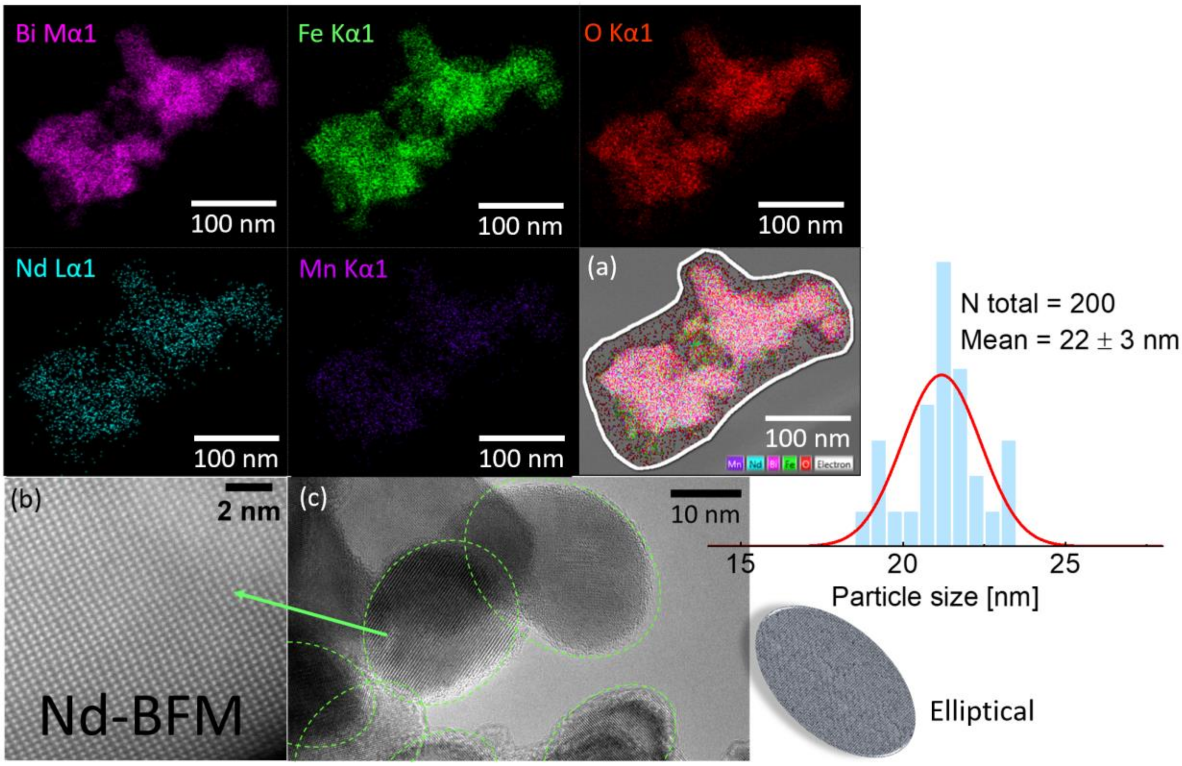

Figure 4.24: HAADF images for elemental distribution in right side of image with an overlay for Nd-BFM NPs. HRTEM image at the bottom (b-c). In right graph the particle size distribution is shown from different areas.

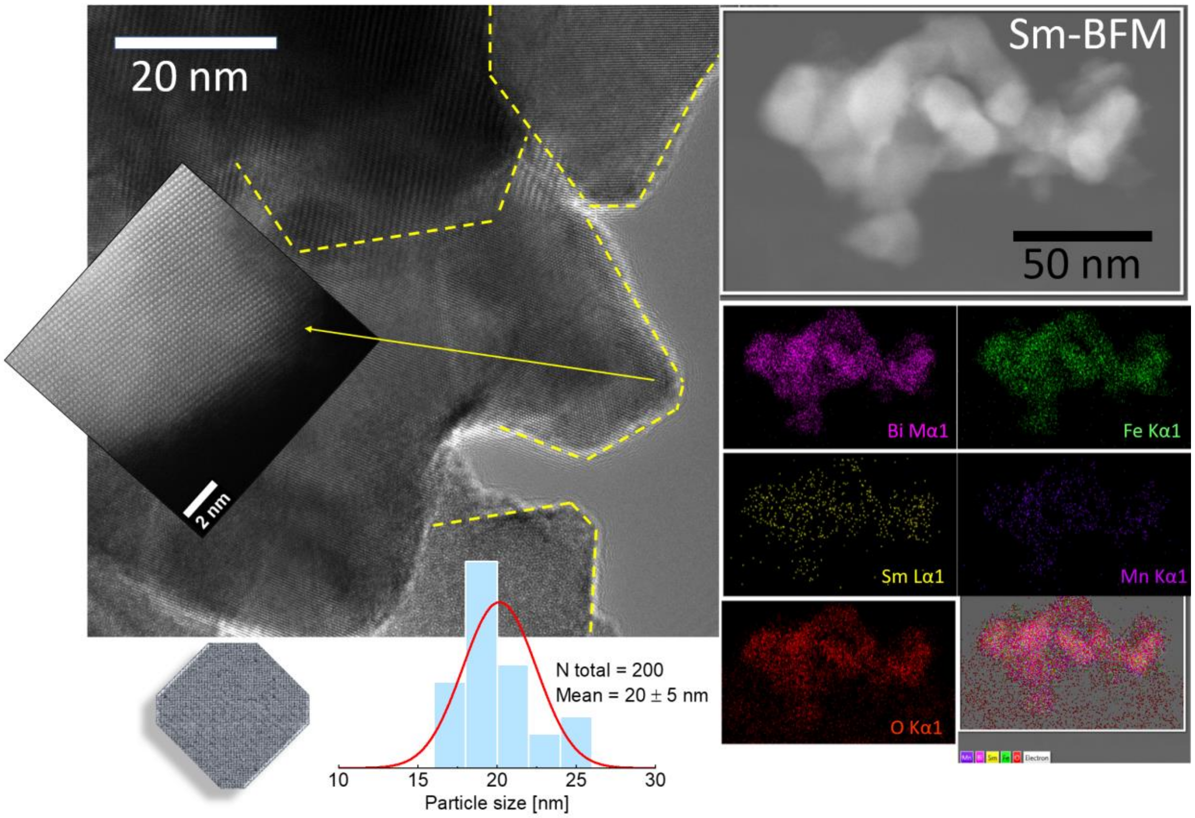

Figure 4.25: High-resolution TEM image of Sm-BFM NPs on left side, the STEM image of edge of NPs. In the bottom graph the particle size distribution is shown from different areas. HAADF images for the elemental distribution on the right side of the image with an overlay.

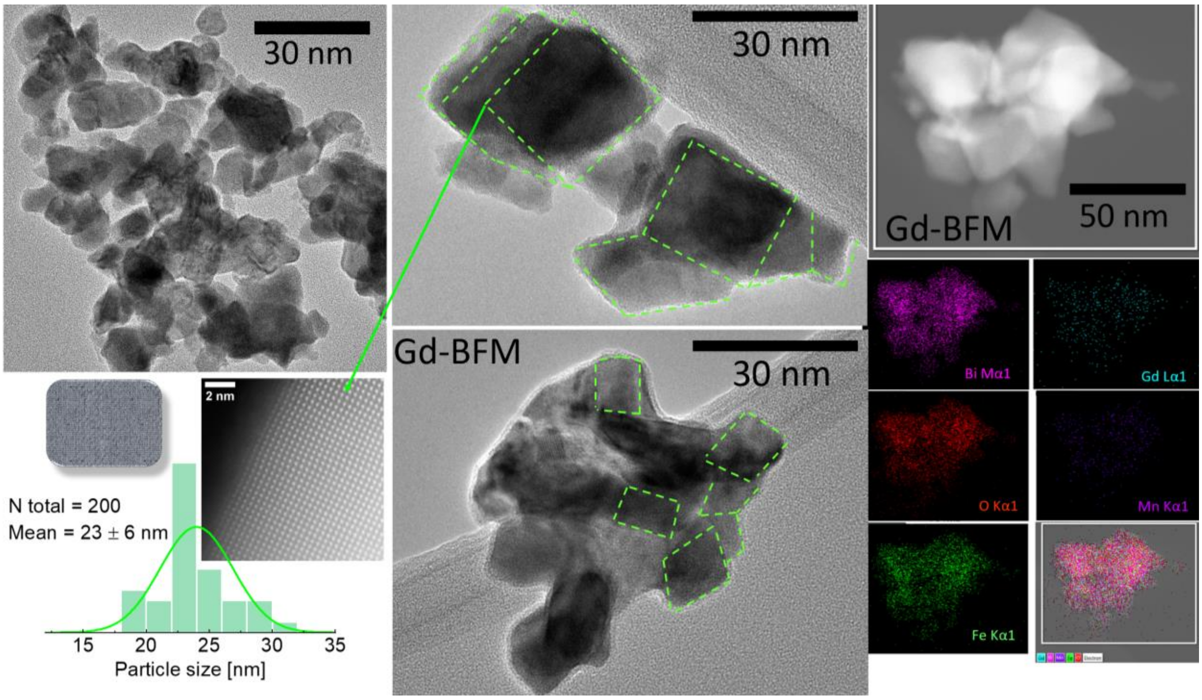

Figure 4.26: TEM image of Gd-BFM NPs on left side, and high-resolution images in the center. The STEM image of the edge of Gd-BFM NPs marked by a green arrow. The schematic of the individual particle morphology is nearly rectangular. In bottom left graph the particle size distribution is shown from different areas. HAADF images of Gd-BFM for elemental distribution are shown on right side of image with an overlay.

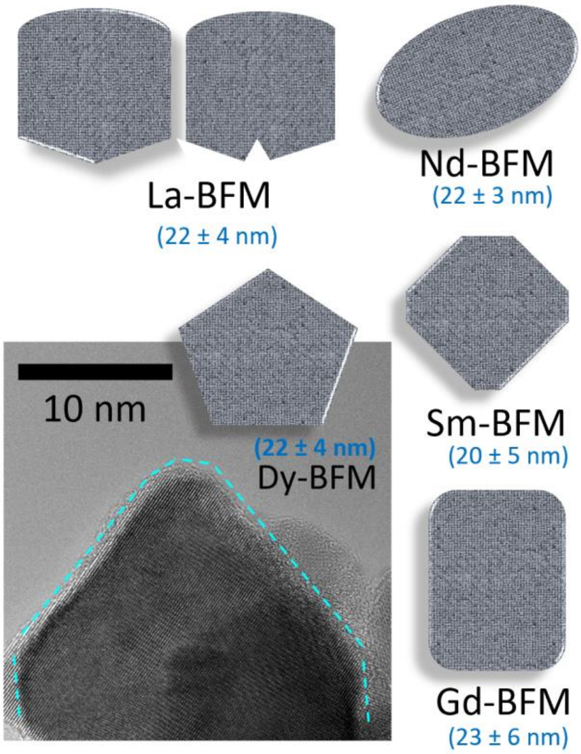

Figure 4.27: The estimated average morphology of lanthanides (La, Nd, Sm, Gd and Dy) doped BFM NPs.

The surfaces of NPs are composed of facets, which are specific crystal planes or facets that can have different arrangements of atoms. These facets can exhibit different surface energies, surface reactivity, and electronic properties, which can significantly impact the catalytic activity of NPs in various chemical reactions, including both catalytic reactions and photocatalysis.

Different facets of NPs can exhibit varying levels of catalytic activity due to several factors including the availability of active sites, surface reactivity, and electronic properties. For example, high-energy facets with a higher number of active sites, can have high surface reactivity leading to enhanced catalytic activity. In contrast, low-energy facets can lead to low surface reactivity may have fewer active sites, resulting in lower catalytic activity.[328–330]

There are different facets of Ba doped BFM NPs found using SAED images as shown in Figure 4.21. For instance, 1BBFM and 5BBFM are exposed with {012} facets compared 2BBFM and 3BBFM with {104} facets. Based on the photocatalytic activity of these doped NPs, the {012} facets provide higher surface reactivity and more active sites for the photoreaction discussed in the chapter 7 “Catalysis”.

Similarly, involving the use of NPs to facilitate light-driven catalytic reactions, facet-dependent activity has been reported.[329] For example, in photocatalytic water splitting, where water is split into hydrogen and oxygen using light energy, it has been found that different facets of semiconductor NPs, such as titanium dioxide (TiO_2), exhibit varying photocatalytic activity. For instance, TiO_2 NPs with {001} facets show higher photocatalytic activity compared to those with {101} facets, as the {001} facets provide better charge separation and transfer properties, leading to more efficient photocatalysis.[330] Understanding the facet-dependent activity of NPs can enable the design and engineering of NPs with enhanced catalytic performance for various applications.

There are several other factors that can contribute to a size reduction of the NPs and changes in morphology when doping is involved. The size and chemical properties of the dopant material can also play a role in determining the size and morphology of NPs. Smaller dopant ions or atoms can substitute into the NP lattice more easily, leading to smaller NPs. The chemical properties of the dopant, such as its electronic configuration, can affect the crystalline structure and surface energy of the NPs leading to changes in size and morphology. The concentration of the dopant material used during the synthesis of NPs can significantly impact the size and morphology of the resulting NPs. Higher dopant concentrations can lead to smaller NPs due to increased nucleation and growth rates, resulting in finer morphology.

4.5.2 Specific surface area and pore volume

The surface area of the NPs affects the number of active sites available for the reaction. Therefore, the larger the surface area of the NPs, the higher the catalytic activity. In NPs, a larger proportion of their atoms are located on their surface. This leads to a higher density of catalytic sites. Additionally, the small size of NPs allows for a greater degree of surface atom rearrangement, which can lead to increased reactivity and selectivity. NPs with a high aspect ratio (i.e., a high ratio of length to width) have a larger surface area per unit volume than those with a low aspect ratio.

Agglomeration of Nanoparticles

However, when NPs agglomerate, the surface area per unit mass decreases as the total surface area of the agglomerate is less than the sum of the surface areas of individual NPs. Agglomeration can occur due to various reasons such as van der Waals forces, electrostatic interactions, or gravitational forces, among others. Agglomeration can also affect the physical and chemical properties of NPs, such as their surface chemistry. These changes can further impact their catalytic activity and selectivity, as well as dispersibility and stability. To prevent agglomeration and maintain the surface area of NPs, various techniques can be employed such as surface modification, stabilizing agents, and control of processing conditions. These techniques can help to maintain the dispersion and stability of NPs, prevent agglomeration, and preserve their catalytic activity. Potentially at the cost that stabilizes themselves affect the surface state.

Nanoscale particles exhibit distinct characteristics compared to larger particles, as they tend to agglomerate more readily. Agglomerates are macroscopically perceived as a single particle, but they can break down into their primary particles. These primary particles can have different geometric forms, such as spherical, cuboidal, or pentagonal, as seen in doped BFM NPs. Primary particles typically agglomerate to form larger units through weak physical interactions, such as adhesion at the corners or edges, resulting in the formation of agglomerates, or aggregates. The total surface area of agglomerates is not significantly different from the sum of the specific surface areas of the primary particles, as shown in Figure 4.28b. Larger agglomerates can further break down into smaller agglomerates or smaller agglomerates can stick to form larger ones upon loner ultrasonication, depending on the size distribution of the primary particles (assuming similar geometry and chemical composition).

Aggregates of Nanoparticles

Aggregates form when primary particles begin to crystallize and develop a common crystalline structure. Aggregates are formed by the fusion of primary particles, which grow together and align side by side, resulting in a reduction of the total specific surface area compared to the sum of the surface areas of the primary particles. For example, five primary particles may form an agglomerate through adhesion, which then converts into a larger aggregate when crystal growth occurs. Although the original geometry of the primary particles is still discernible in the aggregate, the particles are fused together. The specific surface area of an aggregate is smaller than the sum of its original primary particles. The schematic of aggregation is shown in Figure 4.28c.

To differentiate between agglomerates and aggregates, nanoscale particles are transferred into aqueous or alcoholic suspension and examined using TEM after ultrasonic treatment. Ultrasonic treatment for 10 minutes leads to a significant increase in the number of agglomerates on a defined area under TEM, with, for example, 10 agglomerates observed before ultrasonic treatment becoming 100 agglomerates after treatment. In other words, larger agglomerates break down into smaller agglomerates. Agglomerates tend to deagglomerate in aqueous solutions. From the TEM studies and SEM images in Figure 4.29, we can say that the BFO and doped BFO NPs synthesized by the modified sol-gel method are agglomerated instead of aggregated. As also confirmed by ultrasonication testing under TEM. From Ba doped BFM NPs the SEM images unveil the large agglomeration and also there are many pores visible in between these agglomerates. The study of pore size is essential for catalytic applications, which we will discuss later.

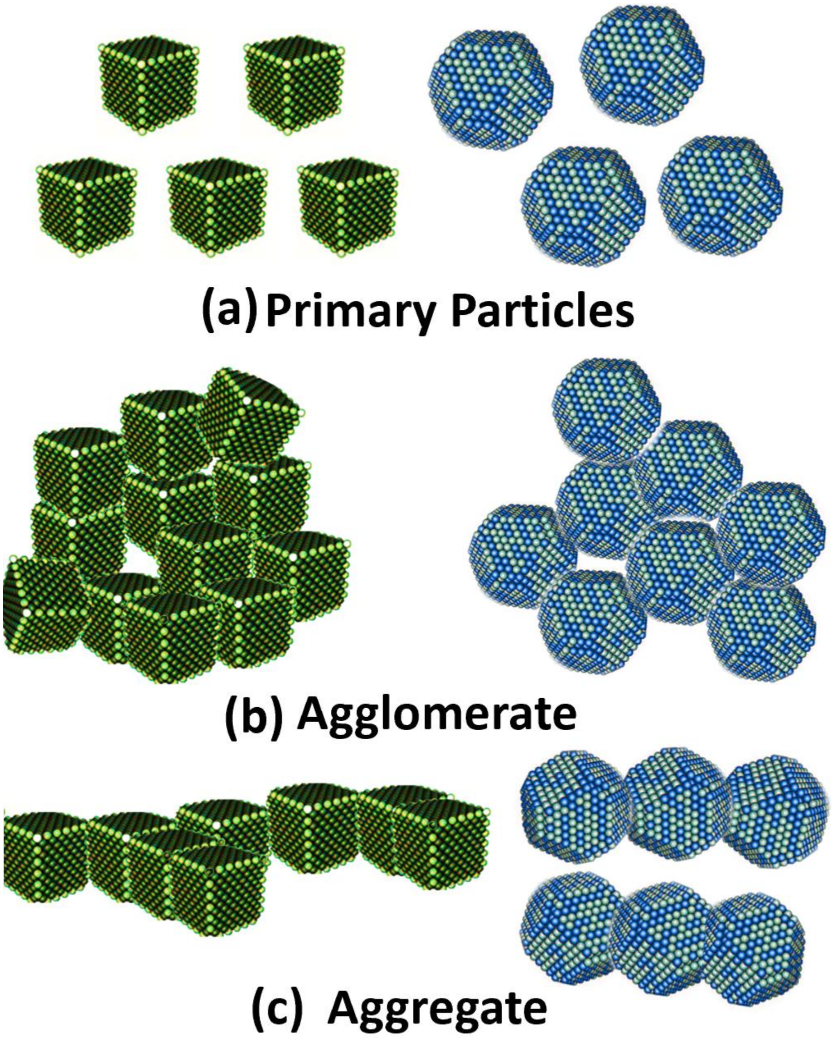

Figure 4.28: The difference among agglomerates and aggregates from primary particles of cuboidal and spherical shapes. (Here agglomeration by physical interactions of primary particles leads to form agglomerates, whereas aggregates are formed by temperature treatment of primary particles causing an assembly of primary particles that have grown together and are aligned side by side.)

The general behaviour of primary particles, particularly their tendency to agglomerate, increases as the particle size decreases.[331] Solubility also generally increases with decreasing particle size.[331–333]

Specific surface area of nanoparticles

Doping BFO and BFM NPs leads to an alteration in the overall specific surface area. The trend of surface area is plotted in Figure 4.30. From Figure 4.30a, we observe that Mn doping in BFO NPs slightly reduces surface area that can be due to large agglomeration in BFM NPs.

Further 1% Ba doping into BFM NPs causes a sudden increase in the surface area that can be due to less agglomeration of 1BBFM as compared to BFKM NPs. Further doping of Ba leads to slightly reduce surface area but still for 5BBFM the surface area is larger than for BFM NPs. This shows that Ba doping leads to reduced agglomeration and increases the specific surface area of the NPs.

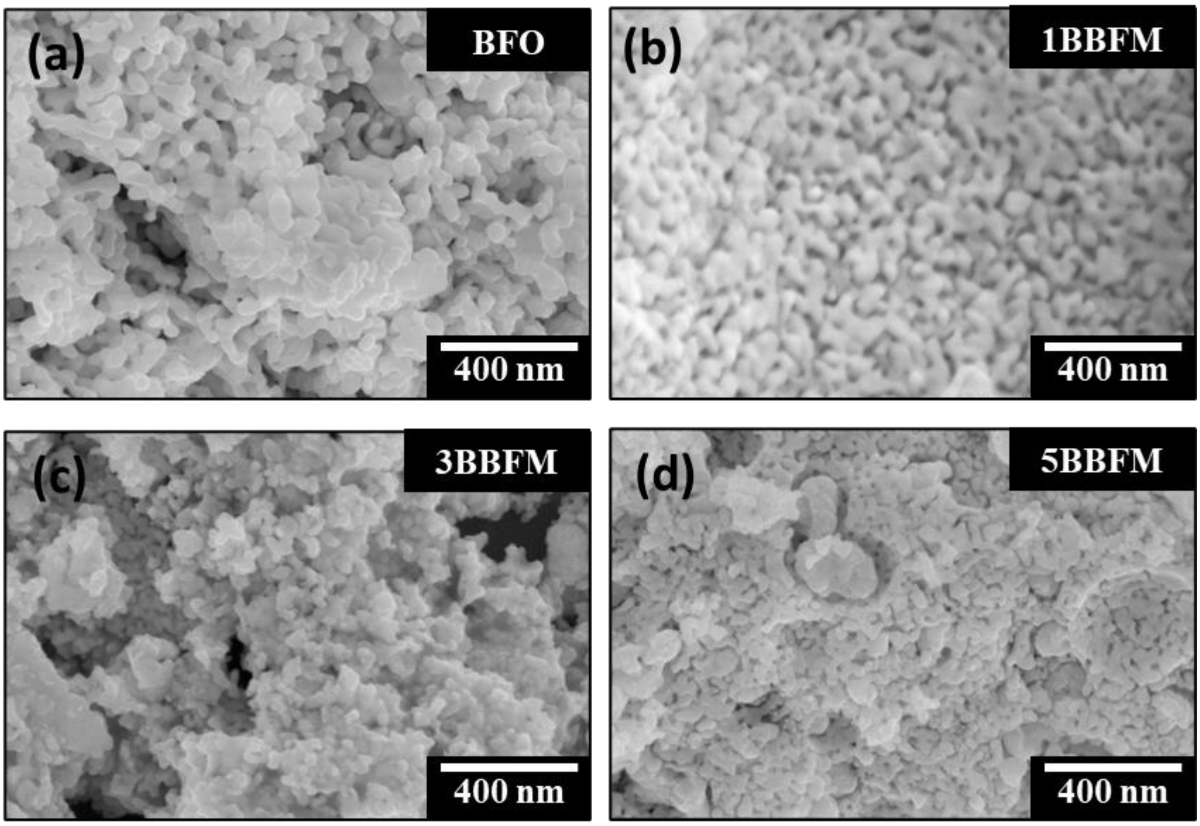

Figure 4.29: SEM images of undoped and Ba and Mn co-doped BFO NPs. [© 2021 Nanoscale Advances] [150]

The MDT doping in BFM NPs also increases the specific surface area of BFM NPs Figure 4.30b. These MDT doped BFM NPs are utilised as piezo-photocatalysts (see chapter 7 "catalysis"). Trivalent Dy-BFM has the largest surface area among the MDT doped BFM NPs. The rare earth doped BFM NPs exhibits larger surface area than BFM itself as shown in Figure 4.30c. All rare-earth and MDT doped BFM NPs are utilised as electrocatalysts of hydrogen evolution reaction (HER) discussed in chapter 7 "catalysis". Among the RE-doped BFM NPs, still Dy-BFM has largest specific surface area, and interestingly Ca-BFM has larger surface area than other RE-doped BFM NPs, which is due to less agglomeration in divalent doped BFM NPs. However, we it important to note down that smaller particle are expected to have larger surface area, so Dy-BFM NPs has smaller size than Ca-BFM, but still the size of Ag-BFM is larger than Dy-BFM, though its specific surface area is less than Dy one due to larger agglomeration in Ag-BFM NPs.

Pore size distribution and pore volume

Pore volume refers to the amount of space inside the NPs that is available for other molecules or particles to occupy. NPs with high pore volume can have a larger surface area available for reactions, which can enhance their catalytic activity. However, NPs with high pore volume can also be more prone to agglomeration due to the increased likelihood of NP-NP interactions. The relation between pore volume and agglomeration in metal oxide NPs is complex and depends on several factors such as the size, shape, and surface chemistry of the NPs, as well as the surrounding environment.

Generally, the pore volume of an NP increases with increasing pore size. The relationship between pore size and pore volume can be influenced by the shape and structure of the NPs. For example, NPs with a high density of small, interconnected pores may have a larger pore volume than a nanoparticle with larger, isolated pores of the same total volume. This is because the interconnected pores occupy a greater volume of space within the NP than the isolated pores. So, the relationship between pore size and pore volume of NPs depends on the type and density of pores present in the NP, as well as the overall shape and structure of the NP.

There is typically a relationship between pore size and surface area in NPs. In general, the smaller the pore size, the greater the surface area of the NPs. This is because smaller pores create more surface area per unit volume than larger pores. NPs with a high density of small pores will have a greater surface area than NPs with the same volume but fewer and larger pores. This is because the small pores create more surface area on the interior of the nanoparticle, which is accessible to the surrounding environment. However, it's important to note that the relationship between pore size and surface area is not always straightforward and can be influenced by other factors, such as the shape and structure of the NPs. Additionally, some types of pores, such as closed pores, may not contribute to the surface area of the NPs at all. The pore volume and pore size distribution of a porous material can affect the diffusion and transport of NPs within the material. The size of the pores can have a significant impact on the catalytic activity of a material.

In general, smaller pores tend to be more beneficial for catalysis than larger pores. Micropores, which have a diameter of less than 2 nm, are particularly beneficial for catalysis. This is because the small size of the micropores allows for a higher surface area-to-volume ratio, which means that there are more active sites available for catalysis. Additionally, the small size of the micropores can create a confined environment that can enhance the selectivity of the catalytic reaction by preventing unwanted reactions.

Mesopores, which have a diameter of 2-50 nm, can also be beneficial for catalysis, but to a lesser extent than micropores. The larger size of the mesopores means that there are fewer active sites available for catalysis, but the larger pore size can allow for easier diffusion of reactants and products, which can increase the overall reaction rate.

Macropores, which have a diameter of more than 50 nm, are generally not beneficial for catalysis. The larger pore size means that there are fewer active sites available for catalysis, and the diffusion of reactants and products is not significantly enhanced by the larger pore size. The method of Barrett, Joyner, and Halenda (BJH) is a procedure for calculating pore size distributions from experimental isotherms using the Kelvin model of pore filling. It applies only to the mesopore and small macropore size range. The BJH method is suitable for the treatment of cylindrical pore models with a pore diameter larger than 5 nm. When calculating pores with a diameter of less than 5 nm by BJH method, a 20 % error is generated. While for a diameter less than 10 nm, the pore size can be underestimated. Therefore, it is not suitable to use the BJH method when analysing fine micropores. However, Mercury intrusion porosimetry can also be used, this technique involves applying a known amount of pressure to the nanoparticles with mercury and measuring the volume of mercury that enters the pores. The porosity can be calculated from the volume of mercury that enters the pores per unit pressure yielding the pore size distribution.

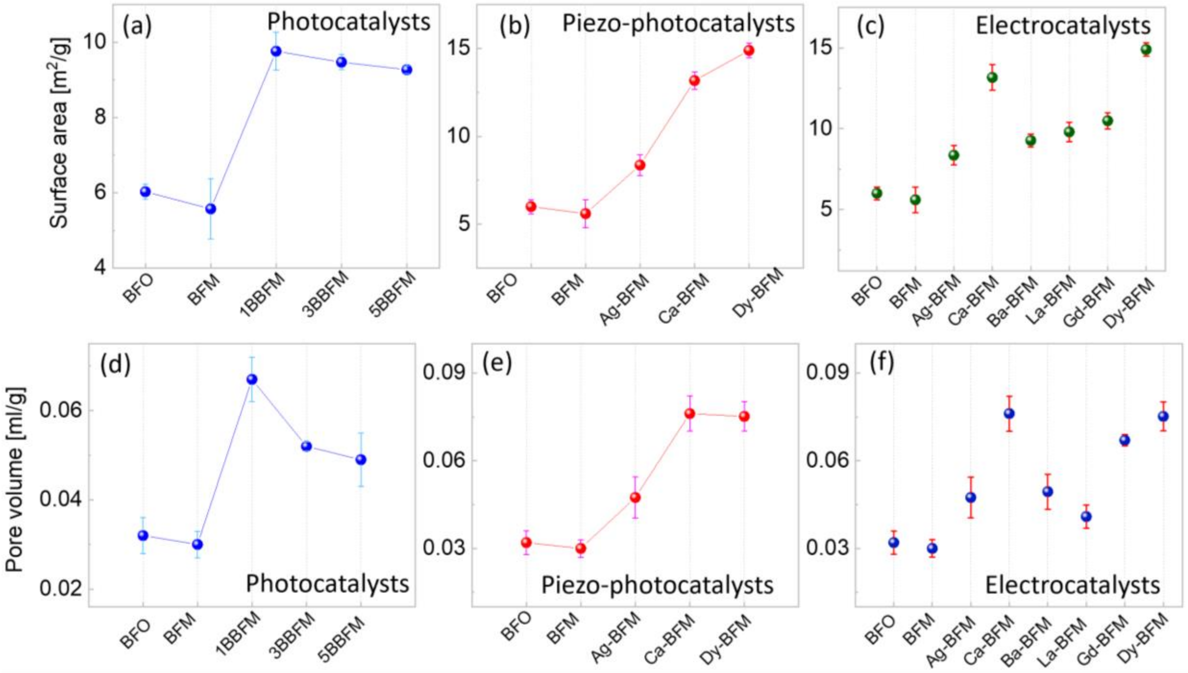

Figure 4.30: Surface area trend of NPs. Photocatalysts: 1-5 mol % Ba doped BFM NPs (a). Piezo-photocatalysts: Ag, Ca and Dy doped BFM NPs (b). Electrocatalysts: doped-BFM NPs and undoped BFO NPs (c). The pore volume of NPs (d-f). Photocatalysts: 1-5 mol % Ba doped BFM NPs (d). Piezo-photocatalysts: Ag, Ca and Dy doped BFM NPs (e). Electrocatalysts: doped-BFM NPs and undoped BFO NPs (f).

The pore volume of NPs is shown in Figure 4.30d-f. The trend of divalent doping amount into BFM NPs is shown in Figure 4.30d, where we observe that 1BBFM has the largest pore volume among pristine BFO/BFM and the other Ba doped BFM NPs. The pre volume reduces upon further doping of Ba into BFM NPs. in MDT doped BFM NPs, we observe larger pore volume for Dy-BFM and Ca-BFM than Ag-BFM and BFM itself, and for the case of lanthanide doped BFM NPs, there is not a linear trend of pre volume. La-BFM has less pore volume as compared to Gd-BFM and Dy-BFM NPs. The Dy-BFM and Ca-BFM NPs has largest pore volume among all doped BFM NPs.

The pore size distributions are shown in Figure 4.31, using BJH modelling. It is evident that the BFO NPs possess pore size ranging around 50 nm with a broad distribution of pore size as indicated by the large full width at half maximum (FWHM). With Mn doping, there is a slight decrease in pore size, but there still remains a considerable distribution of mesopores resulting in a smaller pore volume overall.

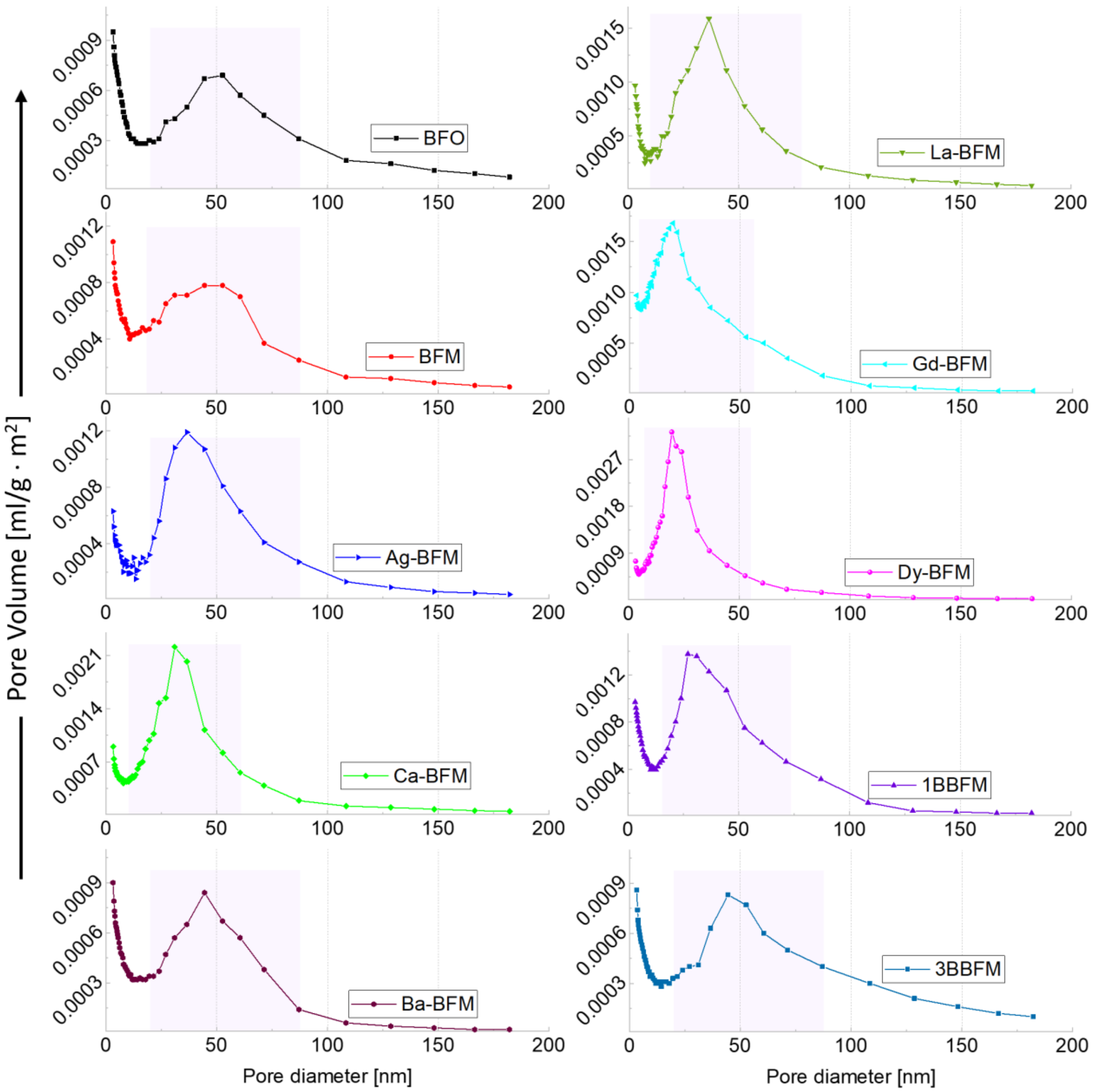

Figure 4.31: The pore size distribution (PSD). Pore volume versus pore diameter curves of undoped and doped BFO NPs based on the BJH model.

Intriguingly, upon Ag doping, the pore size distribution of BFM NPs becomes narrower, which leads to an increase in pore volume due to a small reduction in average pore sizes. Doping with divalent Ca leads to a sudden increase in pore volume, which is attributed to the narrower pore size distribution (smaller FWHM than Ag-BFM) and smaller pores compared to

Ag-BFM NPs. However, divalent Ba results in a broader pore size distribution with larger pore size even than Ag-BFM, leading to a reduction in total pore volume. This can potentially be due to significant agglomeration in Ba-BFM NPs. In contrast, trivalent La doping in BFO NPs also results in a broad pore size distribution of mesopores around 50 nm. Nonetheless, doping with Gd and Dy individually into BFM NPs causes a narrow pore size distribution similar to Ca-BFM NPs, with pore sizes smaller than those in Ca-BFM NPs. As a result, the total pore volume of these trivalent-doped BFM NPs is sufficiently large.

4.6 Conclusion

In this chapter, the structural changes in BFO NPs have been widely explored due to doping. The doping has been explored from single doping at Bi-and Fe-sites to co-doping from different group of elements from the periodic table including alkaline earth metal, transition metals, and rare-earth lanthanide metals. Foremost we find that the tolerance factor of BFO NPs alters the cause of the mismatched ionic radii of these dopants, which influence the local and long-range ordering in doped BFO NPs.

The presence of dopants was confirmed based on EDX and HAADF. All the doping and host elements are homogeneously distributed within the NPs. The confirmation of the oxidation states of the elements is done using XPS. At the surface of NPs, Bi^{3+} and Fe^{3+} are confirmed using 4*f* XPS spectra of Bi and 2*p* XPS spectra of Fe. For the core level oxidation states confirmation, we have utilised EXNES, which also confirms presence of Bi^{3+} and Fe^{3+} in the bulk of the samples.

The presence of the Jahn-teller cation (Mn^{3+}) is found on the surface of NPs, mostly in BFM NPs, Ag-BFM, Ca-BFM, and Ba-BFM NPs. The trivalent cation doped BFM NPs mainly consist of the Mn^{4+} ion even on the surface. EXANES confirms the presence of Mn^{4+} ion in the bulk of NPs. The results show the different chemical environment of NPs on the surface as compared to its bulk.

The oxygen vacancy was estimated using XPS spectra of O 1*s* for all NPs. We find that small amount of oxygen vacancy of BFO NPs reduces upon single doping of Mn, Ba, and Co. Upon mono-, di-, and tri-valent cation doping into BFM NPs, we find that divalent Ba causes increase in oxygen vacancy concentration, but Ca does not. The trivalent Gd also causes formation of oxygen vacancies, and Dy-BFM shows large peak associated with surface absorbed oxygen which can also affiliated to oxygen vacancies.

The crystal structure was solved using XRD, and EXAFS. All NPs consist of a single phase with rhombohedral crystal structure. Rietveld refinement show that the lattice parameters and corresponding unit cell volume get largely affected due to larger sized Ba doping in the BFO NPs at Bi-site, as compared to only Co and Mn doping at Fe-site. Further co-doping of the ion at Bi-site in BFM NPs leads to a decrease in hexagonal UCV.

The crystallite size of doped BFM NPs is found to be smaller than BFM itself, except for the 1BBFM case. There is an inversely proportional relation between crystallite size and microstrain in doped BFM NPs. The highest microstrain is found in Ag-BFM and Sm-BFM NPs.

The Fe-O-Fe bond angle gets reduced from 133° to 131° due to Gd doping in BFM NPs. The reduction in Fe-O-Fe bond angle can cause an increment in magnetic properties of doped BFM NPs. The local Bi-O bond distances are calculated using EXAFS spectra, where the BiO_{12} cuboctahedron plays a crucial role for ferroelectric properties of BFO NPs. The two shorter and two longer bonds of Bi-O in the BiO_{12} cuboctahedron were affected largely and differently for each dopant. The Bi-O $(1.1)_3$ bond is largely shortened by Nd, Sm doping but becomes longer for Gd doping. The Bi-O $(1.2)_3$ bond get shortened due to Gd doping and becomes longer for Dy doping. Whereas the La, Sm and Nd dopings shorten the Bi-O $(1.3)_3$ and Bi-O $(1.4)_3$ bonds in the BiO_{12} cuboctahedron of BFM NPs, which has similar bond distance as BFO NPs. The monovalent dopant shortens Bi-O $(1.3)_3$ and Bi-O $(1.4)_3$ bonds but does not significantly affect the shorter bonds of BiO_{12} cuboctahedron. However, the divalent cation dopants shorten the Bi-O $(1.1)_3$ and Bi-O $(1.2)_3$ i.e., shorter bond of BiO_{12} cuboctahedron as well as the longer Bi-O $(1.3)_3$ and Bi-O $(1.4)_3$ bonds too. This alteration in bond distances can explain the changes in ferroelectric and piezoelectric properties of doped BFM NPs see in chapter 7 “catalysis” PFM results.

We find that doped BFM NPs consist of different morphology and size, from spherical to pentagonal to elliptical. The different morphologies and average sizes of these NPs affect the specific surface area and pore size distribution, which can be crucial to explain the catalytic activity of doped BFM NPs. Of course, the different morphologies of doped BFM NPs lead to different magnetic anisotropy, which can be interesting to explain the magnetic properties of doped BFM NPs.

Magnetism in doped-BFO NPs

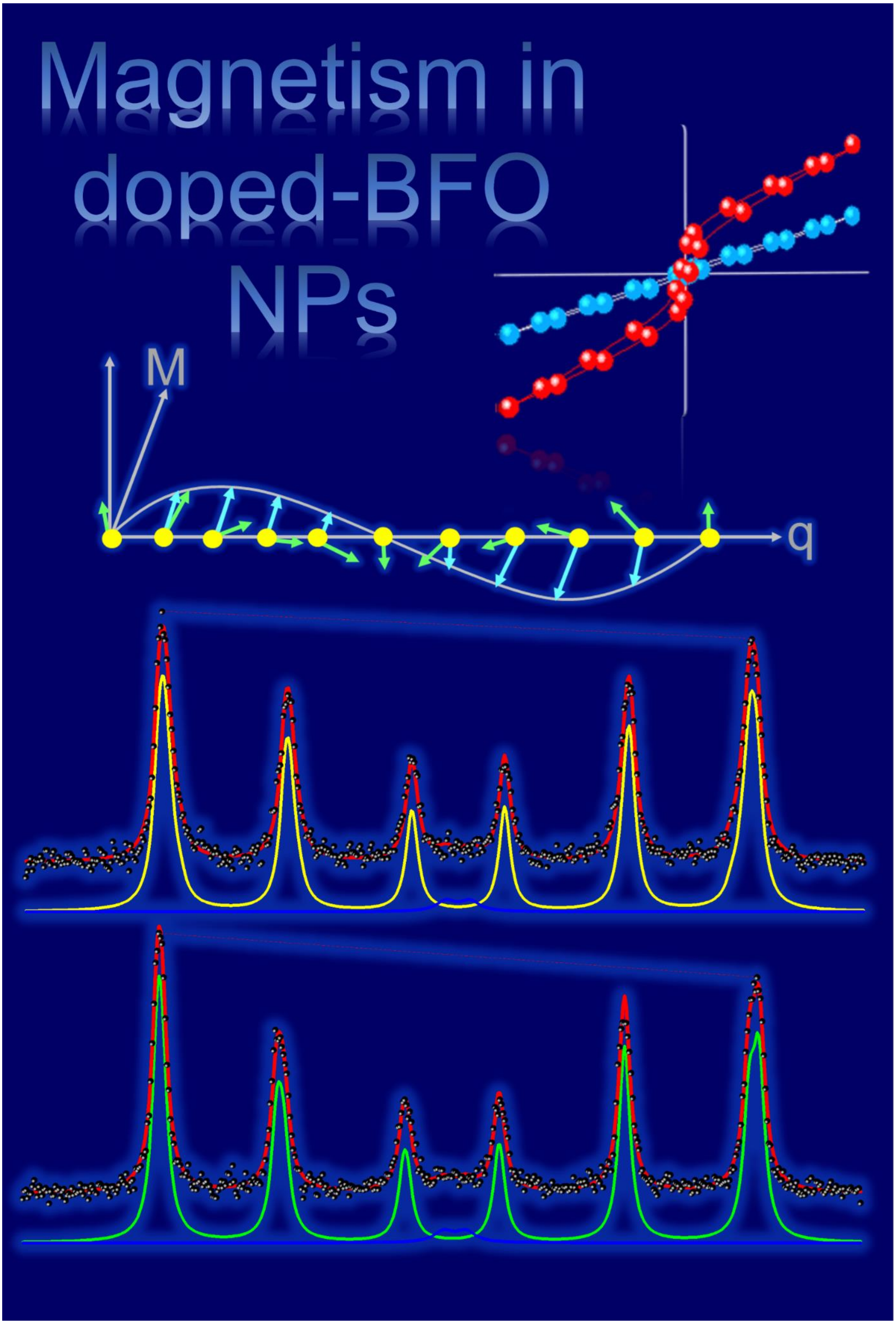

5 Magnetism in doped BFO NPs and hyperthermia studies

5.1 Introduction

The magnetic properties of BFO NPs are particularly intriguing and can be manipulated by the application of temperature,[315,334] pressure,[335] and electric fields[336,337]. This makes it a promising candidate for use in the development of magnetic tunnel junctions (MTJs), which are crucial building blocks of spintronic devices such as magnetic random-access memories (MRAM).[338] In an MTJ, a thin layer of BFO act as a spin filter controlling the flow of spin-polarized electrons between two magnetic electrodes. The spin-orbit coupling of BFO leads to the Rashba effect,[339] which allows for the manipulation of the spins of the electrons in a controllable manner.

Unfortunately, BFO NPs only exhibit weak effective magnetisation due to the antiferromagnetic ordering,[68] which limits its direct use in many magnetic applications.[68,71] Nevertheless, the magnetisation of BFO can be increased by introducing different types of dopants (magnetic or nonmagnetic), for example; Mn, Co, and Ni or Ba, Ca and La. In literature the increase of remanent magnetization of BFO NPs due to doping are explained by the Fe-O-dopant exchange interaction.[185,187,229,230,340–344] Dopants like Ca, La, Sc, and Zn, into BFO NPs have been shown to significantly impact their magnetic properties.[185] The increase in magnetisation upon lanthanides (like Gd, La and Dy) doping in BFO NPs has also obtained significant interest in recent years.[345–349] In Table 1,[187,230,340–343,350] the introduction of magnetic and non-magnetic ions shows increase of the magnetization of the BFO NPs. For 54 nm sized pristine BFO NPs, the remanent (M_r) and maximum magnetization ($M_{\max}$) values are reported 0.051 Am^2kg^{-1} and 0.474 $A\ m^2kg^{-1}$ (0.027 µB/Fe), respectively.[68]

Table 1: Comparison of M_r/M_{max} ratio in single-doped and co-doped BFO NPs.

Doped BFO NPs	Size (nm)	$M_r/M_{\max}$	Reference
$Bi_{0.9}Dy_{0.1}FeO_3$	300-600	5.5	[348]
$Bi_{1-x}Dy_xFeO_3$	30-70	0.47	[349]
$Bi_{1-x}Nd_xFeO_3$	26-74	0.44	[351]
$Bi_{1-x}La_xFeO_3$	100	0.19	[352]
$Bi_{1-x}Ba_xFeO_3$	50-200	0.76	[353]
$Bi_{1-x}Gd_xFeO_3$	21-34	2.23	[345]
$Bi_{1-x}Gd_xFeO_3$	42-59	0.1	[346]
$BiFe_{1-x}Mn_xO_3$	50-100	0.04	[354]
$BiFe_{0.95}Co_{0.05}O_3$	39	0.42	[355]
$Bi_{1-x}Ba_xFe_{1-y}Nb_yO_3$	32	0.36-2	[356]
$Bi_{1-x}Ca_xFe_{1-y}Co_yO_3$	20-70	0.81	[357]
$Bi_{0.8}La_{0.2}Fe_{1-y}Co_yO_3$	50	0.57	[347]
$Bi_{1-x}Gd_xFe_{1-y}Co_yO_3$	60	0.37-2	[358]
$Bi_{1-x}Sm_xFe_{1-y}Mn_yO_3$	16	0.17-5	[359]

Upon doping, the increment in magnetic properties of BFO NPs can be due to many factors. The foremost factor is the superexchange interactions between the magnetic ions at the Fe-site from antiferromagnetic to ferromagnetic crossover, e.g., from Fe^{3+}-O-Mn^{3+} to Fe^{3+}-O-Mn^{4+}, respectively.[10] One additional reason is the variation of the Fe-O-Fe bond angle by a few degrees due to doping, which can influence super-exchange interactions[360] i.e., far from the crossover between antiferromagnetic (153°) and ferromagnetic exchange that occurs usually below 133°.[325] As per EXAFS and XRD results, the Fe-O-Fe bond angle is found to be around 133° for BFO NPs, which develop local ferromagnetism and suppose to disrupts the long-range antiferromagnetic ordering.[361] BFO NPs synthesised in this work, also exhibit average Fe-O-Fe bond angle around 133° see chapter 4, Figure 4.18.

Second reason can be alteration in the magnetic anisotropy due to the different morphologies of doped BFO NPs.[315] Third can be due to distortion in the crystal structure and the developed microstrain cause of reduced crystallite size, which may cause modification of incommensurate magnetic spin cycloid.[10] Pristine BFO NPs of size ~54 nm maintain the cycloidal spin modulation despite the fact that their size is below the period of the modulation in bulk, 62 nm.[69] However, dopants can suppress or distort the spin cycloid,[10] or cause further canting of local spins. Fourth is the presence of uncompensated spins at the surface of NPs due to reduced particle size.[64] The surface and interface of the NPs can significantly contribute to the net magnetic moment. In addition, the presence of defects such as oxygen vacancies can also contribute to an increase in magnetisation via the formation of the Fe^{2+} state for the overall charge compensation in the NPs. Another mechanism for the improvement of magnetic properties is the formation of structural defects in the crystal lattice. The dopant ions can introduce vacancies and interstitials, leading to structural defects. The creation of magnetic clusters can also be one of the reasons, which still needs discussion.[27] The dopant ions aggregate to form magnetic clusters, thereby enhancing magnetic ordering.[362–364]

The effect of doping at the Bi- site and Fe- site on the magnetic properties of BFO NPs has not been studied comparatively. In this chapter, we study the change in magnetic properties of BFO NPs, upon different dopants at the Bi-site and at Fe-site. Factors like type of dopants, concentration of the dopants, Fe-O-Fe bond angle, microstrain, and particle morphology are being correlated.

** In this chapter the magnetic hystereses are recorded by Dr. Soma Salamon, and Mössbauer spectra are recorded by Dr. Joachim Landers.*

5.2 Magnetism in single doped BFO NPs

Non-magnetic Ba^{2+} is substituted at Bi site, and magnetic Mn: $[Ar]3d^5 4s^2$ and Co: $[Ar]3d^7 4s^2$ are substituted at the Fe-site ($[Ar\ 3d^6 4s^2]$) individually. Ba is diamagnetic and does not have a magnetic moment. For high spin $Fe^{3+} = 3d^5 4s^0$ ($t_{2g}^3\ e_g^2$,) the calculated magnetic moment is 5.92 μ_B/Fe, and for high spin $Fe^{2+} = 3d^6 4s^0$ ($t_{2g}^4 e_g^2$), 4.90 μ_B/Fe.[298] The high spin $Mn^{4+}=[Ar]3d^3 4s^0$ has magnetic moment of 3.87 μ_B/Mn,[298] and high spin $Co^{3+} = [Ar]3d^6 4s^0$ has a calculated magnetic moment of 4.9 μ_B/Co and experimentally often a μ_{eff} of 5.4 μ_B/Co.[299]

In Figure 5.1, the hysteresis loops are shown at 300 K, manifest the changes in maximum magnetization, coercive field, and shape of the hysteresis. From Figure 5.1a,b, we observe that single doping increases the maximum magnetization ($M_{\max}$) of BFO NPs at both temperatures 300 K and at 5 K. At 5 K, Co doping has the largest influence on $M_{\max}$ as compared to other dopants. Interestingly, the non-magnetic ion Ba also affects the magnetization of the BFO NPs, significantly. Ba doped BFO NPs (Ba-BFO) has more *S*-shaped characteristic of hysteresis as compared to Mn doped BFO NPs (BFM). Unfortunately, due to technical errors no magnetic measurements for BFC NPs at 5 K. However, one can compare magnetic measurements of BFC at 300 K with other NPs.

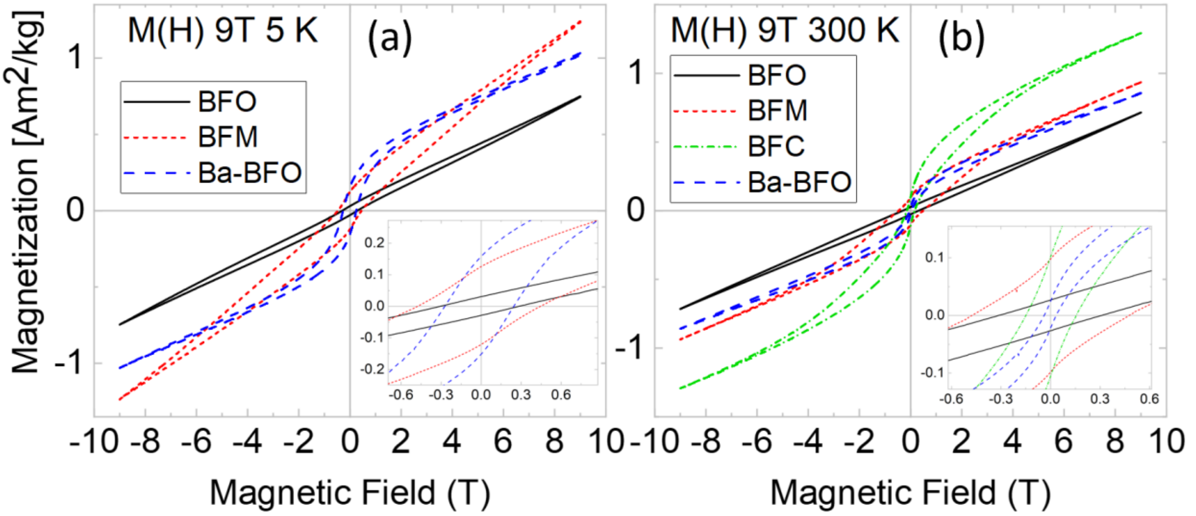

Figure 5.1: Magnetic hysteresis loops at 5 K (a), and at 300 K (b) for single doped BFO NPs. [Doping concentration 5 mol %]

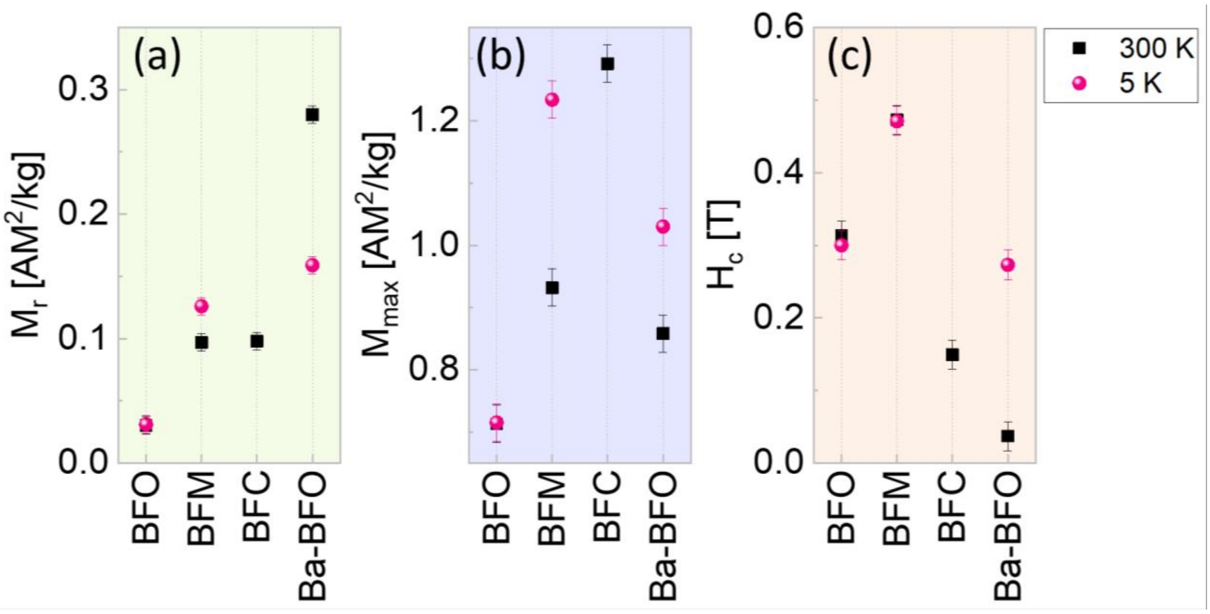

Figure 5.2: Comparison of magnetic values of single-doped and undoped BFO NPs at 5 K and 300 K.

The magnetic values were extracted using the hysteresis and have compared them in Figure 5.2. In Figure 5.2, the remnant magnetization (Mr) value is increasing upon single doping. M_r

is the residual magnetic moment of magnetic material refers to the amount of magnetization that remains in the material after being subjected to an external magnetic field. A highest M_r value for Ba doping at 300 K (shown by black squares) is found, whereas for Co and Mn doping there is no significant difference in M_r values at 300 K, but larger than pristine BFO NPs. The highest M_r value for Ba-BFO at 300 K can be explained by its most distorted rhombohedral unit cell due to larger sized dopant at Bi-site see chapter 4 [Figure 4.15].

From Figure 5.2b Co doping consists of the largest M_{max} value at 300 K, after BFM NPs, which can be due to larger magnetic moment of Co^{3+} than Fe^{3+}. Whereas, at 5 K, the M_{max} value of BFM NPs increases further, and similarly for Ba-BFO NPs. The large M_{max} value of BFC, can be due to its smallest Fe-O-Fe bond angle among single-doped BFO NPs. In addition, microstrain was found to be largest for BFC NPs,[Figure 4.17] due to smallest average crystallite size. These structural changes can lead to high probability of local ferromagnetic exchange interactions which disrupts long-range antiferromagnetic ordering. The large M_{max} value of BFC may also attribute to the larger magnetic moment of Co^{3+} than Fe. The reduction of magnetization at 300 K as compared to at 5 K is due to the reduction of thermal energy at low temperatures, which reduces the magnitude of magnetic fluctuations and increases the stability of magnetic ordering.

From Figure 5.2c, Mn doping increases the coercive field most among all doped and undoped NPs at 300 K and at 5 K. The coercive field of a magnetic particle is a measure of the strength of an external magnetic field required to reverse the direction of magnetization of the particle. In the case of BFO, the coercive field is influenced by a variety of factors, including particle size, temperature, and the presence of impurities or dopants. We can observe that temperature has a limited impact on the coercive field of BFO NPs, but dopants definitely alter it. Co doping and Ba doping both reduce the coercive field of BFO NPs at 300 K.

The increased H_c due to Mn doping, can be due to smaller particle size of BFM NPs than BFO [Figure 4.20, chapter 4], as H_c usually increases upon reduction of particle size for NPs and reaches a maxima/limit afterwards it drops in superparamagnetic state.[365] Nevertheless, there is a ferromagnetic superexchange interaction [Fe^{3+}-O-Mn^{4+}] in BFM NPs due to presence of Mn^{4+} in major amount [XPS results, chapter 4]. Such interaction can contribute to overall magnetization of BFM NPs, therefore further doping influence at Bi-site on magnetic properties of BFM NPs is interesting to probe.

5.3 Magnetism in non-magnetic ion doped at Bi-site in BFM NPs

For 5 mol % non-magnetic ion doping, Ag, Ca, and La are substituted at Bi site in BFM NPs to investigate their effects on magnetic properties of BFM NPs. The valence states of these dopants are +1, +2 and +3, respectively. The hystereses were recorded at 300 K and at 5 K as shown in Figure 5.3a-b. The loops become more *S*-shaped for Ag-BFM as compared to other NPs at 5 K and at 300 K. Interestingly the loop of BFM does not open as much, upon doping Ca and La neither at 5 K nor at 300 K. For quantitative comparison, the M_{max}, H_C, M_r are plotted in Figure 5.4.

The M_r value is highest for monovalent Ag doped BFM at both temperatures followed by trivalent La doped BFM. This may be due to the smallest Fe-O-Fe bond angle [Figure 4.18], since reduction in Fe-O-Fe bond angle leads to increase in local ferromagnetism in BFO NPs.[361,366] At 300 K, divalent Ca doping reduces the M_r for BFM NPs. However, at 5 K there is a more rise in M_r for Ca-BFM than BFM NPs. The rise of M_r is almost similar for doped BFM NPs, except for BFM NPs itself.

From Figure 5.4b, it can be seen that dopants increase the M_{max} value of the BFM NPs. Ag-BFM has the largest M_{max} value at both temperatures followed by divalent Ca. Trivalent La has the lowest M_{max} value among the codoped BFM NPs at 300 K and 5 K. The order of M_{max} can be explained based on Fe-O-Fe bond angle as shown in Figure 4.18f, [chapter 4]. Ag doping has smaller the Fe-O-Fe bond angle than BFM NPs. However, there is increase of Fe-O-Fe bond angles from Ag to Ca to La doping, which is inverse to the reduction of the M_{max} values upon these non-magnetic doping in same order. The relationship between Fe-O-Fe bond angle and M_{max} ordering explain the magnetic properties in non-magnetic doped BFM NPs.

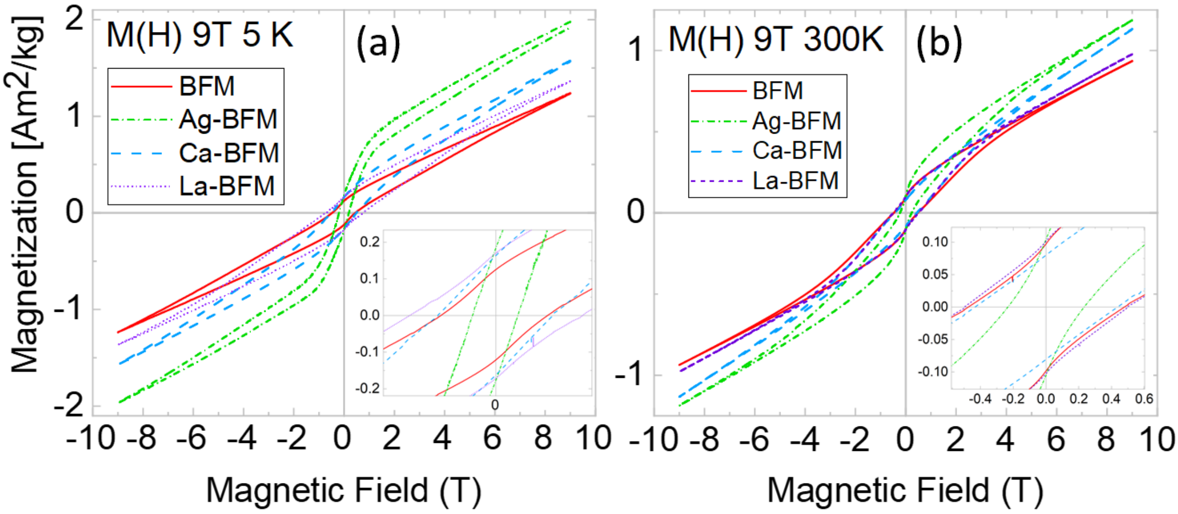

Figure 5.3: Magnetic hysteresis loops at 5 K (a), and at 300 K (b) for non-magnetic ion doped BFM NPs.

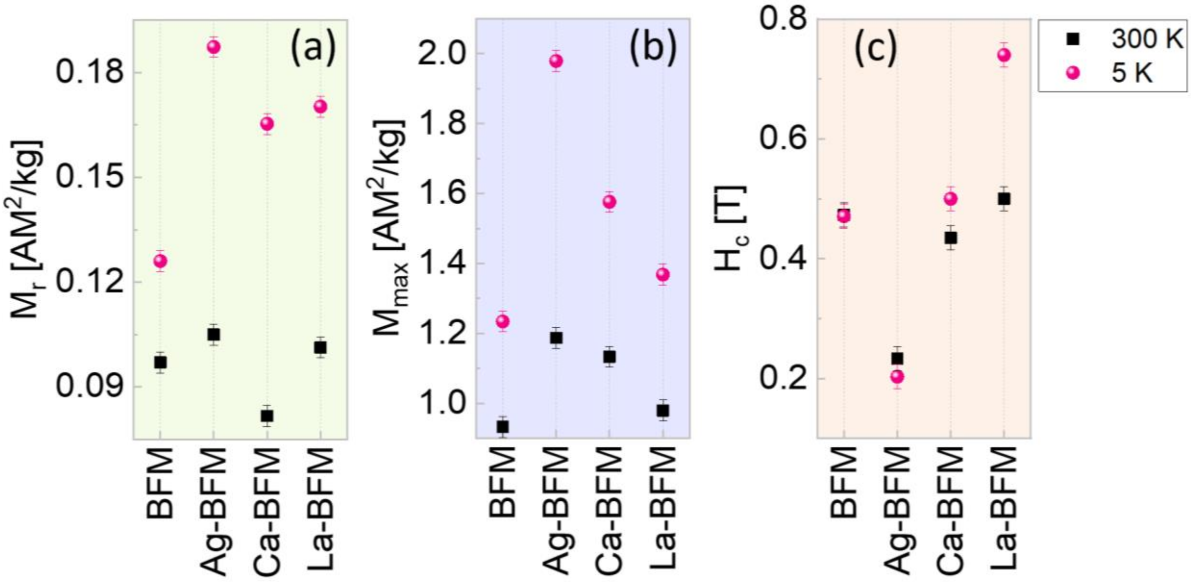

Figure 5.4: Comparison of values from the magnetic hystereses of non-magnetic ions (Ag^+, Ca^{2+}, and La^{3+}) doped BFM NPs at 5 K and 300 K.

In Figure 5.4c, the H_c values are shown at 300 K and at 5 K. Non-magnetic dopants at the Bi site do not raise the H_c values at 300 K. La-BFM has similar H_c as BFM NPs at 300 K. Whereas Ag and Ca doping reduce the H_c value. Ag-BFM has lowest H_c even lower than the BFM NPs at both temperatures. At 5 K there is a significant increase in H_c for La-BFM NPs, but not for Ag and Ca doped ones. One of the sources for the change in the coercivity of NPs can be the magnetic shape anisotropy. Doping by non-magnetic ion reduces the particle size of BFM NPs from 35 nm to 18 nm. Ag-BFM has smallest size (~18 nm), but there is no significant average particle size difference among other codoped samples. In addition, the shape of the BFM NPs is spherical, for Ag-BFM NPs it is elliptical, for Ca-BFM NPs it becomes distorted elliptical, and for the La-BFM NPs consist of an irregular rectangular shape with triangular edges. The different shapes can cause variation in the sensitivity of dipole-dipole magnetostatic interactions between NPs to their shapes. The shape of NPs can influence its magnetic properties in different ways.[365]

The non-magnetic ions are quite effective to alter the magnetic properties of BFM NPs. In terms of coercive field only La-BFM raise H_c at 5 K, whereas Ag and Ca decrease H_c of the BFM NPs. Contradictory to this, Ag-BFM has the highest M_{max} among all non-magnetic doped samples at both temperatures.

5.4 Role of concentration of non-magnetic dopant at the Bi site in BFM NPs

"1 to 5 mol % divalent Ba was doped at the Bi-site into BFM NPs to study the influence on its magnetic properties. Figure 5.5 shows the magnetization hysteresis loops, M(H), measured at 5 K and at 300 K. The magnetic values M_{max}, H_c, and M_r are plotted in Figure 5.6a-c. Upon 1% Ba doping the hysteresis loop becomes slightly narrower than BFM at both temperatures, further doping of 2% Ba widens it even more than BFM. However, upon 3% doping the loops shrink back like 1% Ba codoped BFM, and for 5% Ba the hysteresis has the least opening. 2% Ba doping brings the largest H_c value and further doping causes a reduction in coercive field (Figure 5.6c). This trend is similar at both temperatures. There is a raise in the H_c value at 5 K for Ba codoped BFM NPs, but not for BFM NPs. This may be due to the magnetic anisotropy of codoped NPs which can be different than pristine BFM NPs. BFM NPs are bigger in size than Ba doped ones. There is not a large difference between particle size of codoped Ba-BFM NPs. Nevertheless, introducing Ba into the system brings slight modification in shape of the NPs. Doping by 1% Ba provides more facets to the BFM NPs and has nearly hexagonal shape. 2% Ba doping causes more cuboidal shape with longer edges, and 3 % Ba reduces the longer edge making the particle more symmetrical, whereas 5% Ba doping results more octahedral shaped NPs with many facets but more symmetrical. Such changes in shape of NPs can alter magnetic anisotropies in Ba doped BFM NPs, which may be one of the reasons. In addition, divalent Ba incorporation is responsible for overall charge imbalance which cause some level of defect in spite of Mn^{+4} presence of Mn^{3+} to maintain charge neutrality to the overall system.

In Figure 5.6a, the trend of the M_r values for Ba doping into BFM NPs is shown. We observe that at 5 K, 5% Ba doped has the highest M_r value followed by 1% Ba doped sample. The anomaly by 1% Ba doping can be explained based on the creation of defects in the system via charge imbalance which leads to different magnetic anisotropy comparative to 5% Ba doped BFM and BFM NPs. For 2, 3 , and 5 % there is linear increase in M_r value with respect to M_r value of BFM NPs. This can be explained by decreased particle size upon Ba, which may lead to increase in magnetic anisotropy. When the magnetic anisotropy is increased, the magnetic moments tend to be more aligned, which contributes to an increase in the remanent magnetization. We must not ignore the contribution of distorted crystal structure caused by a certain amount of doping, which acts as a major factor as in the case of 1 % Ba-BFM NPs. [chapter 4]

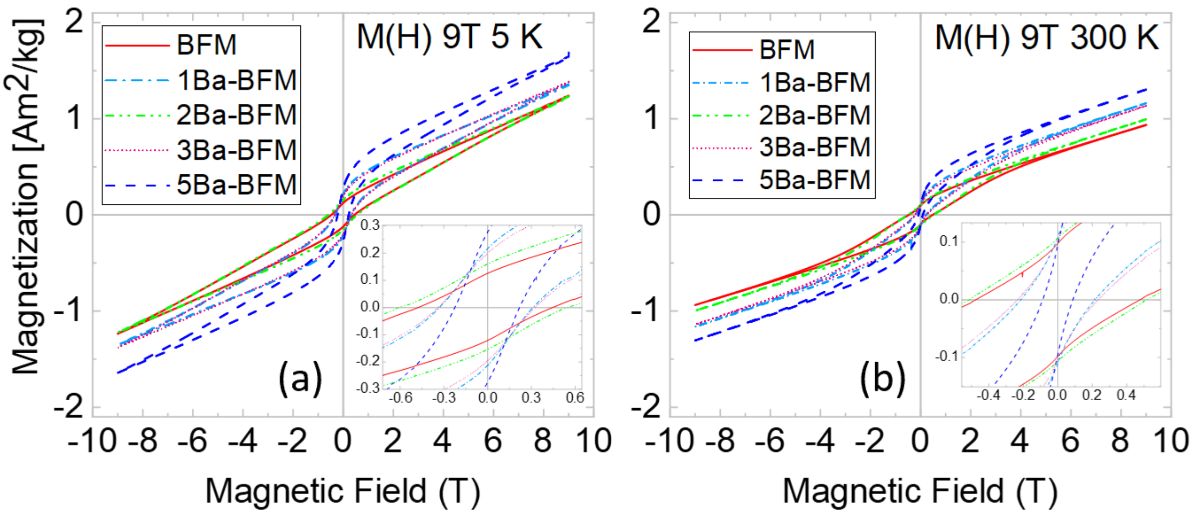

Figure 5.5: Magnetic hysteresis loops at 5 K (a), and at 300 K (b) for non-magnetic Ba doped BFM NPs.

As seen in Figure 5.6b, there is an increase in M_{max} value upon substituting Ba into BFM NPs, 5% Ba has highest M_{max} value. There is a linear increase observed from 2 to 5 % Ba doping.

However, 1 % Ba doping has larger $M_{\max}$ value than 2 % Ba doping, that can be explained based on the smallest Fe-O-Fe bond angle in 1 % Ba-BFM NPs and for 5 % Ba- BFM NPs.

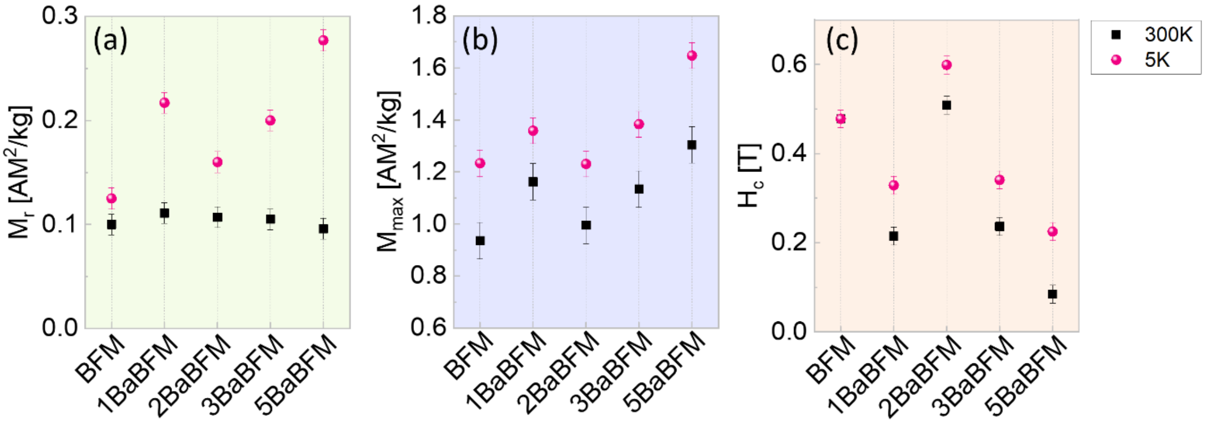

Figure 5.6: Effect on magnetic hysteresis parameters upon changing the doping concentration of the nonmagnetic ion Ba into BFM NPs at 5 K and 300 K.

The concentration of doping influences the magnetic properties of BFM NPs. For a large M_r value, 5 % Ba doping is best. However, for largest coercive field value, 2 % Ba doping is the best choice. 1 % Ba doping is the most interesting composition due to the interplay of defects and magnetic anisotropy.”[d]

5.5 Magnetism in rare-earth magnetic ion doped BFM NPs

In rare-earth, lanthanides like Nd, Sm, Gd, and Dy are opted for 5 mol % substitution at the Bi-site in BFM NPs.

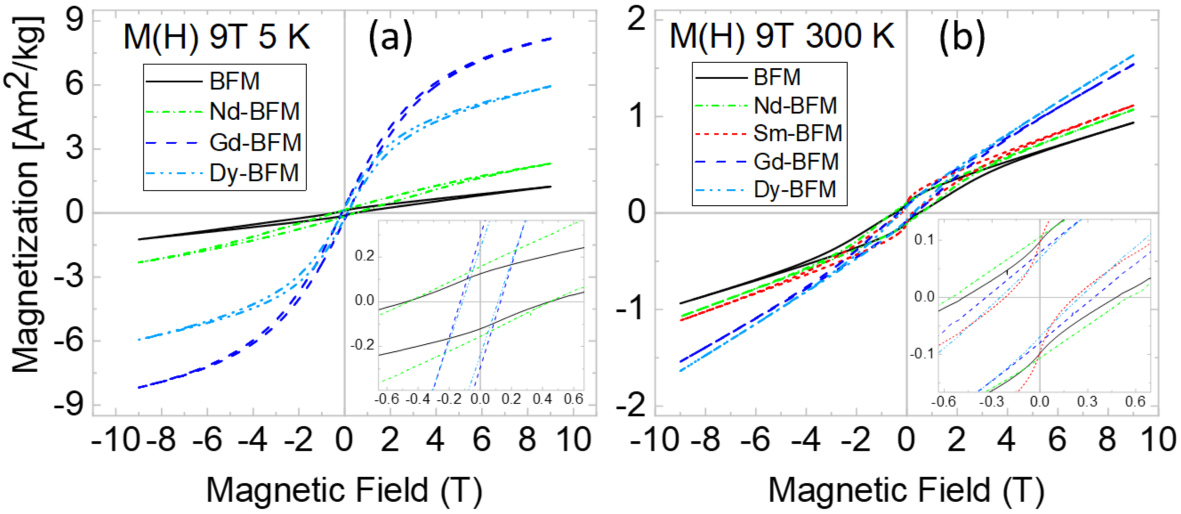

Figure 5.7: Magnetic hysteresis loops at 5 K (a), and at 300 K (b) for rare earth (Nd^{3+}, Sm^{3+}, Gd^{3+} and Dy^{3+}) magnetic ion doped BFM NPs.

---

[d] This paragraph is based on (Dubey et al Journal of Physical Chemistry C 2022, https://doi.org/10.1021/acs.jpcc.0c05778)

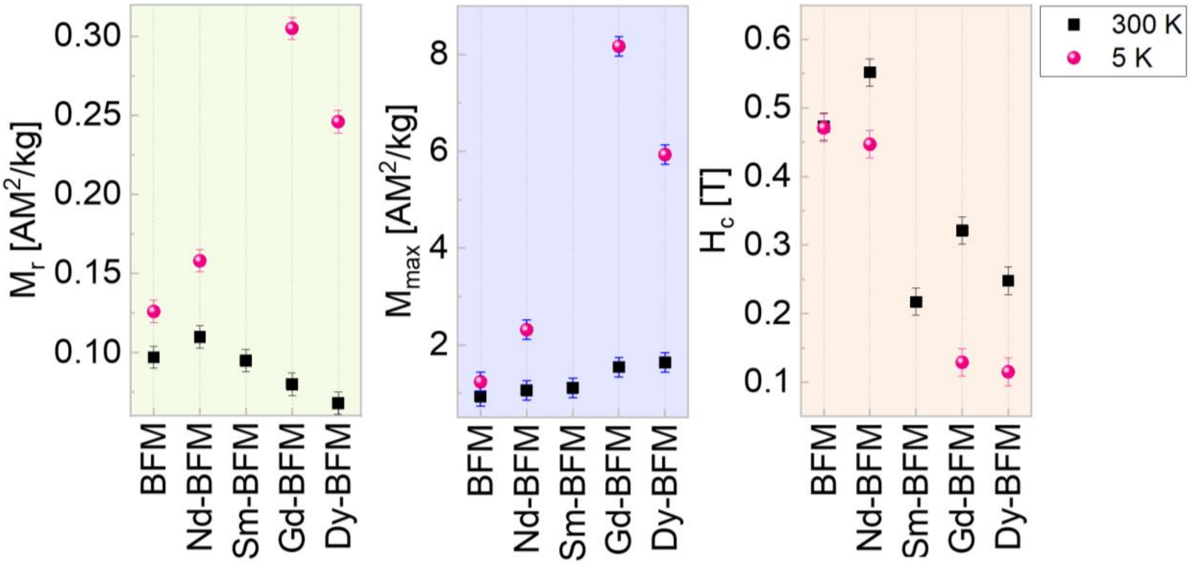

Figure 5.8: Comparison of magnetic values of rare-earth magnetic ions (Nd^{3+}, Sm^{3+}, Gd^{3+} and Dy^{3+}) doped BFM NPs at 5 K and 300 K.

All dopants are trivalent and are magnetic in nature and consists of μ_{eff} Nd^{3+}: 3.44 μB, Sm^{3+}: 1.64 μB, Gd^{3+}: 7.97 μB, Dy^{3+}: 10.6 μB respective magnetic moments.[367,368] Among these elements, Dy (ground term: $^6H_{15/2}$) has the highest magnetic moment, due to its highest number of unpaired electrons in the 3+ oxidation state.[367]

The magnetic hysteresis loops of rare-earth ion doped BFM NPs are shown in Figure 5.7. Due to technical reason, we could not record hysteresis of Sm-BFM at 5 K. From Figure 5.7b, rare-earth ion doping increases the M_{max} at 300 K. Nd opens the hysteresis larger than BFM NPs, whereas Sm makes it quite narrow. A double hysteresis kind of behaviour is observed for Sm-BFM NPs, this is likely due to the presence of two magnetic phases with different magnetic properties. Gd and Dy doping cause large increase in M_{max} value, but both doping reduces the coercivity of BFM NPs. Similar effects were observed at 5 K, where Gd and Dy doping decrease the coercivity of BFM NPs (Figure 5.7a). However, Nd doping retains the coercivity of BFM NPs at 5 K. Gd doped BFM NPs has sharp S-shaped hysteresis with highest M_{max} at 5 K.

There is a large increase in M_r and M_{max} values at 5 K for Gd-BFM and for Dy-BFM. This could be due to large magnetic moments of Gd and Dy ions as compared to other elements. At 300 K, the upon Nd doping into BFM the M_r increased however Sm, Gd and Dy doping lead to linear drop of M_r. However, there is a linear increase of M_{max} upon RE-doping in BFM NPs at 300 K. Such increase in M_{max} may be due to more reduced Fe-O-Fe bond angle for Gd and Dy than for Nd [Chapter 4]. These magnetic ions can also participate in uncompensated spins at the surface of BFM NPs, where their individual magnetic spin can contribute to increase the net effective magnetic moment. The surface area is found to be largest for Dy-BFM, followed by Gd, Sm and Nd, so larger surface area would assist a greater number of uncompensated spins at the surface. In addition, the RE-doped BFM NPs have different particle shape [Figure 4.27] namely, elliptical for Nd-BFM, pentagonal for Dy-BFM, rectangular for Gd-BFM, which leads to changes in the magnetic anisotropy in these NPs.

From Figure 5.8c, at 300 K there is a nonlinear change in H_c upon RE doping, Nd increase the coercivity, however other dopants reduce it. At 5 K the *H*c reduces and smaller than at 300 K for RE-doped BFM NPs. This can be due to reduced magnetic interactions at 5 K for these NPs. Such changes in H_c can be due to different shape of these NPs [Figure 4.27].

5.6 Temperature dependent in-situ Magnetic properties

In the study of magnetic materials, the temperature dependence of magnetization is commonly characterized by zero-field cooled (ZFC) and field-cooled (FC) curves. In ZFC measurements, the sample is first cooled from a high temperature to the measurement temperature in the absence of an external magnetic field (zero-field). Subsequently, an external magnetic field is applied, and the magnetic response of the sample is measured as a function of temperature. Conversely, in FC measurements, the sample is cooled from a high temperature to the measurement temperature in the presence of an external magnetic field, and the magnetic response is measured as a function of temperature. As explained in Figure 5.9. Upon heating, the magnetic ordering of BFO NPs decreases, resulting in a reduction of magnetic moment.[369,370] In ZFC curves, the magnetization decreases as a function of increasing temperature, whereas in FC curve the magnetization increases as a function of decreasing temperature.

The magnetization of the NPs was measured as a function of temperature (M-T plots) using a heating rate of 5 K/min. The NPs were first pressed into small 3 mm discs, and then weighed to ensure a consistent amount of material in each measurement. Next, the discs were glued onto a ceramic heater using a cement called Zircar AL-CEM. This helped to ensure that the nanoparticles remained in place during the measurements.

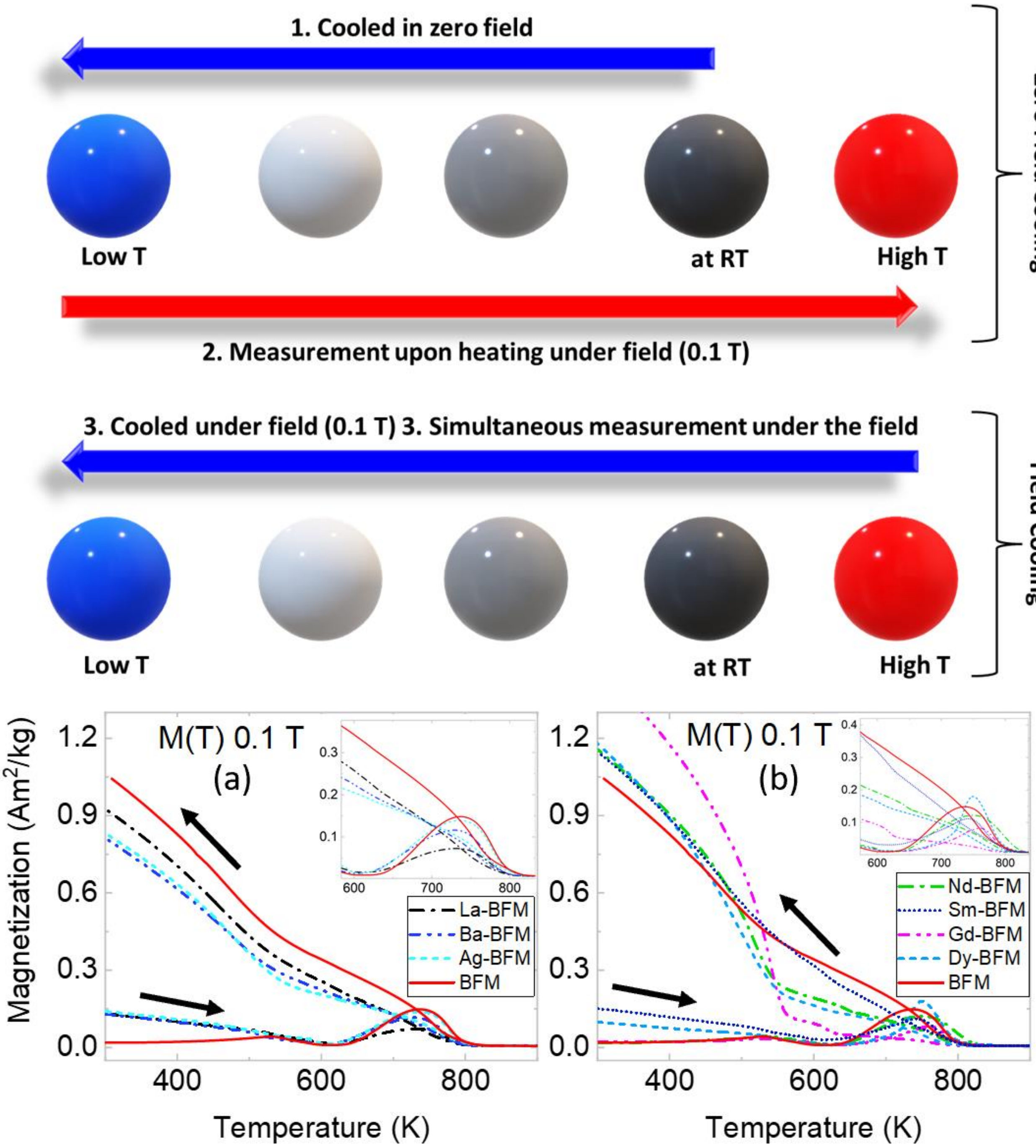

Figure 5.9: Schematic to understand zero field cooling (ZFC) and field cooling (FC) measurements. Temperature dependent magnetization plots for non-magnetic ions (Ag, Ba and La) doped BFM NPs (a), and for magnetic rare-earth ions (Nd, Sm, Gd, and Dy) doped BFM NPs (b) up to 900 K at 0.1 T. (black arrows represent measurement directions)

To ensure accurate measurements, the high temperature M(T) measurements were performed in high vacuum, with a pressure of less than 10^{-5} mbar. This helped to minimize any potential interference from air molecules or other contaminants. To further minimize interference, the sample space was repeatedly purged with helium gas and pumped down after each sample change. This helped to ensure that the measurements were as accurate as possible and that the results obtained were reliable.

“The temperature range from 298 K to 1000 K (727 °C) was scanned in vacuum. BFO is known to decompose near to 850 °C. Therefore, M(T) measurements in the range of the Curie temperature are rarely reported due to the decomposition of BFO or otherwise the occurrence of secondary phases. The temperature dependent in-situ XRD measurements, reveals that decomposition already starts at ~700 °C to mullite ($Bi_2Fe_4O_9$: mullite) and later at ~900 °C to sillenite ($Bi_{25}FeO_{40}$) as well.[315] However, Fe-rich the mullite phase has no significant amount of magnetization.[371] So, the temperature dependent magnetization for RE-doped BFO NPs were collected up to 900 K (627 °C), at magnetic field of 0.1 T from 300 K to 900 K (rising) and back down to 300 K (falling) as shown in Figure 5.9.

For all samples, we observe that the magnetization rises above 630 K and reaches a maximum at about 750 K. Upon cooling, the magnetization continuously increases below 800 K. The magnetization values after cooling back to room temperature are approximately one order of magnitude greater than for as-synthesized NPs. The M(H) curves measured after this heating-cooling cycle, are qualitatively different from those measured before.[315] The hysteresis loops have a pronounced S-shape with a remanent magnetization of 0.2–0.5 Am^2/kg. Such behaviour may indicate the formation of secondary magnetic phases due to partial decomposition of BFO above 630 K.[315] Minor amounts of these phases lie under the XRD detection limit, but their ferrimagnetic response dominates the weak magnetic moment of BFO NPs. However, analysis of the measurements done upon heating below 630 K gives information about the Néel temperature. For BFM NPs we observe an anomaly at the dM/dT(T) dependences around 575 K,[315] which can be attributed to the antiferromagnetic-paramagnetic phase transition.[10] For the Dy-doped BMF NPs this anomaly is also around 575 K, but for Gd- and Nd-doped BMF NPs it shifts to 590 and 600 K, respectively. This indicates that these RE dopants stabilize the antiferromagnetic phase.**”**[e]

5.7 Discussion on magnetism in doped-BFM NPs

The magnetism of doped BFO NPs is influenced by several factors. There is no one single factor which is responsible for overall increase in magnetization of BFO NPs, few major factors are noted followings.

(a) *Uncompensated spins at the surface of NPs:* The effective magnetic moment at the surface of doped/codoped BFO NPs can be more than BFO NPs due to the large surface area to volume ratio. So, the contribution of surface spins to the total magnetic moment of the NPs increases with increasing surface area. In single doped BFO NPs, the surface area of BFC NPs is largest, which lead to largest uncompensated spins at the surface of these NPs. In non-magnetic ion doped BFM NPs, Ca-BFM NPs has largest surface area followed by La-BFM NPs which explains the larger M_{max} of former one. Among RE-doped BFM NPs, the surface area is largest for Dy-BFM NPs followed by Gd-BFM NPs.

---

[e] This paragraph is based on (Dubey et al, Frontiers in Bioengineering and Biotechnology, 2022, http://doi.org/10.3389/fbioe.2022.965146)

(b) *Alteration in incommensurate spin cycloid*: The magnetic incommensurate spin cycloid (periodicity 62 nm) of BFO NPs can be affected by two ways; one it gets disrupted due to smaller particle size (less than 62 nm) or due to presence of dopant at Fe-site with different spin canting angle with respect to Fe, which results to a large net effective magnetic moment. Other way is the suppression of the spin cycloid due to alteration in local Fe-O-Fe bond angle in the crystal lattice. In Chapter 4, from Figure 4.18d-g one can see the changes in the Fe-O-Fe angle upon different dopants incorporation in BFO crystal lattice, which may cause suppression of the spin cycloid. Such local crystal structure changes may result into an increase in net effective magnetic moment of doped BFO NPs.

(c) *Crossover from antiferromagnetic (AFM) to ferromagnetic (FM) superexchange interaction*: The incorporation of Mn and Co at Fe-site may lead to a crossover from AFM to FM superexchange interaction, which contribute to the increase of magnetization of BFO NPs. From the case of Mn doped BFO NPs (BFM), we confirmed such crossover from AFM [Fe^{3+}-O-Mn^{3+}] to FM [Fe^{3+}-O-Mn^{4+}] by XPS and EXAFS results see Chapter 4. For Co doping the measurements and data analysis are under process, so we cannot confirm about BFC NPs. Therefore, we continued studying the magnetic properties of doped BFM NPs.

(d) *Magnetic anisotropies*: The surface anisotropies play important role in magnetic behaviour in NPs. Thus, the increase of magnetization in doped BFO NPs with different morphologies can be due the partial contribution of shape and strain anisotropies, and noncollinear magnetic ordering, which may lead to alteration in local spin canting between magnetic moments.

Apart from these factors, the possibility to have a core-shell structure where core is AFM, and shell is FM can also contribute to a net magnetization in these doped BFO NPs.

5.7.1 Comment on the spin cycloid for Ba doped BFM NPs

In general, the magnetic properties of NPs differ from those of the bulk material due to their small size and high surface-to-volume ratio. In the case of BFO NPs, these differences can lead to a modified magnetic behaviour, such as a change in the magnetization, which can result in a change in the spin cycloid structure and its relationship with the magnetization. Within the cycloid, a part of spins is oriented antiparallelly to another part of spins, resulting in the zero antiferromagnetic vector, where the two antiferromagnetic sublattices are organized along a cycloidal spiral. The spin propagation (q) is along the direction (110) and the cycloidal plane of spin-rotation is (1-10). The Mössbauer spectra can provide information about the magnetic hyperfine field, which is related to the magnetic moment of the material, and the quadrupole splitting, which is associated to the electronic structure of the material. These two parameters can be used to distinguish between different magnetic phases, such as antiferromagnetic, ferrimagnetic, or ferromagnetic phases.

"In Figure 5.10, the Mössbauer spectra recorded at 80 K are shown. They are dominated by the magnetically blocked sextet in agreement with the fundamental antiferromagnetic order. The sextet sub-spectrum was reproduced using a hyperfine field (B_{hf}) distribution with linear coupling of B_{hf} to the nuclear quadrupole level shift 2ε, to approximately describe the fine structure resulting from the spin cycloidal ordering. Its effect is most clearly visible at the outermost right line number '6' (blue background). Essentially, the fine structure of the BFO spectrum is caused by the dependence of the hyperfine field and the nuclear quadruple level shift 2ε, defining the position of the four inner absorption lines relative to the outer lines 1 and 6, on the angle (θ) between the individual spin directions within the cycloidal structure relative to the hexagonal c-axis (polarization direction). BFO is known to exhibit an anisotropic hyperfine magnetic field, which is larger for spins aligned parallel than for those aligned perpendicular to the polarization direction, while 2ε is coupled to the angle θ according to Equation 5.1, where ΔE_{Q} is quadrupole splitting in the paramagnetic doublet state.[372]

$$2\varepsilon\ (\theta) = \ \Delta E_{\mathrm{Q}}(\frac{3cos^2(\theta) - 1}{2}) \tag{5.1}$$

We have observed a typical fine structure as reported for BFO before,[68] which is also influenced by the probability distribution of the spin directions described by the anharmonicity of the spin cycloid.[69] The anharmonic cycloid leads to a higher fraction of spins to be aligned coaxially, rather than perpendicular to the polarization direction, which in turn causes an asymmetry of the peaks. One can observe the left-tilted character of the line, indicative of the typical anharmonic spin structure of BFO,[373] which is clearly absent in all the Mn-doped samples. As this indicates a strong change in the characteristic anharmonic spin cycloidal structure, we can assume that Mn doping either alters the distribution of spin directions (anharmonicity), while conserving the cycloid in general, or distorts the spin cycloidal order to some extent.

Still independent of the Ba-content, the change in fine structure to a more or less symmetric shape indicates dramatic changes in long-range cycloidal ordering, while the local coupling between 2ε and B_{hf} remain existent. This is visible from the sustained total asymmetry of the BFO spectrum (line 1 vs. 6), illustrated by dashed lines, representing the superposition of contributions of different spin directions. It also indicates a distinct change in cycloidal spin order. Upon only Ba-doping, no considerable change in the spectral structure is visible, wherefore one can assume the long-range spin ordering to be largely unaffected. To also consider effects of different temperatures on the magnetic structure of the BFO particles, a room temperature spectrum of the Ba doped sample material is shown for comparison [Figure 5.10). The spectrum displays only moderately higher doublet intensity, presumably caused by a higher but still small superparamagnetic fraction of the smallest particles. The fine structure discussed above is mainly preserved up to this temperature, which is in agreement with previous studies on the temperature dependence of the BFO spin structure, which indicates a transition to a harmonic long range cycloidal order, which is however not reached below 400 K.[69]

These findings are in general agreement with results from XRD, where Ba-doping results in a minor change of the unit cell volume only, without a change in lattice symmetry, presumably explaining the unaltered spin cycloid after doping larger Ba^{+2} ions into BFM NPs. However, it is possible that Ba incorporation has some minor additional effect on the spin cycloid due to a distortion in the primitive rhombohedral lattice, enhanced strain, and charge compensation. For BFM, the dramatic changes in the long-range spin ordering can be correlated to the distinct change in unit cell aspect ratio due to the lattice distortion, which can be one of the reasons for increased remanent magnetization of BFO.

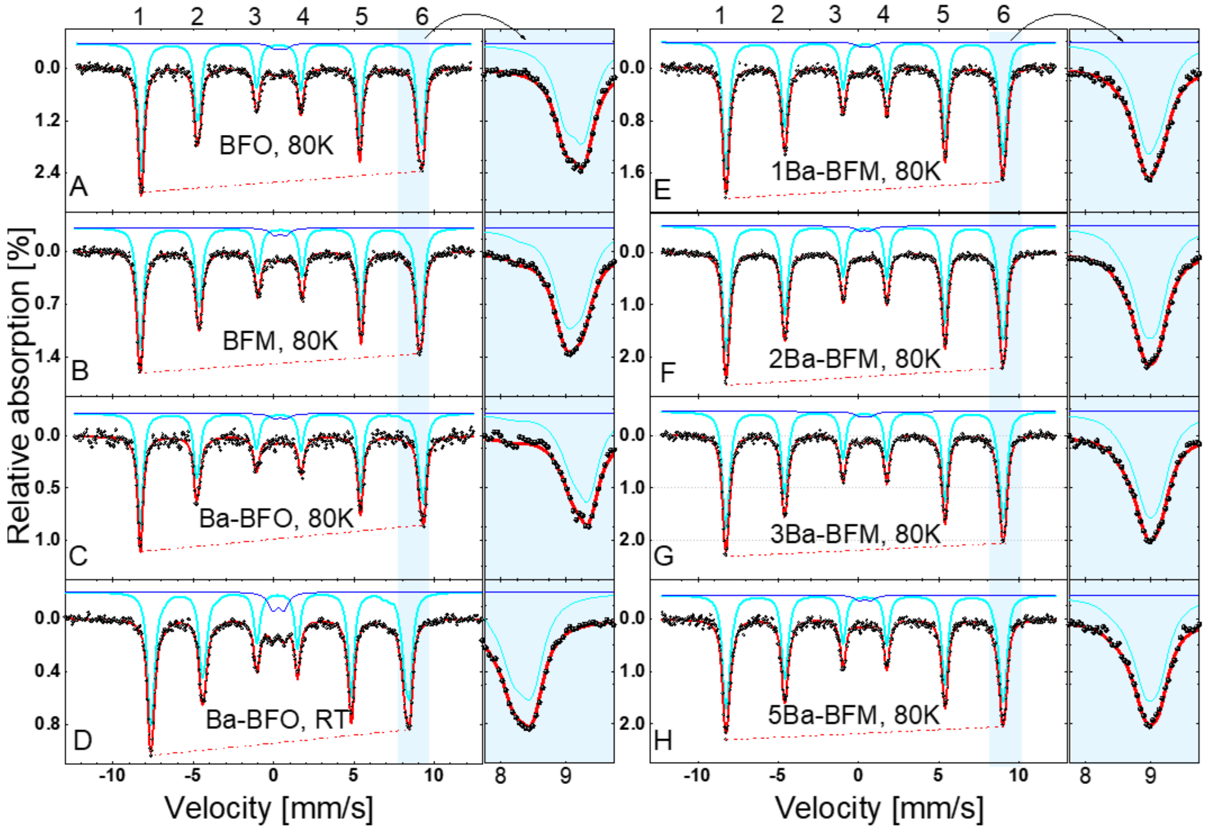

Figure 5.10: Mössbauer spectra of single doped BFO NPs (Mn at Fe-site, and Ba at Bi-site) recorded at 80 K, consisting of a minor superparamagnetic doublet fraction (blue) and a dominant magnetically blocked sextet (light blue), reproduced via a hyperfine field distribution with 2ε linearly coupled to B_{hf}. The sixth peak (cyan background) is shown separately in magnification to the right of each spectrum. [© 2020 The Journal of Physical Chemistry C] [10]

For 1 % to 5 % Ba doping into BFM NPs, the Mössbauer spectra display a much less pronounced asymmetry, which could indicate a decoupling of the spin directions from the cycloidal structure (destruction of spin cycloid), no longer resulting in a distribution, but instead fixed combinations of hyperfine magnetic fields and nuclear quadrupole level shifts. Therefore, in line 6, we see a symmetric structure; in some cases, even a small inclination in the opposite direction as compared to the original BFO sample, which could imply a variation of the cycloidal structure. For BFO NPs, the magnetic phase transition onset was found at 614 K,[10] and for BFM NPs the Néel temperature decreases to 574 K with further broadening of the peak.[10] Further doping of 1 % to 5 % Ba into BFM, does not alter the magnetic transition temperature.[10]

The 5 % Mn doping results in 5 times increase in M_r of BFO NPs, and further 5 % Ba doping doubles it. Mössbauer spectroscopy shows that the pure BFO NPs maintain the cycloidal spin modulation despite the fact that their size is below the period of the modulation in bulk, 62 nm. In addition, doping 5 % of Ba to the pure BFO NPs keeps the same asymmetry in

Mössbauer spectrum. However, adding 5 % of Mn removes such asymmetry of the peaks in the sextet of Mössbauer spectrum, which is considered as a signature of the anharmonic spin modulated structure,[373,374] meaning that the Mn (B-site) doping destroys the cycloidal ordering of spins. The major line asymmetry of the BFO spectra is attributed to an intrinsic anisotropy of the magnetic hyperfine interaction at a site with trigonal symmetry.[374] It becomes less pronounced upon Ba incorporation, which leads to canting between the magnetic moments of the sublattices. That can be one of the reasons of increased ferromagnetic contribution for Ba doping by a local stress driven increase of canting."

In summary, the increase of the magnetization due to Mn dopings is the result of a destructed cycloidal long-range ordering due to Mn-doping and a crossover to the canted antiferromagnetic structure with a weak ferromagnetic moment. The superexchange interaction between Fe^{+3} and Mn^{+3} results in the antiferromagnetic order, while the interaction between Fe^{+3} and Mn^{+4} has ferromagnetic character.[375,376] However other factors like change in particle size, and shape can also contribute to net magnetization.**"**[f]

5.8 The potential of doped BFO NPs in hyperthermia application

Hyperthermia, a form of cancer treatment that utilizes heat to destroy cancer cells, is achieved by elevating the temperature of the targeted tissue. The use of magnetic heating through the application of an alternating magnetic field has proven to be an effective means of achieving hyperthermia. The hyperthermia temperature window refers to the range of temperatures that are suitable for inducing therapeutic effects in cancer treatment through hyperthermia. The temperature range is usually between 40-45 °C, although it can vary depending on the type of cancer and the treatment method being used. The heating efficiency of magnetic nanoparticles (MNPs) in hyperthermia applications is determined by various factors, including the maximum magnetization value. $M_{\max}$ is an important physical property that determines the magnetic response of MNPs to an external magnetic field. The higher $M_{\max}$, the greater their ability to generate heat when exposed to an alternating magnetic field. Therefore, we have utilised rare-earth doped BFM and compared with pristine BFO NPs to test their potential in hyperthermia testing based on their large $M_{\max}$ values as compared to other doped BFM NPs. Nevertheless, it is not just $M_{\max}$ that determines the heating efficiency of MNPs in hyperthermia applications. The particle size, shape, magnetic susceptibility, and material composition, also play a significant role in determining the heating efficiency. In general, MNPs with a high $M_{\max}$ and small particle size are more effective in hyperthermia applications compared to those with low $M_{\max}$ and larger particle size. This is because smaller MNPs can penetrate deeper into the tissue, leading to more effective heating, and the high $M_{\max}$ allows for a stronger magnetic response to the external field.

"To measure hyperthermia, nanopowders were dispersed into water and agar medium by merely mixing them at room temperature without any chemical or thermal treatment. Figure 5.11 depict the change in temperature under an 80 mT AC field for samples with only 1 mg/ml

---

[f] This paragraph is based on (Dubey et al Journal of Physical Chemistry C 2022, https://doi.org/10.1021/acs.jpcc.0c05778)

NPs concentration in both water and agar media. The NPs in water demonstrate the interaction of the system in a general medium, and the NPs in agar, with a 2 % weight solution, simulate the activity of NPs in blood, mimicking the environment inside cells. The 3 mg/ml dispersion of NPs into water and agar mediums were studied at 60 and 80 mT as shown in Figure 3.12. As the concentration increased from 1 mg/ml to 3 mg/ml, the temperature rose faster within the same 5-minute time interval. It was observed that Dy-BFM could produce heat up to ~39°C in water medium within 5 minutes. Similarly, a 3 mg/ml dispersion of NPs in agar shows that a higher concentration of these magnetic NPs could heat more effectively than 1 mg/ml.

The temperatures reached in 5 minutes by applying different AC fields are compared for all NPs in water and agar medium, respectively. The difference in temperature raises as the fields change for each type of NP, as depicted in Figure 5.12. Doping with Gd, Dy, and Nd increases ΔT values as compared to BFM NPs. In water medium, upon increasing the magnetic field, Dy-BFM NPs show a higher temperature rise than Gd and Nd NPs. The difference in heating efficiencies of RE-doped NPs can be due to their different shapes leads to different magnetic anisotropy and maximum magnetization values. Dy-BFM NPs have a higher M_{max} value at 300 K than other NPs and an irregular pentagonal shape,[46] which could be one of the factors behind its heating efficiency.

In agar, again, Dy-BFM has the best results. Among RE-doped samples, Nd-BFM produces the lowest temperature rise compared to other samples may be its due to its elliptical morphology which reduces magnetic anisotropy and its lower M_{max} value than for Dy-BFM NPs. Although the therapeutic window was not reached in either medium, the Dy-BFM sample shows promising features with potential to be further optimized in terms of chemical structure. The improvements in heating efficiencies can be evaluated using the Specific Absorption Rate (SAR).[377]

$$SAR = \frac{\Delta T}{\Delta t}\frac{C_P}{\varphi} \qquad (5.2)$$

ΔT gives the temperature change, Δt gives the change in time, C_p is the heat capacity at constant pressure, and φ is the mass of magnetic material per unit mass of liquid.

The SAR value for the Dy-BFM sample is currently below 30 W/g, which is the highest among the discussed NPs. The SAR value depends on the size, saturation magnetization, and magnetic anisotropy of NPs. Magnetic anisotropy can be adjusted by changing the shape of NPs or modifying the NP surface. Magnetic NPs with high SAR values are in demand for hyperthermia applications as they require lower amounts of material to reach therapeutic temperatures. For spherical and cubic magnetite (Fe_3O_4) NPs, SAR values of 140 and 314 W/g have been reported, respectively.[378] This indicates that different shapes of doped-BFO NPs must be studied to probe the effect of morphology on SAR value. RE-doped BFO NPs exhibit higher M_{max} values than BFM and BFO NPs at RT, which correlates with their improved hyperthermia performance. Furthermore, the distinctive morphology of the RE-doped NPs sets them apart from the pristine BFO and BFM NPs and may contribute to their distinct heating capabilities. Additionally, RE doping reduces the size of BFO/BFM NPs by up to 22 nm, which could further influence the heat generated by the NPs. The NPs concentrations employed in this study were lower than those commonly used for magnetic hyperthermia, suggesting that increasing the concentration of NPs could be explored in future research.

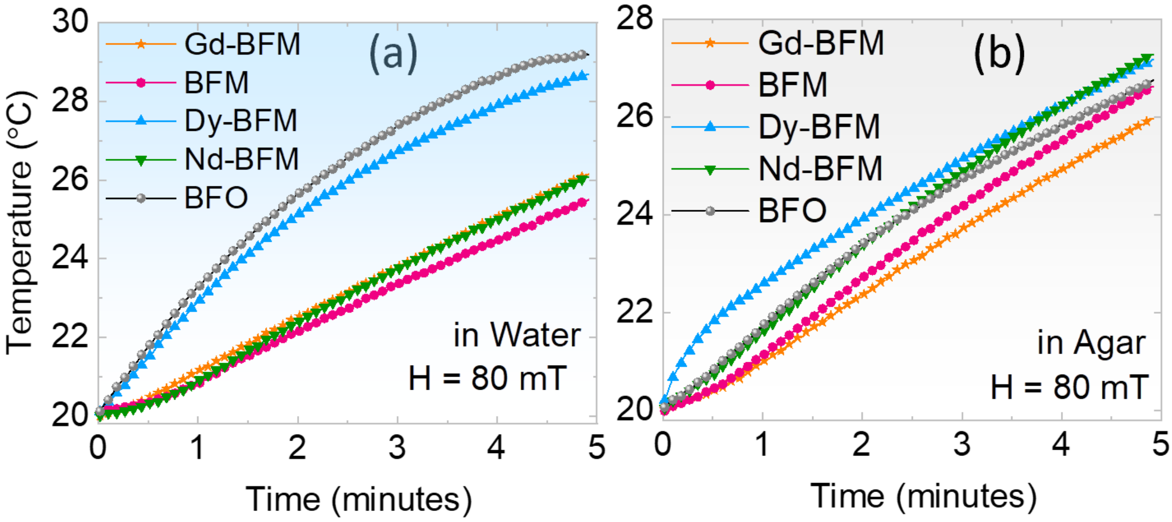

Figure 5.11: Hyperthermia test results of BFO and rare earth doped BFM NPs, the change in temperature due to applied AC field of 80 mT, in water (a), and in agar (b) mediums. [measured by Mr. Supun B Attanayake]

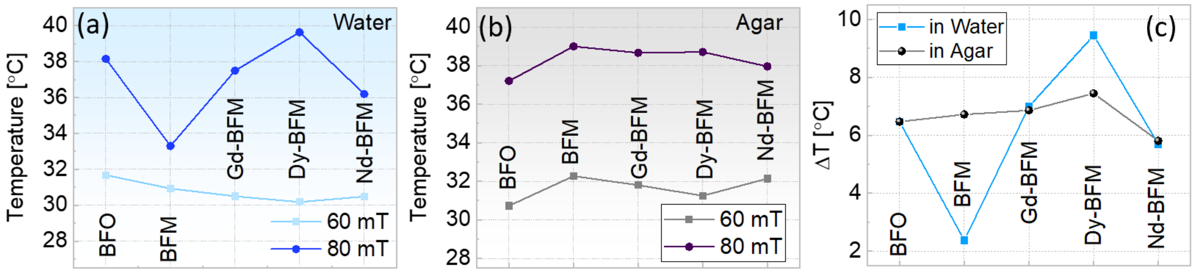

Figure 5.12: Hyperthermia tests at two different fields 60 mT and 80 mT of all doped and undoped BFO NPs, in water (A), and in agar (B) and (C) shows the comparison of temperature difference in both mediums at 3 mg/ml concentrations.

Generally, higher NP concentrations result in a greater temperature rise. However, there is a limit to the concentration of NPs that can be used. As because high concentrations can cause toxicity and other adverse effects. Therefore, it is important to carefully control the concentration of NPs during hyperthermia testing to ensure both safety and efficacy. The high magnetic anisotropy of codoped BFO NPs is a key factor that makes them suitable for magnetic hyperthermia in the treatment of cancer. Their magnetic properties, combined with their biocompatibility, stability, and potential for targeted delivery, make them a promising material for use in hyperthermia applications. Further research is required to fully realize the potential of BFO NPs in this field."[g]

---

[g] This paragraph is based on (Dubey et al, Frontiers in Bioengineering and Biotechnology, 2022, http://doi.org/10.3389/fbioe.2022.965146)

5.9 Conclusions

In this chapter, we have demonstrated that doping magnetic ions at the Fe-site of BFO NPs leads to a significant increase in their total magnetization by modification of the spin cycloid. Further co-doping at the Bi-site leads to even higher magnetization, which is attributed to the distortion in the crystal structure and the resulting changes in the Fe-O-Fe bond angle. The effect of doping on the magnetic properties of NPs is evident, with some dopants increasing the maximum magnetization and remanent magnetization by a factor of two. The coercive field, which is a topic of discussion, is also impacted by doping, with some dopants increasing the coercive field and widening the magnetic hysteresis, while others decrease the coercive field and make the hysteresis more S-shaped.

The magnetic anisotropy of codoped BFO NPs is a key factor that makes them highly suitable for magnetic hyperthermia. NPs with high magnetic anisotropy have a large magnetic moment in a preferred direction, leading to a high magnetic energy density. Doped-BFO NPs possess high magnetic anisotropy, which contributes to their efficiency in converting magnetic energy into heat when exposed to an alternating magnetic field, making them an attractive material for magnetic hyperthermia. Additionally, their small size, stability, and potential for targeted delivery make them a promising option in the field of thermal therapy.

The increased magnetization in BFO NPs can be attributed to a combination of factors, including an increased magnetic anisotropy due to the reduced particle size, changes in spin cycloid, the presence of uncompensated spins and defects at the surface or interface of the particle, and alteration in super-exchange interaction at the Fe-site. The increased coercive field resulting from doping can have a positive impact on the magnetic properties of the material, making it more useful for applications where magnetic stability and resistance to demagnetization are important.

Dopant-Induced Optical Modulations

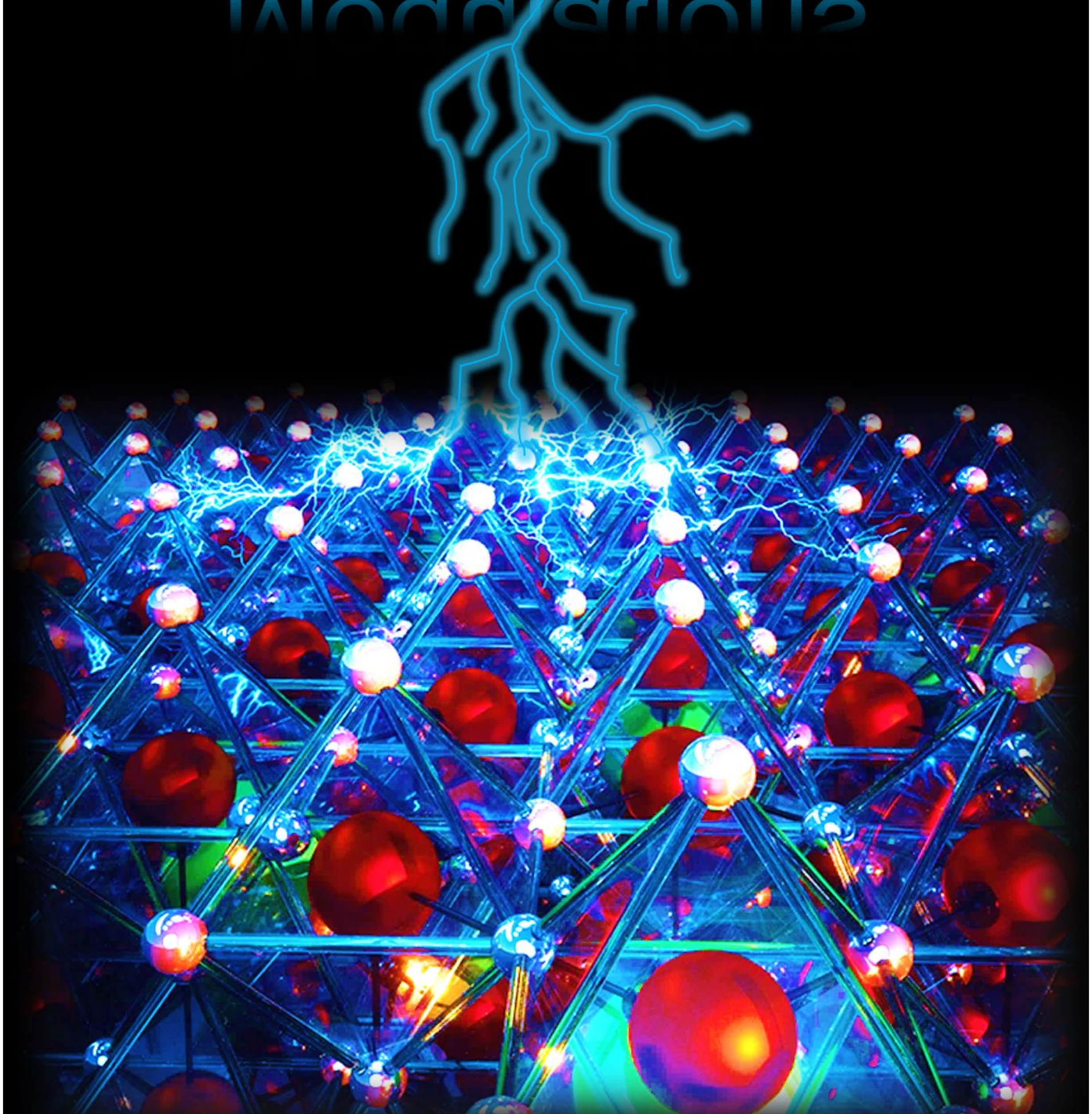

6 Dopant-induced optical modulations

6.1 Introduction

One of the key characteristics of BFO is its optical band gap, which is the energy required to promote an electron from the valence band to the conduction band. The optical band gap of BFO has been extensively studied due to its potential applications in a range of optoelectronic devices, including solar cells, photocatalysts, and photoelectrochemical cells. The band gap of BFO is in the visible range (2.25 eV; 551 eV),[46] making it a promising candidate for solar energy conversion. However, defects in BFO can significantly affect its optical band gap and therefore its optoelectronic properties. Defects such as oxygen vacancies, bismuth vacancies, and iron vacancies can create trap states within the band gap, which can capture charge carriers and reduce their mobility. These trap states can also act as recombination centers for photoexcited carrier, reducing the overall efficiency of optoelectronic devices.

Doping is the intentional introduction of impurity atoms into a material to modify its properties. In the case of BFO, doping can be used to alter its electronic structure and thus affect its optical band gap. The amount of doping is typically specified as a percentage of the total number of atoms in the material. Doping with small amounts of dopant atoms can have a significant effect on the optical band gap of BFO. For example, doping with La, Sr, or Ca has been shown to reduce the band gap of BFO making it more suitable for solar energy conversion applications.[187] The mechanism behind this effect is related to the formation of defect states within the band gap. Doping with dopant atoms introduces new energy levels within the band gap, which can act as traps for charge carriers. These traps can reduce the energy required for electron excitation and thus decrease the apparent optical band gap. In addition, doping can also modify the crystal structure of BFO, which can further affect its electronic and optical properties. It should be noted that the precise effect of doping on the optical band gap of BFO depends on various factors, such as the type and concentration of dopant atoms, the synthesis method, and the measurement conditions. Therefore, an experimental investigation is necessary to determine the optimal doping conditions for a given application. Understanding the role of dopants in the optical band gap of BFO is crucial for optimizing its optoelectronic properties and enhancing its performance in various applications including catalysis.

In this chapter, the light absorption capabilities of BFO and doped BFO NPs are studied based mainly on UV-visible absorption spectroscopy, Raman spectroscopy, and ultraviolet photoelectron spectroscopy methods. For all doped samples we have collected reflection data and transformed them by Kubelka-Munk function (equation 6.1). We have estimated the band gap via Tauc plot. For studying the chare carrier dynamics, we also utilised the transient absorption spectroscopy method.

6.2 Light absorption capabilities of doped BFO NPs

To study the charge carrier generation by light absorption, we have performed UV-Visible absorption measurements. There are different methods to collect absorption spectra of nanopowders. To avoid method related ambiguities in the analysis of the data, we have first compiled the absorption spectra of the pure BFO NPs by using three methods. Figure 6.1 shows the absorbance spectra obtained using the powder DRS method represented by the black line (a), the transmittance of the NPs dispersed in ethanol (blue line) (b), and the transmittance of the drop-cast and dried NPs (red line) (c). The spectra show a weak absorption feature at around ~ 650 nm (1.90 eV) followed by a steep absorption edge at ~ 550 nm (2.25 eV), possibly containing contributions from two different transitions. These results match well with earlier reports for polycrystalline bulk BFO and different sized BFO NPs.[138,379] We observe that the drop cast (red curve) and powder DRS (black curve) methods give well resolved and nearly similar shapes of the spectra, but for the dispersion method (blue curve) we only see the most prominent features of the absorption spectrum, and other important peaks are hidden. Here, we learn the effect of the chosen method on the absorption spectra of BFO NPs. Since these NPs exhibit strong scattering, the peak at ~ 650 nm diminishes in the transmittance measurement of the dispersed NPs, which was conducted in front of an integrating sphere as per device set-up. Therefore, the collection of reflectance measurements in the solid form inside an integrating sphere to compensate scattering is a reliable way to observe the absorption features of these NPs.

Figure 6.1c shows the transformed absorption spectra of doped and undoped BFO NPs via the Kubelka-Munk function ($F(R_\infty)$).[208]

$$F(R_\infty) = K/S = (1 - R_\infty)^2/R_\infty \tag{6.1}$$

$$R_\infty = R_{\text{sample}}/R_{\text{reference}} \tag{6.2}$$

Here, R_∞ is the reflectance of an infinitely thick sample. K and S are the absorption and scattering coefficients.

The band gap of BFO is mainly formed by strong hybridization of Fe 3*d*, O 2*p* and Bi 6*p* orbitals.[380,381] It exhibits a complex electronic structure caused by spin-charge-lattice couplings due to the convolution of charge transfer bands (interatomic transitions) and absorption bands (*d-d* transitions).[382,138] In Figure 6c, the spectrum exhibits four peaks, where peaks at lower energies, are attributed to the crystal field *d-d* transitions.[379] The peak at ~ 2.50 eV corresponds to the band gap of BFO NPs,[382] and peak at ~ 3.34 eV is due to *p*→*d* charge transfer band.[383]

The band edge of an inorganic material is located at the low energy end of the conduction band above the valence band. It is difficult to determine the band edge for transition metal oxides particularly those presenting magnetic order, because there are narrow d bands in the gap, leading to transitions implying localized charges that to some extent can be excited with infrared radiation with a finite probability. The transitions induced by these photons include the d-d transitions, pair excitation, and finally the charge transfer or optical band gap.

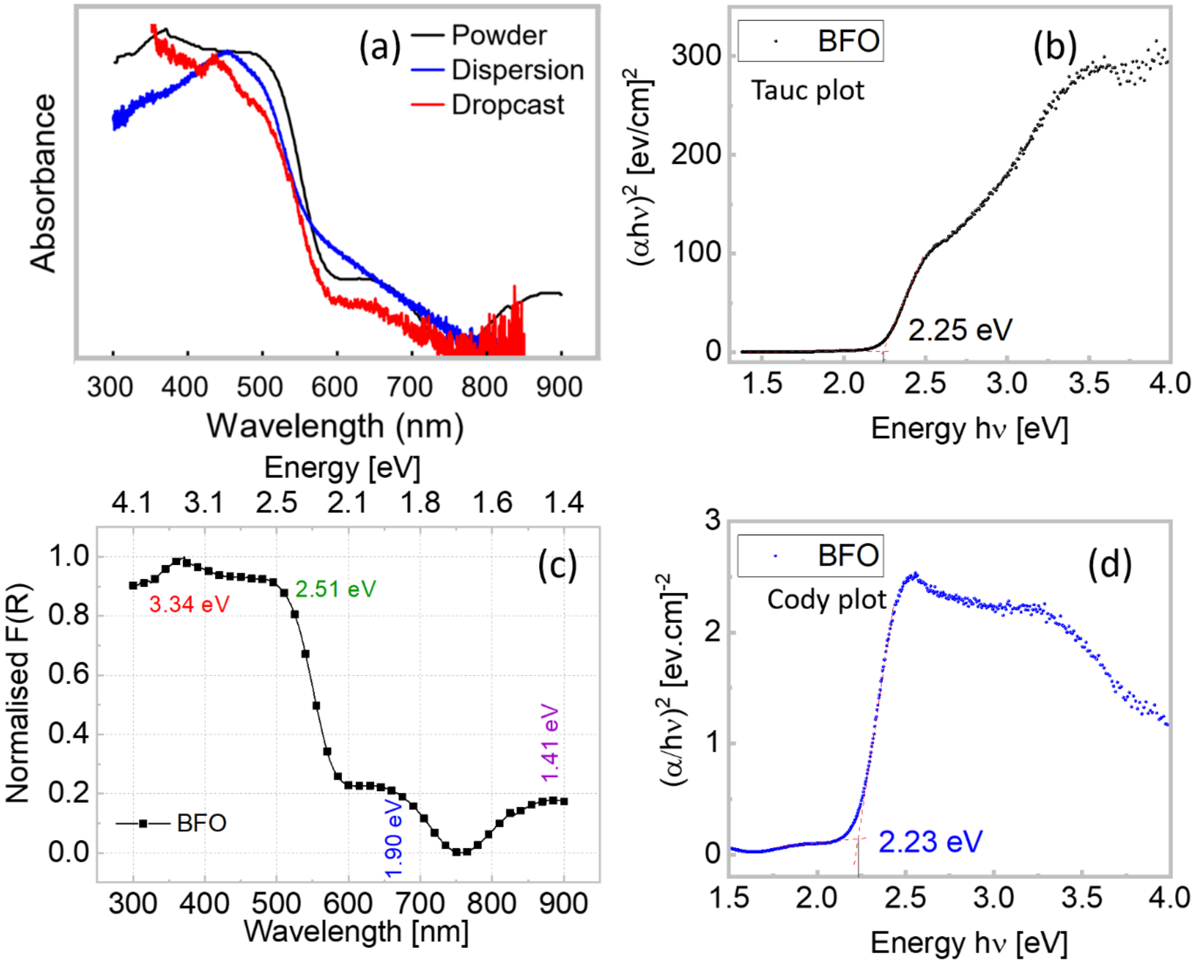

Figure 6.1: (a) Absorbance spectra of BFO NPs obtained by different methods, where the black curve shows transformed reflectance by nanopowder, the blue curve shows absorption spectrum of BFO NPs dispersed in ethanol, and the red curve shows drop cast dispersed BFO NPs onto a Si substrate. (b) Tauc plot for direct band gap approximation, and (d) Cody plot for direct band gap approximation. (Error bar is 0.001 eV), (c). Transformed reflectance spectra equivalent to absorbance spectra collected in DRS set up for BFO NPs.

There are many theories available to estimate the band gap, including most accepted one the Tauc model as described in "the *Materials and Method*" section. In literature, BFO is often considered as a direct band gap semiconductor by both theoretical and experimental proofs,[384,385,386] so having this in consideration for BFO NPs we fit the absorbance data using the Tauc model, and the Cody model as shown in Figure 6.1 b-d. A direct band gap material is one in which the minimum energy required to excite an electron from the valence band to the conduction band, this occurs at a single point in the Brillouin zone, usually at the Γ-point. An indirect band gap material, on the other hand, has its minimum energy at a different point in the Brillouin zone, typically at the edge of the Brillouin zone. To confirm that a material is having direct or indirect band gap, temperature dependent optical studies are a must. For a new material it is very naive to claim the type of band gap based on any available theory and without temperature dependent absorption measurements.

Nevertheless, the Tauc plot is a good fit for a direct or an indirect band gap, one can examine the shape of the curve in the high-energy region. In the case of a direct band gap material, the Tauc plot will have a linear relationship between the absorption coefficient and the photon energy, and the linear fit will have a high R-squared value, indicating a good fit. However, for an indirect band gap material, the Tauc plot will have a non-linear relationship, and a linear fit will not have a high R-squared value, indicating a poor fit.

One advantage of the Cody plot over the Tauc plot is that it allows for the detection of small deviations from linearity near the bandgap, which can result from non-idealities in the material such as impurities or defects. The Cody plot can also provide more accurate bandgap values for materials with a significant Urbach tail, which is a phenomenon that results in a gradual increase in absorption at energies just below the bandgap. However, the Cody method is problematic for materials with a broad absorption edge. The Cody plot can be more sensitive to measurement noise than the Tauc plot, particularly at high absorption levels. This can lead to increased uncertainty in the calculated bandgap energy.

Hence, the Tauc plot is widely used due to its simplicity and ease of interpretation especially for materials with a well-defined bandgap. Additionally, the Tauc method is often preferred for materials with a high absorption coefficient, as the Cody method can be sensitive to measurement noise at high absorption levels.

From both models based on direct band gap, it is evident that the BFO NPs also have a direct band gap nature with an optical bad gap of ~ 2.23-2.25 eV. There is a linear relationship between the absorption coefficient and the photon energy, and the linear fit also has a high R-squared value.

6.2.1 Influence of single doping in BFO NPs

BFO NPs were doped with Mn, and Co at its Fe-site and with Ba at the Bi-site to study the influence of single doping at individual sites on the overall optical band gap of BFO NPs. BFM, BFC, and Ba-BFO were measured by DRS as explained in "*Materials and Techniques*" chapter 2.

From Figure 6.2a we observe that Ba doping at the Bi-site causes a little change in the reflection spectrum of BFO, however Co and Mn doping have a large influence on the reflection spectrum of BFO NPs. Similar observations are found in the absorbance spectra (transformed reflectance spectra) in Figure 6.b. Upon calculating the band gap using the Tauc model for direct band gap approach, [Figure 6 c-f] we find that Ba-BFO does not change the band gap except for a little deviation, whereas Mn and Co doping reduce the band gap of BFO. BFC NPs have the lowest band gap of 2.17 eV.

The large influence of Co and Mn doping and the less effect of Ba doping can be explained by the following arguments.

Co^{3+} and Mn^{3+} are both transition metal cations with partially filled d-orbitals. Co^{3+} is not a Jahn-Teller cation as it does not have a degenerate electronic ground state, while Mn^{3+} is a Jahn-Teller cation and exhibits Jahn-Teller distortion to minimize the energy of its degenerate electronic ground state. The Jahn-Teller effect is a phenomenon that occurs when a non-linear molecular or complex ion has a degenerate electronic ground state.

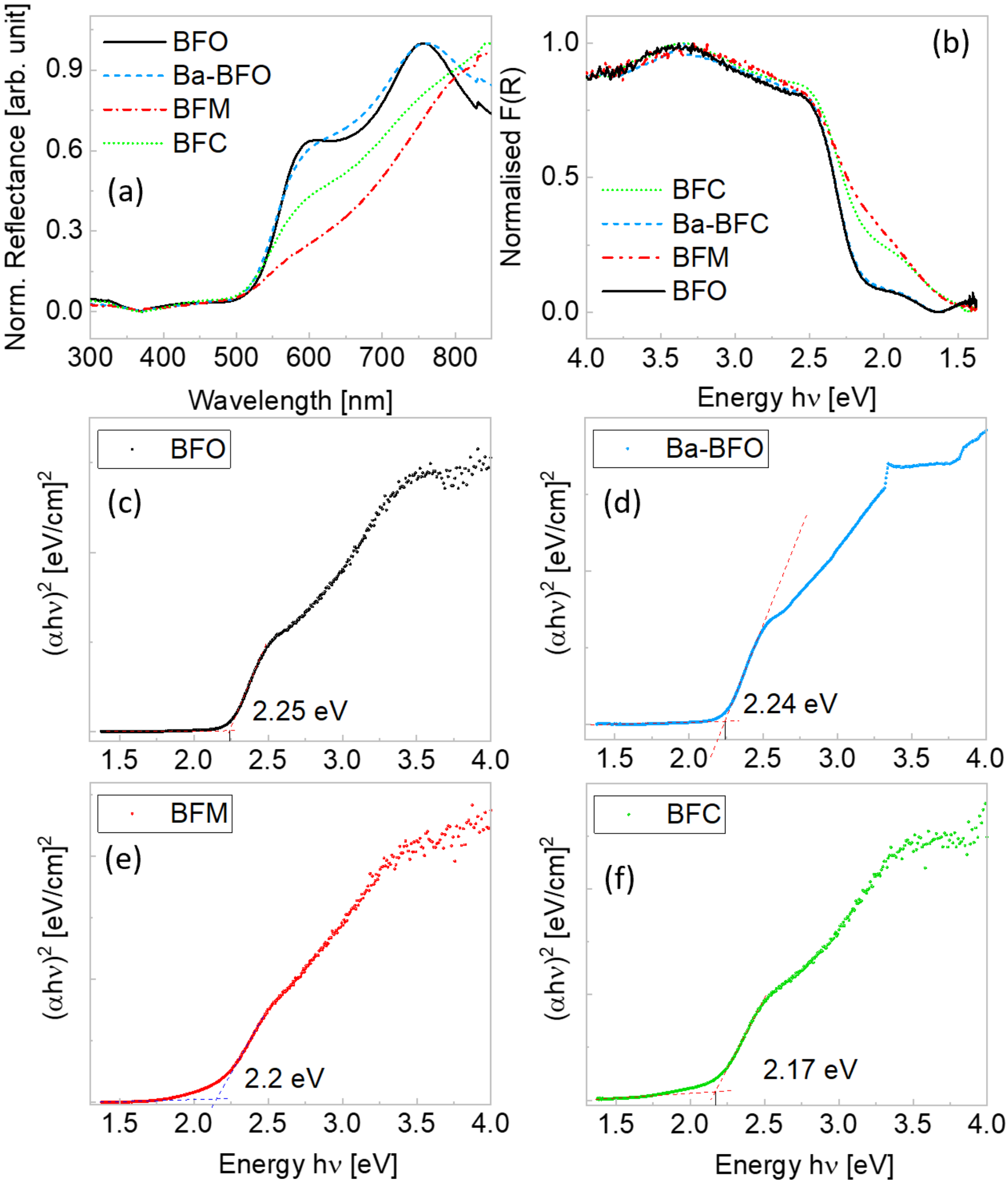

Figure 6.2: (a) The normalised reflectance spectra of BFO, BFM, BFC and Ba-BFO NPs, (b) The normalised absorbance calculated using Kubelka-Munk method, (c-d) Tauc plots for direct band gap approximation. (Error bar is 0.01 eV)

In such case, the symmetry of the electronic shell of the ion is lowered to remove the degeneracy and minimize the energy of the system. Co^{3+} has a partially filled d-orbital configuration of d^6, which has a ground state of $^4T_{2g}$. This ground state is not degenerate, so there is no Jahn-Teller distortion observed in Co^{3+}. Mn^{3+}, on the other hand, has a partially filled d-orbital configuration of d4, which has a degenerate electronic ground state ^4G. Therefore, the symmetry of the Mn^{3+} lowered to remove the degeneracy and minimize the energy of the system. The Jahn-Teller effect can result in a variety of geometries, such as elongation, compression, or distortion of the coordination geometry, depending on the specific system.

In perovskite-like BFO, the optical bandgap is mainly attributed to the Fe 3d orbitals within the FeO_6 octahedral units. These FeO_6 octahedra are the building blocks of the crystal structure of BFO, and the overlap of Fe 3d orbitals within the octahedra contributes to the band structure of the material. However, the Bi 6s and 6p orbitals also play a role in the electronic structure of BFO. The Bi 6s and 6p orbitals hybridize with the O 2p orbitals to form hybrid orbitals that are involved in the bonding with Fe and contribute to the electronic structure of BFO.[138]

In general, doping at the Fe-site is expected to have a stronger influence on the optical bandgap of BFO than doping at the Bi-site, since the Fe 3d orbitals make a larger contribution to the optical bandgap of the material.

The band gap is not much affected by Ba doping, which makes sense since the Fe-site is more involved in band gap determination than Bi. Upon Mn doping at the Fe-site the band gap reduces by 0.5 eV and for Co doping the band gap reduces down to 2.17 eV from 2.25 eV of pristine BFO NPs. This also shows that Cobalt doping has the largest influence on the band gap among other dopants. Whereas Mn doping has a larger influence on the d-d transitions in BFO NPs than cobalt doping due to the distortion in the electronic levels via the Jahn Teller cation asymmetry.

6.2.2 Role of dopant concentration on light absorption of BFM NPs

To study the role of dopant concentration on the optical properties of BFM NPs, we doped 1, 3, and 5 mol % of Ba at the Bi-site and studied the light absorption properties as compared to pristine BFO NPs.

“In Figure 6.3, BFO NPs exhibits peaks at ~ 1.41 eV (879 nm), ~ 1.90 eV (652 nm), ~ 2.50 eV (496 nm), and ~ 3.34 eV (371 nm). The peaks at lower energies, 1.41 eV and 1.90 eV, can be attributed to the crystal field *d-d* transitions $^6A_{1g} \rightarrow {}^4T_{1g}$ and $^6A_{1g} \rightarrow {}^4T_{2g}$ respectively.[379] The peak at ~ 2.50 eV manifests the optical band gap of BFO NPs,[382] and ~ 3.34 eV correspond to *p→d* charge transfer band.[383] Upon Mn incorporation, the global shape of the BFO absorption spectra changes and upon further Ba doping the shape is altered again, which shows the individual effect of these dopants on the electronic structure of BFO NPs.

The $^6A_{1g} \rightarrow {}^4T_{2g}$ transition (~ 1.90 eV) becomes more intense and broader for BFM, which shows a distortion in energy levels due to the Jahn-Teller effect originating from the presence of Mn^{3+} ions as confirmed by XPS analysis in earlier chapters.[10] This peak is even more intense and shifted to a higher energy for 1BBFM. Upon further Ba doping, the absorption peak at ~ 1.98 eV slightly broadens, and the intensity of the peak ~ 2.51 eV increases. One can see that in the photon energy range from 1.6 to 2.50 eV the Ba+Mn co-doped NPs absorb more solar light than the BFM and undoped BFO NPs.

Further co-doping of Ba into BFM increases the unit cell volume and the Mn^{3+} concentration reduces in favor of Mn^{4+}, as per XPS studies on Ba and Mn co-doped BFO NPs and also by Raman [Figure 6.4 b]. It is important to notice that this effect is most significant for the 1BBFM, which also has the largest unit cell volume.[10] For co-doped BFO NPs, two main factors cause important changes in the electronic structure: increased unit cell volume due to bigger Ba^{2+}, and presence of Jahn-Teller cation (Mn^{3+}). In total, the structural distortion leads to an alteration in the Fe-O bond lengths, Fe-O-Fe bond angles [see chapter 4] and influences the *d-d* crystal field transition energy levels[387] and can alter the electronic transition of C_{3v} crystal symmetry of BFO. As per Wei et al. an increase in crystal field splitting due to the reduction in the unit cell volume via doping by rare earth elements leads to a decrease in the energy edge of *d-d* transitions.[388] In our case the increase in unit cell volume due to Ba doping into BFM leads to an increase of the $^6A_{1g}\rightarrow{}^4T_{2g}$ *d-d* transition energies (Figure 6.3). The increase of the light absorption associated with the $^6A_{1g}\rightarrow{}^4T_{2g}$ *d-d* transition due to the doping influences the photocatalytic efficiency significantly.

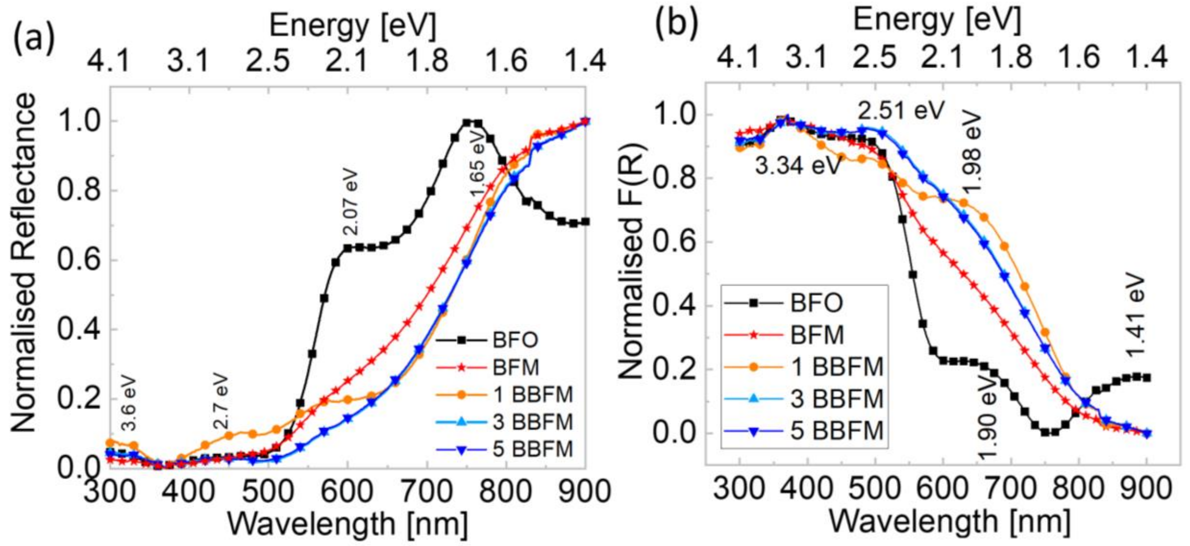

Figure 6.3: (a) Normalised diffuse reflectance spectra, and (b) Kubelka-Munk transformed F(R) normalised absorption spectra for all Ba and Mn co-doped BFO NPs. [© 2021 Nanoscale Advances][150]

To further confirm the presence of the Jahn Teller effect, Raman spectroscopy was used which assesses the phonon density at the Brillouin zone centre so it can provide details about the structural distortions generated by doping. There is a total of 13 Raman active modes for the rhombohedral structure of BFO.[81] In the deconvoluted Raman spectra (Figure 6.4), all 13 Raman active modes ($4A_1 + 9E$) were assigned for pure BFO NPs, which are in good agreement with other reports[78-80] (Appendix Table 3).**”**[h]

“For a better comparison, the normalized Raman spectra with respect to the E(TO1) mode are shown in Figure 6.4. Doping by 5 % Ba does not shift the position of the modes of the BFO Raman spectra but alters the intensity and bandwidth of the modes corresponding to the Bi-O bond vibrations, i.e. modes below 167 cm^{-1} (E(TO1, E(TO2)).[80] The full width at half maximum (FWHM) for the E(TO1) and A_1(TO4) modes (Figure 6.4c) changes significantly after

---

[h] This paragraph is based on (Dubey et al, Nanoscale Advances, 2021, http://doi.org/10.1039/d1na00420d)

Mn and further Ba incorporation into the BFO NPs. The number of the resolved modes decreases after Mn doping into BFO NPs (Appendix). Two prominent bands appear at around 500 cm^{-1} and 630 cm^{-1}. The peak near 630 cm^{-1} corresponds to the A_1(TO4) mode, which is regarded as the bending and stretching of BO_6 octahedra via alteration in B-O bonds.[88] Appearance of these bands cannot be due to the structural transition, since this possibility was already ruled out by Rietveld analysis of XRD data. These features display a Jahn-Teller distortion, which is mainly due to the symmetric and asymmetric stretching of basal oxygens of the BO_6 octahedra.[86,87] The relative intensity of Raman modes ($I_{A1(TO4)}/I_{E(TO1)}$) increases upon Mn doping into the BFO NPs whereas Ba doping into 5 % Mn doped BFO decreases it in a non-linear fashion (Figure 6.4).**"**[i]

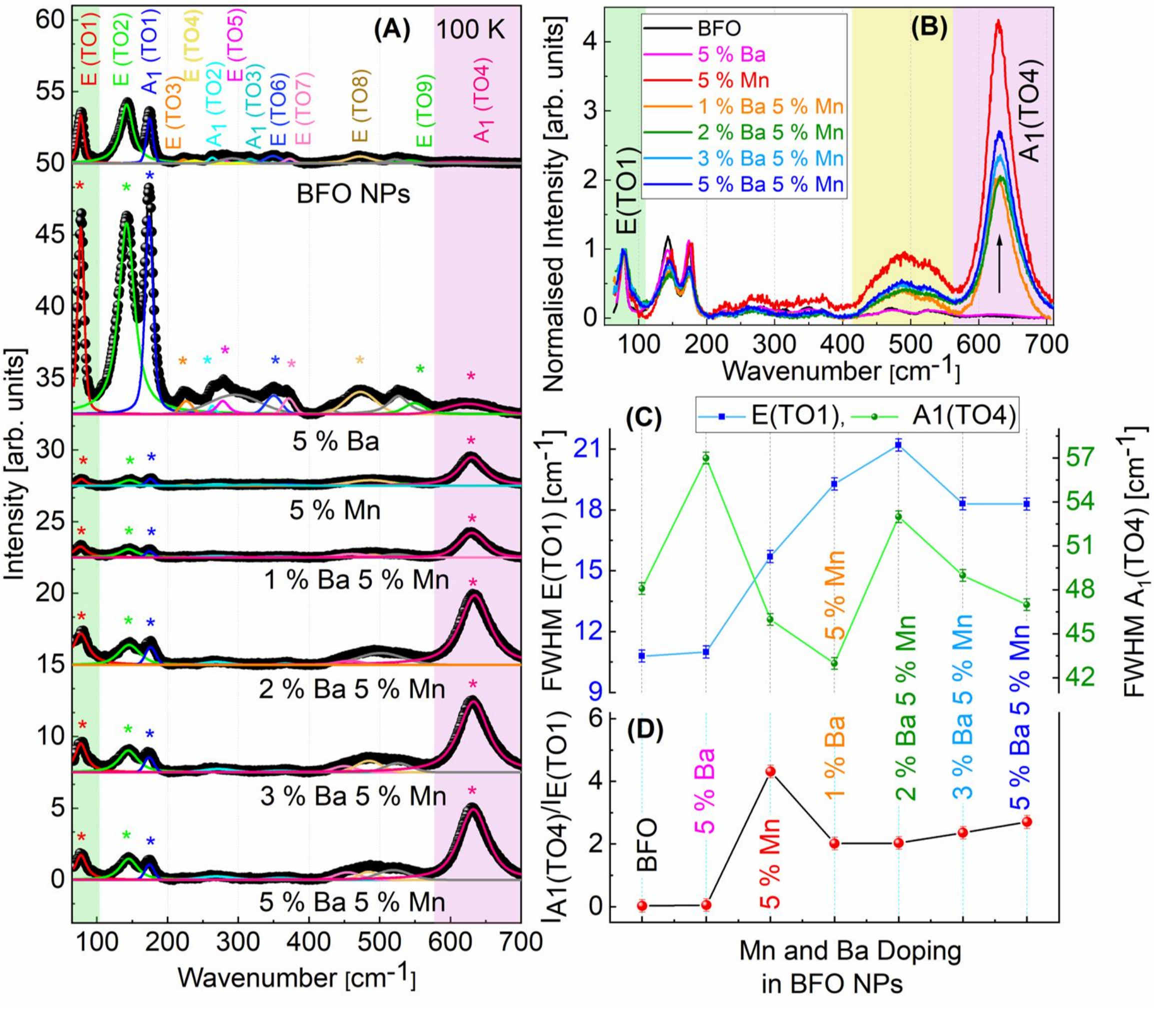

Figure 6.4: Deconvoluted Raman spectra for Ba and Mn doped BFO NPs are shown in panel (A), Normalized Raman spectra with respect to the E(TO1) mode are shown in (B), plot (C) shows a comparative study of FWHM of the E(TO1) and A_1(TO4) modes and plot (D) shows the intensity ratio of E(TO1) and A_1(TO4) mode for all the samples. [© 2020 The Journal of Physical Chemistry C][389]

We can thus conclude that Mn doping results in the appearance of a Jahn-Teller cation on the B-site of the perovskite structure, which can be only Mn^{+3}. Ba doping into 5 % Mn doped BFO NPs changes the shape, position, and bandwidth of Raman modes, which could be due to the

---

[i] This paragraph is based on (Dubey et al, Journal of Physical Chemistry C 2022, https://doi.org/10.1021/acs.jpcc.0c05778)

effect of charge compensation on the FeO_6 or MnO_6 octahedra. There are slight changes in the Tauc plot of BFM due to Ba doping, based on direct band gap approach, these changes are in the lower energy region. 1BBFM has the lowest band gap. The appearance of humps/shoulder in the lower energy region indicate the formation of defect states in the band gap of BFM NPs, due to the incorporation of the divalent Ba ion at the Bi-site. As we know doping of divalent ions at the Bi site will create oxygen vacancies. The oxygen vacancy form trap states in the band gap of BFM NPs, which might be friendly or foe for the catalytic applications.

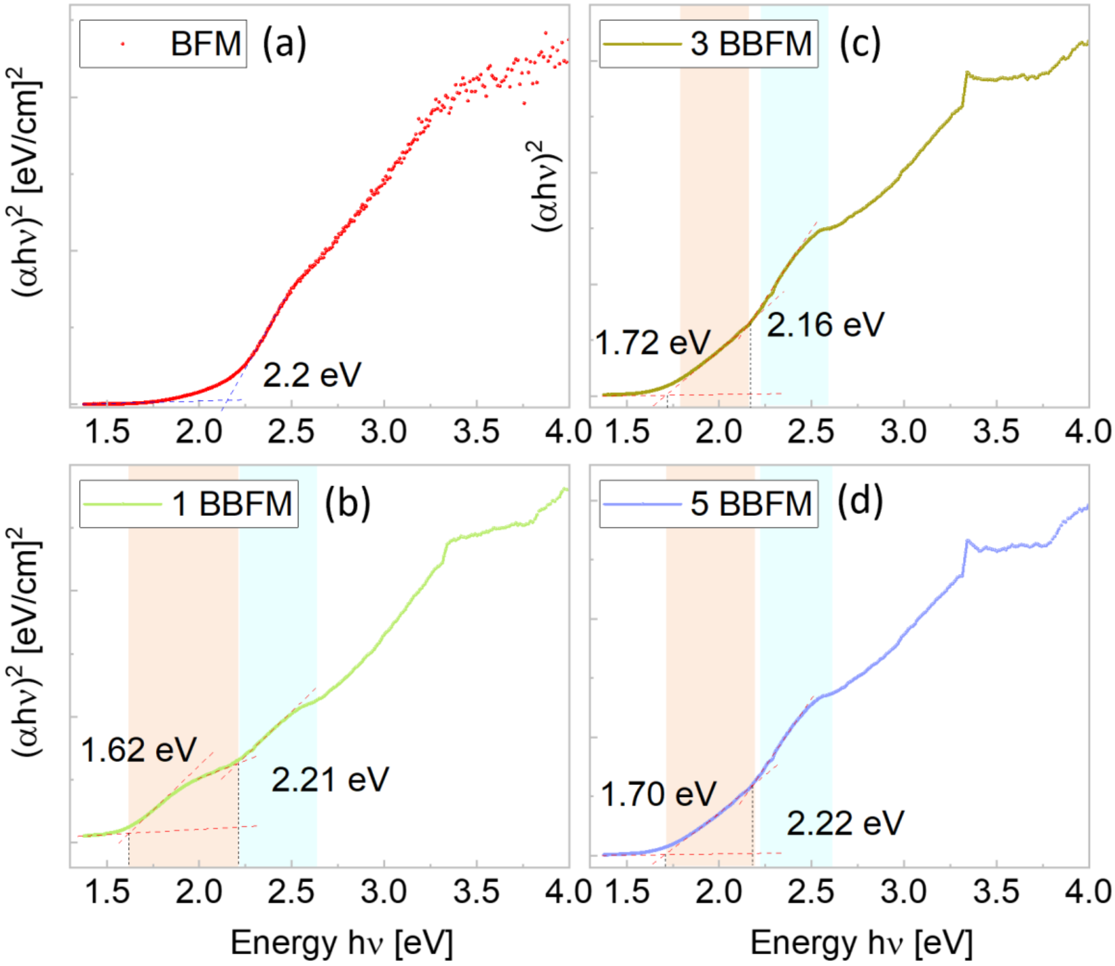

Figure 6.5: Tauc plot for Ba doped BFM NPs with direct band gap approximation. (Error bar is 0.001 eV)

6.2.3 Role of mono-, di, and tri-valent dopant on light absorption of BFM NPs

"We doped monovalent Ag^+, divalent Ca^{2+}, and trivalent Dy^{3+} onto the Bi-site individually in BFM NPs, to study their influence on light absorption. We call these dopants MDT doping, to represent mono-, di-, tri- valent dopants. Since BFM NPs show stronger absorption in the *d-d* transition region than BFO NPs, which is caused by the Jahn-Teller cation (Mn^{3+}).[150] When doping with MDT ions into BFM, we observe an increase in absorption not only in the *d-d* transition range, but also near ~2.5 eV, which shows that the Bi-site substitution increases the total light absorption of the BFM NPs in the visible range from 3.5 to 1.3 eV. Among the MDT doped NPs, the Dy-BFM ones have the strongest absorption around 2.5 eV. The band gap does not alter significantly upon doping, however, there are some transitions that will be analyzed in more detail. [Figure 6.6]

From Figure 6.6b-d, we observe that the band gap of BFM NPs (2.2 eV) has slightly reduced down to 2.07 eV for Ca-BFM NPs. However, among the MDT doped BFM NPs, there is no large difference between the band gaps, which is surprising and interesting. As per the valency these dopants should create different numbers of oxygen vacancies in the BFM NPs, however we have not found any effect of vacancies in the bad gap of BFM NPs."[j]

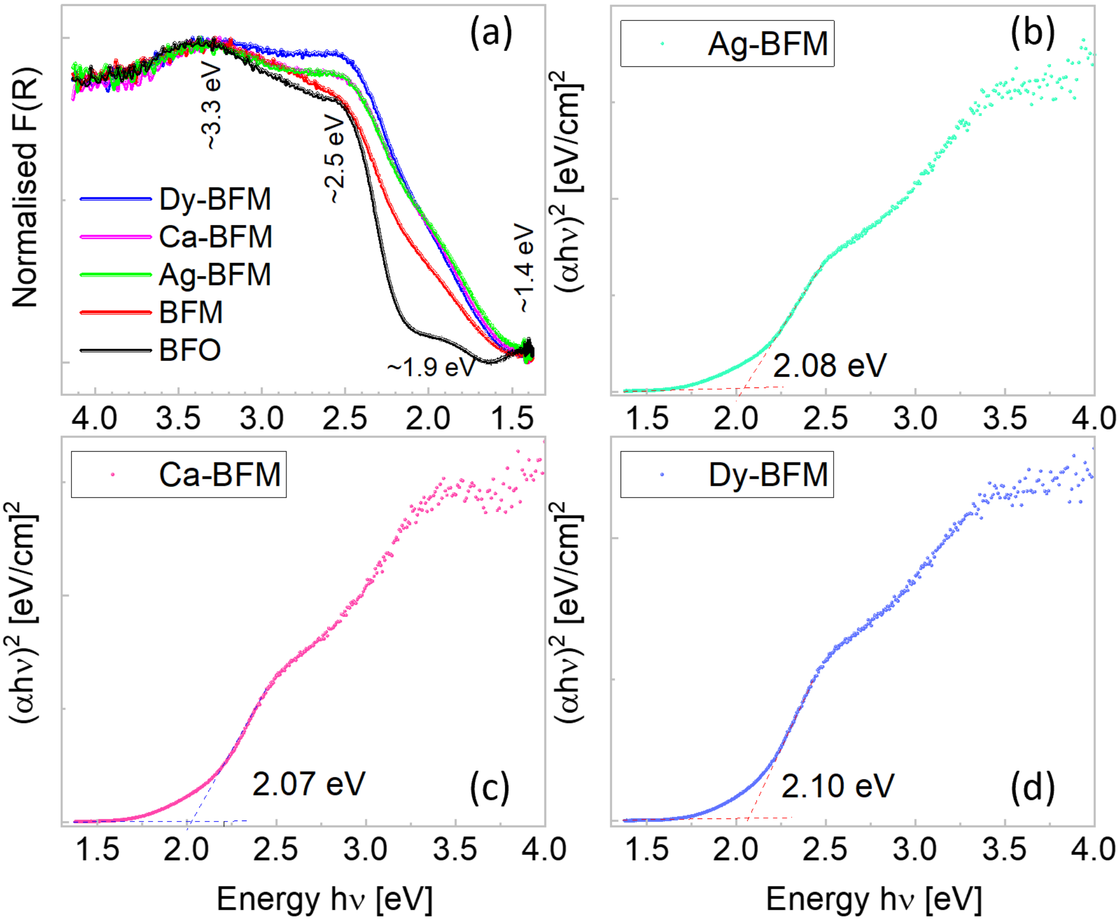

Figure 6.6: (a) Normalised absorbance spectra of Ag, Ca and Dy doped BFM NPs, (b) Tauc plot of Ag doped BFM NPs, (c) Tauc plot of Ca doped BFM NPs, and (d) Tauc plot of Dy doped BFM NPs with direct band gap approximation. (Error bar is 0.01 eV)

It is possible that the presence of oxygen vacancies may not significantly alter the band gap of a material or create defect states within the band gap. This can occur, if the oxygen vacancies are localized in regions of the material that are already rich in defects or if they are effectively passivated by nearby impurities or dopants. To further confirm this, we also studied role of MDT ion doping in BFC NPs in the next section.

---

[j] This paragraph is based on (Dubey et al, Advanced Functional Materials 2022, https://doi.org/10.1002/adfm.202207105)

6.2.3.1 Role of mono-, di, and tri-valent dopant on light absorption of BFC NPs

To understand the effect of MDT ion (Ag, Ca, and Gd) doping into BFC NPs on their light absorption properties we evaluated the DRS data shown in Figure 6.7. For BFC NPs, the band gap is 2.17 eV as shown in Figure 6.2f. Upon MDT doping, the band gap slightly reduced down to 2.05 eV for Ag-BFC NPs. However again among the MDT doped BFC NPs, we have not found significant difference in the band gap similar to MDT doped BFM NPs. This shows that doping at the Bi-site, only has an indirect influence on the band gap alteration as comparative to doping at Fe-site and the effect is less pronounced. Nevertheless, at lower energies the slope of the Tauc plot changes among the MDT doped BFC and also for MDT doped BFM NPs.

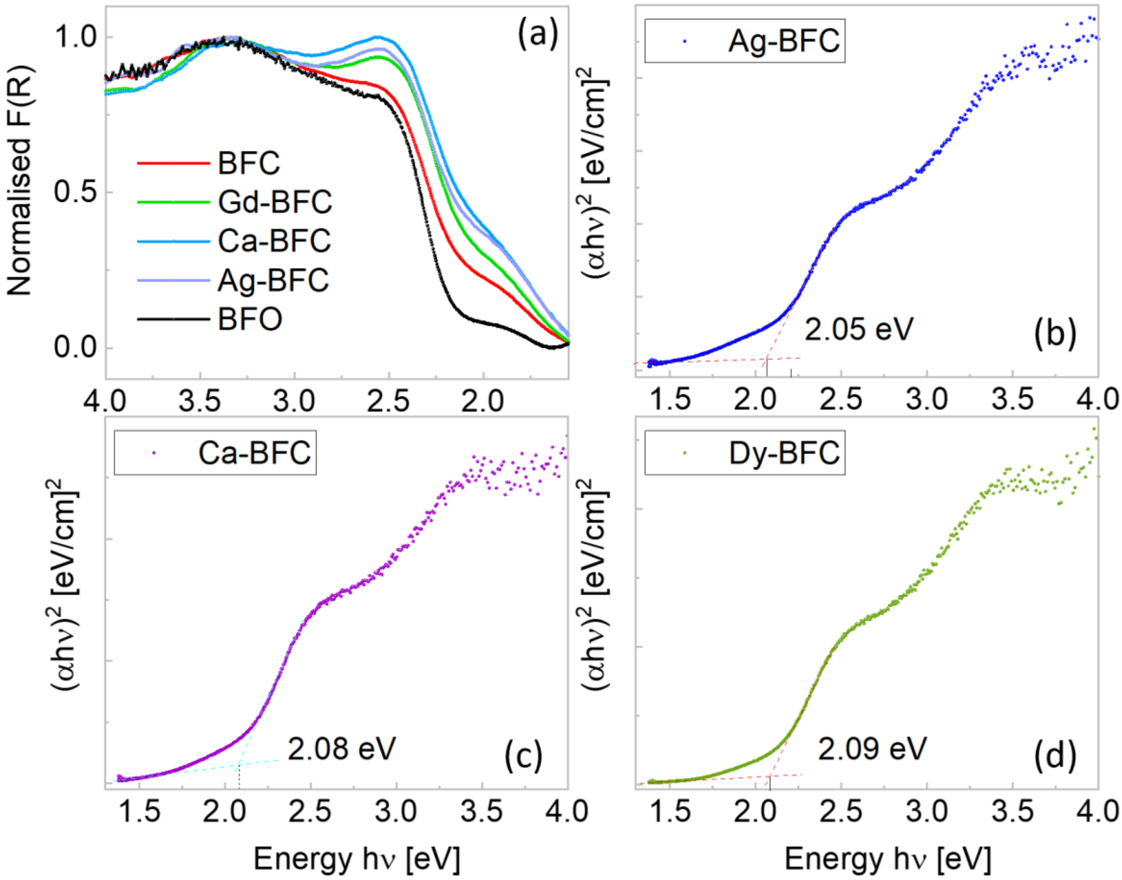

Figure 6.7: (a) Normalised absorbance spectra of Ag, Ca and Dy doped BFC NPs, (b) Tauc plot of Ag doped BFC NPs, (c) Tauc plot of Ca doped BFC NPs, and (d) Tauc plot of Dy doped BFC NPs with direct band gap approximation. (Error bar is 0.01 eV)

6.2.4 Light absorption properties of rare Earth (lanthanides) doped BFM NPs

The trivalent lanthanides (La^{3+}, Nd^{3+}, Sm^{3+}, Gd^{3+}, and Dy^{3+}) were doped at the Bi site into the BFM NPs to study their influence on the light absorption properties. Figure 6.8 shows the reflectance and absorbance spectra. From Figure 6.8b, it is evident that Gd-BFM has the strongest light absorption capability among all RE doped BFM NPs and BFM NPs. La, Dy, Nd, and Sm increase the light absorption but are similar among themselves.

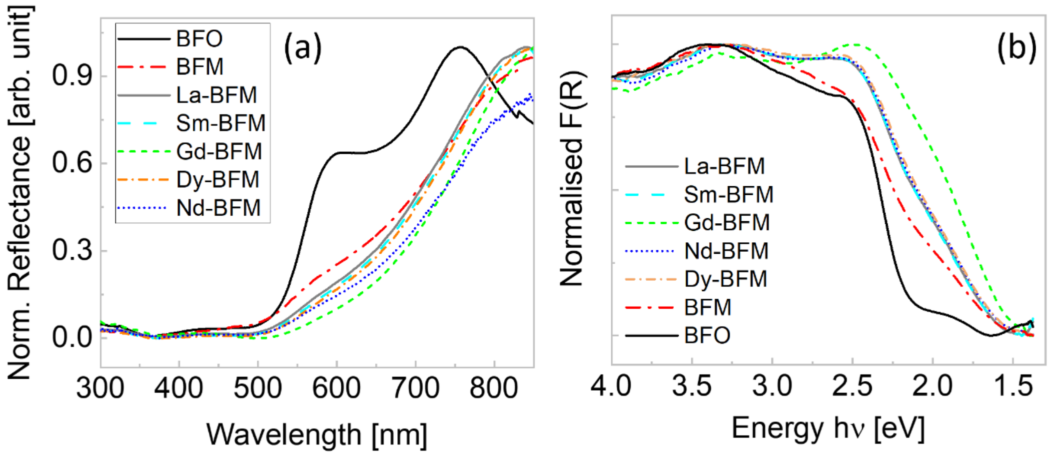

Figure 6.8: Normalised reflectance and normalised absorbance of RE metal doped BFM NPs.

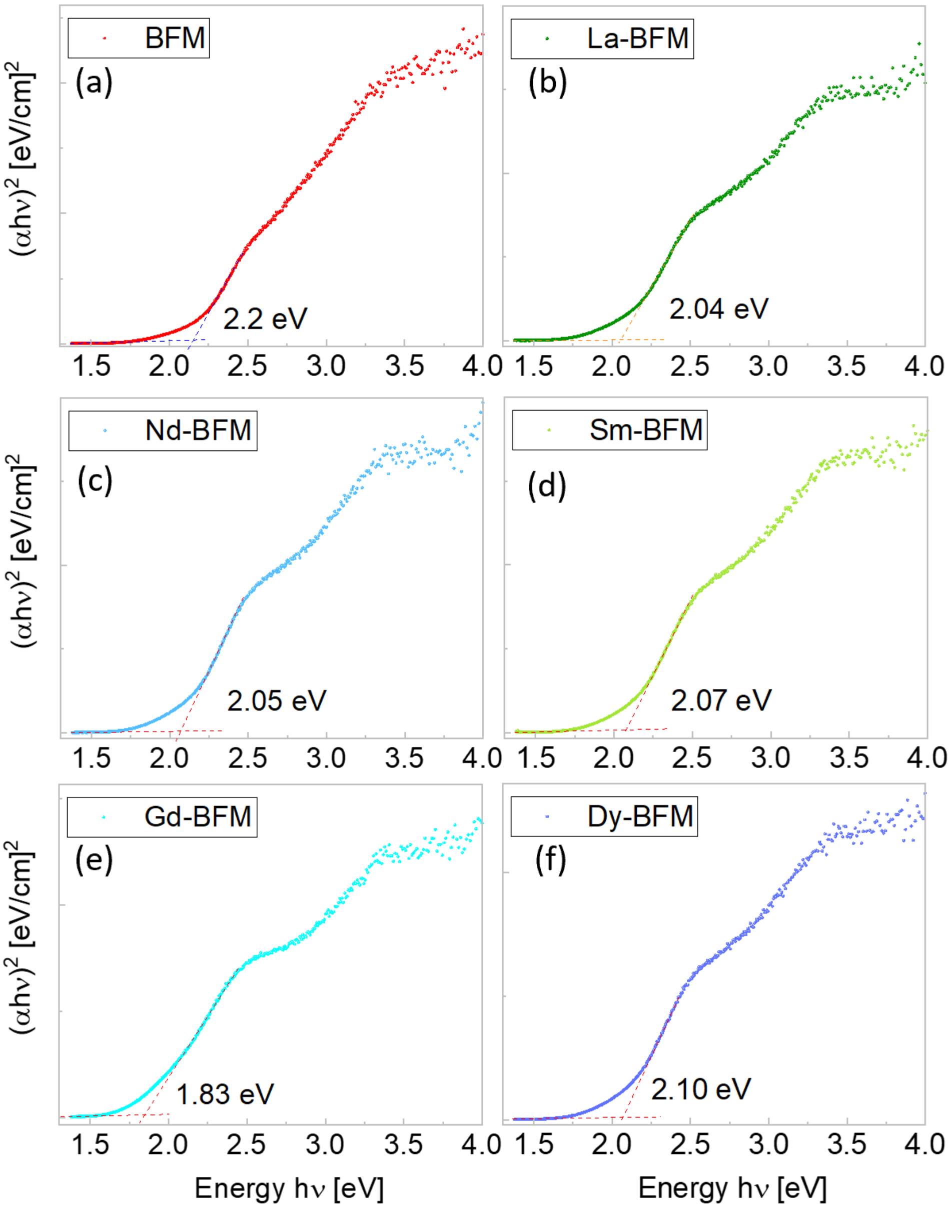

Figure 6.9: Tauc plots of the rare earth lanthanide doped BFM NPs with direct band gap approximation. (Error bar is 0.01 eV)

The Tauc plots for RE-doped BFM NPs are plotted in Figure 6.9. The RE doping has reduced the band gap of BFM NPs significantly, the lowest value is observed for Gd-BFM NPs around 1.83 eV. There is no large difference in the band gaps of La-BFM, Nd-BFM, and Sm-BFM NPs. However, upon Dy-doping the band gap reduces to 2.10 eV, which is still less than BFM NPs.

With seven electrons in the 4f orbitals, Gd^{3+} exhibits a half-filled electronic configuration. This unique electronic structure can have a significant impact on the band structure. Gd^{3+} ions can interact with the O 2p orbitals, which are located near the conduction band minimum of BFM. This interaction can result in a reduction of the band gap due to the larger interaction between the 4*f* electrons of Gd^{3+} and the O 2p orbitals of BFM than the other RE ions.

Crystal field theory can also be used to explain the contribution of f orbitals to the band gap of BFO. In BFO, the t_{2g} levels are completely filled, while the e_g levels are only partially filled in the energy diagram of FeO_6 high spin environment. These levels get further split due to the presence of the Mn Jahn Teller cation for the BFM case. Gd doping can provide interaction with these Mn/Fe *d* orbitals through the *f* orbitals. This interaction can lead to further splitting of the energy levels and an alteration in the band structure of BFM NPs.

6.3 Band edge level estimation

We utilised ultraviolet photoelectron spectroscopy (UPS) to determine the valence band edge of doped BFM NPs. The UPS measures the kinetic energy of electrons ejected from the valence band of the semiconductor material by a photon of known energy as explained in the "materials and method" chapter. We fit a tangent line to the UPS at the point of maximum slope just before the sharp drop in intensity. Afterwards, we extrapolate the tangent line to the photon energy axis to determine the energy at which the valence band edge is located. This energy corresponds to the maximum kinetic energy of electrons in the valence band, using this we calculate the valence band edge relative to the Fermi level.

From Figure 6.11, we observe that upon Mn doping there is a slight decrement in valence band edge. Further doping of monovalent Ag does not change the valence band edge but doping of divalent ions like Ba and Ca reduces the valence edge down to 1.36 eV from 2.0 eV for BFM NPs. Interestingly upon La doping the valence band edge is found to be at 1.65 eV and for Gd-BFM at 1.76 eV.

For Dy-BFM the valence band edge is found to be at the lowest energy of 1.2 eV. Though the UPS spectrum of Dy-BFM is not usual, as other NPs, even after several repetitions of the measurements we find similar result. This can be potentially explained based on the available vacancies in Dy-BFM NPs, as confirmed by the O1s XPS spectra of Dy-BFM NPs [previous chapter 4].

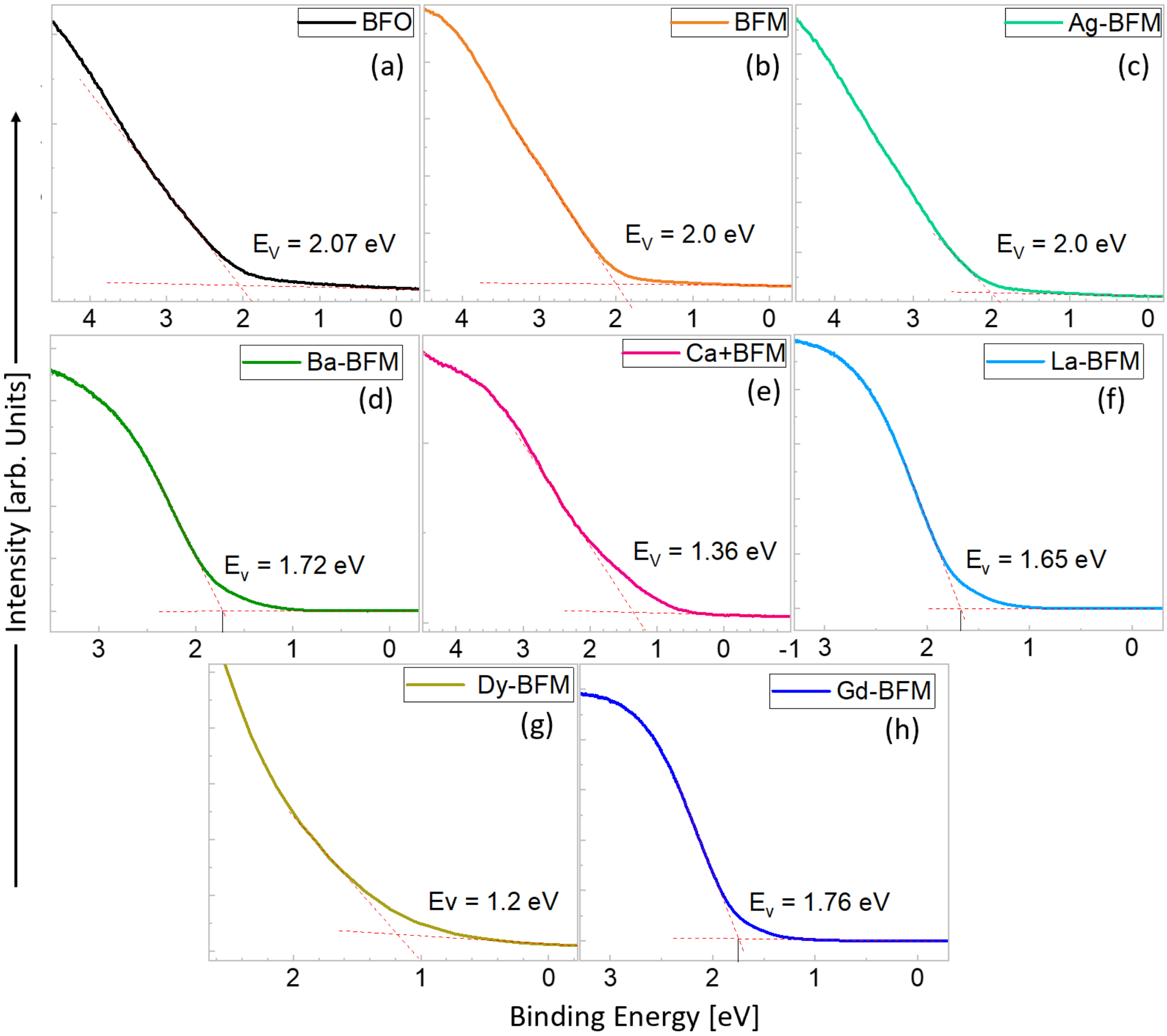

Figure 6.10: Valence edge calculation using UPS spectrum of doped BFM NPs and undoped BFO NPs. (Error bar 0.05 eV)

Using the information of the valence band edge from the UPS dataset and the above studies of band gap from Tauc plots, we estimate the conduction band edge of these materials. The Figure 6.11 shows the estimated conduction and valence band edges and the band gap for doped BFM NPs. The conduction band of Dy-BFM is above 0 eV on the energy scale (towards negative energy) which shows that these doped NPs can be potential candidate for hydrogen generation under light irradiation. Of course, other properties of catalysts must be tested like surface area, and charge transport before final conclusion.

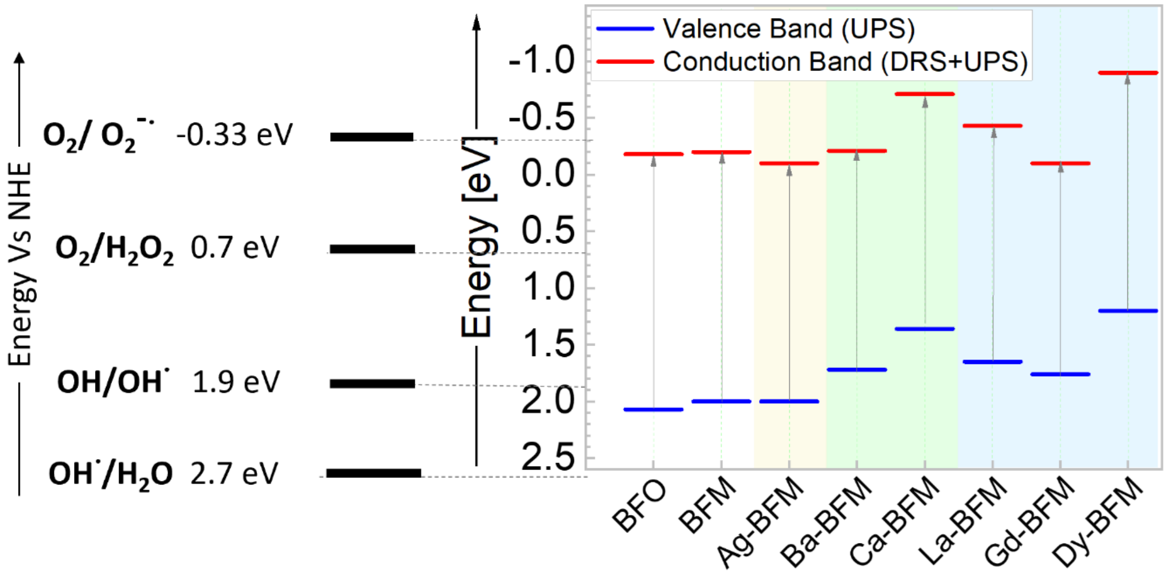

Figure 6.11: The band edge of doped BFM NPs versus normal hydrogen electrode. (Error bar is line thickness)

6.4 Charge carrier dynamics in MDT doped BFM NPs

To unveil the charge carrier dynamics a photocatalyst, various spectroscopic techniques can be employed. For example, transient absorption spectroscopy, time-resolved fluorescence spectroscopy, and time-resolved terahertz spectroscopy can be used to investigate the dynamics of charge carriers in the material.

To study the recombination of photoinduced charge carriers we utilized photoluminescence (PL) spectroscopy. All samples show a broad PL maximum between 500 and 700 nm. The PL intensity and the position of the PL maximum change drastically upon doping [Figure 6.12]. BFO NPs have the highest PL intensity. Doping with Mn reduces it by about four times. Further doping with Ca or Dy does not significantly change the PL, but for Ag-BFM the PL intensity re-increases by a factor of 2.5. Interestingly, the Dy-BFM NPs have the lowest PL intensity among all NPs under study. Upon closer examination, it turns out that the total PL signal is a superposition of two PL peaks at 560-575 and 605-625 nm.

“For the BFO NPs, the main peak at ~562 nm (2.21 eV) corresponds to the emission from the band gap, and the second (lower) peak at ~605 nm (2.05 eV) is due to defect level emission (DLE). Upon doping, a red shift of the peak positions is observed, which can be attributed to an alteration in the electronic energy levels. Since PL emission spectra arise as a result of radiative recombination of electrons and holes, a smaller area of the emission peak corresponds to a lower recombination rate.

It can be seen that the areas of both PL peaks decrease when we dope Mn into BFO [Figure 6.12], whereas the absorption of BFM NPs is higher than that of BFO NPs. This means that BFM NPs have a lower recombination rate of photoinduced charge carriers than BFO NPs, which may be associated with doping-induced trap states inside the band gap. For Ag-BFM NPs, the areas of the PL peaks increase in comparison to BFM. This increase can be due to stronger light absorption by Ag-BFM NPs, as shown previously. For Ca-BFM NPs, we observe that light absorption is similar as Ag-BFM, but the area of the PL peaks is smaller, which indicates a weaker recombination of the charge carriers than in the case of Ag-BFM NPs. Interestingly, Dy-BFM NPs have the strongest light absorption but have the smallest PL peak area among all NPs, which indicates the weakest recombination of charge carriers. In addition, the green peak area corresponding to defect level emission is smallest in the case of Dy-BFM among all.

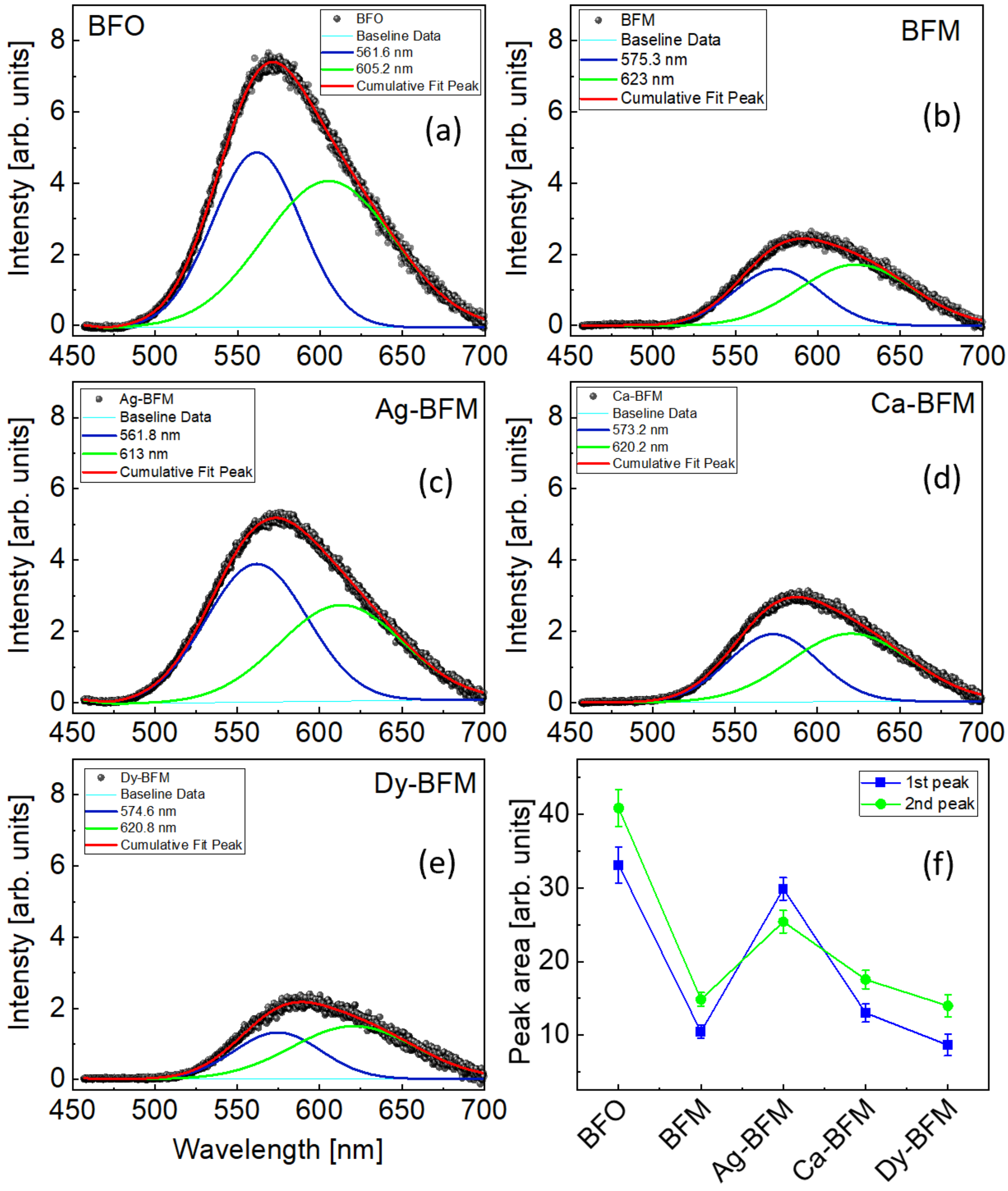

Figure 6.12: Deconvoluted PL spectra of BFO NPs (a), BFM NPs (b), and MDT doped BFM NPs (c-e). Peak area trend for both peaks: green: peak at low energy, blue: peak at high energy.

The time resolved photoluminescence (trPL) decay kinetics of BFO NPs, BFM and Dy-BFM NPs are shown in Figure 6.13. The decay kinetics are fitted by a bi-exponential decay function, $\mathrm{I} =$

$A_1\exp(-t/\tau_1) + A_2\exp(-t/\tau_2)$. The average lifetime of charge carriers is calculated using equation 6.3.

$$\text{Average } \tau = \frac{[(A_1 \cdot \tau_1^2) + (A_2 \cdot \tau_2^2)]}{[(A_1 \cdot \tau_1) + (A_2 \cdot \tau_2)]} \tag{6.3}$$

The average lifetime of these NPs is in the range of a few μs (Table 6.1).

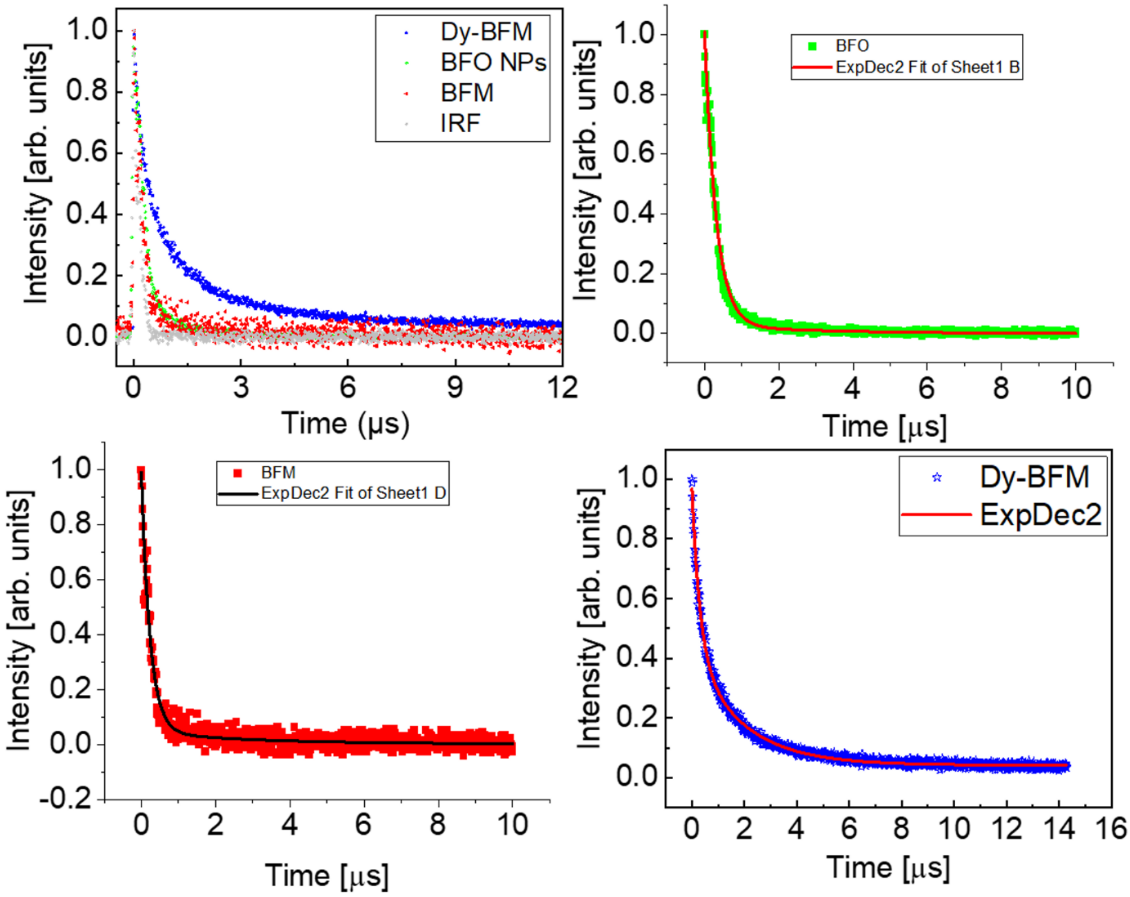

Figure 6.13: Time resolved PL spectra (λ_{ex} = 450 nm) with instrument response function (IRF). Decay kinetics fitted by biexponential function.

From the PL emission decay kinetics, the non-radiative average lifetime is lower for BFM than BFO NPs which is due to the presence of trap states. However, for Dy-BFM, the lifetime is larger than BFO NPs, which manifests less recombination of charge carriers. To understand the charge carrier dynamics, especially in Dy-BFM NPs which can absorb most of the light among all NPs, we utilised transient absorption (TA) spectroscopy. The pump (488 nm, 280 nJ) induced transient absorption signal ΔOD (*t, λ*); optical density, was measured with a continuum probe in the range of 400-850 nm. The absorption band shows a negative sharp GSA feature between 400-530 nm that can be due to bleaching of the ground state[215,216] due to the excitation by the higher intensity pump source as shown in Figure 6.14. Another important feature is the excited state absorption (ESA) spectrum (green region) in the 550-830 nm range [Figure 6.14]. The ESA spectral intensity decreases with increased delay time due to less population of the excited state. One can trace the light-induced reaction from the photogeneration of charges to their almost disappearance. Comparing the TA spectra of BFO NPs recorded at different pump-probe delay times with BFM and Dy-BFM NPs, a qualitative difference can be observed. For BFM NPs, TA spectral intensities are low compared to BFO NPs at the same delay times which manifests a smaller excited state absorption in BFM than BFO. However, for Dy-BFM NPs the spectral intensity is higher than for BFM NPs that means a higher number of carriers is available in the excited states than in BFM.”[k]

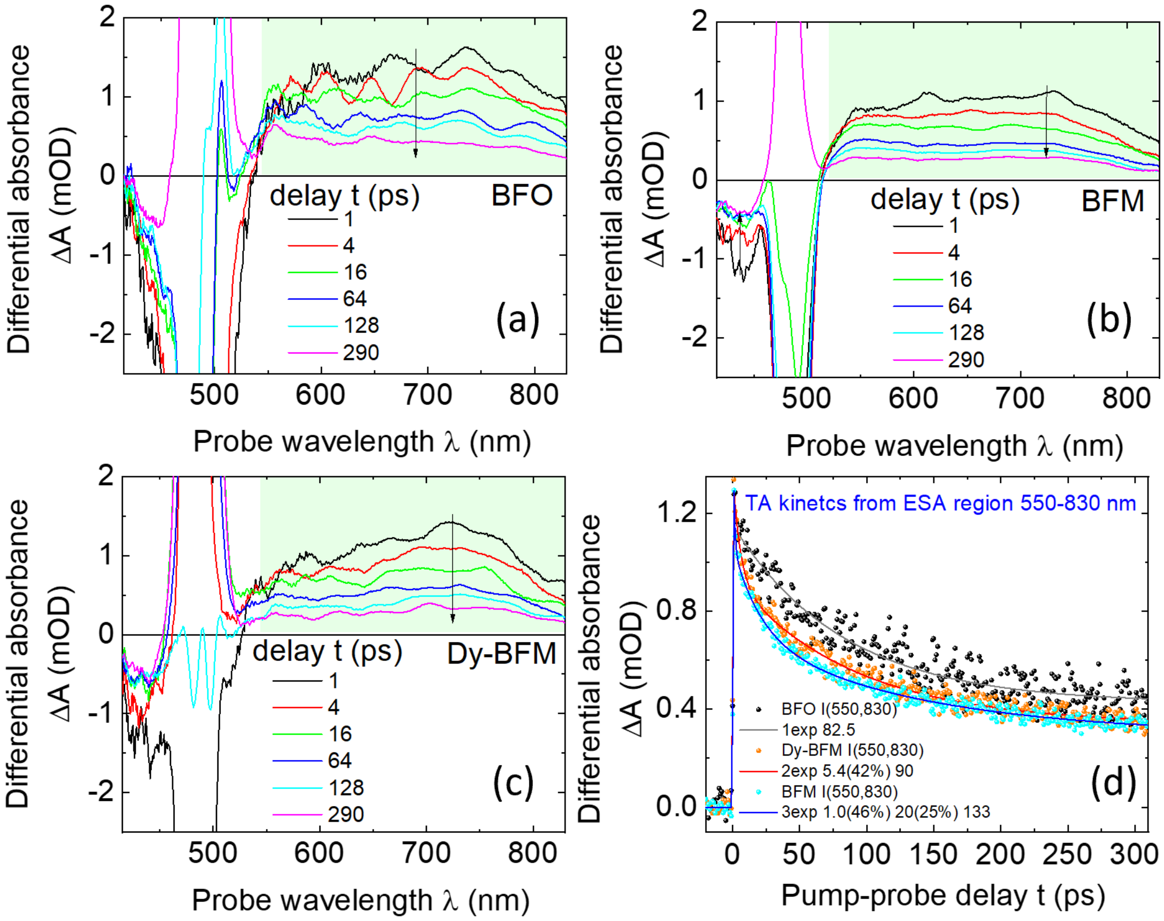

Figure 6.14: The transient absorption spectra recorded following 488 nm excitation at various pump-probe delay times for BFO NPs (c), BFM NPs (d), and Dy-BFM NPs (e). (f) showing the ESA kinetics with fits normalized to the BFO kinetics, ascribed to the excited-state evolution (as the bleach stays constant on this time scale). [© 2022 Advanced Functional Materials][46]

The charge carrier decay dynamics [Figure 6.14] of the TA spectra were analyzed at a probe wavelength of 700 nm. The bi-exponential decay fit of the ESA region for the three samples is shown in Figure 6.15. The bleaching kinetics in the region of 415-450 nm (Figure 6.15d) reveal no change in the long-time behavior unlike the ESA kinetics [Figure 6.15]. In Figure 6.15 the solid lines represent the best fits of the time traces to the sum of the bi-exponential decay function using the following equation 6.4.

$$\Delta A(\tau) = A_1 e^{-t/\tau_1} + A_2 e^{-t/\tau_2} \tag{6.4}$$

---

[k] This paragraph is based on (Dubey et al, Advanced Functional Materials 2022, https://doi.org/10.1002/adfm.202207105)

From Table 6.2, there are two types of components with shorter and longer decay times. The average lifetime is calculated using Equation 6.5.

$$\text{Average } \tau = \frac{[(A_1 * \tau_1) + (A_2 * \tau_2)]}{[A_1 + A_2]} \tag{6.5}$$

BFO NPs possess the longest average lifetime, whereas Dy-BFM possesses the shortest. The shorter decay lifetimes are attributed to the presence of trap-states, which introduce additional pathways for non-radiative recombination of charge carriers.[390]

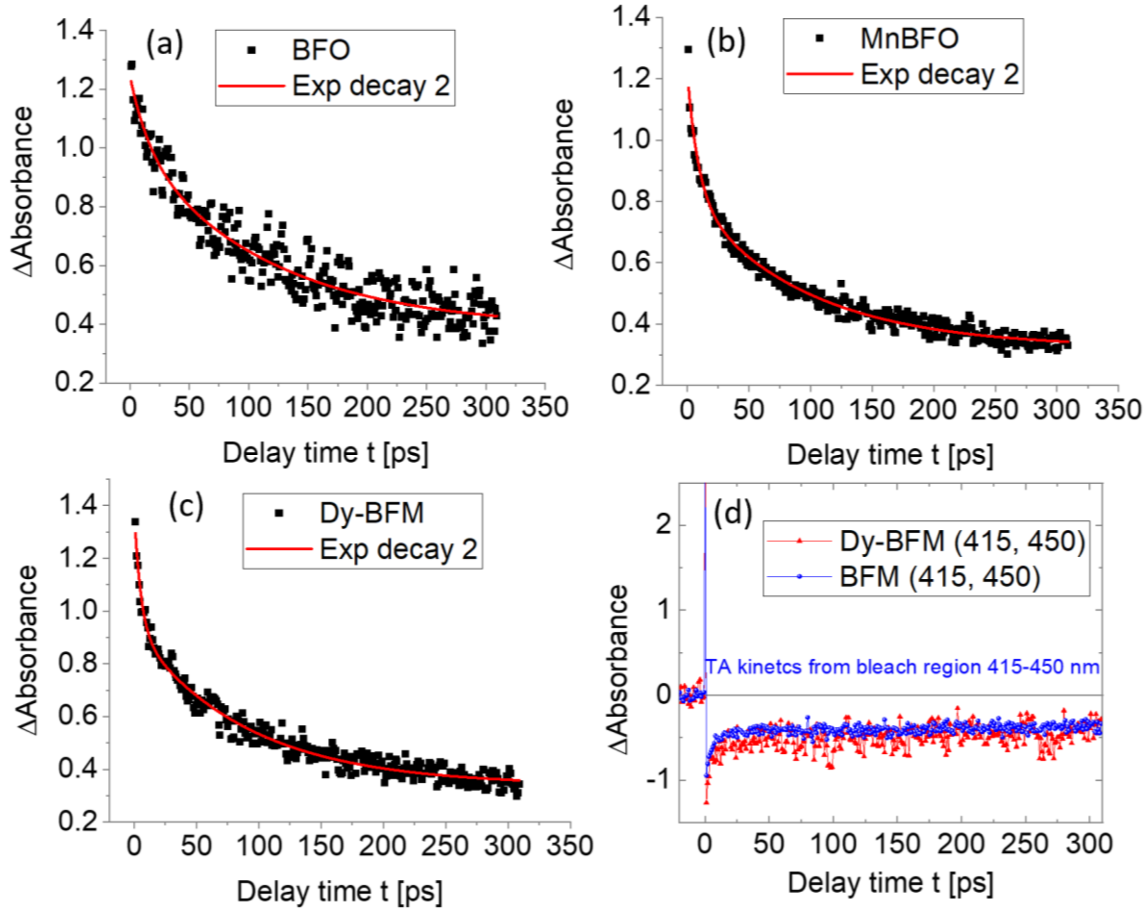

Figure 6.15: ESA decay kinetics λ_{probe} = 700 nm with fits (a-c), should be ascribed to the excited-state evolution, as the bleach stay constant on this time scale of samples and in (d) bleach kinetics reveals no change in the long-time behaviour unlike the ESA kinetics at λ_{probe} = 420 nm.

Table 6.1 Calculated lifetime from time resolved PL decay kinetics using bi-exponential fit.

Exp decay 2	A_1	τ_1 (µs)	A_2	τ_2 (µs)	Average lifetime (µs)
BFO	0.98	0.31	0.03	3.7	1.21
Mn-BFO	0.94	0.23	0.05	2.7	1.17
Dy+Mn BFO	0.54	0.30	0.38	1.9	1.61

Table 6.2: Results of fitting TA decay traces for three samples with a double-exponential decay mode.[l]

Exp decay 2	***A*₁**	**τ₁ (μs)**	***A*₂**	**τ₂ (μs)**
BFO	0.23	16 ± 7	0.62	115 ± 19
BFM	0.29	9 ± 1	0.49	95 ± 5
Dy-BFM	0.44	5 ± 1	0.60	90 ± 4

6.5 Conclusions

Based on the optical results of doped BFO NPs, we can conclude that single doping at the Fe-site has a larger influence on the band gap of BFO NPs as compared to doping at the Bi-site, due to an indirect effect on the energy level of the electronic structure of the BFO NPs mostly contributed by the FeO_6 octahedra. Upon altering the dopant at the Bi-site in Mn doped BFO NPs (BFM), we found that an optimum dopant concentration, like 1 mol % Ba can largely influence the light absorption properties of BFM NPs via creation of oxygen vacancies or creation of defects states in the band gap. The role of ions different valency at the Bi site in BFM and BFC NPs have been discussed, it is found that doping of MDT ion reduces the band gap, but there is no large difference among them, except small deviation at lower energies indicating the presence of defect states in the band gap. In the rare earth (lanthanides) doped BFM NPs, the band gap of Gd-BFM is found to be smallest. From the band energy level diagram, we find that Dy-BFM has the most suitable band edges for the hydrogen evolution reaction under light irradiation due to presence of conduction band at largest energy among the NPs. We also learnt that for Dy-BFM NPs a higher number of charge carriers is available in the excited states than in BFM. Dy-BFM NPs has shorter charge carrier decay component than BFO NPs. The shorter decay lifetimes are attributed to the presence of trap-states, which introduce additional pathways for non-radiative recombination of charge carriers.

---

[l] This table is based on (Dubey et al, Advanced Functional Materials 2022, https://doi.org/10.1002/adfm.202207105)

Exploration of Catalytic Activity in Doped Bismuth Ferrite Nanoparticles

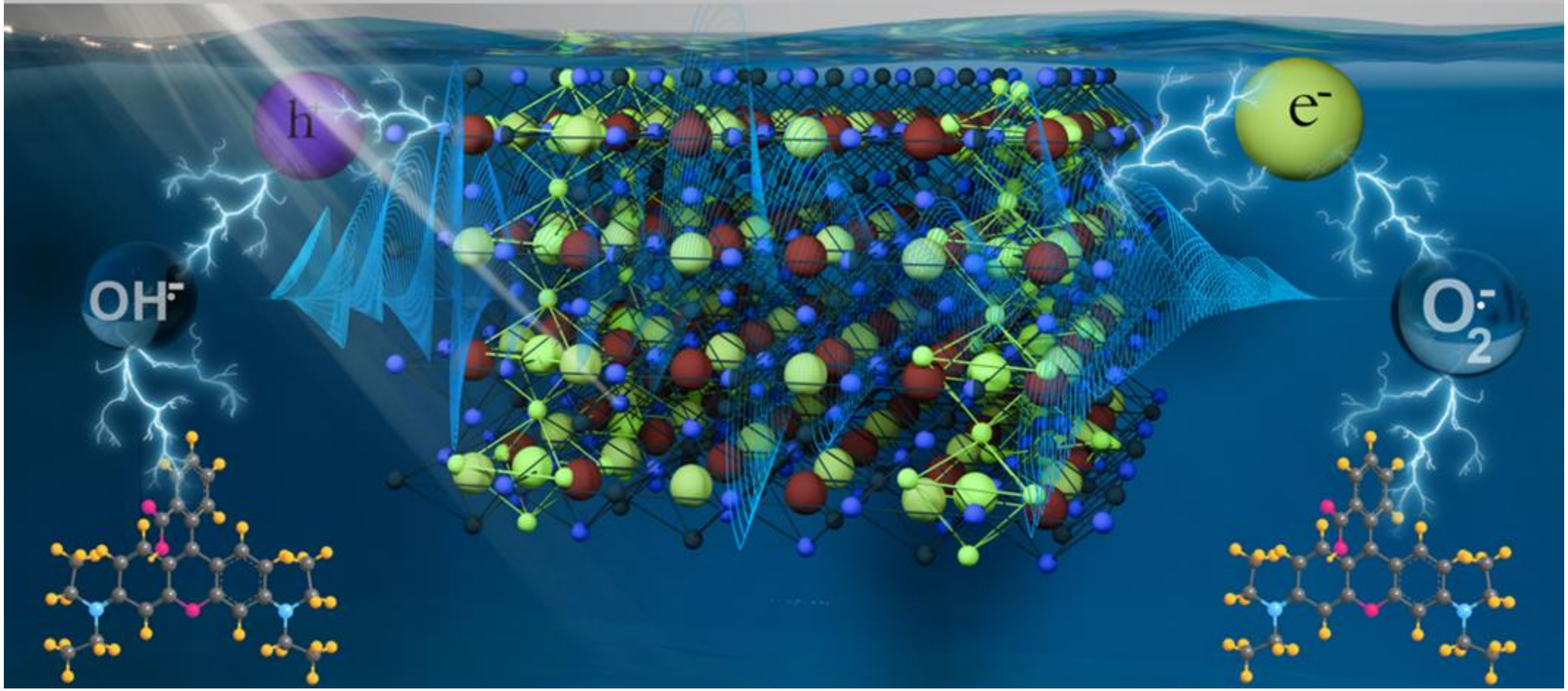

7 Catalytic activities of doped BFO NPs

7.1 Introduction

In this chapter, the photocatalytic (PC), piezo-photocatalytic (PPC), and electrocatalytic (EC) activities of doped BFO NPs are investigated for their potential applications in environmental remediation, energy conversion, and storage. Ferroelectric (FE) NPs have emerged as promising field of catalysts in these processes due to their high surface area, and electric field and stress induced surface activities.[154] FE materials such as Pb(Zr,Ti)O_3, and $Ba_xSr_{1-x}TiO_3$ have been used as photocatalysts due to their polarization-dependent activities.[153,391] It is been argued that intrinsic polarization can be as driving force to suppress the recombination of photoinduced charge carriers.[153,154,391,392]

The photostriction effect in FE materials occurs due to the interaction between light and the polarization of the material.[393,394] When a ferroelectric material is exposed to light, the photons can excite electrons in the material, leading to a redistribution of charge and a change in the polarization. This change in polarization results in a strain in the material. In a nanoparticle if ferroelectric material, the photostriction effect may be further enhanced due to the surface effects. In NPs the surface atoms have different properties compared to the bulk material. This can result in the formation of surface states, which can interact strongly with light, and so stronger with the reactive species from the solution.

Piezo-photocatalysis, involves the coupling of mechanical and light energies to drive chemical reactions. In this process, the non-ferro or ferroelectric catalyst is subjected to an external mechanical force, which induces a change in its polarization and enhances the photocatalytic activity. Ferroelectric materials have been shown to exhibit significant piezoelectric properties, which make them ideal candidates for piezo-photocatalysis.

Electrocatalysis, involves the use of an electric field to drive chemical reactions. Ferroelectric materials have been used as electrocatalysts due to their polarization-dependent reactivity and high stability. The electric field can induce a change in the polarization of the ferroelectric material, which can enhance the efficiency of charge transfer and accelerate the electrocatalytic reaction. In addition, the band bending of ferrocatalysts can boost the electrocatalytic process.

In this chapter, there is an overview of our studies on the catalytic activity of doped BFO NPs. First there is utilization of visible light irradiation to degrade organic pollutants rhodamine B (RhB) and methyl orange (MO), studying the role of dopants in improving the photocatalytic performance of BFO NPs. These findings show that the dopants significantly enhance the efficiency of the photocatalytic reaction, indicating the potential for these NPs to be used in real-world applications. Afterwards there is exploration of the photocatalytic activity of doped BFO NPs supported onto graphene oxide (GO) sheets for the degradation of the plasticizer phthalate. GO sheets provide a stable support structure for the NPs, while the dopants play a crucial role in improving the catalytic performance.

Next, the piezoelectric and FE properties of doped BFO NPs are utilized to degrade the organic dye RhB through piezophotocatalysis (PPC). The piezoelectric and ferroelectric properties enable the NPs to generate an electrical charge when subjected to pressure or mechanical stress, which can be utilise for the efficient dye degradation.

Finally, there is study of catalytic response of doped BFO NPs towards hydrogen evolution reaction (HER) by depositing NPs onto a conductive glassy carbon electrode. The aim is to probe the electrocatalytic activity of doped BFO NPs towards HER.

The catalytic results are promising, for doped BFO NPs, indicating their potential for the development of sustainable energy sources.

7.2 Photocatalytic activity of doped BFO NPs

Photoelectric properties of FE have attracted interest of researchers working in the fields of photovoltaics,[123] photocatalysis (PC)[163], and photoelectrocatalysis[395]. It has been shown that the ferroelectric state is beneficial for PC performance. The positive effect of the FE state on PC was shown in an increased photo-degradation rate of the dye rhodamine B (RhB) when using polar $Ba_{0.8}Sr_{0.2}TiO_3$ NPs (mono domain state) as compared to non-polar $Ba_{0.2}Sr_{0.8}TiO_3$.[391] Similarly, a high photodegradation of methyl orange (MO) was reported when using $BiOIO_3$ nanoplates, which was associated with the local dipole moments of the IO_3 pyramids leading to strong macroscopic polarization.[396] A typical ferroelectric such as tetragonal $BaTiO_3$ also shows increased photodegradation of RhB compared to paraelectric cubic $BaTiO_3$.[397] Zhang et al. showed that orthorhombic $KNbO_3$ exhibits a higher photodegradation rate of RhB compared to monoclinic $KNbO_3$ due to the larger polarity.[392] It was discussed that the internal electric field (depolarization field) inherent to FE materials assists the separation of photo-induced charge carriers.[154] The depolarization field originates from the spontaneous polarization of FE, namely from the bound polarization charges. Typically, the depolarization field is screened, at least partially, by free charge carriers either internally (electrons, holes, charged vacancies or other point defects) or externally (charged species from the environment or surface adsorbates). Nevertheless, even a partially screened depolarization field can be the main driving force for the photo-induced charge carrier separation in single domain FE photocatalysts, as it was observed for $PbTiO_3$ nanoparticles.[153] The depolarization field can increase the chare carrier lifetime (average amount of time that elapses between the generation and annihilation of excited carriers) via mitigating their recombination to the ground state.[395] So that these excited charge carriers diffuse and execute further chemical processes at the surface. Band bending at the surface of FE particles happens due to the interaction of polarization in the proximity of the surface space.

It is considered as the main factor in the charge separation mechanism.[398,399] For positive domains (positive end of the polarization vector points toward the surface) downward band bending happens, whereas in negative domains (negative end of the polarization vector points toward the surface) polarization repels the electrons from the surface and hence upward band bending occurs. Moreover, when we increase the charge carrier density via photoexcitation, the width and height of the Schottky barriers changes, which modifies the interfacial band-bending.[400]

In photocatalysis, the charge migration process requires hundreds of picoseconds. However, the charge recombination in bulk only takes several picoseconds, much faster than charge transport.

**Section 7.2.1 is based on a journal article, published in Nanoscale Advances, Dubey et al 2021.*[150]

7.2.1 Photodegradation of organic dyes: Ba and Mn codoped BFO NPs

"The recycling of wastewater contaminated by organic pollutants is one of the major priorities in our ecosystem. In this area, research is getting promoted on processes that improve the oxidative degradation of organic pollutants. These processes include photocatalysis[401], Fenton oxidation[402], and ozonation[403]. In the advance oxidation processes like heterogeneous photocatalysis, water purification happens on the surface of photocatalysts under the irradiation of photons resulting in the total mineralization of the dyes. The efficiency of the method is based on the formation of the hydroxyl radical $^{\bullet}OH$, which acts as an oxidation agent and is responsible for the photodegradation of the organic pollutants.

In photocatalysis, semiconductors have contributed immensely.[404] The state-of-the-art photocatalytic materials TiO_2 or ZnO can only degrade the pollutants under the UV light, which excludes the visible light range of the solar spectrum. Nevertheless, their application as antibacterial and photoelectrochemical agents are quite promising.[68,69] Presently, there is a demand for photocatalysts, which can utilise maximum range of solar light, and be a low cost and sustainable technology for the wastewater treatment.[405,149] Single phase multiferroic BFO,[72] which is a p-type semiconductor,[406] and features a narrow band gap, non-toxicity and chemical inertness, could be a promising candidate for photocatalytic applications.[407,408]

"BFO and doped BFO NPs are ferroelectric materials.[68,409] It has been shown that in photoferroelectric materials[410] the spatial separation of electrons (e^-) and holes (h^+) and their transfer from bulk to the surface is assisted by the presence of the intrinsic spontaneous polarization electric fields (ISPEF) known as depolarization field.[411] The role of this intrinsic electric field for charge carrier dynamics in the ferroelectric photocatalyst for the photocatalytic redox reactions is fascinating but the mechanisms are still not understood. After poling, a significant enhancement in the visible-light photocatalytic activity of BFO NPs was reported recently.[412] BFO has been studied for the decomposition of organic dyes under UV-visible light irradiation.[413] However, the utilisation of BFO is limited by rapid charge carrier recombination, and the formation of detrimental defect and trap states in the band structure due to oxygen vacancies. Subsequently, different strategies have been developed to improve its photocatalytic efficiency, e.g., by altering the morphology,[414–416] synthesizing composites,[417–420] exploring nanohybrids,[421] and tailoring its properties via doping.[422] "[m]

---

[m] This paragraph is based on (Dubey et al, Nanoscale Advances, 2021, http://doi.org/10.1039/d1na00420d)

A moderate amount of doping of BFO at both Bi- and Fe sites affects its ferroelectric, magnetic and optical properties.[409,322] It has been shown that cation doping can reduce the particle size and alter the band gap of pristine BFO.[423] These fruitful changes increase the surface to volume ratio and enhance the visible light absorption of NPs, which are important parameters for photocatalytic application. In this context, rear-earth metal doping has been widely studied to improve the photocatalytic properties of BFO. RhB was degraded using Gd doped BFO NPs.[424] The exploitation of Gd and Sn co-doped BFO NPs and La and Se co-doped BFO NPs was reported for the photodegradation of several dyes like methylene blue (MB), congo-red (CR) and methyl violet (MV).[425,426] Like this, there are many other reports on Nd, Dy, La, and Sm doped BFO materials based on complicated synthesis methods.[427–430] From economic and environmental point of view rare earth metal doping is not justifiable, especially for water cleaning purposes.

Studies on the photodegradation of dyes by alkaline and transition metal doped BFO NPs are also found to be effective. Single doped BFO NPs like Sc doped BFO NPs and nanofibers were utilised for the photodegradation of MB.[431] Mn doped BFO NPs are able to degrade acid red dye, and Ba doped BFO NPs are effectual to degrade MO.[432,433] The photodegradation of CR using Ba and Mn co-doped and Ca doped BFO nanofibers was reported recently.[434,435] In spite of its calibre in photocatalysis, nanofiber production is difficult and not worthwhile for large-scale application. To overcome this, an economical synthesis route is required with low-cost dopants without compromising the advantageous properties of BFO NPs. Ba and Mn as dopants are inexpensive and amply available elements on earth. It has been shown that these elements are easy to incorporate, and their doping bestows the properties of BFO.[409,354] The versatile oxidation state and similar ionic radius of Mn makes it one of the best transition metals to substitute Fe.

To our knowledge there is no study on Ba and Mn co-doped BFO NPs for photocatalysis. We have chosen 1 to 5 mol % Ba doped $BiFe_{0.95}Mn_{0.05}O_3$ (BFM) NPs as photocatalysts. We studied the role of these dopants in the overall increase of photocatalytic efficiency of the BFO NPs. We find that 1 mol % Ba doped BFM NPs show the best photocatalytic activity among all co-doped NPs examined in this study and can completely degrade MO and RhB dyes within 25 and 60 minutes, respectively, for 10^{-5} M dye concentration. We found that an optimum dopant concentration is the key factor to control the photocatalytic parameters.

7.2.1.1 Results and discussion

For easier readability, here is a repetition of abbreviations for NPs. (5 mol % Mn doped BFO NPs $BiFe_{0.95}Mn_{0.05}O_3$: BFM, 1 mol% Ba doped $Bi_{0.99}Ba_{0.01}Fe_{0.95}Mn_{0.05}O_3$; 1BBFM, 3 mol% Ba doped $Bi_{0.97}Ba_{0.03}Fe_{0.95}Mn_{0.05}O_3$: 3BBFM, 5 mol% Ba doped $Bi_{0.95}Ba_{0.05}Fe_{0.95}Mn_{0.05}O_3$: 5BBFM. The following text is based on a journal article, published in Nanoscale Advances, Dubey et al 2021.[150]

"The result of photodegradation of RhB using the 1BBFM sample is shown in Figure 7.1. The absorbance peak at 550 nm is a characteristic absorption feature of the RhB dye. A decrease in the magnitude of this peak with time indicates a decrease in the concentration of the dye in the solution due to photodegradation, since the absorbance is directly proportional to the concentration of the dye.[436] Figure 7.1b compares the photodegradation of the dye within 180 minutes for all NPs under visible light illumination only (halogen lamp, with 390 nm cut-off filter) at pH = 4.4 of the solution. The photodegradation efficiency of BFM is slightly better than that of BFO NPs. However, incorporating 1 mol % Ba into BFM increases efficiency drastically. For larger barium content in the co-doped NPs, the degree of the photodegradation slightly decreases, but 5BBFM NPs shows better photocatalytic properties than both BFM and BFO NPs. “[n]

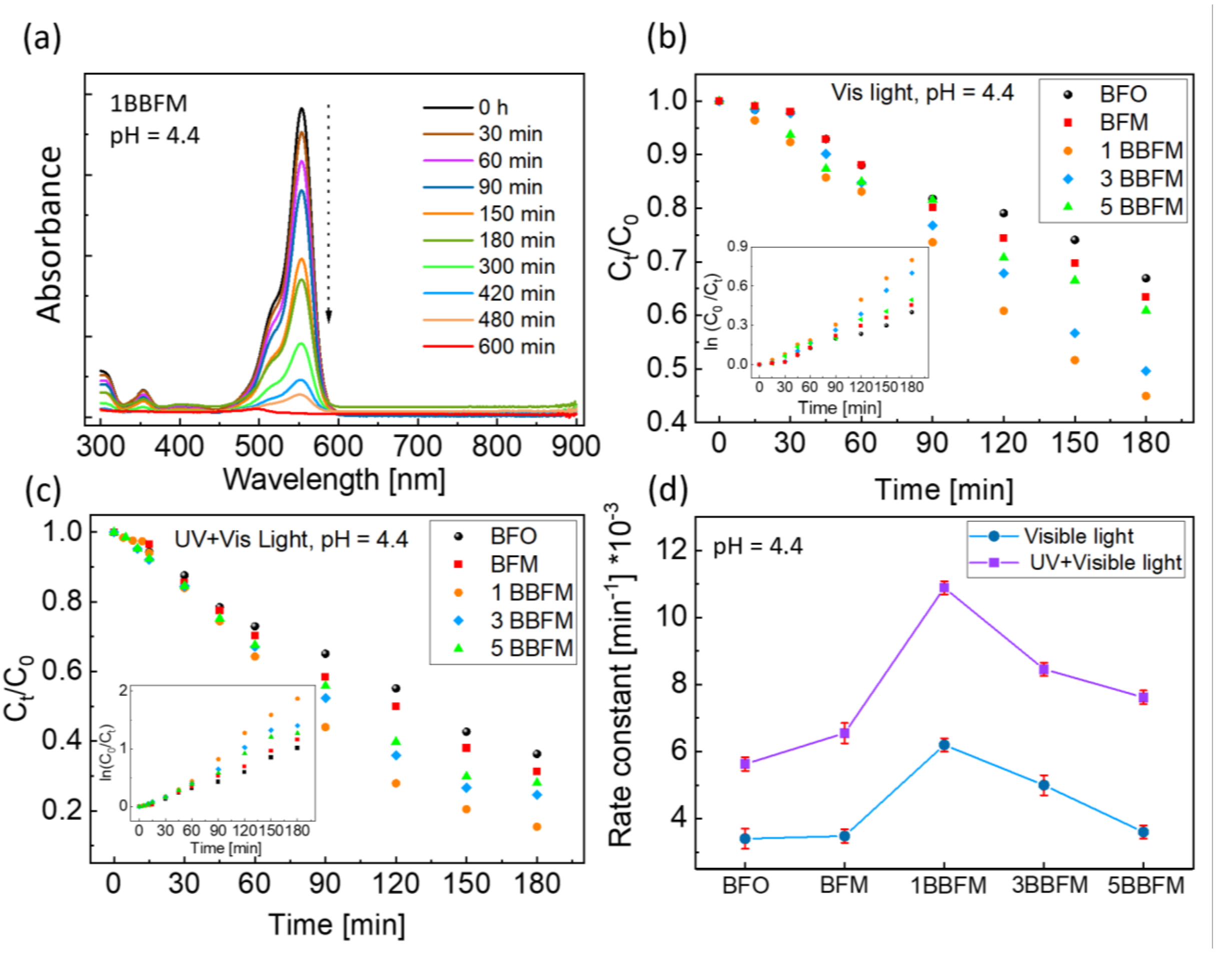

Figure 7.1: Absorption spectra of RhB with respect to time in the presence of 1BBFM NPs under visible light and at normal pH of the RhB solution (pH = 4.4) show the degradation of the RhB dye in (a). The relative concentration of RhB versus time under visible light and UV+visible light (at pH = 4.4) is shown in (b) and (c), respectively. The insets show the kinetics of the photodegradation. (d) Variation of the rate constants (k) for the photocatalysts under visible and UV+visible light excitation at pH = 4.4. [© 2021 Nanoscale Advances][150]

The photodegradation trend under the UV+Visible light source (halogen lamp, without 390 nm filter) at pH = 4.4 is shown in Figure 7.1c, where we observe the same trend as in Figure 7.1b but with a slightly faster degradation for all samples. That shows an effect of UV light together with visible light on the photocatalytic efficiency of the studied NPs, which is due to

---

[n] This paragraph is based on (Dubey et al, Nanoscale Advances, 2021, http://doi.org/10.1039/d1na00420d)

the increase in the number of photons in total.To study the kinetics of PC, Langmuir–Hinshelwood fitting was used.[437]

If the degradation/reaction follows the rate law (equation 7.1) then the reaction has first order kinetics.[438]

$$k \cdot t = \ln\left(C_0/C_t\right) \qquad (7.1)$$

Here, *k* is the rate constant of the reaction, C_0 is the initial concentration of the dye in the dark, and C_t is the concentration of the dye at time *t* during the PC reaction under light. Inserts in Figure 7.1b and 7.1c show the representative time dependencies of $ln\,(C_0/C_t)$ for photocatalytic measurement under visible light and UV + visible illumination up to only 180 min, respectively. From the line fits of $ln\,(C_0/C_t)$ in the time interval from 0 h to 5 h the slope values (rate constant) were obtained. The rate constant values for the doped and undoped NPs in the presence of UV and UV-visible light are plotted in Figure 7.1d. For the 1BBFM NPs the rate constant is maximal and almost twice as high as for the pristine BFO NPs. However, further doping with Ba decreases the rate constant of the photocatalytic reaction under both illumination conditions. In short, doping increases the PC efficiency of the BFO NPs, and the best photocatalyst among all NPs found is 1BBFM under natural condition pH = 4.4.

To further enhance the photocatalytic response of the 1BBFM NPs, we decreased the pH of the dye solution to 2.2 by adding a few drops of dilute HNO_3. For such pH conditions and under UV + visible illumination, 1BBFM completely degraded the dye within 60 minutes (Figure 7.2a). We also performed photodegradation of another organic dye, namely methyl orange under the same conditions. The 1BBFM NPs could completely degrade methyl orange within 25 minutes (Figure 7.2b). From Figure 7.2c, the photodegradation reaction follows first order kinetics for both dyes. The rate constant for RhB photodegradation increased by about 6 times at pH = 2.2 as compared to the solution with pH = 4.4. We observe that the nanopowders are better dispersed in RhB at pH = 2.2 in comparison to pH = 4.4. The zeta potential value of the dispersion increases from 17.2 mV at pH = 4.4 to 39.4 mV at pH = 2.2. This promotes more dye adsorption onto the NPs surface. This can be one of the major causes for the increase in PC efficiency upon decreasing the pH of the solution.

The PC reactions were run at least three times and were found to have similar efficiencies as the first cycle. A representative graph of cycles for 1BBFM is shown in Figure 7.5. The NPs were removed after the PC with the help of a magnet attached to the PC jacketed beaker. For the photocatalyst it is important that it does not self-degrade and remains chemically inert with respect to the dye and solution during the PC reaction. To check the stability of the NPs we have performed XRD measurements for all NPs after the PC and found that they are stable. In Figure 7.6 the XRD patterns of BFO and 1BBFM NPs are shown after PC at pH 2.2 and at pH 4.4 along with TEM images of 1 BBFM sample after PC at pH 2.2. From these results, we conclude that there is no formation of any secondary phase or degradation of the NPs indicating that the NPs recover as a photocatalyst after successful PC. Additionally, we have performed total organic count (TOC) measurements for 1 BBFM [Figure 7.7d] by using a Shimadzu-TOC L device. From the TOC results, we found that all of the RhB was successfully degraded and decayed into CO_2 and H_2O.

Based on these data, the 1BBFM NPs shows the best photodegradation ability. Few questions arose: what could be the reason of 1BBFM to be the best photocatalyst among the NPs under study? How does the overall doping into BFO NPs affect the photocatalysis?

To unveil the possible reasons, we conducted further experiments to study the various parameters crucial for efficient photocatalysis in these samples. Photocatalysis involves the generation of charge carriers (e^- and h^+) upon light absorption by the photocatalyst. Afterwards the charge carriers get separated to diffuse from the bulk to the surface of the NPs competing against their recombination or trapping. In the last step, redox reactions occur at the surface of the NPs driven by the photogenerated charge carriers. Charge carriers not only promote dye reduction, but possibly also react with electron scavengers (e.g., O_2) to form radical anions (e.g., O_2^-), oxidize organic molecules, or react with OH^-/H_2O to form ·OH radicals.[439] So in the next sections, we will discuss about the light absorption by NPs and charge carrier generation, charge carrier recombination and available surface area for the photocatalysis process.

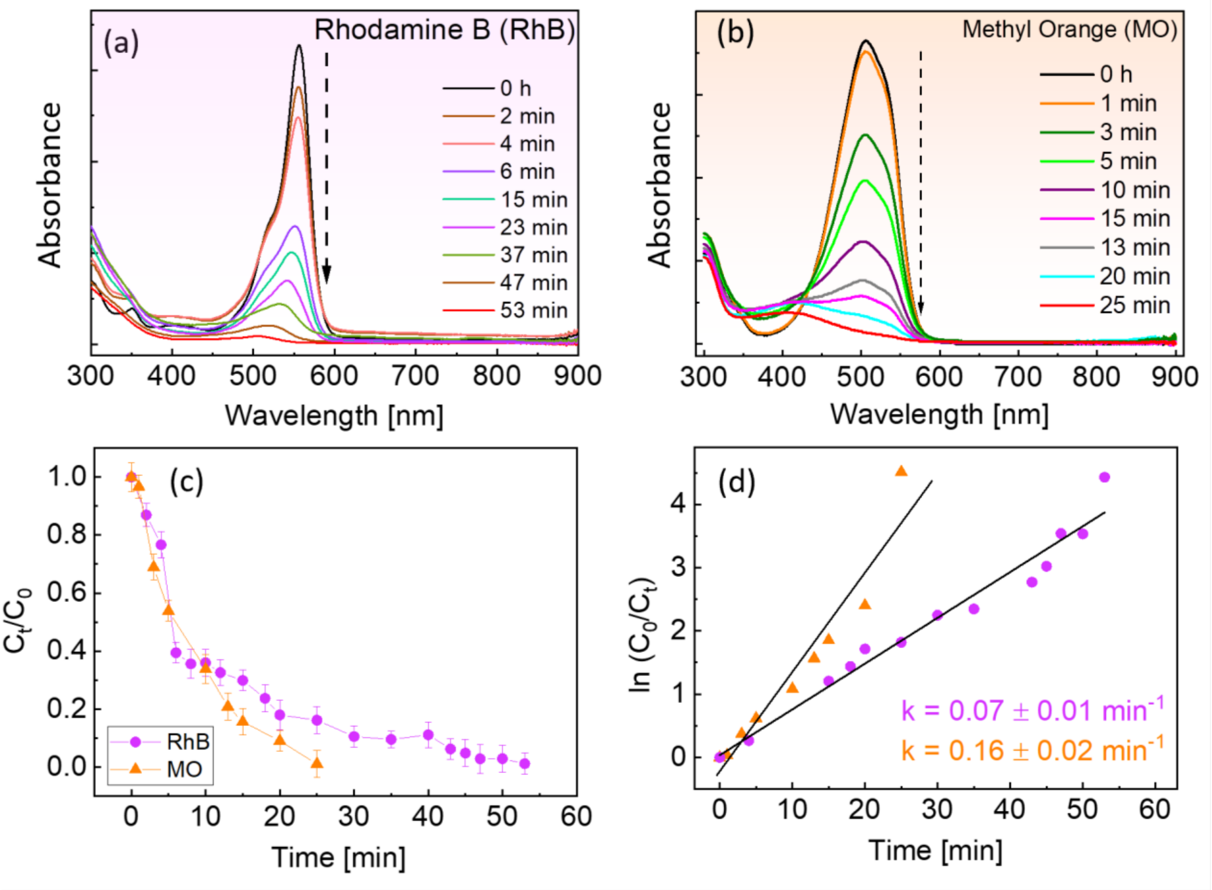

Figure 7.2: Absorbance plots with respect to time of RhB (a) and MO (b) in the presence of 1BBFM NPs at pH = 2.2 under UV+visible illumination. Photodegradation trend C_t/C_0 as a function of time for both dyes (c), where the inset shows the reaction kinetics and rate constant (k) values. [© 2021 Nanoscale Advances][150]

Local ferroelectric properties

After charge carrier generation, their efficient separation also plays a crucial role during the photocatalysis process. In photoferroelectric materials a broad space charge region exists due to internal screening of spontaneous polarization by free charge carriers and defects within the material. The resulting band bending depends on the surface polarity and facilitates the separation of photogenerated charge carriers.[440,441] One can expect that a larger spontaneous polarization of NPs will be beneficial for charge carrier separation and photocatalytic activity.

The influence of Ba and Mn doping on the ferroelectric properties of the BFO NPs was probed by PFM. Figure 7.3 shows PFM images for pure BFO NPs, BFM, 1BBFM and 5BBFM NPs. The first column shows the topography images of the sample surface, while the second column represents the lateral PFM (LPFM) images. The third column shows cross-sections of the PFM image taken for representative NPs. The dark and bright contrasts in the LPFM images correspond to ferroelectric domains with opposite orientation of the in-plane polarization component. The main part of the scanned area shows an intermediate brown contrast corresponding to zero piezoresponse and can be attributed either to the epoxy matrix or to NPs covered by epoxy. From the images, one can see that some NPs are single domain, while others consist of several domains. Mn doping results in a slight increase of the PFM response. 1 mol% Ba doping into BFM NPs further increases the piezoresponse, whereas 5 mol% Ba doping results in both decreasing grain size and PFM signal. The 1BBFM NPs are mostly single domain as shown by the red dotted circles, similar to the BFO and BFM NPs.[10] The local PFM hysteresis loops of 1BBFM [Figure 7.3(f-g)] confirm the switching of the polarization direction by an external electric field confirming the local ferroelectric state. The intensities of the VPFM and LPFM signals depend on the out-of-plane and in-plane components of polarization, respectively.[10] Comparing the normalized PFM response of the 1BBFM NPs with those data, one can see that the intensity of the PFM is about 30 % larger than in the BFM NPs (Figure 7.4). As piezoresponse of a material is proportional to the spontaneous polarization,[68] we can conclude that 1BBFM has a larger spontaneous polarization than the BFO and BFM NPs. This is in good agreement with the data reported for Ba-doped BFO ceramics.[30] The reduction of the polarization can also be partially related to the size effect.[14]

A larger polarization means a larger depolarization field, which can facilitate photoinduced charge carrier separation and may explain the photocatalytic efficiency of the 1BBFM NPs to be best.

Charge carrier recombination

Once the charge carriers are separated, their recombination should be inhibited for their diffusion from the bulk to the surface of the NPs. The PL spectroscopy can be used to identify not only the defect states but the recombination of charge carriers as well.[442] Therefore, the PL spectra of all NPs were measured by excitation of the NPs by a 450 nm (2.75 eV) laser light source.[150] For both, the pristine and doped BFO NPs, we found similar emission peaks, which indicates that no new types of in-band defect levels are formed at this dopant concentration. However, the peaks get slightly shifted, but this effect is not as significant as the change in the total peak area. The 1BBFM sample has the smallest peak area for both emission peaks among the NPs, which is associated with a lower charge carrier recombination,[443] and a less light absorption at ~500 nm (2.48 eV) for 1BBFM. Therefore, the larger PL peak area for the 5BBFM NPs than those for the 1BBFM NPs may correlate with the lower PC efficiency of the 5BBFM sample.

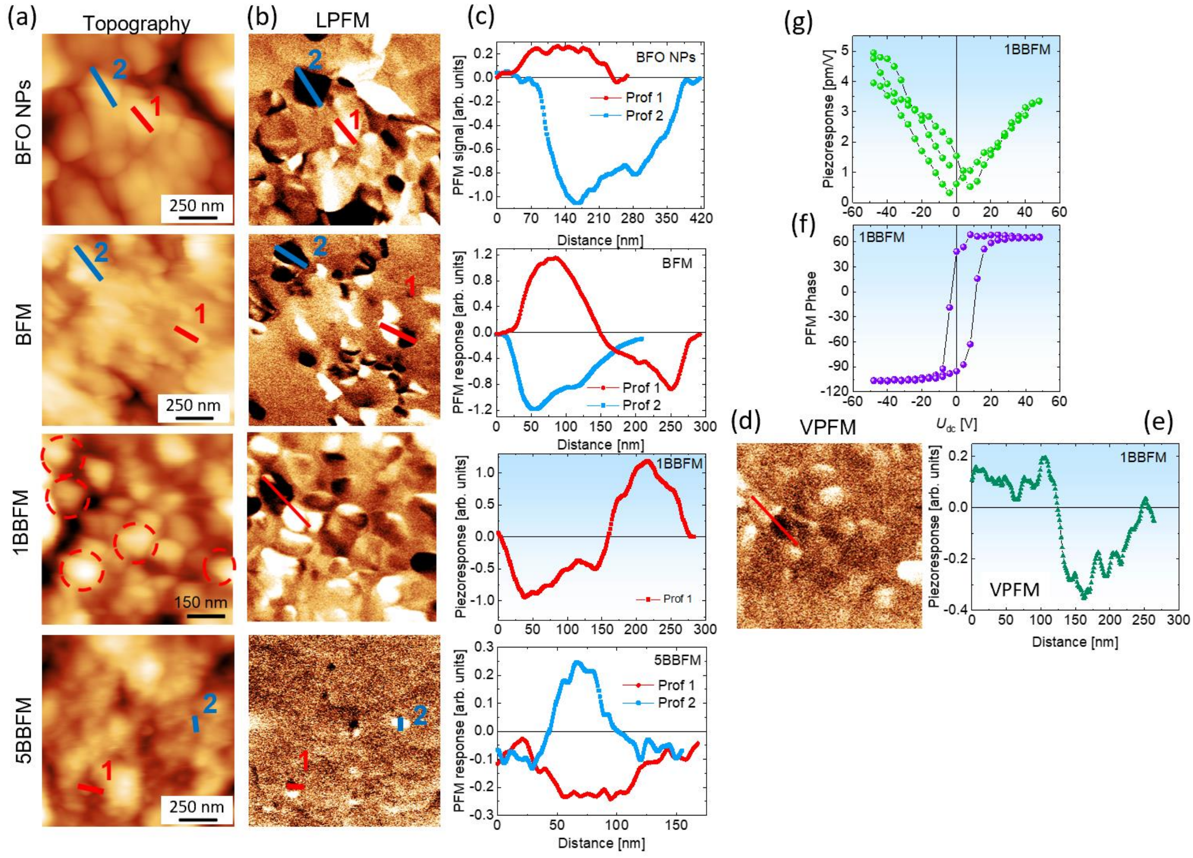

Figure 7.3: Topography (a), lateral PFM image (b), and PFM signal (c) of BFO, BFM, 1BBFM, and 5BBFM from top to bottom. Vertical (c) PFM image of 1BBFM NPs and piezoresponse along the red line in VPFM (e). (The cross-section location is marked by a red line in the corresponding images). The local piezoresponse phase (f) and amplitude (g) hysteresis loops of 1BBFM NPs. [© 2021 Nanoscale Advances][150]

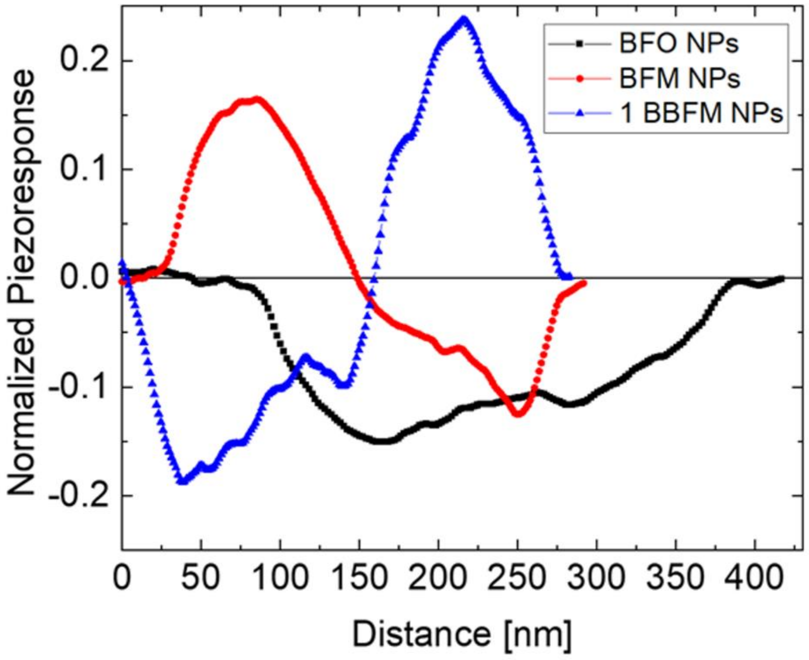

Figure 7.4: Comparison between cross-sections of the vertical PFM signal normalized to the driving voltage for BFO, BFM, and 1BBFM NPs. [© 2021 Nanoscale Advances][150]

Available surface area for photocatalysis

The specific surface area of the co-doped BFO NPs was evaluated using BET measurements as mentioned in the previous chapter 4 [Figure 4.30]. Doping with Mn alone does not lead to a significant change in the surface area, but by adding 1 % Ba the surface area increases considerably. For the samples with more Ba content, the surface area decreases slightly, but they still exhibit more surface area than the pure BFO NPs. The trend of the specific surface area compared to the photodegradation trend at pH = 4.4 under UV+visible light for all NPs is shown in Figure 7.7c.

Surface adsorbed hydroxide groups

Though surface area can be a major factor, other factors also affect the degradation rate of doped NPs. As photocatalysis is a surface-mediated process, not only the available surface area of the NPs plays an important role for their efficiency, but also the surface activity. It has been demonstrated that for a variety of metal-oxides, visible fluorescence is connected to the adsorption and modification of surface adsorbates such as oxygen or -OH_x groups by the excitation light.[66, 67] The evolution of such fluorescence under continuous excitation is hence connected to the surface activity. To support the beneficial properties of our co-doped NPs as compared to pure BFO, we drop cast a dispersion of the NPs in ethanol onto a cleaned Si substrate and conducted PL measurements under UV excitation. The dried NPs were excited with a 325 nm (3.81 eV) laser source in vacuum to collect PL spectra at 290 K and at 5 K. We find the PL spectra in the visible range from 400-700 nm. During continuous illumination, a strong variation of the PL intensity of all samples was observed as exemplified by the spectra of the doped 1BBFM NPs [Figure 7.7 a-b]. No change is detected in the shape of the spectra.

The occurrence of such broad spectra, as well as the observed change in intensity, have been described in literature and are most likely associated with the adsorption of -OH_x groups from the solvent (or atmosphere) onto the NPs surface and their modification under the action of incident laser radiation.[444,445] Although the experiments were conducted under high vacuum, the -OH groups are expected to still persist on the highly porous NPs surfaces and to be trapped between agglomerated particles.

The observed brightening of the PL spectra in the course of illumination manifests light induced surface activity attributed to the modification of adsorbed OH-groups on the surface of the NPs. Comparing the emission intensity change of the pristine and 1BBFM NPs (Figure 9b) reveals a much stronger brightening effect for the 1BBFM sample at both room and cryogenic temperatures. This effect indicates a higher optically induced surface activity of 1BBFM in terms of the adsorption and alteration of attached -OH groups as compared to the pristine BFO NPs. The improved adsorption of -OH groups will lead to increased ·OH radical formation after charge carrier generation. This effect is expected to improve the photocatalytic efficiency of the doped sample in the presence of a dye.

Discussion

The obtained results indicate that the increased photocatalytic efficiency of BFO NPs upon Ba and Mn doping can be explained by a combination of several factors, where the foremost is the change in size and morphology of the NPs. The spherical morphology of the doped BFO NPs under study implies a large surface area, which provides more sites for incoming charge carriers to participate in redox reactions at the surface. The 1BBFM sample has the largest surface area of almost ~ 1.6 times more than that of the pure BFO NPs (Figure 7.7c). The larger surface area and the higher pore volume are major factors in the photocatalytic properties of the co-doped BFO NPs.

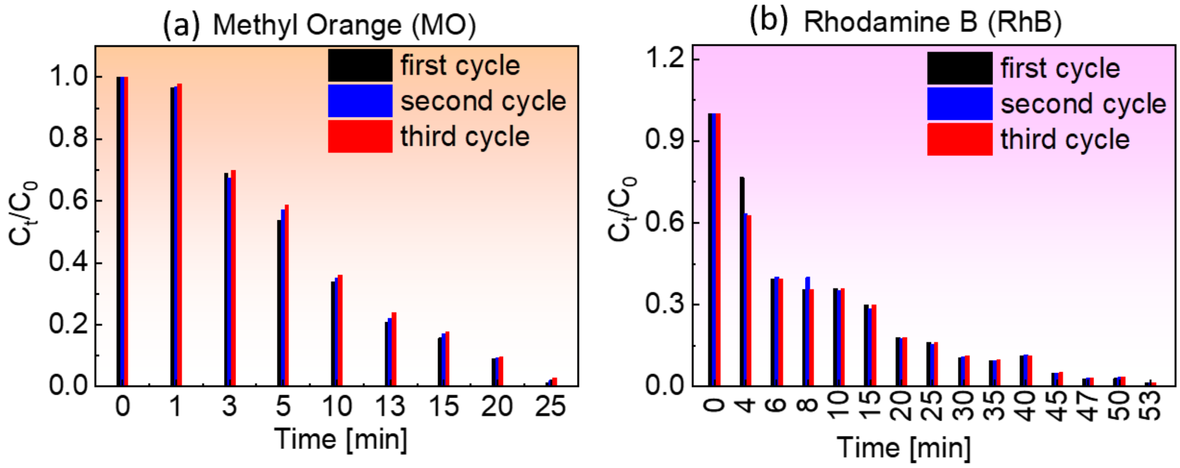

Figure 7.5: Recyclability of 1BBFM co-doped BFO NPs in the degradation of methyl orange (a) and of RhB (b), where Ct/Co is the photodegradation of the dye. [© 2021 Nanoscale Advances][150]

Second, the optical absorption edge in the electronic structure of the BFO NPs is altered due to doping. In the Mn doped BFO NPs, the existence of manganese both as Mn^{3+} (Jahn-Teller cation) and Mn^{4+} in the crystalline lattice was confirmed by XPS and Raman analyses.[10] The presence of a Jahn-Teller cation in the MnO_6 octahedra can distort the electronic structure of BFO by splitting the energy levels further.[387] Upon further co-doping Ba into BFM, the unit cell volume increases and the Mn^{3+} concentration reduces in favor of Mn^{4+}. It is important to notice that this effect is most significant for the 1BBFM, which also has the largest unit cell volume.[10] For co-doped BFO NPs, two main factors cause important changes in the electronic structure: increased unit cell volume due to bigger Ba^{2+}, and presence of Jahn-Teller cation (Mn^{3+}). In total, such structural distortion leads to alteration in Fe-O bond lengths and influences the *d-d* crystal field transition energy levels,[387] and can alter the electronic transition of C_{3v} crystal symmetry of BFO. As per Wei et al. an increase in crystal field splitting due to the reduction in the unit cell volume via doping by rare earth elements leads to a decrease in the energy edge of *d-d* transitions.[388] In our case the increase in unit cell volume due to Ba doping (Chapter 4, Figure 4.15) leads to an increase of the $^6A_{1g} \rightarrow {}^4T_{2g}$ *d-d* transition energies (Chapter 6, Figure 6.3). The increase of the light absorption associated with the $^6A_{1g} \rightarrow {}^4T_{2g}$ *d-d* transition due to the doping influences the photocatalytic efficiency significantly.

Third, the spontaneous polarization of these ferroelectric NPs at room temperature causes band bending, which assists the separation of charge carriers. This effect can also promote the photocatalysis process considerably. The PFM data indicate the larger polarization in the

1BBFM NPs as compared to other NPs under study, which correlates with their best photocatalytic performance.

The fourth factor is the least charge carrier recombination for 1BBFM among all the NPs, as evidenced by the decreased peak area of the PL emission spectra collected at 450 nm.

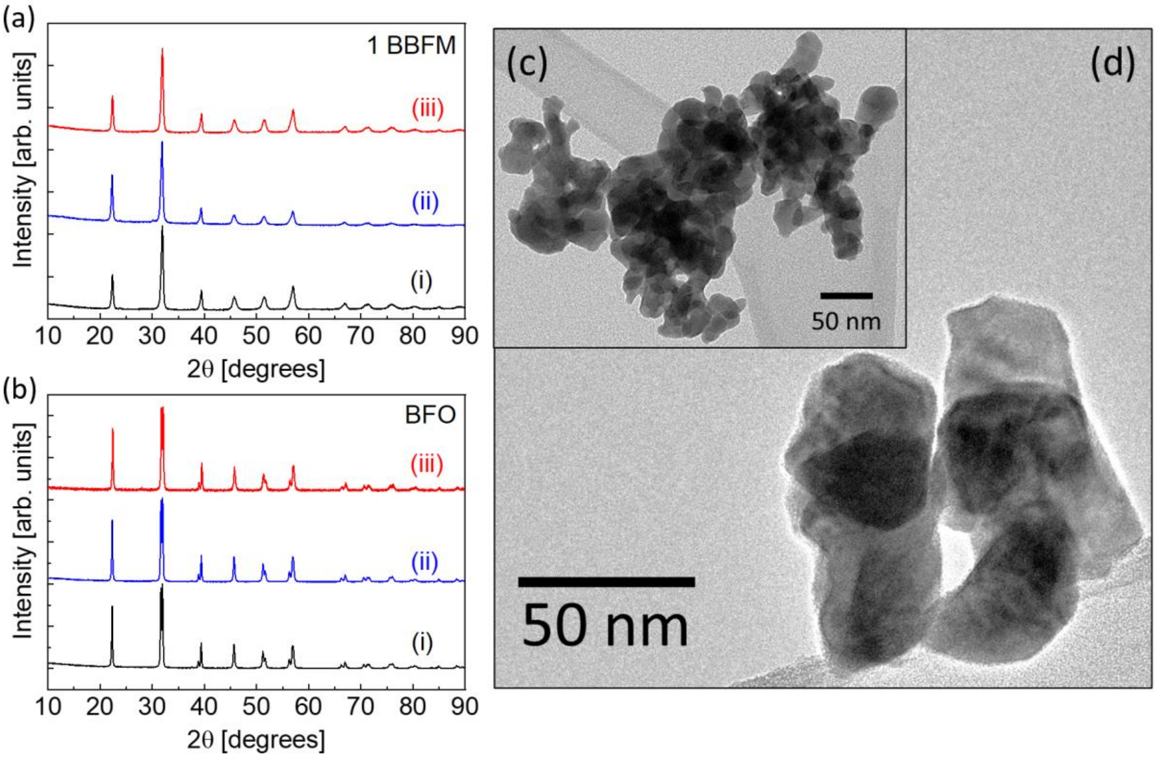

Figure 7.6: XRD diffractograms of photocatalysts before and after photocatalytic (PC) cycles shown in (a) and (b) for 1 mol % Ba 5 mol % Mn co-doped BFO NPs (1BBFM) and BFO NPs, respectively: (i) before photocatalysis, (ii) after 3 PC cycles at pH 4.4 and (iii) after one PC cycle at pH 2.2. The XRD diffractograms of the NPs do not change after PC cycles at both pH conditions, indicating that the NPs are stable, functional, and reusable for further photocatalysis. On the right, (c), and (d) show TEM images of 1BBFM after PC at pH 2.2.

The temporal evolution of the PL intensities collected at 325 nm provides a conclusive link to the catalytic activities of the NPs via adsorbing -OH groups onto their surface. The increasing rate of the PL intensity growth under continuous illumination observed in the 1BBFM sample as compared to the undoped BFO indicates stronger interaction of the nanoparticle surface with adsorbed OH groups. This finding also relates the increased photocatalytic efficiency of the 1BBFM NPs to the increased surface activity.

Conclusions

Ba and Mn co-doped BFO NPs synthesized by the modified sol-gel method show enhanced photocatalytic activity for the degradation of organic dyes (rhodamine B and methyl orange) under UV-visible light. Among them the NPs with 5 mol% Mn and 1 mol% Ba doping show the best results and can degrade MO and RhB dyes in 25 and 60 minutes, respectively, at pH = 2.2. The surface area and pore volume get increased for the doped NPs, while the 1BBFM NPs have the largest surface area and pore volume amidst the NPs under study. The electronic band structure of BFO gets altered due to doping. This increases the light absorption capability of doped NPs in the visible range, in particular between 500 and 800 nm. The larger spontaneous polarization and related depolarization field make the charge carrier separation more effective in the 1BBFM NPs than in the BFO and other doped NPs. The emission spectra show that for 1BBFM the charge carrier recombination is lower than for other NPs. A stronger increase of luminescence from adsorbed species on the co-doped NPs during continuous UV excitation compared to the pristine BFO NPs further indicates an enhanced surface activity.

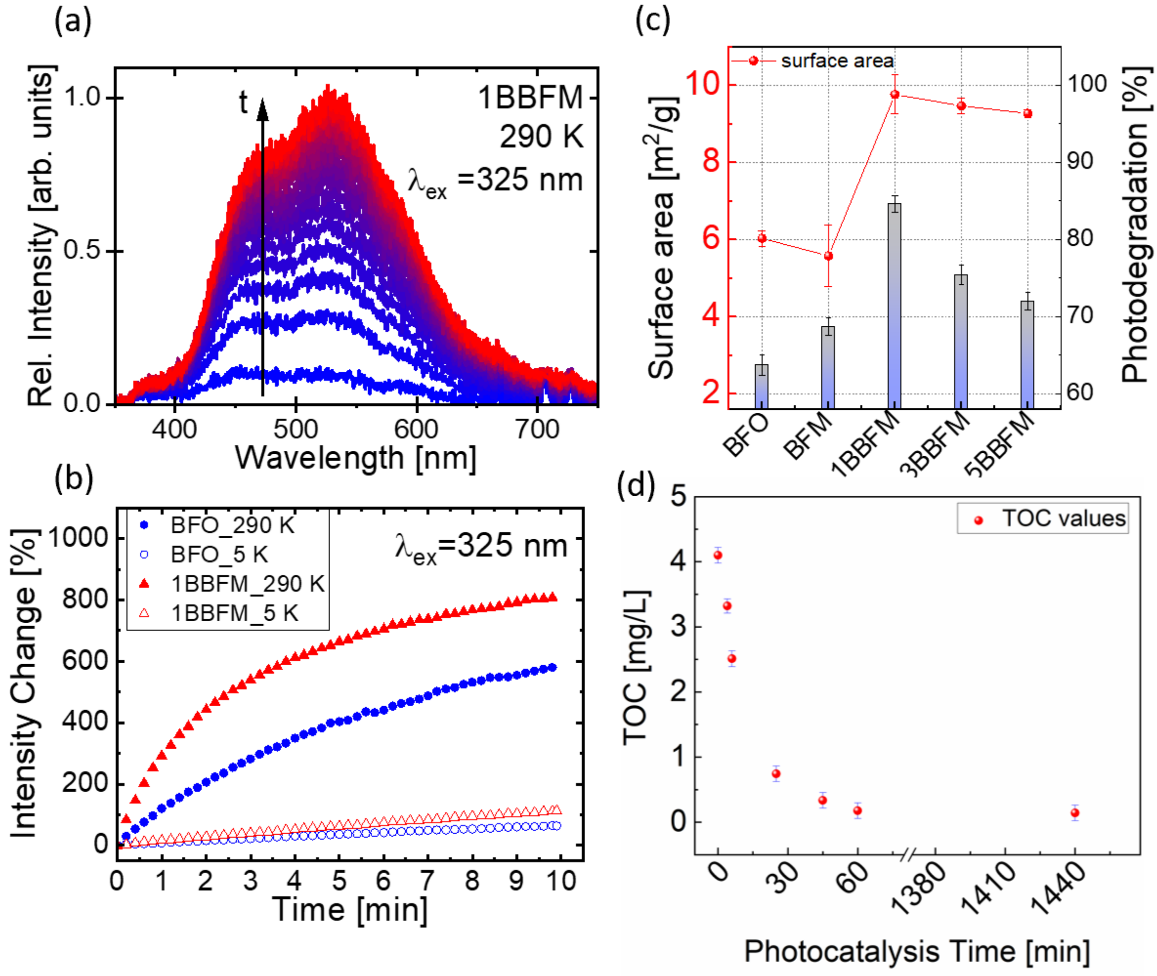

Figure 7.7: (a) The illumination time (t) dependent emission spectra of 1BBFM NPs at 290 K with 325 nm excitation. (b) The change in intensity versus illumination time in minutes at 290 K and 5 K for pristine BFO NPs (blue) and 1BBFM NPs (red), respectively. (c) The specific surface area trend (red) versus doping in BFO NPs is compared to the relative photodegradation (vertical bars) of RhB under UV+visible light (pH = 4.4) up to 180 minutes. (d) Total organic count (TOC) values after photocatalysis at pH 2.2 for 1BBFM photocatalysts. The TOC value was also recorded after 24 h (1440 min), and it matches with the total photodegradation time ~60 min.

Overall, the maximum photocatalytic efficiency for the 1BBFM NPs is attributed to the cooperative effect of increased light absorption, a larger surface area, more effective charge separation, and less recombination of photogenerated charge carriers. The dopant concentration is a key factor in controlling the parameters of the photocatalytic process. In our case doping with 1 mol % Ba into BFM NPs is proven to be optimal for the photocatalysis efficiency."

7.2.2 Photodegradation of plasticizer: doped BFO+GO nanocomposites

Microplastics have become a significant concern for the delicate balance of our planet, owing to their high resistance to degradation and tendency to accumulate in living organisms.[446] Adding to this concern is the use of plasticizers in plastic materials, aimed at enhancing their flexibility and durability. While plasticizers themselves are not microplastics, they can exacerbate the problem of microplastic pollution through a variety of means. Firstly, some plasticizers can leach out of the plastic material over time, as they are not chemically bound to it, thus entering the environment as separate chemicals. This is particularly evident in the case of phthalate plasticizers, frequently used in flexible PVC plastics utilized in medical devices and food packaging. As these materials break down, the phthalates can be released into the environment as microplastics. As an additional concern, certain microplastics are comprised of plasticizers themselves. For example, microbeads found in some toothpastes and exfoliating scrubs are made of plastic materials that include plasticizers such as polyethylene glycol (PEG). The degradation of notorious plasticizers like dibutyl phthalate (DBP) has become a subject of increasing concern due to their persistent nature in the environment and potential toxicity to living organisms.[447–449] DBP like other plasticizers are widely used in a variety of consumer products, including plastics, adhesives, and coatings, which is quite harmful on the long term.[450] Photocatalytic degradation is a promising approach for breaking down plasticizers into smaller, less toxic compounds.[451]

In photodegradation, the UV radiation generates reactive oxygen species (ROS) using photocatalyst and solvent, which reacts with DBP to degrade it. The degradation pathways usually involve the generation of ROS, such as hydroxyl radicals (•OH), and superoxide radicals ($•O_2^-$), which react with DBP to form intermediate products and eventually lead to complete mineralization. These radicals attack the C-C bond and aromatic ring of DBP, leading to the formation of intermediate products such as mono butyl phthalate (MBP), monoethyl phthalate (MEP), and phthalic acid. The intermediate products are further degraded to form CO_2 and H_2O.

In this context, a number of photocatalysts, including TiO_2,[452] ZnO,[453–455] Fe_2O_3,[456] $MnFe_2O_4$,[457] WO_3,[458] and Bi_2WO_6,[459] and $BiVO_4$[460] have been studied for their photodegradation efficiency against several phthalates and organic dyes. Using Bi_2O_3-TiO_2 it has been possible to degrade Cr(VI)/Pb(II)-DBP mixed pollutants under visible light.[461] 95 % of removal of DBP was achieved with Fe and Ag co-doped ZnO.[453] The photocatalytic activity of Bi and Cu co-doped $SrTiO_3$ NPs are reported to be higher than only Bi doped $SrTiO_3$ against DBP.[462] TiO_2 nanotubes have 7.7 times higher photocatalytic activity towards DBP than TiO_2 NPs due to larger surface area.[463] alfa- Fe_2O_3 could degrade 94 % of DBP in the presence of 30 % H_2O_2.[464] Carbon black modified TiO_2 films shows 1.4 times higher degradation rate than bare TiO_2 films.[465]

Interestingly, graphene oxide (GO) has emerged as a promising material for photocatalysis, particularly when it is bound with semiconductor oxide NPs. One of the key advantages of combining GO and oxide NPs is that GO can serve as a support material for the NPs, providing a large surface area for photocatalytic reactions to occur. This large surface area increases the number of active sites for the degradation of organic contaminants. In addition, the presence of GO can also modify the electronic structure of the oxide NPs, leading to improved photocatalytic activity. The combination of GO and TiO_2 NPs has lead to synergistic effects that enhance the photocatalytic performance of TiO_2.[466] Nanocomposite of GO and TiO_2 have shown to produce more efficient charge transfer and to increase the production of ROS. Furthermore, the oxygen-containing functional groups on the surface of GO can also act as electron traps and scavengers, which can reduce the recombination of electrons and holes and improve the stability of the photocatalyst.

Several other studies also investigated the degradation of DBP using the BiOI/BiOCl heterojunction and Bi_2WO_6/CdS composite photocatalysts under visible light irradiation.[451] These studies have identified many intermediate by-products, including phthalic acid, MEP, and MBP, and dimethyl phthalate which were formed during the degradation process.

Despite the recent advancements in the photodegradation of phthalate, there are still some research loopholes and limitations that need to be address. Existing problems are a wide band gap of the photocatalysts, high recombination rate of photoinduced charge carriers, and sluggish and incomplete photodegradation of DBP. The studies on the photodegradation of DBP have estimated different intermediate products vary depending on the photocatalyst used, which leads to a lack of understanding of the reaction mechanisms involved in the DBP photodegradation. The identification of the intermediate products and their potential environmental impacts are critical to assess the feasibility of photocatalytic degradation as a sustainable and safe method for DBP removal.[467]

Ferroelectric-photocatalysts,[468,469] for example Ba and Mn doped BFO NPs show high photocatalytic efficiency than pristine BFO NPs.[150] Another Example is Bi_4NbO_8Br, where the internal spontaneous polarization result in a significant band bending in its electronic structure and greatly promote the migration and separation of charge carriers under visible light irradiation.[470] In case of GO-$BaTiO_3$ nanocomposites for dye photodegradation, a high photocatalytic efficiency is ascribed to the synergistic effects of intrinsic polarization in $BaTiO_3$ NPs and superior electron transport of reduced GO on improving the separation and transport of the photogenerated charge carriers.[471] When TiO_2 is supported on $BiFeO_3$ films in TiO_2/$BiFeO_3$ heterostructures, the photogenerated electrons and holes in ferroelectric $BiFeO_3$ are driven in opposite directions to reduce their chance of recombination.[472] A study found that, BFO nanosheet with single domain show nine times higher photocatalytic activity under visible-light irradiation compared to the polydomain, due to the unidirectional depolarization field as evident by piezoresponse force microscopy (PFM), and spatially resolved surface photovoltage spectroscopy (SRSPS).[473] Additionally, for the case of Ag_2O/$PbTiO_3$ composite a high photodegradation performance against organic dyes has been reported, which was attributed to the ferroelectric polarization of $PbTiO_3$ promoting the separation of photogenerated electrons and holes at the interface.[474]

The state of the art is that bisphenol A was degraded successfully using a BFO and reduced GO composite.[418] Congo red dye was also degraded six times faster in presence of GO supported BFO, than pristine BFO alone.[475] Since GO is an electron acceptor the photogenerated electrons can be easily transferred and hence a larger number of charge carriers will be available for the redox reaction at the surface. Zeng et. al used a heterogeneous photo-Fenton system to degrade several phthalic acid esters (PAEs) in presence of vermiculite supported BFO (VMT-$BiFeO_3$).[476] The photo-Fenton reaction is different from normal photocatalysis under UV light alone, because it involves the use of H_2O_2 and a catalyst in addition to the irradiation by light. In the photo-Fenton reaction, the catalyst (BFO) activates the H_2O_2 and creates hydroxyl free radicals, which are highly reactive and can oxidize a wide range of pollutants, including PAEs. However, a high concentration of H_2O_2 can cause harm to living organisms and aquatic life, and it can also react with other chemicals to produce harmful by-products.

In the following section, we study the photocatalytic degradation of phthalates under UV irradiation using pristine BFO NPs, BFO NPs supported onto GO sheets (BFO-GO), BFM NPs supported onto GO sheets (BFM-GO) and Ag doped BFM NPs onto GO sheets (ABFM-GO) as catalysts.

7.2.2.1 Results and discussion

The AFM images and height profiles of GO sheets are shown in Figure 7.8. Height retraces represents the thickness of layers of GO. On the micrometre scale, the layers display a uniform morphology. However, the graphene layers are overlapping each other as AFM specimens are prepared by drop-casting the dispersion of the GO onto a smooth substrate surface (ITO). Such a morphology is common to the unreduced graphene oxide sheets. The main purpose of interacting BFO NPs with GO layer is to reduce agglomeration of ligand-free BFO NPs that reduces their total surface area. A large surface area of photocatalyst can provide larger number of active sites for redox reactions at the surface. Therefore, interacting BFO NPs with GO can reduce the agglomeration as shown in a schematic of Figure 7.8.

To investigate this, we utilised SEM to image GO and nanocomposites, as shown in Figure 7.8a-d. In Figure 7.8b-d, the SEM images of GO supported NPs are shown with comparison of pristine GO (Figure 7.8a). Each sheet of GO holds NPs all over of its vast surface. The agglomeration is least for ABFM-GO system, which is due to smallest particle size of ABFM NPs than BFM and BFO NPs.[46] The high crystallinity of supported NPs is confirmed using high resolution TEM imaging. The corresponding selected area diffraction pattern shown in Figure 7.8 e-f manifests 101 and 012 lattice planes of *R*3*c* crystal structure of BFO. In the elemental distribution mapping collected in EDX mode all elements are homogeneously distributed all over the sheet covered with NPs. An EDX mapping of BFO-GO nanocomposites is shown in Figure 7.8. The colour scale of elements shows their concentration. This also confirms that BFO NPs are decorated on top of GO sheet.

To study the crystallinity of the synthesized GO from graphene, we measured their XRD patterns, as shown in Figure 7.9a. For graphite a peak near 26° (002) 2θ (interlayer distance "l" = 0.34 nm) is the characteristic peak associated with an organized layer to layer structure. After oxidation of graphite, the peaks shift to lower angle due to the increment in interlayer spacing of the graphite structure via oxygen containing functional groups, as we observe in the XRD pattern of GO. The peak at ~10.7° ("l" = 0.82 nm) belongs to (001) and the peak near

~43° displays (100) planes of GO.[477] We compared the XRD patterns of pristine BFO and BFO-GO and doped BFO-GO nanocomposites as shown in Figure 7.9b. The diffractogram peaks for nanocomposites correlate with the rhombohedral (*R*3*c*) crystal structure like pristine BFO NPs. The diffraction patterns represent single phase of all nanocomposites. The crystallite size and microstrain of NPs attached to GO were calculated using Rietveld refinement fits.

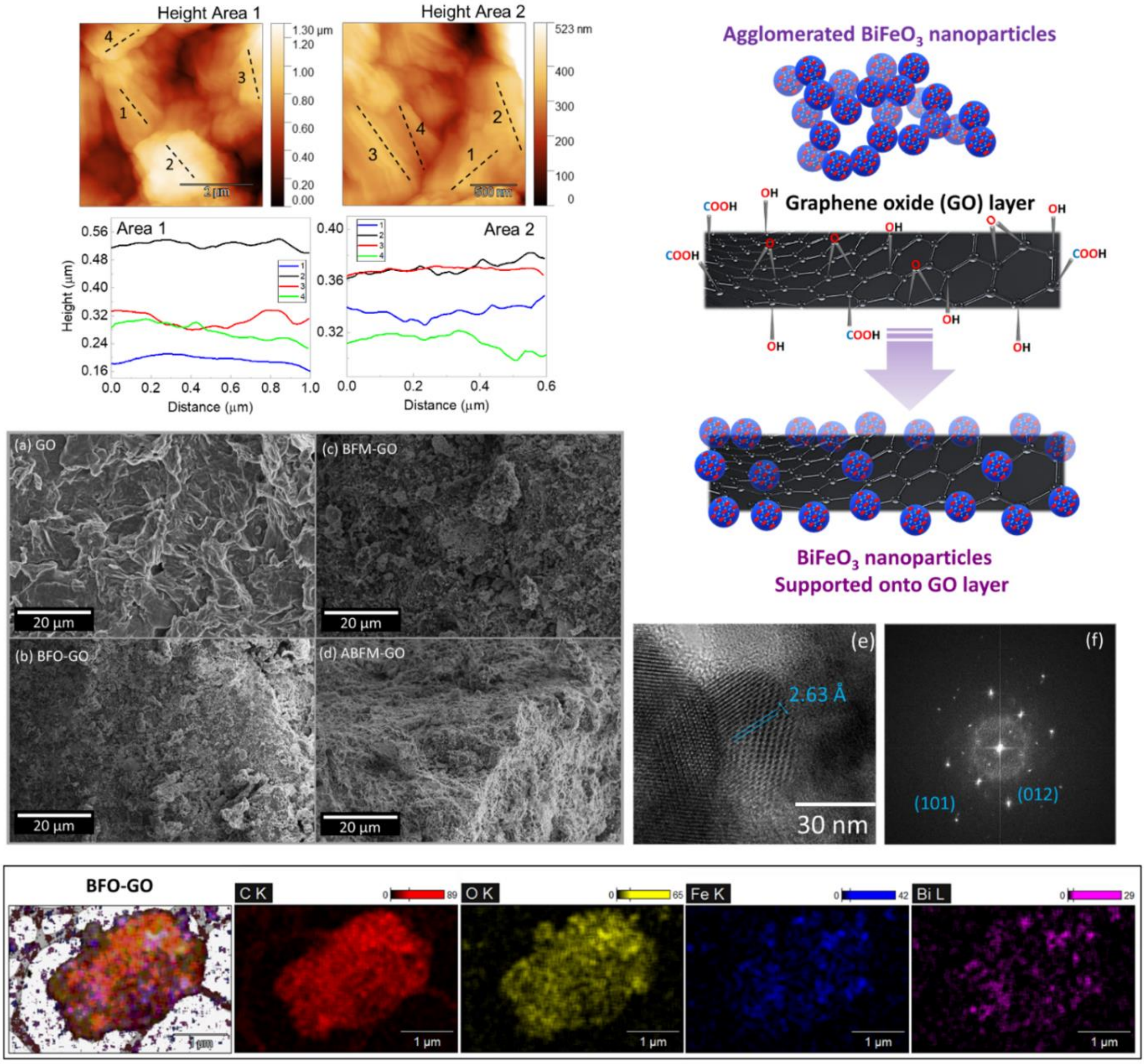

Figure 7.8: The AFM height retrace of graphene oxide sheet (GO) and depth profile of the line of interest on the GO nanosheets from two different areas 1, and 2. On the right side, a scheme shows the functionalisation of the GO layer by interacting with BFO NPs. The SEM images (a-d) of GO nanosheets, BFO+GO composite and doped BFO+GO composites. (e-f) The high-resolution TEM image of crystalline BFO NPs onto GO layer with SAED pattern for lattice plane corresponding to a rhombohedral crystal. At the bottom HAADF images are shown for the elemental distribution in BFO-GO nanocomposite, where the first image is an overlay of all elements.

We found similar crystallite sizes of nanocomposites as for their pristine counterpart NPs [Appendix].[46] The average microstrain of the NPs in the nanocomposite is found to be slightly less than free-standing BFO NPs, which can be due to bonding of oxygen containing groups of GO with the nanoparticle surface. In Figure 7.9b, the peak corresponding to GO is not observable, which is due to its interaction with BFO NPs.

When BFO NPs and doped BFO NPs weakly interact with GO, the *R*3*c* crystal symmetry is retained. These results also suggest the ferroelectric properties, of BFO, BFM, and ABFM NPs should not change as their crystal structure is not affected by interacting with GO layer. Ag-BFM NPs consist highest piezoresponse among all NPs and hence highest local polarization confirmed by switching spectroscopy in PFM mode.[46] This retained property can be useful of photocatalysis.

Interaction of BFO NPs with GO layer

To investigate the interaction between BFO NPs and GO, we analysed the IR spectra of GO, pristine BFO NPs, and BFO-GO nanocomposites, as depicted in Figure 7.9c, where the peak intensity is normalised. For pristine BFO NPs, two intense peaks at approximately 552 and 444 cm^{-1} are indicative of Fe-O stretching and bending vibrations of octahedral FeO_6 groups in the perovskite moiety of BFO NPs. Additionally, the broad absorption band in the 3500-3000 cm^{-1} range is attributed to O-H stretching, caused by surface adsorbed hydroxide groups from the solvent onto the surface of the NPs.

The IR spectrum of GO displays characteristic oxygen functional groups. The peak positions are estimated and associated with -C=O stretching vibration, C=C stretching vibration, -OH deformation, -C-O stretching vibration, -C-O-C stretching, and -O- bending vibrations. This indicates the presence of carboxylic acid, ester, anhydrides, alcohol, and epoxy groups on the basal planes of the GO sheets. The IR spectrum of BFO+GO composites is represented by the solid red line. The peak area of -OH deformation mode related to carboxylic groups on GO has decreased, along with the peak areas attributed to the C=O, C=C, C-OH, C-O, C-O-C stretching modes. This suggests that the oxygen-containing groups of pristine GO weakly interact with BFO NPs through van der Waal forces.

The increase in peak intensity near 552 cm^{-1} and 444 cm^{-1} is due to bending and stretching modes of Fe-O bonds in perovskite BFO, compared to pure BFO NPs illustrated by dotted blue lines. The IR analysis of BFO+GO composite samples reveals the interaction between GO and BFO NPs. We obtained similar results for other doped-BFO NPs, as shown in Figure 7.9d. The peak intensity near the 552 cm^{-1} and 444 cm^{-1} ranges for doped BFO+GO nanocomposites is higher than BFO+GO, indicating stronger Fe-O stretching and bending vibrations of octahedral FeO_6 groups due to the presence of Mn at the Fe-site.

The Raman spectra of GO and BFO+GO composite is shown in Figure 7.9(e-f). Two fundamental vibrations are observed for GO at ~1330 and 1590 cm^{-1}. These characteristic peaks belong to D type vibration and G type vibration, respectively. Difference in peak intensity ratio (I_D/I_G value) of D and G vibration in BGO sample represents the interaction of BFO NPs with GO layers. The ratio of peaks is slightly larger for BGO than that of GO, which can be due to reduction of sp^2 hybridized carbon.[478] In the Raman spectrum of BFO+GO composite, peaks below 800 cm^{-1} are due to BFO NPs. These peaks are assigned as 13 modes ($4A_1$ + 9E) for rhombohedral structure of BFO similar as previously synthesized BFO NPs.[10] The first three intense peaks correspond to E(TO1), E(TO2) and A_1(TO1) of BFO NPs, changes significantly for doped BFO NPs attached to GO. The peak correspond to Bi-O at lowest wavenumber is slightly affected by Mn doping into BFO NPs, however it is more affected when further Ag is doped into Mn-doped BFO NPs. These bond vibrations become broader and slightly shifted towards higher wavenumber due to presence of Ag as dopant at Bi-site.

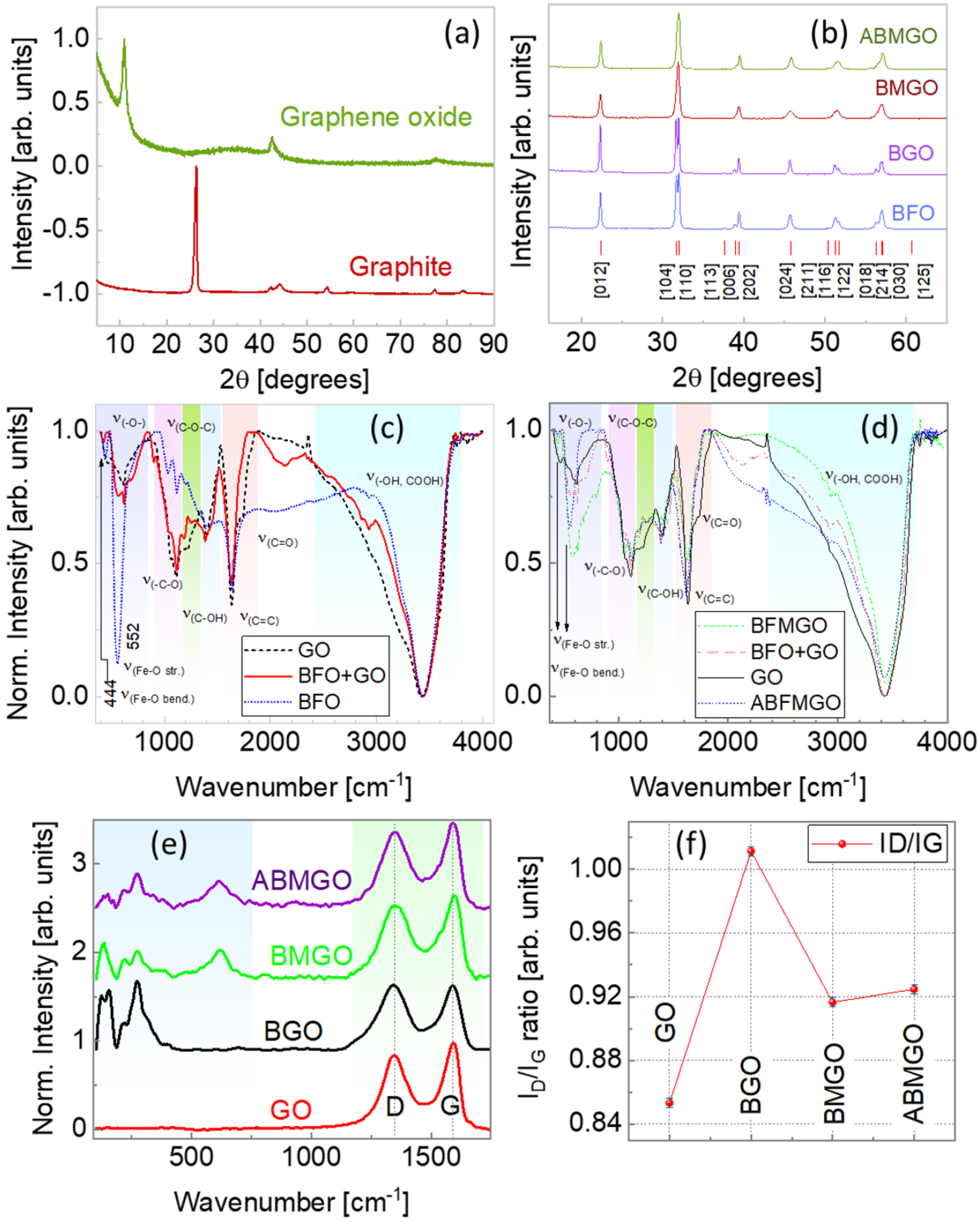

Figure 7.9: XRD diffractogram of graphite and graphene oxide (a), diffractograms of pristine BFO and BFO+GO nanocomposites along with doped BFO+GO nanocomposites (b), Infra-red spectra of GO, pristine BFO and BFO+GO nanocomposite (c), Infra-red spectra of GO and doped BFO+GO nanocomposites (d), and Raman spectra of GO and nanocomposites (e) with intensity ratio trend for all samples.

The intensity ratio (I_D/I_G value) for doped-BFO+GO nanocomposites is less than BFO+GO, but larger than pristine GO, may be due to different type of interaction of doped-BFO NPs with groups onto GO layer than BFO NPs. These changes manifest the interaction of doped and undoped BFO NPs with GO layer.

To further confirm the interaction of GO with BFO NPs, we measured XPS spectra of BFO+GO and doped BFO-GO nanocomposites, as shown in Figure 7.10. The XPS spectra was compared with pristine BFO NPs and pure GO. From Figure 7.10, the C1s spectra of GO typically exhibit four distinct peaks at binding energies of around 288.7 eV, 287.7 eV, 286.8 eV, and 284.7 eV. These peaks correspond to different types of carbon atoms in the material, each with different bonding environments. The peak at 288.72 is assigned to the carbonyl groups (C=O) on the surface of GO. These carbonyl groups are formed during the oxidation process and are known to play an important role in the reactivity and functionality of the material. The peaks at 287.7 and 286.7 eV are attributed to the epoxide groups (C-O-C) present in GO. Epoxide groups are another common functional group formed during the oxidation process, and they can also be used for further modification of the material. The peak at 284.7 eV is associated with the C-C bonds in sp^2 hybridized carbon atoms. These carbon atoms are part of the graphene lattice and are typically not involved in oxidation or functionalization.

In BFO-GO nanocomposite (BGO), we observe that the C1s peaks of pristine BFO slightly shifted towards higher energy [Figure 7.10c]. Moreover, the peak area increases a lot especially for peaks at 288.7 eV and for peak at 287 eV, and for peak at 284.7 eV. We have shown the comparison in the Appendix for C 1s peaks. The observed shift in the C1s peaks of BFO in the BFO-GO composite to slightly higher binding energies, along with the increased peak areas, can be attributed to the interaction between BFO and GO at their interface. The shift to slightly higher binding energies can also be explained by a charge transfer or a change in the electronic structure of BFO due to the interaction with GO. This interaction can modify the bonding environment of the carbon atoms present on the surface of the BFO NPs, which can cause a shift in the C1s peak position towards higher binding energies. The increase in peak areas can be attributed to the increased surface area of the BFO NPs when they are in contact with the GO sheets in the composite. This results in a greater number of carbon atoms in different functional groups being exposed to the X-ray beam during XPS analysis, leading to an increase in the intensity of the C1s peaks. Additionally, the interaction between BFO and GO can lead to changes in the surface chemistry of the BFO NPs, such as the formation of new functional groups or the modification of existing ones. This can also contribute to the increase in peak areas observed in the C1s spectrum.

Comparing of the C 1s of BFO-GO nanocomposite with pristine GO; we find that there is again a slight shift of peak positions towards higher energy for the nanocomposite. However, the peak area of nanocomposite is smaller than GO. The shift in peak positions of the C1s peaks of GO towards higher energy in the BFO-GO nanocomposite can be attributed to the interaction between BFO and GO at their interface.

The extent of the shift in peak positions is usually small, as the interaction between BFO and GO may be weak, and the number of carbon atoms experiencing significant changes in their electronic environment is limited. The decrease in peak area in the C1s spectrum of the

BFO+GO composite, when compared to GO, can be attributed to the presence of BFO NPs on the surface of GO. The BFO NPs can cover the surface of GO and decrease the number of carbon atoms in different functional groups being exposed to the X-ray beam during XPS analysis, leading to a decrease in peak intensity. Additionally, the interaction between BFO and GO can also lead to changes in the surface chemistry of GO, such as the removal of some functional groups or the modification of existing ones, which can also contribute to the decrease in peak area observed in the C1s spectrum. This can be confirmed further by analysing and comparing the O1s spectra.

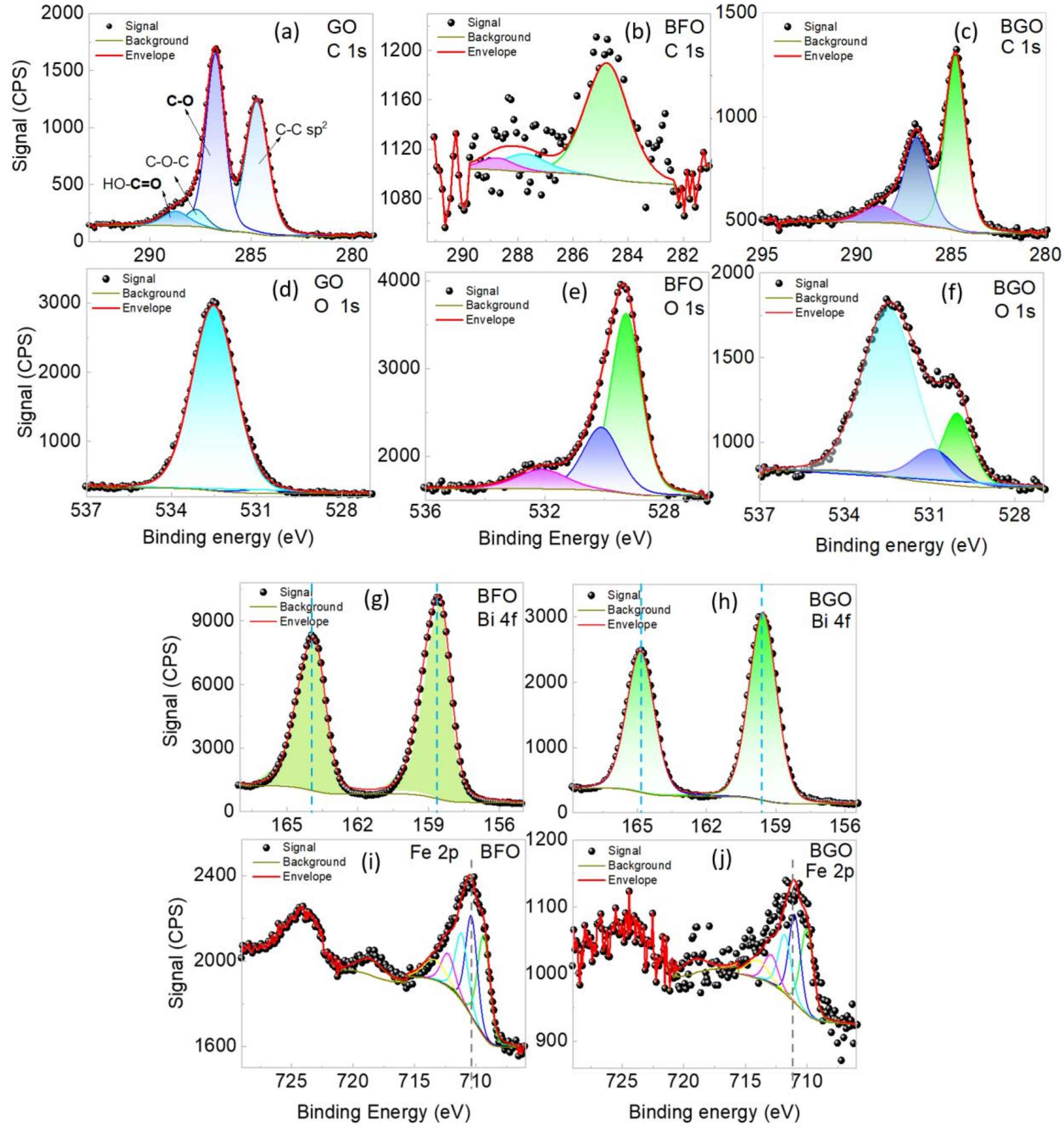

Figure 7.10: (a-b) The XPS spectra of C 1s of (a) GO, (b) BFO, and (c) of BGO nanocomposite. O 1s XPS spectra of (d) GO, (e) BFO, and (f) BGO. XPS spectra of Bi 4f of (g) BFO, and (h) BGO. XPS spectra of Fe 2p of (i) BFO, and (j) BGO.

The comparison of O 1s spectra for each material is shown in Appendix. The O 1s spectrum of GO typically exhibits peaks at binding energies around 532.5 eV and 531.8 eV, which correspond to different types of oxygen atoms in GO. The peak at 532.5 eV is attributed to the oxygen atoms in carboxyl (COOH) groups. Carboxyl groups are formed during the oxidation of graphene and are known to be important functional groups that can be used for further modification of the material. The peak at 531.8 eV is associated with the oxygen atoms in epoxy (C-O-C) and hydroxyl (OH) groups. The higher intensity of the carboxyl peak compared to the hydroxyl and epoxy peaks indicates a higher degree of oxidation and a greater number of carboxyl groups on the surface of the GO.

For BFO-GO nanocomposite, we find three O1s peaks at 532.3 eV, 531 eV, and at 530 eV. The slight shift in peak positions towards lower energy for the O1s peaks in the BFO-GO nanocomposite can be attributed to the formation of new chemical bonds between BFO and GO or the breaking of some of the existing bonds, resulting in changes to the electronic environment of the oxygen atoms. The peak at ~532.5 eV in the BFO+GO composite has a lower peak area than the corresponding peak in pure GO, which suggests that there are fewer oxygen atoms in the BFO-GO nanocomposite with the same chemical environment as in pure GO. This can be due to the formation of new bonds between oxygen atoms in BFO and GO or the breaking of some of the existing oxygen bonds. The peak at 531 eV in the BFO-GO nanocomposite has a higher peak area than the corresponding peak in pure GO, which suggests that there are more oxygen atoms in the BFO-GO nanocomposite with the same chemical environment as in pure GO. The peak at ~530 eV in the BFO+GO composite is a new peak that is not present in the pure GO spectrum. This peak can be attributed to the formation of new oxygen-containing species resulting from the interaction between BFO and GO.

Comparing the O1s spectra of pristine BFO and BFO-GO nanocomposite, we find that pristine BFO has three peaks at 532, 530, 529.3. these peaks shift slightly towards higher energy. The peak area of peak at 532 increases a lot, whereas the peak areas of peaks at 530 and 529.3 decreases for BFO-GO nanocomposite. The increase in peak area of the peak at 532 eV indicates the increase in the concentration of oxygen atoms bonded to BFO in the composite. This suggests that some oxygen atoms from GO have transferred to BFO, leading to the formation of new bonds. The decrease in peak area of peaks at 530 and 529.3 eV in BFO-GO nanocomposite as compared to pristine BFO suggests that some oxygen atoms from BFO have transferred to GO, leading to the breakage of some bonds in BFO. The decrease in the peak area can be attributed to the decrease in the concentration of oxygen atoms bonded to BFO in the composite.

The overall observations suggest that there is a transfer of oxygen atoms between BFO and GO, leading to the formation of new bonds and the breakage of existing bonds. The direction of charge transfer is from BFO to GO, as the peak area 532 eV of oxygen atoms bonded to BFO in the nanocomposite increases, indicating that BFO has donated electrons to GO. This indicates that the BFO-GO nanocomposite has a higher concentration of electron-deficient oxygen species compared to pristine BFO.

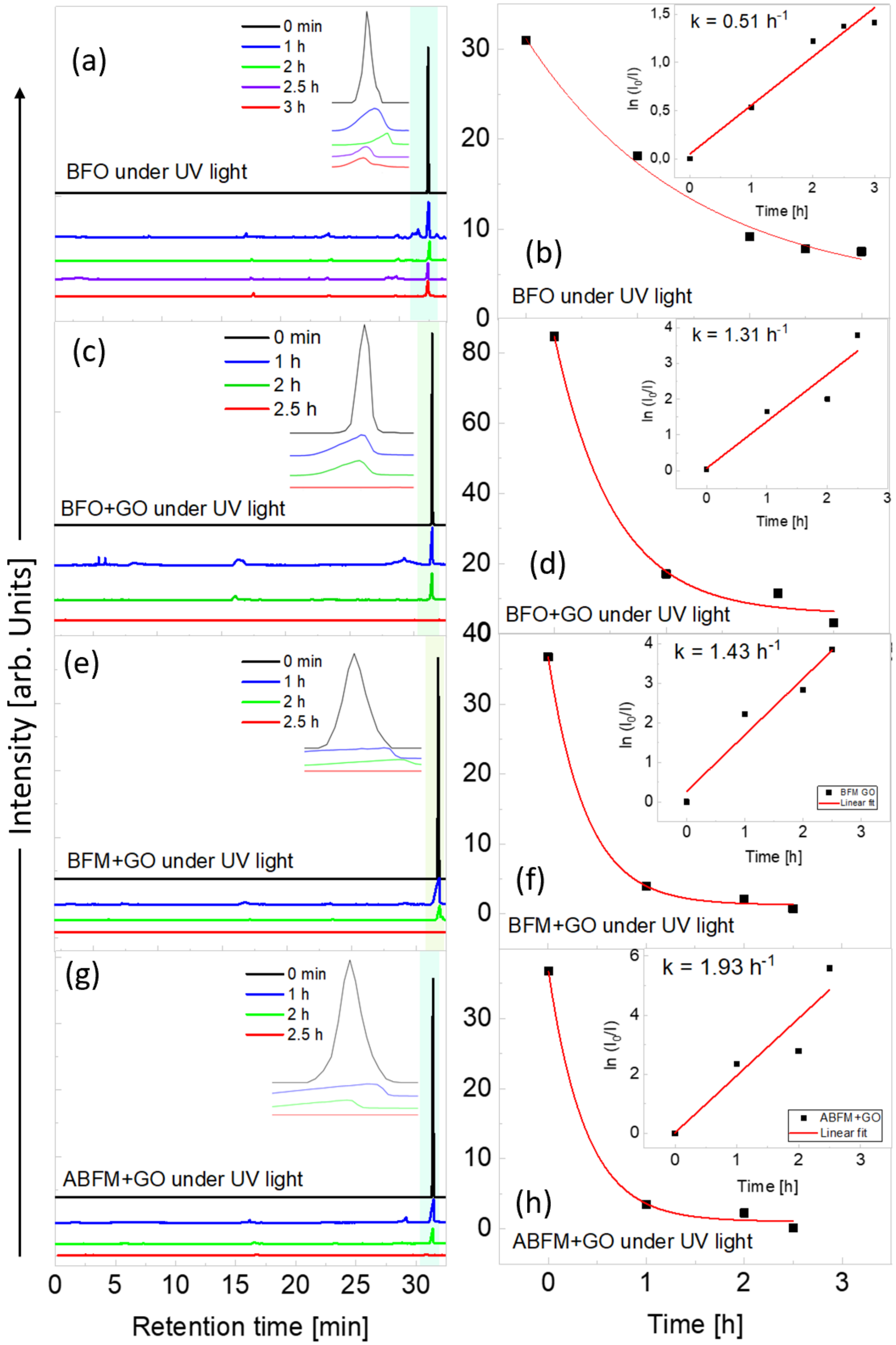

Figure 7.11: Photocatalytic degradation of DBP. GC-MS chromatograms for different UV irradiation times (a) for

pristine BFO as photocatalyst, (c) for BFO+GO composite (e) for BFM+GO composite and (g) for ABFM+GO composite. The decrease of peak intensity at a retention time ~33 min (attributed to DBP) and the corresponding kinetics in the inset (b) for pristine BFO, (d) for BFO+GO composite, (f) for BFM+GO composite, and (h) for ABFM+GO composite.

Photodegradation of Di-butyl phthalate (DBP)

Our study aimed to examine the photodegradation of DBP in aqueous solution using undoped and doped BFO+GO composites. We utilized the GC-MS techniques to analyse the results. Figure 7.11 shows the chromatograms for the degradation of DBP under different UV exposure times. Figure 7.11a indicates the presence of DBP at a retention time of ~35 minutes. A continuous exposure to UV light using pristine BFO as a photocatalyst results in the reduction of DBP over time. Although 3 hours of UV exposure did not completely degrade DBP using only BFO, we observed the appearance of new peaks at lower retention times in the 1–3-hour chromatograms, indicating the degradation of DBP. These degraded products are later discussed in the mass spectra. Figure 7.11b shows a reduction in peak intensity at 35 minutes, with an inset indicating a rate constant of 0.51 h^{-1} for the degradation reaction. We found that although the degradation process was slow, BFO NPs are capable of partially degrading DBP. When BFO NPs are decorated onto GO, we observe almost a complete degradation of DBP in 2.5 hours, as indicated by a peak reduction to near zero at a retention time of 32 minutes in Figure 7.11c. BFO-GO nanocomposite has a faster degradation rate with a rate constant of 1.31 h^{-1}, which is almost 2.57 times higher than BFO NPs alone. For doped BFO-GO nanocomposites, DBP was degraded for up to 2.5 hours by both BFM+GO and ABFM+GO composites, similar to undoped BFO+GO. The photodegradation reactions are faster for doped BFO-GO nanocomposites than the undoped ones, as seen in Figure 7.11 f-h. These findings show that BFO-GO nanocomposites are effective in degrading DBP. Doped BFO-GO nanocomposites exhibit faster reaction kinetics than the undoped ones, especially ABFM-GO has a rate constant 1.93 h^{-1} which is 1.5 times faster than for BFO-GO nanocomposite.

The mass spectra of the products formed during the photodegradation of DBP using pristine BFO NPs under UV light are shown in Figure 7.12. DBP has a molecular formula of $C_{16}H_{22}O_4$, which corresponds to a molecular mass of 278. Therefore, we observe a molecular ion peak at m/z 278 in the mass spectrum of 0 min photodegradation of DBP. Based on the obtained products from the mass spectra, we propose a plausible reaction mechanism for BFO NPs shown in Figure 7.12 (a-i). We could confirm at least nine products formed upon photodegradation of DBP at different times of exposure to UV light. From our proposed plausible mechanism, DBP (m/z 278) degrades to MBP by losing one butyl chain, and MBP (m/z 222) further degrades to phthalic acid (m/z 166) upon losing a butyl chain. The loss of a water molecule from phthalic acid leads to the formation of phthalic anhydride (m/z 149), which undergoes aromatic ring cleavage to form 3-hydroxy butanoic acid (m/z 105), whereas it can also form benzene (m/z 77) upon losing CO and CO_2 molecules. The obtained benzene may undergo final mineralization to form CO_2 and H_2O, which are undetectable by mass spectrometry. If one wants to study the mineralization of DBP, then the total organic carbon (TOC) technique can be used, including both organic and inorganic carbon, so that one can determine the extent of mineralization to CO_2. There is another parallel mechanism happening when BFO acts as a photocatalyst, where DBP is photodegraded by losing both -OC_4H_9 groups to form Benzene-1,2-dicarbaldehyde (phthalaldehyde; m/z 134). phthalaldehyde further degrades to 2-hydroxybenzaldehyde (salicylaldehyde; m/z 122) by losing one CO group. Similarly, the big organic compounds like MBP further degrade to butyl 2-hydroxybenzoate (m/z 194) by losing CO_2, and phthalic acid degrades to 2-carboxybenzaldehyde (m/z 150).

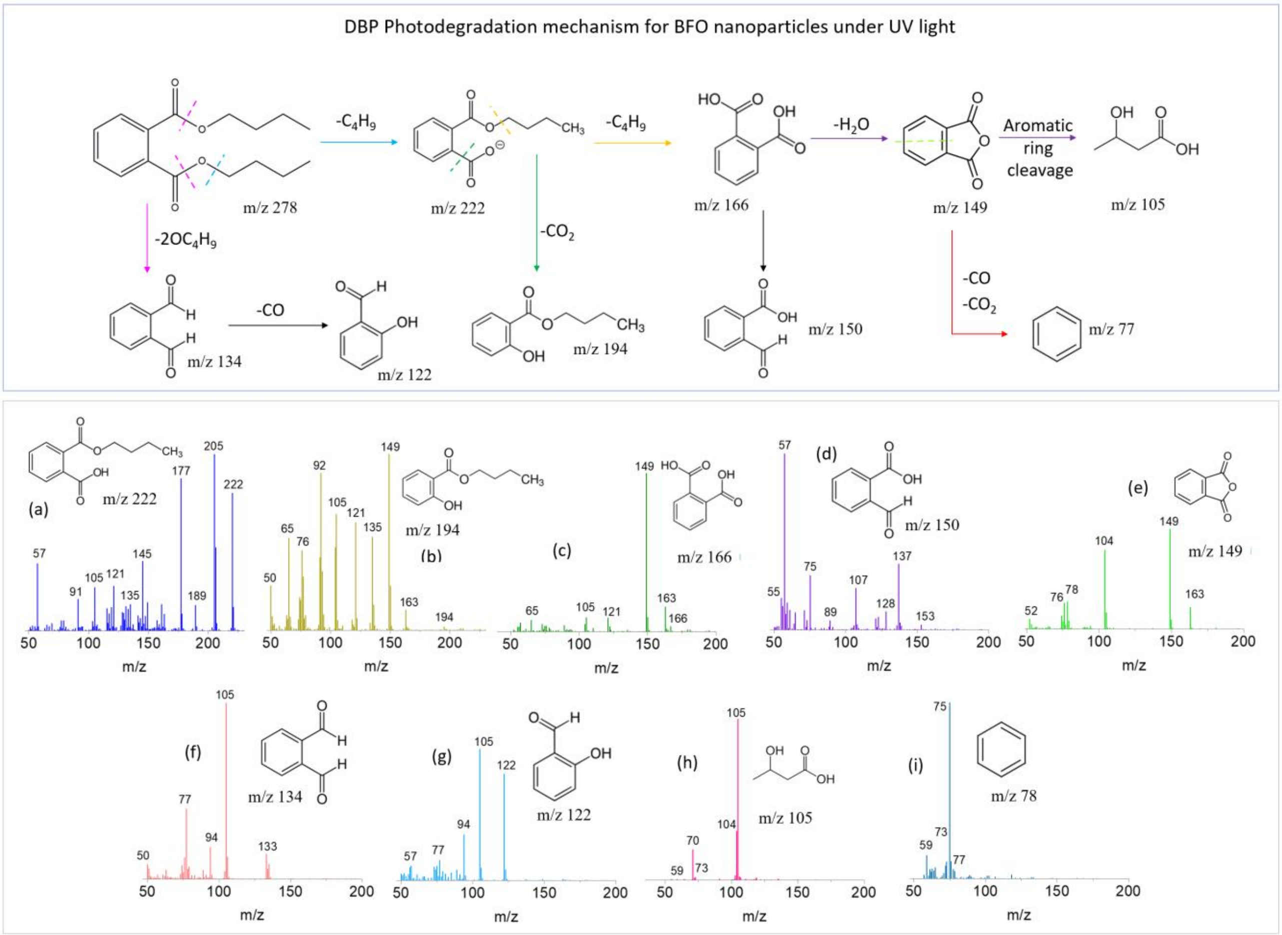

Figure 7.12: Proposed plausible mechanism of photodegradation of DBP using pristine BFO NPs under UV light, (a-f) mass spectrum of by-products formed during continuous irradiation of UV light till 3 h while photodegradation of DBP in presence of BFO NPs.

When BFO NPs are supported on GO, a slightly different photodegradation mechanism occurs. Figure 7.13 (a-i) shows the mass spectra of individual products formed upon photodegradation of DBP using the BFO+GO composite, and a plausible mechanism based on these products.

The BFO+GO photocatalyst directly degrades DBP to phthalic acid (m/z 166) by losing both butyl groups, which further degrades to phthalic anhydride. Phthalic anhydride undergoes aromatic ring cleavage and degrades to 3-hydroxy butanoic acid (m/z 105) and 2-methyl butanoic acid (m/z 102). It also degrades to benzoic acid (m/z 122) by losing one CO group. phthalic acid undergoes several steps to form smaller organics, one of which is the formation of catechol (m/z 111) by losing two CO groups, which further degrades to hydroquinone (m/z

108). In another step, phthalic acid degrades to 2-carboxybenzaldehyde (m/z 150), which further breaks down to 2-hydroxy benzoic acid (m/z 138) by losing a CO group.

We estimate that these products can be completely mineralized to form CO_2 and H_2O, as we observe a reduction in peak intensity of these products at their respective retention times in chromatograms obtained at 2.5 hours.

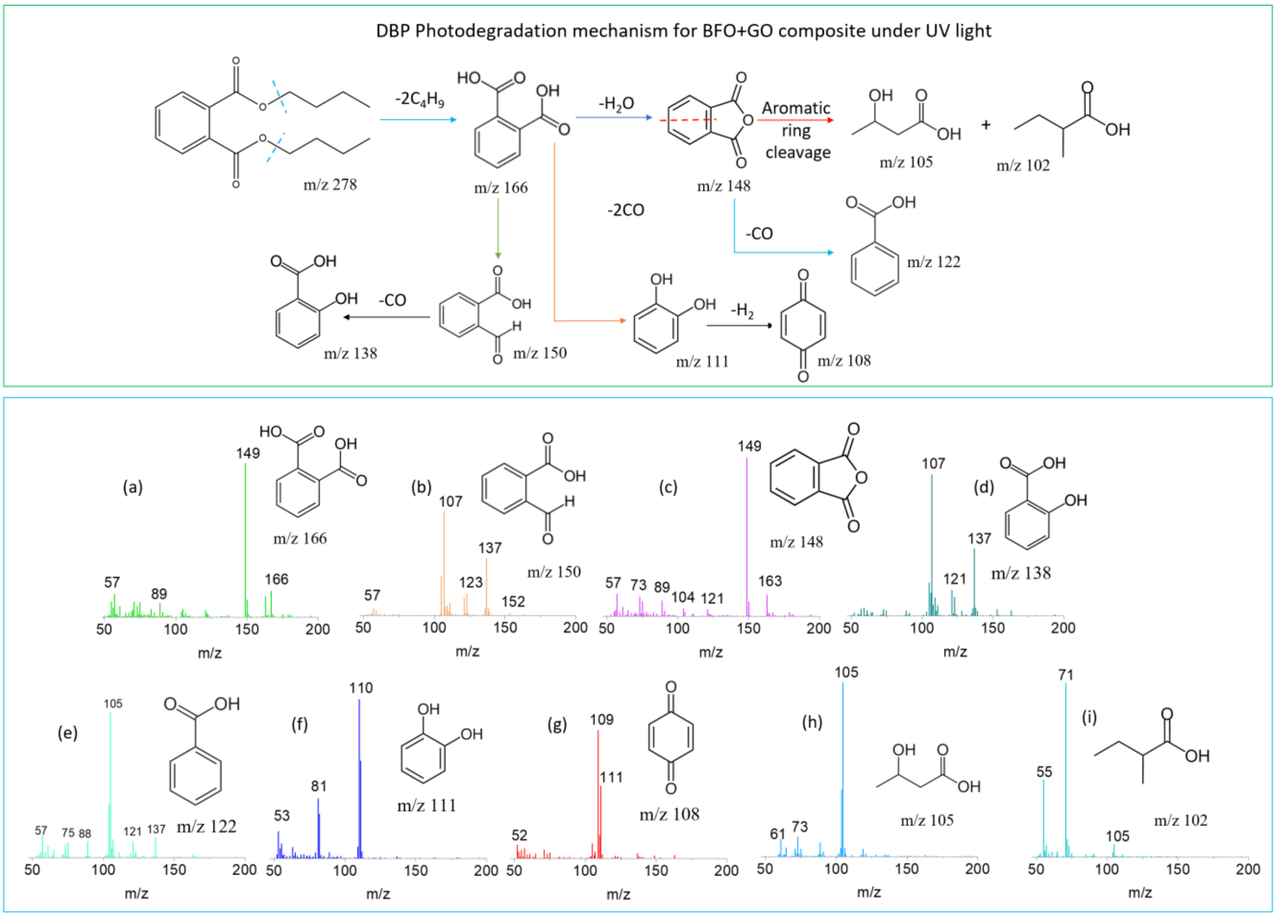

Figure 7.13: Proposed plausible mechanism of photodegradation of DBP using composite of BFO NPs and graphene oxide (BFO+GO) under UV light, (a-i) mass spectrum of by-products formed during continuous irradiation of UV light while photodegradation of DBP in presence of BFO+GO composite.

BFM-GO and ABFM-GO nanocomposites undergo a degradation mechanism that is comparable to, but slightly different from the mechanism observed in BFO-GO nanocomposites. In Figure 7.14(a-l), we present the mass spectra of the formed products, which illustrate that 13 products are generated during the photodegradation of DBP, exceeding the number of products observed in BFO+GO composites alone. They comprise a combination of product types obtained from BFO NPs as a photocatalyst and the BFO+GO composite. The doped BFO-GO nanocomposite is apparently a more effective and superior photocatalyst than both the BFO-GO nanocomposite and BFO NPs. We have proposed a plausible mechanism, based on obtained 13 products. Specifically, our analysis indicates that DBP degrades primarily to MBP (m/z 222), which further decomposes into phthalic acid (m/z 166) and butyl 2-hydroxybenzoate (m/z 194). The butyl 2-hydroxybenzoate (m/z 194) subsequently degrades to 2-hydroxybenzaldehyde (m/z 122) and ultimately breaks down to benzene. Phthalic acid (m/z 166) undergoes degradation to phthalic anhydride (m/z 148), which in turn breaks down to benzaldehyde (m/z 105) and finally to benzene. Additionally, phthalic anhydride (m/z 148) undergoes degradation to 3-hydroxybutanoic acid and 2-methylbutanoic acid (m/z 102). Phthalic acid also undergoes several degradation steps, resulting in the formation of catechol (m/z 111), hydroquinone (m/z 108), 2-carboxybenzaldehyde (m/z 150), 2-hydroxybenzoic acid (m/z 138), and finally benzene. Additionally, MBP (m/z 222) breaks down into salicylaldehyde (m/z 122) and ultimately into benzene.

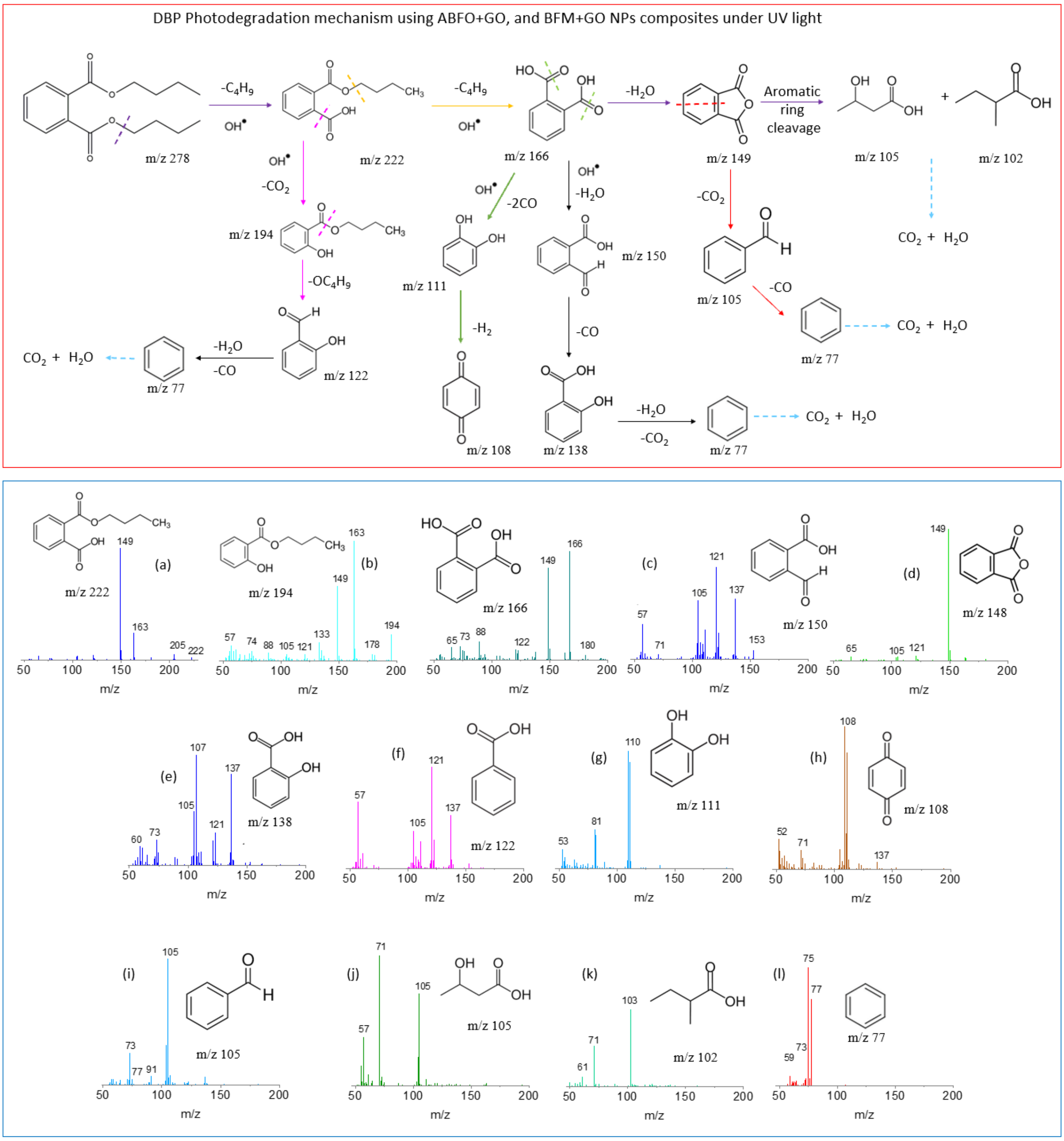

Figure 7.14: Proposed plausible mechanism of photodegradation of DBP using composite of ABFO NPs and graphene oxide (ABFO+GO) and BFM+GO composite under UV light, (a-l) mass spectrum of by-products formed during continuous irradiation of UV light during photodegradation of DBP in presence of both composites.

Discussion

The pristine BFO NPs could not degrade all DBP for up to 3 h of continuous exposure of UV light, whereas BFO+GO could do so. This may be due to low surface area of BFO NPs than BFO+GO composite as shown in Figure 7.15b. A larger surface area of BFO-GO nanocomposite compared to pristine BFO NPs can facilitates a larger number of active sites for redox reactions to occur at the surface of the photocatalyst, more for doped BFO-GO nanocomposites. In addition, the presence of GO in the nanocomposite also facilitates the transfer of charge carriers and prevents their recombination. In UV range more light absorption have been found for BFO-GO nanocomposite than BFO NPs, but without significant change in band gap of BFO NPs, as shown in Figure 7.15a. The band gap of pristine BFO is observed at 520 nm,[46,150] which is similar to our previous studies on BFO NPs. Upon interacting with GO, new energy levels at higher energy less than 300 nm. This could be due to an increment in the known "weak-transitions" in BFO (p-d charge transfers occuring at ~3.4 eV, ~4.5 eV, and (p+d)-p charge transfer happens at ~5.2 eV)[138,150] due to engagement of O 2p orbitals of GO with conduction band levels of BFO formed by involvement of FeO_6. Such, transitions lead to an increase in number of photogenerated photons in the BFO+GO nanocomposite as compared to pristine BFO NPs.

The doped ABFM+GO has the fastest photodegradation kinetics among all used photocatalysts. This is due to the highest surface area and also due to the presence of higher piezoresponse (proportional local polarization) in ABFM NPs,[46] which lead to a enhanced charge separation efficiency and reduced electron-hole recombination rate as compared to BFM+GO and BFO+GO nanocomposites.

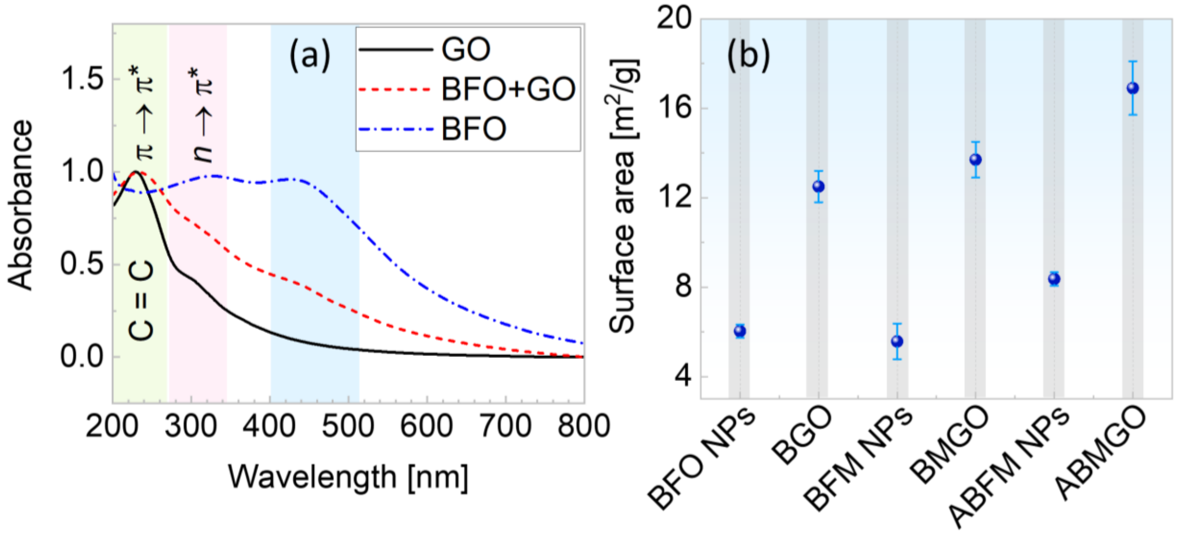

Figure 7.15: Absorbance spectra of GO, BFO and BFO+GO nanocomposites (a). Surface area trend of free standing BFO, BFM and ABFM NPs, and of their nanocomposites with GO (b).

Doped and pristine BFO-GO nanocomposite have formed new products which pristine BFO NPs did not. GO can act as a reducing agent and reduce some of the degraded products to form new compounds. Additionally, GO can also absorb some of the degradation products, preventing their further reaction like dimerization. The obtained products upon photodegradation of DBP are relatively safer than than that of DBP. DBP is known to be toxic to aquatic organisms and has been classified as a probable human carcinogen. The obtained products, such as benzaldehyde and benzoic acid, are commonly used in food flavourings and have low toxicity. In comparison to DBP, both catechol and hydroquinone have a lower potential to bioaccumulate and persist in the environment, reduce the long-term risk. However, their toxicity profiles may still make them a concern for human and environmental health. The obtained intermediate products are generally safer than DBP, they still need to be properly managed and disposed of to prevent harm to the environment and human health.

Conclusion

Poriferous BFO-GO photocatalysts were prepared using the temperature assisted gelation method. Our study finds that BFO+GO composites are effective in degrading DBP in aqueous solutions under UV light irradiation, and the addition of GO to BFO NPs as supporting material enhances the photodegradation rate. The degradation is studied using gas chromatography. Doped BFO+GO nanocomposites, especially ABFM+GO, showed faster reaction kinetics than others. The increase in efficiency is due to the high surface area, namely the number of active sites, available for the photocatalytic reaction. The larger intrinsic polarization in doped BFO NPs (ferroelectric-catalysts), mitigates recombination of photoinduced charge carriers.

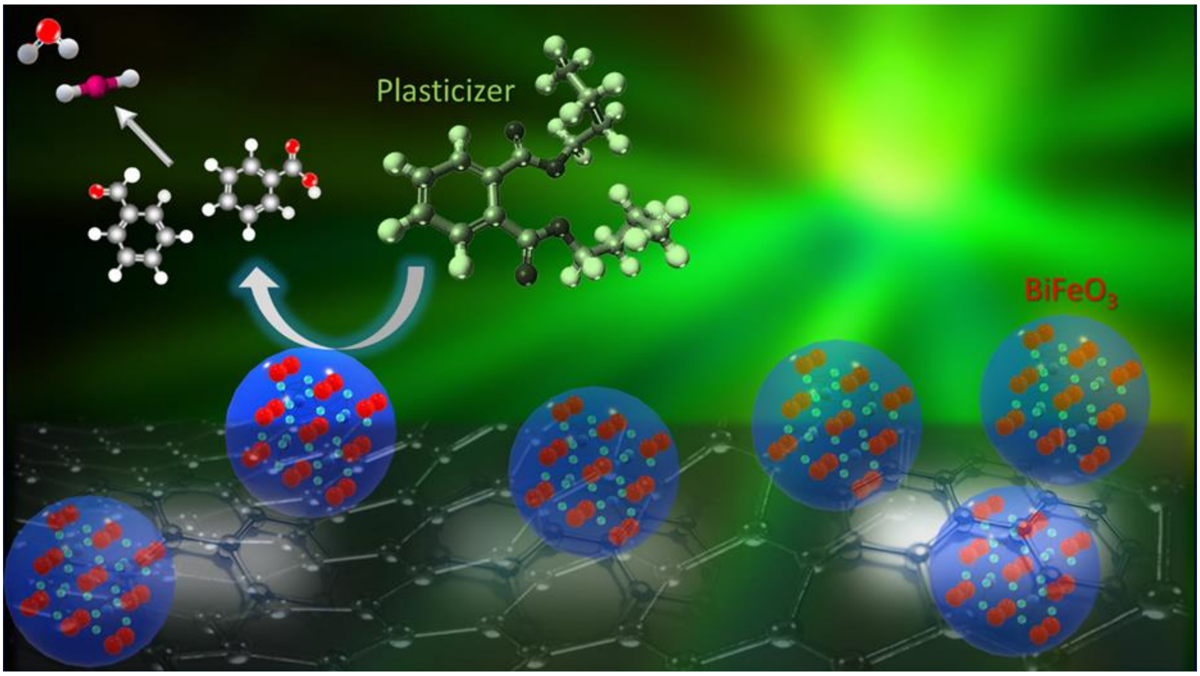

Figure 7.16: The green mercury lamp emits ultraviolet radiation to facilitate the photodegradation of di-butyl phthalate (DBP) in the presence of ferroelectric doped-BFO NPs supported on GO sheets.

In addition, the mechanism of degradation of BFO+GO and doped BFO+GO nanocomposites were found to be slightly different than pristine BFO NPs. DBP degrades to MBP and phthalic acid by losing one and/or both- butyl chains, and further degrades to other products by losing additional functional groups. When BFO NPs are supported onto GO, a slightly different photodegradation mechanism occurs, resulting in the formation of new intermediate products such as benzaldehyde, benzoic acid, and hydroquinone within 1 to 2 h [Figure 7.16]. These intermediate products further decompose to CO_2 and H_2O in 2.5 h for ABFM+GO and BFM+GO nanocomposites.

7.3 Piezo-photocatalytic activity of doped BFO NPs

**This section is based on a journal article, published in Adv. Func. Mater., 2022.*[46]

Piezo-photocatalysis is a combination of piezoelectricity and photoactivity. Piezoelectric materials can produce polarized positive charges on one end of the unit and negative charges on the other end under stress or strain. Driven by the polar state, photoinduced electron and hole pairs can be efficiently separated and propelled to migrate in opposite directions, which benefits the migration of bulk charges to surface active sites and allows them to participate in various photocatalytic reactions.

In a recent report, a piezo-photocatalytic system was fabricated by braiding ZnO nanowires vertically onto carbon fibres. Under UV illumination, electron-hole pairs were generated from the ZnO nanowires and rapidly migrated to the opposite surfaces as a result of periodic pressure-induced polarization fields, efficiently degrading MB. By increasing the frequencies of the applied force, the MB decomposition was accelerated. The piezoelectric-assisted photocatalytic activity of ZnO nanowires was improved by silver doping. The photoexcitation and strain derived from mechanical bending largely increase the local conductance and effectively reduce the potential barrier height by producing a positive piezopotential, rendering enhanced charge carrier transfer. $ZnSnO_3$ is a piezoelectric material with a higher piezoelectric coefficient than ZnO. Vertically aligned $ZnSnO_3$ nanowires on FTO glass show higher UV photocatalytic activity for MB degradation under stress than without applied stress. The enhancement was ascribed to the reduced recombination of photoinduced electron-hole pairs and reinforced mobility of these charge carriers resulting from the energy band distortion caused by stress-induced piezoelectric polarization. The authors further surveyed the synergistic mechanism for piezo-photocatalysis by piezo-assisted photocatalytic degradation of MB over single-crystal $Zn_{1-x}SnO_3$ nanowires, and quantitatively verified the corresponding Schottky-barrier modulation under various applied stresses. Under ultrasonic vibration, the photodegradation rate of $Zn_{1-x}SnO_3$ is about four times higher than that of $Zn_{1-x}SnO_3$ nanowires in the absence of stress and is mainly attributed to the band bending and depolarizing field created by the alternating ultrasonic vibrations.[153,157,395]

Although oxide FE are chemically robust, they usually have a large band gap and a short charge carrier diffusion length, which limits their implementation in photoelectric applications. Therefore, significant attention has been given to narrowing the band gap of oxide perovskites without compromising their electronic and other unique functional properties to exploit the maximum amount of solar energy. There are several approaches, like defect engineering, heterojunction design, and metal oxide modifications to reduce the charge carrier recombination rate.[479]

The influence of heterovalent dopants at the Bi-site on the ferroelectric, optical and photocatalytic properties to our knowledge has not been studied extensively. In this section, we study the effect of mono-, di-, and trivalent doping on the photocatalytic activity of BFM NPs in relation to the doping induced variation of the optical properties, distortion of the crystal structure and nanoscale ferroelectricity. Where, mono- (Ag^+), di- (Ca^{2+}) and tri- (Dy^{3+})

valent cation doped: MDT; $BiFeO_3$: BFO, $BiFe_{0.95}Mn_{0.05}O_3$: BFM, $Bi_{0.99}Ag_{0.05}Fe_{0.95}Mn_{0.05}O_3$: Ag-BFM; $Bi_{0.95}Ca_{0.05}Fe_{0.95}Mn_{0.05}O_3$: Ca-BFM; $Bi_{0.95}Dy_{0.05}Fe_{0.95}Mn_{0.05}O_3$: Dy-BFM. We also abbreviate a few terms used during photocatalysis, absence of ultrasonication; non-US, and presence of ultrasonication; US.

7.3.1 Results and discussion

To study the role of MDT dopants on the photocatalytic (PC) performance of BFM NPs, we carried out experiments on the photodegradation of the organic dye rhodamine B (RhB). According to our previous work, lowering the pH value to 2.2 helps to improve the PC rate by reducing dispersion settling.[150] We also noticed similar results for MDT-doped BFM NPs, where at a pH of 2.2 the PC rate is higher than at pH = 4.4. Figure 7.17 shows the absorption spectra of the RhB dye in the process of photo-stimulated degradation in the presence of various NPs. Figure 7.19 shows the time required for the total degradation of RhB at pH 2.2 and the corresponding rate constant [Figure 7.17].

“The degradation of the dye in the presence of MDT-doped NPs occurs faster than in the case of BFM or BFO NPs. The order of the rates for total degradation is: Dy-BFM > Ca-BFM > Ag-BFM > BFM > BFO. Dy-BFM NPs are capable of degrading all dye within 60 minutes. It should be noted that the observed PC activity of the NPs follows a similar trend as the surface area of the NPs [previous chapter]. Therefore, it can be concluded that the degradation rate is strongly influenced by the surface area of NPs, since a large surface provides more reaction sites for photocatalysis. In addition, the total light absorption by Dy-BFM is also the highest among all NPs, which contributes to the creation of the largest number of photoinduced charge carriers. **„**[o]

We also studied photocatalysis assisted by ultrasonication (US) keeping the other conditions as before (pH 2.2, UV-visible light). The absorption spectra of RhB in the presence of US at pH 2.2 are shown in previous optical chapter. The total degradation trend and the rate constant are shown in Figure 7.19. We found that photodegradation of RhB under US conditions occurs faster than under non-US condition. Moreover, the order of the NPs in terms of the photocatalysis effectiveness changes and becomes: Ag-BFM > Dy-BFM > Ca-BFM > BFM ~ BFO. The increase of the PC performance under US conditions indicates that factors other than the surface area or light absorbance may play a role. It has been discussed in literature that such an enhancement of the photocatalytic activity can be related to the hydrostatic piezoelectric effect and the underlying ferroelectric properties of NPs.[156]

---

[o] This paragraph is based on (Dubey et al, Advanced Functional Materials 2022, https://doi.org/10.1002/adfm.202207105)

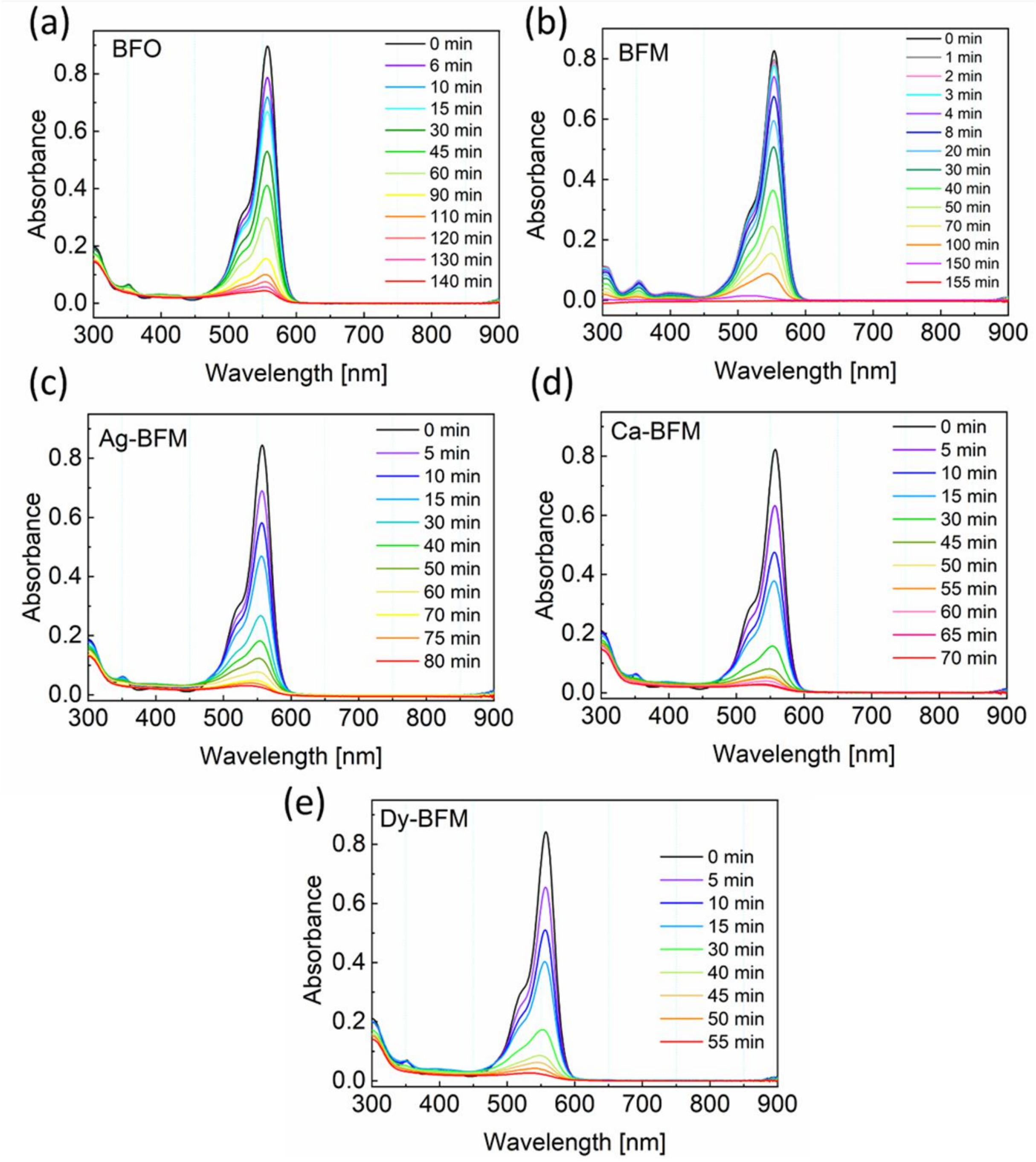

Figure 7.17: Photocatalysis at pH 2.2: absorption spectra of Rhodamine B degrading in presence of photocatalysts; BFO NPs (a), BFM NPs (b), Ag-BFM (d), Ca-BFM (e), and Dy-BFM (e). [© 2022 Advanced Functional Materials][46]

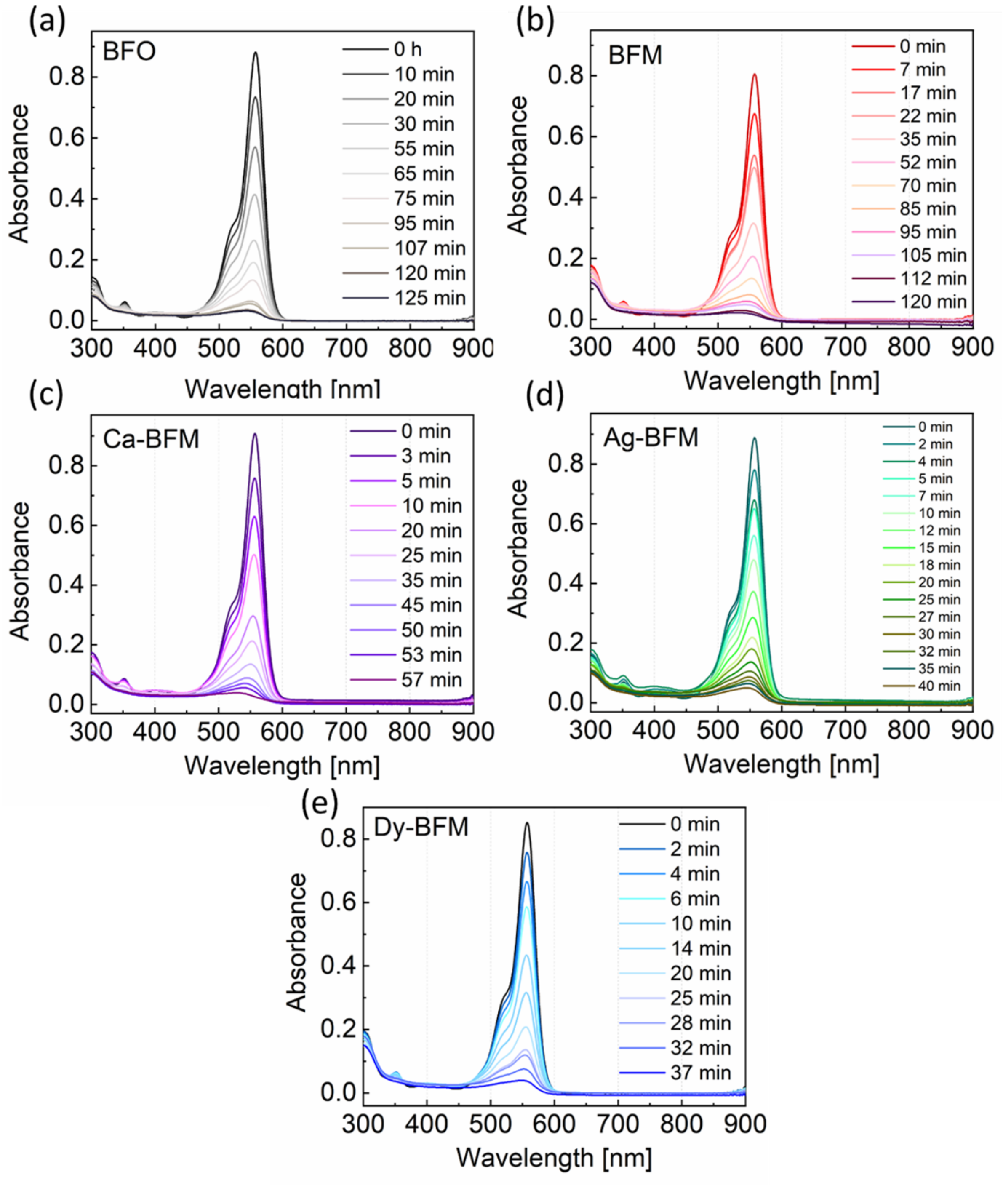

Figure 7.18: Photocatalysis at pH 2.2 and in the presence of ultrasonication (US). The absorption spectra represent the degradation of the Rhodamine B with time for MDT-doped BFO NPs (a-e). [© 2022 Advanced Functional Materials][46]

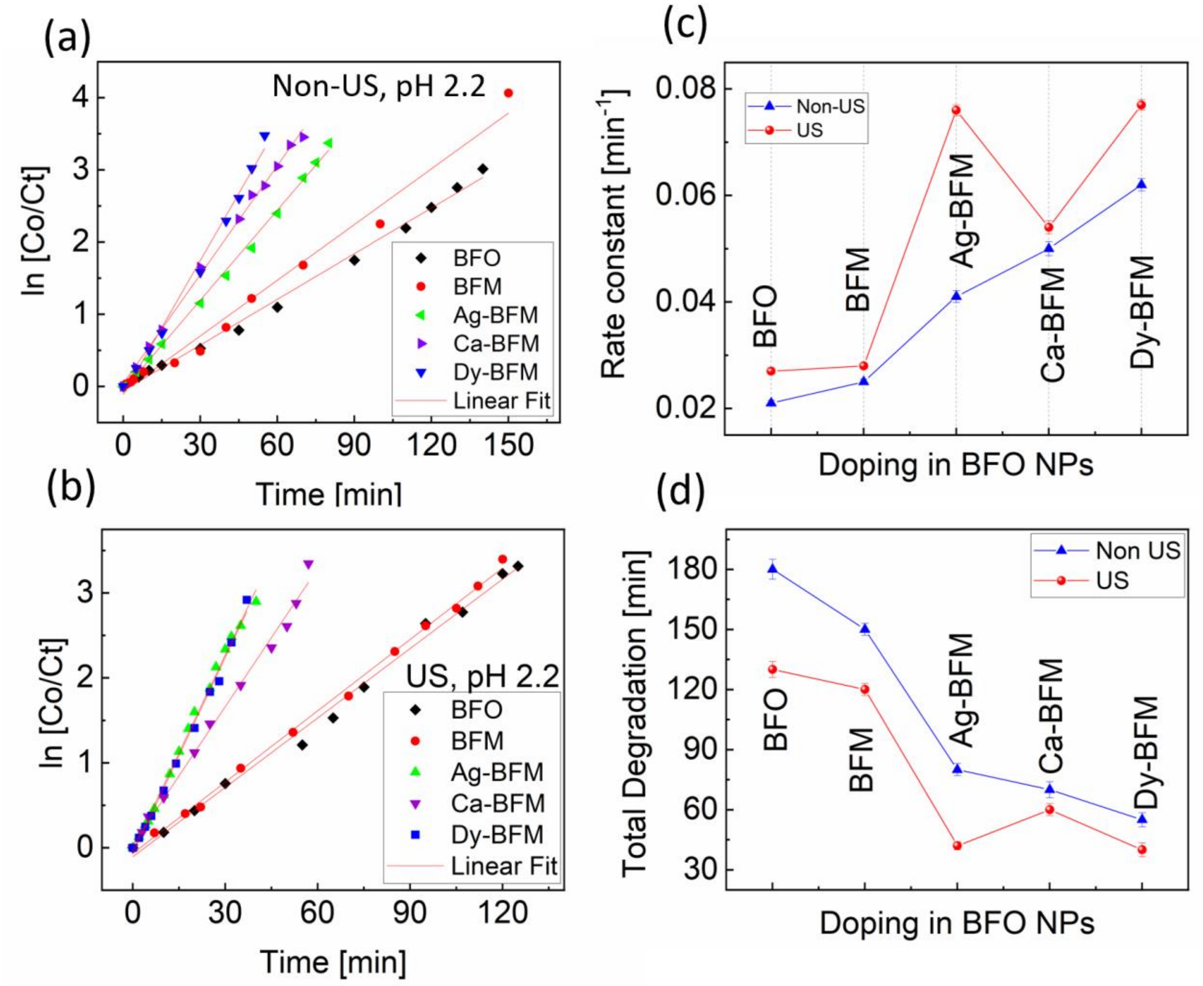

Figure 7.19: Reaction kinetics of photocatalysis in non-ultrasonication (non-US), and ultrasonication (US) conditions at pH 2.2.and (c-d) shows the rate constant and total degradation time trend under both conditions. [© 2022 Advanced Functional Materials][46]

Photocatalytic mechanism

During photocatalysis, charge carriers (electrons: e^- and holes: h^+) are generated upon light absorption by the NPs. Without recombination these charge carriers should migrate from the bulk to the particle's surface, where they produce active species: the oxygen radical, $O_2^{\cdot}$, and the hydroxide radical, $OH^{\cdot}$, from water. The generation of $O_2^{\cdot}$ and $OH^{\cdot}$ happens at certain energy balance conditions, as shown in Figure 9. To form these active species the conduction band (CB) and valence band (VB) of the photocatalyst must be levelled to transfer the charge carriers e^- and h^+ into the water and enable the water to split, photocatalytically. Therefore, we need to estimate the positions of the CB and the VB for the NPs. The positions of VB maxima can be obtained from Ultraviolet Photoelectron Spectroscopy (UPS) data [Optical Chapter]. Adding the band gap (E_g) width available from the DRS results [Optical Chapter] we can predict the positions of the CB minima as discussed in Optical Chapter. According to the energy levels diagram we can conclude that the BFO NPs are not able to produce $O_2^{\cdot}$ radicals since the electrons cannot be transferred. To produce the $OH^{\cdot}$ radicals the VB edge suits quite well. So, BFO NPs mainly produce $OH^{\cdot}$ radical to degrade RhB. From the estimated CB edge value of BFO, it should be able to produce hydrogen [H^+/H_2: 0 eV] via water splitting. For BFM

NPs, the positions of the CB and VB edges are similar to those in BFO. Therefore, it can be assumed that both types of NPs are sources of the formation of $OH^{\cdot}$ radicals. For Ag-BFM NPs, the CB edge is lower than energy level of $O_2/O_2^{\cdot}$ so they cannot produce $O_2^{\cdot}$. However, $OH^{\cdot}$ radicals can be produced easily. Hence $OH^{\cdot}$ radicals are responsible for photocatalysis on Ag-BFM NPs similar to BFO NPs. Whereas, in the case of Ca-BFM and Dy-BFM $O_2^{\cdot}$ radicals are easily produced as per positions of their CB and VB levels [Figure 7.24d]. The undoped BFO, BFM and monovalent doped BFM NPs produce $OH^{\cdot}$ radicals to degrade RhB dye, but di-, and tri- valent doped BFM NPs generate $O_2^{\cdot}$ radicals to accomplish the RhB degradation.

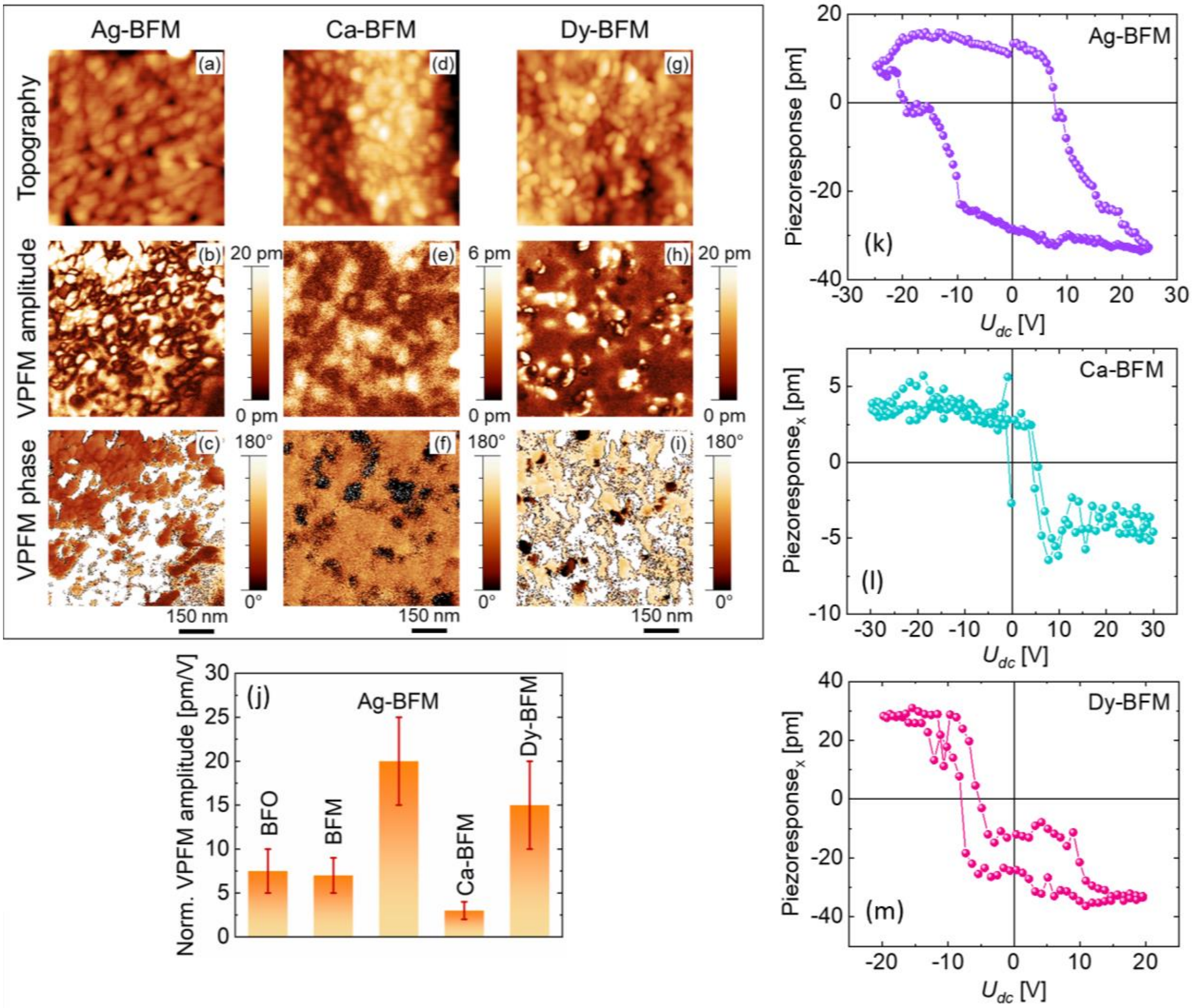

Figure 7.20A: Piezoresponse force microscopy (PFM) images for MDT-doped BFO NPs in black box (a-i). Topmost pictures represent topography. The middle ones show the normalized vertical PFM amplitude. The lowest row of images are vertical phase images. Comparison of VPFM amplitude (j). Piezoresponse hysteresis loops (k-m) for MDT -doped BFO NPs respectively. [© 2022 Advanced Functional Materials][46]

Several factors jointly play a role in determining the final photocatalytic activity of doped BFO NPs. The smaller size of the NPs leads to an advantageously large surface area and therefore, a large number of active sites per volume of photocatalyst becomes available to promote PC. In addition, different dopants like Ag, Ca and Dy and Mn can act as new active sites on the surface of BFO NPs, which may facilitate the redox reactions faster and effectively.

The ferroelectric nature of the NPs is linked to the photocatalytic activity.[154,163] The mechanism is not entirely clear yet, but it is assumed that the spontaneous polarization results in a depolarization electric field, which promotes the separation of photoinduced charge carriers.

Photocatalytic mechanism in an ultrasonication (US) environment

"Ultrasonic treatment has been widely used to drive chemical reactions.[480] Ultrasonication generates alternating low-pressure and high-pressure waves in liquids, leading to the formation of liquid void bubbles and their violent collapse in very short times (a few microseconds). This phenomenon is termed cavitation and causes high-speed impinging liquid jets and strong hydrodynamic shear-forces. The cavitation bubble can collapse near or at the surface of particles with lots of energy. This generates shock waves, which are usually used to remove contaminants from the surface of the particles. When the bubbles collapse, local pressure of the order of 135 MPa can be reached.[481,482] This effect is also used to deagglomerate nanometer-size materials. The pressure provided by the ultrasonicator nevertheless is not enough to distort the pristine crystal structure of BFO.[483] Ultrasonication (480 W, 40 kHz) can induce a piezoelectric effect in presence of light irradiation. When a ferroelectric material, like MDT doped-BFO NPs, experiences a hydrostatic stress, the induced displacement of ions causes an alteration in the polarization resulting in a release of the screening charges that can participate in catalysis [Figure 7.20].

The hydrostatic piezoelectric effect induces a change of the polarization $\Delta P = -p(2d_{31} + d_{33})$. Taking the piezoelectric coefficient for bulk BFO d_{31} = - 4.5 pC/N and d_{33} = 18 pC/N,[484,485] one can estimate that a pressure of 135 MPa acting on a NP upon ultrasonication decreases its polarization by $\Delta P = 0.12\ \mu C/cm^2$. This will lead to an excess of free charge carriers near to the surface of NPs. Before the hydrostatic stress is removed, and before this excess charge is compensated by external screening (H^+ and OH^- ions in solution), it can be used for a redox reaction to degrade the dye. The efficiency of such a mechanism of piezocatalysis depends on the balance between the rate of the redox reaction of charge carriers with adsorbed species, the external and internal screening rate, and the pressure release time."[p]

---

[p] This paragraph is based on (Dubey et al, Advanced Functional Materials 2022, https://doi.org/10.1002/adfm.202207105)

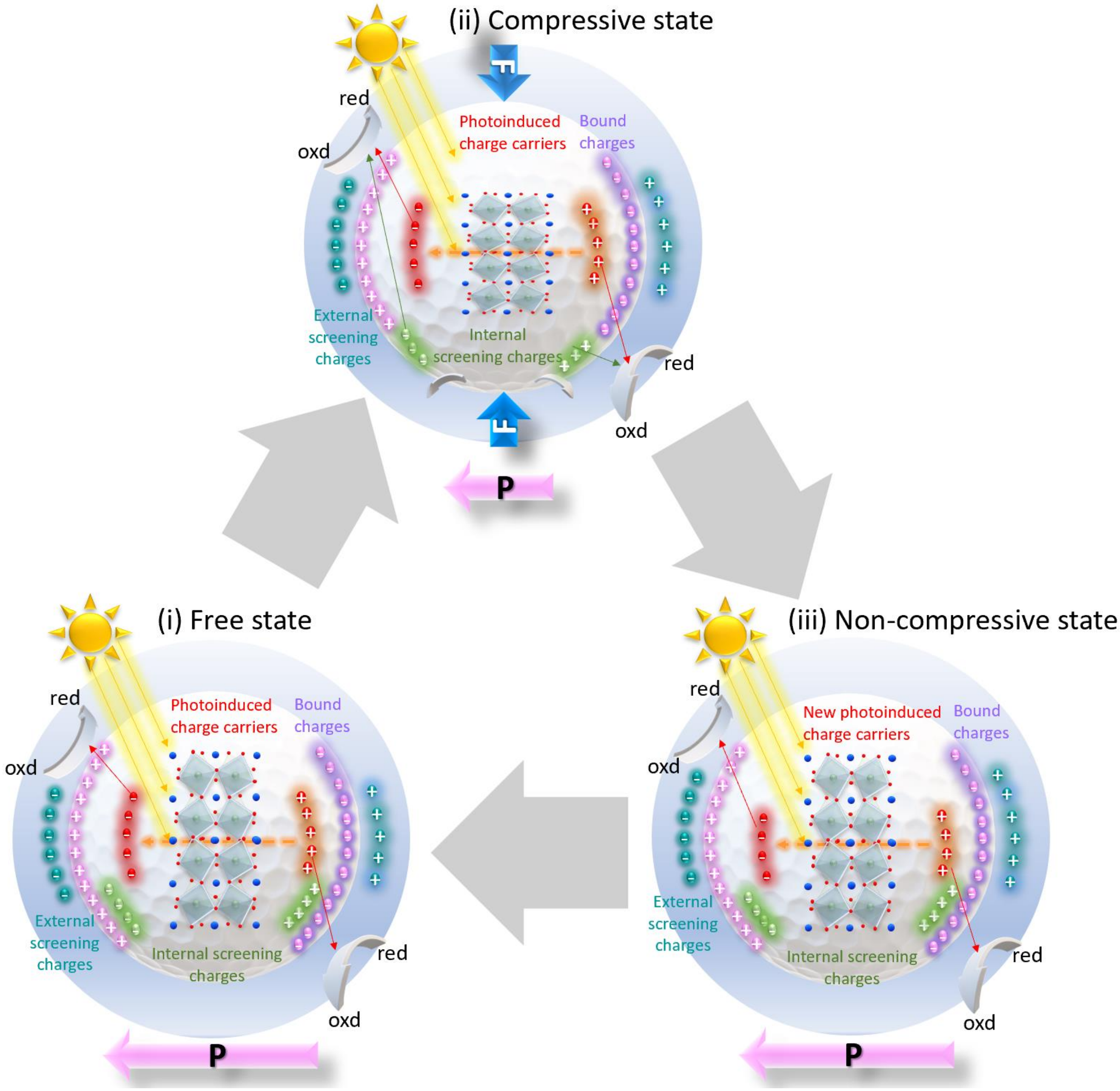

Figure 7.20: Schematic for the role of screening charges in piezo-photocatalysis depending upon the change of polarization (as per material's piezoelectric coefficients) by applied external stress. [© 2022 Advanced Functional Materials][46]

In our understanding, the enhancement of the PC effectiveness under US treatment can be caused by three major factors. *First*, ultrasonic treatment provides a more efficient interaction of dye molecules with the surface of nanoparticles due to intensive mixing. *Second*, it breaks NPs agglomerates and increases the active surface area. *Third*, ultrasonication induces the hydrostatic piezoelectric effect increasing the density of charges that can participate in the redox reactions.[155] Despite the fact that Ag-BFM NPs have a smaller surface area and exhibit lower light absorption and stronger recombination of photoinduced charge carriers, which is confirmed by the PL spectra, than Dy-BFM NPs, they show better PC performance under ultrasonic conditions. This can be explained by a stronger effect of the third factor. Indeed, the Ag-BFM NPs have a greater piezoresponse than the Dy-BFM ones, and, consequently, the hydrostatic piezo-effect will generate more surface charges for reactions with dye molecules. This led to a faster decrease in the concentration of the latter.

Conclusion

"We have compared the effect of the mono-, di- and tri-valent cation doping at the Bi-site on the photocatalytic efficiency and ferroelectric properties of Mn-doped BFO NPs. Monovalent doped Ag-BFM NPs and trivalent doped Dy-BFM NPs have increased polarization in comparison to both pristine and Mn-doped BFO NPs, due to favorable distortion of their crystal structure, confirmed from EXAFS data. On the contrary, divalent Ca doping weakens the ferroelectric properties in the same way as was shown for doping with Ba.

We studied the photocatalytic efficiency of MDT doped BFO NPs via mineralization of the RhB dye. We found that under normal conditions, Dy-BFM NPs exhibit the highest photocatalytic activity due to the largest surface area, the highest light absorption coefficient, the slowest recombination of photoinduced charge carriers, and a large polarization. Most of the nanoparticles are single domain ferroelectrics, where the spontaneous polarization creates an internal depolarization field. Though this field can be screened, but even a partially screened depolarization field can be a driving force for the photo-induced charge carrier separation in such single domain FE photocatalysts. The importance of the large polarization and related piezoresponse becomes obvious for ultrasound assisted photocatalytic degradation of the dye. In this case, a significant improvement of the photocatalytic activity is observed for the Ag-BFM NPs, which have the largest polarization among the measured compositions. Piezoresponse (polarization) becomes especially important factor under ultrasonic conditions for ferroelectric photocatalysts.

The spontaneous polarization and the piezoelectric effect substantially affect the photocatalytic properties of the nanoparticles. Therefore, development of narrow band gap ferroelectric NPs with a large hydrostatic piezoelectric coefficient is promising to achieve better photocatalytic efficiency.**"**[q]

---

[q] This paragraph is based on (Dubey et al, Advanced Functional Materials 2022, https://doi.org/10.1002/adfm.202207105)

7.4 Electrocatalytic response of doped BFO NPs

Hydrogen is a sustainable and environmentally friendly fuel, which potentially could replace the traditional fossil fuels. The electrocatalytic hydrogen evolution reaction (HER) is a method of energy conversion and storage, where the electricity generated from solar, and wind can be converted into chemical energy. The mechanism for the HER involves two steps first, the process starts with the Volmer reaction, followed by either Heyrovsky or Tafel reactions, as shown below, where M represents the catalyst. The hydrogen evolution reaction is the cathodic reaction in electrochemical water splitting. The HER is a classic example of a two-electron transfer reaction with one catalytic intermediate and offers the potential to produce H_2.

Table 7.1: Reaction steps for hydrogen evolution reaction in alkaline and acidic medium.

	Water reduction	**Hydronium ion reduction**	**Tafel slope**$(\alpha = 0.5)$
Volmer reaction	$H_2O + e^- \rightarrow 2OH^- + H_{ad}$	$H_3O^+ + e^- \rightarrow H_{ad} + H_2O$	120 mV/dec
Heyrovsky reaction	$H_{ad} + H_2O + e^- \rightarrow H_2$	$H_{ad} + H^+ + e^- \rightarrow H_2$	40 mV/dec
Tafel reaction	$H_{ad} + H_{ad} \rightarrow H_2$	$H_{ad} + H_{ad} \rightarrow H_2$	30 mV/dec

The random distribution of multiple active sites among NPs causes unexpected long reaction paths which would give rise to undesirable transport and reaction resistance. As per some literature, the strong adsorption of OH^- ions on catalysts in alkaline can retard the water dissociation process and deactivate the active site for further hydrogen combination. Hence an optimal adsorption of OH^- onto catalyst is needed for high-performance catalyst. So, the creation of such catalysts where there are short reaction paths for water dissociation, hydroxide desorption, and hydrogen adsorption simultaneously is highly desirable to boost the alkaline HER kinetics. It has been found in case of other transition metal oxides that pure materials are show low hydrogen-adsorption ability and low electrical conductivity. Design of an ideal catalysts with multiple active sites is a challenge. The active sites highly depend upon the nature of the surface of NPs, the morphology of NPs, and the electrolyte composition in catalytic performance.

Engineering the active site is one of the main necessities to enhance the catalytic performance of catalysts. Doping the electrocatalyst with different elements can create new active sites on the surface of catalysts, which can participate in electrochemical reaction and boost the HER activity. In addition, defect creation is another tool to provide feasible and efficient method to alter the number of active sites in catalysts. Anionic and cationic vacancies accelerate the catalytic activity via enhancing the electronic conductivity and optimizing the adsorption energy.

7.4.1 Results and Discussion

The details of experimental set up have been discussed in the "Materials and Technique" chapter. In brief, 4.5 µL of the NPs dispersion is drop-casted onto glassy carbon's (GC) surface for working electrode. The electrocatalyst loading always kept 0.2 mg/cm^2 for all samples. All electrochemical tests are carried out in 1 M KOH electrolyte (alkaline medium). Pt coil is the counter electrode of HER, and Ag/AgCl as the reference electrode. The measured potential was calibrated with reference to the reversible hydrogen electrode (RHE); E (vs. RHE) = E (vs. Ag/AgCl) + 0.059 pH + 0.197.

Cyclic voltagrams are collected for all doped BFM NPs and compared with pristine BFO NPs. These NPs were deposited onto glassy carbon (GC). For reference it was also measured in same conditions as other electrocatalysts. [Figure 7.21]

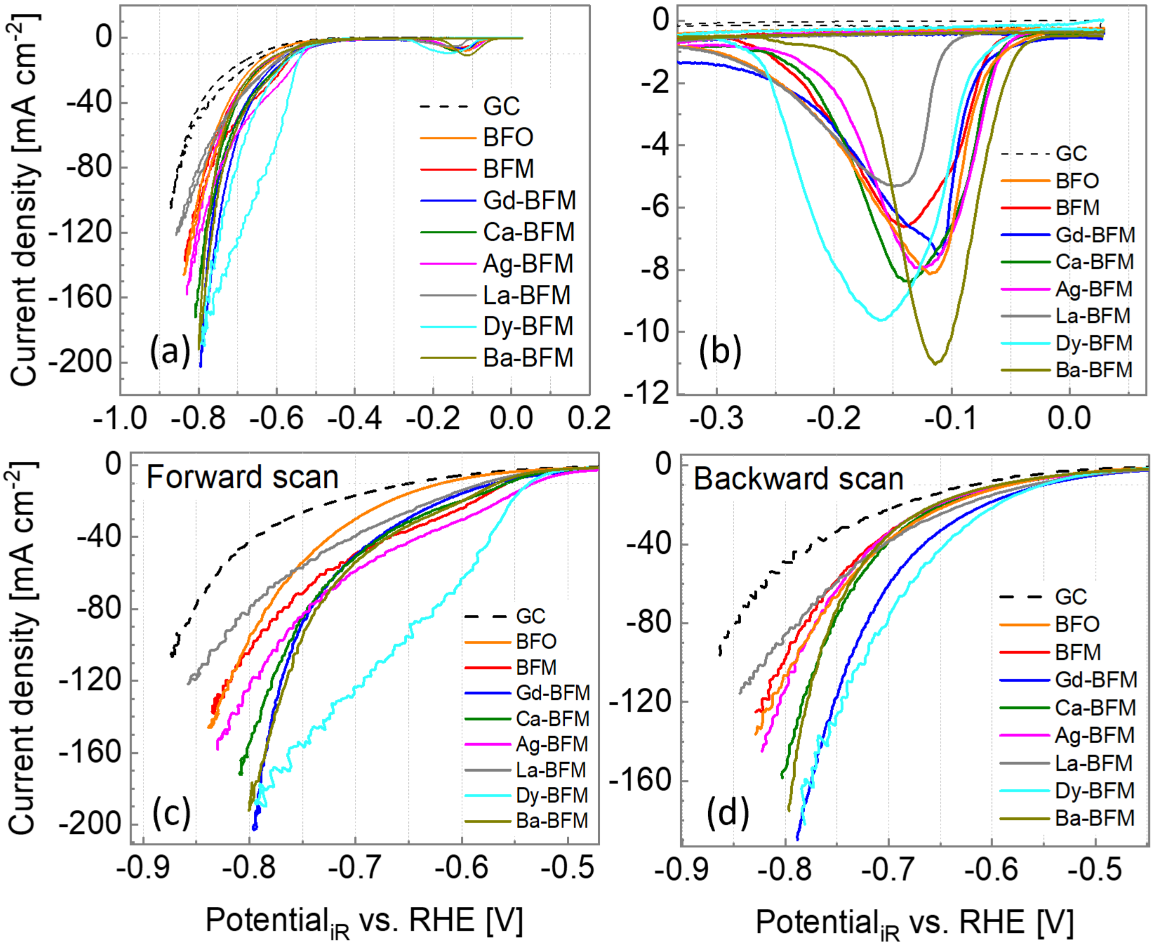

Figure 7.21: Cyclic voltammetry (CV) of BFO and doped BFO NPs along with reference glassy carbon at scan rate 5 mV s^{-1}(a), zoomed in of first downwards peak of CV plot (b). Forward scan and backward scans (c), and (d) respectively. [measured by Dr. Ignacio S. Moltó]

From Figure 7.21, we observe that all the NPs have lower overpotential than GC, which means they have catalytic response towards water splitting and especially towards HER. The overpotential value corresponding to the current density (*j*) of 10 mA/cm^2 is used to compare the activities among different catalysts. We have compared the overpotential values from the forward and backward scans of voltagrams shown in Figure 7.23. We can observe that Dy-BFM has the least overpotential value among all the electrocatalysts used here, and pristine BFO NPs has the least catalytic response. There is a trend of catalytic response based on the overpotential calculated from both scans.

- *Overpotential in forward scan*

Ag-BFM < Dy-BFM < Ca-BFM ~ BFM < Ba-BFM < Gd-BFM < La-BFM < BFO < GC

- *Overpotential in backward scan*

Dy-BFM < Gd-BFM < La-BFM < BFO < Ca-BFM < Ag-BFM ~ BFM < Ba-BFM < GC

Such trend of HER activity can be based on several factors: First defects and oxygen vacancies, second the charge carrier resistance for the deposited electrocatalyst in the solution, the available specific surface area of catalysts (which is different than and usually less than active surface area of electrocatalyst), and microstrain of the electrocatalyst.

We have doped monovalent, divalent, and trivalent cations into BFM NPs. This doping creates different number of oxygen amounts in the doped electrocatalysts, as can be seen from following K-M equations. Monovalent Ag doped BFM has the highest number oxygen vacancy due to charge imbalance, whereas the trivalent doping does not induce vacancies due to the overall charge neutrality in the system.

$$MnO_2 + Bi_2O_3 \rightarrow Mn_{Fe}^{\cdot} + e^{'} + Bi_{Bi}^{x} + 5O_{O}^{x} \tag{7.1}$$

$$Ag_2O + Fe_2O_3 \rightarrow 2Ag_{Bi}^{''} + \mathbf{2V_{O}^{\cdot\cdot}} + 2Fe_{Fe}^{x} + 4O_{O}^{x} \tag{7.2}$$

$$2BaO + Fe_2O_3 \rightarrow 2Ba_{Bi}^{'} + \boldsymbol{V_{O}^{\cdot\cdot}} + 2Fe_{Fe}^{x} + 5O_{O}^{x} \tag{7.3}$$

$$Dy_2O_3 + Fe_2O_3 \rightarrow 2Dy_{Bi}^{x} + 2Fe_{Fe}^{x} + 6O_{O}^{x} \tag{7.4}$$

The defects on the surface of the electrocatalysts can be friend or foe, it depends upon their suitable activity towards the species to be adsorbed or desorb as shown in Figure 7.24 b. From the O1s XPS spectra for these electrocatalysts, [Figure 7.22] we find that for the case of Dy, there is a high intensity peak attribute to adsorbed oxygen on the surface of material, which is not the case for La-BFM or Gd-BFM NPs. The presence of adsorbed oxygen on the surface of materials corresponds to its surface activity, large oxygen vacancies. The surface activity can also be due to the presence of particular ion (Dy^{3+}) on the surface, which can be new active site.

This shows that the presence of these dopants on the surface of the catalyst can play the role as active sites, from Figure 7.22, one can say that Ba, Gd and mostly Dy dopants are acting as active sites due to their presence on the surface leading to more activity as compared to Ag, Ca, and La case.

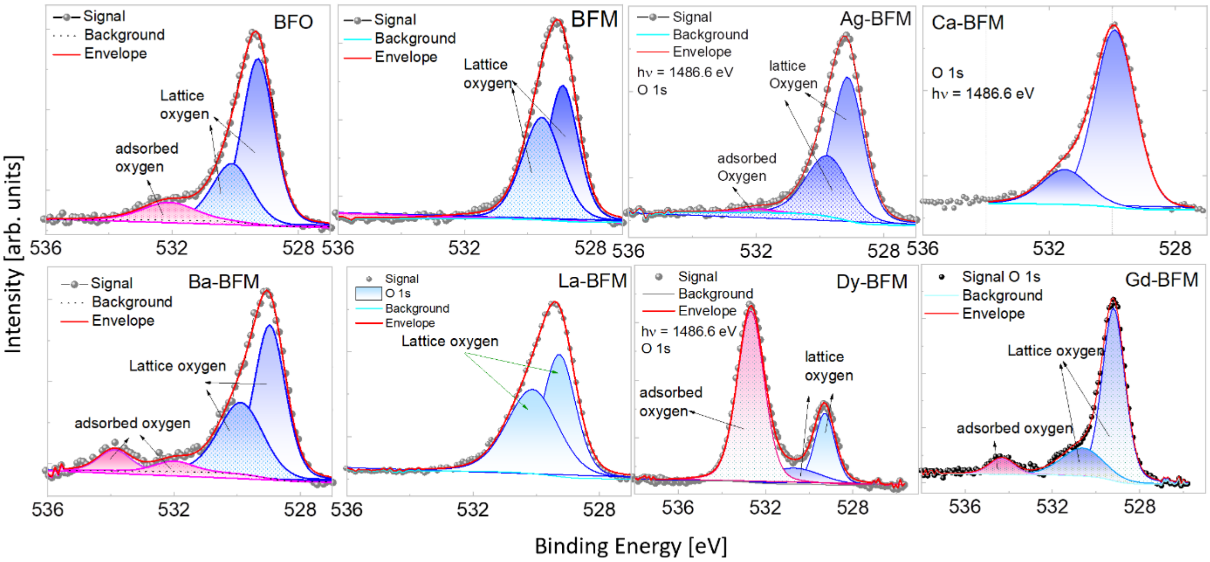

1. *Lattice oxygen: Bi-O-Fe and Fe-O-Fe*
2. *Surface adsorbed oxygen: O in the vicinity of the oxygen vacancy*

Figure 7.22 The O 1s XPS spectra of doped BFO NPs, blue region represents lattice oxygen and pink region shows surface adsorbed oxygen.

Charge transfer resistance (CTR) are measured using electrochemical impedance spectroscopy (EIS) in which an AC voltage is applied to the electrode and the resulting current is measured. From the resulting impedance spectrum, the CTR is determined. The results are shown in Figure 7.23 where the Nyquist and Bode plots are shown to understand the electrical equivalent circuit and to calculate the CTR shown in Figure 7.24b.

The CTR represents the resistance of the electron transfer at the electrode-electrolyte interface during the HER process. In HER, protons from the electrolyte are reduced to hydrogen on the electrode surface. The reduction reaction involves the transfer of electrons from the electrode to the protons, which is a charge transfer process. The resistance of this charge transfer process is represented by CTR. A high CTR can limit the rate of HER by slowing down the electron transfer process, while a low CTR can promote HER by facilitating the electron transfer process.

We find that Dy-BFM has the least CTR after Gd-BFM one among other electrocatalyst. The highest CTR is for BFO NPs, and then Ag-BFM NPs, which can be due to many vacancies and trap states in this system.

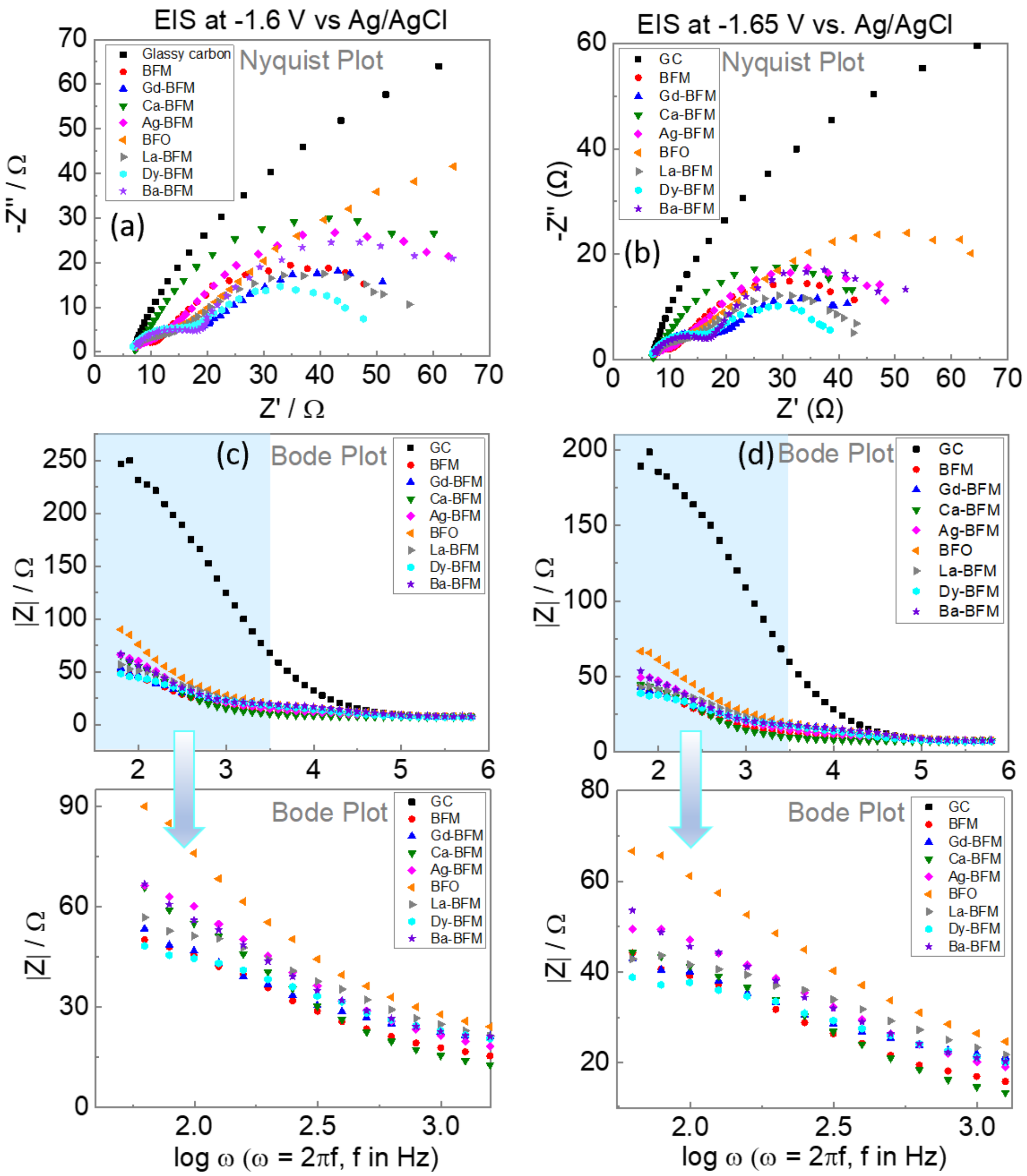

Figure 7.23: Nyquist plots for all doped and undoped NPs (a-b) at different potential. The Bode plots for all electrocatalysts at different potentials (c-d). [measured by Dr. Ignacio S. Moltó]

One other factor is the microstrain of the NPs which has linear relation with the crystallite size of NPs as shown in Figure 7.24 f-g. The microstrain of NPs can significantly affect their electrocatalytic activity, especially for electrochemical reactions that involve lattice strain or surface restructuring. The surface strain due to the lattice mismatch between the crystal planes can create defects on the surface that can improve or reduce the electrocatalytic activity. In most of cases, it is found that microstrain can enhance the HER activity of NPs, by improving the surface reactivity and increasing the number of active sites via surface defects.[167,171,173,486]

We observe that Ag-BFM has the highest microstrain among the doped BFM NPs (see chapter 4), and afterwards Dy-BFM has the microstrain value, so this case explains the less activity in Ag-BFM than Dy -BFM due to higher microstrain which leads to reduction in electronic conductivity.

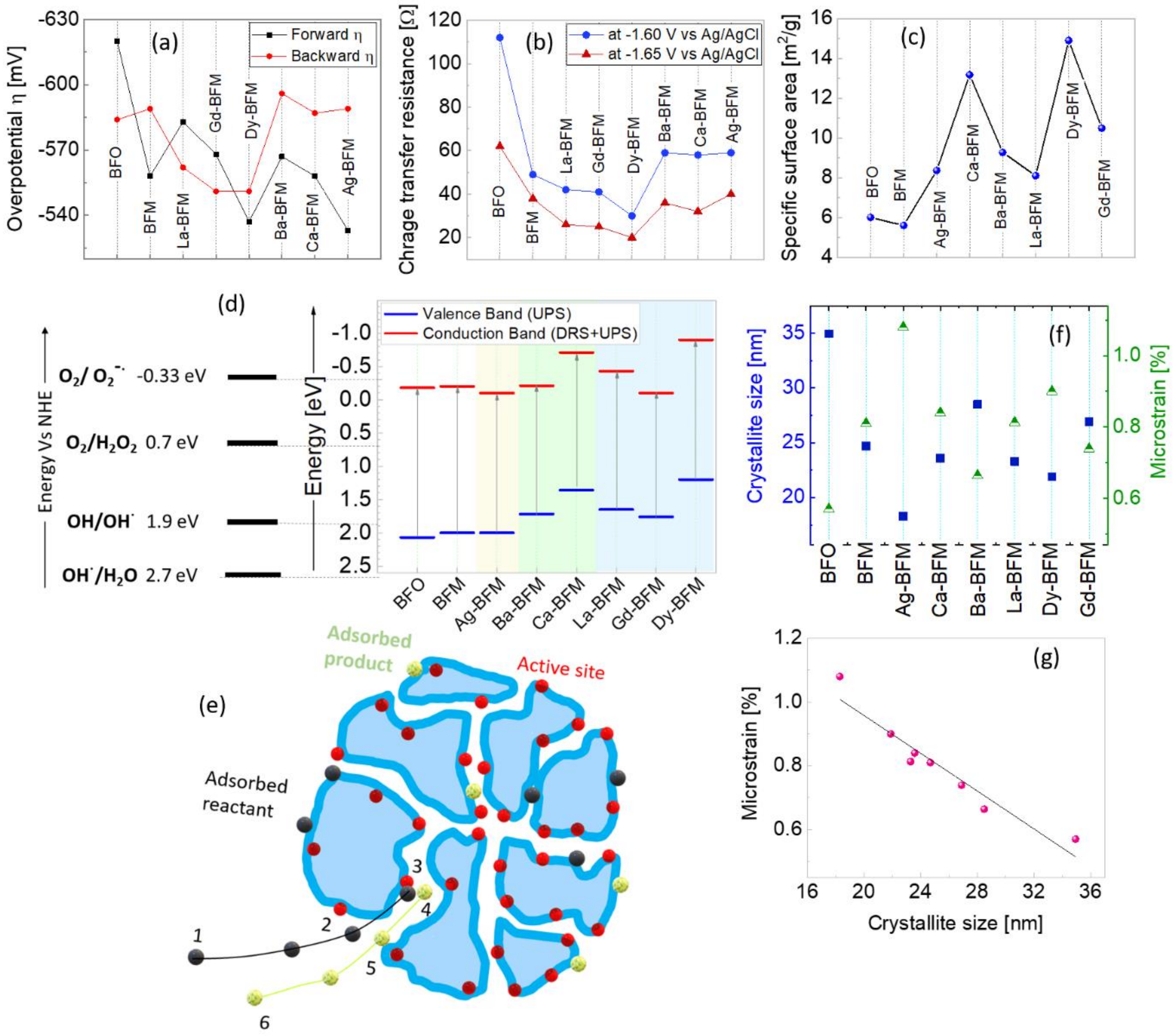

Figure 7.24: The trend of overpotential for forward and backward scan (a), The chare transfer resistance trend (b). The specific surface area trend (c), The Band edge estimation chart based on absorption and UPS data (d). The schematic of active sites on the surface of electrocatalyst (e), and the crystallite size and microstrain trend (f-g) for doped BFM NPs and undoped BFO NPs.

Conclusions

In this study, we investigated the HER activity of doped BFM NPs and compared them with pristine BFO NPs. Our results indicate that Dy-BFM exhibits the best HER activity, as evidenced by its low overpotential value. We explain the observed trend of overpotential by considering the oxygen vacancies in the system due to aliovalent doping and the surface reactivity of the dopant, which we confirmed using XPS studies. The available surface area also plays a significant role in determining the overpotential trend in these catalysts.

Furthermore, we found that the charge transfer resistance trend also contributes to lowering the overpotential of the catalyst by changing the electron transfer rate at the electrode-electrolyte interface during HER.

Many factors can affect the active sites of these electrocatalysts, and establishing a relationship among them is complex since everything is interconnected. However, we can summarize the key factors that influence the HER activity of these catalysts as follows: having a large surface area is advantageous, having low charge transfer resistance, having active ions on the surface of the catalyst, such as Dy in this case, and having an intrinsic microstrain of the catalyst that can tune the surface activity differently.

7.5 Conclusions

In this chapter, we explored the catalysis world quite broadly from photocatalysis to piezophotocatalysis to electrocatalysis using the ferroelectric NPs.

Starting with **photocatalysis**, we observe that the amount of dopants plays a crucial role in determining the overall photocatalytic performance of the catalyst. The photocatalytic (PC) efficiency of the visible light absorber Ba doped BFM NPs as compared to BFO NPs is reported for the degradation of the organic pollutant's rhodamine B (RhB) and methyl orange (MO). 1 mol% Ba-doped-BFM NPs degrade both dyes within 60 and 25 minutes under UV-visible light illumination, respectively. The Ba and Mn co-doping up to 5 mol% in BFO NPs increases the specific surface area, the energy of the d–d transitions, and PC efficiency of the BFO NPs. The maximum PC efficiency found in 1 mol% Ba doped BFM NPs is attributed to a cooperative effect of factors like its increased light absorption ability, large surface area, active surface, reduced recombination of charge carriers, and spontaneous polarization to induce charge carrier separation. The 1 mol% Ba and 5 mol% Mn co-incorporation is found to be the optimum dopant concentration for photocatalytic applications.

To mitigate the negative impact of the plasticizer (phthalate: DBP), we could successfully photodegrade DBP under UV light irradiation within a mere 2.5 hours. We employed the GC-MS technique for an in-depth analysis. It was found that both undoped and doped BFO functionalized with GO had higher photodegradation efficiency than pristine BFO NPs. Furthermore, the photodegradation process of DBP generated various by-products, such as phthalic acid, benzoic acid, benzaldehyde, and 3-methyl butyric acid, as intermediates before achieving complete mineralization into carbon dioxide and water. This process is achieved through the cleavage of both aliphatic and aromatic branches of DBP. The successful degradation of DBP through photodegradation using ferrocatalysts functionalized with GO represents a significant scientific breakthrough.

The **piezophotocatalysis** activity of ferroelectric photocatalysts doped-BFM NPs are studied under ultrasonication and in acidic conditions. It is found that doping enhances the photocatalytic activity of the ferroelectric NPs approximately three times. The correlation of the photocatalytic activity with structural, optical, and electrical properties of the doped NPs is established. The increase of spontaneous polarization by the mono- and tri-valent doping is one of the major factors in enhancing the photocatalytic performance along with other factors such as stronger light absorption in the visible range, low recombination rate of charge carriers, and larger surface area of NPs. A-site doping of BFO NPs by divalent elements suppresses the spontaneous polarization, whereas trivalent (Dy3+) and monovalent (Ag+) cations provide an increase of polarization. The depolarization field in these single domain NPs acts as a driving force to mitigate recombination of the photoinduced charge carriers.

The **electrocatalysis** using doped BFM NPs towards HER is investigated as preliminary tests. We found that Dy-BFM exhibits the best HER activity, as it requires lowest overpotential value among all NPs. The key factors that influence the HER activity of these catalysts as follows: having a large surface area is advantageous, having low charge transfer resistance, having active ions on the surface of the catalyst, and the microstrain of the catalyst.

The conduction and valence band edge levels of these electrocatalysts are shown in Figure 7.24 d, suggests that their HER activity performance can further increase under photoexcitation, i.e., via photoelectrocatalysis.

8. Outlook and Emerging Frontiers

BFO NPs exhibit multifunctional properties and have been extensively studied, particularly in relation to doping engineering and structure-properties correlations. BFO NPs are highly investigated as single-phase multiferroic materials due to their room-temperature ferroic orderings. These NPs have potential applications in sensors, spintronics, catalysis, photovoltaics, and cancer treatments.

We optimised three synthesis routes for phase pure BFO NPs: hydrothermal, modified sol-gel Pechini method, and pulsed laser ablation in liquid method. The hydrothermal method yielded more irregular shaped BFO NPs, while the modified Pechini method provided cuboidal morphology and the PLAL method gave a spherical shape of BFO NPs. In terms of being less time consuming, easy, eco-friendly, and reproducible, the modified Pechini method is the best for synthesizing various doped BFO NPs, as one can easily control the parameters and optimize the reaction to synthesize high-quality NPs.

We extensively investigated the structural changes in BFO NPs through doping with various elements. The doping experiments encompassed single doping at Bi- and Fe-sites, as well as co-doping with elements from different groups in the periodic table such as alkaline earth metals, transition metals, and rare-earth lanthanide metals. One of the findings of this research is the alteration of the tolerance factor of BFO NPs due to the mismatched ionic radii of the dopants, which significantly impacts the local and long-range ordering within the doped BFO NPs. Within the particle, a homogeneous distribution is found for both doping and host elements. Surface analysis revealed the presence of Bi^{3+} and Fe^{3+} ions using 4*f* XPS spectra of Bi and 2*p* XPS spectra of Fe. Core level oxidation states were confirmed using EXAFS which also confirmed the presence of Bi^{3+} and Fe^{3+}. Interestingly, trivalent cation doped BFM NPs predominantly consisted of Mn^{4+} ions even on the surface. EXANES analysis confirmed the presence of Mn^{4+} ions within the bulk of the BFM NPs. The minor presence of Jahn-Teller cations (specifically Mn^{3+}) was observed on the surface of NPs, confirmed by XPS and Raman. These results indicate a distinct chemical environment on the NP surface compared to the bulk.

Oxygen vacancy estimation was conducted using XPS spectra of O 1s. Divalent Ba doping increases the concentration of oxygen vacancies, while Ca doping does not have a significant effect. Trivalent Gd doping and Dy-BFM NPs exhibit the formation of oxygen vacancies, with the latter showing a large peak associated with surface absorbed oxygen, which can also be attributed to oxygen vacancies.

The crystal structure of the doped NPs was studied using XRD and EXAFS. All NPs exhibited a single phase with a rhombohedral crystal structure. Rietveld refinement analysis demonstrated that lattice parameters and unit cell volume were significantly affected by larger-sized Ba doping at the Bi-site, in contrast to Co and Mn doping at the Fe-site. The crystallite size of doped BFM NPs was generally smaller compared to pure BFM. Moreover, an inverse relationship was observed between crystallite size and microstrain in doped BFM NPs.

The Fe-O-Fe bond angle was reduced from 133° to 131° due to Gd doping in BFM NPs, potentially enhancing the magnetic properties of the doped NPs. The calculation of local Bi-O bond distances using EXAFS spectra revealed that the BiO_{12} cuboctahedron plays a crucial role in the ferroelectric properties of BFO NPs. The shorter and longer bonds of Bi-O in the BiO_{12} cuboctahedron were significantly and differentially affected by each dopant.

There is a diverse range of morphologies and sizes, ranging from spherical to pentagonal to elliptical shapes for doped BFO NPs. These distinct morphologies and average sizes influenced the specific surface area and pore size distribution, potentially contributing to the catalytic activity of doped BFM NPs. Additionally, the different morphologies of doped BFM NPs resulted in varied magnetic anisotropy, which adds further interest to exploring the magnetic properties of these NPs.

The magnetism of doped BFO NPs is influenced by a combination of factors. It is evident that there is no singular factor solely responsible for the overall increase in magnetization of BFO NPs, but rather a number of significant factors are at play. Firstly, the presence of uncompensated spins at the surface of NPs contributes to the total magnetic moment, with a larger surface area leading to a greater contribution of surface spins. In the case of single doped BFO NPs, the surface area of BFC NPs is the largest, resulting in the largest number of uncompensated spins. Similarly, non-magnetic ion doped BFM NPs exhibit larger surface areas, with Ca-BFM NPs having the highest surface area and consequently a larger maximum magnetization, followed by La-BFM NPs. Among RE-doped BFM NPs, Dy-BFM NPs have the largest surface area, followed by Gd-BFM NPs. Secondly, alterations in the incommensurate spin cycloid of BFO NPs can impact their magnetism. Disruption of the cycloid can occur due to smaller particle sizes or the presence of dopants at the Fe-site with different spin canting angles, leading to a larger net effective magnetic moment. Additionally, changes in the local Fe-O-Fe bond angle within the crystal lattice can suppress the spin cycloid, potentially resulting in an increase in the net effective magnetic moment of doped BFO NPs.

Furthermore, the incorporation of Mn and Co at the Fe-site can cause a crossover from antiferromagnetic (AFM) to ferromagnetic (FM) superexchange interaction, contributing to the increased magnetization of BFO NPs. XPS results support such crossover for Mn-doped BFO NPs. Magnetic anisotropies, particularly surface anisotropies, may add into the magnetic behaviour of NPs. The magnetization enhancement observed in doped BFO NPs with different morphologies can be attributed, at least partially, to the influence of shape and strain anisotropies, as well as noncollinear magnetic ordering, leading to alterations in local spin canting between magnetic moments.

In conclusion, the magnetism of doped BFO NPs is a complex interplay of factors including surface spins, incommensurate spin cycloid alterations, AFM-to-FM crossover, and magnetic anisotropies. During hyperthermia testing, only 1 mg/ml dispersion of RE doped BFM NPs into water and agar can increase the temperature of dispersion under applied AC magnetic field of 60–80 mT. We observed that Dy-BFM dispersion in water, can heat up to ~39° C at 80 mT, which is close to the hyperthermia window of 40–45° C required for hyperthermia tests as per the standards. These results indicate that an increased concentration of NPs can make them suitable for hyperthermia tests and other biomedical applications.

The investigations into the optical properties of doped BFO NPs have shed light on the significant impact of Fe-site doping on the band gap, the influence of different dopants at the Bi-site, and the unique characteristics of rare earth-doped NPs. Our findings indicate that single doping at the Fe-site has a more pronounced effect on the band gap of BFO NPs compared to doping at the Bi-site. This effect is primarily attributed to the indirect influence on the electronic structure energy levels, with the FeO_6 octahedra playing a significant role. By exploring different dopants at the Bi-site in BFM NPs, we discovered that an optimal dopant concentration, such as 1 mol% Ba, can greatly impact the light absorption properties of BFM NPs. This influence is achieved through the creation of oxygen vacancies or defect states within the band gap. The role of ions with different valencies at the Bi-site in both BFM and BFC NPs has been extensively discussed. It was observed that doping with MDT ions reduces the band gap, although the differences among them are relatively minor, except for slight deviations at lower energies, indicating the presence of defect states in the band gap.

In the case of rare earth (lanthanides) doped BFM NPs, Gd-BFM exhibited the smallest band gap. Analysis of the band energy level diagram revealed that Dy-BFM NPs possess the most suitable band edges for the water splitting under light irradiation, with a conduction band located at the highest energy level among the NPs. Additionally, Dy-BFM NPs exhibited a higher number of available charge carriers in the excited states compared to BFM NPs. Furthermore, the shorter decay lifetimes observed in Dy-BFM NPs can be attributed to the presence of trap-states, which introduce additional pathways for non-radiative recombination of charge carriers.

The comprehensive study on the photocatalytic, piezophotocatalytic, and electrocatalytic activities of doped BFO NPs has provided valuable insights into their performance and potential applications. The incorporation of 1 mol% Ba in BFM NPs resulted in the highest photocatalytic performance, attributed to factors such as increased light absorption ability, large surface area, reduced charge carrier recombination, and spontaneous polarization facilitating charge carrier separation. Additionally, the co-incorporation of 1 mol% Ba and 5 mol% Mn in BFO NPs proved to be the optimal dopant concentration for photocatalytic applications for dye photodegradation.

Furthermore, the successful photodegradation of the plasticizer DBP using ferrocatalysts supported onto GO is achieved. The process was accompanied by the generation of various intermediate by-products before achieving complete mineralization into carbon dioxide and water. This process involved the cleavage of both aliphatic and aromatic branches of DBP, demonstrating the potential of doped BFO functionalized with GO for mitigating the negative impact of phthalates.

The piezophotocatalytic activity of ferroelectric doped-BFM NPs was investigated under ultrasonication and acidic conditions. Doping significantly enhanced the photocatalytic activity, primarily through increased spontaneous polarization, stronger light absorption in the visible range, reduced charge carrier recombination, and larger surface area of the NPs. Divalent, trivalent, and monovalent dopants exhibited different effects on the spontaneous polarization, with depolarization field acting as a driving force to mitigate charge carrier recombination.

Additionally, the preliminary tests on the electrocatalytic activity of doped BFM NPs towards HER revealed that Dy-BFM exhibited the most promising HER activity, requiring the lowest overpotential value. Factors such as a large surface area, low charge transfer resistance, presence of active ions on the catalyst surface, and microstrain influenced the HER activity of these catalysts.

Overall, these findings provide valuable insights into the design and optimization of doped BFM NPs for enhanced photocatalytic, photodegradation, piezophotocatalytic, and electrocatalytic applications, highlighting the importance of dopant concentration and its impact on various catalytic properties.

In future the multiferroic properties and catalytic activities of PLAL synthesized BFO NPs, and for the doped ones should be explored, as this method produces narrow size distributed small NPs of size ~10-20 nm. One of the potential utilizations for BFO NPs can be in magnetic biomedicine. These NPs can be functionalized with biological molecules and used as magnetic contrast agents for imaging in magnetic resonance imaging (MRI). In addition, doped BFO NPs can further be researched for magnetic hyperthermia. For doped BFO NPs the magnetoelectric coefficient can be measured and studied which can be useful in applications like magneto-electronics, where the magnetic and electronic properties of the material can be used for information processing and data storage. Controlling the photocatalytic activity of doped BFO NPs through external magnetic fields is a promising approach for improving the efficiency of magneto-photocatalysis.

Doped BFM NPs demonstrate tunable optical properties and enhanced catalytic performance in photocatalysis, piezophotocatalysis, and electrocatalysis for HER. These findings highlight their potential for applications in environmental remediation, energy conversion, and catalytic processes, emphasizing the significance of exploring and understanding the properties of doped BFO NPs for future scientific advancements.

Future research can build upon these findings to explore the multifaceted properties of doped BFM NPs and their practical utilization in various technological advancements.

References

(1) Pàmies, P.; Stoddart, A. Materials for Drug Delivery. *Nat. Mater.* **2013**, *12* (11), 957. https://doi.org/10.1038/nmat3798.

(2) Li, W.; Peng, A.; Wu, H.; Quan, Y.; Li, Y.; Lu, L.; Cui, M. Anti-Cancer Nanomedicines: A Revolution of Tumor Immunotherapy. *Front. Immunol.* **2020**, *11* (December), 1–13. https://doi.org/10.3389/fimmu.2020.601497.

(3) Baum, Z. J.; Diaz, L. L.; Konovalova, T.; Zhou, Q. A. Materials Research Directions Toward a Green Hydrogen Economy: A Review. *ACS Omega* **2022**, *7* (37), 32908–32935. https://doi.org/10.1021/acsomega.2c03996.

(4) Terna, A. D.; Elemike, E. E.; Mbonu, J. I.; Osafile, O. E.; Ezeani, R. O. The Future of Semiconductors Nanoparticles: Synthesis, Properties and Applications. *Mater. Sci. Eng. B Solid-State Mater. Adv. Technol.* **2021**, *272* (June), 115363. https://doi.org/10.1016/j.mseb.2021.115363.

(5) Derfus, A. M.; Chan, W. C. W.; Bhatia, S. N. Probing the Cytotoxicity of Semiconductor Quantum Dots. **2004**.

(6) Kovalenko, M. V. Opportunities and Challenges for Quantum Dot Photovoltaics. *Nat. Nanotechnol.* **2015**, *10* (12), 994–997. https://doi.org/10.1038/nnano.2015.284.

(7) Xiao, D.; Qi, H.; Teng, Y.; Pierre, D.; Kutoka, P. T.; Liu, D. Advances and Challenges of Fluorescent Nanomaterials for Synthesis and Biomedical Applications. *Nanoscale Res. Lett.* **2021**. https://doi.org/10.1186/s11671-021-03613-z.

(8) Yakout, S. M. Spintronics and Innovative Memory Devices : A Review on Advances in Magnetoelectric BiFeO 3. **2021**, 317–338.

(9) Kossar, S.; Amiruddin, R.; Rasool, A.; Giridharan, N. V; Dhayanithi, D.; Kumar, M. C. S. Ferroelectric Polarization Induced Memristive Behavior in Bismuth Ferrite (BiFeO3) Based Memory Devices. *Superlattices Microstruct.* **2020**, 106726. https://doi.org/10.1016/j.spmi.2020.106726.

(10) Dubey, A.; Escobar Castillo, M.; Landers, J.; Salamon, S.; Wende, H.; Hagemann, U.; Gemeiner, P.; Dkhil, B.; Shvartsman, V. V.; Lupascu, D. C. Effect of Mn and Ba Codoping on a Magnetic Spin Cycloid of Multiferroic Bismuth Ferrite Nanoparticles. *J. Phys. Chem. C* **2020**, *124* (40), 22266–22277. https://doi.org/10.1021/acs.jpcc.0c05778.

(11) Filipev, V. S.; Smolyaninov, N. P.; Fesenko, E. G.; Belyaev, I. N. Formation of BiFeO3 and Determination of Unit Cell. *Kristallografiya* **1960**, *5*, 958–960.

(12) Smolenskii, G. A.; Isupov, V. A.; Krainik, N. N. The Coexistence of the Ferroelectric and Ferromagnetic States. *Izv Akad Nauk SSSR, Seriya Fiz.* **1961**, *25*, 1333–1339.

(13) Kiselev, S. V; Ozerov, R. P.; Zhdanov, G. S. Detection of Magnetic Order in Ferroelectric BiFeO3 by Neutron Diffraction. *Sov Phys Dokl.* **1963**, *7*, 742.

(14) Tickner, J.; Geiser, K.; Baima, S.; Tickner, J.; Geiser, K.; Baima, S. Transitioning the Chemical Industry : The Case for Addressing the Climate , Toxics , and Plastics Crises. *Environ. Sci. Policy Sustain. Dev.* **2021**, *63* (6), 4–15. https://doi.org/10.1080/00139157.2021.1979857.

(15) Schmid, H. Multi-Ferroic Magnetoelectrics. *Ferroelectrics* **1994**, *162*, 317.

(16) Spaldin, N. A.; Fiebig, M. The Renaissance of Magnetoelectric Multiferroics. *Science (80-.).* **2005**, *309* (July), 391–393.

(17) Smolenskii, G. A.; Ioffe, V. A. Communications de Colloque International de Magnetism de Grenoble (France). *2-6 Jullet. Commun. No. 1.* **1958**.

(18) Bokov, V. A.; Mylnikova, I. E.; Smolenskii, G. Ferroelectric-Antiferromagnetic Crystals. *Zhurnal Eksp I Teor Fiz* **1962**, *42*, 643–646.

(19) Lottermoser, T.; Meier, D. A Short History of Multiferroics; De Gruyter, **2020**; Vol. 6, pp 1–15.

(20) P Coeuré; Guinet, F.; Peuzin, J. C.; Buisson, G.; Bertaut, E. F. Ferroelectric Properties of Hexagonal Orthomanganites of Yttrium and Rare Earths. *Proc Int Meet Ferroelectr Prag.* **1966**.

(21) Venevtsev, Y. N.; Zhdanov, G. S.; Solov'ev, S. N.; Bezus, E. V; Ivanova, V. V; Fedulov, S. A. Crystal Chemical Studies of Substances with Perovskite-Type Structure and Special Dielectric Properties. *Kristallografiya.* **1960**, *5*, 620–6.

(22) Ascher, E.; Rieder, H.; Schmid, H.; Stossel, H. Some Properties of Ferromagnetoelectric Nickel Iodine Boracite, Ni3B7O13I. *J. Appl. Phys* **1966**, *37*, 1404–1405.

(23) Hill, N. A. Why Are There so Few Magnetic Ferroelectrics? *J. Phys. Chem. B* **2000**, *104* (29), 6694–6709. https://doi.org/10.1021/jp000114x.

(24) Fiebig M; Lottermoser Th; Frohlich D; Goltsev A V; Pisarev R V. Observation of Coupled Magnetic and Electric Domains. *Nature* **2002**, *419* (6909), 815–818. https://doi.org/10.1038/nature01093.1.

(25) Kimura, T.; Goto, T.; Shintani, H.; Ishizaka, K.; Arima, T.; Tokura, Y. Magnetic Control of Ferroelectric Polarization. *Nature* **2003**, *426* (6962), 55–58. https://doi.org/10.1038/nature02018.

(26) Hur, N.; Park, S.; Sharma, P. A.; Ahn, J. S.; Guha, S.; Cheong, S. W. Electric Polarization Reversal and Memory in a Multiferroic Material Induced by Magnetic Fields. *Nature* **2004**, *429* (6990), 392–395. https://doi.org/10.1038/nature02572.

(27) Catalan, G.; Scott, J. F. Physics and Applications of Bismuth Ferrite. *Adv. Mater.* **2009**, *21* (24), 2463–2485. https://doi.org/10.1002/adma.200802849.

(28) Chi, Z. H.; Xiao, C. J.; Feng, S. M.; Li, F. Y.; Jin, C. Q. Manifestation of Ferroelectromagnetism in Multiferroic BiMnO3. *J. Appl. Phys.* **2005**, *103519* (98), 1–6. https://doi.org/10.1063/1.2131193.

(29) Tehrani, S.; Member, S.; Slaughter, J. O. N. M.; Deherrera, M.; Engel, B. N.; Rizzo, N. D.; Salter, J.; Durlam, M.; Dave, R. W.; Janesky, J.; Butcher, B.; Smith, K. E. N.; Grynkewich, G. Magnetoresistive Random Access Memory Using Magnetic Tunnel Junctions. *IEEE Conf. Pap.* **2003**, *91* (5), 703–714. https://doi.org/10.1109/JPROC.2003.811804.

(30) Awschalom, D. D. *Handbook of Spintronics*; Xu, Y., Awschalom, D., Nitta, J., Eds.; Springer, 2016.

(31) Moreau, J. M.; Michel, C.; Gerson, R.; James, W. J. Ferroelectric BiFeO3 X-Ray and Neutron Diffraction Study. *J. Phys. Chem. Solids* **1971**, *32*, 1315–1320.

(32) Kubel, F.; Schmid, H. Structure of a Ferroelectric and Ferroelastic Monodomain Crystal of the Perovskite BiFeO3. *Acta Crystallogr. Sect. B* **1990**, *46* (6), 698–702. https://doi.org/10.1107/S0108768190006887.

(33) Smolenskii, G. A.; Chupis, I. E. Ferroelectromagnets. *Uspekhi Fiz. Nauk* **1982**, *25* (137), 475–493.

(34) Kiselev, S. V.; Ozerov, R. P.; Zhdanov, G. S. Detection of Magnetic Order in Ferroelectric BiFeO3 by Neutron Diffraction. *Sov. Phys. Dokl.* **1963**, *7*, 742–744.

(35) Roginskaya, Y.; Tomashpol'Skiĭ, Y.; Venevtsev, Y.; Petrov, V.; Zhdanov, G. The Nature of the Dielectric and Magnetic Properties of BiFeO3. *Sov. J. Exp. Theor. Phys.* **1966**, *23* (1), 47.

(36) Tokura, Y. Multiferroics as Quantum Electromagnets. *Science (80-.).* **2006**, *312* (June), 1481. https://doi.org/10.1126/science.1125227.

(37) Bibes, M. Towards a Magnetoelectric Memory. *Nat. Mater.* **2008**, *7* (June), 425.

(38) Baek, S. H.; Jang, H. W.; Folkman, C. M.; Li, Y. L.; Winchester, B.; Zhang, J. X.; He, Q.; Chu, Y. H.; Nelson, C. T.; Rzchowski, M. S.; Pan, X. Q.; Ramesh, R.; Chen, L. Q.; Eom, C. B. Ferroelastic Switching for Nanoscale Non-Volatile Magnetoelectric Devices. *Nat. Mater.* **2010**, *9* (4), 309–314. https://doi.org/10.1038/nmat2703.

(39) R. Ramesh and N. A. Spladin. Multiferroics: Progress and Prospects in Thin Films. *Nat. Mater.* **2007**, *6* (Jan), 21–29. https://doi.org/10.1038/nmat1805.

(40) Kadomtseva, A. M.; Popov, Y. F.; Pyatakov, A. P.; Vorob'Ev, G. P.; Zvezdin, A. K.; Viehland, D. Phase Transitions in Multiferroic BiFeO3 Crystals, Thin-Layers, and Ceramics: Enduring Potential for a Single Phase, Room-Temperature Magnetoelectric "Holy Grail." *Phase Transitions* **2006**, *79* (12), 1019–1042. https://doi.org/10.1080/01411590601067235.

(41) I. Sosnowska, M. Loewenhaupt, W. I. F. David, R. M. I. Investigation of the Unusual Magnetic Spiral Arrangement in BiFeO3. *Phys. B* **1992**, *195*, 117–118.

(42) Ederer, C.; Spaldin, N. A. Weak Ferromagnetism and Magnetoelectric Coupling in Bismuth Ferrite. *Phys. Rev. B - Condens. Matter Mater. Phys.* **2005**, *71* (6), 1–4. https://doi.org/10.1103/PhysRevB.71.060401.

(43) D.Megau, H.; C.N.W.Darlington. Geometrical and Structual Relations in the Rhombohedral Perobskites. *Acta Crystallogr. Sect. A* **1975**, *31*, 161–173.

(44) SEBASTIA, M. T. ABO3 TYPE PEROVSKITES-Chapter 6; Elsevier Ltd, 2008. https://doi.org/10.1016/B978-0-08-045330-9.00006-6.

(45) V. Goldschmidt, T. Barth, G. Lunde, W. H. Z. Geometrical Distribution Law of the Elements: VII Summary of the Chemistry of Crystals. *Skr. Nor. Vidensk. Akad* **1926**, *1*, 1–117.

(46) Dubey, A.; Keat, C. H.; Shvartsman, V. V; Yusenko, K. V; Castillo, M. E.; Buzanich, A. G.; Hagemann, U.; Kovalenko, S. A.; Stähler, J.; Lupascu, D. C. Mono-, Di-, and Tri-Valent Cation Doped BiFe0.95Mn0.05O3 Nanoparticles: Ferroelectric Photocatalysts. *Adv. Funct. Mater.* **2022**, *2207105*, 1–16. https://doi.org/10.1002/adfm.202207105.

(47) Shannon, R. D. Revised Effective Ionic Radii and Systematic Studies of Interatomic Distances in Halides and Chalcogenides. *Acta Crystallogr. Sect. A* **1976**, *32* (5), 751–767. https://doi.org/10.1107/S0567739476001551.

(48) Palewicz, A.; Przeniosło, R.; Sosnowska, I.; Hewat, A. W. Atomic Displacements in BiFeO3 as a Function of Temperature: Neutron Diffraction Study. *Acta Crystallogr. Sect. B Struct. Sci.* **2007**, *63* (4), 537–544. https://doi.org/10.1107/S0108768107023956.

(49) Glazer, A. M. The Classification of Tilted Octahedra in Perovskites. *Acta Crystallogr. Sect. B Struct. Crystallogr. Cryst. Chem.* **1972**, *28* (11), 3384–3392. https://doi.org/10.1107/s0567740872007976.

(50) Glazer, A. M. Simple Ways of Determining Perovskite Structures. *Acta Crystallogr. Sect. A* **1975**, *31* (6), 756–762. https://doi.org/10.1107/S0567739475001635.

(51) Howard, C. J.; Stokes, H. T. Group-Theoretical Analysis of Octahedral Tilting in Perovskites. *Acta Crystallogr. Sect. B Struct. Sci.* **1998**, *54* (6), 782–789. https://doi.org/10.1107/S0108768198004200.

(52) Ravindran, P.; Vidya, R.; Kjekshus, A.; Fjellvåg, H.; Eriksson, O. Theoretical Investigation of Magnetoelectric Behavior in BiFe O3. *Phys. Rev. B - Condens. Matter Mater. Phys.* **2006**, *74* (22). https://doi.org/10.1103/PhysRevB.74.224412.

(53) Diéguez, O.; Aguado-Puente, P.; Junquera, J.; Íñiguez, J. Domain Walls in a Perovskite Oxide with Two Primary Structural Order Parameters: First-Principles Study of BiFeO3. *Phys. Rev. B - Condens. Matter Mater. Phys.* **2013**, *87* (2), 1–11. https://doi.org/10.1103/PhysRevB.87.024102.

(54) Weingart, C.; Spaldin, N.; Bousquet, E. Noncollinear Magnetism and Single-Ion Anisotropy in Multiferroic Perovskites. *Phys. Rev. B - Condens. Matter Mater. Phys.* **2012**, *86* (9), 1–11. https://doi.org/10.1103/PhysRevB.86.094413.

(55) Park, J.; Le, M. D.; Jeong, J.; Lee, S. Structure and Spin Dynamics of Multiferroic BiFeO3. *J. Phys. Condens. Matter* **2014**, *26* (433202), 33. https://doi.org/10.1088/0953-8984/26/43/433202.

(56) Wani, W. A.; Naaz, N.; Venkataraman, B. H.; Kundu, S.; Ramaswamy, K. Significantly Reduced Leakage Current Density in Mn-Doped BiFeO3 Thin Films Deposited Using Spin Coating Technique. *J. Phys. Conf. Ser.* **2021**, *2070* (1). https://doi.org/10.1088/1742-6596/2070/1/012088.

(57) Okuma, G.; Watanabe, S.; Shinobe, K.; Nishiyama, N.; Takeuchi, A. Processing-Induced Defects Formed during Sintering of Hierarchical Powder Packings. *Sci. Rep.* **2019**, No. July, 1–9.

https://doi.org/10.1038/s41598-019-48127-y.

(58) Shvartsman, V. V.; Kleemann, W.; Haumont, R.; Kreisel, J. Large Bulk Polarization and Regular Domain Structure in Ceramic BiFe O3. *Appl. Phys. Lett.* **2007**, *90* (17), 1–4. https://doi.org/10.1063/1.2731312.

(59) Royen, P.; Swars, K. System Bismuth Oxide-Iron Oxide in Range 0 to 55 Mol % Iron Oxide. *Angew. Chemie* **1957**, *69* (24), 779.

(60) Tomashpolskii, Y. Y.; Venevtsev, Y. N.; Zhdanov, G. S. Electron Diffraction Study of the Crystal Structure of BiFeO3. *Dokl. Akad. Nauk SSSR* **1963**, *153* (6), 1313–1314.

(61) Plakhtii, V. P.; IMaltsev, E.; Kaminkev, D. M. Investigation of Some Compounds of Perovskite Structure by Neutron Diffraction. *Izv. Akad. Nauk SSSR, Ser. Fiz.* **1964**, *28* (3), 436–439.

(62) Ghosh, S.; Dasgupta, S.; Sen, A.; Maiti, H. S. Low-Temperature Synthesis of Nanosized Bismuth Ferrite by Soft Chemical Route. *J. Am. Ceram. Soc.* **2005**, *88* (5), 1349–1352. https://doi.org/10.1111/j.1551-2916.2005.00306.x.

(63) Shetty, S.; Palkar, V. R.; Pinto, R. Size Effect Study in Magnetoelectric BiFeO3 System. *Pramana - J. Phys.* **2002**, *58* (5–6), 1027–1030. https://doi.org/10.1007/s12043-002-0211-4.

(64) Park, T. J.; Papaefthymiou, G. C.; Viescas, A. J.; Moodenbaugh, A. R.; Wong, S. S. Size-Dependent Magnetic Properties of Single-Crystalline Multiferroic BiFeO3 Nanoparticles. *Nano Lett.* **2007**, *7* (3), 766–772. https://doi.org/10.1021/nl063039w.

(65) Jaiswal, A.; Das, R.; Maity, T.; Vivekanand, K.; Adyanthaya, S.; Poddar, P. Temperature-Dependent Raman and Dielectric Spectroscopy of Bifeo 3 Nanoparticles: Signatures of Spin-Phonon and Magnetoelectric Coupling. *J. Phys. Chem. C* **2010**, *114* (29), 12432–12439. https://doi.org/10.1021/jp102450z.

(66) Selbach, S. M.; Tybell, T.; Einarsrud, M.; Grande, T. Size-Dependent Properties of Multiferroic BiFeO 3 Nanoparticles. **2007**, No. 13, 6478–6484.

(67) Chattopadhyay, S.; Kelly, S. D.; Palkar, V. R.; Fan, L.; Segre, C. U. Investigation of Size Effects in Magnetoelectric BiFeO3. *Phys. Scr. T* **2005**, *T115*, 709–713. https://doi.org/10.1238/Physica.Topical.115a00709.

(68) Castillo, M. E.; Shvartsman, V. V.; Gobeljic, D.; Gao, Y.; Landers, J.; Wende, H.; Lupascu, D. C. Effect of Particle Size on Ferroelectric and Magnetic Properties of BiFeO3 Nanopowders. *Nanotechnology* **2013**, *24* (35). https://doi.org/10.1088/0957-4484/24/35/355701.

(69) Landers, J.; Salamon, S.; Escobar Castillo, M.; Lupascu, D. C.; Wende, H. Mössbauer Study of Temperature-Dependent Cycloidal Ordering in BiFeO3 Nanoparticles. *Nano Lett.* **2014**, *14* (11), 6061–6065. https://doi.org/10.1021/nl5031375.

(70) Mazumder, R.; Sujatha Devi, P.; Bhattacharya, D.; Choudhury, P.; Sen, A.; Raja, M. Ferromagnetism in Nanoscale BiFeO3. *Appl. Phys. Lett.* **2007**, *91* (6), 91–94. https://doi.org/10.1063/1.2768201.

(71) Park, T. J.; Papaefthymiou, G. C.; Viescas, A. J.; Moodenbaugh, A. R.; Wong, S. S. Size-Dependent Magnetic Properties of Single-Crystalline Multiferroic BiFeO3 Nanoparticles. *Nano Lett.* **2007**, *7* (3), 766–772. https://doi.org/10.1021/nl063039w.

(72) Goswami, S.; Bhattacharya, D.; Choudhury, P.; Ouladdiaf, B.; Chatterji, T. Multiferroic Coupling in Nanoscale BiFeO3. *Appl. Phys. Lett.* **2011**, *99* (7), 1–4. https://doi.org/10.1063/1.3625924.

(73) Selbach, S. M.; Tybell, T.; Einarsrud, M.; Grande, T. Size-Dependent Properties of Multiferroic BiFeO3 Nanoparticles. *Chem. Mater.* **2007**, *19* (13), 6478–6484.

(74) Gao, F.; Chen, X.; Yin, K.; Dong, S.; Ren, Z.; Yuan, F.; Yu, T.; Zou, Z.; Liu, J. M. Visible-Light Photocatalytic Properties of Weak Magnetic BiFeO3 Nanoparticles. *Adv. Mater.* **2007**, *19* (19), 2889–2892. https://doi.org/10.1002/adma.200602377.

(75) Fischer, P.; Polomska, M.; Sosnowska, I.; Szymanski, M. Temperature Dependence of the Crystal and Magnetic Structures of BiFeO3. *J. Phys. C Solid State Phys.* **1980**, *13* (10), 1931–1940.

https://doi.org/10.1088/0022-3719/13/10/012.

(76) Sosnowska, I.; Neumaier, T. P.; Steichele, E. Spiral Magnetic Ordering in Bismuth Ferrite. *J. Phys. C Solid State Phys.* **1982**, *15* (23), 4835–4846. https://doi.org/10.1088/0022-3719/15/23/020.

(77) Zalesskiĭ, A. V.; Zvezdin, A. K.; Frolov, A. A.; Bush, A. A. 57Fe NMR Study of a Spatially Modulated Magnetic Structure in BiFeO3. *JETP Lett.* **2000**, *71* (11), 465–468. https://doi.org/10.1134/1.1307994.

(78) Lebeugle, D.; Colson, D.; Forget, A.; Viret, M.; Bonville, P.; Marucco, J. F.; Fusil, S. Room-Temperature Coexistence of Large Electric Polarization and Magnetic Order in BiFe O3 Single Crystals. *Phys. Rev. B - Condens. Matter Mater. Phys.* **2007**, *76* (2), 1–8. https://doi.org/10.1103/PhysRevB.76.024116.

(79) Tab Ares-Muñoz, C.; Rivera, J. P.; Bezinges, A.; Monnier, A.; Schmid, H. Measurement of the Quadratic Magnetoelectric Effect on Single Crystalline Bife03. *Jpn. J. Appl. Phys.* **1985**, *24*, 1051–1053. https://doi.org/10.7567/JJAPS.24S2.1051.

(80) Das, R.; Kim, N. P.; Attanayake, S. B.; Phan, M. H.; Srikanth, H. Role of Magnetic Anisotropy on the Hyperthermia Efficiency in Spherical Fe3−xCoxO4 (X = 0–1) Nanoparticles. *Appl. Sci.* **2021**, *11* (3), 1–10. https://doi.org/10.3390/app11030930.

(81) Simeonidis, K.; Liébana-Viñas, S.; Wiedwald, U.; Ma, Z.; Li, Z. A.; Spasova, M.; Patsia, O.; Myrovali, E.; Makridis, A.; Sakellari, D.; Tsiaoussis, I.; Vourlias, G.; Farle, M.; Angelakeris, M. A Versatile Large-Scale and Green Process for Synthesizing Magnetic Nanoparticles with Tunable Magnetic Hyperthermia Features. *RSC Adv.* **2016**, *6* (58), 53107–53117. https://doi.org/10.1039/c6ra09362k.

(82) Gilchrist, R. K.; Shorey, W. D.; Hanselman, R. C.; Parrott, J. C.; Taylor, C. B. Selective Inductive Heating of Lymph Nodes. *Ann. Surg.* 1957, pp 596–606. https://doi.org/10.1097/00000658-195710000-00007.

(83) Thorat, N. D.; Bohara, R.; Yadav, H. M.; Otari, S. V; Pawar, S. H.; Tofail, S. A. M. *Multifunctional Magnetic Nanostructures for Cancer Hyperthermia Therapy*; Elsevier Inc., 2016. https://doi.org/10.1016/B978-0-323-47347-7.00021-5.

(84) Kekalo, K.; Baker, I.; Meyers, R.; Shyong, J. Magnetic Nanoparticles with High Specific Absorption Rate at Low Alternating Magnetic Field. *Nano Life* **2015**, *05* (02), 1550002. https://doi.org/10.1142/s1793984415500026.

(85) Obaidat, I. M.; Issa, B.; Haik, Y. Magnetic Properties of Magnetic Nanoparticles for Efficient Hyperthermia. *Nanomaterials* **2014**, *5* (1), 63–89. https://doi.org/10.3390/nano5010063.

(86) Kirchmayr, H. Magnetic Anisotropy. *Encycl. Mater. Sci. Technol. Encycl. Mater. Sci. Technol. (Second Ed.* **2001**, 4754–4757.

(87) Xie, Y.; Zhan, Q.; Hu, Y.; Hu, X.; Chi, X.; Zhang, C.; Yang, H.; Xie, W. Magnetocrystalline Anisotropy Imprinting of an Antiferromagnet on an Amorphous Ferromagnet in FeRh / CoFeB Heterostructures. *NPG Asia Mater.* **2020**. https://doi.org/10.1038/s41427-020-00248-x.

(88) Baberschke, K. *Anisotropy in Magnetism Lecture Notes in Physics*; 2001. https://doi.org/https://doi.org/10.1007/3-540-44610-9_3.

(89) Potrč, T.; Kralj, S.; Nemec, S.; Kocbeka, P.; Kreft, M. E. The Shape Anisotropy of Magnetic Nanoparticles: An Approach to Cell-Type Selective and Enhanced Internalization. *Nanoscale* **2023**, 1–8. https://doi.org/10.1039/d2nr06965b.

(90) Lisjak, D.; Mertelj, A. Anisotropic Magnetic Nanoparticles: A Review of Their Properties, Syntheses and Potential Applications. *Prog. Mater. Sci.* **2018**, 218. https://doi.org/10.1016/j.pmatsci.2018.03.003.

(91) Khurshid, H.; Alonso, J.; Nemati, Z.; Phan, M. H.; Mukherjee, P.; Fdez-Gubieda, M. L.; Barandiarán, J. M.; Srikanth, H. Anisotropy Effects in Magnetic Hyperthermia: A Comparison between Spherical and Cubic Exchange-Coupled FeO/Fe3O4 Nanoparticles. *J. Appl. Phys.* **2015**, *117* (17), 1–5. https://doi.org/10.1063/1.4919250.

(92) Moreno, R.; Poyser, S.; Meilak, D.; Meo, A.; Jenkins, S.; Lazarov, V. K.; Vallejo-Fernandez, G.; Majetich, S.; Evans, R. F. L. The Role of Faceting and Elongation on the Magnetic Anisotropy of Magnetite Fe3O4

Nanocrystals. *Sci. Rep.* **2020**, *10* (1), 1–14. https://doi.org/10.1038/s41598-020-58976-7.

(93) Bell, A. J.; Comyn, T. P.; Stevenson, T. J. Expanding the Application Space for Piezoelectric Materials. *APL Mater.* **2021**, *010901* (9), 1–7. https://doi.org/10.1063/5.0035416.

(94) Manbachi, A.; Cobbold, R. S. C. Development and Application of Piezoelectric Materials for Ultrasound Generation and Detection. *Ultrasound* **2011**, *19* (4), 187–196. https://doi.org/10.1258/ult.2011.011027.

(95) Pandey, R. K.; Dutta, J.; Brahma, S.; Rao, B.; Liu, C. P. Review on ZnO-Based Piezotronics and Piezoelectric Nanogenerators: Aspects of Piezopotential and Screening Effect. *JPhys Mater.* **2021**, *4* (4). https://doi.org/10.1088/2515-7639/ac130a.

(96) Acosta, M.; Novak, N.; Rojas, V.; Patel, S.; Vaish, R.; Koruza, J.; Rossetti, G. A.; Rödel, J. BaTiO3-Based Piezoelectrics: Fundamentals, Current Status, and Perspectives. *Appl. Phys. Rev.* **2017**, *4* (4). https://doi.org/10.1063/1.4990046.

(97) Qi, Y.; McAlpine, M. C. Nanotechnology-Enabled Flexible and Biocompatible Energy Harvesting. *Energy Environ. Sci.* **2010**, *3* (9), 1275–1285. https://doi.org/10.1039/c0ee00137f.

(98) Wang, Z. l. Novel Nanostructures of ZnO for Nanoscale Photonics , Optoelectronics , Piezoelectricity , and Sensing. *Appl. Phys. A* **2007**, *15*, 7–15. https://doi.org/10.1007/s00339-007-3942-8.

(99) Shrout, T. R.; Zhang, S. J. Lead-Free Piezoelectric Ceramics : Alternatives for PZT ? *J Electroceram* **2007**, *19*, 111–124. https://doi.org/10.1007/s10832-007-9047-0.

(100) Fu, H.; Cohen, R. E. Polarization Rotation Mechanism for Ultrahigh Electromechanical Response in Single-Crystal Piezoelectrics. *Nature* **2000**, *403*, 281–283. https://doi.org/https://doi.org/10.1038/35002022.

(101) Park, S.; Wada, S.; Rehrig, P. W.; Liu, S.; Cross, L. E.; Shrout, T. R. Crystallographic Engineering in High-Performance Piezoelectric Crystals. In *Smart Structures and Materials, Smart Materials Technologies, Proceedings*; 1999; Vol. 3675, pp 2–9. https://doi.org/https://doi.org/10.1117/12.352781.

(102) Wang, K.; Li, J. (K,Na)NbO3 -Based Lead-Free Piezoceramics : Phase Transition , Sintering and Property Enhancement. *J. Adv. Ceram.* **2012**, *1* (1), 24–37. https://doi.org/10.1007/s40145-012-0003-3.

(103) Abbasipour, M.; Khajavi, R.; Akbarzadeh, A. A Comprehensive Review on Piezoelectric Polymeric and Ceramic Nanogenerators. *Adv. Eng. Mater.* **2022**, *24* (2101312), 1–24. https://doi.org/10.1002/adem.202101312.

(104) Nye, J. F. *Physical Properties of Crystals, Their Representation by Tensors and Matrices*; Oxford University Press, 1957.

(105) Burianova, L.; Hana, P.; Panos, S.; Furman, E.; Zhang, S.; Shrout, T. R. Hydrostatic Piezoelectric Coefficient Dh of PZT Ceramics and PZN-PT and PYN-PT Single Crystals. *J. Electroceramics* **2004**, *13* (1–3), 443–448. https://doi.org/10.1007/s10832-004-5139-2.

(106) Zheng, T.; Wu, J. Effects of Site Engineering and Doped Element Types on Piezoelectric and Dielectric Properties of Bismuth Ferrite Lead-Free Ceramics. *J. Mater. Chem. C* **2015**, *3* (43), 11326–11334. https://doi.org/10.1039/c5tc02203g.

(107) Zhang, Y.; Roscow, J.; Lewis, R.; Khanbareh, H.; Yu, V.; Xie, M.; Bowen, C. R. Understanding the Effect of Porosity on the Polarisation- Fi Eld Response of Ferroelectric Materials. *Acta Mater.* **2018**, *154*, 100–112. https://doi.org/10.1016/j.actamat.2018.05.007.

(108) Poplavko, Y.; Yakymenko, Y. Pyroelectricity. *Funct. Dielectr. Electron.* **2020**, 131–159. https://doi.org/10.1016/b978-0-12-818835-4.00004-3.

(109) Schrodinger, E. Habil. Thesis. *Sitz. Berichte Akad, Wiss. Wien* **1912**, *121* (27).

(110) Valasek, J. Piezo-Electric and Allied Phenomena in Rochelle Salt. *Phys. Rev.* **1921**, *17* (4), 475–481. https://doi.org/10.1103/PhysRev.17.475.

(111) Busch, G.; Scherrer, P. Eine Neue Seignette-Elektrische Substanz. *Naturwissenschaften* **1935**, *23*, 737.

(112) Hippel, A. Von; Breckenridge, R. G.; Chesley, F. G.; Tisza, L. High Dielectric Constant Ceramics. *Ind. Eng. Chem.* **1946**, *38* (11), 1097.

(113) Kittel, C. Theory of Antiferroelectric Crystals. *Phys. Rev.* **1951**, *82* (5), 729–732. https://doi.org/10.1103/PhysRev.82.729.

(114) Smolenskii, G. A.; Isupov, V. A. BaTi1-XSnxO3 Ceramics. *Zh. Tekh. Fiz.* **1954**, *24*, 1375.

(115) Teague, J. R.; Gerson, R.; James, W. J. Dielectric Hysteresis in Single Crystal BiFeO3. *At. Energy* **1970**, *8* (90), 1073–1074.

(116) Bergman, J. G.; McFee, J. H.; Crane, G. R. Pyroelectricity and Optical Second Harmonic Generation in Polyvinylidene Fluoride Films. *Appl. Phys. Lett.* **1971**, *18* (5), 203–205. https://doi.org/10.1063/1.1653624.

(117) Wang, J.; Neaton, J. B.; Zheng, H.; Nagarajan, V.; Ogale, S. B.; Liu, B.; Viehland, D.; Vaithyanathan, V.; Schlom, D. G.; Waghmare, U. V; Spaldin, N. A.; Rabe, K. M.; Wuttig, M.; Ramesh, R. Epitaxial BiFeO3 Multiferroic Thin Film Heterostructures. *Science (80-.).* **2003**, *299*, 1719–1722.

(118) Miller, W. The Crystallographic Groups. *Pure Appl. Math.* **1972**, *50*, 16–60. https://doi.org/doi.org/10.1016/S0079-8169(08)60959-9.

(119) Shih, W. Y.; Shih, W. H.; Aksay, I. A. Size Dependence of the Ferroelectric Transition of Small BaTiO3 Particles: Effect of Depolarization. *Phys. Rev. B* **1994**, *50* (21), 15575–15585. https://doi.org/10.1103/PhysRevB.50.15575.

(120) Ren, W.; Bellaiche, L. Size Effects in Multiferroic BiFeO3 Nanodots: A First-Principles-Based Study. *Phys. Rev. B - Condens. Matter Mater. Phys.* **2010**, *82* (11), 1–4. https://doi.org/10.1103/PhysRevB.82.113403.

(121) Abdelsamie, A.; You, L.; Wang, L.; Li, S.; Gu, M.; Wang, J. Crossover between Bulk and Interface Photovoltaic Mechanisms in a Ferroelectric Vertical Heterostructure. *Phys. Rev. Appl.* **2022**, *17* (2), 1. https://doi.org/10.1103/PhysRevApplied.17.024047.

(122) Lupascu, D. C.; Anusca, I.; Etier, M.; Gao, Y.; Lackner, G.; Nazrabi, A.; Sanlialp, M.; Trivedi, H.; Ul-Haq, N.; Schröder, J. *Semiconductor Effects in Ferroelectrics*; 2018; Vol. 581. https://doi.org/10.1007/978-3-319-68883-1_3.

(123) Paillard, C.; Bai, X.; Infante, I. C.; Guennou, M.; Geneste, G.; Alexe, M.; Kreisel, J.; Dkhil, B. Photovoltaics with Ferroelectrics: Current Status and Beyond. *Adv. Mater.* **2016**, *28* (26), 5153–5168. https://doi.org/10.1002/adma.201505215.

(124) Yang, M.-M.; Alexe, M. Domain Walls: From Fundamental Properties to Nanotechnology Concepts. In *Photoelectric Effects at Domain Walls*; Oxford, 2020.

(125) Butler, K. T.; Frost, J. M.; Walsh, A. Ferroelectric Materials for Solar Energy Conversion: Photoferroics Revisited. *Energy Environ. Sci.* **2015**, *8* (3), 838–848. https://doi.org/10.1039/c4ee03523b.

(126) Nakamura, M.; Horiuchi, S.; Kagawa, F.; Ogawa, N.; Kurumaji, T.; Tokura, Y.; Kawasaki, M. Shift Current Photovoltaic Effect in a Ferroelectric Charge-Transfer Complex. *Nat. Commun.* **2017**, *8* (1), 1–5. https://doi.org/10.1038/s41467-017-00250-y.

(127) Piskunov, S.; Heifets, E.; Eglitis, R. I.; Borstel, G. Bulk Properties and Electronic Structure of SrTiO3, BaTiO 3, PbTiO3 Perovskites: An Ab Initio HF/DFT Study. *Comput. Mater. Sci.* **2004**, *29* (2), 165–178. https://doi.org/10.1016/j.commatsci.2003.08.036.

(128) Fina, I.; Paillard, C.; Dkhil, B. Photoferroelectric Oxides. *arXiv* **2017**, No. October. https://doi.org/DOI:10.1016/j.apsusc.2019.03.312.

(129) Alexe, M.; Hesse, D. Tip-Enhanced Photovoltaic Effects in Bismuth Ferrite. *Nat. Commun.* **2011**, *2* (1). https://doi.org/10.1038/ncomms1261.

(130) Sharma, K.; Singh, A. Advances in Photovoltaic Behavior of Ferroelectric BiFeO3. *J. Nanosci. Technol.* **2018**, *4* (5), 348–352.

(131) Yang, Y.; Paillard, C.; Xu, B.; Bellaiche, L. Photostriction and Elasto-Optic Response in Multiferroics and Ferroelectrics from First Principles. *J. Phys. Condens. Matter* **2018**, *30* (7). https://doi.org/10.1088/1361-648X/aaa51f.

(132) Zeches, R. J.; Rossell, M. D.; Zhang, J. X.; Hatt, A. J.; He, Q.; Yang, C. H.; Kumar, A.; Wang, C. H.; Melville, A.; Adamo, C.; Sheng, G.; Chu, Y. H.; Ihlefeld, J. F.; Erni, R.; Ederer, C.; Gopalan, V.; Chen, L. Q.; Schldin, D. G.; Spaldin, N. A.; Martin, L. W.; Ramesh, R. A Strain-Driven Morphotropic Phase Boundary in BifeO3. *Science (80-.).* **2009**, *326* (5955), 977–980. https://doi.org/10.1126/science.1177046.

(133) Kundys, B.; Viret, M.; Colson, D.; Kundys, D. O. Light-Induced Size Changes in BiFeO3 Crystals. *Nat. Mater.* **2010**, *9* (10), 803–805. https://doi.org/10.1038/nmat2807.

(134) Bai, X. Size and Doping Effect on the Structure, Transitions and Optical Properties of Multiferroic BiFeO3 Particles for Photocatalytic Applications, Universite Paris Saclay, 2016.

(135) Kundys, B.; Viret, M.; Meny, C.; Da Costa, V.; Colson, D.; Doudin, B. Wavelength Dependence of Photoinduced Deformation in BiFeO3. *Phys. Rev. B - Condens. Matter Mater. Phys.* **2012**, *85* (9), 1–4. https://doi.org/10.1103/PhysRevB.85.092301.

(136) Lejman, M.; Vaudel, G.; Infante, I. C.; Gemeiner, P.; Gusev, V. E.; Dkhil, B.; Ruello, P. Giant Ultrafast Photo-Induced Shear Strain in Ferroelectric BiFeO 3. *Nat. Commun.* **2014**, *5*, 1–7. https://doi.org/10.1038/ncomms5301.

(137) Sherman, D. M. The Electronic Structures of Fe3+ Coordination Sites in Iron Oxides: Applications to Spectra, Bonding, and Magnetism. *Phys. Chem. Miner.* **1985**, *12* (3), 161–175. https://doi.org/10.1007/BF00308210.

(138) Ramachandran, B.; Dixit, A.; Naik, R.; Lawes, G.; Rao, M. S. R. Charge Transfer and Electronic Transitions in Polycrystalline BiFeO 3. *Phys. Rev. B - Condens. Matter Mater. Phys.* **2010**, *82* (1), 1–4. https://doi.org/10.1103/PhysRevB.82.012102.

(139) Sheu, Y. M.; Trugman, S. A.; Park, Y. S.; Lee, S.; Yi, H. T.; Cheong, S. W.; Jia, Q. X.; Taylor, A. J.; Prasankumar, R. P. Ultrafast Carrier Dynamics and Radiative Recombination in Multiferroic BiFeO 3. *Appl. Phys. Lett.* **2012**, *100* (24). https://doi.org/10.1063/1.4729423.

(140) Varignon, J.; Bibes, M.; Zunger, A. Origin of Band Gaps in 3d Perovskite Oxides. *Nat. Commun.* **2019**, *10* (1), 1–11. https://doi.org/10.1038/s41467-019-09698-6.

(141) Bredas, J. L. Mind the Gap! *Mater. Horizons* **2014**, *1* (1), 17–19. https://doi.org/10.1039/c3mh00098b.

(142) Burkert, F.; Kreisel, J.; Kuntscher, C. A. Optical Spectroscopy Study on the Photo-Response in Multiferroic BiFeO3. *Appl. Phys. Lett.* **2016**, *109* (18). https://doi.org/10.1063/1.4966548.

(143) Farrauto, R. J. *Handbook of Industrial Chemistry and Biotechnology*; 2017. https://doi.org/10.1007/978-3-319-52287-6.

(144) Strunk, J. *Heterogeneous Photocatalysis*; 2021. https://doi.org/10.3390/books978-3-0365-6295-7.

(145) Jackson, S. D.; Hargreaves, J. S. J. *Metal Oxide Catalysis*; Wiley VCH Verlag GmbH and Co. kGaA, 2009.

(146) Malato, S.; Pilar Fernandez-Ib ´ a´nez, M. I. M.; Oller, I. M. ˜; Polo-Lopez, I. *Functional Nanostructured Materials and Membranes for Water Treatment Risk Analysis of Water Pollution Photocatalysis Activated Carbon for Water and Wastewater Treatment Biological Wastewater Treatment Ozonation of Water and Waste Water*; 2013.

(147) Védrine, J. C. Heterogeneous Catalysis on Metal Oxides. *Catalysts* **2017**, *7* (11). https://doi.org/10.3390/catal7110341.

(148) Ertl, G.; Knözinger, H.; Weitkamp, J. *Handbook of Heterogeneous Catalysis*; 2008; Vol. 1–5. https://doi.org/10.1524/zpch.1999.208.part_1_2.274.

(149) Chatterjee, D.; Dasgupta, S. Visible Light Induced Photocatalytic Degradation of Organic Pollutants. *J. Photochem. Photobiol. C Photochem. Rev.* **2005**, *6* (2–3), 186–205.

https://doi.org/10.1016/j.jphotochemrev.2005.09.001.

(150) Dubey, A.; Schmitz, A.; Shvartsman, V. V.; Bacher, G.; Lupascu, D. C.; Castillo, M. E. Role of Cooperative Factors in the Photocatalytic Activity of Ba and Mn Doped BiFeO3nanoparticles. *Nanoscale Adv.* **2021**, *3* (20), 5830–5840. https://doi.org/10.1039/d1na00420d.

(151) Kalz, K. F.; Kraehnert, R.; Dvoyashkin, M.; Dittmeyer, R.; Gläser, R.; Krewer, U.; Reuter, K.; Grunwaldt, J. D. Future Challenges in Heterogeneous Catalysis: Understanding Catalysts under Dynamic Reaction Conditions. *ChemCatChem* **2017**, *9* (1), 17–29. https://doi.org/10.1002/cctc.201600996.

(152) Schlögl, R. Heterogeneous Catalysis. *Angew. Chemie - Int. Ed.* **2015**, *54* (11), 3465–3520. https://doi.org/10.1002/anie.201410738.

(153) Liu, Y.; Ye, S.; Xie, H.; Zhu, J.; Shi, Q.; Ta, N.; Chen, R.; Gao, Y.; An, H.; Nie, W.; Jing, H.; Fan, F.; Li, C. Internal-Field-Enhanced Charge Separation in a Single-Domain Ferroelectric PbTiO3 Photocatalyst. *Adv. Mater.* **2020**, *32* (7), 1–7. https://doi.org/10.1002/adma.201906513.

(154) Li, L.; Salvador, P. A.; Rohrer, G. S. Photocatalysts with Internal Electric Fields. *Nanoscale* **2014**, *6* (1), 24–42. https://doi.org/10.1039/c3nr03998f.

(155) Mushtaq, F.; Chen, X.; Hoop, M.; Torlakcik, H.; Pellicer, E.; Sort, J.; Gattinoni, C.; Nelson, B. J.; Pané, S. Piezoelectrically Enhanced Photocatalysis with BiFeO3 Nanostructures for Efficient Water Remediation. *iScience* **2018**, *4*, 236–246. https://doi.org/10.1016/j.isci.2018.06.003.

(156) Woo, J. W. F. Piezoelectricity under Hydrostatic Pressure. *Phys. Rev. B* **1971**, *4* (4), 1218–1220. https://doi.org/10.1103/PhysRevB.4.1218.

(157) Li, S.; Zhao, Z.; Zhao, J.; Zhang, Z.; Li, X.; Zhang, J. Recent Advances of Ferro-, Piezo-, and Pyroelectric Nanomaterials for Catalytic Applications. *ACS Appl. Nano Mater.* **2020**, *3* (2), 1063–1079. https://doi.org/10.1021/acsanm.0c00039.

(158) Ooka, H.; Huang, J.; Exner, K. S. The Sabatier Principle in Electrocatalysis: Basics, Limitations, and Extensions. *Front. Energy Res.* **2021**, *9* (May), 1–20. https://doi.org/10.3389/fenrg.2021.654460.

(159) Kalinin, S. V.; Bonnell, D. A. Local Potential and Polarization Screening on Ferroelectric Surfaces. *Phys. Rev. B - Condens. Matter Mater. Phys.* **2001**, *63* (12), 1–13. https://doi.org/10.1103/PhysRevB.63.125411.

(160) Efe, I.; Spaldin, N. A.; Gattinoni, C. On the Happiness of Ferroelectric Surfaces and Its Role in Water Dissociation: The Example of Bismuth Ferrite. *J. Chem. Phys.* **2021**, *154* (2). https://doi.org/10.1063/5.0033897.

(161) Kalinin, S. V.; Kim, Y.; Fong, D. D.; Morozovska, A. N. Surface-Screening Mechanisms in Ferroelectric Thin Films and Their Effect on Polarization Dynamics and Domain Structures. *Reports Prog. Phys.* **2018**, *81* (3). https://doi.org/10.1088/1361-6633/aa915a.

(162) Li, Y.; Li, J.; Yang, W.; Wang, X. *Implementation of Ferroelectric Materials in Photocatalytic and Photoelectrochemical Water Splitting*; 2020; Vol. 5. https://doi.org/10.1039/d0nh00219d.

(163) Chen, F.; Huang, H.; Guo, L.; Zhang, Y.; Ma, T. The Role of Polarization in Photocatalysis. *Angewandte Chemie - International Edition*. 2019. https://doi.org/10.1002/anie.201901361.

(164) Grigoriev, S. A.; Fateev, V. N.; Bessarabov, D. G.; Millet, P. Current Status, Research Trends, and Challenges in Water Electrolysis Science and Technology. *Int. J. Hydrogen Energy* **2020**, *45* (49), 26036–26058. https://doi.org/10.1016/j.ijhydene.2020.03.109.

(165) Wang, S.; Lu, A.; Zhong, C. J. Hydrogen Production from Water Electrolysis: Role of Catalysts. *Nano Converg.* **2021**, *8* (1). https://doi.org/10.1186/s40580-021-00254-x.

(166) Kim, B.-J. Perovskites as Electrocatalysts for Oxygen Evolution Reaction for Alkaline Water Electrolysis, ETH Zurich, 2019. https://doi.org/https://doi.org/10.3929/ethz-b-000346869.

(167) Pan, Y. Development of Perovskite Materials for Electrocatalysis, University of Southern Queensland

Australia, 2021.

(168) Carmo, M.; Lüke, W.; Stolten, D. Electrocatalysts for the Hydrogen Evolution Reaction. In *PEM Electrolysis for Hydrogen Production*; Taylor & Francis Group, 2015; p 22. https://doi.org/10.1002/9781119829584.ch5.

(169) Zhao, G.; Sun, W. Electrochemical Hydrogen Evolution Reaction. *Wiley Online Books* **2022**, 87–118.

(170) Santos, E.; Quaino, P.; Schmickler, W. Theory of Electrocatalysis: Hydrogen Evolution and More. *Phys. Chem. Chem. Phys.* **2012**, *14* (32), 11224–11233. https://doi.org/10.1039/c2cp40717e.

(171) Shilpa, R.; Sibi, K. S.; Kumar, S. R. S.; Pai, R. K.; Rakhi, R. B. *Electrocatalysts for Hydrogen Evolution Reaction*; 2023; Vol. 42. https://doi.org/10.1016/j.ijhydene.2017.02.125.

(172) Ma, J. *Photo- and Electro-Catalytic Processes*; Wiley VCH, 2022.

(173) Vogt, C.; Weckhuysen, B. M. The Concept of Active Site in Heterogeneous Catalysis. *Nat. Rev. Chem.* **2022**, *6* (2), 89–111. https://doi.org/10.1038/s41570-021-00340-y.

(174) Karki, S. B.; Andriotis, A. N.; Menon, M.; Ramezanipour, F. Enhancement of Electrocatalytic Activity for Both Hydrogen and Oxygen Evolution Reactions of a Perovskite Oxide. *J. Phys. Chem. C* **2022**, *126* (47), 20011–20019. https://doi.org/10.1021/acs.jpcc.2c05651.

(175) Si, C.; Zhang, W.; Lu, Q.; Guo, E.; Yang, Z.; Chen, J.; He, X.; Luo, J. Recent Advances in Perovskite Catalysts for Efficient Overall Water Splitting. *Catalysts* **2022**, *12* (6). https://doi.org/10.3390/catal12060601.

(176) Zou, X.; Zhang, Y. Noble Metal-Free Hydrogen Evolution Catalysts for Water Splitting. *Chem. Soc. Rev.* **2015**, *44* (15), 5148–5180. https://doi.org/10.1039/c4cs00448e.

(177) Kemball, C. Hugh Stott Taylor. *R. Soc. Publ.* **1975**, *21* (April 1974), 517–547.

(178) Kistiakowsky, G. B.; Flosdorf, E. W.; Taylor, H. S. HEATS OF ADSORPTION ON POISONED AND HEAT-TREATED CATALYSTS. *Lab. Phys. Chem. Princet. Univ.* **1927**, *49* (1924), 2200–2206.

(179) Li, G.; Zhang, D.; Qiao, Q.; Yu, Y.; Peterson, D.; Zafar, A.; Kumar, R.; Curtarolo, S.; Hunte, F.; Shannon, S.; Zhu, Y.; Yang, W.; Cao, L. All the Catalytic Active Sites of MoS2 for Hydrogen Evolution. *J. Am. Chem. Soc.* **2016**, *138* (51), 16632–16638. https://doi.org/10.1021/jacs.6b05940.

(180) Kluge, R. M.; Haid, R. W.; Stephens, I. E. L.; Calle-Vallejo, F.; Bandarenka, A. S. Monitoring the Active Sites for the Hydrogen Evolution Reaction at Model Carbon Surfaces. *Phys. Chem. Chem. Phys.* **2021**, *23* (16), 10051–10058. https://doi.org/10.1039/d1cp00434d.

(181) Garlyyev, B.; Fichtner, J.; Piqué, O.; Schneider, O.; Bandarenka, A. S.; Calle-Vallejo, F. Revealing the Nature of Active Sites in Electrocatalysis. *Chem. Sci.* **2019**, *10* (35), 8060–8075. https://doi.org/10.1039/c9sc02654a.

(182) Somorjai, G. A.; McCrea, K. R.; Zhu, J. Active Sites in Heterogeneous Catalysis: Development of Molecular Concepts and Future Challenges. *Top. Catal.* **2002**, *18* (3–4), 157–166. https://doi.org/10.1023/A:1013874202404.

(183) Ricca, C.; Aschauer, U. Mechanisms for Point Defect-Induced Functionality in Complex Perovskite Oxides. *Appl. Phys. A Mater. Sci. Process.* **2022**, *128* (12), 1–8. https://doi.org/10.1007/s00339-022-06210-8.

(184) Ricca, C.; Niederhauser, N.; Aschauer, U. Local Polarization in Oxygen-Deficient LaMn O3 Induced by Charge Localization in the Jahn-Teller Distorted Structure. *Phys. Rev. Res.* **2020**, *2* (4), 1–6. https://doi.org/10.1103/PhysRevResearch.2.042040.

(185) Yang, C. H.; Kan, D.; Takeuchi, I.; Nagarajan, V.; Seidel, J. Doping BiFeO 3: Approaches and Enhanced Functionality. *Phys. Chem. Chem. Phys.* **2012**, *14* (46), 15953–15962. https://doi.org/10.1039/c2cp43082g.

(186) Silva, J.; Reyes, A.; Esparza, H.; Camacho, H.; Fuentes, L. BiFeO3: A Review on Synthesis, Doping and Crystal Structure. *Integr. Ferroelectr.* **2011**, *126* (1), 47–59.

https://doi.org/10.1080/10584587.2011.574986.

(187) Gebhardt, J.; Rappe, A. M. Doping of BiFeO3: A Comprehensive Study on Substitutional Doping. *Phys. Rev. B* **2018**, *98* (12), 1–16. https://doi.org/10.1103/PhysRevB.98.125202.

(188) Kröger, F. A.; Vink, H. J. Relations between the Concentrations of Imperfections in Crystalline Solids. *Solid State Phys. - Adv. Res. Appl.* **1956**, *3* (C), 307–435. https://doi.org/10.1016/S0081-1947(08)60135-6.

(189) Larowska, D.; Brien, J. M. O.; Senge, M. O.; Burdzinski, G.; Lewandowska-andralojc, A. Graphene Oxide Functionalized with Cationic Porphyrins as Materials for the Photodegradation of Rhodamine B. *J. Phys. Chem. C* **2020**, *124*, 15769–15780. https://doi.org/10.1021/acs.jpcc.0c03907.

(190) Chen, D.; Feng, H.; Li, J. Graphene Oxide: Preparation, Functionalization, and Electrochemical Applications. *Chem. Rev.* **2012**, *112* (11), 6027–6053. https://doi.org/10.1021/cr300115g.

(191) Brisebois, P. P.; Siaj, M. Harvesting Graphene Oxide-Years 1859 to 2019: A Review of Its Structure, Synthesis, Properties and Exfoliation. *J. Mater. Chem. C* **2020**, *8* (5), 1517–1547. https://doi.org/10.1039/c9tc03251g.

(192) Caglioti, G.; Paoletti, A.; Ricci, F. P. Choice of Collimators for a Crystal Spectrometer for Neutron Diffraction. *Nucl. Instruments* **1958**, *3* (4), 223–228. https://doi.org/10.1016/0369-643X(58)90029-X.

(193) Rietveld, H. M. A Profile Refinement Method for Nuclear and Magnetic Structures. *J. Appl. Crystallogr.* **1969**, *2* (2), 65–71. https://doi.org/10.1107/s0021889869006558.

(194) Scherrer, P. Bestimmung Der Größe Und Der Inneren Struktur von Kolloidteilchen Mittels Röntgenstrahlen. *Nachrichten von der Gesellschaft der Wissenschaften zu Göttingen, Math. Klasse* **1918**, 98–100.

(195) Miranda, M. A. R.; Sasaki, J. M. The Limit of Application of the Scherrer Equation. *Acta Crystallogr. Sect. A Found. Adv.* **2018**, *74* (1), 54–65. https://doi.org/10.1107/S2053273317014929.

(196) Gleichmann, N. SEM vs TEM. *Technol. Networks- Anal. Sep.* **2020**, 1–8.

(197) Suresh Kumar, P.; Korving, L.; Keesman, K. J.; van Loosdrecht, M. C. M.; Witkamp, G. J. Effect of Pore Size Distribution and Particle Size of Porous Metal Oxides on Phosphate Adsorption Capacity and Kinetics. *Chem. Eng. J.* **2019**, *358* (September 2018), 160–169. https://doi.org/10.1016/j.cej.2018.09.202.

(198) Braunauer, S.; Emmett, P. H.; Teller, E. Adsorption of Gases in Multimolecular Layers. *J. Am. Chem. Soc.* **1938**, 309–319. https://doi.org/10.1016/j.fuel.2016.10.086.

(199) Barrett, E. P.; Joyner, L. G.; Halenda, P. P. The Determination of Pore Volume and Area Distributions in Porous Substances. I. Computations from Nitrogen Isotherm. *Vol. Area Distrib. Porous Subst.* **1951**, *73* (1948), 373–380.

(200) Sing, K. S. W.; Everett, D. H.; Haul, R. A. W.; Moscou, L.; Pierotti, R. A.; Rouquerol, J.; Siemieniewska, T. Reporting Physisorption Data for Gas/Solid Systems with Special Reference to the Determination of Surface Area and Porosity. *Pure Appl. Chem.* **1985**, *57* (4), 603–619. https://doi.org/10.1351/pac198557040603.

(201) Steinhardt, R. G.; Serfass, E. J. X-Ray Photoelectron Spectrometer for Chemical Analysis. *Anal. Chem.* **1951**, *23* (11), 1585–1590. https://doi.org/10.1021/ac60059a019.

(202) Tougaard, S. Practical Guide to the Use of Backgrounds in Quantitative XPS. *J. Vac. Sci. Technol. A* **2021**, *39* (1), 011201. https://doi.org/10.1116/6.0000661.

(203) Ramaker, D. E.; Mojet, B. L.; Koningsberger, D. C.; O'Grady, W. E. Understanding Atomic X-Ray Absorption Fine Structure in x-Ray Absorption Spectra. *J. Phys. Condens. Matter* **1998**, *10* (39), 8753–8770. https://doi.org/10.1088/0953-8984/10/39/013.

(204) Riesemeier, H.; Ecker, K.; Görner, W.; Müller, B. R.; Radtke, M.; Krumrey, M. Layout and First XRF Applications of the BAMline at BESSY II. *X-Ray Spectrom.* **2005**, *34* (2), 160–163. https://doi.org/10.1002/xrs.750.

(205) Lutz, C.; Hampel, S.; Ke, X.; Beuermann, S.; Turek, T.; Kunz, U.; Guilherme Buzanich, A.; Radtke, M.; Fittschen, U. E. A. Evidence for Redox Reactions during Vanadium Crossover inside the Nanoscopic Water-Body of Nafion 117 Using X-Ray Absorption near Edge Structure Spectroscopy. *J. Power Sources* **2021**, *483*, 229176. https://doi.org/10.1016/J.JPOWSOUR.2020.229176.

(206) Ravel, B.; Newville, M. ATHENA, ARTEMIS, HEPHAESTUS: Data Analysis for X-Ray Absorption Spectroscopy Using IFEFFIT. *J. Synchrotron Radiat.* **2005**, *12* (4), 537–541. https://doi.org/10.1107/S0909049505012719.

(207) Newville, M. IFEFFIT: Interactive XAFS Analysis and FEFF Fitting. *J. Synchrotron Radiat.* **2001**, *8* (2), 322–324. https://doi.org/10.1107/S0909049500016964.

(208) Kubelka, P.; Munk, F. Ein Beitrag Zur Optik Der Farbanstriche. *J. Tech. Phys.* **1931**, *12*, 593.

(209) J. Tauc, R. Grigorovici, A. V. Optical Properties and Electronic Structure of Amorphous Germanium. *Phys. stat. sol.* **1966**, *15*, 627–637. https://doi.org/10.1007/s10812-016-0329-7.

(210) Cody, G. D.; Brooks, B. G.; Abeles, B. Optical Absorption above the Optical Gap of Amorphous Silicon Hydride. *Sol. Energy Mater.* **1982**, *8* (1–3), 231–240. https://doi.org/10.1016/0165-1633(82)90065-X.

(211) Pankove, J. I. Optical Process in Semiconductors. *J. Electrochem. Soc.* **1975**, *119* (5), 450.

(212) Makuła, P.; Pacia, M.; Macyk, W. How To Correctly Determine the Band Gap Energy of Modified Semiconductor Photocatalysts Based on UV-Vis Spectra. *J. Phys. Chem. Lett.* **2018**, *9* (23), 6814–6817. https://doi.org/10.1021/acs.jpclett.8b02892.

(213) Berera, R.; van Grondelle, R.; Kennis, J. T. M. Ultrafast Transient Absorption Spectroscopy: Principles and Application to Photosynthetic Systems. *Photosynth. Res.* **2009**, *101* (2–3), 105–118. https://doi.org/10.1007/s11120-009-9454-y.

(214) Kanal, F. Femtosecond Transient Absorption Spectroscopy – Technical Improvements and Applications to Ultrafast Molecular Phenomena, Julius-Maximilians-Universitat Wurzburg, 2015.

(215) Kovalenko, S. A.; Schanz, R.; Hennig, H.; Ernsting, N. P. Cooling Dynamics of an Optically Excited Molecular Probe in Solution from Femtosecond Broadband Transient Absorption Spectroscopy. *J. Chem. Phys.* **2001**, *115* (7), 3256–3273. https://doi.org/10.1063/1.1380696.

(216) Kovalenko, S. A.; Dobryakov, A. L.; Ruthmann, J.; Ernsting, N. P. Femtosecond Spectroscopy of Condensed Phases with Chirped Supercontinuum Probing. *Phys. Rev. A - At. Mol. Opt. Phys.* **1999**, *59* (3), 2369–2384. https://doi.org/10.1103/PhysRevA.59.2369.

(217) Moreno, J.; Dobryakov, A. L.; Ioffe, I. N.; Granovsky, A. A.; Hecht, S.; Kovalenko, S. A. Broadband Transient Absorption Spectroscopy with 1- and 2-Photon Excitations: Relaxation Paths and Cross Sections of a Triphenylamine Dye in Solution. *J. Chem. Phys.* **2015**, *143* (2). https://doi.org/10.1063/1.4926574.

(218) Ioffe, I. N.; Quick, M.; Quick, M. T.; Dobryakov, A. L.; Richter, C.; Granovsky, A. A.; Berndt, F.; Mahrwald, R.; Ernsting, N. P.; Kovalenko, S. A. Tuning Stilbene Photochemistry by Fluorination: State Reordering Leads to Sudden Polarization near the Franck-Condon Region. *J. Am. Chem. Soc.* **2017**, *139* (42), 15265–15274. https://doi.org/10.1021/jacs.7b09611.

(219) Raman, C. V.; Krishnan, K. S. A New Type of Secondary Radiation. *Nature* **1928**, *121* (3048), 501–502. https://doi.org/10.1038/121501c0.

(220) Mangamma, G.; Das, B. K.; Ramachandran, B.; Ramachandra Rao, M. S.; Sairam, T. N. Interplay of Piezoresponse and Magnetic Behavior in Bi0.9A0.1FeO2.95 (A = Ba, Ca) and Bi0.9Ba0.05Ca0.05FeO2.95 Co-Doped Ceramics. *RSC Adv.* **2022**, *12* (4), 2443–2453. https://doi.org/10.1039/d1ra08141a.

(221) Dittmer-gobeljic, D. Polar Microstructure and Nanoscale Electromechanical Behavior of Lead-Free Piezoelectric Ceramics, University of Duisburg Essen, 2015.

(222) TWI news. *What Are Nanoparticles? Definition, Size Uses and Properties.*; 2023.

(223) Abid, N.; Khan, A. M.; Shujait, S.; Chaudhary, K.; Ikram, M.; Imran, M.; Haider, J.; Khan, M.; Khan, Q.;

Maqbool, M. Synthesis of Nanomaterials Using Various Top-down and Bottom-up Approaches, Influencing Factors, Advantages, and Disadvantages: A Review. *Adv. Colloid Interface Sci.* **2022**, *300*, 102597. https://doi.org/10.1016/J.CIS.2021.102597.

(224) Wang, Y.; He, J.; Liu, C.; Chong, W. H.; Chen, H. Thermodynamics versus Kinetics in Nanosynthesis. *Angew. Chemie - Int. Ed.* **2015**, *54* (7), 2022–2051. https://doi.org/10.1002/anie.201402986.

(225) An, K.; Somorjai, G. A. Size and Shape Control of Metal Nanoparticles for Reaction Selectivity in Catalysis. *ChemCatChem* **2012**, *4* (10), 1512–1524. https://doi.org/10.1002/cctc.201200229.

(226) Byrappa, K.; Adschiri, T. Hydrothermal Technology for Nanotechnology. *Prog. Cryst. Growth Charact. Mater.* **2007**, *53* (2), 117–166. https://doi.org/10.1016/j.pcrysgrow.2007.04.001.

(227) Dimesso, L. Pechini Processes: An Alternate Approach of the Sol–Gel Method, Preparation, Properties, and Applications. In *Handbook of Sol-Gel Science and Technology*; Springer, 2016; pp 1–22. https://doi.org/10.1007/978-3-319-19454-7.

(228) Zhang, Q.; Sando, D.; Nagarajan, V. Chemical Route Derived Bismuth Ferrite Thin Films and Nanomaterials. *J. Mater. Chem. C* **2016**, *4* (19), 4092–4124. https://doi.org/10.1039/c6tc00243a.

(229) Gao, T.; Chen, Z.; Huang, Q.; Niu, F.; Huang, X.; Qin, L.; Huang, Y. A Review: Preparation of Bismuth Ferrite Nanoparticles and Its Applications in Visible-Light Induced Photocatalyses. *Rev. Adv. Mater. Sci.* **2015**, *40* (2), 97–109.

(230) Wang, N.; Luo, X.; Han, L.; Zhang, Z.; Zhang, R.; Olin, H.; Yang, Y. Structure, Performance, and Application of BiFeO3 Nanomaterials. *Nano-Micro Lett.* **2020**, *12* (1). https://doi.org/10.1007/s40820-020-00420-6.

(231) Wang, X.; Yang, C.; Zhou, D.; Wang, Z.; Jin, M. Chemical Co-Precipitation Synthesis and Properties of Pure-Phase BiFeO3. *Chem. Phys. Lett.* **2018**, *713* (July), 185–188. https://doi.org/10.1016/j.cplett.2018.09.043.

(232) Tomina, E. V.; Kurkin, N. A.; Korol', A. K.; Alekhina, Y. A.; Perov, N. S.; Jiyu, F.; Mittova, I. Y.; Nguyen, T. A.; Bui, V. X. Spray Pyrolysis Synthesis, Electrical and Magnetic Properties of HoxBi1-XFeO3 Nanocrystals. *J. Mater. Sci. Mater. Electron.* **2022**, *33* (32), 24594–24605. https://doi.org/10.1007/s10854-022-09170-0.

(233) Cao, W.; Chen, Z.; Gao, T.; Zhou, D.; Leng, X.; Niu, F.; Zhu, Y.; Qin, L.; Wang, J.; Huang, Y. Rapid Synthesis of Single-Phase Bismuth Ferrite by Microwave-Assisted Hydrothermal Method. *Mater. Chem. Phys.* **2016**, *175*, 1–5. https://doi.org/10.1016/j.matchemphys.2016.02.067.

(234) Mostafavi, E.; Ataie, A.; Ahmadzadeh, M. Characterization of Nano-Structured Multiferroic Bismuth Ferrite Produced via Solid State Reaction Route. *Adv. Mater. Res.* **2014**, *829*, 683–687. https://doi.org/10.4028/www.scientific.net/AMR.829.683.

(235) Siebeneicher, S.; Waag, F.; Castillo, M. E.; Shvartsman, V. V.; Lupascu, D. C.; Gökce, B. Laser Fragmentation Synthesis of Colloidal Bismuth Ferrite Particles. *Nanomaterials* **2020**, *10* (2). https://doi.org/10.3390/nano10020359.

(236) Han, J. T.; Huang, Y. H.; Wu, X. J.; Wu, C. L.; Wei, W.; Peng, B.; Huang, W.; Goodenough, J. B. Tunable Synthesis of Bismuth Ferrites with Various Morphologies. *Adv. Mater.* **2006**, *18* (16), 2145–2148. https://doi.org/10.1002/adma.200600072.

(237) Zhang, H.; Kajiyoshi, K. Hydrothermal Synthesis and Size-Dependent Properties of Multiferroic Bismuth Ferrite Crystallites. *J. Am. Ceram. Soc.* **2010**, *93* (11), 3842–3849. https://doi.org/10.1111/j.1551-2916.2010.03953.x.

(238) Sun, X.; Liu, Z.; Yu, H.; Zheng, Z.; Zeng, D. Facile Synthesis of BiFeO3 Nanoparticles by Modified Microwave-Assisted Hydrothermal Method as Visible Light Driven Photocatalysts. *Mater. Lett.* **2018**, *219*, 225–228. https://doi.org/10.1016/j.matlet.2018.02.052.

(239) Wang, X.; Lin, Y.; Ding, X.; Jiang, J. Enhanced Visible-Light-Response Photocatalytic Activity of Bismuth Ferrite Nanoparticles. *J. Alloys Compd.* **2011**, *509* (23), 6585–6588.

https://doi.org/10.1016/j.jallcom.2011.03.074.

(240) Das, N.; Majumdar, R.; Sen, A.; Maiti, H. S. Nanosized Bismuth Ferrite Powder Prepared through Sonochemical and Microemulsion Techniques. *Mater. Lett.* **2007**, *61* (10), 2100–2104. https://doi.org/10.1016/j.matlet.2006.08.026.

(241) Wang, Y.; Hu, Y.; Fei, L.; Zhang, Y.; Yuan, J.; Gu, H. Synthesis of Bismuth Ferrite Nanoparticles via a Wet Chemical Route at Low Temperature. *J. Nanomater.* **2011**, *2011*. https://doi.org/10.1155/2011/797639.

(242) Siebeneicher, S.; Waag, F.; Castillo, M. E.; Shvartsman, V. V.; Lupascu, D. C.; Gökce, B. Laser Fragmentation Synthesis of Colloidal Bismuth Ferrite Particles. *Nanomaterials* **2020**, *10* (2). https://doi.org/10.3390/nano10020359.

(243) Ghosh, S.; Dasgupta, S.; Sen, A.; Maiti, H. S. Low Temperature Synthesis of Bismuth Ferrite Nanoparticles by a Ferrioxalate Precursor Method. *Mater. Res. Bull.* **2005**, *40* (12), 2073–2079. https://doi.org/10.1016/j.materresbull.2005.07.017.

(244) Sachse, E.; Escobar-Castillo, M.; Waag, F.; Bilal Gökce; Salamon, S.; Landers, J.; Wende, H.; Lupascu, D. C. Laser Ablation of NiFe2O4 and CoFe2O4 Nanoparticles. *Nanomaterials* **2022**, *12* (1872), 1–13. https://doi.org/10.1007/s10948-021-05968-x.

(245) Huang, H.; Lai, J.; Lu, J.; Li, Z. Pulsed Laser Ablation of Bulk Target and Particle Products in Liquid for Nanomaterial Fabrication. *AIP Adv.* **2019**, *9* (1). https://doi.org/10.1063/1.5082695.

(246) S. Reich, A. Letzel, A. Menzel, N. Kretzschmar, B. Gokce, S. B. and A. P. Nanoscale Pulsed Laser Ablation in Liquids Dynamics. *Nanoscale* **2019**, *11*, 6962–6969. https://doi.org/10.1039/c9nr01203f.

(247) Sternlicht, H.; Rheinheimer, W.; Mehlmann, A.; Rothchild, A.; Hoffmann, M. J.; Kaplan, W. D. The Mechanism of Grain Growth in SrTiO3. *GRC Conf. Solid State Stud. Ceram.* **2018**.

(248) Bokov, D.; Turki Jalil, A.; Chupradit, S.; Suksatan, W.; Javed Ansari, M.; Shewael, I. H.; Valiev, G. H.; Kianfar, E. Nanomaterial by Sol-Gel Method: Synthesis and Application. *Adv. Mater. Sci. Eng.* **2021**, *2021*. https://doi.org/10.1155/2021/5102014.

(249) Walton, R. I. Perovskite Oxides Prepared by Hydrothermal and Solvothermal Synthesis: A Review of Crystallisation, Chemistry, and Compositions. *Chem. - A Eur. J.* **2020**, *26* (42), 9041–9069. https://doi.org/10.1002/chem.202000707.

(250) Castillo, M. E.; Shvartsman, V. V.; Gobeljic, D.; Gao, Y.; Landers, J.; Wende, H.; Lupascu, D. C. Effect of Particle Size on Ferroelectric and Magnetic Properties of BiFeO3 Nanopowders. *Nanotechnology* **2013**, *24* (35). https://doi.org/10.1088/0957-4484/24/35/355701.

(251) Chen (1996) - Grain Growth in CeO2 - Dopant Effects, Defect Mechanism and Solute Drag.Pdf.

(252) Caballero, A. C.; Fernändez, J. F.; Moure, C.; Durán, P.; Fierro, J. L. G. Dopant Distribution and Grain Growth Control in BaTiO3 Ceramics Doped with ZnO-SiO2-P2O5. *J. Eur. Ceram. Soc.* **1997**, *17* (10), 1223–1230. https://doi.org/10.1016/s0955-2219(96)00230-0.

(253) Bodišová, K.; Galusek, D.; Švančárek, P.; Pouchlý, V.; Maca, K. Grain Growth Suppression in Alumina via Doping and Two-Step Sintering. *Ceram. Int.* **2015**, *41* (9), 11975–11983. https://doi.org/10.1016/j.ceramint.2015.05.162.

(254) Milak, P.; Minatto, F. D.; Faller, C.; De Noni, A.; Klegues Montedo, O. R. The Influence of Dopants in the Grain Size of Alumina - A Review. *Mater. Sci. Forum* **2015**, *820* (September), 280–284. https://doi.org/10.4028/www.scientific.net/MSF.820.280.

(255) Masahiro Yoshimura. History of Hydrothermal. *Handb. Hydrothermal Technol.* **2001**, 53–81.

(256) Gan, Y. X.; Jayatissa, A. H.; Yu, Z.; Chen, X.; Li, M. Hydrothermal Synthesis of Nanomaterials. *J. Nanomater.* **2020**, *2020*. https://doi.org/10.1155/2020/8917013.

(257) Chen, C.; Cheng, J.; Yu, S.; Che, L.; Meng, Z. Hydrothermal Synthesis of Perovskite Bismuth Ferrite Crystallites. *J. Cryst. Growth* **2006**, *291* (1), 135–139. https://doi.org/10.1016/j.jcrysgro.2006.02.048.

(258) Zhou, M.; Li, W.; Du, Y.; Kong, D.; Wang, Z.; Meng, Y.; Sun, X.; Yan, T.; Kong, D.; You, J. Hydrothermal Synthesis of Bismuth Ferrite Fenton-like Catalysts and Their Properties. *J. Nanoparticle Res.* **2016**, *18* (11). https://doi.org/10.1007/s11051-016-3665-x.

(259) Bucci, G.; Gadelrab, K.; Carter, W. C. Mesoscale Model for Ostwald Ripening of Catalyst Nanoparticles. *J. Electrochem. Soc.* **2021**, *168* (5), 054515. https://doi.org/10.1149/1945-7111/abf970.

(260) Viswanatha, R.; Sarma, D. D. *Growth of Nanocrystals in Solution*; 2007. https://doi.org/10.1002/9783527611362.ch4.

(261) Baldan, A. Progress in Ostwald Ripening Theories and Their Applications to Nickel-Base Superalloys. Part I: Ostwald Ripening Theories. *J. Mater. Sci.* **2002**, *37*, 2171–2202.

(262) Ostwald, W. *Lehrbuch Der Allgemeinen Chemie*; W. Engelmann: Leipzig, Germany, 1896; Vol. 2.

(263) Wagner, C. L. Theorie Der Alterung von Niederschlägen Durch Umlösen (Ostwald-Reifung). *Zeitschrift für Elektrochemie, Berichte der Bunsengesellschaft für Phys. Chemie* **1961**, 581–591. https://doi.org/DOI:10.1002/BBPC.19610650704.

(264) Navas, D.; Fuentes, S.; Castro-alvarez, A. Review on Sol-Gel Synthesis of Perovskite and Oxide Nanomaterials. **2021**.

(265) M P Pechini. Method of Preparing Lead and Alkaline Earth Titanates and Niobates and Coating Method Using the Same to Form a Capacitor, 1967.

(266) Olav, T.; Sunde, L.; Grande, T.; Einarsrud, M. *Modified Pechini Synthesis of Oxide Powders and Thin Films*; Klein, L., Aparicio, M., Jitianu, A., Eds.; 2016. https://doi.org/10.1007/978-3-319-19454-7.

(267) Barcikowski, S., Amendola, V., Lau, M., Marzun, G., Rehbock, C., Reichenberger, S., Zhang, D., Gökce, B. *Handbook of & Processing of Colloids*, Second.; Duisburg-Essen Publications online, 2019. https://doi.org/https://doi.org/10.17185/duepublico/70584.

(268) Zhang, D.; Gökce, B.; Barcikowski, S. Laser Synthesis and Processing of Colloids: Fundamentals and Applications. *Chem. Rev.* **2017**, *117* (5), 3990–4103. https://doi.org/10.1021/acs.chemrev.6b00468.

(269) Kruusing, A. Underwater and Water-Assisted Laser Processing: Part 2-Etching, Cutting and Rarely Used Methods. *Opt. Lasers Eng.* **2004**, *41*, 329–352.

(270) Kang, H. W.; Lee, H.; Welch, A. J. Laser Ablation in a Liquid-Confined Environment Using a Nanosecond Laser Pulse. *J. Appl. Phys.* **2008**, *103*, 1–6. https://doi.org/10.1063/1.2905314.

(271) Hwang, D. J.; Choi, T. Y.; Grigoropoulos, C. P. Liquid-Assisted Femtosecond Laser Drilling of Straight and Three-Dimensional Microchannels in Glass. *Appl. Phys. A Mater. Sci. Process.* **2004**, *79*, 605–612. https://doi.org/10.1007/s00339-004-2547-8.

(272) Rehbock, C.; Jakobi, J.; Gamrad, L.; van der Meer, S.; Tiedemann, D.; Taylor, U.; Kues, W.; Rath, D.; Barcikowski, S. Current State of Laser Synthesis of Metal and Alloy Nanoparticles as Ligand-Free Reference Materials for Nano-Toxicological Assays. *Beilstein J. Nanotechnol.* **2014**, *5*, 1523–1541. https://doi.org/10.3762/bjnano.5.165.

(273) Lam, J.; Lombard, J.; Dujardin, C.; Ledoux, G.; Merabia, S.; Amans, D. Dynamical Study of Bubble Expansion Following Laser Ablation in Liquids. *Appl. Phys. Lett.* **2016**, *108*, 1–5. https://doi.org/10.1063/1.4942389.

(274) Kang, H. W.; Lee, H.; Welch, A. J. Laser Ablation in a Liquid-Confined Environment Using a Nanosecond Laser Pulse. *J. Appl. Phys.* **2008**, *103* (8). https://doi.org/10.1063/1.2905314.

(275) Kim, K. K.; Roy, M.; Kwon, H.; Song, J. K.; Park, S. M. Laser Ablation Dynamics in Liquid Phase: The Effects of Magnetic Field and Electrolyte. *J. Appl. Phys.* **2015**, *117*, 1–7. https://doi.org/10.1063/1.4913253.

(276) Gregory Stacy, J.; Thomas Vestrand, W. Gamma-Ray Astronomy. *Encylopedia of Physical Science and Technology*; 1992; Vol. 6, pp 397–432. https://doi.org/10.1080/00107519208219534.

(277) Tanabe, R.; Nguyen, T. T. P.; Sugiura, T.; Ito, Y. Bubble Dynamics in Metal Nanoparticle Formation by Laser Ablation in Liquid Studied through High-Speed Laser Stroboscopic Videography. *Appl. Surf. Sci.* **2015**, *351*, 327–331. https://doi.org/10.1016/j.apsusc.2015.05.030.

(278) O'Malley, S. M.; Zinderman, B.; Schoeffling, J.; Jimenez, R.; Naddeo, J. J.; Bubb, D. M. Nanosecond Laser-Induced Shock Propagation in and above Organic Liquid and Solid Targets. *Chem. Phys. Lett.* **2014**, *615*, 30–34. https://doi.org/10.1016/j.cplett.2014.09.061.

(279) Tanabe, R.; Nguyen, T. T. P.; Sugiura, T.; Ito, Y. Bubble Dynamics in Metal Nanoparticle Formation by Laser Ablation in Liquid Studied through High-Speed Laser Stroboscopic Videography. *Appl. Surf. Sci.* **2015**, *351*, 327–331. https://doi.org/10.1016/j.apsusc.2015.05.030.

(280) Menéndez-Manjón, A.; Chichkov, B. N.; Barcikowski, S. Influence of Water Temperature on the Hydrodynamic Diameter of Gold Nanoparticles from Laser Ablation. *J. Phys. Chem. C* **2010**, *114*, 2499–2504. https://doi.org/10.1021/jp909897v.

(281) Tsuji, T.; Thang, D. H.; Okazaki, Y.; Nakanishi, M.; Tsuboi, Y.; Tsuji, M. Preparation of Silver Nanoparticles by Laser Ablation in Polyvinylpyrrolidone Solutions. *Appl. Surf. Sci.* **2008**, *254*, 5224–5230. https://doi.org/10.1016/j.apsusc.2008.02.048.

(282) Tomko, J.; Naddeo, J. J.; Jimenez, R.; Tan, Y.; Steiner, M.; Fitz-Gerald, J. M.; Bubb, D. M.; O'Malley, S. M. Size and Polydispersity Trends Found in Gold Nanoparticles Synthesized by Laser Ablation in Liquids. *Phys. Chem. Chem. Phys.* **2013**, *1* (1), 1–100. https://doi.org/10.1039/c5cp01965f.

(283) De Giacomo, A.; De Bonis, A.; Dell'aglio, M.; De Pascale, O.; Gaudiuso, R.; Orlando, S.; Santagata, A.; Senesi, G. S.; Taccogna, F.; Teghil, R. Laser Ablation of Graphite in Water in a Range of Pressure from 1 to 146 Atm Using Single and Double Pulse Techniques for the Production of Carbon Nanostructures. *J. Phys. Chem. C* **2011**, *115*, 5123–5130. https://doi.org/10.1021/jp109389c.

(284) Fazio, E.; Gökce, B.; De Giacomo, A.; Meneghetti, M.; Compagnini, G.; Tommasini, M.; Waag, F.; Lucotti, A.; Zanchi, C. G.; Ossi, P. M.; Dell'aglio, M.; D'urso, L.; Condorelli, M.; Scardaci, V.; Biscaglia, F.; Litti, L.; Gobbo, M.; Gallo, G.; Santoro, M.; Trusso, S.; Neri, F. Nanoparticles Engineering by Pulsed Laser Ablation in Liquids: Concepts and Applications. *Nanomaterials* **2020**, *10*, 1–50. https://doi.org/10.3390/nano10112317.

(285) Franzel, L.; Phumisithikul, K.; Bertino, M. F.; Carpenter, E. E. Synthesis of Multiphasic Inhomogeneous Mo/MoC Nanoparticles by Pulsed Laser Ablation. *J. Nanoparticle Res.* **2013**, *15*, 1–6. https://doi.org/10.1007/s11051-013-2032-4.

(286) Sasaki, K.; Takada, N. Liquid-Phase Laser Ablation. *Pure Appl. Chem.* **2010**, *82* (6), 1317–1327. https://doi.org/10.1351/PAC-CON-09-10-23.

(287) Nath, A.; Khare, A. Laser-Induced High-Pressure and High-Temperature Conditions at the Titanium–Water Interface and Their Implication on TiO_2 Nanoparticles. *J. Opt. Soc. Am. B* **2012**, *29* (3), 351–356. https://doi.org/10.1364/josab.29.000351.

(288) Liu, Q. X.; Yang, G. W.; Zhang, J. X. Phase Transition between Cubic-BN and Hexagonal BN upon Pulsed Laser Induced Liquid-Solid Interfacial Reaction. *Chem. Phys. Lett.* **2003**, *373* (1–2), 57–61. https://doi.org/10.1016/S0009-2614(03)00580-3.

(289) Shih, C. Y.; Wu, C.; Shugaev, M. V.; Zhigilei, L. V. Atomistic Modeling of Nanoparticle Generation in Short Pulse Laser Ablation of Thin Metal Films in Water. *J. Colloid Interface Sci.* **2017**, *489*, 1–41. https://doi.org/10.1016/j.jcis.2016.10.029.

(290) Nichols, W. T.; Sasaki, T.; Koshizaki, N. Laser Ablation of a Platinum Target in Water. II. Ablation Rate and Nanoparticle Size Distributions. *J. Appl. Phys.* **2006**, *100*, 1–6. https://doi.org/10.1063/1.2390641.

(291) Liu, H.; Chen, F.; Wang, X.; Yang, Q.; Bian, H.; Si, J.; Hou, X. Influence of Liquid Environments on Femtosecond Laser Ablation of Silicon. *Thin Solid Films* **2010**, *518*, 5188–5194. https://doi.org/10.1016/j.tsf.2010.04.043.

(292) Streubel, R.; Bendt, G.; Gökce, B. Pilot-Scale Synthesis of Metal Nanoparticles by High-Speed Pulsed Laser

Ablation in Liquids. *Nanotechnology* **2016**, *27* (20), 1–9. https://doi.org/10.1088/0957-4484/27/20/205602.

(293) De Giacomo, A.; Dell'Aglio, M.; Santagata, A.; Gaudiuso, R.; De Pascale, O.; Wagener, P.; Messina, G. C.; Compagnini, G.; Barcikowski, S. Cavitation Dynamics of Laser Ablation of Bulk and Wire-Shaped Metals in Water during Nanoparticles Production. *Phys. Chem. Chem. Phys.* **2013**, *15*, 3083–3092. https://doi.org/10.1039/c2cp42649h.

(294) Oseguera-Galindo, D. O.; Martínez-Benítez, A.; Chávez-Chávez, A.; Gómez-Rosas, G.; Pérez-Centeno, A.; Santana-Aranda, M. A. Effects of the Confining Solvent on the Size Distribution of Silver NPs by Laser Ablation. *J. Nanoparticle Res.* **2012**, *14*, 1–6. https://doi.org/10.1007/s11051-012-1133-9.

(295) Bauer, F.; Michalowski, A.; Kiedrowski, T.; Nolte, S. Heat Accumulation in Ultra-Short Pulsed Scanning Laser Ablation of Metals. *Opt. Express* **2015**, *23* (2), 1035–1043. https://doi.org/10.1364/oe.23.001035.

(296) Dubey, A.; Ismadi, M.; Salamon, S.; Waag, F.; Gokce, B.; Escobar, M.; Wende, H.; Lupascu, D. C. Nanosecond Laser Ablation in Liquid for the Synthesis of Multiferroic Doped BFO Nanoparticles. *Submitted* **2023**.

(297) Zaaba, N. I.; Foo, K. L.; Hashim, U.; Tan, S. J.; Liu, W. W.; Voon, C. H. Synthesis of Graphene Oxide Using Modified Hummers Method: Solvent Influence. *Procedia Eng.* **2017**, *184*, 469–477. https://doi.org/10.1016/j.proeng.2017.04.118.

(298) Matthey, J. *Magnetic Susceptibility*; 2004.

(299) Meyers, H. P. *Introductory Solid State Physics*, second.; Taylor & Francis, 1997.

(300) Saburo Mori. Magnetic Properties of Several Phases of Barium Orthoferrite BaFeOx. *J. Phys. Soc. Japan* **1970**, *28* (1), 1–7. https://doi.org/10.1143/JPSJ.28.44.

(301) Bagwaiya, T.; Khade, P.; Reshi, H. A.; Bhattacharya, S.; Shelke, V.; Kaur, M.; Debnath, A. K.; Muthe, K. P.; Gadkari, S. C. Investigation on Gas Sensing Properties of Ag Doped BiFeO3. *AIP Conf. Proc.* **2018**, *1942*, 1–5. https://doi.org/10.1063/1.5028910.

(302) Albino, G. M.; Perales-Pérez, O.; Renteria-Beleño, B.; Cedeño-Mattei, Y. Effect of Ca and Ag Doping on the Functional Properties of BiFeO3 Nanocrystalline Powders and Films. *Mater. Res. Soc. Symp. Proc.* **2014**, *1675*, 105–111. https://doi.org/10.1557/opl.2014.778.

(303) Li, Q.; Zhang, W.; Wang, C.; Ma, J.; Ning, L.; Fan, H. Ag Modified Bismuth Ferrite Nanospheres as a Chlorine Gas Sensor. *RSC Adv.* **2018**, *8* (58), 33156–33163. https://doi.org/10.1039/C8RA06247A.

(304) Newman, D. The Orbit-Lattice Interaction for Lanthanide Ions. I. Determination of Empirical Parameters. *Aust. J. Phys.* **1978**, *31* (1), 79. https://doi.org/10.1071/ph780079.

(305) Grieshammer, S. The Effect of Defect Interactions on the Reduction of Doped Ceria. *Phys. Chem. Chem. Phys.* **2021**, *23* (17), 10321–10325. https://doi.org/10.1039/d1cp00925g.

(306) Kuo, J. J.; Wood, M.; Slade, T. J.; Kanatzidis, M. G.; Snyder, J. Systematic Over-Estimation of Lattice Thermal Conductivity in Materials with Electrically-Resistive Grain Boundaries. *Energy Environ. Sci.* **2020**, *13*, 1250–1258.

(307) Biesinger, M. C.; Payne, B. P.; Grosvenor, A. P.; Lau, L. W. M.; Gerson, A. R.; Smart, R. S. C. Resolving Surface Chemical States in XPS Analysis of First Row Transition Metals, Oxides and Hydroxides: Cr, Mn, Fe, Co and Ni. *Appl. Surf. Sci.* **2011**, *257* (7), 2717–2730. https://doi.org/10.1016/j.apsusc.2010.10.051.

(308) Yamashita, T.; Hayes, P. Analysis of XPS Spectra of Fe 2+ and Fe 3+ Ions in Oxide Materials. *Appl. Surf. Sci.* **2008**, *254* (8), 2441–2449. https://doi.org/10.1016/j.apsusc.2007.09.063.

(309) Wandelt, K. Photoemission Studies of Adsorbed Oxygen and Oxide Layers. *Surf. Sci. Rep.* **1982**, *2* (1), 1–121. https://doi.org/10.1016/0167-5729(82)90003-6.

(310) Yin, L.; Adler, I.; Tsang, T.; Matienzo, L. J.; Grim, S. O. PARAMAGNETISM AND SHAKE-UP SATELLlTES IN X-RAY PHOTOELEflRON SPECTRA The Phenomenon of Satellites in the X-Ray Photo- Has Been Well

Documented . At Present , While There Is Consensus That These Satellites Originate from the Shake-up Process , the Details . **1974**, *24* (1).

(311) Gupta, R. P.; Sen, S. K. Calculation of Multiplet Structure of Core p -Vacancy Levels. II. *Phys. Rev. B* **1975**, *12* (1), 15–19. https://doi.org/10.1103/PhysRevB.12.15.

(312) Grosvenor, A. P.; Kobe, B. A.; Biesinger, M. C.; McIntyre, N. S. Investigation of Multiplet Splitting of Fe 2p XPS Spectra and Bonding in Iron Compounds. *Surf. Interface Anal.* **2004**, *36* (12), 1564–1574. https://doi.org/10.1002/sia.1984.

(313) Nascimento, V. B.; De Carvalho, V. E.; Paniago, R.; Soares, E. A.; Ladeira, L. O.; Pfannes, H. D. XPS and EELS Study of the Bismuth Selenide. *J. Electron Spectros. Relat. Phenomena* **1999**, *104* (1–3), 99–107. https://doi.org/10.1016/s0368-2048(99)00012-2.

(314) J. P. Schaffer, A. Saxena, S. D. Antolovich, T. H. Sanders, and J. S. B. W. *The Science and Design of Engineering Materials*; WCB/McGraw-Hill, 1999.

(315) Dubey, A.; Salamon, S.; Attanayake, S. B.; Ibrahim, S.; Landers, J.; Castillo, M. E.; Wende, H.; Srikanth, H.; Shvartsman, V. V; Lupascu, D. C. Rare-Earth Doped BiFe0.05Mn0.05O3 Nanoparticles for Potential Hyperthermia Applications. *Front. Bioeng. Biotechnol.* **2022**, 1–19.

(316) Firet, N. J.; Blommaert, M. A.; Burdyny, T.; Venugopal, A.; Bohra, D.; Longo, A.; Smith, W. A. Operando EXAFS Study Reveals Presence of Oxygen in Oxide-Derived Silver Catalysts for Electrochemical CO 2 Reduction. *J. Mater. Chem. A* **2019**, *7* (6), 2597–2607. https://doi.org/10.1039/c8ta10412c.

(317) Gholam, T.; Ablat, A.; Mamat, M.; Wu, R.; Aimidula, A.; Bake, M. A.; Zheng, L.; Wang, J.; Qian, H.; Wu, R.; Ibrahim, K. An Experimental Study of the Local Electronic Structure of B-Site Gallium Doped Bismuth Ferrite Powders. *Phys. Lett. Sect. A Gen. At. Solid State Phys.* **2017**, *381* (29), 2367–2373. https://doi.org/10.1016/j.physleta.2017.05.007.

(318) Wang, Z.; Wang, L. Role of Oxygen Vacancy in Metal Oxide Based Photoelectrochemical Water Splitting. *EcoMat* **2021**, *3* (1), 1–13. https://doi.org/10.1002/eom2.12075.

(319) Wang, Z.; Mao, X.; Chen, P.; Xiao, M.; Monny, S. A.; Wang, S.; Konarova, M.; Du, A.; Wang, L. Understanding the Roles of Oxygen Vacancies in Hematite-Based Photoelectrochemical Processes. *Angew. Chemie - Int. Ed.* **2019**, *58* (4), 1030–1034. https://doi.org/10.1002/anie.201810583.

(320) Barreca, D.; Gasparotto, A.; Milanov, A.; Tondello, E.; Devi, A.; Fischer, R. A. Nanostructured Dy2O3 Films: An XPS Investigation. *Surf. Sci. Spectra* **2007**, *14* (1), 52–59. https://doi.org/10.1116/11.20080702.

(321) Cullity B. D. Elements Of X Ray Diffraction https://archive.org/details/elementsofxraydi030864mbp/page/n8/mode/2up (accessed Jan 29, 2020).

(322) Dubey, A.; Castillo, M. E.; Shvartsman, V. V.; Lupascu, D. C.; Salamon, S.; Wende, H. Tuning the Optical, Structural and Multiferroic Properties of Bismuth Ferrite Nanoparticles by Doping with Ba. *IEEE* **2019**, 1–4. https://doi.org/10.1109/ISAF43169.2019.9034963.

(323) Chowdhury, Z. Z.; Akbarzadeh, O.; Sagadevan, S. Lattice Strain Analysis of a Mn-Doped CdSe QD System Using Crystallography Techniques. *Process. MDPI* **2019**, *7*, 639.

(324) Volkova, L. M.; Marinin, D. V. Crystal Chemistry Aspects of the Magnetically Induced Ferroelectricity InTbMn2O5 and BiMn2O5. *J. Phys. Condens. Matter* **2009**, *21* (1). https://doi.org/10.1088/0953-8984/21/1/015903.

(325) Volkova, L. M.; Marinin, D. V. Magnetoelectric Ordering of BiFeO3 from the Perspective of Crystal Chemistry. *J. Supercond. Nov. Magn.* **2011**, *24* (7), 2161–2177. https://doi.org/10.1007/s10948-011-1178-5.

(326) Modak, P.; Lahiri, D.; Sharma, S. M. Correlation between Structure and Ferromagnetism in Nano-BiFeO3. *J. Phys. Chem. C* **2016**, *120* (15), 8411–8416. https://doi.org/10.1021/acs.jpcc.6b02822.

(327) Laraib, I.; Carneiro, M. A.; Janotti, A. Untangling the Effects of Octahedral Rotation and Ionic Displacements on the Electronic Structure Of. *Phys. Rev. B* **2021**, *104* (3), 1–7.

https://doi.org/10.1103/PhysRevB.104.035159.

(328) Li, Y.; Tsang, S. C. E. Unusual Catalytic Properties of High-Energetic-Facet Polar Metal Oxides. *Acc. Chem. Res.* **2021**, *54* (2), 366–378. https://doi.org/10.1021/acs.accounts.0c00641.

(329) Pal, J.; Pal, T. Faceted Metal and Metal Oxide Nanoparticles: Design, Fabrication and Catalysis. *Nanoscale* **2015**, *7* (34), 14159–14190. https://doi.org/10.1039/c5nr03395k.

(330) Rudel, H. E.; Lane, M. K. M.; Muhich, C. L.; Zimmerman, J. B. Toward Informed Design of Nanomaterials: A Mechanistic Analysis of Structure-Property-Function Relationships for Faceted Nanoscale Metal Oxides. *ACS Nano* **2020**, *14* (12), 16472–16501. https://doi.org/10.1021/acsnano.0c08356.

(331) Kwon, S.; Messing, G. L. The Effect of Particle Solubility on the Strength of Nanocrystalline Agglomerates: Boehmite. *Nanostructured Mater.* **1997**, *8* (4), 399–418. https://doi.org/10.1016/S0965-9773(97)00180-3.

(332) Gosens, I.; Post, J. A.; de la Fonteyne, L. J. J.; Jansen, E. H. J. M.; Geus, J. W.; Cassee, F. R.; de Jong, W. H. Impact of Agglomeration State of Nano- and Submicron Sized Gold Particles on Pulmonary Inflammation. *Part. Fibre Toxicol.* **2010**, *7* (1), 37. https://doi.org/10.1186/1743-8977-7-37.

(333) Sun, J.; Wang, F.; Sui, Y.; She, Z.; Zhai, W.; Wang, C.; Deng, Y. Effect of Particle Size on Solubility, Dissolution Rate, and Oral Bioavailability: Evaluation Using Coenzyme Q10 as Naked Nanocrystals. *Int. J. Nanomedicine* **2012**, *7*, 5733–5744. https://doi.org/10.2147/IJN.S34365.

(334) Dang, T. T.; Schell, J.; Boa, A. G.; Lewin, D.; Marschick, G.; Dubey, A.; Noll, C.; Beck, R.; Zyabkin, D. V; Glukhov, K.; Yap, I. C. J.; Gerami, A. M.; Lupascu, D. C. Temperature Dependence of the Local Electromagnetic Field at the Fe Site in Multiferroic Bismuth Ferrite. *Phys. Rev. B* **2022**, *054416*, 1–15. https://doi.org/10.1103/PhysRevB.106.054416.

(335) Ramazanoglu, M.; Ratcliff, W.; Yi, H. T.; Sirenko, A. A.; Cheong, S. W.; Kiryukhin, V. Giant Effect of Uniaxial Pressure on Magnetic Domain Populations in Multiferroic Bismuth Ferrite. *Phys. Rev. Lett.* **2011**, *107* (6). https://doi.org/10.1103/PhysRevLett.107.067203.

(336) Quickel, T. E.; Schelhas, L. T.; Farrell, R. A.; Petkov, N.; Le, V. H.; Tolbert, S. H. Mesoporous Bismuth Ferrite with Amplified Magnetoelectric Coupling and Electric Field-Induced Ferrimagnetism. *Nat. Commun.* **2015**, *6*, 1–7. https://doi.org/10.1038/ncomms7562.

(337) Ramesh, R. Electric Field Control of Magnetism Using Multiferroic Bismuth Ferrite. *Funtai Oyobi Fummatsu Yakin/Journal Japan Soc. Powder Powder Metall.* **2014**, *61* (SUPLL.1). https://doi.org/10.2497/jjspm.61.S19.

(338) Ramesh, R. Electric Field Control of Magnetism Using Multiferroic Bismuth Ferrite. *J. Japan Soc. Powder Powder Metall.* **2014**, *61* (S1), S19–S24. https://doi.org/10.2497/jjspm.61.s19.

(339) Ahmad, T.; Jindal, K.; Tomar, M.; Jha, P. K. Theoretical Insight of Origin of Rashba-Dresselhaus Effect in Tetragonal and Rhombohedral Phases of BiFeO3. *Phys. Chem. Chem. Phys.* **2023**, *25* (7), 5857–5868. https://doi.org/10.1039/d2cp04852c.

(340) Salak, A. N.; Cardoso, J. P. V.; Vieira, J. M.; Shvartsman, V. V.; Khalyavin, D. D.; Fertman, E. L.; Fedorchenko, A. V.; Pushkarev, A. V.; Radyush, Y. V.; Olekhnovich, N. M.; Tarasenko, R.; Feher, A.; Čižmár, E. Magnetic Behaviour of Perovskite Compositions Derived from BiFeO3. *Magnetochemistry* **2021**, *7* (11), 1–12. https://doi.org/10.3390/magnetochemistry7110151.

(341) Yin, L.; Mi, W. Progress in BiFeO3-Based Heterostructures: Materials, Properties and Applications. *Nanoscale* **2020**, *12* (2), 477–523. https://doi.org/10.1039/c9nr08800h.

(342) Bukharaev, A. A.; Zvezdin, A. K.; Pyatakov, A. P.; Fetisov, Y. K. Straintronics: A New Trend in Micro- and Nanoelectronics and Material Science. *Uspekhi Fiz. Nauk* **2018**, *188* (12), 1288–1330. https://doi.org/10.3367/ufnr.2018.01.038279.

(343) Liu, Y. Q.; Wang, Y. J.; Zhang, J.; Wu, Y. H.; Zhang, Y. J.; Wei, M. B.; Yang, J. H. The Effect of Structural Phase Transition on the Magnetic Properties of BiFeO3 Thin Films. *J. Mater. Sci. Mater. Electron.* **2015**,

26 (3), 1283–1290. https://doi.org/10.1007/s10854-014-2608-5.

(344) Sando, D.; Barthélémy, A.; Bibes, M. BiFeO3 Epitaxial Thin Films and Devices: Past, Present and Future. *J. Phys. Condens. Matter* **2014**, *26* (47). https://doi.org/10.1088/0953-8984/26/47/473201.

(345) Hu, W.; Chen, Y.; Yuan, H.; Li, G.; Qiao, Y.; Qin, Y.; Feng, S. Structure, Magnetic, and Ferroelectric Properties of Bi1-XGdxFeO3 Nanoparticles. *J. Phys. Chem. C* **2011**, *115*, 8869–8875.

(346) Mohan, S.; Subramanian, B.; Bhaumik, I.; Gupta, P. K.; Jaisankar, S. N. Nanostructured Bi(1-x)Gd(x)FeO3-a Multiferroic Photocatalyst on Its Sunlight Driven Photocatalytic Activity. *RSC Adv.* **2014**, *4* (32), 16871–16878. https://doi.org/10.1039/c4ra00137k.

(347) Qian, F. Z.; Jiang, J. S.; Jiang, D. M.; Wang, C. M.; Zhang, W. G. Improved Multiferroic Properties and a Novel Magnetic Behavior of Bi 0.8La0.2Fe1-XCoxO3 Nanoparticles. *J. Magn. Magn. Mater.* **2010**, *322* (20), 3127–3130. https://doi.org/10.1016/j.jmmm.2010.05.045.

(348) Arora, M.; Sati, P. C.; Chauhan, S.; Singh, H.; Yadav, K. L.; Chhoker, S.; Kumar, M. Structural, Magnetic and Optical Properties of Bi1-XDy XFeO3 Nanoparticles Synthesized by Sol-Gel Method. *Mater. Lett.* **2013**, *96*, 71–73. https://doi.org/10.1016/j.matlet.2012.12.114.

(349) Muneeswaran, M.; Giridharan, N. V. Effect of Dy-Substitution on the Structural, Vibrational, and Multiferroic Properties of BiFeO 3 Nanoparticles. *J. Appl. Phys.* **2014**, *214109* (115), 1–10.

(350) Zhang, Q.; Sando, D.; Nagarajan, V. Chemical Route Derived Bismuth Ferrite Thin Films and Nanomaterials. *J. Mater. Chem. C* **2016**, *4* (19), 4092–4124. https://doi.org/10.1039/c6tc00243a.

(351) Gautam, A.; Singh, K.; Sen, K.; Kotnala, R. K.; Singh, M. Crystal Structure and Magnetic Property of Nd Doped BiFeO3 Nanocrytallites. *Mater. Lett.* **2011**, *65* (4), 591–594. https://doi.org/10.1016/j.matlet.2010.11.002.

(352) Chaudhuri, A.; Mandal, K. Enhancement of Ferromagnetic and Dielectric Properties of Lanthanum Doped Bismuth Ferrite Nanostructures. *Mater. Res. Bull.* **2012**, *47* (4), 1057–1061. https://doi.org/10.1016/j.materresbull.2011.12.034.

(353) Chauhan, S.; Arora, M.; Sati, P. C.; Chhoker, S.; Katyal, S. C.; Kumar, M. Structural, Vibrational, Optical, Magnetic and Dielectric Properties of Bi1-XBaxFeO3 Nanoparticles. *Ceram. Int.* **2013**, *39* (6), 6399–6405. https://doi.org/10.1016/j.ceramint.2013.01.066.

(354) Chauhan, S.; Kumar, M.; Chhoker, S.; Katyal, S. C.; Singh, H.; Jewariya, M.; Yadav, K. L. Multiferroic, Magnetoelectric and Optical Properties of Mn Doped BiFeO 3 Nanoparticles. *Solid State Commun.* **2012**, *152* (6), 525–529. https://doi.org/10.1016/j.ssc.2011.12.037.

(355) Khan, U.; Adeela, N.; Javed, K.; Riaz, S.; Ali, H.; Iqbal, M.; Han, X. F.; Naseem, S. Influence of Cobalt Doping on Structural and Magnetic Properties of BiFeO3 Nanoparticles. *J. Nanoparticle Res.* **2015**, *17* (11), 1–9. https://doi.org/10.1007/s11051-015-3233-9.

(356) Godara, S.; Kumar, B. Effect of Ba-Nb Co-Doping on the Structural, Dielectric, Magnetic and Ferroelectric Properties of BiFeO3 Nanoparticles. *Ceram. Int.* **2015**, *41* (5), 6912–6919. https://doi.org/10.1016/j.ceramint.2015.01.145.

(357) Chauhan, S.; Kumar, M.; Chhoker, S.; Katyal, S. C.; Jewariya, M.; Suma, B. N.; Kunte, G. Structural Modification and Enhanced Magnetic Properties with Two Phonon Modes in Ca-Co Codoped BiFeO3 Nanoparticles. *Ceram. Int.* **2015**, *41* (10), 14306–14314. https://doi.org/10.1016/j.ceramint.2015.07.062.

(358) Vijayasundaram, S. V.; Suresh, G.; Mondal, R. A.; Kanagadurai, R. Substitution-Driven Enhanced Magnetic and Ferroelectric Properties of BiFeO3 Nanoparticles. *J. Alloys Compd.* **2016**, *658*, 726–731. https://doi.org/10.1016/j.jallcom.2015.10.250.

(359) Arya, G. S.; Sharma, R. K.; Negi, N. S. Enhanced Magnetic Properties of Sm and Mn Co-Doped BiFeO3 Nanoparticles at Room Temperature. *Mater. Lett.* **2013**, *93*, 341–344. https://doi.org/10.1016/j.matlet.2012.11.131.

(360) Seo, J. W.; Fullerton, E. E.; Nolting, F.; Scholl, A.; Fompeyrine, J.; Locquet, J. P. Antiferromagnetic LaFeO3 Thin Films and Their Effect on Exchange Bias. *J. Phys. Condens. Matter* **2008**, *20* (26). https://doi.org/10.1088/0953-8984/20/26/264014.

(361) Lahiri, D.; Chattopadhyay, S.; Kaduk, J.; Shibata, T.; Shevchenko, E. V.; Palkar, V. R. XAFS Investigation of the Correlation of Bi-Sublattice Disorder with Ferromagnetism of Multiferroic BiFeO 3 Nanoparticle. *Mater. Res. Express* **2019**, *6* (4). https://doi.org/10.1088/2053-1591/aaf9eb.

(362) Yan, X.; Wu, J.; Lei, X.; He, L.; Guo, W.; Kuang, X.; Yin, C. Magnetic Clusters and Ferromagnetic Spin Glass in the Novel Hexagonal Perovskite 12R-Ba4SbMn3O12. *RSC Adv.* **2023**, *13* (17), 11234–11240. https://doi.org/10.1039/d3ra00607g.

(363) Okajima, Y.; Kohn, K.; Siratori, K. Magnetic Relaxation and Possible Ferromagnetic Clusters in Defect Perovskite LaNiO2.70. *J. Magn. Magn. Mater.* **1995**, *140–144* (PART 3), 2149–2150. https://doi.org/10.1016/0304-8853(94)01404-3.

(364) Németh, Z.; Klencsár, Z.; Kuzmann, E.; Homonnay, Z.; Vértes, A.; Greneche, J. M.; Bódogh, M. Relaxation of Magnetic Clusters in Sr and Fe Doped Cobaltate Perovskites. *Hyperfine Interact.* **2008**, *184* (1–3), 63–68. https://doi.org/10.1007/s10751-008-9767-9.

(365) Mody, V. V; Singh, A.; Wesley, B. Basics of Magnetic Nanoparticles for Their Application in the Field of Magnetic Fluid Hyperthermia. *Eur. J. Nanomedicine* **2013**, *5* (1), 11–21. https://doi.org/10.1515/ejnm-2012-0008.

(366) Da Silva, K. L.; Trautwein, R. S.; Da Silva, R. B.; Fabián, M.; Čižmár, E.; Holub, M.; Skurikhina, O.; Harničárová, M.; Girman, V.; Menzel, D.; Becker, K. D.; Hahn, H.; Šepelák, V. Suppression of the Cycloidal Spin Arrangement in BiFeO3 Caused by the Mechanically Induced Structural Distortion and Its Effect on Magnetism. *Front. Mater.* **2021**, *8* (December), 1–9. https://doi.org/10.3389/fmats.2021.717185.

(367) Cotton, S. *Lanthanide and Actinide Chemistry*; 2006. https://doi.org/10.1002/0470010088.

(368) Sorace, L.; Gatteschi, D. Electronic Structure and Magnetic Properties of Lanthanide. *Wiley VCH* **2015**, *2*, 1–26. https://doi.org/10.1002/9783527673476.ch1.

(369) Huang, F.; Wang, Z.; Lu, X.; Zhang, J.; Min, K.; Lin, W.; Ti, R.; Xu, T.; He, J.; Yue, C.; Zhu, J. Peculiar Magnetism of BiFeO3 Nanoparticles with Size Approaching the Period of the Spiral Spin Structure. *Sci. Rep.* **2013**, *3*, 1–7. https://doi.org/10.1038/srep02907.

(370) Szafraniak-Wiza, I.; Andrzejewski, B.; Hilczerb, B. Magnetic Properties of Bismuth Ferrite Nanopowder Obtained by Mechanochemical Synthesis. *Acta Phys. Pol. A* **2014**, *126* (4), 1029–1031. https://doi.org/10.12693/APhysPolA.126.1029.

(371) Zhao, J.; Liu, T.; Xu, Y.; He, Y.; Chen, W. Synthesis and Characterization of Bi2Fe4O9 Powders. *Mater. Chem. Phys.* **2011**, *128* (3), 388–391. https://doi.org/10.1016/j.matchemphys.2011.03.011.

(372) C Blaauw, F. van der W. Magnetic and Structural Properties of BiFeO3. *J. Phys. C Solid State Phys* **1973**, *6*, 1422–1431.

(373) Sando, D.; Agbelele, A.; Rahmedov, D.; Liu, J.; Rovillain, P.; Toulouse, C.; Infante, I. C.; Pyatakov, A. P.; Fusil, S.; Jacquet, E.; Carrétéro, C.; Deranlot, C.; Lisenkov, S.; Wang, D.; Le Breton, J. M.; Cazayous, M.; Sacuto, A.; Juraszek, J.; Zvezdin, A. K.; Bellaiche, L.; Dkhil, B.; Barthélémy, A.; Bibes, M. Crafting the Magnonic and Spintronic Response of BiFeO3 Films by Epitaxial Strain. *Nat. Mater.* **2013**, *12* (7), 641–646. https://doi.org/10.1038/nmat3629.

(374) Lebeugle, D.; Colson, D.; Forget, A.; Viret, M. Very Large Spontaneous Electric Polarization in BiFeO3 Single Crystals at Room Temperature and Its Evolution under Cycling Fields. *Appl. Phys. Lett.* **2007**, *91* (2), 10–13. https://doi.org/10.1063/1.2753390.

(375) Goodenough, J. B. Theory of the Role of Covalence in the Perovskite-Type Manganites [La,M(II)]MnO3. *Phys. Rev.* **1955**, *100* (2), 564–573. https://doi.org/10.1103/PhysRev.100.564.

(376) Goodenough, J. B. Magnetism and the Chemical Bond. *Intersci. Wiley New York* **1963**, *16*, 394.

(377) Wildeboer, R. R.; Southern, P.; Pankhurst, Q. A. On the Reliable Measurement of Specific Absorption Rates and Intrinsic Loss Parameters in Magnetic Hyperthermia Materials. *J. Phys. D. Appl. Phys.* **2014**, *47* (49). https://doi.org/10.1088/0022-3727/47/49/495003.

(378) Martinez-Boubeta, C.; Simeonidis, K.; Makridis, A.; Angelakeris, M.; Iglesias, O.; Guardia, P.; Cabot, A.; Yedra, L.; Estradé, S.; Peiró, F.; Saghi, Z.; Midgley, P. A.; Conde-Leborán, I.; Serantes, D.; Baldomir, D. Learning from Nature to Improve the Heat Generation of Iron-Oxide Nanoparticles for Magnetic Hyperthermia Applications. *Sci. Rep.* **2013**, *3*, 1–8. https://doi.org/10.1038/srep01652.

(379) Bai, X.; Wei, J.; Tian, B.; Liu, Y.; Reiss, T.; Guiblin, N.; Gemeiner, P.; Dkhil, B.; Infante, I. C. Size Effect on Optical and Photocatalytic Properties in BiFeO3 Nanoparticles. *J. Phys. Chem. C* **2016**, *120* (7), 3595–3601. https://doi.org/10.1021/acs.jpcc.5b09945.

(380) Neaton, J. B.; Ederer, C.; Waghmare, U. V.; Spaldin, N. A.; Rabe, K. M. First-Principles Study of Spontaneous Polarization in Multiferroic BiFeO 3. *Phys. Rev. B - Condens. Matter Mater. Phys.* **2005**, *71* (1), 1–8. https://doi.org/10.1103/PhysRevB.71.014113.

(381) Clark, S. J.; Robertson, J. Band Gap and Schottky Barrier Heights of Multiferroic BiFeO3. *Appl. Phys. Lett.* **2007**, *90* (13), 1–4. https://doi.org/10.1063/1.2716868.

(382) Ramirez, M. O.; Kumar, A.; Denev, S. A.; Podraza, N. J.; Xu, X. S.; Rai, R. C.; Chu, Y. H.; Seidel, J.; Martin, L. W.; Yang, S. Y.; Saiz, E.; Ihlefeld, J. F.; Lee, S.; Klug, J.; Cheong, S. W.; Bedzyk, M. J.; Auciello, O.; Schlom, D. G.; Ramesh, R.; Orenstein, J.; Musfeldt, J. L.; Gopalan, V. Magnon Sidebands and Spin-Charge Coupling in Bismuth Ferrite Probed by Nonlinear Optical Spectroscopy. *Phys. Rev. B - Condens. Matter Mater. Phys.* **2009**, *79* (22), 1–9. https://doi.org/10.1103/PhysRevB.79.224106.

(383) Pisarev, R. V.; Moskvin, A. S.; Kalashnikova, A. M.; Rasing, T. Charge Transfer Transitions in Multiferroic BiFeO3 and Related Ferrite Insulators. *Phys. Rev. B - Condens. Matter Mater. Phys.* **2009**, *79* (23), 1–16. https://doi.org/10.1103/PhysRevB.79.235128.

(384) Moubah, R.; Schmerber, G.; Rousseau, O.; Colson, D.; Viret, M. Photoluminescence Investigation of Defects and Optical Band Gap in Multiferroic BiFeO 3 Single Crystals. *Appl. Phys. Express* **2012**, *5* (3), 3–6. https://doi.org/10.1143/APEX.5.035802.

(385) Palai, R.; Katiyar, R. S.; Schmid, H.; Tissot, P.; Clark, S. J.; Robertson, J.; Redfern, S. A. T.; Catalan, G.; Scott, J. F. Alpha Phase and Gamma-Beta Metal-Insulator Transition in Multiferroic BiFeO3. *Phys. Rev. B* **2008**, *77* (1), 014110. https://doi.org/10.1103/PhysRevB.77.014110.

(386) Kumar, A.; Rai, R. C.; Podraza, N. J.; Denev, S.; Ramirez, M.; Chu, Y. H.; Martin, L. W.; Ihlefeld, J.; Heeg, T.; Schubert, J.; Schlom, D. G.; Orenstein, J.; Ramesh, R.; Collins, R. W.; Musfeldt, J. L.; Gopalan, V. Linear and Nonlinear Optical Properties of BiFeO3. *Appl. Phys. Lett.* **2008**, *92* (12), 1–4. https://doi.org/10.1063/1.2901168.

(387) Burns, R. G. *Mineralogical Applications of Crystal Field Theory*, second edi.; Cambridge University Press, 1993. https://doi.org/10.1017/CBO9780511524899.

(388) Wei, J.; Wu, C.; Liu, Y.; Guo, Y.; Yang, T.; Wang, D.; Xu, Z.; Haumont, R. Structural Distortion, Spin-Phonon Coupling, Interband Electronic Transition, and Enhanced Magnetization in Rare-Earth-Substituted Bismuth Ferrite. *Inorg. Chem.* **2017**, *56* (15), 8964–8974. https://doi.org/10.1021/acs.inorgchem.7b00914.

(389) Dubey, A.; Castillo, M. E.; Landers, J.; Salamon, S.; Wende, H.; Hagemann, U.; Gemeiner, P.; Dkhil, B.; Shvartsman, V. V; Lupascu, D. C. E Ff Ect of Mn and Ba Codoping on a Magnetic Spin Cycloid of Multiferroic Bismuth Ferrite Nanoparticles. **2020**. https://doi.org/10.1021/acs.jpcc.0c05778.

(390) Cheng, H.; Feng, Y.; Fu, Y.; Zheng, Y.; Shao, Y.; Bai, Y. Understanding and Minimizing Non-Radiative Recombination Losses in Perovskite Light-Emitting Diodes. *J. Mater. Chem. C* **2022**, *10* (37), 13590–13610. https://doi.org/10.1039/d2tc01869a.

(391) Wang, Y.; Zhang, M.; Liu, J.; Zhang, H.; Li, F.; Tseng, C. W.; Yang, B.; Smith, G.; Zhai, J.; Zhang, Z.; Dunn, S.; Yan, H. Domain Wall Free Polar Structure Enhanced Photodegradation Activity in Nanoscale

Ferroelectric BaxSr1-XTiO3. *Adv. Energy Mater.* **2020**, *10* (38). https://doi.org/10.1002/aenm.202001802.

(392) Zhang, T.; Lei, W.; Liu, P.; Rodriguez, J. A.; Yu, J.; Qi, Y.; Liu, G.; Liu, M. Insights into the Structure-Photoreactivity Relationships in Well-Defined Perovskite Ferroelectric KNbO3 Nanowires. *Chem. Sci.* **2015**, *6* (7), 4118–4123. https://doi.org/10.1039/c5sc00766f.

(393) Kreisel, J.; Alexe, M.; Thomas, P. A. A Photoferroelectric Material Is More than the Sum of Its Parts. *Nat. Mater.* **2012**, *11* (4), 260. https://doi.org/10.1038/nmat3282.

(394) Fina, I.; Paillard, C.; Dkhil, B. Photoferroelectric Oxides. **2017**, 1–10.

(395) Li, Y.; Li, J.; Yang, W.; Wang, X. Implementation of Ferroelectric Materials in Photocatalytic and Photoelectrochemical Water Splitting. *Nanoscale Horizons* **2020**, *5* (8), 1174–1187. https://doi.org/10.1039/d0nh00219d.

(396) Wang, W.; Huang, B.; Ma, X.; Wang, Z.; Qin, X.; Zhang, X.; Dai, Y.; Whangbo, M. H. Efficient Separation of Photogenerated Electron-Hole Pairs by the Combination of a Heterolayered Structure and Internal Polar Field in Pyroelectric BiOIO3 Nanoplates. *Chem. - A Eur. J.* **2013**, *19* (44), 14777–14780. https://doi.org/10.1002/chem.201302884.

(397) Cui, Y.; Briscoe, J.; Dunn, S. Effect of Ferroelectricity on Solar-Light-Driven Photocatalytic Activity of BaTiO3 - Influence on the Carrier Separation and Stern Layer Formation. *Chem. Mater.* **2013**, *25* (21), 4215–4223. https://doi.org/10.1021/cm402092f.

(398) Kalinin, S. V.; Bonnell, D. A.; Alvarez, T.; Lei, X.; Hu, Z.; Ferris, J. H.; Zhang, Q.; Dunn, S. Atomic Polarization and Local Reactivity on Ferroelectric Surfaces: A New Route toward Complex Nanostructures. *Nano Lett.* **2002**, *2* (6), 589–593. https://doi.org/10.1021/nl025556u.

(399) Bhardwaj, A.; Burbure, N. V.; Rohrer, G. S. Enhanced Photochemical Reactivity at the Ferroelectric Phase Transition in Ba1-XSrxTiO3. *J. Am. Ceram. Soc.* **2010**, *93* (12), 4129–4134. https://doi.org/10.1111/j.1551-2916.2010.04002.x.

(400) Peter, L. M. Photoelectrochemistry: From Basic Principles to Photocatalysis. *RSC Energy Environ. Ser.* **2016**, No. 14, 1–28. https://doi.org/10.1039/9781782622338-00001.

(401) Nasrollahzadeh, M.; Sajjadi, M.; Iravani, S.; Varma, R. S. Green-Synthesized Nanocatalysts and Nanomaterials for Water Treatment: Current Challenges and Future Perspectives. *J. Hazard. Mater.* **2021**, *401* (May 2020), 123401. https://doi.org/10.1016/j.jhazmat.2020.123401.

(402) Thomas, N.; Dionysiou, D. D.; Pillai, S. C. Heterogeneous Fenton Catalysts: A Review of Recent Advances. *J. Hazard. Mater.* **2021**, *404*, 124082. https://doi.org/10.1016/j.jhazmat.2020.124082.

(403) M. J. G. Salazar. Development and Application of Titanium Dioxide Coated Magnetic Particles for Photocatalytic Oxidation of Aqueous Phase Organic Pollutants, Technischen Universität Berlin, Berlin, 2010.

(404) Fresno, F.; Portela, R.; Sú Arez, S.; Coronado, J. M. Photocatalytic Materials: Recent Achievements and near Future Trends. *J. Mater. Chem. A* **2014**, *2*, 2863. https://doi.org/10.1039/c3ta13793g.

(405) Lee, K. M.; Lai, C. W.; Ngai, K. S.; Juan, J. C. Recent Developments of Zinc Oxide Based Photocatalyst in Water Treatment Technology: A Review. *Water Res.* **2016**, *88*, 428–448. https://doi.org/10.1016/j.watres.2015.09.045.

(406) Xu, Q.; Sobhan, M.; Yang, Q.; Anariba, F.; Ong, K. P.; Wu, P. The Role of Bi Vacancies in the Electrical Conduction of BiFeO3:A First-Principles Approach. *Dalt. Trans.* **2014**, *43*, 10787. https://doi.org/10.1039/c4dt00468j.

(407) Irfan, S.; Zhuanghao, Z.; Li, F.; Chen, Y. X.; Liang, G. X.; Luo, J. T.; Ping, F. Critical Review: Bismuth Ferrite as an Emerging Visible Light Active Nanostructured Photocatalyst. *J. Mater. Res. Technol.* **2019**, *8* (6), 6375–6389. https://doi.org/10.1016/j.jmrt.2019.10.004.

(408) Gao, T.; Chen, Z.; Huang, Q.; Niu, F.; Huang, X.; Qin, L.; Huang, Y. A Review: Preparation of Bismuth Ferrite

Nanoparticles and Its Applications in Visible Light Induced Photocatalyses. *Rev. Adv. Mater. Sci* **2015**, *40*, 97–109.

(409) Dubey, A.; Escobar Castillo, M.; Landers, J.; Salamon, S.; Wende, H.; Hagemann, U.; Gemeiner, P.; Dkhil, B.; Shvartsman, V. V.; Lupascu, D. C. Supp-Effect of Mn and Ba Codoping on a Magnetic Spin Cycloid of Multiferroic Bismuth Ferrite Nanoparticles. *J. Phys. Chem. C* **2020**, *124* (40), 22266–22277. https://doi.org/10.1021/acs.jpcc.0c05778.

(410) Fridkin, V. M. *Photoferroelectrics*; New York Sciences, 1979.

(411) He, J.; Zhao, Y.; Jiang, S.; Song, S. Photocatalysis Within Intrinsic Spontaneous Polarization Electric Field. *Sol. RRL* **2020**, *2000446*, 1–16. https://doi.org/10.1002/solr.202000446.

(412) Huang, G.; Zhang, G.; Gao, Z.; Cao, J.; Li, D.; Yun, H.; Zeng, T. Enhanced Visible-Light-Driven Photocatalytic Activity of BiFeO3 via Electric-Field Control of Spontaneous Polarization. *J. Alloys Compd.* **2019**, *783*, 943–951. https://doi.org/10.1016/j.jallcom.2019.01.017.

(413) Lam, S. M.; Sin, J. C.; Mohamed, A. R. A Newly Emerging Visible Light-Responsive BiFeO3 Perovskite for Photocatalytic Applications: A Mini Review. *Mater. Res. Bull.* **2017**, *90*, 15–30. https://doi.org/10.1016/j.materresbull.2016.12.052.

(414) Mohan, S.; Subramanian, B.; Sarveswaran, G. A Prototypical Development of Plasmonic Multiferroic Bismuth Ferrite Particulate and Fiber Nanostructures and Their Remarkable Photocatalytic Activity under Sunlight. *J. Mater. Chem. C* **2014**, *2*, 6835. https://doi.org/10.1039/c4tc01038h.

(415) Bharathkumar, S.; Sakar, M.; Balakumar, S. Experimental Evidence for the Carrier Transportation Enhanced Visible Light Driven Photocatalytic Process in Bismuth Ferrite (BiFeO 3) One-Dimensional Fiber Nanostructures. *J. Phys. Chem. C* **2016**, *120*, 18811–18821. https://doi.org/10.1021/acs.jpcc.6b04344.

(416) Ruby, S.; Rosaline, D. R.; Inbanathan, S. S. R.; Anand, K.; Kavitha, G.; Srinivasan, R.; Umar, A.; Hegazy, H. H.; Algarni, H. Sunlight-Driven Photocatalytic Degradation of Methyl Orange Based on Bismuth Ferrite (BiFeO 3) Heterostructures Composed of Interconnected Nanosheets . *J. Nanosci. Nanotechnol.* **2019**, *20* (3), 1851–1858. https://doi.org/10.1166/jnn.2020.17174.

(417) Zhang, Y.; Schultz, A. M.; Salvador, P. A.; Rohrer, G. S. Spatially Selective Visible Light Photocatalytic Activity of TiO 2 /BiFeO 3 Heterostructures. *J. Mater. Chem.* **2011**, *21*, 4168. https://doi.org/10.1039/c0jm04313c.

(418) Soltani, T.; Lee, B. K. Sono-Synthesis of Nanocrystallized BiFeO3/Reduced Graphene Oxide Composites for Visible Photocatalytic Degradation Improvement of Bisphenol A. *Chem. Eng. J.* **2016**, *306*, 204–213. https://doi.org/10.1016/j.cej.2016.07.051.

(419) Prakash Bajpai, O.; Mandal, S.; Ananthakrishnan, R.; Mandal, P.; Khastgir, D.; Chattopadhyay, S. Structural Features, Magnetic Properties and Photocatalytic Activity of Bismuth Ferrite Nanoparticles Grafted on Graphene Nanosheets. *New J. Chem* **2018**, *42*, 10712. https://doi.org/10.1039/c8nj02030b.

(420) Fatima, S.; Ali, S. I.; Iqbal, M. Z. Congo Red Dye Degradation by Graphene Nanoplatelets / Doped Bismuth Ferrite Nanoparticle Hybrid Catalysts under Dark and Light Conditions. *Catalysts* **2020**, *10*, 367. https://doi.org/10.3390/catal10040367.

(421) Iqbal, M. A.; Tariq, A.; Zaheer, A.; Gul, S.; Ali, S. I.; Iqbal, M. Z.; Akinwande, D.; Rizwan, S. Ti 3 C 2-MXene/Bismuth Ferrite Nanohybrids for Efficient Degradation of Organic Dyes and Colorless Pollutants. *ACS Omega* **2019**, *4*, 20530–20539. https://doi.org/10.1021/acsomega.9b02359.

(422) Tong, H.; Ouyang, S.; Bi, Y.; Umezawa, N.; Oshikiri, M.; Ye, J. Nano-Photocatalytic Materials: Possibilities and Challenges. *Adv. Mater.* **2012**, *24* (2), 229–251. https://doi.org/10.1002/adma.201102752.

(423) Medhi, R.; Marquez, M. D.; Lee, T. R. Visible-Light-Active Doped Metal Oxide Nanoparticles: Review of Their Synthesis, Properties, and Applications. *ACS Appl. Nano Mater.* **2020**, *3*, 6156–6185. https://doi.org/10.1021/acsanm.0c01035.

(424) Zhang, N.; Chen, D.; Niu, F.; Wang, S.; Qin, L.; Huang, Y. Enhanced Visible Light Photocatalytic Activity of

Gd-Doped BiFeO 3 Nanoparticles and Mechanism Insight. *Sci. Rep.* **2016**, *6*, 26467. https://doi.org/10.1038/srep26467.

(425) Irfan, S.; Li, L.; Saleemi, A. S.; Nan, C.-W. Enhanced Photocatalytic Activity of La 3+ and Se 4+ Co-Doped Bismuth Ferrite Nanostructures †. *J. Mater. Chem. A* **2017**, *5*, 11143–11151. https://doi.org/10.1039/c7ta01847a.

(426) Irfan, S.; Rizwan, S.; Shen, Y.; Li, L.; Butt, S.; Nan, C.-W. The Gadolinium (Gd 3+) and Tin (Sn 4+) Co-Doped BiFeO 3 Nanoparticles as New Solar Light Active Photocatalyst. *Sci. Rep.* **2017**, *7*, 42493. https://doi.org/10.1038/srep42493.

(427) Esmaili, L.; Gholizadeh, A. The Effect of Nd and Zr Co-Substitution on Structural, Magnetic and Photocatalytic Properties of Bi1-XNdxFe1-XZrxO3 Nanoparticles. *Mater. Sci. Semicond. Process.* **2020**, *118*, 105179. https://doi.org/10.1016/j.mssp.2020.105179.

(428) Syed Irfan, Yang Shen, Syed Rizwan, Huan Chun Wang, Sadaf Khan, C. W. N. Band-Gap Engineering and Enhanced Photocatalytic Activity of Sm and Mn Doped BiFeO3 Nanoparticles. *J. Am. Ceram. Soc.* **2016**, *100*, 31–40. https://doi.org/10.1111/jace.14487.

(429) Sakar, M.; Balakumar, S.; Saravanan, P.; Bharathkumar, S. Compliments of Confinements: Substitution and Dimension Induced Magnetic Origin and Band-Bending Mediated Photocatalytic Enhancements in Bi1-XDyxFeO3 Particulate and Fiber Nanostructures. *Nanoscale* **2015**, *7* (24), 10667–10679. https://doi.org/10.1039/c5nr01079a.

(430) Maleki, H. Photocatalytic Activity, Optical and Ferroelectric Properties of Bi0.8Nd0.2FeO3 Nanoparticles Synthesized by Sol-Gel and Hydrothermal Methods. *J. Magn. Magn. Mater.* **2018**, *458*, 277–284. https://doi.org/10.1016/j.jmmm.2018.03.043.

(431) Sakar, M.; Balakumar, S.; Saravanan, P.; Bharathkumar, S. Particulates vs. Fibers: Dimension Featured Magnetic and Visible Light Driven Photocatalytic Properties of Sc Modified Multiferroic Bismuth Ferrite Nanostructures. *Nanoscale* **2016**, *8* (2), 1147–1160. https://doi.org/10.1039/c5nr06655g.

(432) Zhang, Y.; Yang, Y.; Dong, Z.; Shen, J.; Song, Q.; Wang, X.; Mao, W.; Pu, Y.; Li, X. Enhanced Photocatalytic Activity of Ba Doped BiFeO3 by Turning Morphologies and Band Gap. *J. Mater. Sci. Mater. Electron.* **2020**, *31* (18), 15007–15012. https://doi.org/10.1007/s10854-020-04064-5.

(433) Ponraj, C.; Vinitha, G.; Daniel, J. Visible Light Photocatalytic Activity of Mn-Doped BiFeO3 Nanoparticles. *Int. J. Green Energy* **2019**, *17* (1), 71–83. https://doi.org/10.1080/15435075.2019.1688158.

(434) Wang, H.-C.; Lin, Y.-H.; Feng, Y.-N.; Shen, Y. Photocatalytic Behaviors Observed in Ba and Mn Doped BiFeO 3 Nanofibers. *J. Electroceramics* **2013**, *31*, 271–274. https://doi.org/10.1007/s10832-013-9818-8.

(435) Feng, Y.-N.; Wang, H.-C.; Luo, Y.-D.; Shen, Y.; Lin, Y.-H. Ferromagnetic and Photocatalytic Behaviors Observed in Ca-Doped BiFeO 3 Nanofibres. *J. Appl. Phys* **2013**, *113*, 146101. https://doi.org/10.1063/1.4801796.

(436) Ingle, Jr. J. D, and Crouch, S. . R. *Spectrochemical Analysis*; 1988.

(437) Keith J. Laidler, J. H. M. *Physical Chemistry*; Benjamin-Cummings Pub Co, 1982.

(438) Ollis, D. F. Kinetics of Photocatalyzed Reactions: Five Lessons Learned. *Front. Chem.* **2018**, *6* (AUG), 1–7. https://doi.org/10.3389/fchem.2018.00378.

(439) Qiao, L.; Zhang, S.; Xiao, H. Y.; Singh, D. J.; Zhang, K. H. L.; Liu, Z. J.; Zu, X. T.; Li, S. Orbital Controlled Band Gap Engineering of Tetragonal BiFeO3 for Optoelectronic Applications. *J. Mater. Chem. C* **2018**, *6* (5), 1239–1247. https://doi.org/10.1039/c7tc04160h.

(440) Fang, L.; You, L.; Liu, J.-M. Ferroelectrics in Photocatalysis. *Ferroelectr. Mater. Energy Appl.* **2018**, 265–309. https://doi.org/10.1002/9783527807505.ch9.

(441) Jones, P. M.; Dunn, S. Photo-Reduction of Silver Salts on Highly Heterogeneous Lead Zirconate Titanate. *Nanotechnology* **2007**, *18*, 185702. https://doi.org/10.1088/0957-4484/18/18/185702.

(442) Brus, L. E. A Simple Model for the Ionization Potential, Electron Affinity, and Aqueous Redox Potentials of Small Semiconductor Crystallites. *J. Chem. Phys.* **1983**, *79* (11), 5566–5571. https://doi.org/10.1063/1.445676.

(443) Vincenzo Balzani; Paola Ceroni; Alberto Juris. *Photochemistry and Photophysics: Concepts, Research, Applications*; Wiley-VCH, 2014.

(444) Van Dijken, A.; Meulenkamp, E. A.; Vanmaekelbergh, D.; Meijerink, A. Influence of Adsorbed Oxygen on the Emission Properties of Nanocrystalline ZnO Particles. *J. Phys. Chem. B* **2000**, *104* (18), 4355–4360. https://doi.org/10.1021/jp993998x.

(445) Guo, H.; Ke, Y.; Wang, D.; Lin, K.; Shen, R.; Chen, J.; Weng, W. Efficient Adsorption and Photocatalytic Degradation of Congo Red onto Hydrothermally Synthesized NiS Nanoparticles. *J. Nanoparticle Res.* **2013**, *15* (1475), 1–12. https://doi.org/10.1007/s11051-013-1475-y.

(446) Chen, J.; Wu, J.; Sherrell, P. C.; Chen, J.; Wang, H.; Zhang, W. xian; Yang, J. How to Build a Microplastics-Free Environment: Strategies for Microplastics Degradation and Plastics Recycling. *Adv. Sci.* **2022**, *9* (6), 1–36. https://doi.org/10.1002/advs.202103764.

(447) Paluselli, A.; Aminot, Y.; Galgani, F.; Net, S.; Sempéré, R. Occurrence of Phthalate Acid Esters (PAEs) in the Northwestern Mediterranean Sea and the Rhone River. *Prog. Oceanogr.* **2017**, *163*, 221–231. https://doi.org/10.1016/j.pocean.2017.06.002.

(448) Weschler, C. J.; Salthammer, T.; Fromme, H. Partitioning of Phthalates among the Gas Phase, Airborne Particles and Settled Dust in Indoor Environments. *Atmos. Environ.* **2008**, *42* (7), 1449–1460. https://doi.org/10.1016/j.atmosenv.2007.11.014.

(449) Pelletier, M.; Glorennec, P.; Mandin, C.; Le Bot, B.; Ramalho, O.; Mercier, F.; Bonvallot, N. Chemical-by-Chemical and Cumulative Risk Assessment of Residential Indoor Exposure to Semivolatile Organic Compounds in France. *Environ. Int.* **2018**, *117* (October 2017), 22–32. https://doi.org/10.1016/j.envint.2018.04.024.

(450) Ghosh, S.; Sahu, M. Phthalate Pollution and Remediation Strategies: A Review. *J. Hazard. Mater. Adv.* **2022**, *6*, 100065. https://doi.org/10.1016/j.hazadv.2022.100065.

(451) Pang, X.; Skillen, N.; Gunaratne, N.; Rooney, D. W.; Robertson, P. K. J. Removal of Phthalates from Aqueous Solution by Semiconductor Photocatalysis : A Review. *J. Hazard. Mater.* **2021**, *402* (May 2020), 123461. https://doi.org/10.1016/j.jhazmat.2020.123461.

(452) Wang, C.; Zeng, T.; Gu, C.; Zhu, S.; Zhang, Q. Photodegradation Pathways of Typical Phthalic Acid Esters Under. **2019**, *7* (December), 1–11. https://doi.org/10.3389/fchem.2019.00852.

(453) Akbari-Adergani, B.; Saghi, M. H.; Eslami, A.; Mohseni-Bandpei, A.; Rabbani, M. Modeling and Optimization of a Nanophotocatalytic Process Using Fe, Ag-ZnO under Visible LED Irradiation for Dibutyl Phthalate Removal from Aqueous Environment. *Environ. Technol.* **2018**, *39* (12), 1566–1576. https://doi.org/10.1080/09593330.2017.1332693.

(454) Kumar, S. G.; Rao, K. S. R. K. Zinc Oxide Based Photocatalysis: Tailoring Surface-Bulk Structure and Related Interfacial Charge Carrier Dynamics for Better Environmental Applications. *RSC Adv.* **2015**, *5* (5), 3306–3351. https://doi.org/10.1039/c4ra13299h.

(455) Tasso Guaraldo, T.; Wenk, J.; Mattia, D. Photocatalytic ZnO Foams for Micropollutant Degradation. *Adv. Sustain. Syst.* **2021**, *5* (5). https://doi.org/10.1002/adsu.202000208.

(456) Liu, Y.; Sun, N.; Hu, J.; Li, S.; Qin, G. Photocatalytic Degradation Properties of α-Fe2 O3 Nanoparticles for Dibutyl Phthalate in Aqueous Solution System. *R. Soc. Open Sci.* **2018**, *5* (4), 172196. https://doi.org/10.1098/rsos.172196.

(457) Wang, Z.; Ma, H.; Zhang, C.; Feng, J.; Pu, S.; Ren, Y.; Wang, Y. Enhanced Catalytic Ozonation Treatment of Dibutyl Phthalate Enabled by Porous Magnetic Ag-Doped Ferrospinel MnFe2O4 Materials: Performance and Mechanism. *Chem. Eng. J.* **2018**. https://doi.org/10.1016/j.cej.2018.07.177.

(458) Malannata, E. M.; Spitaleri, L.; Gulino, A.; Balsamo, S. A.; Scirè, S.; Fiorenza, R. Removal of Phthalates from Water by Unconventional La-Based/WO3 Photocatalysts. *Eur. J. Inorg. Chem.* **2022**, No. 20, 1–11. https://doi.org/10.1002/ejic.202200183.

(459) Wang, C.; Zeng, T.; Gu, C.; Zhu, S.; Zhang, Q.; Luo, X. Photodegradation Pathways of Typical Phthalic Acid Esters Under UV, UV/TiO2, and UV-Vis/Bi2WO6 Systems. *Front. Chem.* **2019**, *7*, 1–11. https://doi.org/10.3389/fchem.2019.00852.

(460) Mitoraj, D.; Lamdab, U.; Kangwansupamonkon, W.; Pacia, M.; Macyk, W.; Wetchakun, N.; Beranek, R. Revisiting the Problem of Using Methylene Blue as a Model Pollutant in Photocatalysis: The Case of InVO4/BiVO4 Composites. *J. Photochem. Photobiol. A Chem.* **2018**, *366*, 103–110. https://doi.org/10.1016/j.jphotochem.2018.02.023.

(461) You, S.; Hu, Y.; Liu, X.; Wei, C. Synergetic Removal of Pb(II) and Dibutyl Phthalate Mixed Pollutants on Bi2O3-TiO2 Composite Photocatalyst under Visible Light. *Appl. Catal. B Environ.* **2018**, *232*, 288–298. https://doi.org/10.1016/j.apcatb.2018.03.025.

(462) Jamil, T. S.; Abbas, H. A.; Youssief, A. M.; Mansor, E. S.; Hammad, F. F. The Synthesis of Nano-Sized Undoped, Bi Doped and Bi, Cu Co-Doped SrTiO3 Using Two Sol–Gel Methods to Enhance the Photocatalytic Performance for the Degradation of Dibutyl Phthalate under Visible Light. *Comptes Rendus Chim.* **2017**, *20* (2), 97–106. https://doi.org/10.1016/j.crci.2016.05.022.

(463) He, G.; Zhang, J.; Hu, Y.; Bai, Z.; Wei, C. Dual-Template Synthesis of Mesoporous TiO2 Nanotubes with Structure-Enhanced Functional Photocatalytic Performance. *Appl. Catal. B Environ.* **2019**, *250*, 301–312. https://doi.org/10.1016/j.apcatb.2019.03.027.

(464) Liu, Y.; Sun, N.; Hu, J.; Li, S.; Qin, G. Photocatalytic Degradation Properties of α-Fe2 O3 Nanoparticles for Dibutyl Phthalate in Aqueous Solution System. *R. Soc. Open Sci.* **2018**, *5* (4). https://doi.org/10.1098/rsos.172196.

(465) Li, L.; Zhu, W.; Chen, L.; Zhang, P.; Chen, Z. Photocatalytic Ozonation of Dibutyl Phthalate over TiO2 Film. *J. Photochem. Photobiol. A Chem.* **2005**, *175* (2–3), 172–177. https://doi.org/10.1016/j.jphotochem.2005.01.020.

(466) Tang, B.; Chen, H.; Peng, H.; Wang, Z.; Huang, W. Graphene Modified TiO 2 Composite Photocatalysts : Mechanism , Progress and Perspective. **2018**, *8* (105), 27–30. https://doi.org/10.3390/nano8020105.

(467) Som, I.; Roy, M.; Saha, R. Advances in Nanomaterial-Based Water Treatment Approaches for Photocatalytic Degradation of Water Pollutants. *ChemCatChem* **2020**, *12* (13), 3409–3433. https://doi.org/10.1002/cctc.201902081.

(468) Liu, L.; Huang, H. Ferroelectrics in Photocatalysis. *Chem. - A Eur. J.* **2022**, *28* (16). https://doi.org/10.1002/chem.202103975.

(469) He, J.; Zhao, Y.; Jiang, S.; Song, S. Photocatalysis Within Intrinsic Spontaneous Polarization Electric Field. *Sol. RRL* **2021**, *5* (6), 1–16. https://doi.org/10.1002/solr.202000446.

(470) Xu, R.; Wang, Y.; Cui, D.; Du, K.; Shi, Z.; Zhang, H.; Xu, Z.; Hao, W.; Du, Y. Boosting Light-Driven Photocatalytic Water Splitting of Bi4NbO8Br by Polarization Field. *Sol. RRL* **2022**, *6* (9), 1–7. https://doi.org/10.1002/solr.202200365.

(471) Jiang, S.; Zhao, R.; Ren, Z.; Chen, X.; Tian, H.; Wie, X.; Li, X.; Shen, G.; Han, G. A Reduced Graphene Oxide (RGO)-Ferroelectrics Hybrid Nanocomposite as High Efficient Visible-Light-Driven Photocatalyst. *ChemistrySelect* **2016**, *1* (18), 6020–6025. https://doi.org/10.1002/slct.201601505.

(472) Zhang, Y.; Salvador, P. A.; Rohrer, G. S. Ferroelectric-Enhanced Photocatalysis with TiO2/BiFeO 3. *Energy Technol. 2014 Carbon Dioxide Manag. Other Technol.* **2014**, 15–24. https://doi.org/10.1002/9781118888735.ch2.

(473) He, J.; Liu, Y.; Qu, J.; Xie, H.; Lu, R.; Fan, F.; Li, C. Boosting Photocatalytic Water Oxidation on Photocatalysts with Ferroelectric Single-domain. *Adv. Mater.* **2023**, *2210374*, 2210374. https://doi.org/10.1002/adma.202210374.

(474) Chen, F.; Ren, Z.; Gong, S.; Li, X.; Shen, G.; Han, G. Selective Deposition of Silver Oxide on Single-Domain Ferroelectric Nanoplates and Their Efficient Visible-Light Photoactivity. *Chem. - A Eur. J.* **2016**, *22* (34), 12160–12165. https://doi.org/10.1002/chem.201601456.

(475) Li, Z.; Shen, Y.; Yang, C.; Lei, Y.; Guan, Y.; Lin, Y.; Liu, D.; Nan, C. W. Significant Enhancement in the Visible Light Photocatalytic Properties of BiFeO3-Graphene Nanohybrids. *J. Mater. Chem. A* **2013**, *1* (3), 823–829. https://doi.org/10.1039/c2ta00141a.

(476) Zeng, H.; Li, X.; Hao, W.; Zhang, L.; Wei, T.; Zhao, X.; Liu, Y.; Li, J. Determination of Phthalate Esters in Airborne Particulates by Heterogeneous Photo-Fenton Catalyzed Aromatic Hydroxylation Fluorimetry. *J. Hazard. Mater.* **2016**, *324-B*, 250–257. https://doi.org/10.1016/j.jhazmat.2016.10.055.

(477) Stobinski, L.; Lesiak, B.; Malolepszy, A.; Mazurkiewicz, M.; Mierzwa, B.; Zemek, J.; Jiricek, P.; Bieloshapka, I. Graphene Oxide and Reduced Graphene Oxide Studied by the XRD, TEM and Electron Spectroscopy Methods. *J. Electron Spectros. Relat. Phenomena* **2014**, *195* (August), 145–154. https://doi.org/10.1016/j.elspec.2014.07.003.

(478) Ren, Y.; Nan, F.; You, L.; Zhou, Y.; Wang, Y.; Wang, J.; Su, X.; Shen, M.; Fang, L. Enhanced Photoelectrochemical Performance in Reduced Graphene Oxide/BiFeO3 Heterostructures. *Small* **2017**, *13* (16). https://doi.org/10.1002/smll.201603457.

(479) Raizada, P.; Soni, V.; Kumar, A.; Singh, P.; Parwaz Khan, A. A.; Asiri, A. M.; Thakur, V. K.; Nguyen, V. H. *Surface Defect Engineering of Metal Oxides Photocatalyst for Energy Application and Water Treatment*; Elsevier Ltd, 2021; Vol. 7. https://doi.org/10.1016/j.jmat.2020.10.009.

(480) Santos, H. M.; Lodeiro, C.; Capelo-Martínez, J. L. The Power of Ultrasound. *Ultrasound Chem. Anal. Appl.* **2009**, 1–16. https://doi.org/10.1002/9783527623501.CH1.

(481) Azar, L. Cavitation in Ultrasonic Cleaning and Cell Disruption. *Control. Environ.* **2009**, 14–17.

(482) Henglein, A.; Gutiérrez, M. Sonochemistry and Sonoluminescence: Effects of External Pressure. *J. Phys. Chem.* **1993**, *97* (1), 158–162. https://doi.org/10.1021/j100103a027.

(483) Chandiramouli, R.; Nagarajan, V. First-Principles Studies on Band Structure and Mechanical Properties of BiFeO3 Ceramics under High Pressure. *Process. Appl. Ceram.* **2017**, *11* (2), 120–126. https://doi.org/10.2298/PAC1702120C.

(484) Graf, M.; Sepliarsky, M.; Machado, R.; Stachiotti, M. G. Dielectric and Piezoelectric Properties of BiFeO3 from Molecular Dynamics Simulations. *Solid State Commun.* **2015**, *218*, 10–13. https://doi.org/10.1016/J.SSC.2015.06.002.

(485) Jian, G.; Xue, F.; Guo, Y.; Yan, C. Orientation Dependence of Elastic and Piezoelectric Properties in Rhombohedral BiFeO3. *Mater. 2018, Vol. 11, Page 2441* **2018**, *11* (12), 2441. https://doi.org/10.3390/MA11122441.

(486) Linnemann, J.; Kanokkanchana, K.; Tschulik, K. Design Strategies for Electrocatalysts from an Electrochemist's Perspective. *ACS Catal.* **2021**, *11* (9), 5318–5346. https://doi.org/10.1021/acscatal.0c04118.

(487) Chen, P.; Xu, X.; Koenigsmann, C.; Santulli, C.; Wong, S. S.; Musfeldt, J. L.; Bifeo, S. Size-Dependent Infrared Phonon Modes and Ferroelectric Phase Transition in BiFeO3 Nanoparticles. *Scan. Electron Microsc.* **2010**, *1*, 2–4.

(488) Porporati, A. A.; Tsuji, K.; Valant, M.; Axelsson, A. K.; Pezzotti, G. Raman Tensor Elements for Multiferroic BiFeO3 with Rhombohedral R3c Symmetry. *J. Raman Spectrosc.* **2010**, *41* (1), 84–87. https://doi.org/10.1002/jrs.2394.

(489) Hermet, P.; Goffinet, M.; Kreisel, J.; Ghosez, P. Raman and Infrared Spectra of Multiferroic Bismuth Ferrite from First Principles. *Phys. Rev. B - Condens. Matter Mater. Phys.* **2007**, *75* (22), 3–6. https://doi.org/10.1103/PhysRevB.75.220102.

Appendix

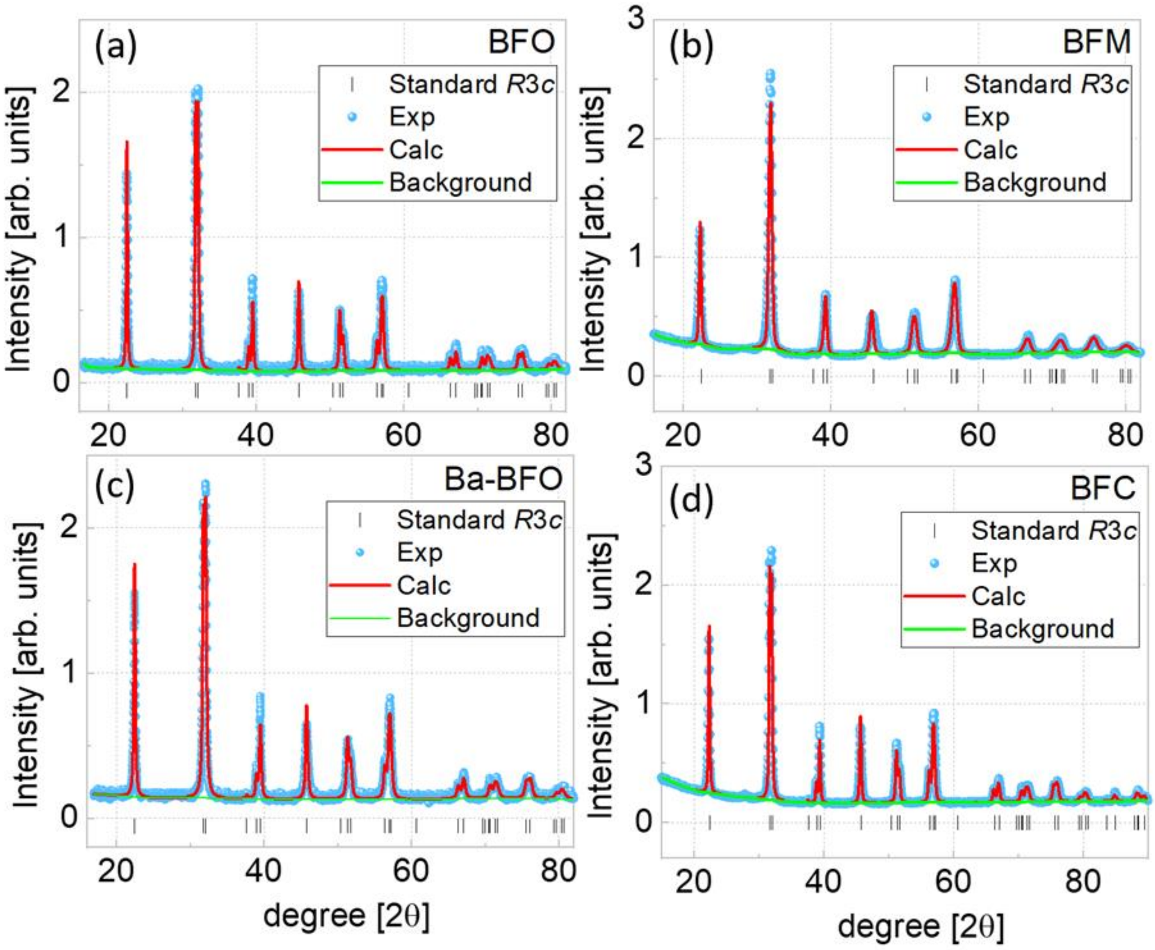

Figure A1: The Rietveld fit of XRD diffractograms of single-doped BFO NPs.

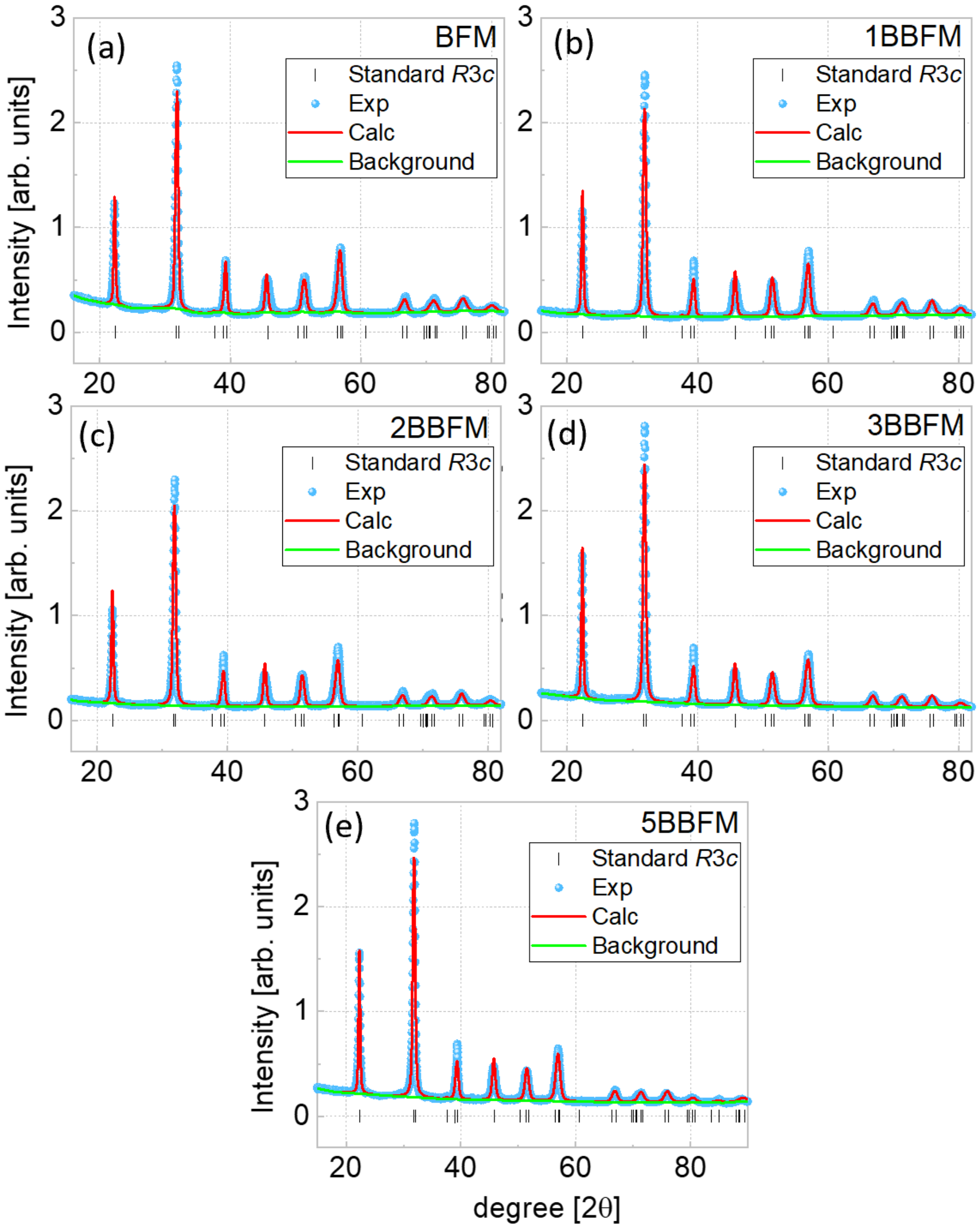

Figure A2: Rietveld fit of Ba doped BFM NPs, with R3c standard pattern shown by black vertical lines.

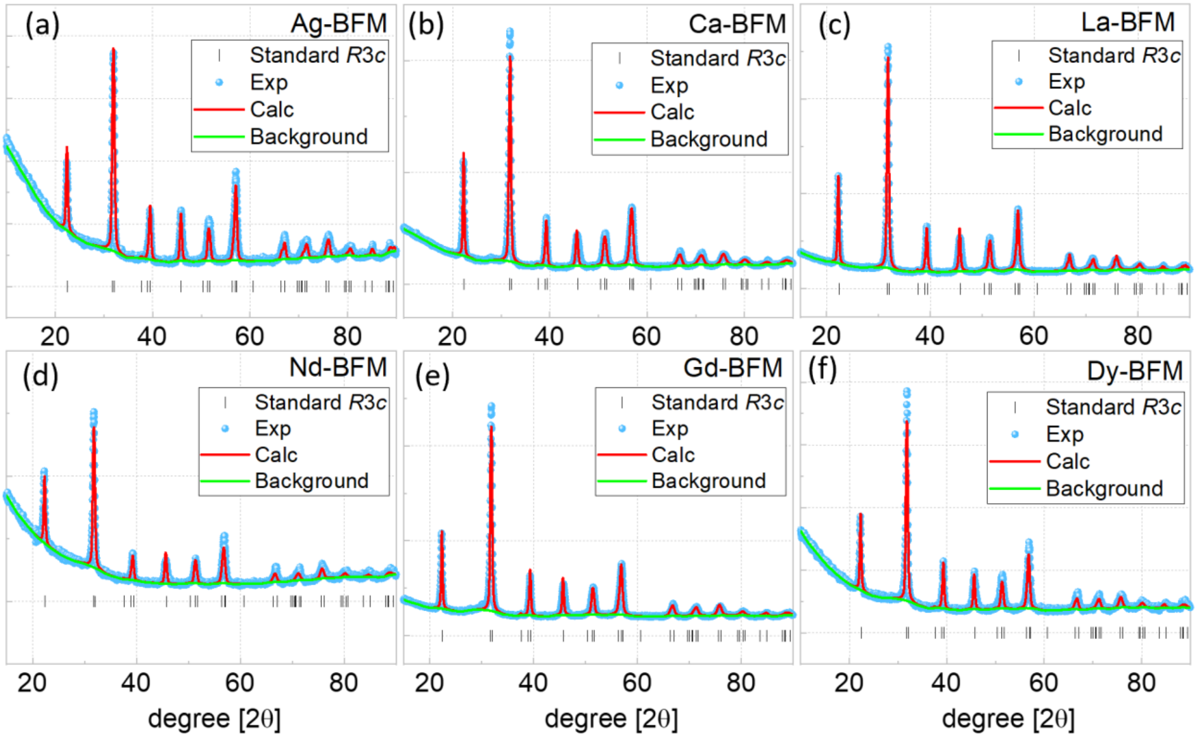

Figure A3: The Rietveld fits of mono-, di-, and tri-valent cation doped BFM NPs.

Table A1 : The goodness of fit parameter calculated by R_{wp} and R_{exp} values after the fit.

Material	**Goodness of fit** **(χ^2)**
BFO	1.45
BFM	1.67
BFC	1.71
Ba-BFO	1.25
Ag-BFM	1.85
Ca-BFM	1.58
La-BFM	1.69
Nd-BFM	1.48
Sm-BFM	1.69
Gd-BFM	1.48

Dy-BFM	1.03
1BBFM	1.84
2BBFM	1.59
3BBFM	1.02
5BBFM	1.24

Table A2: :Raman mode of rhombohedral BFO NPs.

Source of Raman Modes	**Wavenumber [cm^{-1}]**			
	BFO NPs (*)	Chen_2010[487]	Porporati_2010[488]	Hermet_2007[489]
E (TO1)	77	77.3	76	102
E (TO2)	142	133.9	136	152
A_1 (TO1)	175	150.5	-	167
E (TO3)	223	226.2	-	237
E (TO4)	238	-	261	263
A_1 (TO2)	263	-	-	266
E (TO5)	278	279.1	281	274
-	291	-	-	-
A_1 (TO3)	317	318.7	-	318
E (TO6)	349	351.8	320	335
E (TO7)	373	383.5	372	378
-	433	-	-	-
E (TO8)	472	444.1	444	409
-	522	-	-	
E (TO9)	542	536.8	530	509
A_1 (TO4)	615	575.5	-	517

(*) this work.

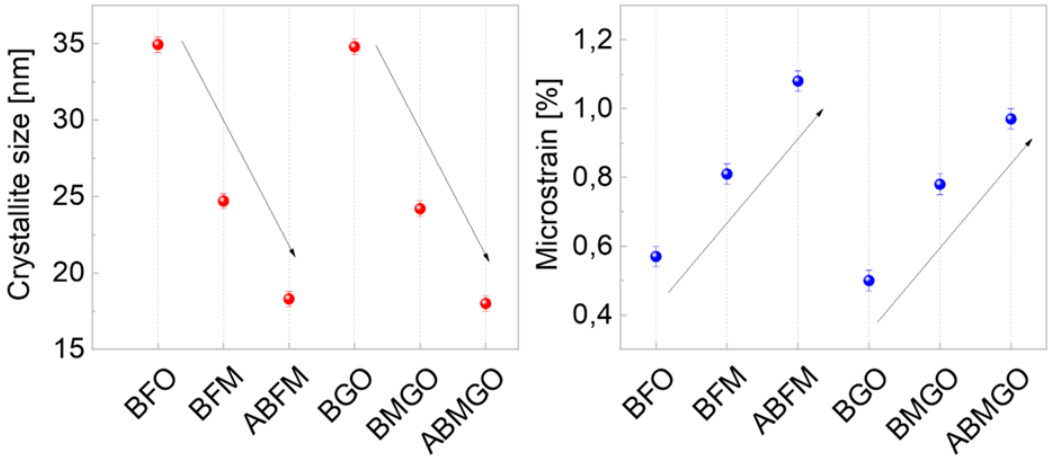

Figure A4: Crystallite size (left) and Microstrain (right) trend of free standing BFO and doped BFO NPs, and NPs supported onto GO layer (nanocomposites).

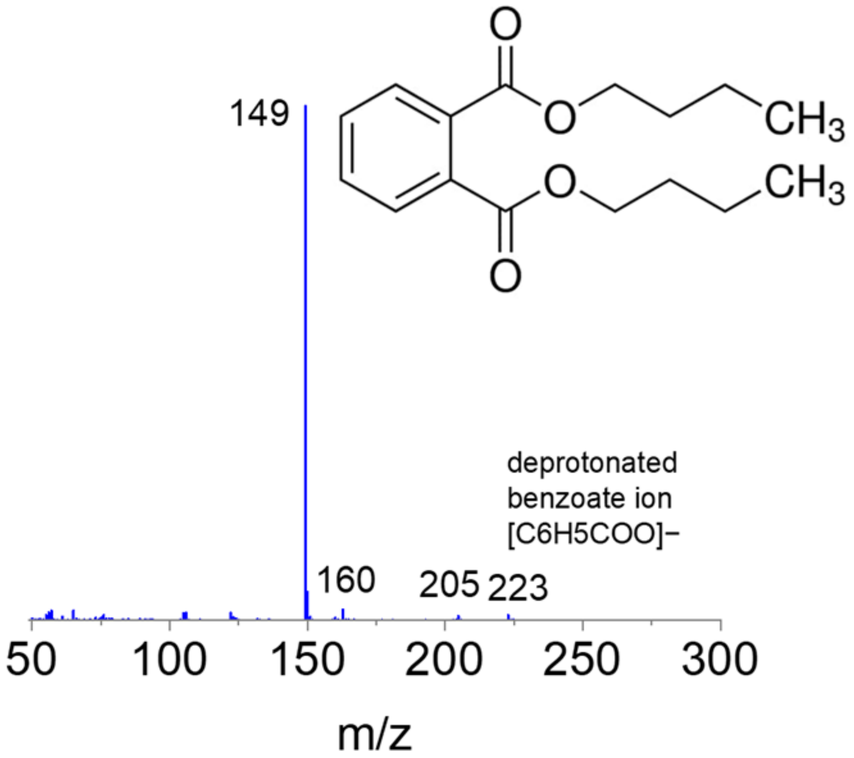

Figure A5: Mass spectrum of DBP. The spectrum matches well with NIST data set.

Table A3: FWHM and peak area values of C 1s XPS deconvoluted peaks of GO, pristine BFO and BFO-GO nanocomposite.

Materials	***C1s Peak 1 (eV)***		***C1s Peak 2 (eV)***		***C1s Peak 3 (eV)***		***C1s Peak 3 (eV)***	
	FWHM (eV)	*Area (eV)*	*FWHM (eV)*	*Area (eV)*	*FWHM (eV)*	*Area (eV)*	*FWHM (eV)*	*Area (eV)*
GO	**288.72**		**287.72**		**286.77**		**284.72**	
	1.51	228	1.2	215.54	1.09	2007	1.32	1833
BFO	**288.77**		**287.77**		**-**		**284.77**	
	1.54	17.68	1.87	31.84	-	-	1.86	206.66
BFO-GO	**289**		**288**		**287**		**285**	
	2.14	203.95	2	46.77	1.58	795.36	1.28	1293.84

Table A4: FWHM and peak area values of O 1s XPS deconvoluted peaks of GO, pristine BFO and BFO-GO nanocomposites.

Materials	***O1s Peak 1 (eV)***		***O1s Peak 2 (eV)***		***O1s Peak 3 (eV)***	
	FWHM (eV)	*Area (eV)*	*FWHM (eV)*	*Area (eV)*	*FWHM (eV)*	*Area (eV)*
GO	**532.5**		**531.8**		-	
	1.79	5482	1.7	107.3	-	-
BFO	**532**		**530**		**529.3**	
	1.96	518.4	1.48	1275	1.2	2945
BFO-GO	**532.3**		**531**		**530**	
	2.24	2548.5	1.77	433	1.24	632.2

"The curriculum vitae is not included in the online version for data protection reasons."

Iti Shubham

Om